ADVANCES IN HEAT TRANSFER

Volume I

Thomas F. Irvine, Jr. &
James P. Hartnett

Advances in
HEAT TRANSFER

Edited by

Thomas F. Irvine, Jr.
State University of New York at Stony Brook
Stony Brook, Long Island
New York

James P. Hartnett
Department of Mechanical Engineering
University of Delaware
Newark, Delaware

Volume 1

1964

ACADEMIC PRESS • New York • London

ACADEMIC PRESS INC.
111 Fifth Avenue, New York 3, New York

United Kingdom Edition published by
ACADEMIC PRESS INC. (LONDON) LTD.
Berkeley Square House, London W.1

LIBRARY OF CONGRESS CATALOG CARD NUMBER: 63-22329

PRINTED IN THE UNITED STATES OF AMERICA

LIST OF CONTRIBUTORS

R. D. CESS, *State University of New York at Stony Brook, Stony Brook, Long Island, New York*
THEODORE R. GOODMAN, *Oceanics, Incorporated, Plainview, New York*
G. LEPPERT, *Stanford University, Stanford, California*
A. V. LUIKOV, *Heat and Mass Transfer Institute, Minsk, U.S.S.R.*
C. C. PITTS, *Stanford University, Stanford, California*
MARY F. ROMIG, *The RAND Corporation, Santa Monica, California*
MARIO SILVESTRI, *Politecnico di Milano, Italy*

PREFACE

In launching a new publication series at this time when publications are appearing at an explosive rate it is of paramount importance to establish the necessity of the new venture. Obviously the strongest argument for initiating a new publication is that it fills a void; that it performs a function not accomplished by the existing literature. This is precisely the reason for the appearance of the new *Advances in Heat Transfer*—it is intended to fill the significant gap between the regularly scheduled journals, both national and international, and the university level textbooks on the subject of heat transfer.

Research in heat transfer during the past decade has grown at an astonishing rate primarily due to the problems associated with the growth of the atomic energy industry, and the aerodynamics and astronautics efforts throughout the world. During this period, development of new instrumentation and refinement of high speed computers have improved our experimental and analytical capacities, and accordingly we have been able to attack new and more complex problems as well as dissect classical problems in a much more definitive fashion. The results of these research efforts are normally published as individual articles in national and international journals. It is understandable that such journal articles, because of space limitations, assume the reader to be well aware of the existing state of knowledge, and so present in an abbreviated and concise manner the new piece of information. It is extremely difficult for a nonspecialist to make engineering use of individual papers appearing in such a journal. It is clear from time to time—as a given area in heat transfer evolves to a definitive state—that a review article or a monograph which starts from widely understood principles and develops the topic in a logical fashion would be of value to the engineering and scientific community. It is the hope that *Advances in Heat Transfer* will fulfill this function.

T. F. IRVINE, JR.
J. P. HARTNETT

December, 1963

The Interaction of Thermal Radiation with Conduction and Convection Heat Transfer[1]

R. D. CESS

State University of New York at Stony Brook, Stony Brook, New York

I. Introduction

The interaction of radiation upon other modes of heat transfer (i.e., conduction and convection) is an area which has recently aroused considerable attention. Basically, such interaction effects may be broken

[1] A portion of the work described herein was supported by the National Science Foundation through Grant Number G-19189.

down into two main categories. The first involves radiation passing through an absorbing-emitting medium such as water vapor or quartz, for which net radiant energy is transferred to or from each element of the medium. Consequently, the conduction or convection process may be thought of as one involving heat sources and sinks. Due to the fact that the analytical expression for the source-sink effect must be formulated in terms of emissive power, problems of this type are of course nonlinear. In addition, radiation to or from an element will take place over paths of finite length resulting in an integral expression for the source-sink term, and consequently the equation expressing conservation of energy will be an integrodifferential equation.

The second category involves radiation interaction through the boundary conditions of the conduction or convection process. One example is transient conduction in a solid with radiation at the surface as treated, for example, in (*1*), (*2*) and (*3*); while in convection processes the boundary condition along the heated or cooled surface may be altered due to radiation exchange.

It is not the purpose of the present article to furnish a comprehensive survey of the literature, particularly since excellent summaries of existing work on absorbing media have recently been compiled by Viskanta (*4*) and Hottel (*5*). Instead, the aim is to illustrate only the most basic effects of radiation upon the other modes of heat transfer, and to this end extremely simple physical models will be employed. Admittedly, such simplifications do not always correspond to reality. Since problems involving radiation interaction generally contain a large number of parameters, emphasis will often be placed upon evaluating only first-order radiation effects. Although such results certainly do not give a complete solution to the problem, they do serve the useful purpose of indicating under what conditions radiation effects need even be considered.

II. Radiation Equations for Absorbing Media

Although energy transfer by radiation has been of interest to physicists for a relatively long period of time, it is only recently that the fundamental equations describing energy transfer in an absorbing medium have been developed for application to engineering systems. Such derivations may be found in the work of Viskanta (*4*), Usiskin and Sparrow (*6*), and Goulard (*7*). A similar development will be given herein making use of the simplifying assumptions as follow[2]:

(1) The medium is gray; i.e., the absorption coefficient is independent of wave length.

[2] For a more complete development taking into account isotropic scattering and an index of refraction other than unity, the reader is referred to (*4*).

(2) The medium is nonscattering, is in "local thermodynamic equilibrium," is a diffuse absorber and emitter, and has an index of refraction of unity.

(3) The bounding surfaces are isothermal, opaque, gray, and diffuse reflectors and emitters.

In addition, the development will be restricted solely to one-dimensional energy transfer.

A. BASIC EQUATIONS FOR ONE-DIMENSIONAL RADIATION

The physical model and coordinate system are illustrated in Fig. 1 and consist of two infinite parallel surfaces separated by an absorbing medium. With the surfaces at different temperatures, radiant energy will pass through the intervening medium, and the problem is to first evaluate the local radiant energy flux $q_r(y)$. To accomplish this, let I be the intensity of radiation passing through a volume element of length ds and unit cross-sectional area as shown in Fig. 1.

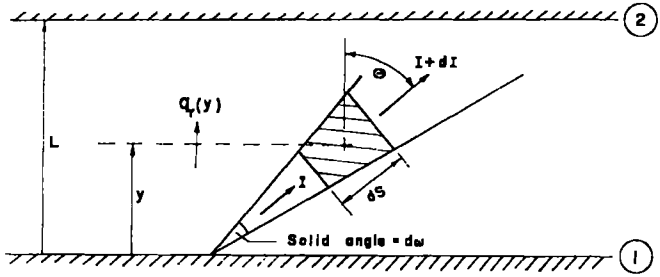

FIG. 1. Physical model and coordinate system.

By the definition of the absorption coefficient a, the amount of intensity I which is absorbed in passing through the length ds is

$$aI\,ds \tag{1}$$

Further, through use of Kirchhoff's law the energy emitted by the volume element is given by (*8*)

$$4ae\,ds$$

where it should be noted that ds also denotes the volume of the element. Since the medium is assumed to be a diffuse emitter, then the energy leaving the element through the solid angle $d\omega$ is correspondingly

$$4ae\,ds\left(\frac{d\omega}{4\pi}\right) = \frac{ae\,ds\,d\omega}{\pi}$$

[3]

and the intensity of emission becomes

$$\frac{ae\,ds}{\pi} \tag{2}$$

It is apparent that the intensity of radiation over the path ds is reduced through absorption in the amount given by Eq. (1) and increased by emission as given by Eq. (2). Thus, the change in intensity dI is simply the difference of these quantities, yielding

$$\frac{dI}{ds} = \frac{ae}{\pi} - aI$$

Upon defining

$$\tau = \int_0^y a\,dy, \quad \mu = \cos\Theta$$

this results in

$$\mu\frac{dI}{d\tau} + I = \frac{e}{\pi} \tag{3}$$

Letting the radiosities of the lower and upper surfaces be R_1 and R_2 respectively, the boundary conditions for Eq. (3) may be expressed as

$$I = \frac{R_1}{\pi}; \qquad \tau = 0, \quad \mu > 0$$

$$I = \frac{R_2}{\pi}; \qquad \tau = \tau_0, \quad \mu < 0$$

where $\tau_0 = \int_0^L a\,dy$. The solution of Eq. (3) is correspondingly

$$I = \frac{R_1}{\pi}\exp\left(-\frac{\tau}{\mu}\right) + \frac{1}{\pi}\int_0^\tau e(t)\exp\left(\frac{t-\tau}{\mu}\right)\frac{dt}{\mu}; \qquad \mu > 0 \tag{4a}$$

$$I = \frac{R_2}{\pi}\exp\left(\frac{\tau_0-\tau}{\mu}\right) - \frac{1}{\pi}\int_\tau^{\tau_0} e(t)\exp\left(\frac{t-\tau}{\mu}\right)\frac{dt}{\mu}; \qquad \mu < 0 \tag{4b}$$

The radiant heat flux may now be obtained through integration of Eqs. (4) with respect to solid angle over the entire enclosing sphere; i.e., with $d\omega = 2\pi\sin\Theta\,d\Theta$, then

$$q_r = 2\pi\int_0^\pi I\cos\Theta\sin\Theta\,d\Theta$$

$$= 2\pi\int_0^1 I\mu\,d\mu - 2\pi\int_0^{-1} I\mu\,d\mu$$

and substituting Eqs. (4a) and (4b) into the first and second integrals respectively

$$q_r = 2R_1E_3(\tau) - 2R_2E_3(\tau_0 - \tau) + 2\int_0^{\tau} e(t)E_2(\tau - t)\,dt - 2\int_{\tau}^{\tau_0} e(t)E_2(t - \tau)\,dt \quad (5)$$

This represents the desired result for the radiant heat flux. The functions $E_n(t)$ are the exponential integrals defined as

$$E_n(t) = \int_0^1 \mu^{n-2}e^{-t/\mu}\,d\mu$$

and are tabulated by Kourganoff (*9*).

It follows that the radiant heat source per unit volume within the medium is $-dq_r/dy$ or $-a\,dq_r/d\tau$, and upon differentiating Eq. (5) there is obtained

$$-\frac{dq_r}{d\tau} = 2R_1E_2(\tau) + 2R_2E_2(\tau_0 - \tau) + 2\int_0^{\tau_0} e(t)E_1(|\tau - t|)\,dt - 4e(\tau) \quad (6)$$

Physically, the first and second terms in this expression represent the energy absorbed by a volume element from the lower and upper surfaces respectively. The third term denotes the energy absorbed from all other elements, while the last term is the energy emitted by the element. One may note that for isothermal conditions ($R_1 = R_2 = e$)

$$-\frac{dq_r}{d\tau} = 2eE_2(\tau) + 2eE_2(\tau_0 - \tau) + 2e\int_0^{\tau_0} E_1(|\tau - t|)\,dt - 4e$$

and since (*10*)

$$\int_0^{\tau_0} E_1(|\tau - t|)\,dt = 2 - E_2(\tau) - E_2(\tau_0 - \tau)$$

then $dq_r/d\tau = 0$. This of course should be expected, since under isothermal conditions there can be no net radiation to or from any element of the medium.

A further consideration in any heat transfer process is the net radiation to or from the bounding surfaces. In the present situation the net radiant transfer is obtained by evaluating Eq. (5) at either surface. For example, the net radiant transfer from surface 1 is

$$q_{r1} = R_1 - 2R_2E_3(\tau_0) - 2\int_0^{\tau_0} e(t)E_2(t)\,dt \quad (7)$$

noting that $E_3(0) = \frac{1}{2}$. Since the first term in this expression, R_1, denotes the radiant energy leaving the surface, then the sum of the second two terms represents the radiation incident upon surface 1. The quantity $2R_2E_3(\tau_0)$ is the energy coming from surface 2, with $2E_3(\tau_0)$ being the

attenuation factor due to the intervening medium. The energy radiated by the medium which is incident upon surface 1 is $2\int_0^{\tau_0} e(t)E_2(t)\,dt$.

So far nothing has been said concerning the radiosities R_1 and R_2, and these will not be known *a priori*. Consider first the lower wall. Since the radiosity R_1 is the sum of the emitted and reflected energies from surface 1, and recalling that the surfaces have been assumed to be gray and opaque so that the reflectivity is $(1 - \epsilon_1)$, then

$$R_1 = \epsilon_1 e_1 + (1 - \epsilon_1)H_1$$

where H_1 is the radiation incident upon surface 1, and from the discussion following Eq. (7)

$$H_1 = 2R_2E_3(\tau_0) + 2\int_0^{\tau_0} e(t)E_2(t)\,dt$$

Consequently

$$R_1 = \epsilon_1 e_1 + 2(1 - \epsilon_1)\left[R_2E_3(\tau_0) + \int_0^{\tau_0} e(t)E_2(t)\,dt\right] \tag{8}$$

In a similar manner, consideration of surface 2 yields

$$R_2 = \epsilon_2 e_2 + 2(1 - \epsilon_2)\left[R_1E_3(\tau_0) + \int_0^{\tau_0} e(t)E_2(\tau_0 - t)\,dt\right] \tag{9}$$

Equations (8) and (9) thus constitute two simultaneous equations for R_1 and R_2. For black surfaces the simple results $R_1 = e_1$ and $R_2 = e_2$ are obtained.

It may be noted from the preceding equations that dependence upon the absorption properties of the medium occurs solely through the dimensionless distance τ. For a constant absorption coefficient, the dimensionless thickness of the absorbing medium is $\tau = aL$, and this is commonly referred to as the optical thickness. Further, as discussed in (7) the quantity $1/a$ may be interpreted as the penetration length for radiation. In other words, if the absorption coefficient is small, then a beam of radiant energy will travel a large distance through the medium before significant attenuation occurs; i.e., the penetration length will be large. On the other hand, if a is large then the penetration length will be short.

From this it may be seen that the optical thickness τ_0 is the ratio of characteristic length L to penetration length and that $1/a$ plays a role analogous to a mean free path while $1/\tau_0$ is analogous to the Knudsen number. For $\tau_0 \ll 1$ the radiation process is referred to as optically thin, whereas it is optically thick for $\tau_0 \gg 1$.

The preceding discussion would indicate that possible simplification of the governing radiation equations might result for the limiting cases of an optically thin or optically thick medium. Fortunately, this is so, and the optically thick approximation will be considered first.

B. OPTICALLY THICK APPROXIMATION

Providing the radiation process is optically thick, the penetration length will be small compared to the characteristic length L of the medium, and the radiation transfer will approach a diffusion process. This occurs since the radiant energy emitted from an element will undergo such rapid attenuation that the transfer process will be dependent solely upon local conditions; i.e., the gradient of emissive power. There is of course a direct analogy to heat conduction in a gas as treated by kinetic theory, for which energy is considered to be transported by gas molecules in traveling a mean free path which is assumed to be an incremental distance. The radiation transfer process may in turn be visualized as one in which energy is transported by photons traveling a "radiation mean free path" or penetration length, and the penetration length is taken to be the incremental distance. This leads to the so-called Rosseland approximation for the radiant heat flux (*11*)

$$q_r = -\frac{4}{3a}\frac{de}{dy} = -\frac{4}{3}\frac{de}{d\tau} \tag{10}$$

The coefficient $\frac{4}{3}$ has been the subject of some controversy (*5*), and perhaps the most straightforward derivation of Eq. (10) is simply a proof that it follows from the asymptotic form of the governing radiation equations applicable to an optically thick medium. For this purpose, consider a slab of thickness L bounded by black surfaces and within which only radiation transfer takes place. Hence, since there is no mechanism other than radiation by which energy can be transferred to or from an element, it follows that $dq_r/d\tau = 0$. Letting

$$\varphi(\tau) = \frac{e(\tau) - e_1}{e_2 - e_1}$$

Eq. (6) may thus be expressed with the aid of (*10*) as

$$\int_0^{\tau} \varphi(\tau - t)E_1(t)\,dt + \int_0^{\tau_0-\tau} \varphi(\tau + t)E_1(t)\,dt + E_2(\tau_0 - \tau) = 2\varphi(\tau) \tag{11}$$

In that Eq. (10) predicts the emissive power within the slab to vary linearly with distance, a solution of Eq. (11) will be assumed of the form $\varphi = \tau/\tau_0$. Upon substituting this into Eq. (11) and performing the indicated integrations, the left side of Eq. (11) becomes

$$\frac{1}{2\tau_0}[(\tau_0 - \tau)E_3(\tau_0 - \tau) - e^{-(\tau_0-\tau)} - \tau E_3(\tau) + e^{-\tau}] + 2\frac{\tau}{\tau_0}$$

In order for $\varphi = \tau/\tau_0$ to be a solution of Eq. (11), the above quantity in brackets must vanish. This is obviously not the case. However, the bracketed term will vanish provided τ and $\tau_0 - \tau$ are large, since for $t \gg 1$ (*10*)

$$tE_n(t) \sim e^{-t}$$

So, the emissive power will vary linearly with distance providing the medium is optically thick. It should be realized, however, that no matter how optically thick the medium might be, the assumption that τ and $\tau_0 - \tau$ are everywhere large will always fail at the boundaries, and this is a shortcoming of the Rosseland approximation.

To evaluate the heat flux across the slab, Eq. (5) may be expressed as

$$\frac{q_r}{e_1 - e_2} = 2E_3(\tau_0 - \tau) + 2\int_0^{\tau_0-\tau} \varphi(\tau + t)E_2(t)\,dt - 2\int_0^{\tau_0} \varphi(\tau - t)E_2(t)\,dt$$

and substituting into this equation $\varphi = \tau/\tau_0$ together with the asymptotic expression $tE_n(t) \sim e^{-t}$, there is obtained

$$q_r = -\frac{4}{3}\frac{e_2 - e_1}{\tau_0}$$

Consequently, for an infinitesimal slab of thickness $d\tau$

$$q_r = -\frac{4}{3}\frac{de}{d\tau}$$

which is precisely Eq. (10). It has thus been shown that the Rosseland approximation is indeed an asymptotic form of the governing radiation equations.

C. Optically Thin Approximation

The optically thin approximation applies for $\tau_0 \ll 1$, and the radiation equations derived in Section II,A may be simplified through use of the relations (*9*)

$$E_2(t) = 1 + 0(t), \quad E_3(t) = \tfrac{1}{2} - t + 0(t^2) \tag{12}$$

which are the first terms of the power series expansions of $E_2(t)$ and $E_3(t)$. For example, considering black surfaces ($R_1 = e_1$ and $R_2 = e_2$) Eq. (5) reduces to

$$q_r = e_1(1 - 2\tau) - e_2(1 - 2\tau_0 + 2\tau) + 2\int_0^{\tau} e(t)\,dt - 2\int_{\tau}^{\tau_0} e(t)\,dt \tag{13}$$

and it follows that for black surfaces the source-sink expression becomes

$$-\frac{dq_r}{d\tau} = 2e_1 + 2e_2 - 4e \tag{14}$$

The physical interpretation of Eq. (14) is readily apparent. The quantity $4e$ represents the energy emitted per unit volume from an element, since $4ae$ is the actual emission per unit volume (*8*). In turn, $2e_1$ and $2e_2$ denote the energy absorbed by the element from the lower and upper surfaces respectively. Thus, under optically thin conditions every element of the medium exchanges radiation directly with the bounding surfaces and no intermediate attenuation of the radiant energy takes place. An optically thin medium is therefore commonly referred to as a medium with negligible self-absorption.

D. ABSORPTION COEFFICIENTS

Although a considerable amount of data has been obtained concerning the emissivity of gases, very little information is available regarding the mean absorption coefficient a. As illustrated by Goulard (*7*), the conversion of emissivity data to absorption coefficients may be accomplished in the following manner.

From the discussion following Eq. (7), the rate of energy per unit surface area emitted by the gas slab and incident upon the lower surface is

$$q_{rg} = 2\int_0^{\tau_0} e(t)E_2(t)\,dt \tag{15}$$

Now, by the usual definition of gas emissivity, ϵ, the energy emitted by an *isothermal* slab of gas may be expressed by

$$q_{rg} = \sigma\epsilon T^4 \tag{16}$$

with T the gas temperature. Thus, letting $e = \sigma T^4$ be a constant in Eq. (15), and equating Eqs. (15) and (16)

$$\epsilon = 2\int_0^{\tau_0} E_2(t)\,dt$$

or

$$\epsilon = 1 - 2E_3(\tau_0) \tag{17}$$

However, if this expression were employed to evaluate the absorption coefficient from emissivity data, it would be found that a is dependent upon the gas thickness L, whereas actually the absorption coefficient depends solely upon the state of the gas.[3]

[3] When the assumption of a gray gas is not applicable, a will also depend upon the incident radiation.

At this point is should be reemphasized that the concept of gas emissivity refers to an isothermal gas, and a radiating gas can approach isothermal conditions only in the limit as $\tau_0 \to 0$. Thus, from Eqs. (12) and (17) with $\tau_0 = aL$, the relationship between gas emissivity and absorption coefficient is found to be

$$a = \tfrac{1}{2}\left(\frac{\epsilon}{L}\right)_{L\to 0} \tag{18}$$

The absorption coefficient may therefore be evaluated from emissivity data through extrapolation of the quantity ϵ/L.

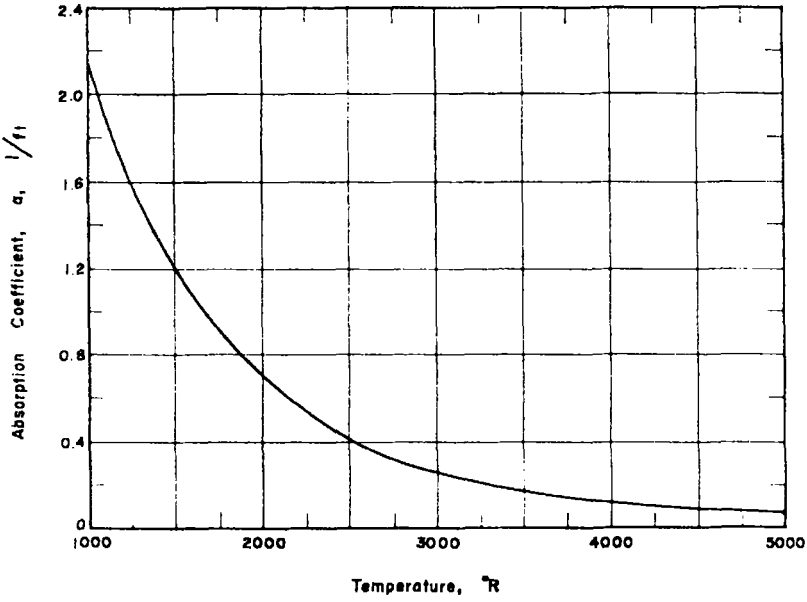

FIG. 2. Absorption coefficient of water vapor at one atmosphere pressure.

This procedure has presently been applied both to water vapor and carbon dioxide at a pressure of 1 atmosphere, and the results are shown in Figs. 2 and 3. The emissivity data were taken from Figs. 4–13 and 4–15 of Hottel's chapter in McAdams (*12*), and Fig. 4–16 of (*12*) was utilized to correct the pressure of the water vapor from 0 to 1 atmosphere. Figures 4–14 and 4–16 of (*12*) may be employed in order to apply the results of Figs. 2 and 3 to pressures other than 1 atmosphere.

Values of ϵ/L for high-temperature air have been tabulated by Kivel and Bailey (*13*), and since their results were obtained for optically thin conditions, Eq. (18) may be applied directly with no extrapolation necessary. These results are given in Fig. 4 where ρ_0 denotes standard

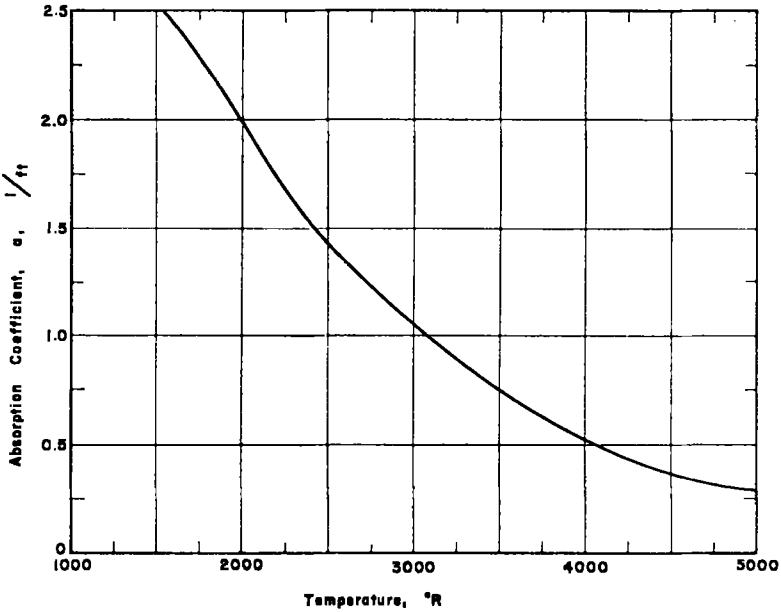

FIG. 3. Absorption coefficient of carbon dioxide at one atmosphere pressure.

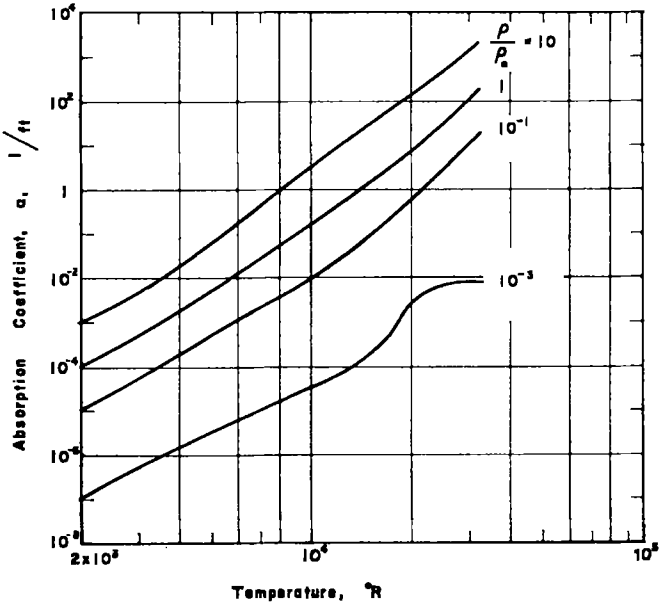

FIG. 4. Absorption coefficient of air.

density. Further information on the emissivity of high-temperature air has recently been summarized by Thomas (*14*).

III. Pure Radiation in an Absorbing Medium

Before considering the application of the foregoing radiation equations to problems involving conduction and convection, the simpler situation of pure radiation transfer in an absorbing medium will be investigated. For convenience, radiation between parallel black plates which are infinite in extent will be assumed. It is of interest to first note that if the plates are separated by a nonabsorbing rather than absorbing medium, the radiant heat transfer from one plate to the other is simply

$$q_r = e_1 - e_2$$

If the space between the plates is instead occupied by an absorbing gas, the effect upon the net radiant heat transfer q_r will be similar to that of placing a radiation shield between the plates. One would thus expect the heat transfer to be decreased as the absorption ability (or optical thickness) of the intervening medium is increased.

Since radiation is assumed to be the only mode of heat transport or addition within the medium, then from conservation of energy $dq_r/d\tau = 0$. Again letting φ be the dimensionless emissive power of the gas defined as

$$\varphi = \frac{e - e_1}{e_2 - e_1}$$

Eq. (6) gives

$$\int_0^\tau \varphi(t)E_1(\tau - t)\,dt + \int_\tau^{\tau_0} \varphi(t)E_1(t - \tau)\,dt + E_2(\tau_0 - \tau) = 2\varphi(\tau) \quad (19)$$

It should be noted that Eq. (19) is linear in φ due to the neglect of conduction or convection. The integral equation is, however, singular since $E_1(t)$ possesses a logarithmic singularity at the origin. Numerical results for $\varphi(\tau)$ have been obtained by Usiskin and Sparrow (*6*) through numerical integration of Eq. (19) using an iterative procedure, and by Viskanta and Grosh (*15*) through application of the method of undetermined parameters. The results of (*15*) are illustrated in Fig. 5, and the limiting solutions for $\tau = 0$ and $\tau = \infty$ readily follow from the optically thin and optically thick approximations. From Eq. (14) for an optically thin medium with $dq_r/d\tau = 0$

$$e = \frac{e_1 + e_2}{2} \quad (20)$$

such that $\varphi = \frac{1}{2}$. Conversely, with q_r constant Eq. (10) illustrates that [12]

the gas emissive power will vary linearly with distance between plates for optically thick conditions such that $\varphi = \tau/\tau_0$.

To evaluate the net radiant heat transfer from one wall to the other, Eq. (7)[4] in terms of $\varphi(\tau)$ becomes

$$\frac{q_r}{e_1 - e_2} = 2E_3(\tau_0) + 2\int_0^{\tau_0} \varphi(t)E_2(t)\,dt \tag{21}$$

Thus, with φ known the radiant energy transfer may be evaluated through integration of the above equation. This has been accomplished in (*6*) and (*15*), and the results of (*15*) are illustrated in Fig. 6. As expected, the heat transfer decreases with increasing optical thickness.

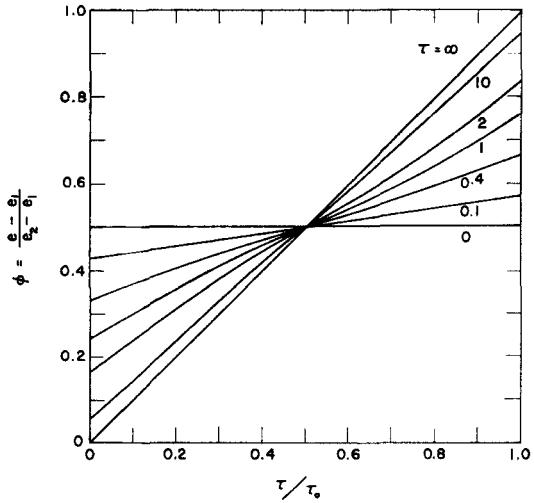

FIG. 5. Variation of dimensionless emissive power between parallel black plates from (*15*).

Following Hottel (*5*), optically thin and optically thick results are also shown in Fig. 6. The optically thin expression for q_r is obtained by substituting Eq. (20) into Eq. (21), giving

$$\frac{q_r}{e_1 - e_2} = 1 - \tau_0$$

while the optically thick result

$$\frac{q_r}{e_1 - e_2} = \frac{4}{3\tau_0}$$

follows directly from Eq. (10). Figure 6 thus conveniently serves to

[4] The subscript 1 may be droped since q_r is constant.

illustrate the applicability of the optically thin and optically thick approximations.

It should be noted from Fig. 5 that a discontinuity in emissive power, and hence temperature, exists at the surfaces. This is due to the neglect of conduction within the medium, conduction being the only process by which continuity of temperature can be insured. This temperature jump may be thought of as analogous to the discontinuity in velocity between fluid and bounding surface which arises in nonviscous flow analyses, the velocity jump resulting from the neglect of viscosity.

It is worth mentioning that nowhere in the preceding analysis has the absorption coefficient been assumed to be independent of temperature.

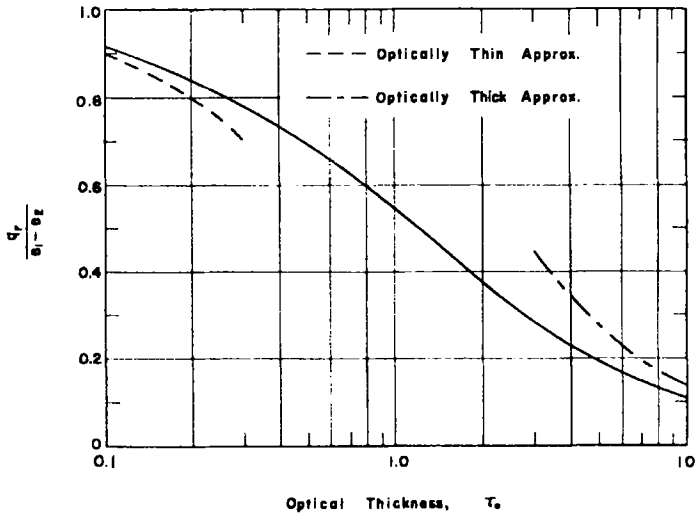

FIG. 6. Heat transfer between parallel black plates from (*15*).

Actually, the results as presented are valid for any variation of the absorption coefficient with temperature, and a given variation $a(T)$ need be utilized only in the evaluation of the optical thickness τ_0. If the absorption coefficient is independent of temperature, then $\tau_0 = aL$, while if a is temperature dependent the relationship between L and τ_0 is

$$L = \int_0^{\tau_0} \frac{d\tau}{a(\tau)} \tag{22}$$

The conversion of $a(T)$ to $a(\tau)$ is accomplished through use of the known emissive-power profiles, which yield $T(\tau)$.

As a simple example, consider the absorbing medium to be water vapor and the distance between plates to be sufficiently large such that

the optically thick approximation may be employed. Thus $\varphi = \tau/\tau_0$, and from the definition of φ

$$T = \left[T_1^4 - (T_1^4 - T_2^4) \frac{\tau}{\tau_0} \right]^{1/4}$$

Over moderate temperature ranges, the absorption coefficient of water vapor can be approximated by

$$a = CT^{-n}$$

So, combining this with the preceding equation

$$a = C \left[T_1^4 - (T_1^4 - T_2^4) \frac{\tau}{\tau_0} \right]^{-n/4}$$

and substituting into Eq. (22)

$$\tau_0 = \frac{(n+4)CL}{4} \frac{(T_1^4 - T_2^4)}{(T_1^{n+4} - T_2^{n+4})}$$

Letting $T_1 = 2000°\text{R}$ and $T_2 = 1000°\text{R}$, it is found from Fig. 2 that $C = 135{,}000$ and $n = 1.6$. Further, taking $L = 10$ ft, the above expression yields $\tau_0 = 9.5$. Assuming, on the other hand, a constant value of the absorption coefficient corresponding to the mean temperature of 1500°R, then $\tau_0 = 12.0$. The assumption of a constant absorption coefficient evaluated at the mean temperature between plates thus leads to an error of 26% for the optical thickness. Since under optically thick conditions q_r varies as $1/\tau_0$, the heat transfer will be underestimated by 21% through the assumption of a constant absorption coefficient.

Although the results of Figs. 5 and 6 are directly applicable only to black surfaces, Viskanta and Grosh (*15*) have discussed their extension to gray surfaces through the following procedure. It is easily shown (*15*) that Figs. 5 and 6 apply to gray surfaces through replacing e_1 and e_2 by R_1 and R_2 respectively. Further, upon substitution of the emissive-power profiles given in Fig. 5 into Eqs. (8) and (9), subsequent integration yields two simultaneous algebraic equations for R_1 and R_2. This determination of the radiosities then gives all the necessary information for radiation between gray surfaces.

Viskanta and Grosh have, in fact, recently applied this procedure to the parallel plate system for the case of equal plate emissivities ($\epsilon_1 = \epsilon_2$). Their results, recast in terms of the present nomenclature, are listed in Table I, and, as would be expected, illustrate a reduction in heat transfer with decreasing plate emissivity.

An alternate approach to radiation heat transfer between gray plates has recently been employed by Howell and Perlmutter (*17*). Instead of

TABLE I
HEAT TRANSFER RESULTS FOR RADIATION BETWEEN PARALLEL GRAY PLATES (*16*)

τ_0	ϵ	$q_r/(e_1 - e_2)$
0.1	1.0	0.916
	0.9	0.761
	0.5	0.330
	0.1	0.052
1.0	1.0	0.553
	0.9	0.493
	0.5	0.265
	0.1	0.050
10.0	1.0	0.109
	0.9	0.107
	0.5	0.090
	0.1	0.038

formulating the problem in terms of an integral equation, the Monte Carlo method was applied. Heat transfer results were presented for the two plates having equal emissivities, and these results are shown in Fig. 7. The curve for $\epsilon = 1.0$ is in excellent agreement with (*15*), while the

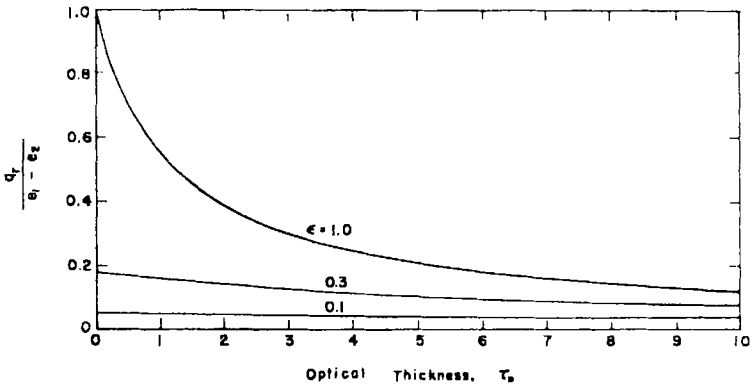

FIG. 7. Heat transfer between parallel gray plates from (*17*).

results for $\epsilon = 0.1$ are in corresponding agreement with Table I. For $\tau_0 = 0$, the values for $\epsilon = 0.1$ and $\epsilon = 0.3$ coincide with the well-known expression (*18*)

$$\frac{q_r}{e_1 - e_2} = \frac{\epsilon}{2 - \epsilon}$$

for parallel plates with equal emissivities and separated by a nonabsorbing medium.

IV. Combined Conduction and Radiation in an Absorbing Medium

The problem previously considered of heat transfer between infinite parallel plates separated by an absorbing medium will now be extended to include conduction as well as radiation within the medium. It will be assumed that the absorption coefficient and thermal conductivity of the medium are independent of temperature, and the plates will initially be considered as black surfaces. The first complete formulation of this problem was recently presented by Viskanta and Grosh (*19*).

The temperature distribution within the medium is described by the energy equation as applied to simultaneous conduction and radiation, and for the present one-dimensional problem with constant thermal conductivity this is

$$k\frac{d^2T}{dy^2} - \frac{dq_r}{dy} = 0 \tag{23}$$

Correspondingly, employing Eq. (6) with $R_1 = e_1$ and $R_2 = e_2$ since the surfaces are assumed black, the energy equation becomes an integro-differential equation of the form

$$ka\frac{d^2T}{d\tau^2} = 4e(\tau) - 2\int_0^{\tau_0} e(t)E_1(|\tau - t|)\,dt - 2e_1E_2(\tau) - 2e_2E_2(\tau_0 - \tau) \tag{24}$$

Unlike the previous problem of pure radiation, which resulted in solely an integral equation, the above equation necessitates two boundary conditions. Since the inclusion of conduction requires continuity of temperature, these conditions are

$$T = T_1; \quad y = 0$$

$$T = T_2; \quad y = L$$

It may further be noted that Eq. (24) is nonlinear as a result of the conduction term appearing on the left side.

An additional quantity of importance is the net heat transfer from one plate to the other. Because the system is in steady state, this may be determined by evaluating the heat transfer from or to either surface. Choosing the lower surface, the radiative contribution to the total heat transfer is given by Eq. (7) with the R's replaced by e's, while the conduc-

tive contribution is

$$-k\left(\frac{dT}{dy}\right)_{y=0}$$

The total heat transfer between plates may thus be expressed by

$$q = -\left(\frac{dT}{dy}\right)_{y=0} + e_1 - 2e_2E_3(\tau_0) - 2\int_0^{\tau_0} e(\tau)E_2(\tau)\,d\tau \qquad (25)$$

Dimensionless quantities similar to those employed by Viskanta and Grosh (*19*) will now be defined as

$$N = \frac{ka}{4\sigma T_1^3}, \quad \Theta = \frac{T}{T_1}, \quad \Theta_2 = \frac{T_2}{T_1}$$

Equation (24) correspondingly becomes

$$N\frac{d^2\Theta}{d\tau^2} = \Theta^4(\tau) - \tfrac{1}{2}E_2(\tau) - \tfrac{1}{2}\Theta_2^4E_2(\tau_0 - \tau) - \tfrac{1}{2}\int_0^{\tau_0}\Theta^4(t)E_1(|\tau - t|)\,dt \qquad (26)$$

with the boundary conditions

$$\Theta(0) = 1, \quad \Theta(\tau_0) = \Theta_2$$

In addition, the equation for heat transfer between plates, Eq. (25), may be expressed in dimensionless form as

$$\frac{q}{\sigma T_1^4} = -4N\left(\frac{d\Theta}{d\tau}\right)_{\tau=0} + 1 - 2\Theta_2^4E_3(\tau_0) - 2\int_0^{\tau_0}\Theta^4(\tau)E_2(\tau)\,d\tau \qquad (27)$$

Equations (26) and (27) illustrate that both the dimensionless temperature distribution, $\Theta(\tau)$, and dimensionless heat transfer, $q/\sigma T_1^4$, depend upon three parameters; τ_0, Θ_2 and N. The appearance of Θ_2, which was not present in the preceding pure radiation solution, is a result of the nonlinearity of the present problem, while N may be regarded as a measure of the relative importance of conduction versus radiation. In the limit as N goes to zero the present problem reduces to that of the preceding section, while for large N the heat transfer process approaches that of pure conduction.

Equation (26) has been solved numerically using an iteration procedure by Viskanta and Grosh (*19*) for several combinations of the governing parameters, and the heat transfer was subsequently evaluated using an equation similar to Eq. (27). Their results, actually taken from (*16*), are listed in Table II. Additional heat transfer results have recently been presented by Einstein (*20*) for Θ_2 of 0.2 and 0.8 with N and τ_0 ranging up

to 1.56 and 3.0 respectively. The geometry employed by Einstein actually differed slightly from that considered here, in that the width of the plates was taken to be finite and equal to ten times the spacing between plates.

It is again of interest to investigate the limiting cases of optically thick and optically thin radiation. Consider first the optically thick situation. Temperature profiles for combined conduction and optically thick radiation have been discussed by Viskanta and Grosh (*21*), while the local

TABLE II
HEAT TRANSFER RESULTS FOR COMBINED CONDUCTION AND RADIATION BETWEEN BLACK PLATES (*16*)

τ_0	Θ_2	N	$q/\sigma T_1^4$	q/q(approx.)
0.1	0.5	0	0.859	1.00
		0.01	1.074	1.01
		0.1	2.88	1.01
		1.0	20.88	1.00
		10.0	200.88	1.00
1.0	0.5	0	0.518	1.00
		0.01	0.596	1.11
		0.1	0.798	1.11
		1.0	2.600	1.03
		10.0	20.60	1.00
1.0	0.1	0	0.556	1.00
		0.01	0.658	1.11
		0.1	0.991	1.08
		1.0	4.218	1.01
		10.0	36.60	1.00
10.0	0.5	0	0.102	1.00
		0.01	0.114	1.10
		0.1	0.131	1.07
		1.0	0.315	1.04
		10.0	2.114	1.01

heat flux is obtained by combining Eq. (10) with the conduction law, yielding

$$q = -\left(k + \frac{16\sigma T^3}{3a}\right)\frac{dT}{dy}$$

Following Einstein (*20*), this may be integrated, recalling that q is a constant, to give

$$q = \frac{k}{L}(T_1 - T_2) + \frac{4\sigma}{3aL}(T_1^4 - T_2^4) \qquad [19]$$

or, in dimensionless form

$$\frac{q\tau_0}{\sigma T_1^4} = 4N(1 - \theta_2) + \tfrac{4}{3}(1 - \theta_2^4) \tag{28}$$

One may note that the optical thickness τ_0 has been eliminated as a separate parameter through combination with the dimensionless heat transfer term.

A comparison of Eq. (28) with the results of Table II for $\theta_2 = 0.5$ and $\tau_0 = 10$ is shown in Fig. 8. The maximum discrepancy between the two results is 23% for $N = 0$; i.e., for pure radiation. As N increases the difference in turn decreases, with the error being only ½% for $N = 10$. The reason for this is that the optically thick approximation is concerned solely with the radiation process, and any resulting error should diminish with an increasing influence of conduction (increasing N).

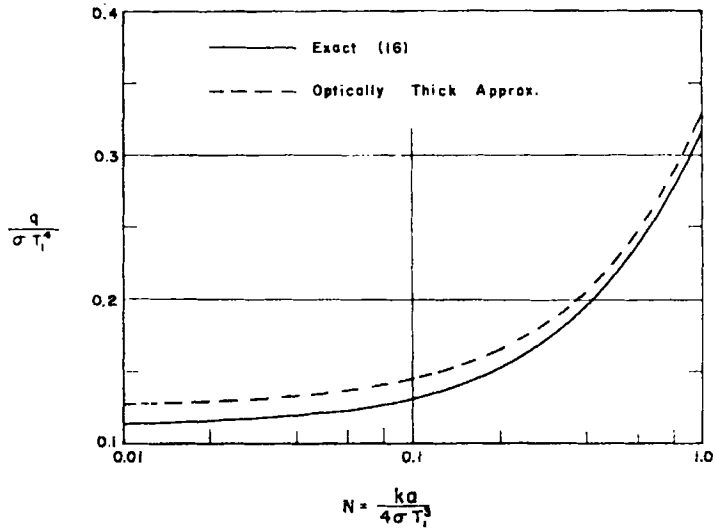

FIG. 8. Heat transfer for combined conduction and radiation between parallel black plates, $\theta_2 = 0.5$ and $\tau_0 = 10$.

Turning next to the optically thin approximation, combination of Eqs. (14) and (23) with subsequent reduction to dimensionless form yields

$$N\frac{d^2\theta}{d\tau^2} = \theta^4 - \tfrac{1}{2}\theta_2^4 - \tfrac{1}{2} \tag{29}$$

as the equation describing the temperature profile within the medium. The boundary conditions are again

$$\theta(0) = 1, \quad \theta(\tau_0) = \theta_2$$

while combination of Eq. (13) with the conduction law gives the heat transfer between plates as

$$\frac{q}{\sigma T_1^4} = -4N\left(\frac{d\Theta}{d\tau}\right)_{\tau=0} + 1 - \Theta_2^4(1 - 2\tau_0) - 2\int_0^{\tau_0} \Theta^4(\tau)\, d\tau \qquad (30)$$

Inspection of Eq. (29) reveals that the temperature profile, $\Theta(\tau)$, for optically thin conditions is no longer dependent upon three parameters, but instead τ and N combine to yield dependence upon the two parameters $\tau_0/\sqrt{N}$ and Θ_2. From Eq. (30), however, the dimensionless heat transfer is still a function of three parameters.

To this writer's knowledge, no solutions to Eqs. (29) and (30) are presently available for comparison with the results of Table II. Numerical results for an optically thin problem have been obtained by Goulard (*7*), but these are based upon thermal conductivity and absorption coefficient varying with temperature.

In addition to studying combined conduction and radiation between black plates, Viskanta and Grosh (*16*) have extended their analysis to include gray plates. It was assumed that the plates had equal emissivities, and heat transfer results were presented for $\epsilon = 0.1$, 0.5, and 0.9. These results for the case of $\epsilon = 0.1$ are illustrated in Table III.

At this point it is certainly evident that problems involving combined conduction and radiation in an absorbing media contain a multitude of parameters, the number being four for gray plates with equal emissivities. It would consequently be advantageous to have some sort of simplified procedure available for estimating heat transfer, and one such method has been proposed by Einstein (*20*). This procedure simply assumes that the two modes of heat transfer can be superimposed with no regard for their mutual interaction. Thus, the radiation transfer q_r is evaluated as though there were no conduction taking place; in other words, from Fig. 6 for black surfaces or Table I for gray surfaces. The heat transfer due to conduction is in turn calculated as if there were no radiation transfer occurring, so that

$$q_c = \frac{k}{L}(T_1 - T_2)$$

or, in dimensionless form

$$\frac{q_c}{\sigma T_1^4} = \frac{4N}{\tau_0}(1 - \Theta_2)$$

The total heat transfer is then taken as the sum of the two separate heat rates, $q = q_r + q_c$.

Einstein found that this approximate procedure, when compared to his complete calculations for $\Theta_2 = 0.2$ and 0.8 with black surfaces, under-

predicted heat transfer by no more than 9%. A further comparison has presently been made with the $\epsilon = 1.0$ results of Viskanta and Grosh and is illustrated in Table II by the column q/q(approx.), where q(approx.) denotes heat transfer evaluated by the superposition approach. It may be noted that the maximum discrepancy is roughly 11%, and this comparison lends further support to Einstein's approach.

TABLE III
HEAT TRANSFER RESULTS FOR COMBINED CONDUCTION AND RADIATION BETWEEN GRAY PLATES, $\epsilon = 0.1$ (*16*)

τ_0	Θ_2	N	$q/\sigma T_1^4$	q/q(approx.)
0.1	0.5	0	0.049	1.00
		0.01	0.267	1.07
		0.1	2.078	1.01
		1.0	20.08	1.00
		10.0	200.08	1.00
1.0	0.5	0	0.047	1.00
		0.01	0.156	2.33
		0.1	0.393	1.59
		1.0	2.245	1.10
		10.0	20.25	1.01
1.0	0.1	0	0.051	1.00
		0.01	0.22	2.55
		0.1	0.591	1.44
		1.0	3.752	1.03
		10.0	36.22	1.00
10.0	0.5	0	0.036	1.00
		0.01	0.090	2.37
		0.1	0.115	2.05
		1.0	0.297	1.26
		10.0	2.107	1.03

The largest errors in the superposition method arise for intermediate values of N. This should be expected, since in the limit of either very small or very large N the heat transfer process approaches that of pure radiation or pure conduction respectively, and the superposition procedure becomes exact. Table II further illustrates that, with respect to optical thickness, the largest differences between q and q(approx.) exist for intermediate values of τ_0. For $\tau_0 = 0$ the heat transfer process is again that of pure conduction, while for large τ_0 Einstein has pointed out that the superposition approach is exact since Eq. (28), which applies for

optically thick conditions, simply represents the sum of pure conduction and pure radiation heat transfer.

In order to assess the applicability of the superposition method to gray rather than black surfaces, an additional comparison is illustrated in Table III for the plates having an emissivity of 0.1. From this it is seen that very substantial errors arise, and it would appear that the superposition approximation is therefore applicable only for high surface emissivities.

V. Laminar Flow of an Absorbing Gas across a Flat Plate

As a final example of heat transfer in absorbing media, consideration will be given to combined convection and radiation. The only basic difference between this process and one of combined conduction and radiation is that the medium is now allowed to move relative to the bounding surfaces with some prescribed velocity distribution. Essentially, convective heat transfer can be broken down into two general areas; internal or duct flows, and external or boundary layer flows. A rather detailed analysis pertaining to the first area, consideration of fully developed heat transfer for flow of an absorbing medium between parallel plates, has been presented by Viskanta (*22*). The second area, boundary layer flow of an absorbing medium, is not nearly as amenable to analysis, and it is with this type of combined convection and radiation process that the present section will be concerned.

Sidorov (*23*) has considered combined convection and radiation for laminar flow across a flat plate, but obtains a solution in an extremely approximate fashion. The optically thin approximation has been applied to boundary layer heat transfer by several authors, for example, Howe (*24*) and Koh and DeSilva (*25*). In these analyses the gas (high-temperature air) within the boundary layer was assumed to emit but not absorb thermal radiation. This assumption is valid providing the surface and the gas outside the boundary layer are relatively cold. Results based upon the optically thick approximation have been presented by Viskanta and Grosh (*26*) for laminar flow across a wedge. This analysis thus serves as a limiting solution for the case in which the optical thickness of the boundary layer is large.

In many situations involving boundary layer flow of absorbing gases, the interaction between convection and radiation will not be appreciable. To assess under what conditions this neglect of interaction effects is permissible, the following analysis will deal with evaluating first-order interaction effects upon boundary layer heat transfer. The particular case of laminar flow across a flat plate will be considered.

A. THEORETICAL MODEL

The physical model and coordinate system are illustrated in Fig. 9. Steady laminar flow of a constant-property fluid with negligible viscous dissipation is assumed, and the boundary condition at the plate surface is taken to be that of a constant temperature. In order to keep the number of parameters to a minimum, it will further be assumed that the plate surface is black. No appreciable difficulty would be encountered in extending the analysis to a gray surface. As usual, the free-stream fluid is considered to be infinite in extent. It should be emphasized, however, that in the present situation "infinite in extent" additionally refers to optical conditions. Thus, all radiation emitted by the plate must eventually be absorbed by the fluid, while the fluid will in turn be the sole source of radiation incident upon the plate.

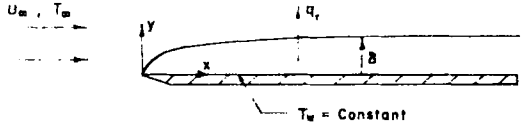

FIG. 9. Physical model and coordinate system for boundary layer flow of an absorbing gas.

Before discussing the mathematical model to be used in the present analysis, it is of interest to investigate possible limiting solutions for the case in which the fluid is a very weak absorber. Under such a condition, it would be expected that absorption and emission effects within the thermal boundary layer would exert a negligible influence upon the convection process. Correspondingly, the convective heat transfer q_{cw} at the plate surface would be that for pure convection, and, expressing this in terms of the convective Nusselt number, defined as

$$\mathrm{Nu} = \frac{q_{cw}x}{(T_w - T_\infty)k}$$

and taking for example Pr = 1.0, one has the well-known result

$$\frac{\mathrm{Nu}}{\sqrt{\mathrm{Re}}} = 0.332 \tag{31}$$

where Re is the Reynolds number defined as $\mathrm{Re} = u_\infty x/\nu$.

To obtain an expression for the radiative heat transfer q_{rw} at the plate surface, it may be noted that under the condition of weak absorption the radiation field will extend far out into the fluid since only gradual attenuation of radiation occurs, and, correspondingly, temperature gradients will

be small throughout most of the fluid. It may thus be assumed that as far as radiation is concerned the fluid is essentially isothermal and at the free-stream temperature T_∞. Equation (17) illustrates that the emissivity of an infinite isothermal fluid is unity, and therefore the net radiation exchange between plate and fluid is

$$q_{rw} = e_w - e_\infty \tag{32}$$

First-order corrections to Eqs. (31) and (32) will now be considered, and it will first be necessary to formulate the energy equation as applies to the present boundary layer problem. Under the assumptions previously mentioned, the complete energy equation is

$$\rho c_p \left(u \frac{\partial T}{\partial x} + v \frac{\partial T}{\partial y} \right) = - \operatorname{div} \bar{q}_c - \operatorname{div} \bar{q}_r \tag{33}$$

where the bar denotes a vector quantity, and

$$\bar{q}_c = -k \operatorname{grad} T$$

As is well known, if the Peclet number, defined as $\mathrm{Pe} = u_\infty x/\alpha$, is sufficiently large, then conduction in the x-direction will be negligible such that $\operatorname{div} q_c \simeq \partial q_{cy}/\partial y$, where the subscripts x and y will be used to denote the x and y components. Equation (33) then becomes

$$\rho c_p \left(u \frac{\partial T}{\partial x} + v \frac{\partial T}{\partial y} \right) = k \frac{\partial^2 T}{\partial y^2} - \operatorname{div} \bar{q}_r \tag{34}$$

A similar criterion for the neglect of radiation in the x-direction will now be determined. Perhaps the simplest means of accomplishing this is to investigate under what conditions radiation in the flow direction is negligible compared to convection, since convection in the flow direction will, under most conditions, be a predominate term in the energy equation. The requirement is thus that

$$\rho c_p u \frac{\partial T}{\partial x} \gg \frac{\partial q_{rx}}{\partial x} \tag{35}$$

The order of magnitude of $u\partial T/\partial x$ is estimated in the usual manner to be

$$u \frac{\partial T}{\partial x} \sim u_\infty \frac{(T_w - T_\infty)}{x} \tag{36}$$

In order to predict the magnitude of $\partial q_{rx}/\partial x$, it may be noted from Fig. 6 that the optically thick approximation will overestimate radiation heat transfer when applied to conditions which are not optically thick. Thus, in the present situation a conservative criterion would at most result through use of the optically thick approximation. The order of

magnitude of $\partial q_{rx}/\partial x$ will consequently be estimated from

$$q_{rx} = -\frac{4}{3a}\frac{\partial e}{\partial x} = -\frac{16\sigma T^3}{3a}\frac{\partial T}{\partial x}$$

giving

$$\frac{\partial q_{rx}}{\partial x} \sim \frac{16\sigma T^3}{3a}\frac{(T_w - T_\infty)}{x^2} \tag{37}$$

From this, together with Eqs. (35) and (36), the condition for radiation transfer in the x-direction to be negligible is

$$\frac{u_\infty x}{16\sigma T^3/3a\rho c_p} \gg 1 \tag{38}$$

As pointed out by Viskanta and Grosh (*26*), the quantity $16\sigma T^3/3a$ can be interpreted as a "radiative conductivity." The dimensionless group appearing above may in turn be considered as a "radiative Peclet number."

With radiation neglected in the x-direction, and again letting q_r denote radiation in the y-direction, Eq. (34) becomes

$$u\frac{\partial T}{\partial x} + v\frac{\partial T}{\partial y} = \alpha\frac{\partial^2 T}{\partial y^2} - \frac{a}{\rho c_p}\frac{\partial q_r}{\partial \tau} \tag{39}$$

The absorption-emission term, $\partial q_r/\partial \tau$, is given by Eq. (6) with $\tau_0 \to \infty$, $R_1 = e_w$ and $e(\tau)$ replaced by $e(x,\tau)$, such that

$$-\frac{\partial q_r}{\partial \tau} = 2e_w E_2(\tau) + 2\int_0^\infty e(x,t)E_1(|\tau - t|)\,dt - 4e(x,\tau) \tag{40}$$

It will now be assumed that thermal conduction within the fluid is restricted to a thin region of thickness δ adjacent to the plate surface, which is simply the conventional thermal boundary layer, and that this boundary layer is optically thin (i.e., $\tau_\delta = a\delta \ll 1$). The optically thin boundary layer, however, represents only a portion of the entire temperature field, since radiation emitted by the plate will pass virtually unattenuated through this layer. Consequently, it is necessary to consider not only the boundary layer, but also an adjacent radiation layer which is not optically thin and within which temperature gradients, and thus conduction effects, may be assumed small.

In other words, it has been assumed that conduction within the fluid is restricted to a thermal boundary layer whose thickness is small compared to the penetration length. Adjacent to this boundary layer is a radiation layer having a thickness of the same magnitude as the penetration length, and within which thermal conduction is neglected. In carrying out the solution to this assumed model, the temperature profile within

the radiation layer must first be determined. From this the temperature at the outer edge of the thermal boundary layer is obtained, and the boundary layer solution follows.

B. RADIATION LAYER

The energy equation applicable to the radiation layer is given by Eqs. (39) and (40) with $u = u_\infty$, $v = 0$, and the conduction term in Eq. (39) deleted. Thus

$$\frac{\rho c_p u_\infty}{a}\frac{\partial T}{\partial x} = 2e_w E_2(\tau) + 2\int_0^\infty e(x,t)E_1(|\tau - t|)\,dt - 4e(x,\tau) \qquad (41)$$

Since radiation transfer in the x-direction has been neglected, the boundary condition for this equation is

$$T = T_\infty; \qquad x = 0$$

The solution of Eq. (41) may be accomplished through successive approximations. In light of previous discussion, the first approximation will be taken as $T = T_\infty$, and substituting this (i.e., $e = e_\infty$) into the right side of Eq. (41) and performing the integrations, there is obtained

$$T = T_\infty + (e_w - e_\infty)E_2(\tau)\left(\frac{2ax}{\rho c_p u_\infty}\right) + \cdots \qquad (42)$$

The second term on the right side of this equation thus represents the change in fluid temperature due to radiation exchange with the plate. Since only first-order effects are being considered, higher-order terms in Eq. (42) will not be investigated.

Equation (42) may now be employed to evaluate the boundary condition at the outer edge of the thermal boundary layer. Letting this temperature be T_δ, and since $E_2(\tau_\delta) = 1 + 0(\tau_\delta) \simeq 1$, then

$$T_\delta = T_\infty + (e_w - e_\infty)\left(\frac{2ax}{\rho c_p u_\infty}\right) + \cdots \qquad (43)$$

The fact that T_δ differs from T_w is the result of neglecting conduction within the radiation layer. It may be seen that the solution for the radiation layer is in a sense analogous to a potential flow solution, from which the potential velocity at the surface is employed as the boundary condition at the outer edge of the velocity boundary layer.

C. THERMAL BOUNDARY LAYER

In order to apply Eqs. (39) and (40) to the optically thin boundary layer ($0 \leq \tau \leq \tau_\delta$), the integral appearing in Eq. (40) will be split into

two parts giving

$$-\frac{\partial q_r}{\partial \tau} = 2e_w E_2(\tau) + 2\int_0^{\tau_\delta} e(x,t)E_1(|\tau - t|)\,dt + 2\int_{\tau_\delta}^{\infty} e(x,t)E_1(|\tau - t|)\,dt - 4e(x,\tau) \quad (44)$$

The emissive power occurring in the second integral corresponds to the temperature distribution within the radiation layer. So, making use of Eq. (42) there is obtained

$$e(x,\tau) = e_\infty + 4(e_w - e_\infty)E_2(\tau)\left(\frac{2a\sigma T_\infty^3 x}{\rho c_p u_\infty}\right) + \cdots$$

for $\tau > \tau_\delta$. Upon substituting this into the second integral in Eq. (44) and evaluating the integral for $\tau < \tau_\delta$, one has

$$\int_{\tau_\delta}^{\infty} e(x,t)E_1(|\tau - t|)\,dt = e_\infty + 0\left(\frac{2a\sigma T_\infty^3 x}{\rho c_p u_\infty}\right) + 0(\tau_\delta) \quad (45)$$

The second term on the right is neglected since the present analysis is concerned solely with first-order radiation effects, while $0(\tau_\delta)$ may be neglected due to the fact that the boundary layer is assumed to be optically thin. Equation (45) thus gives the value of the second integral appearing in Eq. (44), whereas the first integral is negligible under optically thin conditions (see, for example, Section II,C). Since $E_2(\tau) \simeq 1$ for $\tau < \tau_\delta$, the form of Eq. (44) applicable to the optically thin boundary layer is therefore

$$-\frac{\partial q_r}{\partial \tau} = 2e_w + 2e_\infty - 4e(x,\tau) \quad (46)$$

Comparing this with Eq. (14), it may be seen that the radiation layer appears as a black surface at temperature T_∞ as far as first-order radiation effects within the boundary layer are concerned.

Upon substituting Eq. (46) into Eq. (39), the applicable form of the boundary layer energy equation is

$$u\frac{\partial T}{\partial x} + v\frac{\partial T}{\partial y} = \alpha\frac{\partial^2 T}{\partial y^2} + \frac{2a\sigma}{\rho c_p}(T_w^4 + T_\infty^4 - 2T^4) \quad (47)$$

The boundary conditions for this equation are

$$T = T_w; \qquad y = 0$$

$$T \to T_\delta; \qquad y \to \infty$$

where T_w is a constant while T_δ is given by Eq. (43). It will now be convenient to define a dimensionless temperature difference and a tem-

perature ratio as

$$\Theta = \frac{T - T_\infty}{T_w - T_\infty}, \quad \lambda = \frac{T_w}{T_\infty}$$

and Eq. (47) becomes

$$u\frac{\partial\Theta}{\partial x} + v\frac{\partial\Theta}{\partial y} = \alpha\frac{\partial^2\Theta}{\partial y^2} + \frac{2a\sigma T_\infty^3}{\rho c_p(\lambda - 1)}\{1 + \lambda^4 - 2[1 + (\lambda - 1)\Theta]^4\} \quad (48)$$

From Eq. (43) the boundary conditions transform to

$$\left.\begin{aligned} \Theta &= 1; \qquad y = 0 \\ \Theta &\to \left(\frac{\lambda^4 - 1}{\lambda - 1}\right)\left(\frac{2a\sigma T_\infty^3 x}{\rho c_p u_\infty}\right); \qquad y \to \infty \end{aligned}\right\} \quad (49)$$

New independent and dependent variables will now be defined as

$$\eta = y\sqrt{\frac{u_\infty}{\nu x}}, \quad \xi = \frac{2a\sigma T_\infty^3 x}{\rho c_p u_\infty}$$

where η is the familiar similarity variable for pure forced convection from a flat plate, while ξ is an expansion parameter which arises since the present convection-radiation problem does not reduce to a similarity solution. The solution of Eq. (48) is now assumed to be of the form

$$\Theta = \Theta_0(\eta) + \Theta_1(\eta)\xi + \cdots \quad (50)$$

Recalling that the velocity components are given by

$$u = u_\infty f', \quad v = \tfrac{1}{2}\sqrt{\frac{u_\infty \nu}{x}}(\eta f' - f) \quad (51)$$

where $f(\eta)$ is the Blasius stream function (*27*), then upon substituting Eqs. (50) and (51) into Eq. (48) and collecting like powers of ξ, there is obtained

$$\frac{1}{\mathrm{Pr}}\Theta_0'' + \tfrac{1}{2}f\Theta_0' = 0 \quad (52)$$

$$\frac{1}{\mathrm{Pr}}\Theta_1'' + \tfrac{1}{2}f\Theta_1' - f'\Theta_1 = -\varphi_0 \quad (53)$$

with

$$\varphi_0 = \frac{1}{\lambda - 1}\{1 + \lambda^4 - 2[1 + (\lambda - 1)\Theta_0]^4\} \quad (54)$$

The boundary conditions upon $\Theta_0(\eta)$ and $\Theta_1(\eta)$ are found from Eqs. (49) to be

$$\Theta_0(0) = 1, \quad \Theta_0(\infty) \to 0$$

$$\Theta_1(0) = 0, \quad \Theta_1(\infty) \to \left(\frac{\lambda^4 - 1}{\lambda - 1}\right)$$

As would be expected, the function $\Theta_0(\eta)$ represents the convective temperature distribution for the case of negligible radiation interaction ($\xi = 0$), while the second term in Eq. (50) denotes the first-order radiation effect upon the temperature profile within the boundary layer. To determine the temperature distribution throughout the entire fluid (combined boundary layer and radiation layer), Eq. (42) may be rephrased as

$$\Theta = \Theta_1(\infty)E_2(\tau)\xi + \cdots$$

and it readily follows from combination of this expression with Eq. (50) that

$$\Theta = \Theta_0(\eta) + \Theta_1(\eta)E_2(\tau)\xi + \cdots \tag{55}$$

represents the temperature distribution throughout the entire fluid. In making use of Eq. (55), it must be remembered that $\eta \to \infty$ corresponds to the outer edge of the thermal boundary layer where τ is still sufficiently small such that $E_2(\tau) \simeq 1$.

D. Heat Transfer Results

It will be convenient to consider separately the radiation and convection contributions to the total heat rate per unit area at the plate surface. To evaluate the radiation heat transfer, Eq. (7) with $R_1 = e_w$, $\tau_0 \to \infty$ and $e(\tau)$ replaced by $e(x,\tau)$ gives

$$q_{rw} = e_w - 2\int_0^\infty e(x,\tau)E_2(\tau)\,d\tau$$

or

$$q_{rw} = (e_w - e_\infty) - 2\int_0^\infty (e - e_\infty)E_2(\tau)\,d\tau \tag{56}$$

At this point it should be noted that

$$\tau_\delta = a\delta \sim \frac{ax}{\sqrt{\mathrm{Re}}}$$

and since the present analysis applies only for small τ_δ as well as small ξ, then any terms of $0(\tau_\delta\xi)$ are negligible in the same sense that $0(\xi^2)$ has been neglected. In line with this, evaluation of the emissive power from Eq. (55) and substitution into Eq. (56) gives the radiation heat

transfer at the wall as

$$\frac{q_{rw}}{e_w - e_\infty} = 1 - \left(\frac{ax}{\sqrt{\mathrm{Re}}}\right)\left(\frac{2}{\lambda^4 - 1}\right) \int_0^\infty \{[1 + (\lambda - 1)\Theta_0]^4 - 1\}\, d\eta + \cdots \quad (57)$$

Comparison of the above with Eq. (32) illustrates that the second term on the right side of Eq. (57) represents the first-order correction to Eq. (32), and that this first-order effect depends upon the optical thickness of the boundary layer but not upon ξ. It may be recalled that Eq. (32) is based upon the assumption that the fluid is isothermal at temperature T_∞, whereas the first-order correction in Eq. (57) corresponds to the temperature profile $\Theta_0(\eta)$. The subsequent departure from this profile by the amount $\Theta_1(\eta)E_2(\tau)\xi$ as indicated in Eq. (55) would in turn appear as a second-order effect in Eq. (57).

It may easily be shown that the quantity

$$\left(\frac{2}{\lambda^4 - 1}\right) \int_0^\infty \{[1 + (\lambda - 1)\Theta_0]^4 - 1\}\, d\eta$$

is positive regardless of the value of λ (of course, $\lambda > 0$). The effect of the first-order term in Eq. (57) is thus to reduce radiation heat transfer with respect to that predicted by Eq. (32). This is physically reasonable since Eq. (32) assumes the fluid to be isothermal at T_∞, whereas the fluid within the boundary layer (and also the radiation layer if higher-order effects are taken into account) actually differs from the free-stream temperature in the direction of T_w, such that radiation exchange between this portion of the fluid and the plate is reduced.

Turning next to the convective heat transfer at the plate surface, this is given by

$$q_{cw} = -k\left(\frac{\partial T}{\partial y}\right)_{y=0}$$

and combining the above with the definition of the Nusselt number

$$\frac{\mathrm{Nu}}{\sqrt{\mathrm{Re}}} = -\left(\frac{\partial \Theta}{\partial \eta}\right)_{\eta=0}$$

so that from Eq. (50)

$$\frac{\mathrm{Nu}}{\sqrt{\mathrm{Re}}} = -\Theta_0'(0) - \Theta_1'(0)\xi + \cdots \quad (58)$$

The first term in this equation corresponds to pure forced convection and reduces to Eq. (31) for Pr = 1.0. It may be seen that the first-order

radiation effect depends upon ξ but not upon the optical thickness of the boundary layer.

Although the foregoing heat transfer results were obtained under the assumption of constant properties, they may be applied without modification to the variable-property situation characterized by

$$\rho u = \text{const} \qquad \rho k = \text{const}$$

$$c_p = \text{const} \qquad a/\rho = \text{const}$$

This may easily be verified through use of Howarth's transformation together with the optical distance expression

$$\tau = \int_0^y a \, dy$$

for variable a.

With the exception of a/ρ = constant, the property variations described above constitute a reasonable first-approximation for most gases. With respect to a/ρ = constant, it may be recalled from Section III that for water vapor in the temperature range 1000° to 2000°R the absorption coefficient varies as $T^{-1.6}$. Consequently a/ρ varies approximately as $T^{-0.6}$, and this is a less severe dependence upon temperature than for a by itself. On the other hand, for high-temperature air the ratio a/ρ will vary more strongly with temperature than for a alone.

E. Numerical Results for $\lambda \to 1$

Although numerical heat transfer results covering a range of values of the parameter λ were not available at the time of completion of this article, illustrative results can be presented for the limiting case of $\lambda \to 1$ (small temperature differences). It may easily be shown that taking $\lambda \to 1$ is the same as assuming linearized radiation.

Turning first to radiation heat transfer at the plate surface, Eq. (57) with $\lambda \to 1$ becomes

$$\frac{q_{rw}}{e_w - e_\infty} = 1 - 2\left(\frac{ax}{\sqrt{\text{Re}}}\right)\int_0^\infty \Theta_0 \, d\eta + \cdots$$

Choosing Pr = 1.0, then from Reynolds' analogy

$$\int_0^\infty \Theta_0 \, d\eta = \int_0^\infty (1 - f') \, d\eta = 1.721$$

and

$$\frac{q_{rw}}{e_w - e_\infty} = 1 - 3.44\left(\frac{ax}{\sqrt{\text{Re}}}\right) + \cdots \tag{59}$$

To evaluate convective heat transfer the solution for $\Theta_1(\eta)$ is necessary, and for $\lambda \to 1$ and Pr = 1.0 Eq. (53) and its boundary conditions reduce [32]

to

$$\Theta_1'' + \tfrac{1}{2}f\Theta_1' - f'\Theta_1 = 8\Theta_0 - 4$$

$$\Theta_1(0) = 0, \quad \Theta_1(\infty) \to 4$$

From this it may be verified that

$$\Theta_1(\eta) = 4[1 + \sigma_2(\eta) - \sigma_1(\eta)]$$

where

$$\sigma_1'' + \tfrac{1}{2}f\sigma_1' - f'\sigma_1 = 0; \qquad \sigma_1(0) = 1, \quad \sigma_1(\infty) \to 0 \tag{60}$$

and

$$\sigma_2'' + \tfrac{1}{2}f\sigma_2' - f'\sigma_2 = \Theta_0; \qquad \sigma_2(0) = 0, \quad \sigma_2(\infty) \to 0 \tag{61}$$

Equation (60) corresponds to forced convection with a linear variation of surface temperature with x, and from (*28*) $\sigma_1'(0)$ may be estimated for Pr = 1 to be $\sigma_1'(0) = -0.541$. Further, Eq. (61) has been solved in (*29*) with application to a nonsteady convection problem, giving $\sigma_2'(0) = -0.876$ for Pr = 1.0. Thus $\Theta_1'(0) = -1.34$, and for Pr = 1.0 Eq. (58) yields

$$\frac{\mathrm{Nu}}{\sqrt{\mathrm{Re}}} = 0.332 + 1.34\xi + \cdots \tag{62}$$

The fact that convection heat transfer is increased due to the interaction of radiation can be explained by investigating the sign of the absorption-emission term $-\partial q_r/\partial\tau$. For example, if the plate is heated ($T_w > T_\infty$) it may be seen from Eq. (46) that $-\partial q_r/\partial\tau$ will be negative near the surface of the plate and positive within the outer portion of the boundary layer. The effect of radiation is thus to impose an effective heat sink within the fluid near the surface, which in turn tends to increase heat transfer from the plate surface. For the opposite extreme of an optically thick boundary layer, Viskanta and Grosh (*26*) have shown that an increase in convective heat transfer occurs only for $\lambda < \frac{1}{2}$.

VI. Boundary Condition Effects upon Forced Convection

The foregoing sections have dealt exclusively with the influence of radiation upon conduction and convection heat transfer as the result of absorption and emission within the medium. In all cases the bounding surfaces were taken to be isothermal, and there was no alteration of the boundary conditions due to the presence of radiation. The present section considers the reverse situation. The medium is assumed to be nonabsorbing, and the only influence of radiation is through altering the boundary conditions of the heat transfer process.

The particular situation to be considered is that of laminar forced convection across a flat plate. Steady flow of a constant-property fluid which is transparent to thermal radiation is assumed, and the physical

model and coordinate system are illustrated in Fig. 10. Heat transfer at the surface takes place through the combined processes of convection with the fluid which has a constant free-stream temperature T_∞ and radiation with the environment which is at temperature T_e.

Consider first the case in which the surface temperature is a prescribed function of x. With this type of boundary condition the fluid is completely oblivious to the presence of radiation since there is neither absorption within the fluid nor does the radiant heat exchange affect the surface temperature $T_w(x)$. Thus, for a prescribed surface temperature there will be no interaction between the two separate modes of heat transfer. The local convective heat transfer coefficient (or convective Nusselt number) can be evaluated by standard methods (*30* and *31*), while the radiation heat transfer is evaluated in the usual manner.

The situation is considerably different, however, for the inverse problem in which the surface heat rate per unit area is a prescribed function of x. Once again there are standard methods available for evaluating

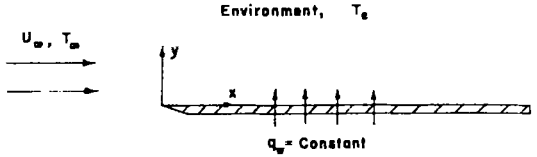

FIG. 10. Physical model and coordinate system for boundary condition effects upon forced convection.

the convective Nusselt number corresponding to a given $q_w(x)$. However, with radiation present the heat rate distribution along the surface which the fluid actually observes may be quite different from that which is prescribed. This is due to the fact that part of the prescribed $q_w(x)$ leaves the surface as radiant energy and in an amount which varies with location. It is thus possible for the convective heat rate to vary with x in a completely different manner than the total prescribed quantity $q_w(x)$, and this results in a mutual interaction between the two modes of heat transfer.

In the present analysis the particular case of a constant surface heat flux is considered, and results will be given for the convective Nusselt number. Once this is known, the surface temperature can readily be obtained through an energy balance.

For laminar flow of a constant-property fluid across a flat plate with negligible viscous dissipation, the energy equation is of the form

$$u\frac{\partial T}{\partial x} + v\frac{\partial T}{\partial y} = \alpha\frac{\partial^2 T}{\partial y^2} \tag{63}$$

As mentioned above, the surface heat rate is taken to be constant, and the boundary conditions for Eq. (63) become

$$\frac{\partial T}{\partial y} = -\frac{q_w}{k} + \frac{\sigma\epsilon}{k}(T^4 - T_s^4); \qquad y = 0 \tag{64a}$$

$$T \to T_\infty, \qquad y \to \infty \tag{64b}$$

where ϵ is the plate emissivity.

The solution of Eq. (63) subject to the boundary conditions (64) may be obtained in the following manner. Two new independent variables will be defined as

$$\eta = y\sqrt{\frac{u_\infty}{\nu x}}, \quad \xi = \frac{\sigma\epsilon T_\infty^3}{k}\sqrt{\frac{\nu x}{u_\infty}}$$

where η is the similarity variable as used previously, while the expansion parameter ξ is defined differently than before. In addition, the fluid temperature will be expressed by the series

$$T - T_\infty = T_\infty[a_1\Theta_1(\eta)\xi + a_2\Theta_2(\eta)\xi^2 + \cdots] \tag{65}$$

with the requirement that $\Theta_1(0) = \Theta_2(0) = \cdots = 1$.

Upon substitution of Eq. (65) into Eq. (63) and collecting like powers of ξ, the quantities $\Theta_n(\eta)$ are found to be the solution of

$$\frac{1}{\mathrm{Pr}}\Theta_n'' + \tfrac{1}{2}f\Theta_n' - \frac{n}{2}f'\Theta_n = 0 \tag{66}$$

satisfying the boundary conditions

$$\Theta_n(0) = 1, \quad \Theta_n(\infty) \to 0$$

The Blasius stream function (*27*) is again denoted by $f(\eta)$. It should be noted (*28*) that Eq. (66) is identical to that representing the fluid temperature for a surface temperature varying as ξ^n (or $x^{n/2}$). Such a result should be expected since the energy equation is linear.

It remains to evaluate the constants a_1, a_2, . . . , and from Eq. (65)

$$T_w - T_\infty = T_\infty(a_1\xi + a_2\xi^2 + \cdots) \tag{67}$$

$$\left(\frac{\partial T}{\partial y}\right)_{y=0} = \frac{\sigma\epsilon T_\infty^4}{k}[a_1\Theta_1'(0) + a_2\Theta_2'(0)\xi^2 + \cdots] \tag{68}$$

Substituting these expressions into Eq. (64a) and collecting like powers of ξ, the constants a_n may be determined. In the following, however, it will be necessary to know only the ratio a_2/a_1, for which it is found that

$$\frac{a_2}{a_1} = \frac{4}{\Theta_2'(0)} \tag{69}$$

The foregoing results may now be expressed in terms of the convective Nusselt number, recalling that

$$\mathrm{Nu} = \frac{q_{cw}x}{(T_w - T_\infty)k} = -\frac{x}{(T_w - T_\infty)}\left(\frac{\partial T}{\partial y}\right)_{y=0}$$

Combining this definition with Eqs. (67) and (68) and dividing one series into the other, there is obtained

$$\frac{\mathrm{Nu}}{\sqrt{\mathrm{Re}}} = -\theta_1'(0) - \frac{a_2}{a_1}[\theta_2'(0) - \theta_1'(0)]\xi + \cdots \tag{70}$$

The quantities $\theta_1'(0)$ and $\theta_2'(0)$ have been evaluated by Donoughe and Livingood (*28*) for Pr = 0.7, giving

$$\theta_1'(0) = -0.4059, \quad \theta_2'(0) = -0.4803$$

So, combining these results with Eqs. (69) and (70), the final expression for the Nusselt number with Pr = 0.7 becomes

$$\frac{\mathrm{Nu}}{\sqrt{\mathrm{Re}}} = 0.406 - 0.620\xi + \cdots \tag{71}$$

As would be expected, the value 0.406 represents $\mathrm{Nu}/\sqrt{\mathrm{Re}}$ for a constant surface heat flux with no effect due to radiation. The second term in Eq. (71) correspondingly denotes the first-order influence of radiation. It is interesting to note that this first-order term does not depend upon either T_e or q_w. However, these quantities enter into the second and higher-order terms in the form of the additional parameter

$$\beta = \frac{q_w}{\sigma\epsilon T_\infty^4} + \left(\frac{T_e}{T_\infty}\right)^4 \tag{72}$$

As discussed in (*32*), there appears to be little use in evaluating higher-order terms in Eq. (71) due to the slow convergence of the series. An alternate approach is to obtain a solution applicable for large ξ, and it was found that an asymptotic expansion exists of the form

$$T - T_\infty \sim T_\infty[b_0\phi_0(\eta) + b_1\phi_1(\eta)\xi^{-1} + \cdots] \tag{73}$$

where $\phi_0(0) = \phi_1(0) = \cdots = 1$ have been chosen for convenience. The functions $\phi_n(\eta)$ and constants b_n are evaluated using essentially the same procedure as in the previous solution for small ξ.

Upon substituting Eq. (73) into Eq. (63) and collecting like powers of ξ, there is obtained

$$\left.\begin{aligned} \frac{1}{\mathrm{Pr}}\phi_n'' + \tfrac{1}{2}f\phi_n' + \frac{n}{2}f'\phi_n = 0 \\ \phi_n(0) = 1, \quad \phi_n(\infty) \to 0 \end{aligned}\right\} \tag{74}$$

and this is the same as Eq. (66) except that the sign of n is reversed. From Eqs. (64a) and (73) it is found that

$$\frac{b_1}{b_0} = \frac{\phi_0'(0)}{4\beta^{3/4}}$$

where β is defined by Eq. (72), while from (*28*)[6] for Pr = 0.7

$$\phi_0'(0) = -0.2927, \quad \phi_1'(0) = 0$$

The asymptotic expansion for the Nusselt number is in turn found to be

$$\frac{\mathrm{Nu}}{\sqrt{\mathrm{Re}}} \sim -\phi_0'(0) + \frac{b_1}{b_0}\phi_0'(0)\xi^{-1} + \cdots \tag{75}$$

such that for Pr = 0.7

$$\frac{\mathrm{Nu}}{\sqrt{\mathrm{Re}}} \sim 0.293 + \frac{0.0214}{\beta^{3/4}}\xi^{-1} + \cdots \tag{76}$$

This obviously applies only for $\beta > 0$. For $\beta = 0$ an asymptotic solution can be obtained by expanding in reciprocal powers of $\xi^{1/4}$ as done by Lighthill (*33*). Further, for pure radiation the wall temperature is given by

$$\frac{T_w}{T_\infty} = \left[\frac{q_w}{\sigma\epsilon T_\infty^4} + \left(\frac{T_e}{T_\infty}\right)^4\right]^{1/4} = \beta^{1/4} \tag{77}$$

and consequently, at least in the limit of large ξ, $\beta < 0$ is not physically possible.

One may note that the first term in Eq. (76) is the value of $\mathrm{Nu}/\sqrt{\mathrm{Re}}$ for pure convection with a constant surface temperature. This is entirely reasonable on physical grounds, since in the limit as ξ becomes large (radiation predominates) the surface temperature will approach the constant value given by Eq. (77). Thus, the *maximum* effect that radiation can exert upon the convection process is to reduce $\mathrm{Nu}/\sqrt{\mathrm{Re}}$ from 0.406 to 0.293.

The limiting results for small and large ξ as given by Eqs. (71) and (76) are illustrated in Fig. 11 together with Lighthill's results (*33*) for $\beta = 0$. Also shown in Fig. 11 is a straight-line fairing between the two limiting solutions, and this should be regarded only as a very crude interpolation.

The fact that the maximum influence of radiation upon convection is to reduce the Nusselt number from that for a uniform surface heat rate to the value for a uniform surface temperature has particular significance with regard to turbulent flow. If the flow is turbulent, this difference is only about 4%, and it may therefore be concluded that for turbulent

[6] $\phi_1'(0) = 0$ for all Pr.

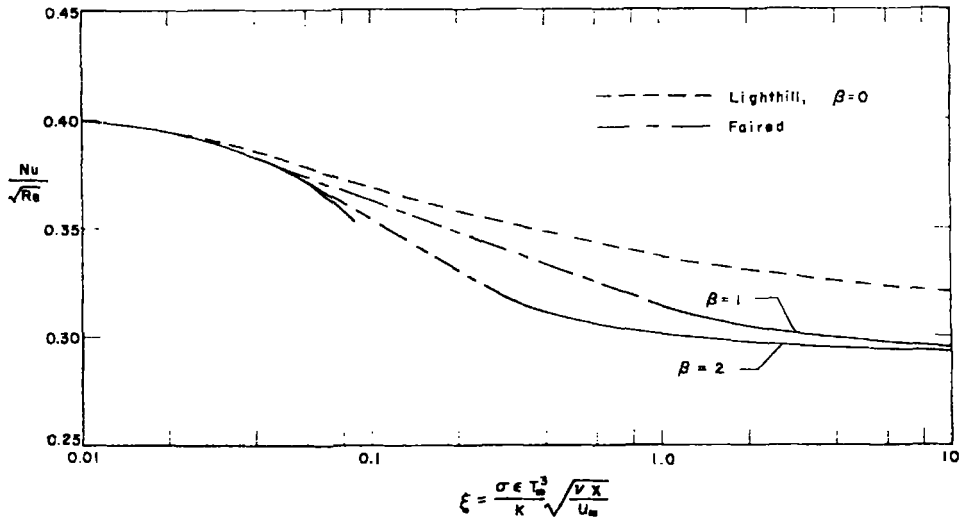

FIG. 11. Variation of the Nusselt number for laminar flow across a flat plate, $Pr = 0.7$.

flow across a flat plate any radiation effects upon the surface boundary condition will have slight effect on the Nusselt number.

VII. Boundary Condition Effects upon Free Convection

As a second example of the influence that radiation may have upon altering convective boundary conditions, free convection from a vertical flat plate will be considered. It is again assumed that the fluid is non-absorbing and that the surface heat flux is uniform. To further simplify

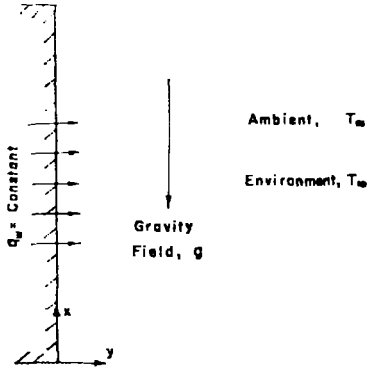

FIG. 12. Physical model and coordinate system for boundary condition effects upon free convection.

the problem, the ambient temperature of the fluid and the environment temperature for radiation exchange will be taken as the same value T_∞. The physical model and coordinate system are illustrated in Fig. 12 for a heated plate. For a cooled plate the gravity force is reversed. In addition to analytical predictions, experimental results have been obtained using ambient air as the nonabsorbing fluid.

A. ANALYSIS

For laminar free convection of a constant-property fluid along a vertical surface, the boundary layer equations are

$$\frac{\partial u}{\partial x} + \frac{\partial v}{\partial y} = 0 \tag{78}$$

$$u\frac{\partial u}{\partial x} + v\frac{\partial u}{\partial y} = \nu\frac{\partial^2 u}{\partial y^2} + g\beta(T - T_\infty) \tag{79}$$

$$u\frac{\partial T}{\partial x} + v\frac{\partial T}{\partial y} = \alpha\frac{\partial^2 T}{\partial y^2} \tag{80}$$

and the boundary conditions become

$$\left.\begin{aligned} \frac{\partial T}{\partial y} &= -\frac{q_w}{k} + \frac{\sigma\epsilon}{k}(T^4 - T_e^4) \\ u &= v = 0 \end{aligned}\right\}; \qquad y = 0 \tag{81a}$$

$$T \to T_\infty, \quad u \to 0; \qquad y \to \infty \tag{81b}$$

Introducing the stream function ψ by the customary definition

$$u = \frac{\partial \psi}{\partial y}, \quad v = -\frac{\partial \psi}{\partial x}$$

then Eq. (78) is automatically satisfied. New independent variables will now be defined as

$$\eta = \frac{C_1 y}{x^{1/5}}, \quad \xi = \frac{\sigma\epsilon T_\infty^3}{kC_1}x^{1/5} \tag{82}$$

and solutions of Eqs. (79) and (80) are assumed to be

$$\psi = C_2 x^{4/5}[F_0(\eta) + F_1(\eta)\xi + \cdots] \tag{83}$$

$$T_\infty - T = \frac{q_w x^{1/5}}{C_1 k}[\Theta_0(\eta) + \Theta_1(\eta)\xi + \cdots] \tag{84}$$

where

$$C_1 = \left(\frac{g\beta q_w}{5k\nu^2}\right)^{1/5}, \quad C_2 = \left(\frac{5^4 g\beta q_w \nu^3}{k}\right)^{1/5} \tag{85}$$

For $\xi = 0$, Eqs. (82) through (85) reduce to the similarity transformation for free convection in the absence of radiation as considered by Sparrow and Gregg (*34*).

Upon substituting Eqs. (83) and (84) into Eqs. (79) and (80) and collecting like powers of ξ, ordinary differential equations describing F_0, Θ_0, F_1 and Θ_1 are obtained as

$$\left.\begin{aligned} F_0''' + 4F_0F_0'' - 3(F_0')^2 &= \Theta_0 \\ \frac{1}{\Pr}\Theta_0'' + 4F_0\Theta_0' - F_0'\Theta_0 &= 0 \end{aligned}\right\} \tag{86}$$

$$\left.\begin{aligned} F_1''' + 4F_0F_1'' - 7F_0'F_1' + 5F_0''F_1 &= \Theta_1 \\ \frac{1}{\Pr}\Theta_1'' + 4F_0\Theta_1' - 2F_0'\Theta_1 &= F_1'\Theta_0 - 5F_1\Theta_0' \end{aligned}\right\} \tag{87}$$

The boundary conditions for these equations are determined in essentially the same manner as in the preceding case of forced convection. Combining Eqs. (83) and (84) with Eqs. (81) gives

$$\left.\begin{aligned} F_0(0) = F_0'(0) = 0, \quad \Theta_0'(0) &= 1 \\ F_0'(\infty) \to (0), \quad \Theta_0(\infty) &\to 0 \end{aligned}\right\} \tag{88}$$

$$\left.\begin{aligned} F_1(0) = F_1'(0) = 0, \quad \Theta_1'(0) &= 4\Theta_0(0) \\ F_1'(\infty) \to 0 \qquad \Theta_1(\infty) &\to 0 \end{aligned}\right\} \tag{89}$$

The foregoing results may now be expressed in terms of the convective Nusselt number and Grashof number, where

$$\mathrm{Gr} = \frac{g\beta x^3(T_w - T_\infty)}{\nu^2}$$

From Eq. (84), recalling that $\Theta_1'(0) = 4\Theta_0(0)$

$$T_w - T_\infty = -\frac{q_w x^{1/5}}{C_1 k}[\Theta_0(0) + \Theta_1(0)\xi + \cdots]$$

$$\left(\frac{\partial T}{\partial y}\right)_{y=0} = -\frac{q_w}{k}[1 + 4\Theta_0(\xi) + \cdots]$$

and combining these with the definitions for Nu and Gr

$$\frac{\mathrm{Nu}}{(\mathrm{Gr})^{1/4}} = \frac{1}{5^{1/4}[-\Theta_0(0)]^{1/4}}\left\{1 + \left[4\Theta_0(0) - \frac{5}{4}\frac{\Theta_1(0)}{\Theta_0(0)}\right]\xi + \cdots\right\} \tag{90}$$

Results for $\Theta_0(\eta)$ and $F_0(\eta)$ have been presented by Sparrow and Gregg (*34*) for Pr of 0.1, 1, 10 and 100. For purposes of the present analysis,

Eqs. (87) subject to the boundary conditions (89) were solved numerically on an IBM 7090 digital computer for Pr = 1.0, and the pertinent results are

$$\Theta_0(0) = -1.357, \quad \Theta_1(0) = 5.463$$

In addition, the functions F_0', F_1' and Θ_0, Θ_1 are illustrated in Figs. 13 and 14 respectively. For Pr = 1.0, Eq. (90) thus gives

$$\frac{\mathrm{Nu}}{(\mathrm{Gr})^{1/4}} = 0.456 - 0.180\xi + \cdots \tag{91}$$

The first term is again the result for pure free convection with no influence of radiation.

In order to make a comparison later with experimental data, it would be advantageous to extend the present analysis to a Prandtl number

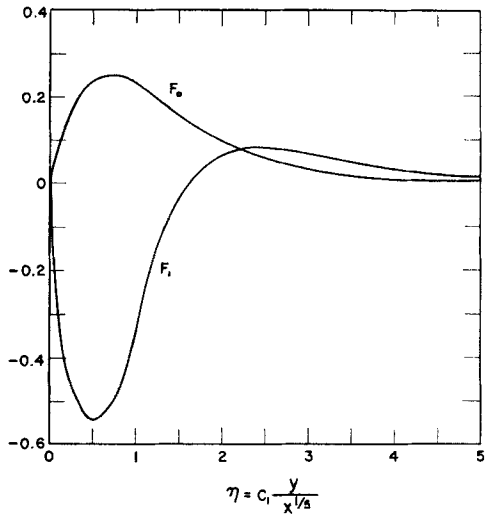

FIG. 13. The functions $F_0(\eta)$ and $F_1(\eta)$ for free convection.

more closely representing that of air. One way to do this, of course, would be to resolve Eqs. (86) and (87). However, from the analysis of Sparrow and Gregg (*35*) it may be found that at least within the Prandtl number range of 0.7 to 1.0 the effect of Prandtl number upon Nusselt number is virtually independent of the surface boundary condition. From the uniform surface temperature results of Ostrach (*36*) the Nusselt number for Pr = 0.72 is found to be lower by the factor 1.12 than for

Pr = 1.0. Thus, applying this factor to Eq. (91) there is obtained for Pr = 0.72

$$\frac{\mathrm{Nu}}{(\mathrm{Gr})^{1/4}} = 0.407 - 0.161\xi + \cdots \tag{92}$$

It is interesting to note what form the preceding results would take if linearized rather than fourth-power radiation had been assumed. Factoring the fourth-power temperature difference in the usual manner, the

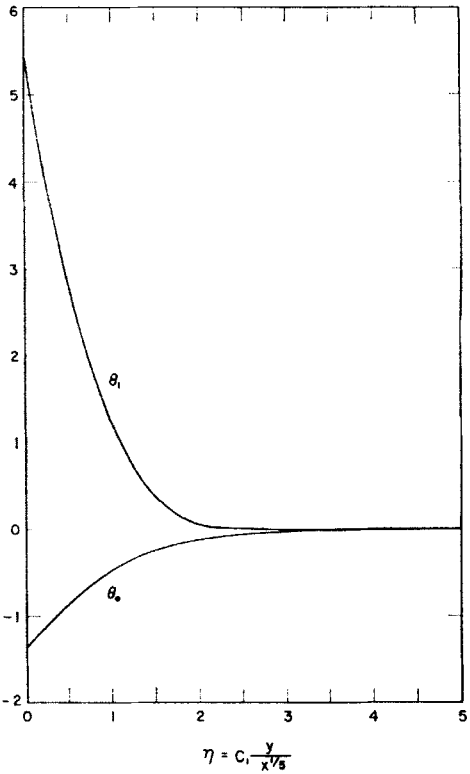

FIG. 14. The functions $\Theta_0(\eta)$ and $\Theta_1(\eta)$ for free convection.

radiant heat transfer between surface and environment may be expressed as

$$q_{rw} = \sigma\epsilon(T_w^2 + T_\infty^2)(T_w + T_\infty)(T_w - T_\infty)$$

and providing T_w does not differ too greatly from T_∞, this may be approximated by

$$q_{rw} = 4\sigma\epsilon T_\infty^3(T_w - T_\infty)$$

So, assuming linearized radiation the boundary condition at the plate

surface becomes

$$\frac{\partial T}{\partial y} = -\frac{q_w}{k} + \frac{4\sigma\epsilon T_\infty^3}{k}(T_w - T_\infty); \qquad y = 0 \tag{93}$$

If Eq. (93) rather than the first of Eqs. (81a) had been employed in the foregoing analysis, the same results would still have been obtained. In other words, the term denoting first-order radiation effects is the same whether fourth-power or linearized radiation is employed, and this holds for forced convection as well. If higher-order terms were considered in Eqs. (91) and (92), the additional parameter

$$\frac{q_w}{\sigma\epsilon T_\infty^4}$$

would arise for fourth-power radiation, whereas this would not be the case if linearized radiation were assumed.

As in the previous section dealing with forced convection, attention will now be directed towards determining asymptotic results for large values of the radiation parameter ξ. To further simplify the problem linearized radiation will be assumed, and the thermal boundary condition at the plate surface is taken to be that given by Eq. (93). As just discussed, the small ξ results are equally applicable to this situation.

A solution of Eqs. (79) and (80) in the form of an asymptotic expansion will now be assumed as

$$\psi \sim 4\nu C_3 x^{3/4}[G_0(\zeta) + G_1(\zeta)\xi^{-5/4} + \cdots] \tag{94}$$

$$T - T_\infty \sim \frac{q_w}{4\sigma\epsilon T_\infty^3}[\phi_0(\zeta) + \phi_1(\zeta)\xi^{-5/4} + \cdots] \tag{95}$$

where

$$\zeta = \frac{C_3 y}{x^{1/4}}, \quad C_3 = \frac{1}{2}\left(\frac{g\beta q_w}{\sigma\epsilon T_\infty^3 \nu^2}\right)^{1/4} \tag{96}$$

For $\xi = 0$, this reduces to the similarity transformation for free convection from an isothermal plate with the temperature difference between plate and ambient equal to $q_w/4\sigma\epsilon T_\infty^3$.

Upon substituting Eqs. (94) and (95) into Eqs. (79) and (80) and collecting like powers of ξ, there is obtained

$$\left.\begin{aligned} G_0''' + 3G_0G_0'' - 2(G_0')^2 &= -\phi_0 \\ \frac{1}{\mathrm{Pr}}\phi_0'' + 3G_0\phi_0' &= 0 \end{aligned}\right\} \tag{97}$$

$$\left.\begin{aligned} G_1''' + 3G_0G_1'' - 3G_0'G_1' + 2G_0''G_1 &= -\phi_1 \\ \frac{1}{\mathrm{Pr}}\phi_1'' + 3G_0\phi_1' + G_0'\phi_1 &= -2G_1\phi_0' \end{aligned}\right\} \tag{98}$$

The boundary conditions are easily found to be

$$\left.\begin{aligned} G_0(0) = G_0'(0) = 0, \quad \phi_0(0) = 1 \\ G_0'(\infty) \to 0, \quad \phi_0'(\infty) \to 0 \end{aligned}\right\} \tag{99}$$

$$\left.\begin{aligned} G_1(0) = G_1'(0) = 0, \quad \phi_1(0) = \frac{5^{1/4}}{8}\phi_0'(0) \\ G_1'(\infty) \to 0, \quad \phi_1'(\infty) \to 0 \end{aligned}\right\} \tag{100}$$

Heat transfer results may now be determined in eactly the same manner as before. By incorporating Eq. (95) into the definitions for Nu

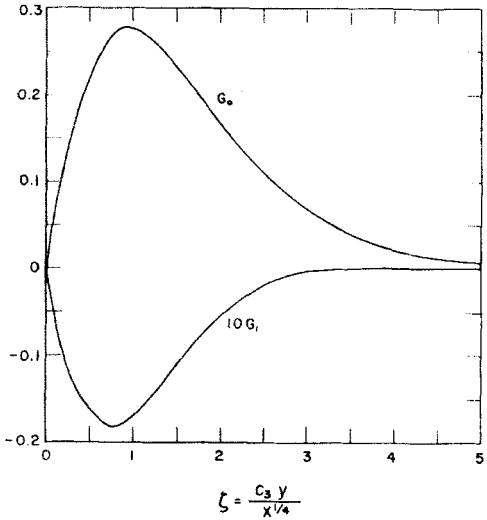

FIG. 15. The functions $G_0(\zeta)$ and $G_1(\zeta)$ for free convection.

and Gr, there is obtained

$$\frac{\mathrm{Nu}}{(\mathrm{Gr})^{1/4}} \sim -\frac{1}{\sqrt{2}}\{\phi_0'(0) + [\phi_1'(0) - \tfrac{5}{4}\phi_0'(0)\phi_1(0)]\xi^{-5/4} + \cdots\} \tag{101}$$

It is readily observed that, as for forced convection, the first term in the above expression represents heat transfer from a constant-temperature plate.

Tabulated values of $G_0(\eta)$ and $\phi_0(\eta)$ given by Ostrach (*36*) for Pr = 0.72 were used as input data in solving Eqs. (98) numerically on an IBM 1620 digital computer. The results of primary interest are

$$\phi_0'(0) = -0.505, \quad \phi_1'(0) = 0.042$$

and the functions G_0', G_1' and ϕ_0, ϕ_1 are illustrated in Figs. 15 and 16 respectively. It follows that for Pr = 0.72 the Nusselt number expression becomes

$$\frac{\mathrm{Nu}}{(\mathrm{Gr})^{1/4}} \sim 0.357 + 0.007\xi^{-5/4} + \cdots \tag{102}$$

Equations (92) and (102) thus represent for Pr = 0.72 the solutions for small and large ξ respectively. It should be emphasized that if fourth-

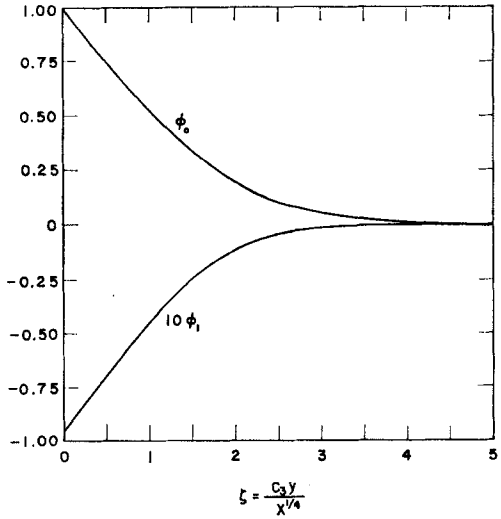

FIG. 16. The functions $\phi_0(\zeta)$ and $\phi_1(\zeta)$ for free convection.

power rather than linearized radiation had been employed, the additional parameter

$$\frac{q_w}{\sigma\epsilon T_\infty{}^4}$$

would appear in the coefficient of the second term in Eq. (102).

B. EXPERIMENTAL RESULTS

To augment the foregoing analytical results, an experimental investigation was undertaken concerning free convection from a vertical flat plate having a uniform surface heat flux. Free convection rather than forced convection was chosen solely as the result of the lesser equipment requirements of the former as compared to the latter. On the other hand, the analyses have indicated that the influence of radiation through altering the convective boundary conditions is considerably less for free rather than forced convection. Consequently, the advantage of experi-

mental simplicity is somewhat offset by the fact that a smaller effect had to be observed.

It was decided to use room air as the nonabsorbing fluid and to employ moderate temperature differences so that the assumption of linearized radiation would be appropriate. From the previous section it was shown that the influence of radiation is dependent upon the parameter ξ defined as

$$\xi = \frac{\sigma\epsilon T_\infty^3 x^{1/5}}{kC_1} = \frac{\sigma\epsilon T_\infty^3}{k}\left(\frac{5k\nu^2 x}{g\beta q_w}\right)^{1/5}$$

With the ambient temperature T_∞ fixed, the only way of varying ξ for

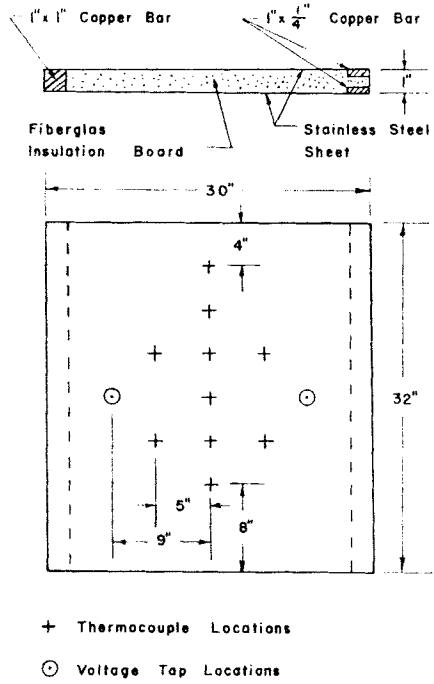

FIG. 17. Free convection apparatus.

a given plate emissivity would be to vary either x or q_w. However, since these quantities are raised to the 1/5 power in the above expression, significant variations in ξ could not easily be obtained in this manner. It was thus decided to produce the main variations in ξ through altering the emissivity of the surface.

The experimental apparatus consisted of a vertical test plate as illustrated schematically in Fig. 17. The test plate was constructed of 26

gage (0.018 inches thick) type 304 stainless steel. An identical stainless steel sheet was used as a guard plate and was separated from the test plate by a one-inch-thick fiberglas insulation board.

Both the test and guard plates were heated by passing an alternating current through them, thus producing a locally uniform heat generation within the plates. The two plates were connected in series by a one-inch-square copper bus bar as shown in Fig. 17. The plates were checked for uniformity in thickness and no variations greater than 1% were found. Power to the test plate was measured by a Weston Model 432 wattmeter, and the voltage taps for the wattmeter were soldered to the inside surface of the plate as shown in Fig. 17.

Surface temperatures were measured by copper-constantan thermocouples located vertically along the center of the test plate and soldered to the inside surface. Additional thermocouples were located on both the test and guard plates to serve as a check on horizontal and transverse temperature gradients. Thermocouple emf was measured by a self-balancing Leeds and Northrup K-3 potentiometer.

The radiation environment for the test plate consisted of a four-foot-square plywood box open on one side. The test plate was then located so as to face into the box, and the minimum gray-body view factor was calculated to be 0.99ϵ with ϵ plate emissivity. Thus, the box was sufficiently large to closely approximate an infinite environment, since the gray-body view factor between the plate and an infinite environment is ϵ. The combined ambient-environment temperature T_∞ was taken to be the average of the inner surface temperatures of the box.

Three surface finishes on the plate were employed; polished stainless steel, bronze radiator paint, and black lacquer. The emissivity of these surfaces was measured using a radiometer similar to that described in (*37*), giving the following values in the temperature range of 100° to 140°F:

Polished stainless steel $\epsilon = 0.20$

Bronze radiator paint $\epsilon = 0.52$

Black lacquer $\epsilon = 0.96$

The apparatus was operated at a surface heat rate of 46 Btu/hr ft^2, which corresponds to a current of approximately 240 amps. The temperature difference between plate surface and ambient ranged from 28° to 61°F depending upon location and surface emissivity. In evaluating the convective heat transfer coefficient (and hence Nusselt number) the only additional information required was the convective heat rate from the plate surface, and this was determined by subtracting the radiation heat

rate $\sigma\epsilon(T_w^4 - T_\infty^4)$ from the total. In reducing the data to the form $\mathrm{Nu}/\mathrm{Gr}^{1/4}$ as a function of ξ, the air properties, with the exception of β, were evaluated at the local reference temperature

$$T_r = T_w - 0.38(T_w - T_\infty)$$

while the coefficient of thermal expansion was taken to be $\beta = 1/T_\infty$. This is the procedure that has been recommended by Sparrow and Gregg (*38*).

The experimental data are illustrated in Fig. 18 and correspond to a Grashof number range of 1.6×10^7 to 1.3×10^9. Also shown in Fig. 18 are the limiting solutions for small and large ξ, Eqs. (92) and (102), as

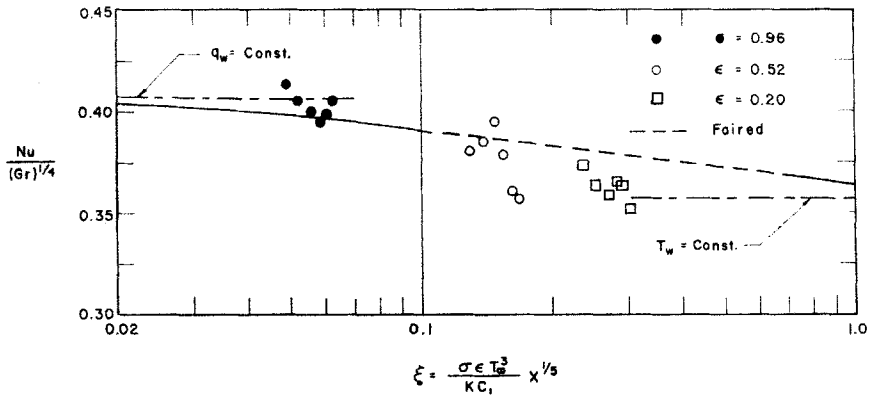

FIG. 18. Comparison of experimental and theoretical results for free convection from a vertical plate.

represented by the solid curves, while the broken curve denotes a straight-line fairing between the two limiting solutions. It may be seen that the data are in reasonably good agreement with the analytical and faired curves, the maximum discrepancy being 8%.

SYMBOLS

a	absorption coefficient
c_p	specific heat at constant pressure
e	black-body emissive power, σT^4
Gr	Grashof number, $g\beta x^3(T_w - T_\infty)/\nu^2$
H	incident radiation
I	intensity of radiation, time-rate of radiant energy transfer per unit solid angle per unit area normal to pencil of rays
k	thermal conductivity
L	distance between plates
Nu	Nusselt number, $q_{cw}x/(T_w - T_\infty)k$
Pr	Prandtl number ν/α
q	heat rate per unit area
R	radiosity, total radiant energy leaving a surface per unit time per unit area (i.e., sum of emitted and reflected radiation)
Re	Reynolds number, $u_\infty x/\nu$
t	dummy variable of integration

T	absolute temperature
u	velocity component in x-direction
v	velocity component in y-direction
x	distance measured along surface
y	distance measured normal to surface
α	thermal diffusivity
β	coefficient of thermal expansion
δ	boundary layer thickness
ϵ	total hemispherical emissivity
Θ	angle measured from normal
μ	absolute viscosity
μ	cos Θ
ν	kinematic viscosity
ρ	density
σ	Stefan-Boltzmann constant
τ	optical distance, $\int_0^y a\,dy$
τ_0	optical thickness, $\int_0^L a\,dy$
ω	solid angle

Subscripts:

1	lower plate
2	upper plate
c	conduction or convection
r	radiation
w	wall
∞	free-stream conditions

REFERENCES

1. J. C. Jaeger, *Proc. Cambridge Phil. Soc.* **46,** 634 (1950).
2. P. L. Chambre, *J. Appl. Phys.* **30,** 1683 (1959).
3. S. S. Arbarbanel, "On Some Problems in Radiative Heat Transfer," OSR Technical Report 59-531, April 1959.
4. R. Viskanta, "Heat Transfer in Thermal Radiation Absorbing and Scattering Media," AEC Research and Development Report ANL-6170, May 1960.
5. H. C. Hottel, "Some Problems in Radiative Transport," Lecture presented at International Heat Transfer Conference, Boulder, Colorado, 1961.
6. C. M. Usiskin and E. M. Sparrow, *Intern. J. Heat Mass Transfer* **1,** 28 (1960).
7. R. Goulard and M. Goulard, *Intern. J. Heat Mass Transfer* **1,** 81 (1960).
8. E. R. G. Eckert and R. M. Drake, "Heat and Mass Transfer," p. 391. McGraw-Hill, New York, 1959.
9. V. Kourganoff, "Basic Methods in Transfer Problems," Oxford Univ. Press (Clarendon), Oxford, 1952.
10. S. Chandrasekhar, "Radiative Transfer," pp. 373–374. Dover, New York, 1960.
11. J. O. Hirschfelder, C. F. Curtis, and R. Byron Bird, "Molecular Theory of Gases and Liquids," pp. 723–726. Wiley, New York, 1954.
12. W. H. McAdams, "Heat Transmission," pp. 82–86. McGraw-Hill, New York, 1954.
13. B. Kivel and K. Bailey, "Tables of Radiation from High Temperature Air," AVCO Research Report 21, December 1957.
14. P. D. Thomas, *J. Aerospace Sci.* **29,** 477 (1962).
15. R. Viskanta and R. J. Grosh, "Heat Transfer in a Thermal Radiation Absorbing and Scattering Medium," Intern. Heat Transfer Conf. Boulder, Colorado, 1961, p. 820.
16. R. Viskanta and R. J. Grosh, *Intern. J. Heat Mass Transfer* **5,** 729 (1962).
17. J. R. Howell and M. Perlmutter, "Monte Carlo Solution of Thermal Radiation Through Radiant Media Between Gray Walls," to be published in *J. Heat Transfer*
18. W. H. McAdams, "Heat Transmission," p. 63. McGraw-Hill, New York, 1954.
19. R. Viskanta and R. J. Grosh, *J. Heat Transfer* **84,** 63 (1962).
20. T. H. Einstein, "Radiant Heat Transfer with Flow and Conduction," to be issued as NASA Technical Report R-154 (1963).
21. R. Viskanta and R. J. Grosh, *Am. Rocket Soc. J.* **31,** 839 (1961).

22. R. Viskanta, "Interaction of Heat Transfer by Conduction, Convection and Radiation in a Radiating Fluid," to be published in *J. Heat Transfer*
23. E. A. Sidorov, "Radiant-Convective Heat Exchange in an Absorbing Medium," U. S. Atomic Energy Comission Translation AEC-Tr-4511.
24. J. T. Howe, "Radiation Emission Effects of the Equilibrium Boundary Layer in the Stagnation Region," NASA TN D-1031, 1961.
25. J. C. Y. Koh and C. N. DeSilva, *Am. Rocket Soc. J.* **32,** 739 (1962).
26. R. Viskanta and R. J. Grosh, *Intern. J. Heat Mass Transfer* **5,** 795 (1962).
27. H. Schlichting, "Boundary Layer Theory," pp. 116–121. McGraw-Hill, New York, 1960.
28. P. L. Donoughe and J. N. B. Livingood, "Exact Solutions of Laminar-Boundary-Layer Equations with Constant Property Values for Porous Wall with Variable Temperature," NACA Report 1229, 1958.
29. E. M. Sparrow and J. L. Gregg, "Prandtl Number Effects on Unsteady Forced-Convection Heat Transfer," NACA TN 4311, 1958.
30. M. Tribus and J. Klein, "Forced Convection from Nonisothermal Surfaces," p. 211. Heat Transfer Symposium, University of Michigan Press, Ann Arbor, Michigan, 1953.
31. J. P. Hartnett, E. R. G. Eckert, R. Birkebak, and R. L. Sampson, "Simplified Procedures for the Calculation of Heat Transfer to Surfaces with Non-Uniform Temperatures," WADC TR 56-373, ASTIA Doc. No. AD 110540, 1956.
32. R. D. Cess, *Appl. Sci. Res. Sect. A* **10,** 430 (1962).
33. M. J. Lighthill, *Proc. Roy. Soc. (London), Ser. A* **202,** 359 (1950).
34. E. M. Sparrow and J. L. Gregg, *J. Heat Transfer* **78,** 435 (1956).
35. E. M. Sparrow and J. L. Gregg, *J. Heat Transfer* **80,** 379 (1958).
36. S. Ostrach, "An Analysis of Laminar Free-Convection Flow and Heat Transfer About a Flat Plate Parallel to the Direction of the Generating Body Force," NACA Report 1111, 1953.
37. E. R. G. Eckert, J. P. Hartnett, and T. F. Irvine, Jr., *Jet Propulsion* **26,** 280 (1956).
38. E. M. Sparrow and J. L. Gregg, *J. Heat Transfer* **80,** 879 (1958).

Application of Integral Methods to Transient Nonlinear Heat Transfer

THEODORE R. GOODMAN

Oceanics, Inc., Plainview, New York

THEODORE R. GOODMAN

I. Introduction

The field equations which describe a physical phenomenon are frequently nonlinear. However, the analytical investigator linearizes them whenever possible in order to take advantage of the principle of superposition. The linear representation is an approximation, and can be expected to reproduce the true behavior fairly well whenever the nonlinearities are weak in some sense. Conversely, if the nonlinearities are strong, they must be included in order to explain the observed behavior. An example of the latter case, taken from the field of mechanics, is the hard or soft spring. Examples from the field of fluid mechanics are boundary layer growth and shock wave propagation.

In the field of heat transfer, and more especially heat conduction, the transient heat conduction equation is linearized by assuming the thermal properties to be independent of temperature; furthermore, the boundary conditions are also taken to be linear. When dealing with heat conduction in solids, the linear approximation is often quite acceptable. As a matter of fact, virtually all of the well-known treatise of Carslaw and Jaeger (*1*) is devoted to a presentation of solutions of linear transient heat conduction problems. However, if the temperature in the solid varies over a wide range the thermal properties become temperature dependent, the field equation becomes nonlinear, and the solution cannot be obtained by any of the elegant methods which Carslaw and Jaeger demonstrate. On the other hand, if the temperature level itself becomes high, radiation or change of phase may occur, and, as a consequence, the boundary conditions become nonlinear, and once again the elegant methods fail. The purpose of this chapter is to present a mathematical technique, called the integral method, by which approximate solutions to nonlinear transient heat conduction problems can be obtained. Such problems need not be linearized, because the technique is elastic enough to encompass all nonlinearities. The integral method reduces the nonlinear boundary value problem to an ordinary initial value problem whose solution can frequently be expressed in closed analytical form. The integral method can also be used to obtain approximate solutions to linear problems with complicated spacially-dependent thermal properties, and problems where convection as well as conduction is involved. The versatility of the method will be demonstrated by the presentation of many examples in the subsequent text.

In order to introduce those concepts which are basic to the integral method, we will use the method to obtain the solution to a very simple linear problem. Let us assume there is a semiinfinite slab extending over positive x. Initially, the temperature T is $-T_\infty$, and at the surface $x = 0$

the heat flux, $F(t)$, is given for time $t > 0$. If α is the thermal diffusivity, the heat conduction equation is

$$\alpha \frac{\partial^2 T}{\partial x^2} = \frac{\partial T}{\partial t}, \quad x > 0, \quad t > 0 \tag{1}$$

If k is the thermal conductivity, the boundary condition is

$$k \frac{\partial T}{\partial x} = -F(t) \qquad x = 0, \quad t > 0 \tag{2}$$

We now define a quantity $\delta(t)$ called the penetration distance. Its properties are such that for $x > \delta(t)$ the slab, for all practical purposes, is at an equilibrium temperature and there is no heat transferred beyond this point. The penetration distance is analogous to the boundary layer thickness in fluid mechanics. If Eq. (1) is multiplied by dx and integrated from 0 to δ, the resulting equation is called the heat-balance integral. The temperature will be compelled to satisfy the heat-balance integral, but not the original heat conduction equation, Eq. (1). The heat conduction equation will, thereby, be satisfied only on the average. This averaged equation is analogous to the momentum integral in boundary layer theory. Integral methods were first introduced by von Karman and Pohlhausen (*2*) in order to solve nonsimilar boundary layer problems in fluid mechanics. A modern account of the Karman-Pohlhausen method and a bibliography may be found in Schlichting (*3*). The method is, however, equally appropriate for solving any problem governed by a diffusion-type equation. Such problems as the nonsteady heat conduction in solids, the nonsteady flow of fluids through porous media, the mixing of two species, and (in the social sciences) the spreading of rumors all obey equations of this type. The integral method will be developed here in the context of heat transfer. The solutions thus obtained, although not exact, are often sufficiently accurate for engineering purposes.

The heat-balance integral obtained by averaging Eq. (1) in the manner described, becomes

$$\frac{d}{dt}(\theta + T_\infty \delta) = \alpha \left[\frac{\partial T}{\partial x}(\delta,t) - \frac{\partial T}{\partial x}(0,t) \right] \tag{3}$$

where

$$\theta = \int_0^{\delta(t)} T \, dx \tag{4}$$

But, since there is no heat transferred beyond $x = \delta$,

$$\frac{\partial T}{\partial x}(\delta,t) = 0 \tag{5}$$

Let us assume that T can be represented by a second-degree polynomial in x of the form: $T = \beta_0 + \beta_1 x + \beta_2 x^2$, where the coefficients β_i may depend on t. Applying Eqs. (2, 5) and the condition

$$T(\delta,t) = -T_\infty \tag{6}$$

the temperature profile must take the form

$$T = -T_\infty + \frac{F}{2k\delta}(\delta - x)^2 \tag{7}$$

Substituting into Eq. (4), it is seen that

$$\theta = -T_\infty \delta + \frac{\delta^2 F}{6k} \tag{8}$$

Introducing Eqs. (2, 5, 8) into the heat-balance integral, Eq. (3), gives the following ordinary differential equation to be solved for δ:

$$\frac{1}{6}\frac{d}{dt}(\delta^2 F) = \alpha F \tag{9}$$

By virtue of the initial condition, $\delta(0) = 0$,

$$\delta = \sqrt{(6\alpha)}\left[\frac{1}{F(t)}\int_0^t F(t_1)\,dt_1\right]^{1/2} \tag{10}$$

If $F(t)$ is constant this reduces to

$$\delta = \sqrt{(6\alpha t)} \tag{11}$$

The surface temperature is obtained by setting $x = 0$ in Eq. (7) and applying Eq. (10). The result is

$$T(0,t)[\equiv z] = -T_\infty + \sqrt{(3/2)}\,\sqrt{\alpha}\left[F(t)\int_0^t F(t_1)\,dt_1\right]^{1/2}\Big/ k \tag{12}$$

If $F(t)$ is constant this reduces to

$$z = -T_\infty + \sqrt{(3/2)}\,\sqrt{\alpha}\,F\,\sqrt{t}/k \tag{13}$$

The exact solution of this problem is given on page 75 of (*1*), and for a constant value of F, the result is

$$T(0,t) = -T_\infty + \sqrt{(4/\pi)}\,\sqrt{\alpha}\,F\,\sqrt{t}/k \tag{14}$$

By comparing Eqs. (13) and (14) it is seen that the results are of the same form, differing only by a numerical factor. Since $\sqrt{(4/\pi)} = 1.13$ and $\sqrt{(3/2)} = 1.23$, the error is about 9%. This error can be reduced by using a less primitive temperature profile than that represented by

Eq. (7), and also by using other methods which will be presented in the sections below. However, considering the crudity of the method, and of the assumed profile, it is remarkable that Eqs. (13) and (14) agree as well as they do. At interior points, where the temperature is lower, the per cent error is necessarily greater, but the temperatures are still fairly well represented.

It will be required, for subsequent development, to know the value of δ when $z = 0$. From Eqs. (10, 12) the result is

$$\delta_m = 2T_\infty k/F(t_m) \tag{15}$$

where t_m is the time at which $z = 0$ occurs, and can be obtained from Eq. (12) for variable heat flux, or from Eq. (13) for constant heat flux. Using Eq. (13), the result is

$$t_m = \frac{2}{3}\frac{T_\infty{}^2 k^2}{\alpha F^2} \tag{16}$$

All of the fundamental concepts basic to the integral method appear in the simple example presented above. Much of the material presented below will be devoted to the demonstration of the proper application of the method for various practical heat transfer problems. Included are problems in both conduction and convection, problems involving a change of phase, problems with polar and spherical symmetry, problems with nonlinear boundary conditions, and problems with temperature-dependent thermal properties.

Historically, the first applications of the integral method to solve the diffusion equation, Eq. (1), were made by Landahl (*4*) in the field of biophysics. Landahl was specifically concerned with the spread of a concentrate. In all the problems with which he dealt, the profile was chosen to be linear, and this is, of course, the most primitive profile possible. (An exception is one case which used an exponential profile, but the end result was dismissed as being no significant improvement over the result obtained using a linear profile.) Landahl subsequently applied his version of the integral method to a variety of nonlinear problems governed by an equation of the diffusion type (*5*, *6*). The case of concentration-dependent properties was discussed by Macey (*7*) but still using a linear profile. A presentation of some of this early work appears in Rashevsky (*8*).

A more sophisticated approach was adopted by Veinik (*9*) in applying the integral method to heat conduction problems. He always assumed the profile to be a polynomial, and applied the integral method to a great number of cases. None of these early investigators were concerned with a rational approach toward improving the accuracy of the integral method.

Although we will also apply the integral method to a number of cases, nevertheless, the objective of this article is to acquaint the reader with the integral method as a mathematical technique. With this purpose in mind, the applications will be used primarily for illustrative purposes. The integral method has been advanced beyond the rudimentary stage by virtue of the efforts of many investigators whose work will be discussed. Thus, in addition to presenting examples of the application of the method, we will also present techniques for improving the accuracy of the method; we will compare the method with other related methods; we will demonstrate the limitations of the method, and suggest how these limitations may be overcome.

II. The Linear Heat Conduction Equation with Fixed Boundaries

In this section, we will consider problems involving the transient heat conduction equation in one space variable. Thermal properties will be taken to be constant so that the governing equation is linear. Both linear and nonlinear boundary conditions will be considered. The crude second degree polynomial for the temperature profile, which was assumed in the example problem presented in Section I, will usually be discarded in favor of a more convenient or appropriate profile.

A. THE SEMIINFINITE SLAB

The temperature distribution in a semiinfinite slab, initially at zero temperature [$T_\infty = 0$] and subject to a very general boundary condition, has been obtained by Goodman (*10*) [see also (*17*)] using the integral technique. In Section I the solution was obtained assuming the surface heat flux to be a prescribed function of time. A generalization of this condition is the assumption that the heat flux is a prescribed function of surface temperature and time:

$$\frac{\partial T}{\partial x}(0,t) = -f[z,t] \tag{17}$$

The temperature profile will be taken to be a cubic, in which case four conditions are required to determine the four constants. Three of these conditions are Eqs. (5, 6, 17) which are the natural conditions. An additional derived condition can be obtained by differentiating Eq. (6) with respect to time and applying Eqs. (1, 5). The resulting derived condition is

$$\frac{\partial^2 T}{\partial x^2}(\delta,t) = 0 \tag{18}$$

Equation (18) is sometimes called the smoothing condition because it

tends to make the profile go smoothly into the ambient temperature. Clearly, the cubic profile must take the form

$$T = \frac{z}{\delta^3}(\delta - x)^3 \tag{19}$$

where

$$\delta = 3z/f(z,t) \tag{20}$$

Equation (20) expresses a relationship between surface temperature and the penetration distance. As a consequence, there is really only one unknown function of time in Eq. (19), and this will be obtained from the heat-balance integral. Upon integrating Eq. (1) from $x = 0$ to $x = \delta$ and applying Eqs. (5, 17) we obtain

$$\alpha f = \frac{d\theta}{dt} \tag{21}$$

By substituting Eq. (19) into Eq. (4) and performing the integration, we obtain the quantity θ in terms of z and δ. After eliminating δ by using Eq. (20), we obtain the following ordinary differential equation for z:

$$\tfrac{4}{3}\alpha f(z,t) = \frac{d}{dt}\left(\frac{z^2}{f(z,t)}\right) \tag{22}$$

The proper initial condition is $z = 0$ when $t = 0$. If the function $f(z,t)$ is dependent on both z and t Eq. (22) must be integrated numerically. However, there are two cases for which Eq. (22) can be integrated analytically: when f depends solely on z, and when f depends solely on t.

Case (a)—If f is independent of t, the solution is

$$\tfrac{4}{3}\,\alpha t = \int_0^z \frac{[2z_1 f(z_1) - z_1^2 f'(z_1)]\,dz_1}{[f(z_1)]^3} \tag{23}$$

Case (b)—If f is independent of z, the problem becomes identical to the one solved in Section I, except that the profile in Section I is a quadratic, whereas here it is a cubic. We are therefore able to compare the results obtained using a quadratic profile with those obtained using a cubic profile. The result is

$$z = \left[\tfrac{4}{3}\,\alpha f(t) \int_0^t f(t_1)\,dt_1\right]^{1/2} \tag{24}$$

which is, of course, the cubic profile equivalent of Eq. (12).

1. Applications of Goodman's Solution

If f is constant, Eq. (24) reduces to

$$z = \sqrt{\tfrac{4}{3}}\, f \sqrt{\alpha t} \tag{25}$$

which is the cubic profile equivalent of Eq. (13). Since $\sqrt{4/3} = 1.15$, and the exact factor $\sqrt{4/\pi} = 1.13$, the error has been reduced from 9% to 2% by using a cubic instead of a quadratic profile.

As an example of Eq. (23) suppose

$$f(z) = \frac{h}{k}(z' - z) \tag{26}$$

where h and z' are constants and represent, respectively, the heat transfer coefficient and the ambient temperature of the surrounding medium. The result is

$$\frac{4}{3}\left(\frac{h}{k}\right)^2 \alpha t = \frac{1}{2}\left\{\frac{1}{[1 - (z/z')]^2} - 1\right\} + ln\,[1 - (z/z')] \tag{27}$$

The exact solution is given both analytically and graphically on page 72 of (*1*). To the scale of the graph presented there, it is impossible to detect any error in Eq. (27).

Equation (23) may be applied to a nonlinear problem. Suppose

$$f(z) = (H/k)(z + T_0)^4 \tag{28}$$

This represents a slab of absolute temperature T_0 radiating into a sink of absolute temperature zero. The result is

$$\frac{\alpha t H^2 T_0^6}{k^2} = \frac{3}{2\eta^8}\left[\frac{\eta^2}{6} - \frac{3\eta}{7} + \frac{1}{4}\right] + \frac{1}{56} \tag{29}$$

where

$$\eta = 1 + z/T_0 \tag{30}$$

This problem has been solved by Jaeger (*11*) by numerical integration of the heat conduction equation. In this case also, it is impossible to detect any error in Eq. (29) when it is superimposed on the graph which Jaeger presents.

Schneider (*12*) has generalized the solution given by Eq. (29) to a slab of finite thickness (plate) radiating into a sink of finite temperature. The case of zero sink temperature can be expressed in closed form; other cases must be integrated numerically. For further details see Schneider's paper. (See Section II, B, however, for a general discussion of slabs of finite thickness.)

Chambre (*13*) has considered, from a different point of view, the semi-infinite slab with a boundary condition of the form of Eq. (17) without t dependence (although there is no reason, in principle, why t dependence could not have been included). Since the field equation is linear, the surface temperature can be expressed as a convolution-type integral in

terms of the surface heat flux using standard methods (e.g., LaPlace transforms). Then, by virtue of Eq. (17), Chambre is led to the following nonlinear integral equation for the surface temperature:

$$z(t) = z_0 + \sqrt{\frac{\alpha}{\pi}} \int_0^t \frac{f[z(\tau)]\, d\tau}{(t-\tau)^{1/2}} \tag{31}$$

where z_0 is the initial temperature of the slab [$\equiv -T_\infty$]. Upon substituting an approximate solution into the right-hand side of Eq. (31), he is led to an improved solution which he again substitutes into the right-hand side. By continuing in this way, very accurate results can be obtained after only a few iterations, provided, of course, that the initial guess is reasonably accurate. It is clear that this method of attack could be used for any problem in which the nonlinearities appear only in the boundary conditions; for, if the differential equation is linear, an integral equation can always be derived. Schapker (*14*) has discussed the derivation of such integral equations. In using the integral equation approach together with an iteration procedure, two questions arise: the convergence of the iteration procedure, and the choice of the initial guess. For the semiinfinite slab, Chambre has outlined the convergence proof and the conditions under which it is valid. The best choice for the initial guess, as suggested by Chambre, is the solution obtained by the integral method. Thus, the iteration scheme becomes a technique for improving the integral method. Arbarbanel (*15*) has also used the integral equation approach, together with an iteration procedure. He has applied the technique to the slab of finite thickness and the sphere, each of which is subjected to the radiation boundary condition. He does not, however, use the integral method to obtain the initial guess in the iteration procedure.

2. The Step in Surface Temperature

A case of special interest is the semiinfinite slab initially at zero temperature whose face is suddenly raised to temperature T_s. Applying Eqs. (5, 6, 18) with $T_\infty \equiv 0$, together with the boundary condition

$$T(0,t) = T_s \tag{32}$$

the cubic profile must take the form

$$T = T_s[1 - x/\delta]^3 \tag{33}$$

Substituting into Eqs. (3, 4) we are led to a differential equation for δ whose solution is

$$\delta = \sqrt{24\alpha t} \tag{34}$$

The surface heat flux is, therefore,

$$k \left.\frac{\partial T}{\partial x}\right|_0 = -\frac{\sqrt{\frac{3}{8}}T_s k}{\sqrt{\alpha t}} \tag{35}$$

The exact solution of this problem is given on page 63 of (*1*) and is identical to Eq. (35) except that the numerical factor $\sqrt{\frac{3}{8}} = .602$ is replaced by $\sqrt{1/\pi} = .564$. The error is about 7%. Reynolds and Dolton (*16*) have used the integral method to analyze this problem, but their result differs from the one presented here because of a different selection of the derived condition on the cubic profile. Instead of using the smoothing condition, Eq. (18), they obtain a derived condition by differentiating Eq. (32) and applying Eq. (1). They are then led to a surface heat flux of the form of Eq. (35) except that the numerical factor is replaced by $\sqrt{\frac{9}{32}} = .530$. The error in this case is about 6%. This difference in approach is illustrative of a general property of the integral method; viz., the choice of profile is never unique, and the error in the final solution depends, to a large extent, on a judicious choice of the profile. Thus, there is a certain ambiguity in the method, which can only be resolved by investing it with mathematical rigor. For those problems to which it applies, Chambre's iteration scheme (*13*) is precisely the rigor required; for, by virtue of the convergence proof, we have a guarantee that, whatever the assumed profile, we can come as close to the correct solution as desired. For the particular case under consideration, the iteration can be said to converge in one step; for, by substituting Eq. (35) (which has the same form as the exact solution) into Eq. (31), the surface temperature is seen to be indeed a constant, but the wrong constant. It may then be adjusted, and the iteration is complete.

The solution for the step in temperature given by Eqs. (33, 34) can be used to generate an approximate solution for the semiinfinite slab with arbitrary time-dependent surface temperature $T_s(t)$ by use of Duhamel's integral:

$$T(x,t) = T_s(0)[1 - x/\delta(t)]^3 + \int_0^t T_s'(\tau)[1 - x/\delta(t-\tau)]^3 d\tau \tag{36}$$

where $\delta(t)$ is given by Eq. (34).

3. Internal Heat Generation

Suppose there is internal heat generation $q(t)$ per unit time per unit volume, and the surface temperature is fixed at zero. Initially, the slab is at zero temperature. Equation (1) is replaced by

$$\frac{\partial T}{\partial t} - \alpha \frac{\partial^2 T}{\partial x^2} = \frac{q(t)}{\rho c} \tag{37}$$

Assume once again a cubic profile. Two of the natural conditions are: Eq. (5), and Eq. (32) with $T_s = 0$. The third natural condition is obtained by applying Eq. (37) far from the boundary where no temperature gradient exists:

$$T(\delta,t) = \frac{Q(t)}{\rho c} \equiv \frac{1}{\rho C}\int_0^t q(t)\,dt \tag{38}$$

The derived condition can be obtained by differentiating Eq. (38) and applying Eqs. (5, 37). The result is once again Eq. (18), and the heat balance integral takes the form

$$\frac{d}{dt}\left[\theta - \frac{Q(t)\delta}{\rho c}\right] = -\alpha\frac{\partial T}{\partial x}(0,t) \tag{39}$$

The temperature profile is

$$T = \frac{Q}{\rho c}[1 - (1 - x/\delta)^3] \tag{40}$$

The solution is

$$\delta = \left[\frac{24\alpha\int_0^t Q^2\,dt}{Q^2}\right]^{1/2} \tag{41}$$

B. THE SLAB OF FINITE THICKNESS

Goodman (*17*) has obtained the temperature distribution in a slab of thickness l, initially at zero temperature, and subject to boundary condition Eq. (17) at $x = 0$ and to the isothermal condition at $x = l$:

$$T(l,t) = 0 \tag{42}$$

Initially, the effect of the boundary condition at $x = l$ is not felt, and the slab behaves as though it were semiinfinite. For this initial stage, therefore, Eq. (22) applies. As soon as $\delta = l$, however, the initial stage is complete, and the time at which this occurs can be obtained by setting $\delta = l$ in Eq. (20). In the second stage, the concept of penetration distance has no meaning, and, consequently, only three conditions are required to specify the coefficients of the cubic profile. Two of these are the two natural conditions, Eqs. (17, 42). The third condition can be derived by differentiating Eq. (42) with respect to time and applying Eq. (1):

$$\frac{\partial^2 T}{\partial x^2}(l,t) = 0 \tag{43}$$

The cubic temperature profile must then take the form:

$$T = \left(\frac{3}{2}\frac{z}{l} - \frac{1}{2}f\right)(l - x) + \frac{1}{2l^2}\left(f - \frac{z}{l}\right)(l - x)^3 \tag{44}$$

The surface temperature, z, will be determined from the heat-balance integral, where, in this case, the integration extends from 0 to l. We are then led to the following differential equation for z:

$$\frac{12\alpha}{l^2}\left[f(z,t) - \frac{z}{l}\right] = \frac{d}{dt}\left[5\frac{z}{l} - f(z,t)\right] \tag{45}$$

Once again, there are two cases for which the equation can be integrated directly: when f depends solely on z, and when f depends solely on t.

Case (a)—If f is independent of t, the solution is:

$$\frac{12\alpha}{l^2}(t - t_0) = \int_{z_0}^{z} \frac{\frac{5}{l} - f'(z_1)}{f(z_1) - z_1/l}\,dz_1, \quad t \geq t_0 \tag{46}$$

The constants t_0 and z_0 define the end of the initial stage and the beginning of the second stage. These constants may be determined from the semiinfinite slab solution when $\delta = l$. Explicitly, set $\delta = l$ in Eq. (20) to determine z_0, and set $z = z_0$ in Eq. (23) to determine t_0.

Case (b)—If f is independent of z, the solution is:

$$z = \frac{l}{5}f(t) + \left[z_0 - \frac{l}{5}f(t_0)\right]e^{-(12\alpha/5l^2)(t-t_0)} + \frac{48\alpha}{25l}\int_{t_0}^{t} f(t_1)e^{-(12\alpha/5l^2)(t-t_1)}\,dt_1 \qquad t \geq t_0 \tag{47}$$

The constants t_0 and z_0 in this case are determined by setting $\delta = l$ in Eq. (20), and $t = t_0$ in Eq. (24).

1. Application of Goodman's Solution

Only one simple application of the general formulas will be presented, viz. the case f = constant. Equation (47) then reduces to:

$$z = fl[1 - .814\exp(-2.4\alpha t/l^2)] \qquad t > t_0 \tag{48}$$

The exact solution appears on p. 113 of (*1*) in terms of an infinite series of eigenfunctions. For large time, it is sufficient to retain only the first eigenfunction. If this is done, the result is:

$$z = fl\left[1 - \frac{8}{\pi^2}\exp - \frac{\pi^2}{4}\alpha t/l^2\right] \tag{49}$$

By comparing Eqs. (48) and (49), it is seen that the exact value of the eigenvalue is $\pi^2/4 = 2.467$ instead of 2.4, while the exact coefficient of the exponential is $8/\pi^2 = .811$ instead of .814. In Section VII it will be demonstrated how the integral method may be used to generate the

higher eigenfunctions and eigenvalues, while simultaneously improving the accuracy.

2. The Step in Surface Temperature

Reynolds and Dolton (*16*) have carried out the calculation of the temperature in a finite slab initially at zero temperature, whose surface temperature is suddenly raised to T_s, and whose far surface, $(x = l)$, is insulated:

$$\frac{\partial T}{\partial x}(l,t) = 0 \tag{50}$$

The derived condition for the cubic profile is obtained by differentiating Eq. (32) and applying Eq. (1):

$$\frac{\partial^2 T}{\partial x^2}(0,t) = 0 \tag{51}$$

The profile is then of the form:

$$\frac{T}{T_s} = 1 + \gamma\left[\frac{x}{l} - \frac{1}{3}\left(\frac{x}{l}\right)^3\right] \tag{52}$$

where the parameter γ satisfies the differential equation:

$$\frac{d\gamma}{dt} + \frac{12}{5}\frac{\alpha}{l^2}\gamma = 0 \tag{53}$$

which is obtained from the heat-balance integral. The initial condition which we will apply to Eq. (53) is slightly different from the one used by Reynolds and Dolton (*16*) because the solution in the initial stage is different (see Section II, A, 2). By equating the surface temperature gradient with that for the initial stage at the time when $\delta = l$, we are led to the condition $\gamma(t_0) = -3$. The complete solution is:

$$\gamma = -3e^{-[12/5(\alpha/l^2)t - 1/10]} \tag{54}$$

The exact solution appears on page 101 of (*1*) in terms of an infinite series of eigenfunctions. The first term of the series is:

$$\gamma = \frac{l}{T_s}\frac{\partial T}{\partial x}(0,t) = -2e^{(-\pi^2/4)(\alpha/l^2)t} \tag{55}$$

A numerical comparison between Eqs. (54, 55) demonstrates the accuracy.

C. PROFILES REPRESENTED BY FUNCTIONS OTHER THAN POLYNOMIALS

Up to this point, all profiles have been represented by polynomial expressions. It is sometimes more advantageous to use some other type

of profile which invariably takes the form of a nonalgebraic function multiplied by a polynomial. The advantage of so doing lies in the greater accuracy achievable. This will be illustrated by three examples.

1. Polar and Spherical Symmetry

Lardner and Pohle (*18*) have demonstrated that, for problems involving polar or spherical symmetry, the polynomial representation of the profile is inappropriate because the solution does not tend to the proper form of the steady state solution in the limit for large time. They argue that the volume into which heat diffuses does not remain the same for equal increments of r (radius) as in the planar case, and, as a consequence, a modification in the assumed profile is necessary. Indeed, in the case of polar symmetry, the heat conduction equation becomes:

$$\frac{\partial}{\partial t}(rT) = \alpha \frac{\partial}{\partial r}\left(r \frac{\partial T}{\partial r}\right) \tag{56}$$

The heat-balance integral becomes:

$$\frac{d\theta}{dt} = \alpha r \frac{\partial T}{\partial r}\Bigg|_a^b \tag{57}$$

where

$$\theta = \int_a^b rT\, dr \tag{58}$$

and the suggested form of the profile is:

$$T = (\text{polynomial in } r)\ lnr \tag{59}$$

Similarly, in the case of spherical symmetry, since the steady state solution is proportional to $1/r$, the suggested profile is:

$$T = \frac{(\text{polynomial in } r)}{r} \tag{60}$$

Lardner and Pohle then proceed to solve an explicit case having polar symmetry using both a polynomial profile, and a profile in the form of Eq. (59). By comparing the results with the known exact solution of the problem, they clearly demonstrate the superiority of Eq. (59). For further details, the reader is referred to Lardner and Pohle's paper.

2. One Fluid Heat Exchanger

Reynolds and Dolton (*16*) have applied the integral method to the transient cooling of a single-fluid heat exchanger. The exchanger consists of a tube of length l through which the fluid flows. At time zero-minus, the exchanger is in steady state, with the wall temperature held at

$T_w = T_i$ by an appropriate heat source. At time zero, the heat source is removed and the exchanger cools. It is assumed that conduction is absent in both the tube and the fluid, and the heat which is exchanged between them is proportional to the temperature difference. The wall and fluid temperatures are then functions only of time (t) and the longitudinal distance along the tube (x). An energy balance in the solid leads to the equation:

$$\frac{d}{dt}\int_0^l T_w\,dx + \beta\int_0^l (T_w - T_f)\,dx = 0 \tag{61}$$

where T_f is the temperature of the fluid. The energy balance in the fluid is obtained assuming that the change of energy storage in the fluid is small compared with the energy transferred to it from the wall:

$$\frac{dT_f}{dx} = \frac{\alpha}{l}(T_w - T_f) \tag{62}$$

If the wall temperature were constant, the solution would be:

$$T_i - T_f = T_i e^{-\alpha x/l} \tag{63}$$

This steady state solution suggests we assume a profile of the form:

$$T_i - T_f = T_i e^{-ax/l} \tag{64}$$

where a is a time-dependent parameter to be determined. This assumed form is chosen in the same spirit as Lardner and Pohle's profiles for polar and spherical symmetry. In both cases, the form is suggested by the steady state solution. If the wall temperature is also assumed to have an exponential profile, such that Eq. (62) is satisfied uniformly, it must take the form:

$$T_i - T_s = T_i\left(1 - \frac{a}{\alpha}\right)e^{-ax/l} \tag{65}$$

Substituting Eqs. (64, 65) into Eq. (61), Reynolds and Dolton are led to the following differential equation for a:

$$\left\{\frac{1}{a^2} - \frac{e^{-a}}{a(1-e^{-a})} + \frac{1}{\alpha}\frac{e^{-a}}{1-e^{-a}}\right\}\frac{da}{dt} + \frac{\beta}{\alpha} = 0 \tag{66}$$

subject to the initial condition $a(0) = \alpha$. From a graphical comparison of the exact solution [see page 123 of Bateman (*19*)] with the one obtained by integrating Eq. (66), they conclude that the results agree quite well for $\alpha < 5$, which is the range of most practical heat exchangers.

3. Heat Conduction in Rods

The heat conduction equation in a rod of constant cross section is given, for example, in Chapter IV of (*1*):

$$\frac{\partial T}{\partial t} = \alpha \frac{\partial^2 T}{\partial x^2} - \nu T \tag{67}$$

where ν is related to the heat transfer coefficient between the rod and its surroundings. The steady state solution for a semi-infinite rod whose end $x = 0$ is maintained at constant temperature T_s is:

$$T = T_s e^{-\sqrt{\frac{\nu}{\alpha}}x} \tag{68}$$

Now suppose that at time zero-minus, the rod is at zero temperature, and at time zero, the end temperature is suddenly raised to T_s. We assume a profile of the form

$$T = T_s e^{-x/b} \tag{69}$$

which is suggested from the steady state solution, Eq. (68). Upon integrating Eq. (67) from $x = 0$ to $x = \infty$, the heat balance integral becomes

$$\frac{\partial \theta}{\partial t} = -\alpha \frac{\partial T}{\partial x}(0,t) - \nu\theta \tag{70}$$

where

$$\theta = \int_0^\infty T\, dx \tag{71}$$

After performing the indicated operations, there is obtained the following differential equation for b:

$$\frac{db}{dt} = \frac{\alpha}{b} - \nu b \tag{72}$$

subject to the condition $b(0) = 0$. The solution is

$$b = \sqrt{\frac{\alpha}{\nu}}\sqrt{1 - e^{-2\nu t}} \tag{73}$$

The temperature gradient at $x = 0$ is

$$\frac{\partial T}{\partial x} = -\frac{T_s\sqrt{\frac{\nu}{\alpha}}}{\sqrt{1 - e^{-2\nu t}}} \tag{74}$$

The exact solution of this problem is given on p. 135 of (*1*). The exact

temperature gradient at $x = 0$ is given by:

$$\frac{\partial T}{\partial x} = -T_s \sqrt{\frac{\nu}{\alpha}} \left[1 + \frac{e^{-\nu t}}{\sqrt{\nu \pi t}} \right] \tag{75}$$

Equations (74, 75) are shown plotted in Fig. 1. The accuracy of the approximate solution can be improved by using a profile consisting of a polynomial multiplied by an exponential, where additional constraints can be derived by differentiating the boundary condition at $x = 0$.

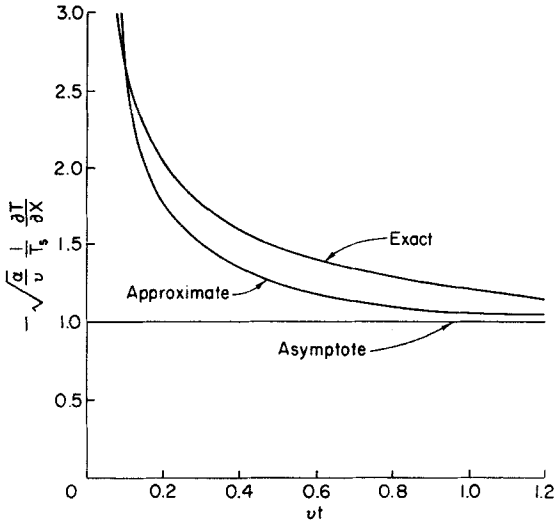

FIG. 1. Temperature gradient time history at the end of a semiinfinite rod with isothermal end—comparison between exact and integral solution.

D. CONCLUDING REMARKS

The examples presented above are not intended to be exhaustive, but merely illustrative of the manner in which the integral method reduces a heat transfer problem to an ordinary differential equation. As pointed out by Reynolds and Dolton (*16*), the integral method is really a generalization of the "lumped parameter" method in which the temperature of the thermal capacitor is no longer idealized as constant, but is allowed to have some spatial distribution.

In all the problems considered in this section, the initial temperature has been assumed to be constant or, more usually (and with no loss in generality), zero. No consideration has been given to problems in which there is an initial distribution of temperature. The reason for this is that the integral method, as presented, cannot deal with problems of

this type. One possible approach to this type of problem is to utilize a theorem of Goodman (*20*) which states that the solution of any linear problem can always be expressed in terms of its adjoint; the adjoint is merely another heat conduction problem with time running backwards which *always* has zero initial temperature. The integral method can thus be employed indirectly to solve linear problems with nonuniform initial temperature; for, by solving the adjoint problem using the integral method, and then applying Goodman's theorem which relates the actual problem to its adjoint, the solution to the actual problem may be obtained. Other approaches which are applicable to both linear and nonlinear problems will be presented in Section VII where generalizations of the integral method are presented.

III. Temperature-Dependent Thermal Properties

When the thermal properties depend on temperature, Eq. (1) is replaced by

$$\rho c \frac{\partial T}{\partial t} = \frac{\partial}{\partial x}\left(k \frac{\partial T}{\partial x}\right) \tag{76}$$

Both k and ρc are here assumed to be temperature-dependent. At this point, we make a transformation of the dependent variable as suggested by Goodman (*21*):

$$v = \int_0^T \rho c \, dT \tag{77}$$

The quantity v is a single valued function of the temperature T. In terms of the new variable, the heat conduction equation, Eq. (76), becomes

$$\frac{\partial v}{\partial t} = \frac{\partial}{\partial x}\left[\alpha(v) \frac{\partial v}{\partial x}\right] \tag{78}$$

A. THE SEMIINFINITE SLAB

The slab is assumed to be initially at zero temperature. At the surface, either the temperature or the heat flux is prescribed:

$$T = T_s, \qquad x = 0 \tag{79a}$$

$$k \frac{\partial T}{\partial x} = -F(t) \quad x = 0 \tag{79b}$$

The designations a and b will continue to refer, respectively, to the case of prescribed surface temperature and prescribed surface heat flux.

In terms of the transformed variable v, the boundary condition becomes

$$v = v_s, \qquad x = 0 \tag{80a}$$

$$\frac{\partial v}{\partial x} = -F(t)/\alpha_s \quad x = 0 \tag{80b}$$

We will adopt a cubic profile for v. The assumption that v is a polynomial does not lead to the correct steady state limit; however, the polynomial representation is adequate provided the thermal properties of the material do not vary rapidly with temperature. This characteristic applies to most materials. The cubic must take the form

$$v = v_s(1 - x/\delta)^3 \tag{81a}$$

$$v = \frac{F\delta}{3\alpha_s}(1 - x/\delta)^3 \tag{81b}$$

Upon integrating Eq. (78) from $x = 0$ to $x = \delta$ and applying Eqs. (81), we obtain the following heat balance integrals:

$$\frac{d\theta}{dt} = 3\alpha_s v_s/\delta \tag{82a}$$

$$\frac{d\theta}{dt} = F(t) \tag{82b}$$

where, in both cases,

$$\theta = \int_0^\delta v\, dx \tag{83}$$

Substituting Eqs. (81) into Eq. (83), and using the results in Eqs. (82), we obtain the following differential equations for δ:

$$\frac{d}{dt}\left(\frac{v_s\delta}{4}\right) = \frac{3\alpha_s v_s}{\delta} \tag{84a}$$

$$\frac{d}{dt}\left(\frac{F\delta^2}{12\alpha_s}\right) = F \tag{84b}$$

Notice that only the thermal properties at the surface are involved when the problem is cast in terms of the transformed variable v. The solutions of Eqs. (84), subject to the initial condition $\delta(0) = 0$, are

$$\delta = \frac{2\sqrt{6}}{v_s}\left[\int_0^t \alpha_s v_s^2\, dt\right]^{1/2} \tag{85a}$$

$$\delta = 2\sqrt{3}\left[\frac{\alpha_s}{F}\int_0^t F\, dt\right]^{1/2} \tag{85b}$$

Equations (77, 81a, 85a) comprise the solution for prescribed surface temperature in terms of quadratures. For prescribed surface heat flux, the solution would correspondingly be given by Eqs. (77, 81b, 85b), except that the diffusivity at the surface α_s is given in terms of the surface temperature which is not yet known. However, v_s may be determined in terms of δ by setting $x = 0$ in Eq. (81b). Upon eliminating δ between the resulting equation and Eq. (85b), the following transcendental equation for v_s is obtained:

$$\sqrt{\alpha_s}\, v_s = \sqrt{4/3}\, F^{1/2} \left[\int_0^t F\, dt \right]^{1/2} \tag{86}$$

Once v_s and therefore α_s has been determined as a function of time by solving Eq. (86), the complete solution is given by Eqs. (77, 81b, 85b).

As an application of Eq. (85a), suppose the prescribed surface temperature is a step, so that v_s is constant. Since α_s depends solely on v_s, α_s is also constant, and Eq. (85a) reduces to

$$\delta = \sqrt{24 \alpha_s t} \tag{87}$$

which is a generalization of Eq. (34). Upon substituting into Eq. (81a) we obtain

$$\frac{v}{v_s} = \left[1 - \frac{x}{2\sqrt{6\alpha_s t}} \right]^3 \tag{88}$$

Suppose that ρc is constant. By virtue of Eq. (77), v is then proportional to u. At the same time, let $k = k_0(1 + \alpha T/T_s)$ describe the temperature variation of the thermal conductivity. It follows that $\alpha_s = k_0(1 + \alpha)/\rho c$. Let $y = x\sqrt{\rho c}/2\sqrt{k_0 t}$, and Eq. (88) then becomes

$$\frac{T}{T_s} = \left[1 - \frac{y}{\sqrt{6(1 + \alpha)}} \right]^3 \tag{89}$$

This closed form solution is plotted in Fig. 2, and compared with the exact solution of Yang (*22*). Also shown in Fig. 2 is a comparison of $-d/dy\ (T/T_s)\ y = 0$ as calculated exactly by Yang, and as calculated approximately from Eq. (89). The heat flux at the surface is directly proportional to this quantity.

B. OTHER GEOMETRIC CONFIGURATIONS

The transformation given by Eq. (77) is generally applicable to all problems with temperature-dependent thermal properties. For example, upon applying the transformation to problems with polar symmetry we

obtain

$$\frac{\partial}{\partial t}(rv) = \frac{\partial}{\partial r}\left(\alpha r \frac{\partial v}{\partial r}\right) \tag{90}$$

The finite slab with variable thermal properties and an insulated far boundary has been analyzed by Koh (*23*) using the integral method. Koh assumes an exponential profile, although there does not appear to be any rationale for so doing.

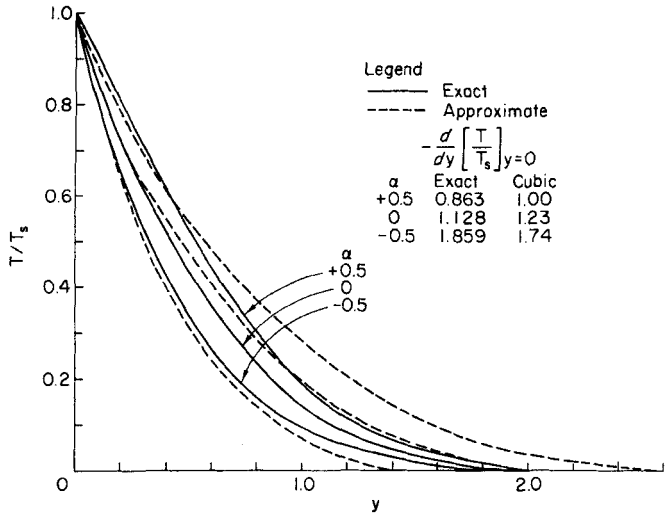

FIG. 2. Temperature profiles in a semiinfinite slab with linear dependence of thermal conductivity on temperature—comparison between exact and integral solution using cubic profile (*21*).

IV. Problems Involving a Change of Phase

Problems in which melting or freezing occur fall into two categories. For some materials, there is no distinct line of demarcation between the liquid and solid phases. These materials are called glassy, and the two phases are distinguished mainly by a gradual change in the physical properties of the material. If the fluid phase can flow, the problem becomes one of fluid mechanics with a coupling between the energy and momentum equations because the viscosity is strongly temperature-dependent and increases rapidly into the "solid" phase. Such fluid flow problems are beyond the scope of the present article and will not be considered. Other materials possess a definite line of demarcation between the liquid and solid phases, called the melt line. Typical of such materials are the metals and ice. We will deal exclusively with materials of this type.

In addition to melting, heated materials may also vaporize by passing through a liquid phase or by sublimating, provided the temperature becomes high enough or the vapor pressure is low enough. When vaporization occurs there is always a vaporization line. Examples of all of these cases will be presented, and we will concentrate on problems in one space dimension. It will be assumed in all problems that the thermal properties in each phase are constants, but they will, in general, be different constants in each phase. Conditions in the solid phase will be designated by a subscript 2, and in the liquid phase by a subscript 1. The field equation in each phase will be Eq. (1) with the appropriate subscript. Throughout these problems, a quadratic profile in each phase will be used. Let $x = s(t)$ define the location of the melt line. The melting temperature will always be taken to be zero, thus,

$$T[s(t),t] = 0 \tag{91}$$

From a heat balance across the melt line

$$k_2 \frac{\partial T_2}{\partial x} - k_1 \frac{\partial T_1}{\partial x} = \pm \rho_2 L \frac{ds}{dt}, \; x = s(t) \tag{92}$$

where L is the latent heat of melting, and the upper sign is to be taken for freezing problems and the lower sign for melting problems. This equation states, in mathematical terms, that the difference between the heat flux entering and leaving the melt line equals the latent heat absorbed or emitted.

Goodman (*24*) has solved a number of problems involving a change of phase, some of which will now be presented. All of these problems have one feature in common: viz., there is a temperature variation in only one phase. This feature offers tremendous mathematical simplifications in the analysis. Some of the problems are correctly formulated in this way, while for others this formulation constitutes an approximation. In the latter case, Evans *et al.* (*25*) have presented a discussion of the effect of the approximation on the meaning of the results.

A. MELTING OF A SOLID WITH STEP IN SURFACE TEMPERATURE[1]

In accordance with the approximation mentioned above, it will be assumed that the solid is at the melting temperature. Equation (92) then simplifies to

$$\frac{\partial T}{\partial x}(s,t) = A_1 \frac{ds}{dt} \tag{93}$$

where $A_1 = \rho L/k$, and the subscripts have been dropped since there is

[1] The solution is equally applicable to the freezing of a liquid.

only one phase. The condition at the surface is Eq. (32). Equations (1, 32, 91, 93) constitute a complete statement of the problem. Upon integrating Eq. (1) from $x = 0$ to $x = s$, and applying Eq. (93) we are led to the following heat balance integral:

$$\frac{d\theta}{dt} = -\alpha\left[A_1\frac{ds}{dt} + \frac{\partial T}{\partial x}(0,t)\right] \tag{94}$$

where

$$\theta = \int_0^{s(t)} T\,dx \tag{95}$$

Let T be represented by a second-degree polynomial in x. Two of the three conditions required to determine the constants are Eqs. (32, 91). The third condition is Eq. (93). But in its present form, Eq. (93) is not suitable because the coefficients in the polynomial would involve ds/dt. In turn, θ would involve ds/dt, and the heat-balance integral would then be a second-order differential equation for $s(t)$, whereas there is only one initial condition for s, namely, $s(0) = 0$. To circumvent this difficulty, we will cast Eq. (91) into a different form. By differentiating Eq. (91) with respect to t we obtain:

$$\frac{\partial T}{\partial x}\frac{ds}{dt} + \frac{\partial T}{\partial t} = 0 \tag{96}$$

Upon eliminating ds/dt between Eqs. (93, 96), it follows that

$$\left(\frac{\partial T}{\partial x}\right)^2 = A_1\frac{\partial T}{\partial t} \tag{97}$$

But a partial derivative with respect to time is inadmissable for determining the constants in the polynomial because the constants would then be determined from a differential rather than an algebraic equation. Therefore, we eliminate $\partial T/\partial t$ between Eqs. (1, 97). The third condition then becomes

$$\left(\frac{\partial T}{\partial x}\right)^2 = \alpha A_1\frac{\partial^2 T}{\partial x^2},\ x = s(t) \tag{98}$$

With the third boundary condition in this form, the nonlinearity of the problem becomes self-evident.

If the temperature distribution is given by

$$T = a(x - s) + b(x - s)^2 \tag{99}$$

the quantities a and b are determined by

$$a = \frac{A_1\alpha}{s}[1 - (1 + \mu)^{1/2}]$$
$$b = \frac{as + T_s}{s^2} \tag{100}$$

where

$$\mu = \frac{2T_s}{A_1\alpha} \tag{101}$$

Upon substituting this profile into Eqs. (94, 95) we finally obtain the following differential equation for s:

$$s\frac{ds}{dt} = \frac{6\alpha[1 - (1 + \mu)^{1/2} + \mu]}{5 + \mu + (1 + \mu)^{1/2}} \tag{102}$$

The initial condition $s(0) = 0$ leads to the solution

$$s = K\sqrt{t} \tag{103}$$

where

$$\frac{K}{2\sqrt{\alpha}} = \sqrt{3}\left[\frac{1 - (1 + \mu)^{1/2} + \mu}{5 + (1 + \mu)^{1/2} + \mu}\right]^{1/2} \tag{104}$$

The exact solution is given in the form of Eq. (103) by Carslaw and Jaeger (*1*). A graphical comparison of Eq. (104) with the true variation between $K/2\sqrt{\alpha}$ and μ is given in (*24*) snd shows that the error is about 7% for $\mu = 2.8$, the largest value of μ considered. For smaller values of μ, the per cent error is less.

B. MELTING OF A SOLID WITH GIVEN SURFACE HEAT FLUX[2]

The problem is identical to the preceding one except that the condition at the surface, Eq. (32), is replaced by Eq. (2). The heat-balance integral becomes

$$\frac{d}{dt}(\theta + \alpha A_1 s) = \alpha F(t)/k \tag{105}$$

where θ is given by Eq. (95). Upon integrating and applying the initial condition $s(0) = 0$, we obtain

$$\theta + \alpha A_1 s = \frac{\alpha}{k}\int_0^t F(t_1)\,dt_1 \tag{106}$$

Once again, we assume T to be in the form of a second-degree polynomial. The three conditions for determining the constants are Eqs. (2, 91, 98). After carrying out the required elementary steps we obtain the following

[2] The solution is equally applicable to the freezing of a liquid.

relationship between the location of the melt line and time:

$$\tau = \frac{\sigma}{6}[\sigma + 5 + (1 + 4\sigma)^{1/2}] \tag{107}$$

where

$$\tau = \frac{F(t)}{\alpha k^2 A_1^2} \int_0^t F(t_1)\, dt_1 \tag{108}$$

$$\sigma = \frac{F(t)s}{\alpha A_1 k} \tag{109}$$

The exact solution for F = constant is given in (*25*) in the form of a Taylor series for σ in terms of τ. By expanding Eq. (107) in the same form, it is shown in (*24*) that the coefficients of the first four terms of the series agree, and that the error in the coefficient of the fifth term is about 4%.

The temperature-time history on the surface is given parametrically by Eq. (107) and the following equation:

$$\frac{T(0,t)}{A_1\alpha} = -\frac{1}{4} + \frac{1}{4}(1 + 4\sigma)^{1/2} + \sigma/2 \tag{110}$$

C. MELTING OF A SOLID WITH COMPLETE REMOVAL OF MELT (ABLATION)[3]

In the preceding two problems, a temperature distribution was assumed to exist only in the liquid phase, and the temperature in the solid phase was approximated by a constant. In the present case, since the liquid is immediately removed on formation, there is a temperature distribution in the solid phase only, and this does not constitute an approximation.

It is assumed that the semiinfinite solid slab has been heated by application of a constant heat flux F at the boundary $x = 0$. At time $t = 0$ the melting temperature $T = 0$ is reached on the boundary, and at that time the penetration distance is given by Eq. (15). For positive time the solid melts, and all the melt is immediately swept away by some undisclosed mechanism. (For the case in which the mechanism is aerodynamic shear and pressure forces, Goodman (*26*), by analyzing the fluid flow in the liquid phase, has determined the conditions under which complete removal of melt is a good approximation.) The boundary and melt lines are now indistinguishable and are both located at $x = s(t)$. According to Eq. (92), the boundary condition is

$$F + k\frac{\partial T}{\partial x} = \rho L \frac{ds}{dt}, \quad x = s(t) \tag{111}$$

[3] The solution is equally applicable to a sublimating solid with complete removal of vapor.

Once again, the subscripts have been dropped since there is only one phase. The temperature distribution in the solid is represented by a quadratic which satisfies Eqs. (5, 6, 91). This leads to the following distribution:

$$T = T_\infty \left[-2\left(\frac{x - s}{\delta - s}\right) + \left(\frac{x - s}{\delta - s}\right)^2 \right] \tag{112}$$

The heat balance integral is obtained by averaging Eq. (1) from s to δ. After applying Eq. (111), we obtain

$$\frac{d}{dt}\left(\theta + T_\infty \delta + \frac{\rho L \alpha s}{k}\right) = \frac{\alpha F}{k} \tag{113}$$

where

$$\theta = \int_s^\delta T \, dx \tag{114}$$

Upon substituting Eq. (112) into Eq. (114), and applying the result in Eq. (113), we obtain

$$\frac{\alpha F}{T_\infty k} = \frac{d}{dt}\left[\frac{\delta - s}{3}\right] + \frac{ds}{dt}(1 + \nu_1) \tag{115}$$

where

$$\nu_1 = \alpha \rho L / k T_\infty \tag{116}$$

There are two unknowns in Eq. (115), and consequently another relationship between δ and s is required. This relationship can be obtained from the condition at the melt line. Upon substituting Eq. (112) into Eq. (111) we obtain

$$\rho L \frac{ds}{dt} = F - \frac{2kT_\infty}{\delta - s} \tag{117}$$

Equations (115, 117) are two simultaneous differential equations for s and $(\delta - s)$. The initial conditions are $s(0) = 0$, $\delta(0) = 2T_\infty k/F$. Assume that this pair of equations possesses a steady state solution, i.e., assume ds/dt has a constant value w. It follows from Eq. (117) that $\delta - s$ is constant, and from Eq. (115), it is seen that

$$w = \frac{\alpha F / T_\infty k}{1 + \nu_1} \tag{118}$$

This value of w is precisely the same as obtained by Landau (*27*) using the exact system of equations.

To solve the complete transient equations, eliminate ds/dt between

them and let

$$\zeta = \frac{F(\delta - s)}{T_\infty k} \tag{119}$$

The result is a differential equation for ζ. Let

$$\Omega = F^2 t/\rho L k T_\infty \tag{120}$$

The solution of the differential equation is

$$\Omega = \tfrac{1}{3}\left[\zeta - 2 + 2(1 + \nu_1)\, ln\, \frac{2(1 + \nu_1) - \zeta}{2\nu_1}\right] \tag{121}$$

Upon substituting Eq. (121) into Eq. (117), and defining

$$S = \frac{sF}{T_\infty k} \tag{122}$$

we obtain

$$S = -\tfrac{1}{3}\left[\zeta - 2 + 2\nu_1\, ln\, \frac{2(1 + \nu_1) - \zeta}{2\nu_1}\right] \tag{123}$$

Equations (121, 123) are the equations for the melt line in parametric form. Landau (*27*) has obtained the exact solution for the melt line by integrating the heat conduction equation numerically; it is impossible to distinguish his results, on the scale to which they are plotted, from the solution presented here.

If the applied heat flux is due to aerodynamic friction, and the solid sublimates, the gaseous vapor which is produced will mix in the boundary layer and have a cooling effect. This results in a modification of the boundary condition, Eq. (111). By drawing on the literature of transpiration cooling Adams (*28*) has shown that this modification manifests itself in an effective increase in the latent heat. Otherwise, the problem remains the same. Sutton (*29*) has applied the integral method with the Adams modification, and has assumed a profile in the form

$$T = -T_\infty\{1 - \exp[-(x - s)/\bar{x}]\} \tag{124}$$

It can be shown that the form of this profile approaches the exact steady state value in the limit for large time. Hence, this form may be expected to be more accurate than the polynomial form. Sutton's solution for the location of the melt line is given parametrically by

$$\Omega = (1 + \nu_1)\, ln\, \frac{\nu_1 \zeta}{(1 + \nu_1)\zeta - 1} - \nu_1\left(\frac{1}{\zeta} - 1\right) \tag{125}$$

$$S = \frac{1}{1 + \nu_1}\left[\nu_1 \Omega - \left(\frac{1}{\zeta} - 1\right)\right] \tag{126}$$

where, in this case, ζ is defined to be

$$\zeta = kT_\infty/F\bar{x} \tag{127}$$

Economos (*30*) has carried out experiments in a hypersonic wind tunnel using teflon and lucite hemispherical models and has obtained good agreement with the theoretical values calculated by Sutton.

Blecher and Sutton (*31*) have considered the ablation problem with a pulselike heat input typical of that experienced by a reentry vehicle. By comparing results obtained from the integral method with more simple-minded methods (e.g., a quasi-steady approximation), they conclude that all methods will predict the transient ablation rate fairly well, but that the simpler methods do not predict the temperature profiles correctly. It is difficult to justify this victory for the integral method on the basis of this comparison because no exact solution was calculated, and also because the integral method itself appears to give spurious profiles for pulselike inputs (see Section VI). On the other hand, Altman (*32*) also considered the ablation problem for pulselike inputs and, using polynomial profiles, obtained good agreement with solutions based on finite difference calculations. The spurious results which occur for other problems with pulselike inputs apparently do not take place in the ablation problem; the reason for this remains obscure.

D. OTHER CASES

Goodman (*24*) has presented the solution to two other cases which will only be mentioned here. One case is the melting of a solid due to aerodynamic heating or radiation. This case is similar to those presented in IV,A except that the boundary condition at the surface is given by

$$k\frac{\partial T}{\partial x} = h[T - T_0], \qquad x = 0 \tag{128}$$

where h and T_0 are constants. The second case is the vaporization of a melting solid. Here the solid is assumed to be at the melting temperature and the vapor is immediately removed. Thus, a temperature distribution exists only in the liquid phase. Goodman and Shea (*33*) have considered the melting of a finite slab with temperature distributions in both phases. At the surface $x = 0$ the heat flux is specified to be a constant. The far surface is either insulated or isothermal. Quadratic profiles are assumed in each phase, giving rise to six unknown constants. In addition, the location of the melt line is also unknown. The seven conditions which are used to determine these unknowns are: the two boundary conditions at either end of the slab; Eq. (91) in both phases, Eq. (92),

and the heat balance integrals in each phase. It is interesting to observe that, for the case of the insulated far boundary, the results indicate that the temperature in the solid reaches the melting temperature very rapidly, thereby justifying the approximation, which was made in Section IV,A that the temperature in the solid is equal to the melting temperature from the outset.

Van der Velden and Schaffers (*34*) have independently devised a version of the integral method and applied it to a freezing problem with polar symmetry. They assumed logarithmic type profiles in accordance with the rule presented in Eq. (59), and they report that their results differ by only a few per cent from more exact results.

V. Related Methods

The heat-balance integral technique is not, of course, the only approximate method available to the analytic investigator. We will now briefly consider some other analytical methods which bear a resemblance to the integral method in that they utilize the concept of penetration distance whenever appropriate, and that they are applicable to linear and nonlinear problems alike. The results of these related methods, when applied to some simple cases, will be compared with the corresponding results obtained using the integral method. Two such methods will be presented: Biot's method and Shvets' method.

A. BIOT'S METHOD[4]

Variational principles have been used in mechanics for many years. Recently, applied mathematicians have turned their attention to the formulation of variational principles in heat conduction. Many variational formulations have been published in the decade between 1950 and 1960 [see (*35*) for a bibliography]. The formulation of Biot is remarkable, however, because it constitutes a thermodynamic analogy to Hamilton's principle in mechanics, and thereby leads to the thermodynamic equivalent of Lagrange's formulation of Newton's laws in terms of generalized coordinates. In a series of elegant papers, Biot has developed and applied his variational principle and the Lagrange equations (*36*, *37*, *38*, *39*, *40*, *41*). We are not primarily concerned here with the derivation of the method, but, rather, with its application.

Let $\mathbf{H}$ represent a heat flow vector whose time rate of change $\dot{\mathbf{H}}$ is the heat flux across an area normal to $\mathbf{H}$. Conservation of energy then requires

$$-\rho c\dot{T} = \operatorname{div} \mathbf{H} \tag{129}$$

[4] Most of the material presented in this section was taken from a report by Lardner (*35*).

Let E represent the thermal potential energy, D the dissipation function, Q_i the generalized force, and q_i the generalized coordinate, where

$$E = \tfrac{1}{2} \int \rho c T^2 \, dv$$

$$D = \tfrac{1}{2} \int k|\dot{\mathbf{H}}|^2 \, dv \tag{130}$$

$$Q_i = \int T \frac{\partial \mathbf{H}}{\partial q_i} \, dS$$

The volume integrals are understood to extend to the penetration distance for those problems for which the concept of penetration distance has meaning. The Lagrange formulation of the thermal balance is

$$\frac{\partial E}{\partial q_i} + \frac{\partial D}{\partial \dot{q}_i} = Q_i \tag{131}$$

where the dot denotes time differentiation.

1. The Semiinfinite Slab

Equation (131) can be applied to solve the problem of a semi-infinite slab with constant heat flux F, applied to its surface. Biot has suggested that for the boundary condition of prescribed heat flux two generalized coordinates be used, one being the penetration distance and the other being the surface temperature. One Lagrange equation with respect to either coordinate together with a constraint preserving the overall heat balance will yield two coupled equations for the generalized coordinates. It might be noted that the constraint is identically the heat balance integral. An alternative approach will be presented in which only one generalized coordinate, the penetration distance, appears. The heat flux field can be made to satisfy the boundary conditions $\dot{H}(\delta,t) = 0$ and $\dot{H}(0,t) = F$ if we choose a temperature profile in the form

$$T = \frac{3Ft}{\rho c \delta}\left(1 - \frac{x}{\delta}\right)^2 \tag{132}$$

$\mathbf{H}$ has only one component for a one-dimensional problem, and by applying Eq. (129) we obtain

$$H = Ft\left(1 - \frac{x}{\delta}\right)^3 \tag{133}$$

from which the heat flux field becomes

$$\dot{H} = F\left(1 - \frac{x}{\delta}\right)^3 + \frac{3Ftx}{\delta^2}\,\dot{\delta}\left(1 - \frac{x}{\delta}\right)^2 \tag{134}$$

Upon substituting Eqs. (132–134) into Eqs. (130, 131) we obtain

$$\alpha[(3/35)\delta\dot{\delta}t + (3/42)\delta^2] = (9/10)t \tag{135}$$

The solution of this equation is

$$\delta = 2.81\sqrt{\alpha t} \tag{136}$$

The surface temperature is

$$z = \frac{3Ft}{\rho c\delta} = 1.065\frac{F}{k}\sqrt{\alpha t} \tag{137}$$

Similar analyses can be performed using cubic, exponential, and other profiles. It is not always possible to choose a temperature profile which enables the heat flux field to satisfy the required boundary conditions.

TABLE I

RESULTS FOR CONSTANT FLUX CASE[a]

Profile[b]	Surface temperature	Penetration distance	% Difference
I. Parabolic			
A	1.065	2.81	−5.6
B	1.157	2.59	+2.0
C	1.120	2.68	−0.7
II. Exponential			
A	1.225	0.816	+8.6
B	1.220	0.895	−0.7
C	1.152	0.866	+2.3
III. Cubic			
A	1.105	3.62	−2.0
B	1.14	3.52	+1.0
C	1.123	3.56	−0.5
IV. Heat balance integral			
Parabolic	1.225	2.45	+8.6
Cubic	1.15	3.45	+2.0
V. Exact	1.128		

[a] Data from Lardner (*35*).

[b] A = Heat flow satisfies flux condition.
B = Independent generalized coordinate = surface temperature.
C = Independent generalized coordinate = penetration depth.

In this case, one must fall back on the approach which utilizes two generalized coordinates. In general the penetration distance will be of the form $\delta = (\ )\sqrt{\alpha t}$, and the surface temperature of the form $z = (\ )(F/k)\sqrt{\alpha t}$. Table I presents the values of the bracket for all possible cases together with the exact solution and the result obtained using the integral method. It can be seen that all solutions give results which are accurate to within a few per cent.

2. Melting of a Solid with Complete Removal of Melt

Biot and Daughaday (*41*) have used Lagrangian methods to solve the problem of the melting solid with complete removal of melt which is solved in Section IV,C using the integral method.[5] In their analysis, Biot and Daughaday assume the slab to be initially at zero temperature, and the melting temperature is consequently T_m, a constant. We shall adopt this view. The volume integrals, Eq. (130), must extend from $x = s$ to $x = \delta$. We choose a cubic temperature profile and let the penetration distance be the generalized coordinate.

$$T = T_m\left[1 - \left(\frac{x - s}{\delta - s}\right)\right]^3 \tag{138}$$

The heat flow field is obtained by applying Eq. (129):

$$H = \frac{\rho c T_m}{4}\left[1 - \frac{x - s}{\delta - s}\right]^4 (\delta - s) \tag{139}$$

Upon substituting into Eq. (130) we obtain the following Lagrangian heat flow equation:

$$(\delta - s)\left[\frac{4}{112}\frac{d}{dt}(\delta - s) + \frac{11}{112}\frac{ds}{dt}\right] = \frac{5}{14}\alpha \tag{140}$$

A second relationship between s and δ is derived from the heat-balance integral, Eq. (113). Because the initial temperature is zero and the melting temperature is T_m, Eq. (113) is slightly modified to:

$$\frac{d}{dt}\left(\theta + T_m s + \frac{\rho L \alpha s}{k}\right) = \frac{\alpha F}{k} \tag{141}$$

Whence,

$$\tfrac{1}{4}T_m\frac{d}{dt}(\delta - s) + \left(T_m + \frac{\rho L \alpha}{k}\right)\frac{ds}{dt} = \frac{\alpha F}{k} \tag{142}$$

Equations (140) and (142) must be solved simultaneously for $(\delta - s)$ and s. The initial conditions are derived from a Lagrange analysis prior to melting, specifically the solution III,C of Table I. It is possible to obtain a closed-form solution in parametric form which is similar to that obtained using the integral method, but this will not be carried out. The numerical results show satisfactory correlation with the exact results of Landau (*27*).

[5] Lardner (*42*) has carried out this calculation independently. In the same report Lardner has also used Lagrangian methods to solve the problem presented in Section IV,C, and compared the results both with the exact solution and with the solution obtained using the integral method.

Biot has applied Lagrangian methods to problems with variable thermal properties, and to problems with a variety of nonlinear boundary conditions. He has also generalized the method to those problems for which the thermal and elastic behavior is coupled. We will not, however, present any additional examples.

B. SHVETS' METHOD

An iteration scheme for solving Eq. (1) has been proposed by Shvets (*43*). Consider a semi-infinite slab initially at zero temperature, and subjected to a step of unit temperature at its surface. Let the nth approximation be given by

$$T^n = \sum_{k=0}^{n} T_k \tag{143}$$

where the partial solutions satisfy

$$\alpha \frac{\partial^2 T_k}{\partial x^2} = \frac{\partial T_{k-1}}{\partial t} \tag{144}$$

and the sequence is started by

$$\frac{\partial^2 T_0}{\partial x^2} = 0 \tag{145}$$

Define a penetration distance by the condition $T(\delta,t) = 0$. Then, T_0 must take the form

$$T_0 = (1 - x/\delta) \tag{146}$$

Upon substituting into Eq. (144) and applying the conditions $T(\delta,t) = 0$, $T(0,t) = 1$, we obtain, to the first approximation,

$$T = 1 - \frac{x}{\delta} + \frac{x\dot{\delta}}{6}\left(\frac{x^2}{\delta^2} - 1\right) \tag{147}$$

where the dot denotes differentiation with respect to αt.

To determine δ, we apply Eq. (5), which leads to the following equation:

$$\delta\dot{\delta} = 3 \tag{148}$$

The penetration distance thus becomes

$$\delta = 2.45\sqrt{\alpha t} \tag{149}$$

and the surface heat flux becomes

$$k\frac{\partial T}{\partial x}\bigg|_0 = -\frac{0.61k}{\sqrt{\alpha t}} \tag{150}$$

As noted below Eq. (35), the exact solution is of the same form, except that the numerical factor 0.61 is replaced by 0.564. Shvets' method may be carried out to higher approximations, resulting in higher order differential equations for δ and polynomial profiles of higher degree. The differential equation for δ is always determined by applying Eq. (5) after all the partial solutions have been obtained.

Suppose we wish to apply the same technique to a semiinfinite slab for which the surface heat flux is specified as in Eq. (17). Squire (*44*) has discussed the application of the Shvets method to this problem. The surface temperature z is now unknown, and T_0 may take any one of three forms:

$$T_0 = z(1 - x/\delta) \tag{151a}$$

$$T_0 = f(x - \delta) \tag{151b}$$

$$T_0 = z - fx \tag{151c}$$

Thus, there are three possible ways to proceed. Forms *a* and *c* imply a two-parameter profile, the parameters being the surface temperature z and penetration distance δ. For form *b*, there is but a single parameter: the penetration distance. The possibility of having three choices of profiles and procedures arises here for the same reason that it arose in using Lagrangian methods.

In procedure (a) T satisfies the conditions $T_1(0,t) = 0$, $T_1(\delta,t) = 0$. Two simultaneous equations for the two parameters are derived by applying the boundary conditions Eqs. (5, 17). In procedure (b) T_1 satisfies the conditions $\frac{\partial T_1}{\partial x}(0,t) = 0$, $T_1(\delta,t) = 0$. The equation for the penetration distance is derived by applying the boundary condition Eq. (5). In procedure (c) T satisfies the conditions $T_1(0,t) = 0$, $\frac{\partial T_1}{\partial x}(0,t) = 0$. Two simultaneous equations for the two parameters are derived by applying the boundary condition $T(\delta,t) = 0$ and Eq. (5).

For constant heat flux F, the penetration distance will take the form $\delta = (\ \ ) \sqrt{\alpha t}$ and the surface temperature will take the form

$$z = (\ \ )(F/k) \sqrt{\alpha t}$$

Table II presents the value of the brackets for the three possible cases together with the exact solution and the results obtained using the integral method. It can be seen that the results obtained using Shvets' method for constant heat flux are not very accurate. This is in contrast to the results obtained using Shvets' method for the step in surface temperature where the accuracy was quite acceptable. Of course, higher order approximations are available in order to improve the accuracy,

TABLE II
RESULTS FOR CONSTANT FLUX CASE

Solution	Surface temperature	Penetration distance	% Difference
Case a	1.000	2.000	−13
Case b	0.707	1.414	−37
Case c	1.000	2.000	−13
Heat-balance integral			
Parabolic	1.225	2.45	+8.6
Cubic	1.15	3.45	+2.0
Exact	1.128		

although they soon become rather tedious. The method can, of course, be used to solve nonlinear problems, and Shvets himself has done so by applying it to solve some boundary layer problems, achieving acceptable accuracy in the first approximation.

VI. Pulselike Inputs

Although there are many problems which can be solved successfully by using the integral method, there is a class of problems for which the method provides spurious answers. After we discuss the reason for the failure of the integral method in solving this class of problems we will present the extended integral method which is a method specifically designed to be applied in cases where the ordinary integral method is inapplicable.

In order to appreciate the limitations of the integral method, consider Eq. (12) which expresses the surface temperature in terms of a general time-dependent surface heat flux for a semiinfinite slab. We will assume $T_\infty = 0$ with no loss in generality. Suppose the heat flux $F(t)$ to be pulselike, i.e., suppose it rises to a maximum, falls to zero, and then remains zero. According to Eq. (12) the surface temperature rises to a maximum some time after F_{max}, falls to zero at the same moment that F becomes zero (heat shut-off), and remains zero. However, the exact solution to this linear problem is known, and according to the exact solution, or by physical intuition, we know that for a pulselike surface heat flux, the surface temperature must rise to a maximum and then decay gradually, approaching zero asymptotically. Thus, it is seen that Eq. (12) deviates from the correct value sometime after F_{max}, and is completely spurious just prior to heat shut-off. The same type of failure would occur if a pulselike surface temperature were prescribed and the surface heat flux were sought.

The reason for the failure of the method is clear: the assumed temperature profile, Eq. (19), does not resemble the actual profile when the surface heat flux is pulselike. According to Eq. (19), the profile is monotonic with no inflection points. This is a reasonable profile for an increasing heat flux. When the heat flux is pulselike, on the other hand, the profile will tend to be nonmonotonic after F_{max}, and there is no way in which the form assumed in Eq. (19) can accommodate itself to this tendency.

What is required is a temperature profile which possesses two (or more) time-dependent parameters to be determined by two (or more) conditions. With this view, the heat-balance integral would be one such condition. The totality of conditions would then result in sufficient simultaneous equations to determine all the parameters.

Goodman and Ullah (*45*) have developed a two-parameter method in which one parameter is the penetration distance of a fictitious problem and is known, while the other parameter is determined from the heat-balance integral. Thus, the two parameters are determined successively rather than simultaneously, and the heat-balance integral alone is sufficient to determine both the parameters. This technique will become clearer by the presentation of a simple example.

A. SEMIINFINITE SLAB WITH A PULSELIKE HEAT FLUX

Consider a semiinfinite slab initially at zero temperature, and assume that the temperature satisfies Eq. (1) together with the boundary condition, Eq. (2). A sketch of $F(t)$ is shown in Fig. 3 as the curve ABCD,

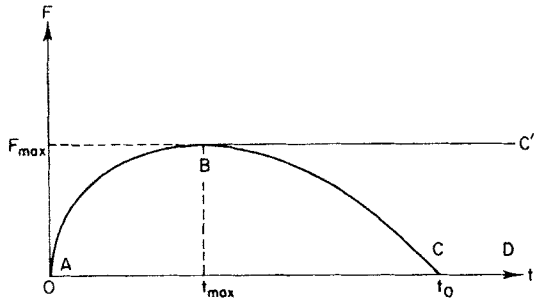

FIG. 3. Sketch of pulselike heat flux.

and the pulselike character of this function will be noted. For simplicity, we will use quadratic temperature profiles. Then, for $0 < t < t_{max}$, the heat flux is increasing, and the solution presented in Section I obtains. In the interval $t > t_{max}$ we assume the temperature to consist of two parts:

$$T(x,t) = T_1(x,t) + T_2(x,t) \tag{152}$$

where T_1 satisfies the conditions of a fictitious problem with boundary condition

$$k\frac{\partial T}{\partial x} = -F_{\max}, \qquad x = 0 \tag{153}$$

In other words, T_1 is the analytic continuation of the solution obtained in the first interval assuming that the heat flux follows the curve ABC′ which is monotonic. We denote the penetration distance associated with T_1 by δ_1; then, an analytical expression for δ_1 can readily be obtained from Eq. (10):

$$\delta_1 = \sqrt{\frac{6\alpha}{F_{\max}}}\left[\int_0^{t_{\max}} F(t)\,dt + F_{\max}(t - t_{\max})\right]^{1/2} \tag{154}$$

We now assume that the surface heat flux associated with T_2 is negative and monotonic and begins at $t_{\max}$ in such a way that the total heat flux follows the curve ABCD, which is the true boundary condition. Associated with the temperature T_2 is a second penetration distance $\delta_2 < \delta_1$ which begins to propagate at $t = t_{\max}$. In other words, T_2 must take the form

$$\begin{aligned} T_2 &= -\frac{(F_{\max} - F)}{2k\delta_2}(x - \delta_2)^2 \qquad && x < \delta_2 \\ &= 0 && x > \delta_2 \end{aligned} \tag{155}$$

We now calculate

$$\theta = \int_0^{\delta_1} T\,dx = \int_0^{\delta_1} T_1\,dx + \int_0^{\delta_2} T_2\,dx$$

$$= \frac{1}{6k}[F_{\max}\delta_1^2 - (F_{\max} - F)\delta_2^2] \tag{156}$$

The heat balance integral gives

$$\int_{\theta(t_{\max})}^{\theta(t)} d\theta = \frac{\alpha}{k}\int_{t_{\max}}^{t} F(t)\,dt \tag{157}$$

or

$$\theta = \frac{\alpha}{k}\int_0^t F\,dt \tag{158}$$

Upon equating Eq. (156) and Eq. (158) and eliminating δ_1 with the aid of Eq. (154), we obtain the value of δ_2:

$$\delta_2 = \left(\frac{6\alpha}{F_{\max} - F}\right)^{1/2}\left[\int_{t_{\max}}^{t}(F_{\max} - F)\,dt\right]^{1/2} \tag{159}$$

Hence, the surface temperature for $t > t_{max}$ is given by

$$z = \sqrt{\frac{3}{2}}\sqrt{\frac{\alpha}{k}}\left[F_{max}^{1/2}\left\{\int_0^{t_{max}}(F - F_{max})\,dt + F_{max}t\right\}^{1/2} - (F_{max} - F)^{1/2}\left\{\int_{t_{max}}^{t}(F_{max} - F)\,dt\right\}^{1/2}\right], \quad t > t_{max} \tag{160}$$

For $t > t_0$, the surface temperature can be obtained by setting $F = 0$ in Eq. (160). This results in

$$z = \sqrt{\frac{3}{2}}\sqrt{\frac{\alpha F_{max}}{k}}\left[\left\{\int_0^{t_{max}}(F - F_{max})\,dt + F_{max}t\right\}^{1/2} - \left\{F_{max}(t - t_{max}) - \int_{t_{max}}^{t_0} F\,dt\right\}\right] \qquad t > t_0 \tag{161}$$

For large time Eq. (161) yields the following asymptotic formula:

$$z \to \frac{1}{2}\sqrt{\frac{3}{2}}\frac{\sqrt{\alpha}}{k\sqrt{t}}\int_0^{t_0} F\,dt \qquad t \gg t_0 \tag{162}$$

If, instead of assuming quadratic profiles, we assume cubic profiles which satisfy the smoothing condition, Eq. (18), the results given in Eqs. (160–162) will remain unaltered except that the numerical factor $\sqrt{3/2}$ will be replaced by $\sqrt{4/3}$.

Figures 4 and 5 show the surface temperature obtained by using the extended integral method for parabolic and triangular heat pulses. The exact solutions of these problems are also known, and the comparisons demonstrate satisfactory agreement.

If the thermal properties are temperature-dependent, the transformation, Eq. (77), can be applied. In this case, the fictitious solution v_1 cannot be obtained explicitly because it depends on the diffusivity which, in turn, depends on the actual temperature, not the fictitious temperature. Nevertheless, the analysis can be carried out symbolically, in which case it is found that for $t < t_{max}$ the solution is given by Eq. (86), and for $t > t_{max}$ the solution is given by

$$\sqrt{\alpha_s}v_s = \sqrt{3/2}\left[F_{max}^{1/2}\left\{\int_0^{t_{max}}(F - F_{max})\,dt + F_{max}t\right\}^{1/2} - (F_{max} - F)^{1/2}\left\{\int_{t_{max}}^{t}(F_{max} - F)\,dt\right\}^{1/2}\right] \tag{163}$$

where quadratic profiles have been assumed. The effect of using cubic profiles can again be obtained by replacing $\sqrt{3/2}$ by $\sqrt{4/3}$. Equation

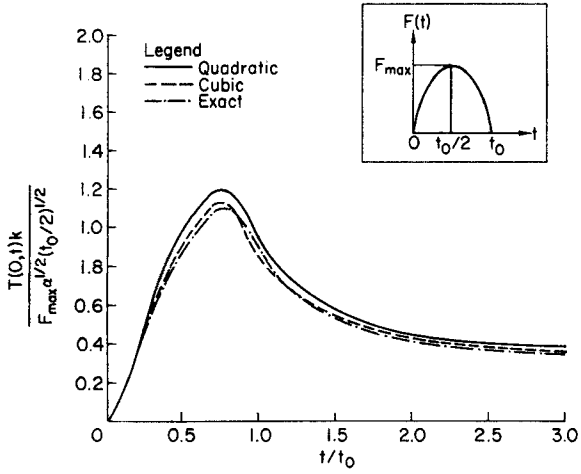

FIG. 4. Temperature time history at the surface of a semiinfinite slab with parabolic surface heat flux—comparison between exact and integral solution with two different profiles (*45*).

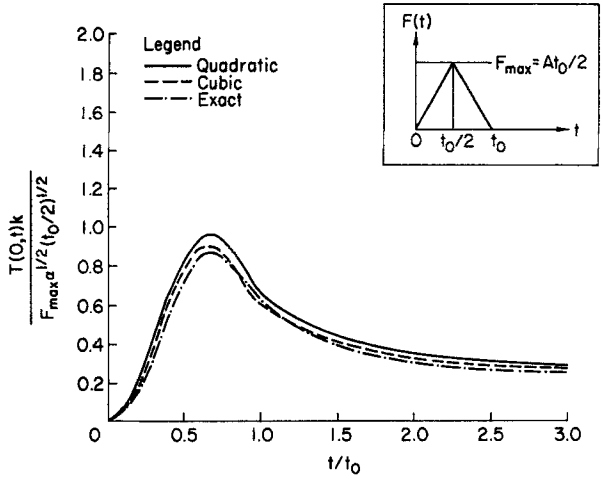

FIG. 5. Temperature time history at the surface of a semiinfinite slab with triangular surface heat flux—comparison between exact and integral solution with two different profiles (*45*).

(163) is the generalization of Eq. (160) for temperature-dependent thermal properties, and is a transcendental equation to be solved for the surface temperature.

B. SEMIINFINITE SLAB WITH PULSELIKE HEAT GENERATION

We will reconsider the problem presented in Section II,A,3, and generalize it in two ways: the thermal properties will be taken to be temperature-dependent, and the cumulative heat generated, $Q(t)$, will be taken to be pulselike, so that heat is first added and then withdrawn. Equation (37) is replaced by

$$\rho c \frac{\partial T}{\partial t} - \frac{\partial}{\partial x}\left(k \frac{\partial T}{\partial x}\right) = q(t) \tag{164}$$

Upon applying the transformation, Eq. (77), we obtain

$$\frac{\partial v}{\partial t} - \frac{\partial}{\partial x}\left(\alpha \frac{\partial v}{\partial x}\right) = q(t) \tag{165}$$

The problem will now be transformed into one satisfying a homogeneous equation with a nonhomogeneous boundary condition. Let

$$v = Q + v' \tag{166}$$

The quantity v' then satisfies Eq. (78) with α dependent on v, and the boundary condition becomes

$$v'(0,t) = -Q(t) \tag{167}$$

In the interval before $Q = Q_{\max}$, the ordinary integral procedure is valid, and the profile is given by

$$v' = -Q(1 - x/\delta)^3 \qquad t < t_{\max} \tag{168}$$

The heat balance integral becomes

$$\frac{d}{dt}\int_0^\delta v'\,dx = -\alpha_s \frac{\partial v'}{\partial x}(0,t) \tag{169}$$

This yields a differential equation for δ, the solution to which is

$$\delta = \left[\frac{24\alpha_s \int_0^t Q^2\,dt}{Q^2}\right]^{1/2} \qquad t < t_{\max} \tag{170}$$

It is to be noted that since the surface temperature of the original problem for v is constant, α_s is constant.

When $t > t_{max}$ the extended integral method must be used. Accordingly, let

$$v' = v_1(x,t) + v_2(x,t) \tag{171}$$

where v_1 satisfies the conditions of a fictitious problem which is the analytic continuation of the solution given above with $Q = Q_{max}$. The penetration distance δ_1, which is associated with v_1, is obtained by substituting $Q = Q_{max}$ in Eq. (170):

$$\delta_1 = \left[\frac{24\alpha_s}{Q^2_{max}}\right]^{1/2}\left[\int_0^{t_{max}} Q^2\,dt + Q^2_{max}(t - t_{max})\right]^{1/2} \tag{172}$$

The profile for v_2 must then be

$$\begin{aligned} v_2 &= (Q - Q_{max})[1 - x/\delta_2]^3 \qquad x < \delta_2 \\ &= 0 \qquad\qquad\qquad\qquad\quad x > \delta_2 \end{aligned} \tag{173}$$

where δ_2 begins to propagate at $t = t_{max}$. The heat balance integral is obtained by integrating Eq. (78) from 0 to δ_1:

$$\frac{d}{dt}\left[\int_0^{\delta_1} v_1\,dx + \int_0^{\delta_2} v_2\,dx\right] = -\alpha_s\left[\frac{\partial v_1}{\partial x} + \frac{\partial v_2}{\partial x}\right]_s \tag{174}$$

Upon subtracting Eq. (169) (with $\delta = \delta_1$, $v' = v_1$) we obtain a differential equation for δ_2 the solution to which is

$$\delta_2 = \left[\frac{24\alpha_s\int_{t_{max}}^{t}(Q_{max} - Q)^2\,dt}{(Q_{max} - Q)^2}\right]^{1/2} \tag{175}$$

The complete solution in the second time interval is then given by

$$v = -Q_{max}(1 - x/\delta_1)^3 - (Q - Q_{max})(1 - x/\delta_2)^3 + Q \tag{176}$$

where it is understood that the first term vanishes for $x > \delta_1$, and the second term vanishes for $x > \delta_2$. The solution after heat shut-off can readily be derived as the analytic continuation of Eqs. (175, 176), by setting $Q = 0$. The surface temperature gradient is shown plotted in Fig. 6 for the triangular heat pulse which is sketched in Fig. 5. In performing these calculations, constant thermal properties have been assumed in order to be able to compare the results with those of an exact solution which is also shown. The comparison indicates that the approximate solution is quite satisfactory. Some temperature profiles for the interval $t_0/2 < t < t_0$ are shown plotted against the dimensionless distance $\xi = x/2\sqrt{\alpha t_0}$ in Fig. 7. Note the reverse profiles for the larger

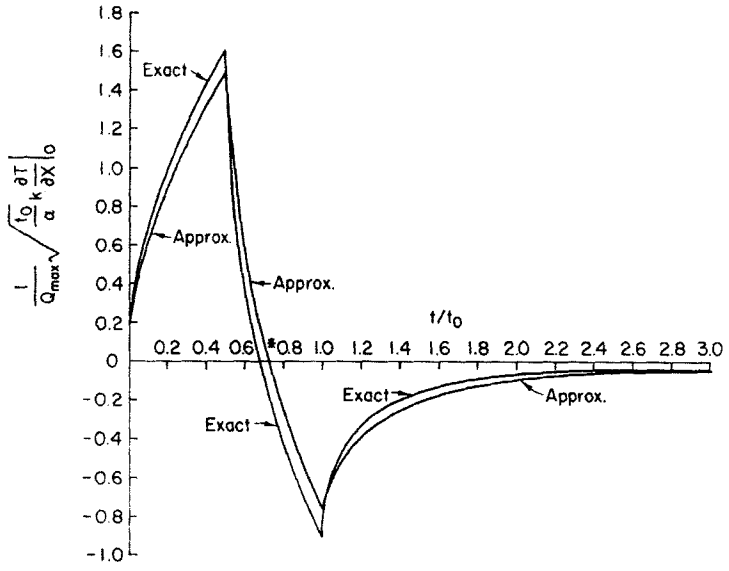

FIG. 6. Surface temperature gradient for semiinfinite slab with triangular cumulative heat generation—comparison between exact and extended integral solution.

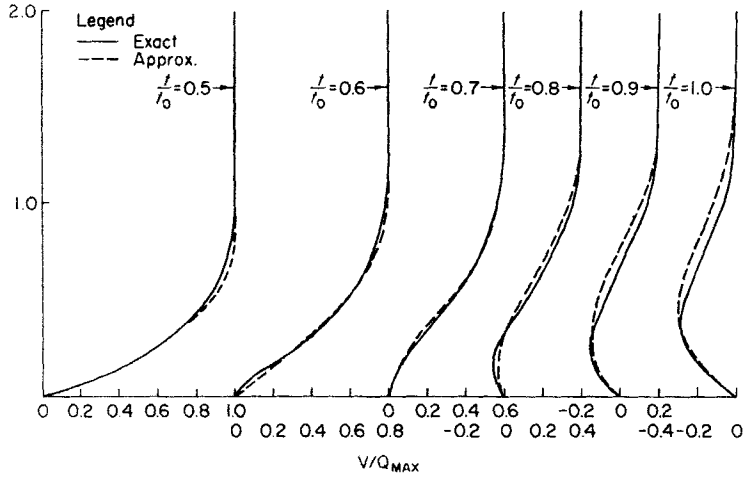

FIG. 7. Temperature profiles during the interval when heat is withdrawn for a semi-infinite slab with cumulative heat generation—comparison between exact and extended integral solution.

values of t, and also note how well the extended integral method represents such profiles.

It might be noted in passing that Eq. (164) bears a resemblance to the momentum equation which governs a steady incompressible laminar boundary layer. In this analogy, x and t become the normal and longitudinal coordinates, respectively, T becomes the longitudinal velocity, k becomes the coefficient of viscosity, ρ is the density, q becomes the pressure gradient (Q becomes the pressure), and the condition of zero surface temperature becomes the no-slip condition. Furthermore, in order to cast the momentum equation into the form of Eq. (164) it is necessary to make an Oseen-type approximation in which momentum is transported with an average velocity c, and the normal velocity is identically zero. The point of zero surface heat flux, which is marked with an asterisk (*) in Fig. 6, then corresponds to the point of separation in the analogy, and a condition for separation can be determined by performing elementary operations on Eq. (176), and applying Eqs. (172, 175). The result is

$$Q^4_{\max} \int_{t_{\max}}^{t} (Q_{\max} - Q)^2 \, dt = (Q_{\max} - Q)^4 \left[\int_0^{t_{\max}} Q^2 \, dt + Q^2_{\max}(t - t_{\max}) \right] \tag{177}$$

A superior separation condition can undoubtedly be derived by applying the extended integral method to the exact boundary layer conditions. Furthermore, the extended integral method also gives promise of being able to predict the flow in the separated region itself. But these problems are beyond the scope of the present article.

C. FINITE SLAB WITH TRIANGULAR HEAT PULSE

Suppose we apply the triangular heat flux as sketched in Fig. 5 to the end $x = 0$ of a finite slab of length l which is insulated at the far end. We assume $t_0/2$ to be greater than the time needed for the thermal layer δ to become equal to l. Assuming that the profiles are quadratic, it is seen that as long as $\delta < l$ the solution is given by Eq. (12) which, for zero initial temperature, becomes

$$z = \sqrt{3/4} \, \frac{A\alpha^{1/2}}{k} \, t^{3/2} \qquad 0 \leq t \leq t_\delta \leq t_0/2 \tag{178}$$

where t_δ is the time at which $\delta = l$, and is given by

$$t_\delta = l^2/3\alpha \tag{179}$$

When $t = t_\delta$ the temperature distribution in the slab is given by

$$T(x,t) = \frac{Al}{6\alpha k} (x - l)^2 \tag{180}$$

which serves as the initial condition for the next time interval. For $t > t_\delta$ the solution is affected by the insulation condition at $x = l$:

$$\frac{\partial T}{\partial x} = 0, \quad x = l \tag{181}$$

The heat balance integral can be derived in the next time interval, and the temperature profile turns out to be

$$T(x,t) = \frac{At}{2kl}(x - l)^2 + \frac{A\alpha t}{2kl}(t - t_\delta), \quad t_\delta \leq t \leq t_0/2 \tag{182}$$

For $t > t_0/2$ the heat flux starts decreasing, and it is necessary to use the extended integral method. Proceeding as in the previous examples, we seek the solution T of a fictitious problem for which $F = F_{\max} = At_0/2$, which is the analytic continuation of Eq. (182). The solution is

$$T_1(x,t) = \frac{At_0}{4kl}(x - l)^2 + \frac{A\alpha t_0}{4kl}\left(2t - \frac{t_0}{2} - t_\delta\right) \qquad t > t_0/2 \tag{183}$$

The solution to the actual problem is then assumed in the form

$$T = T_1(x,t) + T_2(x,t) \qquad t > t_0/2 \tag{184}$$

For time immediately subsequent to $t_0/2$ there is a penetration distance δ_2 associated with T_2, and T_2 takes the form

$$T_2(x,t) = -\frac{A(t - t_0/2)}{2k\delta_2}(x - \delta_2)^2 \tag{185}$$

The heat balance integral then yields

$$\delta_2 = \sqrt{3\alpha(t - t_0/2)} \tag{186}$$

and the complete solution is given by

$$T(x,t) = \frac{At_0}{2kl}(x - l)^2 + \frac{At_0\alpha}{2kl}\left(2t - \frac{t_0}{2} - t_\delta\right) - \frac{A(t - t_0/2)}{2k\sqrt{3\alpha(t - t_0/2)}}(x - \sqrt{3\alpha(t - t_0/2)})^2 \tag{187}$$

As soon as $\delta_2 = l$, the form of T_2 assumed in Eq. (185) becomes inappropriate because the boundary condition at the far end then begins to affect it. The time at which this occurs is denoted by t_{δ_2}, and is given by

$$t_{\delta_2} = t_\delta + t_0/2 \tag{188}$$

When $t > t_{\delta_2}$, Eq. (185) must be replaced by

$$T_2 = a - \frac{A(t - t_0/2)}{2kl}(x^2 - 2lx) \tag{189}$$

where a is an unknown parameter to be determined by applying the

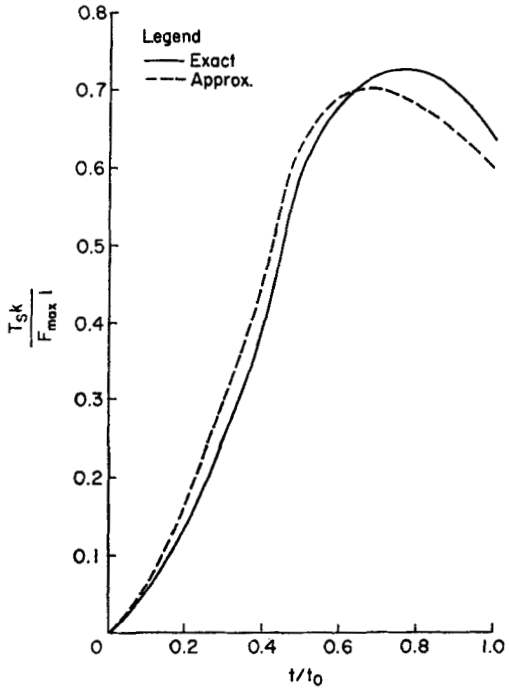

FIG. 8. Temperature time history at the surface of a finite slab with the triangular surface heat flux sketched in Fig. 5 and insulated far end—comparison between exact and extended integral solution ($\alpha t_0/2l^2 = 0.6$) (*45*).

heat balance integral. The solution turns out to be

$$T(x,t) = \frac{A}{2kl}(t_0 - t)(x - l)^2 + \frac{A\alpha t_0}{4kl}(2t - t_{\delta_2}) - \frac{A\alpha(t - t_0/2)}{2kl}(t - t_{\delta_2}), \quad t_{\delta_2} \leq t \leq t_0 \tag{190}$$

Since T_1 and T_2 both satisfy the same boundary conditions applied at the same place, namely Eqs. (2, 181), it is not really necessary to use the extended integral method to derive Eq. (190); the ordinary integral

method suffices. However, the initial condition for the solution in this interval must be taken from Eq. (187) which does require the extended method for its derivation.

When $t > t_0$ the heat is shut off and T becomes constant and uniform:

$$T = \frac{A\alpha t_0^2}{4kl} \qquad t > t_0 \tag{191}$$

A plot of the surface temperature, obtained from Eqs. (178, 182, 187, 190) is presented in Fig. 8 for the special case $\alpha t_0/2l^2 = 0.6$. The exact solution obtained from (*46*) is also shown for purposes of comparison, and agreement is seen to be quite satisfactory.

D. CONCLUDING REMARKS

The extended integral method has been presented and applied to a number of cases involving pulselike inputs. The same technique can be used to generate solutions to problems for inputs which are oscillatory in character simply by allowing a new penetration depth to begin propagating at each maximum and minimum of the input. In practice, the required mathematical manipulations become quite tedious, and no demonstration will be given here.

It might be pointed out that the extended integral method is eminently suited to problems which involve melting and subsequent refreezing, such as those that arise during welding.

VII. Improving the Accuracy

Every solution thus far obtained using the integral method, for which an exact counterpart was available, has been seen to contain small but irrevocable errors in the final numerical results. The question naturally arises as to how to eliminate, or at least reduce, these errors and thereby improve the accuracy. One simple and obvious way which might be used to improve the accuracy is to increase the order of the polynomial used to represent the profile. Each additional parameter which is thereby introduced is then determined from an additional derived constraint applied at the ends of the profile. The smoothing condition, Eq. (18), is typical of such derived constraints. Goodman (*21*) has applied this concept to solve a nonlinear problem, and has demonstrated the improved accuracy achievable using a fourth-degree polynomial over that which can be achieved using a third-degree polynomial. The flaw in this concept is that there is no a priori guarantee that increasing the order of the polynomial will improve the accuracy. Although the accuracy is frequently improved with this technique, it can be demonstrated, none the less, that there are cases for which it actually worsens. An example is

the problem presented in Section II,A,2; in this case a quadratic profile provides a more accurate surface heat flux than a cubic profile. However, because the concept is simple and easy to apply, cubic profiles are generally to be preferred to quadratic profiles, and quartics to cubics.

A much better way to improve the accuracy is to use the iteration scheme of Chambre which has been presented in Section II,A,1. In this case we are guaranteed improvement by virtue of the convergence proof. However, Chambre's method has two unattractive features. The first of these is that the method can be used only for those cases for which an integral equation can be derived. This restricts it to problems with a linear field equation, and allows nonlinearities to appear only in the boundary conditions. The second unattractive feature is that an integral equation must be solved instead of a differential equation. An integral equation is more awkward to solve on a high-speed digital computer than a differential equation, principally because the integral equation contains both fixed and running variables.

We will now present three techniques for improving the accuracy of a solution obtained using the integral method. These techniques can be applied when the nonlinearities appear in the field equation or the boundary conditions or both. The details of these techniques can become rather involved and, due to space limitations, they can be presented only in broad outline. In each technique the improvement is effected by solving an initial value problem involving ordinary differential equations. Such problems are readily adapted to high speed computers.

A. THE METHOD OF WEIGHTED RESIDUALS

Consider a field equation described by a nonlinear operator L:

$$L(T) = 0 \tag{192}$$

Specifically, of course, we are concerned with some form of the heat equation. An approximate solution, T_n, when substituted into the left-hand side of Eq. (192) will result in a residual ϵ_n,

$$L(T_n) = \epsilon_n \tag{193}$$

We seek a solution which makes ϵ_n small in some sense. We multiply it by a weighting factor w_j, and average over-all space. Upon setting the average equal to zero we obtain

$$\int w_j L(T_n)\, dv = 0 \qquad j = 1, 2, \ldots n \tag{194}$$

Our solution will be made to satisfy Eq. (194) instead of Eq. (192). The form of T_n will be taken in such a way as to satisfy the boundary

conditions and to contain n unknown parameters C_{n_j}. By choosing n different weighting factors, there will result precisely the same number of equations as unknowns.

For different selections of the forms of the weighting factor, the method is known by different names. When $w_j = \Delta(x - x_j)$ [Δ is the Dirac delta function], the method is called collocation. If T_n is a linear function of the parameters C_{n_j} and $w_j = \partial T_n/\partial C_{n_j}$, the method is called Galerkin's method. When $w_j = x^j$ or $T_n{}^j$, it is called the method of moments. For the special case of one parameter and $w_1 = 1$, Eq. (194) becomes the heat balance integral, and the method of weighted residuals reduces to the integral method. We will be concerned primarily with the application of these methods to nonlinear problems.

1. *The Method of Collocation*

Collocation is probably the crudest of all methods for solving a differential equation, and is not really a technique for improving the integral method. Nevertheless, it is a special case of the method of weighted residuals, and it does have inherent within it the possibility for self-improvement. The collocation method can be applied to problems having nonzero initial conditions as will be demonstrated. If the boundary condition is such that the temperature is specified, then no collocation point may lie on the boundary. Otherwise the location of the collocation points can be freely chosen. To demonstrate how the method of collocation is to be applied, we will present an example.

Consider a finite slab of length l. The temperature obeys Eq. (1) together with the boundary conditions

$$\frac{\partial T}{\partial x}(0,t) = 0, \quad \frac{\partial T}{\partial x}(l,t) = -f(T_l,t)$$

where T_l is the temperature at $x = l$. The initial temperature distribution is $T(x,0) = g(x)$. The boundary condition at $x = l$ is seen to be nonlinear. Assume a biquadratic profile which automatically satisfies the symmetry requirement imposed by the boundary condition at $x = 0$:

$$T = A + Bx^2 + Cx^4 \tag{195}$$

By satisfying the condition at $x = l$ the parameter B can be eliminated, with the result,

$$T = A - \frac{(f + 4Cl^3)}{2l} x^2 + Cx^4 \tag{196}$$

There are two remaining parameters in Eq. (196), and therefore two collocation points are required. We arbitrarily select these points to be

$x = 0$ and $x = l$. The second derivative of T evaluated at each collocation point is:

$$\left(\frac{\partial^2 T}{\partial x^2}\right)_{x=0} = -\left(\frac{f(T_l,t)}{l} + 4Cl^2\right) \tag{197}$$

$$\left(\frac{\partial^2 T}{\partial x^2}\right)_{x=l} = -\left(\frac{f(T_l,t)}{l} + 8Cl^2\right) \tag{198}$$

The temperature evaluated at each collocation point is

$$T_0 = A \tag{199}$$

$$T_l = A - f(T_l,t)l/2 - Cl^4 \tag{200}$$

where T_0 is the temperature at $x = 0$. We now satisfy Eq. (1) at each of the collocation points. Thus, substituting Eqs. (197, 199) and then Eqs. (198, 200) into Eq. (1), we obtain the following two ordinary differential equations:

$$-\alpha\left(\frac{f(T_l,t)}{l} + 4Cl^2\right) = \frac{dA}{dt} \tag{201}$$

$$-\alpha\left(\frac{f(T_l,t)}{l} - 8Cl^2\right) = \frac{d}{dt}\left(A - \frac{f(T_l,t)}{2} - Cl^4\right) \tag{202}$$

Eqs. (200–202) constitute a set of three simultaneous equations for the three unknowns A, C, T_l. The two initial conditions which must be satisfied are

$$T_0 = A = g(0); \qquad T_l = g(l) \tag{203}$$

It is seen that the original distribution of temperature is accounted for, but only very crudely.

Consider the special case f = constant, $g(x) = 0$. In this case, all of the steps can be carried out analytically, and the final result is

$$T = \underline{\frac{-\alpha f t}{l} + fl\left\{\frac{1 - 3(x/l)^2}{6}\right.} - \tfrac{1}{6}[1 - 6(x/l)^2 + 3(x/l)^4]e^{-12\alpha t/l^2}\Big\} \tag{204}$$

The exact solution to this problem is given on p. 112 of (*1*). A comparison shows that the underlined terms are reproduced exactly, and we may, therefore, expect the longtime solution, as obtained by the method of collocation, to be quite accurate. The remainder of the exact solution is comprised of a series of eigenfunctions. The first eigenvalue is $-\pi^2\alpha/l^2$ which is approximated in Eq. (204) by $-12\alpha/l^2$. The first eigenfunction is $1/\pi^2 \cos \pi x/l$ which is approximated in Eq. (204) by $\frac{1}{6}[1 - 6(x/l)^2 +$

$3(x/l)^4]$. Plots of the approximate and exact first eigenfunction are presented in Fig. 9.

The early time solution, obtained by the method of collocation (or by any form of the method of weighted residuals, for that matter), will never be as accurate as the longtime solution. This shortcoming can be overcome by using the concept of penetration distance for those problems with zero initial temperature. With this view, the time domain will always be divided into two intervals: the interval before the penetration distance reaches the far end, and the interval after this occurrence. As

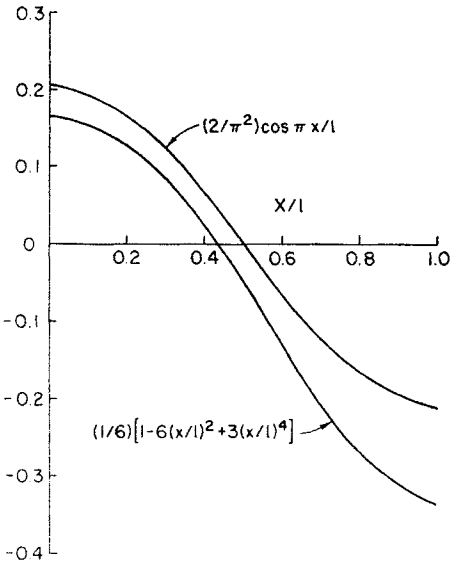

FIG. 9. Approximate and exact first eigenfunction for a slab with constant surface heat flux and insulated far end.

forfeit for the improved accuracy in the first time interval, the solution in the second time interval will be less accurate than the solution obtained without using the concept of penetration distance.

We can, of course, improve the overall accuracy by including additional collocation points. Suppose, for example, we add another term, Dx^6, to the temperature profile in Eq. (195). We can now collocate at the interior point $x = l/2$ as well as at the boundaries. This results in an additional differential equation, and, for the case f = constant, $g = 0$, we obtain approximations to the first two eigenfunctions. Furthermore, the accuracy of the first eigenfunction and eigenvalue is improved over that given in Eq. (204). To this approximation, the first two eigenvalues

are $-9.50\alpha/l^2$ and $-50.5\alpha/l^2$, which are to be compared with the exact values $-\pi^2\alpha/l^2$ and $-4\pi^2\alpha/l^2$, respectively. The additional collocation point also allows for an improved representation of the initial temperature distribution. It can be seen that the more collocation points, the better the representation of the solution. Clearly, this method is not restricted to problems in one space dimension. However, in two space dimensions it becomes more imperative to saturate the spacial domain with collocation points.

In one dimension, the method of collocation is analogous to the problem of curve fitting, where the fit is effected by compelling the assumed analytical representation to pass through the true curve at a specified number of points.

2. *The Method of Moments*

An early, yet quite sophisticated application of the integral method to solve the nonlinear heat conduction equation is presented in a paper by Fujita (*47*) who credits Yamada (*48*) with the original conception. Consider the one-dimensional heat equation with temperature-dependent properties, and let $w_j = x^j$ in Eq. (194). If the spacial domain is the interval $a < x < b$, Eq. (194) becomes

$$\int_a^b x^j L(T_n)dx = 0, \qquad j = 0, 1, 2, \ldots n \tag{205}$$

By virtue of the theorem of moments, any function T_n which satisfies this set of n equations makes $L(T_n)$ vanish at least n times in the interval $a < x < b$. Hence if T_n further satisfies any given initial or boundary condition, such a function may be considered to be an approximate solution of Eq. (192), and we may improve the accuracy by making n moderately large. In practice, of course, n is limited because the calculations become too tedious. The case $n = 0$ is identically the integral method which, as has been amply demonstrated, yields reasonable accuracy whenever it is applied to problems with monotonic inputs.

It has been stated previously that the accuracy of a solution obtained using the integral method might be improved by increasing the order of the polynomial used to represent the profile and applying derived constraints at the ends of the interval. However, as was pointed out, there are cases for which the accuracy actually worsens using this procedure. On the other hand, suppose that we increase the order of the polynomial and only use the natural constraints. The additional parameters can then be determined by using the higher moments. Thus, by virtue of the theorem of moments, we can expect an improved solution.

For example, for the case of temperature-dependent thermal properties,

Eq. (78) is the basic field equation. Then, for $j = 1$ the weighting factor is x. After integrating by parts we obtain

$$\frac{d}{dt}\int_0^\delta xv\,dx = -\int_0^\delta \alpha\frac{\partial v}{\partial x}\,dx \tag{206}$$

where a semiinfinite slab has been assumed, and we have utilized the concept of penetration distance. Equation (206) together with the usual heat balance integral will permit the determination of two parameters in the profile. Notice that in this approximation, the variation of the diffusivity throughout the slab appears, and not merely the diffusivity at the surface.

Fujita has used the method of moments to solve the heat equation with a linear dependence of thermal conductivity on temperature. Initially, the slab is at zero temperature. He divides time into the usual two intervals and employs the concept of penetration distance. The procedure is straightforward and will not be presented here inasmuch as Fujita's complete analysis has been reproduced by Crank (*49*) in a readily accessible reference. It is interesting, however, to compare Fujita's constant diffusivity result in the first interval with the result using only the heat balance integral and a quadratic profile. The latter result for a cubic profile is presented in Section II,A,2, and it is shown there that the surface heat flux is proportional to the numerical factor .602. For a quadratic profile, the factor is .576. Fujita also obtains .576 using zeroth and first moments and a cubic profile. Thus, the loss in accuracy which occurs in going from a quadratic to a cubic profile in the earlier method does not take place with the method of moments.

Suppose the initial temperature were not zero. In this case the concept of penetration distance cannot be applied. However, as in the method of collocation, we can account for nonzero initial conditions by abandoning the concept of penetration distance; but, by doing so, we will forfeit some accuracy in the early time. If the initial temperature is $T(x,0) = g(x)$, then, upon applying the method of moments, we obtain

$$\int_a^b x^j T(x,0)\,dx = \int_a^b x^j g(x)\,dx, \qquad j = 0, 1, 2, \ldots n \tag{207}$$

These equations can be used to generate sufficient initial conditions for all the parameters.

Another possible way to apply the method of moments is to weight the equation with the dependent variable instead of the independent variable:

$$\int_a^b u^j L(T)\,dx = 0, \qquad j = 0, 1, 2, \ldots n \tag{208}$$

The advantage that Eq. (208) has over Eq. (205) is that the differential operator is weighted most where the temperature difference from ambient is greatest. Thus, regions of greater activity are considered to be more important than regions of lesser activity. As an example, for the case of temperature-dependent thermal properties, Eq. (78) is the basic field equation. Then for $j = 1$, we take the weighting factor to be v. After an integration by parts, we arrive at

$$\frac{1}{2}\frac{d}{dt}\int_0^\delta v^2\,dx = v_s\alpha_s\left(\frac{\partial v}{\partial x}\right)_s - \int_0^\delta \alpha(v)\left(\frac{\partial v}{\partial x}\right)^2 dx \tag{209}$$

where a semiinfinite slab has been assumed and we have utilized the concept of penetration distance. Equation (209) together with the usual heat balance integral will permit the determination of two parameters in the profile. This two-parameter technique was introduced by Tani (*50*) to solve a boundary layer problem. As in the case of Eq. (206), the variation of the diffusivity throughout the slab appears, and not merely the diffusivity at the surface.

3. Galerkin's Method

Galerkin's method is another variation of the method of weighted residuals and is mainly applicable to linear problems. It can be applied with ease to complicated two- and three-dimensional regions, and to cases where the thermal properties are neither isotropic nor homogenous. A presentation of the Galerkin method as applied to slabs is given by Schmit (*51*). A proof of the convergence of the method is given by Green (*52*). We will illustrate the method by applying it to solve for the temperature in a circular region of radius a initially at temperature $p(r)$. At the boundary $r = a$ the temperature is maintained at $T = T_0$. We assume a solution in the form

$$T = T_0 + \sum_1^n \phi_k(t)g_k(r) \tag{210}$$

where $g_k(a) = 0$ so as to satisfy the boundary condition. The temperature satisfies Eq. (56). Upon multiplying by $g_j(r)$ and applying the condition that the weighted residual must be zero, we obtain

$$\int_0^a g_j(r)\left[\alpha\frac{\partial}{\partial r}\left(r\frac{\partial T}{\partial r}\right) - r\frac{\partial T}{\partial t}\right]dr = 0 \tag{211}$$

If Eq. (210) is substituted into Eq. (211), and the first term is integrated

by parts, we obtain

$$\sum_1^\infty \phi_k' \int_0^a g_j g_k r\, dr + \alpha \sum_1^\infty \phi_k \int_0^a r g_j' g_k'\, dr = 0 \tag{212}$$

where the prime denotes differentiation.

The initial condition is satisfied by setting $T(r,0) = p(r)$ in Eq. (210), resulting in

$$T_0 + \sum_1^\infty \phi_k(0) g_k(r) = p(r) \tag{213}$$

Upon multiplying Eq. (213) by $rg_j(r)$ and integrating over the interval, we obtain

$$T_0 \int_0^a r g_j\, dr + \phi_k(0) \int_0^a r g_j g_k\, dr = \int_0^a p(r) g_j(r)\, dr \tag{214}$$

Equation (212) is an eigenvalue problem. The characteristic numbers and vectors can be obtained in standard fashion by letting $\phi_k = A_k e^{\omega t}$. Equation (214) represents n simultaneous equations for the n initial values $\phi_k(0)$. If the functions g_k are orthogonal, Eq. (212) will appear in canonical form; that is, the derivatives will be solved for in terms of other quantities; at the same time, in Eq. (214), the initial conditions will be given directly.

Suppose we choose $n = 1$, and select the function g_1 to be

$$g_1 = (r^2 - a^2) \tag{215}$$

This selection does not comply with the form suggested by Lardner and Pohle for problems with polar symmetry (see Eq. (59)). However, Lardner and Pohle's rule must be obeyed only when the concept of penetration distance is being adhered to, which is not the case here. With g_1 given by Eq. (215), Eq. (212) becomes

$$\phi_1' \frac{a^2}{b} + \alpha \phi_1 = 0 \tag{216}$$

Upon choosing $p(r) = 0$, Eq. (214) becomes

$$-\frac{T_0}{4} + \phi_1(0) \frac{a^2}{6} = 0 \tag{217}$$

The solution is, therefore,

$$\phi_1 = \frac{3}{2} \frac{T_0}{a^2} e^{-6\alpha t/a^2} \tag{218}$$

Upon substituting into Eq. (210), the temperature is seen to be

$$T = T_0 - \tfrac{3}{2}T_0\left(1 - \frac{r^2}{a^2}\right)e^{-6\alpha t/a^2} \tag{219}$$

Figure 10 shows the axis temperature as obtained from Eq. (219) and compares it with the exact solution. As in the other forms of the method of weighted residuals, the errors are seen to be largest for early time.

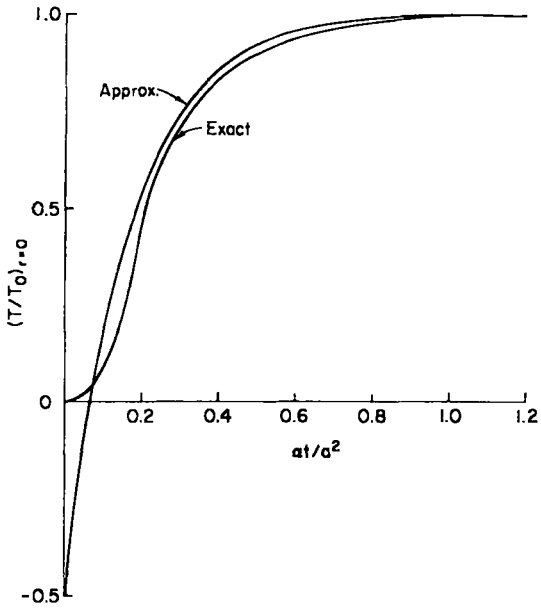

FIG. 10. Axis temperature time history for a circular region of radius a with constant surface temperature—comparison between exact and Galerkin's solution.

These errors can be reduced by using the concept of penetration distance [for $p(r) = 0$]. For a one-parameter profile, such as the one assumed in the foregoing example, Galerkin's method reduces to the equation of the first moment as exemplified by Eq. (209), except that in this case it must be modified to account for polar symmetry. For constant thermal properties the result is

$$\frac{1}{2}\frac{d}{dt}\int_a^{a-\delta} rT^2\,dr = \alpha T_0 a\frac{\partial T}{\partial r}(a) - \alpha\int_a^{a-\delta} r\left(\frac{\partial T}{\partial r}\right)^2 dr \tag{220}$$

The appropriate one parameter profile which satisfies Lardner and Pohle's

rule for problems with polar symmetry is

$$T = T_0 \left\{ 1 + \left[\frac{r}{a - \delta} - 1 - ln\,(1 - \delta/a) \right] \frac{ln\, r/a}{[ln\,(1 - \delta/a)]^2} \right\}, \qquad a - \delta \leq r \leq a \quad (221)$$

The carrying out of the solution is left to the reader.

B. THE METHOD OF YANG

In a series of papers, K. T. Yang (*53*, *54*, *55*, *56*) has developed and demonstrated an improved integral method, and also an error criterion. He has applied the improved integral method to boundary layer problems. steady convection problems, and unsteady conduction problems. The final formulation of the improved method is presented in (*56*), and the description which follows is taken from that paper. We will present the method exclusively in the context of unsteady heat conduction.

The basic aim of the improved integral method is to use the solution obtained from the heat-balance integral to achieve an improved profile. Then, having improved the profile, we can solve the heat-balance integral over again. In theory, the procedure may be repeated as many times as desired. After each iteration, a certain quantity J is calculated. J is defined in such a way that if the solution were exact, J would be zero. By monitoring the magnitude of J at each iteration, we can discover how much our solution has improved. At first glance, it would seem to be superfluous to have such an error criterion, because it might be thought that the quality of the solution after n iterations could be judged by observing whether or not there was a large change from one iteration to the next. But, in practice it becomes necessary to stop after one iteration, and we would like some indication of the improvement effected by this iteration. Hence, the error criterion is an important part of the method.

With these preliminary remarks out of the way, we can now describe the improved integral method in detail. As developed originally by Yang, the method is to be applied only to those cases for which the concept of penetration distance has meaning, i.e., only to semiinfinite slabs with uniform initial temperature. We will restrict our attention to such cases.

Consider the heat equation $L(u) = 0$. Averaging from zero to infinity we obtain

$$I_{\mathrm{I}} + I_{\mathrm{II}} = 0 \quad (222)$$

where

$$I_{\mathrm{I}} = \int_0^1 L\, d\eta, \quad I_{\mathrm{II}} = \int_1^\infty L\, d\eta \quad (223)$$

and $\eta = x/\delta$. To determine the basic integral solution, we let T' be

described by a polynomial (say) in the interval $0 \leq \eta \leq 1$, and $T = 0$ in the interval $1 \leq \eta \leq \infty$. Thus, I_{II} is zero in the first iteration, and Eq. (222) defines the usual heat-balance integral from which the basic integral solution may be obtained.

In the improved integral procedure and in subsequent iterations, the thickness $\delta(t)$ is treated as an auxiliary function defined by the solution to Eq. (222) with I_{II} included. The improvement in the profile is accomplished by first transforming the independent variables from (x,t) to (η,t). For the heat equation with variable thermal properties, Eq. (78), we obtain, in terms of the transformed variable v,

$$\frac{\partial^2 v}{\partial \eta^2} - \left[\frac{\delta \dot{\delta} \eta}{\alpha} + \frac{\alpha'}{\alpha}\frac{\partial v}{\partial \eta}\right]\frac{\partial v}{\partial \eta} = \frac{\delta^2}{\alpha}\frac{\partial v}{\partial t} \tag{224}$$

where the dot denotes differentiation with respect to time and the prime denotes differentiation with respect to v. We now evaluate the coefficient of $\partial v/\partial \eta$ and also the right-hand side of Eq. (224) by using the results already at hand from the basic integral solution. Equation (224) then becomes an ordinary linear differential equation in terms of η with time entering only as a parameter. For brevity, we rewrite Eq. (224) as

$$\frac{d^2 v}{d\eta^2} + P_1 \frac{dv}{d\eta} = P_2 \tag{225}$$

When P_1 and P_2 take values from the basic integral solution they will be denoted by P_{1_0} and P_{2_0} respectively. Equation (225) is readily integrated to yield an improved profile v_1, where the subscript refers to the first iteration. However, both P_1 and P_2 involve v, and v has a composite structure; therefore, Eq. (225) must be integrated separately for the two intervals $0 \leq \eta \leq 1$ and $1 \leq \eta \leq \infty$. Using the subscripts I and II to designate the two intervals, Eq. (225) may be written as

$$\frac{d^2 v_{1_I}}{d\eta^2} + P_{1_{0_I}} \frac{dv_{1_I}}{d\eta} = P_{2_{0_I}}; \qquad \frac{d^2 v_{1_{II}}}{d\eta^2} + P_{1_{0_{II}}} \frac{dv_{1_{II}}}{d\eta} = P_{2_{0_{II}}} \tag{226}$$

which can be solved explicitly. Four constants of integration will appear in the solutions, and these may be determined from two matching conditions at $\eta = 1$, viz.,

$$v_{1_I} = v_{1_{II}}, \quad \frac{dv_{1_I}}{d\eta} = \frac{dv_{1_{II}}}{d\eta}, \quad \eta = 1 \tag{227}$$

together with the prescribed conditions at $\eta = 0$ and $\eta = \infty$. The new profiles must now be resubstituted into the integral equation, Eq. (222), and an improved variation of δ, viz. δ_1, obtained. When $\delta_1(t)$ is sub-

stituted in η, v_1 becomes a known function of x and t and the improved integral solution is complete. The steps may, of course, be repeated treating v_1 as the basic solution, and this results in an iteration procedure.

In applying Eq. (225) we evaluated P_1 and P_2 from the solution obtained in the previous iteration. However, after the solution is at hand we may evaluate the quantity

$$\epsilon_n = \frac{d^2v_n}{d\eta^2} + P_{1_n}\frac{dv_n}{d\eta} - P_{2_n} \tag{228}$$

where the P's are now evaluated from the solution obtained in the current iteration. The smallness of ϵ_n will be a measure of the error, and, if the iteration procedure converges, ϵ_n may be expected to approach zero for all η. In order to account for both positive and negative values of ϵ_n in the interval $0 \leq \eta \leq \infty$ the following error criterion is used:

$$J_n(t) = \int_0^\infty {\epsilon_n}^2\, d\eta = \int_0^1 {\epsilon_{n_I}}^2\, d\eta + \int_1^\infty {\epsilon_{n_{II}}}^2\, d\eta \tag{229}$$

Separate calculations for the two intervals $0 \leq \eta \leq 1$ and $1 \leq \eta \leq \infty$ are necessary in view of Eq. (226). In the actual evaluation of ϵ_n in the nth iteration, Eq. (228) may be simplified by eliminating the second profile derivative as follows:

$$\epsilon_n(t,\eta) = (P_{2,n-1} - P_{2,n}) + (P_{1,n} - P_{1,n-1})\frac{dv_n}{d\eta} \tag{230}$$

By comparing successive values of J, the question of convergence may be readily answered.

As an illustration of the rapidity of the convergence of his method, Yang has "improved" the integral solution for a semi-infinite slab with step-wise surface temperature change and linear variation of thermal conductivity with temperature. The basic solution to this problem is given by Eq. (88) [or Eq. (89)] for an assumed cubic profile. For a quartic profile with an additional derived constraint the solution has been given by Goodman (*21*), and it is this quartic integral solution that Yang uses as the basic solution to start his iteration procedure. The three cases $\alpha = +.5,\ 0,\ -.5$ shown in Fig. 2 were chosen, and the iterated values of $-d/dy\,(T/Ts)_{y=0}$, as shown exactly in Fig. 2, were determined together with the J values. The results are presented in Table III. Notice the large reduction in J from the integral solution to the first iteration. This is significant for the following reason: The sample problem is of the type known as self-similar, i.e., the temperature is a function of the one variable $x/\sqrt{t}$, and not a function of x and t separately. Because the sample problem has this property it is a simple matter to

iterate as many times as desired. Most problems which are encountered are not self-similar, and for those cases, Eq. (225) must be solved repeatedly for each value of the time. Because of the enormous amount of numerical work involved in such a program, it is not practical to carry out Yang's iteration scheme beyond the first improvement. Hence, it is important that a large improvement be effected in the first iteration. The large reduction in J in the first iteration of the sample problem attests to the utility of the method.

TABLE III

RESULTS OBTAINED BY FIVE SUCCESSIVE APPLICATIONS OF YANG'S METHOD[a]

α	Iterations	J	$-\frac{d}{dy}\left(\frac{T}{T_s}\right)_{y=0}$
0.5	0	0.23920	0.865
	1	7.0916×10^{-5}	0.8631
	2	5.7466×10^{-7}	0.8631
	3	5.0310×10^{-7}	0.8632
	4	5.0157×10^{-7}	0.8632
	5	4.9970×10^{-7}	0.8632
0	0	0.25687	1.095
	1	6.7926×10^{-6}	1.1284
	2	1.5519×10^{-6}	1.1284
	3	1.5457×10^{-6}	1.1284
	4	1.5407×10^{-6}	1.1284
	5	1.5366×10^{-6}	1.1284
−0.5	0	0.21789	1.789
	1	5.0568×10^{-5}	1.8603
	2	1.7631×10^{-8}	1.8596
	3	9.9195×10^{-11}	1.8596
	4	9.4097×10^{-11}	1.8596
	5	8.4550×10^{-11}	1.8596

[a] Data from Yang (*56*).

C. THE METHOD OF DORODNITSYN

A generalization of the integral method has been described by Dorodnitsyn (*57*) in which the usual integral method is considered to be the first approximation. Subsequent approximations are obtained by dividing the interval into two or more strips and averaging over each strip. Thus, the values of the dependent variable at the boundary of each strip can be taken as the unknowns, and the number of unknowns is exactly equal to the number of heat balance integrals. Dorodnitsyn (*58*) has generalized this method further by introducing weighting functions in the integral relations in each strip. He has applied the technique to solve a boundary layer problem, but not to solve the (mathematically

simpler) heat equation. Sokolova (*59*), on the other hand, has applied a method similar to Dorodnitsyn's first method to the semiinfinite slab using two intervals $0 < x < (\delta/2)$ and $(\delta/2) < x < \delta$. Parabolic profiles are used in each interval. (Higher order polynomials would require derived constraints which are inadmissable.) Thus, seven parameters arise: three from each parabola plus the penetration distance. The seven conditions which completely define the solution are: the given boundary condition at the surface $x = 0$; the zero temperature and zero heat flux condition at $x = \delta$; the continuity of temperature and heat flux at $x = (\delta/2)$; and the two heat balance integrals in each interval. Much improvement in accuracy is reported over the results obtained using but one interval. Goodman and Shea (*33*) used much the same technique in solving for the melting of finite slabs, but here the division into two intervals arose naturally because of the two phases. Also, the location of the melt line which divides the two intervals was an additional unknown.

The same technique can be applied to a slab of finite length, l. For the linear problem presented in Section II, B, 1, it was shown that the first eigenfunction of the exact solution is reproduced approximately when one interval is used. If we use the two intervals $0 < x < (l/2)$ and $(l/2) < x < l$, the first two eigenfunctions will be reproduced approximately. The approximate first two eigenvalues in this case turn out to be -2.597 and -31.7, which are to be compared with the exact values: -2.467 and -22.2. It is clear that the number of eigenfunctions which can be reproduced approximately will equal the number of intervals which are used. Also the numerical values of the solution will tend to improve as the number of intervals increases.

Landahl (*4*) has also reported improved accuracy using two intervals (for the semiinfinite case) in his applications, but he does not present any details.

VIII. A Nonsteady Convection Problem

Thus far, we have used the integral method to solve various forms of the heat equation in one space dimension only. The field equation in these cases was always reduced to an ordinary differential equation. At this point, we will apply the integral method to a problem in forced convection that was originally solved by Goodman (*60*). This problem involves two space dimensions and time, and the integral method reduces the field equation to a partial differential equation in one less independent variable.

The problem to be considered is the temperature response of an incompressible fluid due to a wall temperature which is uniform but unsteady. The approach adopted uses the integral method to solve for the response

due to a unit step in wall temperature, and then uses Duhamel's integral to generalize to arbitrary wall temperature.

In this section the (x,y) components of convection velocity will be denoted by (u,v). Neglecting viscous dissipation, and assuming constant thermal properties, the temperature is found to obey the following equation:

$$\rho c\left[\frac{\partial T}{\partial t}+u\frac{\partial T}{\partial x}+v\frac{\partial T}{\partial y}\right]=k\frac{\partial^2 T}{\partial y^2} \tag{231}$$

Taking the external temperature to be zero, and assuming a penetration distance $\delta(x,t)$, we find, upon integrating Eq. (231) from $y = 0$ to $y = \delta$,

$$\frac{\partial}{\partial t}\int_0^\delta \rho cT\,dy+\frac{\partial}{\partial x}\int_0^\delta \rho cuT\,dy=-q_s \tag{232}$$

where q_s is the surface heat flux, and the continuity equation for the velocities has been used. We now adopt the approximation that the velocity profile is linear and is given by the first term of a Taylor series expansion near the wall. This approximation can be expected to have greatest validity when the Prandtl number is large, because in that case the penetration distance will be small in comparison with the boundary layer thickness. In practice, the approximation is found to be acceptable when the Prandtl number is of the order unity.

$$u\approx\left(\frac{\partial u}{\partial y}\right)_s y=\frac{\tau_s}{\mu}y \tag{233}$$

where τ_s is the wall shear stress and μ is the coefficient of viscosity. Upon applying Fourier's law, and substituting Eq. (233) into Eq. (232), we obtain

$$\frac{\partial}{\partial t}\int_0^\delta \rho cT\,dy+\frac{\partial}{\partial x}\int_0^\delta \frac{\rho c\tau_s yT}{\mu}\,dy=-q_s=-k\left.\frac{\partial T}{\partial y}\right|_s \tag{234}$$

We now assume a cubic profile which obeys the constraints: $T(x,\delta,t) = 0$; $\partial T/\partial y(x,\delta,t) = 0$; $T(x,0,t) = T_s$; $\partial^2 T/\partial y^2(x,0,t) = 0$. The last condition is a derived constraint, and makes use of Eq. (231) at $y = 0$ and the no-slip conditions. The temperature profile is seen to be of the form

$$T=\frac{T_s}{2}\left[3\left(1-\frac{y}{\delta}\right)^2-\left(1-\frac{y}{\delta}\right)^3\right] \tag{235}$$

Upon substituting into Eq. (234), we obtain

$$\frac{\rho c}{\mu}\alpha\frac{\partial}{\partial x}(\tau_s\delta^2)+\rho c\beta\frac{\partial\delta}{\partial t}=\frac{3}{2}\frac{k}{\delta} \tag{236}$$

where

$$\alpha \equiv 1_2 \int_0^1 \eta\, d\eta[3(1-\eta)^2 - (1-\eta)^3] = 1/10$$

$$\beta \equiv 1/2 \int_0^1 [3(1-\eta)^2 - (1-\eta)^3]\, d\eta = 3/8$$

Thus, Eq. (236) simplifies to

$$\frac{\delta}{15\mu}\frac{\partial}{\partial x}(\tau_s \delta^2) + \frac{\delta}{4}\frac{\partial \delta}{\partial t} = \alpha \tag{237}$$

We now restrict our attention to a flat plate, in which case

$$\tau_s = K_1/\sqrt{x} \tag{238}$$

where K_1 is given, for example, by Schlichting (3, Chapter VIII):

$$K_1 = 0.332\rho U^2 \sqrt{\nu/U} \tag{239}$$

and U is the free stream velocity, $\nu(=\mu/\rho)$ is the kinematic viscosity. Equation (238) becomes

$$\frac{\delta K_1}{15\mu}\frac{\partial}{\partial x}\left(\frac{\delta^2}{\sqrt{x}}\right) + \frac{\delta}{4}\frac{\partial \delta}{\partial t} = \alpha \tag{240}$$

Since the wall temperature is uniform, δ always starts at $x = 0$, and hence, a similarity solution is possible. Let

$$\phi = \left(\frac{K_1}{30\mu\alpha}\right)^{1/4} \delta/\sqrt{x} \tag{241}$$

$$F = 4\alpha\left(\frac{K_1}{30\mu\alpha}\right)^{3/4} t/x \tag{242}$$

Assume $\phi = \phi(F)$. Then Eq. (240) reduces to the following ordinary differential equation:

$$\frac{dF}{d\phi}(1 - \phi^2) = -4\phi^2 F + \phi \tag{243}$$

This equation is linear if F is taken to be the dependent variable. Applying the initial condition $\phi(0) = 0$, we obtain the solution,

$$F = (1-\phi^2)^{1/4} \int_0^\phi \frac{\phi_1\, d\phi_1}{(1-\phi_1^2)^{3/4}} \tag{244}$$

which is shown plotted in Fig. 11.

The equation

$$\phi = 1 \tag{245}$$

is a singular solution of Eq. (243); this solution does not satisfy the initial condition, but is a steady state solution. The complete solution must begin for small F on the curve represented by Eq. (244), and end for large F on the curve represented by Eq. (245). However, the curve of

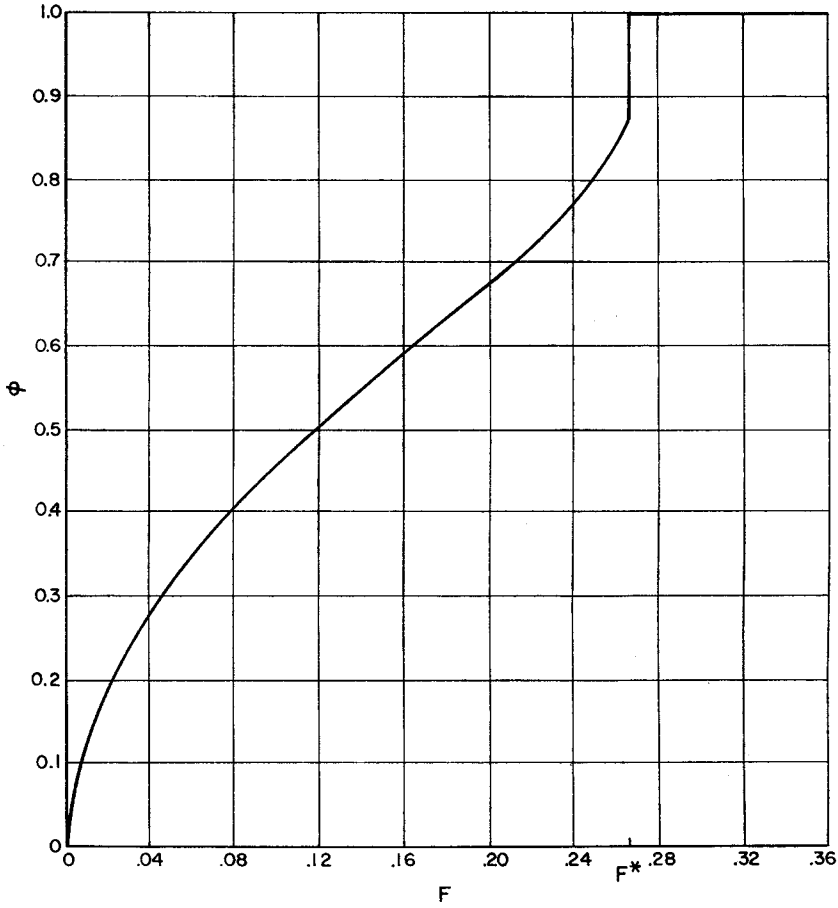

FIG. 11. Transient growth of penetration distance for forced convection on a flat plate with step in surface temperature (*60*).

Eq. (244) turns back on itself, so that for some values of F (time) it is double-valued. This is impossible physically, and somewhere before turning back on itself the solution must jump to $\phi = 1$. This jump will be called a heat wave.

The heat wave must occur at some constant value of F, say F^*. In

order to calculate the value of F^* we must obtain a conservation law across the wave. Such a law can be obtained from Eq. (243). Setting $F = F^*$, and integrating, it is found that

$$\tfrac{1}{2}\phi^2 - \tfrac{4}{3}\phi^2 F^* \tag{246}$$

is conserved across the wave. On the side of the wave where Eq. (244) is applicable, let $\phi = \phi^*$. On the side of the wave where Eq. (245) is applicable, let $\phi = 1$. Hence, applying the conservation law, we obtain

$$F^* = \tfrac{3}{8}\frac{(1 + \phi^*)}{1 + \phi^* + \phi^{*2}} \tag{247}$$

From the numerical solution of Eq. (244) it is found that

$$F^* = 0.266 \tag{248}$$

Now it is clear that for $F > F^*$ the steady state solution prevails, whereas, for $F < F^*$ the solution is transient. Thus, a step in surface temperature will give rise to a starting heat wave which propagates from the leading edge, and whose trajectory is given by $F = F^*$. After this wave has passed any particular station, the heat flux is steady at that station. In order to define the trajectory of the wave more explicitly, substitute Eq. (239) into Eq. (242), and let $F = F^*$. After some simplification we obtain

$$Ut/x = 1.33\mathrm{Pr}^{\frac{1}{2}} \tag{249}$$

where $\mathrm{Pr}(=\mu c/k)$ is the Prandtl number. Hence, the larger the Prandtl number, the slower the wave, and the longer it takes to achieve steady state.

The surface heat flux response to a step in surface temperature can now be determined, and the result is

$$q_s = \frac{3}{2}\frac{kT_s}{\delta} = 0.334kT_s\sqrt{\frac{U}{\nu x}}\,\mathrm{Pr}^{\frac{1}{2}}\frac{1}{\phi} \tag{250}$$

which may be compared with the steady state solution presented by Schlichting (*3*, Chapter XIV). In order to obtain the response to an arbitrary wall temperature variation, we apply Duhamel's integral, with the result that

$$q_s = 0.334k\sqrt{\frac{U}{\nu k}}\,\mathrm{Pr}^{\frac{1}{2}}\left[\int_0^F \frac{dT_s(F_1)}{\phi(F - F_1)} + \frac{T_s(0)}{\phi(F)}\right] \tag{251}$$

The definition of F, Eq. (242), may be simplified with the aid of Eq.

(239). After some manipulation, it is seen that

$$F = \frac{0.20Ut}{\mathrm{Pr}^{1/3}x} \tag{252}$$

Finally, it should be mentioned that Cess (*61*) has solved the same problem by use of La Place transforms. He overcomes the intractability of Eq. (231) by constructing two solutions in the LaPlace transform domain which have the proper behavior for small and large values of the LaPlace transform variable respectively, and then patching them.

IX. A Two-Dimensional Problem

Consider a cylindrical prism having a square cross section bounded by the isothermal surfaces

$$C_0(x,y) = (x^2 - a^2)(y^2 - a^2) = 0 \tag{253}$$

The region is assumed to contain liquid at the melting temperature $T = 0$, and the surfaces are maintained at the temperature $T = -T_0$. During the period of solidification the location of the melt line will be described by the line $C_F(x,y,t) = 0$ which is an isothermal on which $T = 0$. The heat conduction equation is

$$\alpha\left(\frac{\partial^2 T}{\partial x^2} + \frac{\partial^2 T}{\partial y^2}\right) = \frac{\partial T}{\partial t} \tag{254}$$

The boundary conditions are

$$\begin{aligned} &T = -T_0 \text{ on } C_0(x,y) = 0, \quad t > 0 \\ &T = 0 \text{ on } C_F(x,y,t) = 0 \end{aligned} \tag{255}$$

The initial conditions are

$$T = 0 \text{ and } C_F = C_0 = 0, \quad t = 0 \tag{256}$$

Let $V(C_F, C_0)$ be the volume of solidified material at time t per unit depth of boundary in the axial direction. Thus in time Δt the volume of solid increases by an amount $\Delta V(C_f,C_0)$, and there will be set free an amount of heat.

$$\Delta Q = \rho \mathrm{L} \Delta V(C_F,C_0) \tag{257}$$

This must escape by conduction through the solidified material in such a way that the amount of heat that flows outward is

$$\Delta Q = -k\left(\oint \frac{\partial u}{\partial n}\, ds\right)\Delta t \tag{258}$$

where s is the distance measured along the contour $C_f = 0$ in a counter-clockwise direction, and n is the normal. Thus, in the limit as Δt becomes vanishingly small

$$k \oint_{C_F=0} \frac{\partial T}{\partial n}\, ds = -\rho L \frac{dV\ (C_F, C_0)}{dt} \tag{259}$$

where

$$V(C_F, C_0) = \iint_{C_F=0}^{C_0=0} dx\, dy = \iint_{C_F=0}^{C_0=0} dS \tag{260}$$

Upon introducing the dimensionless variables

$$\left.\begin{aligned} \theta &= \frac{T + T_0}{T_0} & \beta &= \frac{\rho L \alpha}{k T_0} \\ \tau &= \frac{t\alpha}{a^2} & v &= \frac{V}{a^2} \\ l &= \frac{s}{a} & \sigma &= \frac{S}{a^2} \\ X &= \frac{x}{a} & Y &= \frac{y}{a^2} \end{aligned}\right\} \tag{261}$$

the above boundary value problem may be written

$$\frac{\partial^2 \theta}{\partial X^2} + \frac{\partial^2 \theta}{\partial Y^2} = \frac{\partial \theta}{\partial \tau} \tag{262}$$

$$\left.\begin{aligned} &\theta = 0 \text{ on } C_0(X,Y) = (X^2 - 1)(Y^2 - 1) = 0, \quad \tau > 0 \\ &\theta = 1 \text{ on } C_F(X,Y,\tau) = 0 \end{aligned}\right\} \tag{263}$$

$$\oint_{C_F=0} \frac{\partial \theta}{\partial n}\, dl = -\beta \frac{dv}{d\tau} \tag{264}$$

where

$$v(C_F, C_0) = \iint_{C_F=0}^{C_0=0} d\sigma$$

$$\theta = 1, \quad \tau = 0 \tag{266}$$

G. Poots (*62*) has solved the above two dimensional heat conduction problem using an integral method. The success of the solution he obtains depends, to a large extent, upon his ability to make intelligent guesses for the shape of the solidification front (melt line) for all time, and for the temperature profiles. Because the problem which he poses contains many symmetries the guesses are likely to be nearly correct.

Note, that at the beginning

$$C_F(X,Y,\tau) = C_0 = (X^2 - 1)(Y^2 - 1) = 0, \quad \tau = 0 \tag{267}$$

It is plausible to assume that for small time C_f will be in the shape of a

square with rounded corners, and must become circular, i.e., of the form $X^2 + Y^2 - f(\tau) = 0$, for times near the finish of the solidification period. Moreover, at the end of the solidification period the solidification front lies on the axis of the prism, $X = Y = 0$. It is thus reasonable to assume the following shape

$$C_F(X,Y,\tau) = (X^2 - 1)(Y^2 - 1) - \epsilon(\tau) = 0 \tag{268}$$

where ϵ is an unknown function of time. The initial condition, Eq. (266), is now replaced by

$$\epsilon = 0 \text{ at } \tau = 0 \tag{269}$$

and, by virtue of Eq. (268), $\epsilon = 1$ at the instant of complete solidification of the prism.

The heat balance integral is derived by integrating both sides of Eq. (262) over the solidified phase bounded by the contours $C_0 = 0$ and $C_F = 0$. Applying Green's theorem to the resulting equation and using the boundary condition Eq. (264), we obtain

$$\beta \frac{dv}{d\tau} + \oint_{C_0=0} \frac{\partial \theta}{\partial n}\, dl = \iint_{C_F=0}^{C_0=0} \frac{d\theta}{d\tau}\, d\sigma \tag{270}$$

We assume for the solidified phase, the one-parameter temperature distribution

$$\theta = \frac{(X^2 - 1)(Y^2 - 1)}{\epsilon} \tag{271}$$

which satisfies, by virtue of Eq. (267), the boundary conditions, Eq. (263). Upon substituting Eq. (271) into the heat-balance integral, Eq. (270), there results a first order differential equation for $\epsilon(\tau)$ to be solved subject to the initial condition Eq. (269). The solution is

$$\tau = \int_0^{\epsilon} \{\tfrac{3}{8}\beta A_0(\epsilon) + A_1(\epsilon)\}\, d\epsilon \tag{272}$$

where

$$A_0 = -\epsilon \frac{dI_0}{d\epsilon} \tag{273}$$

and

$$A_1 = \tfrac{1}{24}\left(\frac{4 - 3I_1}{\epsilon}\right) \tag{274}$$

Defining

$$R(X;\epsilon) = \left\{\frac{1 - \epsilon - X^2}{1 - X^2}\right\} \tag{275}$$

the required integrals

$$I_0 = \int_0^{\sqrt{1-\epsilon}} R^{-1/2}\, dX \tag{276}$$

and

$$I_1 = \int_0^{\sqrt{1-\epsilon}} (2 - 2X^2 + \epsilon) R^{1/2}\, dX \tag{277}$$

can be expressed in terms of complete elliptic integrals. The results are

$$I_0 = E - \epsilon K$$

$$I_1 = \tfrac{1}{3}\{(4 + \epsilon)E - \epsilon(2 + 3\epsilon)K\} \tag{278}$$

where the modulus is $\sqrt{1 - \epsilon}$. Upon using the rules for differentiating E and K we obtain

$$A_0 = \tfrac{1}{2}\epsilon K \tag{279}$$

The functions A_0 and A_1 are tabulated in Table IV correct to six decimal places.

TABLE IV

THE FUNCTIONS A_0 AND A_1 (62).

ϵ	A_0	A_1
0.00	0.000000	0.000000
0.04	0.060322	0.012226
0.08	0.107342	0.021931
0.12	0.149558	0.030715
0.16	0.188741	0.038914
0.20	0.225720	0.046685
0.24	0.260979	0.054122
0.28	0.294833	0.061284
0.32	0.327503	0.068213
0.36	0.359154	0.074943
0.40	0.389913	0.081496
0.44	0.419880	0.087893
0.48	0.449136	0.094149
0.52	0.477748	0.100276
0.56	0.505772	0.106287
0.60	0.533256	0.112190
0.64	0.560241	0.117994
0.68	0.586764	0.123705
0.72	0.612855	0.129329
0.76	0.638542	0.134872
0.80	0.663849	0.140339
0.84	0.688800	0.145734
0.88	0.713413	0.151061
0.92	0.737706	0.156323
0.96	0.761696	0.161524
1.00	0.785398	0.166667

The analysis presented above differs in its application of the integral method from that presented in Section IV in one fundamental respect (aside from the additional dimension). The temperature profile in Section IV possesses two parameters [see e.g., Eq. (99)] one of which is eliminated by applying the heat flux boundary condition at the melt line in a modified form, viz., Eq. (98). The profile in Poots' analysis contains only one parameter ϵ, and it does not satisfy the heat flux condition at the melt line. We may, therefore, expect the results of Poots' analysis to be less accurate than the solutions presented in Section IV. An exact numerical solution of the melting square prism has been obtained by Allen and Severn (*63*) using the method of relaxation for the special case $\beta = 1.5613$. According to this solution the nondimensional time required for the complete solidification of the prism is $\tau = 0.60$. From the integral method Poots obtains $\tau = 0.35$. The integral solution appears to lose accuracy for late time, which accounts for this discrepancy. The solution can, of course, be improved, by using a two-parameter profile together with another condition; for example, the two-dimensional analog of Eq. (98) could be used. Poots recognized the need for an improved solution and chose for his second condition the first moment equation as exemplified in one dimension by Eq. (209). The late time accuracy is considerably improved using this scheme, and the nondimensional time required for the complete solidification of the prism becomes $\tau = 0.52$. For the details of this improved solution the reader is referred to Poots' paper.

X. Concluding Remarks

The integral method and related methods have been presented with emphasis on application to nonsteady heat conduction in one space variable. Examples have been chosen to illustrate various aspects of the method.

There are still questions left unanswered, however. For example, it is not clear how the concept of penetration distance should be used for problems in more than one space variable. The problem presented in Section VIII, while dealing in two-space variables, bypasses this question because the space variable x in that problem is really time-like. The problem presented in Section IX also bypasses the question by utilizing the symmetry properties of the geometry. Another unanswered question is how to use the penetration distance concept when the initial temperature is nonuniform. Questions of convergence, while not altogether ignored, have not been emphasized. In most cases, no convergence proof exists in the literature, and this is especially so for nonlinear cases. It is hoped that, in the course of time, light will be shed on all of these problems.

ACKNOWLEDGMENTS

It is a pleasure to acknowledge the assistance of: my wife, Judith, who helped edit the manuscript and prepare the illustrations; Mrs. D. Walsh, in memoriam, whose editing and typing skills were a *condicio sine qua non*; Professor W. Squire, with whom I corresponded and who pointed out some references which I had overlooked; and, finally, the Air Force Office of Scientific Research, which supported some of my investigations on the integral method.

SYMBOLS

a	radius of circle; also see Eq. (64); also parameter	t	time
		T	temperature
A	slope of linear heat input (see Fig. 5); also parameter	T_∞	negative of initial temperature
		u	velocity
A_1	$\rho L/k$	U	free stream velocity
b	parameter	v	see Eq. (77); also velocity in Section VIII
B	parameter		
c	heat capacity; also parameter	w_j	weighting function
C'	parameter	x	spacial coordinate
D	parameter	y	spacial coordinate in Section VIII
f	see Eq. (17)	z	surface temperature
F	surface heat flux; also see Eq. (242) in Section VIII	z'	ambient temperature of surrounding medium
$g(x)$	initial temperature distribution	α	diffusivity ($= k/\rho c$) also parameter in Eq. (62)
$g_k(r)$	see Eq. (210)		
h	heat transfer coefficient	γ	parameter
H	heat flow vector	δ	penetration distance
J	see Eq. (229)	ϵ_n	residual
k	thermal conductivity	η	x/δ; also see Eq. (30)
l	length of slab	θ	see Eq. (4); also see Eq. (261) in Section IX.
L	latent heat of melting		
Pr	Prandtl number ($= \mu c/k$ in Section VIII)	μ	coefficient of viscosity
		ν	see Eq. (67); also kinematic viscosity ($= \mu/\rho$) in Section VIII
q	internal heat generated per unit volume per unit time; also heat flux in Section VIII	ν_1	see Eq. (116)
		ρ	density
Q	see Eq. (38)	τ_s	surface shear stress
r	radial coordinate	Subscript s refers to surface value	
s	melt line		

REFERENCES

1. H. S. Carslaw and J. C. Jaeger, "Conduction of Heat in Solids." Second Ed., Oxford Univ. Press, London, 1959.
2. K. Pohlhausen, *Z. Angew. Math. Mech.* **1**, 252 (1921).
3. H. Schlichting, "Boundary Layer Theory." Chapter 12. McGraw-Hill, New York, 1955.
4. H. D. Landahl, *Bull. Math. Biophys.* **15**, 49 (1953).
5. H. D. Landahl, *Bull. Math. Biophys.* **15**, 367 (1953).
6. H. D. Landahl, *Bull. Math. Biophys.* **19**, 171 (1957).
7. R. I. Macey, *Bull. Math. Biophys.* **21**, 19 (1959).

8. N. Rashevsky, "Mathematical Biophysics." Third Ed., Vol. I, Chapter 1. Dover, New York, 1960.
9. A. I. Veinik, "Priblizhennii Raschet Protsessov Teploprovodnosti (Approximate Calculation of Heat Conduction Processes)." Gosudarstvenoe Energetiheskoe Izdatelstvo, Moscow, 1959.
10. T. R. Goodman, *J. Aerospace Sci.* **26**, 187 (1959).
11. J. C. Jaeger, *Proc. Cambridge Phil. Soc.* **46**, 634 (1950).
12. P. J. Schneider, *J. Aerospace Sci.* **27**, 546 (1960).
13. P. L. Chambre, *J. Appl. Phys.* **3**, 1683 (1959).
14. R. L. Schapker, *J. Aerospace Sci.* **29**, 883 (1962).
15. S. S. Arbarbanel, *J. Math. Phys.* **39**, 246 (1960).
16. W. C. Reynolds and T. A. Dolton, ASME Paper No. 58-A-248 (1958).
17. T. R. Goodman, AFOSR-TN-58-524 (AD 158337), Allied Res. Assoc. Inc. (1958).
18. T. J. Lardner and F. V. Pohle, *J. Appl. Mech.* **28**, 310 (1961).
19. H. Bateman, "Partial Differential Equations of Mathematical Physics." Cambridge Univ. Press, London, 1959.
20. T. R. Goodman, *Fourth U.S. Natl. Congr. Appl. Mech. Proc., ASME*, 1257 (1962).
21. T. R. Goodman, *J. Heat Transfer* **83**, 83 (1961).
22. K. T. Yang, *J. Appl. Mech.* **25**, 146 (1958).
23. J. C. Y. Koh, *J. Aerospace Sci.* **28**, 989 (1961).
24. T. R. Goodman, *ASME Trans.* **80**, 335 (1958).
25. G. W. Evans, E. Isaacson, and J. K. L. MacDonald, *Quart. Appl. Math.* **8**, 312 (1950).
26. T. R. Goodman, *Third U.S. Natl. Congr. Appl. Mech. Proc., ASME* 735 (1958).
27. H. G. Landau, *Quart. Appl. Math.* **8**, 81 (1950).
28. M. C. Adams, *Am. Rocket Soc. J.* **29**, 625 (1959).
29. G. W. Sutton, Rpt.TIS57SD736, General Electric Co., Philadelphia, Pennsylvania (1957).
30. C. Economos, *Am. Rocket Soc. J.* **32**, 1074 (1962).
31. S. Blecher and G. W. Sutton, *Am. Rocket Soc. J.* **31**, 433 (1961).
32. M. Altman, *Chem. Engrg. Progr. Symp. Series* **57** (1961).
33. T. R. Goodman and J. J. Shea, *J. Appl. Mech.* **27**, 16 (1960).
34. H. A. van der Velden and W. J. Schaffers, *Glückauf* **20**, 1237 (1959).
35. T. J. Lardner, *J. Amer. Inst. Aero. Astro.* **1**, 196 (1963).
36. M. A. Biot, *J. Appl. Phys.* **27**, 240 (1956).
37. M. A. Biot, *J. Aerospace Sci.* **24**, 857 (1957).
38. M. A. Biot, *Seventh Anglo-Amer. Conf. Proc., IAS*, 418 (1959).
39. M. A. Biot, *J. Aerospace Sci.* **26**, 367 (1959).
40. M. A. Biot, *Third U.S. Natl. Cong. Appl. Mech. Proc., ASME*, 1 (1958).
41. M. A. Biot and H. Daughaday, *J. Aerospace Sci.* **29**, 227 (1962).
42. T. J. Lardner, PIBAL Rept. #654, Polytechnic Institute of Brooklyn, Dept. Aerospace Engineering and Applied Mechanics, Brooklyn, New York, (1962).
43. M. E. Shvets, NACA TM 1286 (1951) [translated from *Prikl. Mat. Mekh.* **13**, 257 (1949)].
44. W. Squire, *J. Aerospace Sci.* **26**, 756 (1959).
45. T. R. Goodman and N. Ullah, AFOSR-2261, Allied Research Assoc. Inc. (1962).
46. R. E. Mascola, AVCO Rept. RAD-9(7) TM-60-72 (1960).
47. H. Fujita, *Mem. Coll. Agr. Kyoto Univ.* **59**, 31 (1951).
48. H. Yamada, Rep. *Ryutaikogaku Kenkyusyo* #3, **3**, 29 (1947). [In Japanese.]
49. J. Crank, "The Mathematics of Diffusion." Chapter 9. Oxford Univ. Press (Clarendon), London (1956).

50. I. Tani *J. Aero. Sci.* **21,** 487 (1954).
51. L. A. Schmit, WADC Tech. Rept. 56–287 (AD97326), MIT (1956).
52. J. W. Green, *J. Natl. Bur. Stds.* **51,** 127 (1953).
53. K. T. Yang, *J. Appl. Mech.* **28,** 9 (1961).
54. K. T. Yang, *Intern. Developments Heat Transfer* **1,** 18 (1961).
55. K. T. Yang, *J. Heat Transfer,* **84,** 353 (1962).
56. K. T. Yang, *Fourth U.S. Nat'l Congr. Appl. Mech. Proc. ASME,* 1419 (1962).
57. A. A. Dorodnitsyn, *Ninth Internat'l Cong. Appl. Mech.* **1,** 485 (1957).
58. A. A. Dorodnitsyn, *In* "Advances in Aeronautical Sciences" (T. von Karman, ed.) Vol. 1, p. 207. Pergamon Press, Oxford (1962).
59. Sokolova, I. N., *Am. Rocket Soc. J. Russ. Suppl.* **30,** 375 (1960). [translated from *Energetika i Avtomatica* **3,** 90 (1959).]
60. T. R. Goodman, *J. Heat Transfer* **84,** 347 (1962).
61. R. D. Cess, *J. Heat Transfer* **83,** 274 (1961).
62. G. Poots *Intern. J. Heat Mass Transfer* **5,** 339 (1962).
63. D. N. de G. Allen and R. T. Severn. *Quart. J. Mech. Appl. Math.* **15,** 53 (1962).

Heat and Mass Transfer in Capillary-Porous Bodies

A. V. LUIKOV

Director, Heat and Mass Transfer Institute, B.S.S.R. Academy of Sciences, B.S.S.R., U.S.S.R.

I. Introduction

Heat and mass transfer between capillary-porous bodies and surrounding incompressible liquid accompanied by a change of phase is not only of theoretical interest but also of great practical importance for some technological processes. As is shown below, phase changes (evaporation of a liquid or ice) essentially influence the intensity of heat and mass transfer between a body surface and the surrounding medium (external heat and mass transfer). Heat and mass transfer inside a porous body (internal heat and mass transfer) also has its unique character.

Even now the mechanism of heat and mass transfer in evaporation processes is scantily studied, and analytical investigations do not, therefore, lead to reliable results. The main part of this paper is devoted to the experimental study of heat and mass transfer in evaporation processes. To elucidate peculiarities of heat transfer with simultaneous mass transfer, a dry body (pure heat transfer) and a moist body (heat transfer in

the presence of mass transfer) were investigated simultaneously. Such a comparison makes it possible to establish relations for interconnected heat and mass transfer processes.

II. External Heat and Mass Transfer in Evaporation Processes

Heat and mass transfer between a body surface and a liquid are frequently described by empirical relations of the following form:

$$\mathrm{Nu}_q = A\mathrm{Pr}^m\mathrm{Re}^n; \qquad \mathrm{Nu}_m = A'\mathrm{Sc}^{m'}\mathrm{Re}^{n'} \tag{1}$$

where the constants A, A', m, m', n and n' are determined experimentally and depend both on liquid properties and on the range of the Reynolds number (laminar or turbulent liquid flow).

Investigations of Lebedev (*1*), Polonskaya (*2*), Sergeyev (*3*) and others show that for capillary-porous bodies containing a liquid, relations of the type shown in Eq. (1) are inapplicable. In this case the dimensionless Gukhman number has to be introduced, characterizing the capacity of a moving gas to evaporate liquid. The Gukhman number is a generalized variable which determines the peculiarities of simultaneous heat and mass transfer processes with evaporation.

For more detailed investigation into heat and mass transfer between capillary-porous bodies and humid air, extensive experiments under the various conditions considered below were conducted at the Heat and Mass Transfer Institute.

A. Experimental Procedure

Experiments were carried out in a wind tunnel, 30 meters long with an octahedron-shaped cross section 0.22 square meter in area. The chamber where experiments were conducted is a part of the wind tunnel. The air motion was induced by a fan, the velocity of air motion ranging from 1 to 22 meters per second. Dynamic head was measured by a Pitot tube; exchange of the circulating air in the wind tunnel was made by means of slide valves and an additional channel.

The air was heated by an electric air heater 100 kw in power which consists of eight parallel sections. Two of them were switched into an electrical network to provide automatic control of temperature. Thermistors were used for temperature measurement. The automatic system was of 0.1°C accuracy. Air temperature changed between 25° and 150°C. Air humidity in the tunnel was maintained constant with the help of a special automatic-control system. Relative air humidity varied from 5 to 80%.

Uniformity and stability of an airflow in the tunnel working section

were thoroughly studied. In the wind tunnel there were settling screens which removed the larger eddies and secured a uniform temperature distribution in the airflow. The length of the stabilization portion, i.e., the distance from the screens to the working section, was 4 meters. Velocity and pressure fields were measured by three-channel cylindrical and five-channel spherical probes. The nonuniformity of the velocity field did not exceed 1.0–1.5% of the flow velocity on the axis. The divergence of velocity-vector angles in horizontal and vertical planes was no more than $\pm 1.5°$ (within a flow core). Flow turbulence was also measured with the help of the Loitsyansky-Schwabe version of the hot wire anemometer. The degree of turbulence was 2.5%. Consequently, the wind tunnel secured rather high stability and uniformity of a flow.

To minimize the value of radiant heat transfer, the air at a given temperature circulated over an additional airpipe which was in the working section of the tunnel (See Fig. 1). This arrangement kept the test section walls at the same temperature as the test body. The automatic-control system maintained constant wall temperatures within 10%. The working section of the wind tunnel had glass doors (7) and (8); all the measuring devices were inserted into the tunnel through a bushing (9), placed far from the bodies investigated. The wind tunnel and additional airpipe were insulated thermally from the outside.

1. Experiments on Liquid Evaporation from Free Surface

Initially experiments on heat transfer between the heated air and liquid surface were carried out along with those on heat transfer between the air and a dry body. The liquid was poured into a $45 \times 100 \times 76$ mm metallic pan made of stainless steel. The dry body was made of the same steel in the shape of a hollow parallelepiped $45 \times 100 \times 76$ mm in size. From a vessel [Fig. 1b (4)] water entered this parallelepiped and passing through it into a tank (18) which was weighed.

The experimental procedure was as follows: a dry body (15) and a pan (14) with a liquid, which flowed from a vessel (12), were placed into the working section of the wind tunnel (see Fig. 1b).

Evaporation of various liquids: water, acetone, benzol, and butanol was investigated. Aerodynamic wedges (16) made of heat-insulating material were placed in front of the pan and the dry body. The non-heated length was 176 mm long. The amount of heat transferred from the air to the body was determined by the water rate entering into the metallic parallelepiped (dry body) and by the measured inlet and outlet water temperatures.

The test liquid was supplied to a burette (5), which in turn supplied the liquid to the pressure vessel (12).

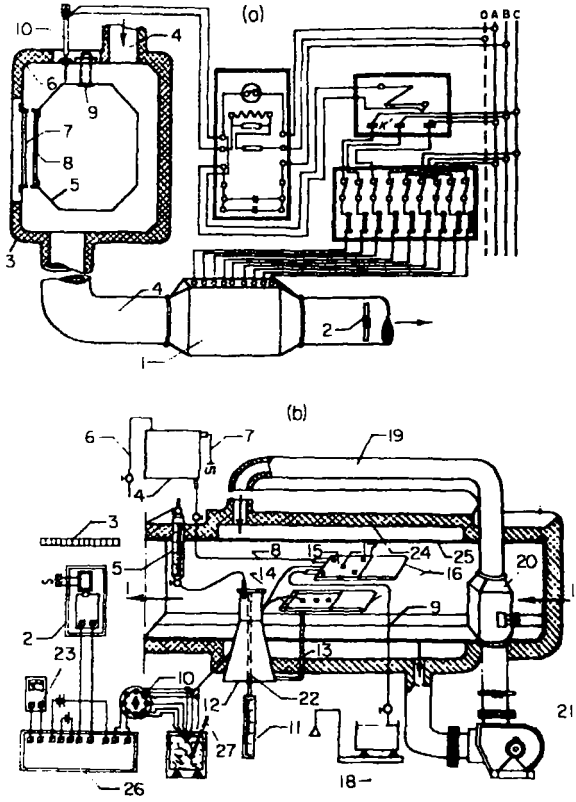

FIG. 1. Schematic drawing of test units for heat and mass transfer investigation. a. Supplementary air line for radiant heat transfer control: 1—electric air heater; 2—slide valve; 3—heat insulation; 4—additional air pipe; 5—internal surface; 6—external surface of working chamber; 7 and 8—glass doors; 9—bush for installation of measuring devices; 10—contact thermometer for air temperature control in additional pipe. b. Schematic drawing of working section; 1—direction of air flow in tunnel; 2—galvanometer; 3—galvanometer scale; 4—pressure tank for water cooling dry body; 5—measuring burette; 6—water cock; 7—overflow pipe; 8—water hose or calorimeter of dry body; 9—outlet of water from calorimeter; 10—commutator; 11—measuring cylinder; 12—pressure vessel; 13—water hose for liquid feed into pan; 14—pan with liquid; 15—dry body; 16—aerodynamic wedges; 17—hot junctions of thermocouples; 18—balance for water; 19—supplementary air pipe; 20—heater; 21—low-pressure fan; 22—connecting pipe; 23—galvanometer; 24—heat insulation; 25—wall of the working section; 26—potentiometer; 27—Dewar flask for cold junctions of thermocouples.

The pressure vessel (12) was connected by a pipe (13) with the pan and an overflow pipe (22) located at the same level as the test surface allowed the maintenance of the same liquid level both in the vessel and in the pan during the whole evaporation process. The small amount of overflow was collected in a measuring cylinder (11). The amount of the evaporating liquid from the pan (14) was determined by readings on the measuring burette (5) and the cylinder (11). The supply of liquid through a hole in the bottom of the pan provided uniform temperature over the pan height.

The temperature of the body surface was maintained constant and equal to that of the evaporating liquid in the pan. Thus, the surface temperature of the liquid and dry body was the same.

The surface temperature of the liquid was measured by three special thermocouples. The temperature was also measured over the liquid height. The heat-transfer coefficient h_d between the dry body and the air was determined according to the rate of water m which passed through the body for the definite time τ and according to the difference of inlet and outlet water temperatures:

$$h_d = \frac{m(t_1 - t_2)}{\tau S_d(t_a - t_s)} \tag{2}$$

where S_d is the heat-transfer surface.

In most cases the contribution of radiant heat transfer is small in comparison with that of convective heat transfer so that it may be neglected. The coefficient h_d is, therefore, equal to the coefficient of convective heat transfer.

In some experiments a correction for radiant heat transfer was introduced which was found both theoretically and from experiments with the additional airpipe (see Fig. 1a).

The heat-transfer coefficient h_e with liquid evaporation was defined by the following formula:

$$h_e = \frac{q_c}{S_e(t_a - t_s)} \tag{3}$$

where S_e is the free liquid surface.

The magnitude of the convective heat flow q_c was determined by the amount of the evaporated liquid with the correction for the value of radiant heat transfer between the bottom, side pan surfaces and the wind-tunnel walls.

The mass-transfer coefficient h_m was found according to the amount of the evaporated liquid m for the time τ

$$h_m = \frac{m}{\tau S_e(p_{va} - p_{vs})} \tag{4}$$

The partial vapor pressure p_{vs} close to a liquid surface was assumed to be equal to that of a saturated vapor at the surface temperature. The partial pressure of water vapor p_{va} in the air was determined by the psychrometric method. When acetone, alcohol and other liquids evaporated, p_{va} was defined by an aspirational method (by the sampling method).

2. Experiments on Drying of Moist Solids

The aim of this experimental set was to compare heat transfer of a dry capillary-porous body with that of a moist capillary-porous body being dried. Dry and moist bodies, each of the same shape of a rectangular

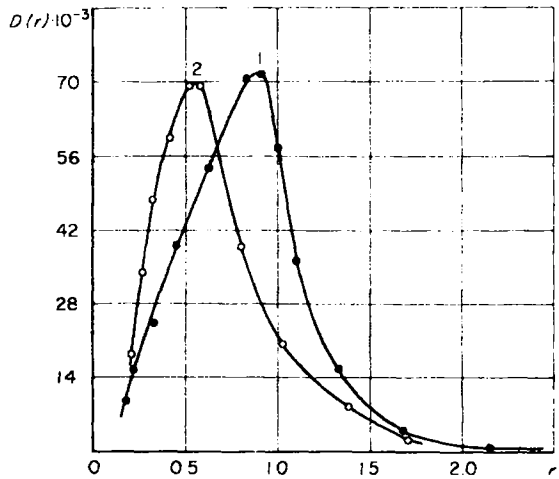

Fig. 2. Distribution of pore radii of porous ceramic bodies with fineness of 1–10 %; 2–2%. Here r is the pore radius in microns and D is the ratio of the pore volume to the body volume.

parallelepiped, 25 × 100 × 187.5 mm, were taken instead of metal models and placed into the wind tunnel.

The capillary-porous bodies were made of porous ceramics which was prepared in the following way: the mixture was composed of *chamotte*[1] (75%), kaolin (12.5%), clay (12%), and liquid glass (0.5%). Particles 8–10 μ in size were obtained after milling the above components. Then dross (suspension of 35% moisture) was made of this mixture which was a material for a ceramic body. The latter was dried first at a temperature of 80°C for 48 hours followed by 8 hours kilning at 1200°C.

Porosity of the ceramics obtained was uniform. The distribution of

[1] A refractory material with a high content (75%) of Al_2O_3.

pore radii is depicted in Fig. 2 as differential curves which show that about 70% of the pores are 0.6–0.8 μ in radius, depending on fineness. Such ceramics may be machined easily and are capable of absorbing large quantities of water (moisture of about 19–20%).

A moist capillary-porous body was shaped as a solid parallelepiped (a brick) and a dry body was a rectangular parallelepiped (a box) made of sheet copper and covered by a thin layer of porous ceramic (see Fig. 3). The water was supplied to the box, which served as a cooler, through connecting pipes. The water temperature was raised by heat transferred

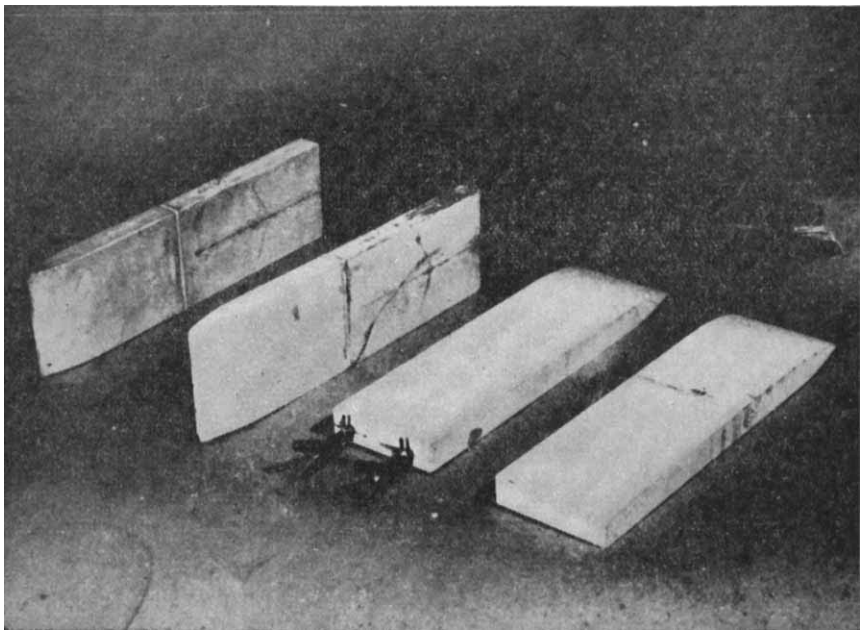

FIG. 3. Dry and moist capillary-porous bodies.

from air to the cooler surface through the layer of porous ceramic and the metal wall of the cooler. The temperature of water in the connecting pipes was measured by thermocouples. Aerodynamic wedges made of the same porous ceramic were located at the frontal part of the models. The length of the unheated wedge was equal to that of the parallelepiped. A teflon packing was inserted between the wedge and the models. The models were machined by a grinder and a shaping machine, and then twelve thermocouples (copper-constantan) were installed in every body to measure the surface temperatures. To decrease heat loss through the wire thermocouples, they were installed in a large section of an isothermal

surface. The thermocouples were calibrated after installation in the body surface to eliminate errors which may have occurred in the process of installation.

In a typical run, dry and wet bodies were placed together in the working section of the tunnel. The surface temperature of the body was controlled to be the same as the wet-bulb temperature by adjusting the amount of cooling water passing through the cooler of the dry body. The moist body was preheated to the wet-bulb temperature and then placed into the tunnel. The body was weighed to determine the amount of the evaporated moisture. For this purpose an automatic balance was used as described by Smolsky (*4*). The accuracy of weighing was $\pm 0.1\%$. The rate of drying was constant. The moisture of the body ranged in the drying process from 19 to 7–9%.

Heat transfer coefficients h_d and h_e and mass transfer coefficient h_m were determined in a similar way. The degree of uncertainty (maximum relative error) was $\pm 6.5\%$ allowing for all the errors.

3. Experiments on Porous Cooling

The process of drying of moist ceramics is unsteady since the moisture content of the body is continuously decreasing. Evaporation does not always occur on the surface. Under severe conditions of drying, even with constant evaporation rate, evaporation takes place inside the body at a certain depth. Hence, comparison of heat transfer of a dry capillary-porous body with that of a moist one with continuous supply of liquid is of great interest. In this case the process will be stationary (the moisture content of the body is maximum and constant) and heat transfer between such a moist body and heated air will be referred as porous cooling by evaporation.

The experiments were carried out in the above tunnel with the same parameters of the heated air. Bodies made of the same porous ceramics were used as models. They were shaped as a sphere, cone, cylinder, and disc. Every body was hollow and detachable and composed of two sections which provided more accurate installation of thermocouples and uniform water supply. The sections were assembled in two ways. One of these methods is depicted in Fig. 4. The joint surfaces of two halves of a body were ground, holes 5 mm in depth were drilled in the walls for pins of a frame inserted between the halves. Liquid cement-phosphate was used to joint the halves with the frame. This method proved of particular value for bodies of revolution. The halves of a body with a slightly curved surface should be jointed by means of a cross and a pin coupling and this is more reliable for bodies of such a shape. The model was placed into the wind tunnel and the surface temperature at various

points as well as the amount of the evaporated liquid was recorded during the run.

B. INTERPRETATION OF DATA

The Nusselt numbers Nu_q and Nu_m were calculated from the experimental data. The thermal conductivity of humid air was found by the formula of Nesterenko (*5*).

The question of proper selection of the physical properties of humid air is of great importance for analysis of the experimental data. These coefficients (k, ν, D, a) are variable and depend on temperature and air humidity. Some investigators assume the temperature of the wall to be

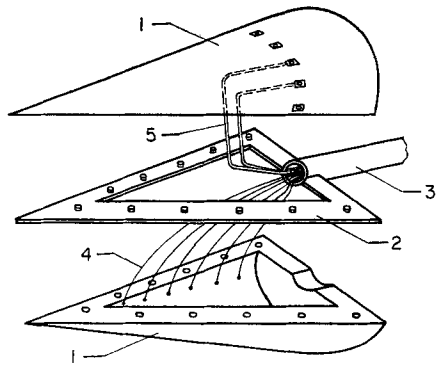

FIG. 4. Schematic drawing of porous body: 1—half of ceramic body; 2—plastic frame with pins; 3—holder; 4—thermocouples; 5—drain.

the characteristic value for evaluating the properties, while others use the mean temperature of the boundary layer, and a third group prefer the temperature outside the boundary layer. In the present work, transfer coefficients were based on the temperature outside the boundary layer t_∞ ($t_\infty = t_a$). This method proved to be the best one for correlation of the experimental points.

1. Liquid Evaporation from a Free Surface

At first it was determined that the heat transfer coefficient with evaporation h_e is greater than that without evaporation h_d (heat transfer coefficient for a metal body). The ratio h_e/h_d ranges between 1.2 and 1.6, depending on temperature t_a and relative air humidity φ. Table I gives data on h_e/h_d for several air temperatures. From Table I it is seen that the value of h_e/h_d increases with the air temperature for all the liquids tested. Consequently, heat transfer with liquid evaporation from a free surface has its own peculiarities, different from that with injection of

TABLE I

EFFECT OF AIR TEMPERATURE t_a ON h_e/h_d OF VARIOUS LIQUIDS

Liquid (h_e/h_d)	Air temperature °C				
	40°	50°	70°	90°	120°
Benzol	1.40	1.44	1.51	1.51	1.63
Acetone	—	1.43	1.47	1.52	1.56
Butanol	1.40	1.44	1.51	1.57	1.60
Water[a]	1.46	1.48	1.51	1.55	—

[a] Constant relative air humidity $\varphi = 16\%$.

an inert gas into a boundary layer through a porous wall. Let us consider this in detail.

In the excellent text by E. Eckert and R. Drake (*6*) it is shown that the heat transfer coefficient with gas injection into a boundary layer h

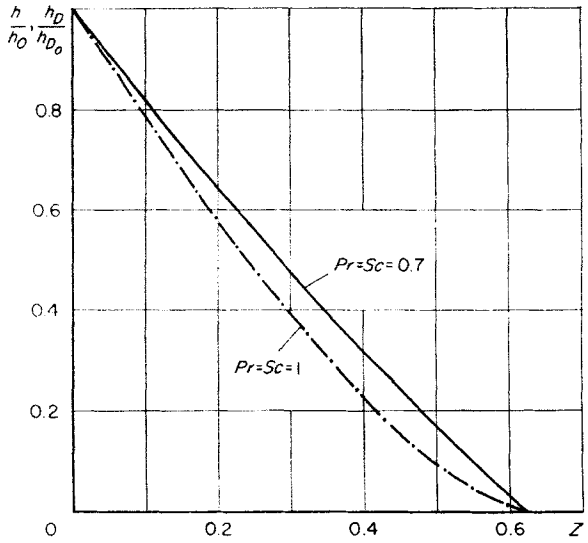

FIG. 5. Relative heat and mass transfer coefficients for laminar flow on flat plate according to E. R. G. Eckert.

is less than the value without injection h_o. The ratio h/h_o decreases with increase in the parameter $Z = (w_s/w_a)\sqrt{\mathrm{Re}_x}$ (see Fig. 5). In the case of liquid evaporation from a free surface the velocity of convective mass transfer w_s, normal to the wall on its surface, is equal to the evaporative mass flux j_s (kg/m²h) divided by the humid-air density ρ (kg/m³), i.e., $w_s = j_s/\rho$.

In our case with water evaporation from a free surface the evaporative mass flux changed from 0.65 to 15.0 kg/m²h and Re_x, from 4.10^4 to 16.10^4. Then, the parameter Z will vary between 0.0007 and 0.09.

Figure 5 shows that for such values of the parameter Z the ratio h/h_o will be equal to 0.99 and 0.83, respectively, i.e., the heat transfer coefficient h will decrease by 17% at most.

We do not deny either the effect of mass transfer on temperature and velocity profiles in a boundary layer in evaporation processes or the theory of injection into a boundary layer through a porous wall. However, under the present conditions this effect was apparently suppressed by other effects which lead to an increase in the heat transfer coefficient with evaporation, as compared with dry wall heat-transfer.

It should be noted, however, that the comparison of the present data with those in Fig. 5 is not completely valid. In these experiments heat and mass transfer occurred on a flat plate and on a liquid surface in a turbulent flow while Fig. 5 illustrates results for a laminar boundary layer. Such a discrepancy made us conduct some additional research, the results of which will be considered below.

From these additional experiments it was found that the mass transfer coefficient h_m (kg/m²h mm Hg) depends on the molecular weight of the evaporating liquid M (see Table II). The mass-transfer coefficient

TABLE II

EFFECT OF MOLECULAR WEIGHT ON MASS TRANSFER COEFFICIENT h_m

Liquid	M kg/mole	h_m kg/m²h mm Hg[a] $w_a = 5$ m/sec	$w_a = 9$ m/sec	$w_a = 14$ m/sec
Water	0.018	0.125–0.185	0.181–0.232	0.269–0.377
Acetone	0.058	0.243–0.271	0.343–0.351	0.489–0.505
Butanol	0.074	0.329–0.366	0.439–0.472	0.570–0.710
Benzol	0.078	0.330–0.370	0.410–0.470	0.729–0.788

[a] Limiting values of mass transfer coefficient, obtained at various air temperature ($27°C < t < 120°C$), are presented.

increases with the molecular weight of the evaporating liquid under other similar conditions. The Nusselt numbers Nu_q and Nu_m are calculated according to the values of h_e and h_m. Calculation results are shown in Fig. 6, from which it follows that the relative humidity φ is an important independent parameter. The slope of the straight lines is equal to 0.8 ($n = n' = 0.8$). If the Gukhman number which accounts for the influence of the relative humidity is introduced, experimental points lie on one

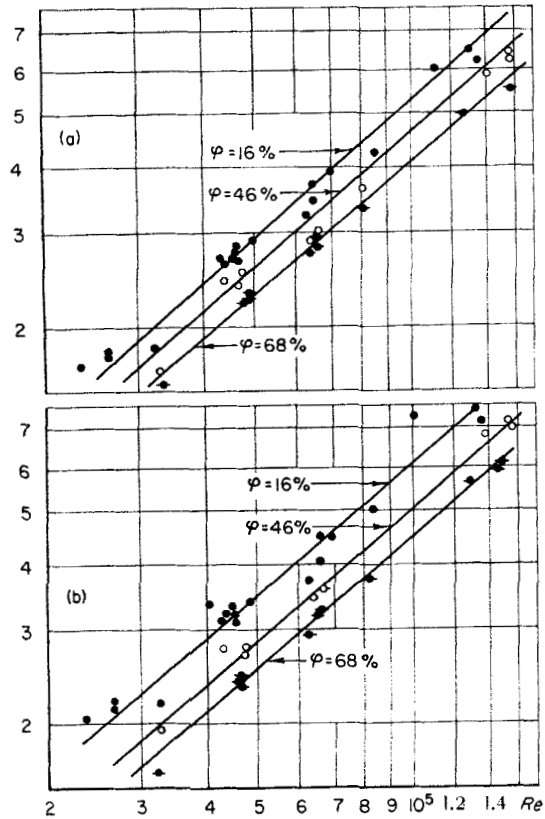

FIG. 6. Heat and mass transfer with water evaporation from free surface (Sergeev's experiments). (a) $Nu_q \cdot 10^{-2}/Pr^{0.33}$ and (b) $(Nu_m/Sc^{0.33}) \cdot 10^{-2}$ are included in vertical line.

straight line $lg(Nu/Re^{0.8}) = f(lg\ Gu)$. The exponent for Gu is equal to 0.2. The experimental data on evaporation of all the test liquids are presented in Fig. 7, on the basis of which the following relations may be written:

$$Nu_q = 0.086Pr^{0.33}Re^{0.8}Gu^{0.2} \tag{5}$$

$$Nu_m = 0.094Sc^{0.33}Re^{0.8}Gu^{0.2} \tag{6}$$

Range of validity: $2 \cdot 10^4 < Re < 2 \cdot 10^5$

$$0{\cdot}02 < Gu < 0{\cdot}19$$

Nesterenko and Dokuchaev (7) obtained similar relations for Re between 3×10^4 and 3×10^5 (see Fig. 8).

Consequently, Gu characterizes the peculiarities of heat and mass transfer in liquid-evaporation processes. In such processes the thermal

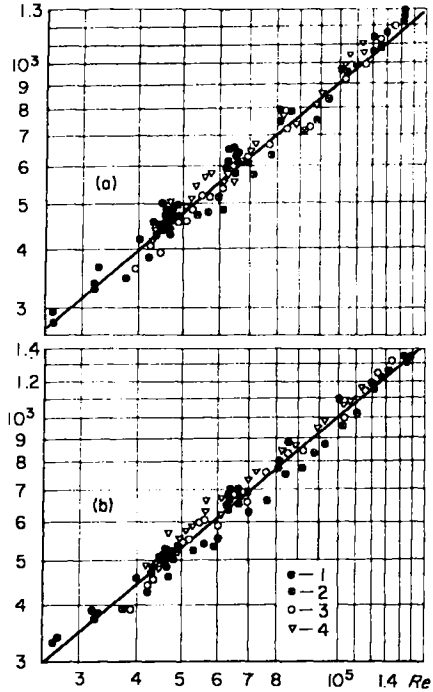

FIG. 7. Heat and mass transfer with liquid evaporation from free surface according to Sergeev's data: 1—water; 2—acetone; 3—benzol; 4—butanol. (a) $Nu_q \cdot Pr^{1/3}Gu^{0.2}$ and (b) $-Nu_m/Sc^{1/3}Gu^{0.2}$ are included in vertical line.

conductivity and diffusion coefficients depend on vapor fraction in the air, i.e., on temperature and relative air humidity. In Sergeyev's experiments the thermal conductivity coefficient of the humid air was calculated by the Nesterenko formula:

$$k = k_o + 0.0041\varphi \tag{7}$$

where k_o is the thermal conductivity of the dry air.

However, the thermal conductivity of the humid air depends to a greater extent on temperature than that of the dry air. Zakharov (*8*) carried out experiments to determine the heat conductivity of humid air over a temperature range from 20° to 60°C. Experimental results are presented in Table III, from which it is seen that at $\varphi = 100\%$ the conductivity changes from 0.0208 kcal/m h°C, at $t = 20$°C up to 0.0478 kcal/m h°C, at $t = 60$°C, i.e., 2.3-fold. With increase in temperature from 20° to 60°C the thermal conductivity of the dry air ($\varphi = 0$) varies only 1.23-fold.

If the Gukhman number appeared only in the relations for the heat

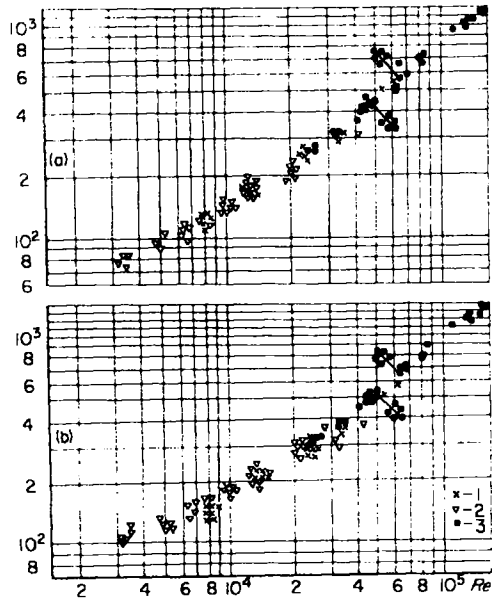

FIG. 8. Plot of $Nu_q/Pr^{0.33}Gu^{0.2}$ and $Nu_m/Sc^{0.33}Gu^{0.2}$ versus Re according to the data by: 1—A. V. Nesterenko; 2—N. F. Dokuchaev; 3—G. T. Sergeev.

transfer Nusselt number, then it might be argued that it characterizes a change in the thermal conductivity of the humid air in the boundary layer. However, the Gukhman number also enters into the formula for Nu_m.

The hypothesis on volumetric evaporation is the most possible explanation of the physical meaning of the Gukhman number Gu. The essence of this hypothesis lies in the fact that from the free liquid surface fine liquid droplets penetrate into the boundary layer. Heat fluctuations of

TABLE III

THERMAL CONDUCTIVITY OF HUMID AIR

$k \cdot 10^2$(KCAL/M H GRAD)

	t°C		
φ%	20	40	60
0	1.78	2.02	2.20
20	1.84	2.29	3.05
40	1.90	2.54	3.74
60	1.96	2.78	4.26
80	2.02	3.00	4.51
100	2.08	3.20	4.78

a liquid-molecule complex (the Papaleksi effect)[2] favors the evacuation of liquid droplets into a boundary layer. The interaction between a humid airflow and liquid surface is, however, the major reason for the removal of liquid droplets.[3]

According to the dynamic-adsorption theory of de Boer (*9*) an evaporation process is a dynamic process of evaporation and condensation. Liquid molecules not only leave the liquid surface (evaporation) but also return continuously from the air (condensation). The evaporation rate is proportional to the difference of the flow of molecules leaving the surface and those returning to the surface. On the basis of Fedyakin's investigations (*10*) condensation occurs nonuniformly along the liquid surface. In the process of condensation there takes place incomplete wetting of the liquid surface by the adsorbed layer of liquefied vapor. In this case on the liquid surface there are droplets which are not firmly bound and consequently are removed by the airflow.

It is of interest to make an approximate calculation of the lifetime of such a droplet in a boundary layer.

Designate the droplet radius by R, then the time necessary for the droplet evaporation, τ (lifetime) will be equal to

$$\tau = \frac{L\rho_e R}{h\,\Delta t} = \frac{L\rho_e R^2}{2k\,\Delta t} \tag{8}$$

where L is the latent heat of evaporation, Δt is the temperature drop between the droplet surface and the air.

Transmission of heat from the air to a droplet proceeds mainly by heat conduction. So the heat transfer coefficient h will be equal to $h = \mathrm{Nu}\, k/R = k/R$, since the Nusselt number for a spherical droplet is unity when the radius is used as the characteristic length. Droplet evaporation occurs under adiabatic[4] conditions, therefore the droplet

[2] See N. D. Papaleksi, "Collected Works," Vol. 1, Published by Academy of Sciences of the U.S.S.R., 1948.

[3] The editors suggest, and the author agrees, the increase in heat transfer may be due to an instability phenomenon. Chandrasekhar ("Hydrodynamic and Hydromagnetic Stability," Oxford Univ. Press, 1961) predicts that surface waves occur for airflow over water for an air velocity of 21 feet per second (approx. 6.5 meters per second). The theory reportedly has been verified experimentally by Francis ("Wave Motions on a Free Oil Surface," Philosophical Magazine, Series 7, Vol. 45, p. 695, 1954). Since many of the reported experiments were above this critical value, it is suggested that surface waves were present—thus increasing the area of heat transfer. The presence of waves would also explain the entrainment of a substantial amount of water in the boundary layer, just as the wind blowing over the waves on an ocean or lake carries a substantial spray of water.

[4] By this we mean that the heat required for evaporation is transferred from the surrounding air by convection.

temperature is equal to the wet-bulb temperature. If it is assumed that $\Delta t = 2°C$, $L = 580$ kcal/°C, then for the droplet with the radius $R = 0.01$ mm its lifetime will be of order $\tau = 0.004$ second. In reality, however, it will be less because in the process of evaporation the droplet radius continuously decreases. For a droplet with $R = 0.001$ mm its lifetime will be 100 times less, since τ is directly proportional to the square of the radius.

Liquid-droplet evaporation in a boundary layer is called volumetric evaporation. It is volume-vapor source in a boundary layer and a heat sink. For a flat plate the laminar boundary layer equations for transfer of a two-component mixture (humid air) will be as follows:

Continuity

$$\frac{\partial(\rho w_x)}{\partial x} + \frac{\partial(\rho w_y)}{\partial y} = 0 \tag{9}$$

Momentum[5]

$$\rho w_x \frac{\partial w_x}{\partial x} + \rho w_y \frac{\partial w_x}{\partial y} = \frac{\partial}{\partial y}\left(\mu \frac{\partial w_x}{\partial y}\right) \tag{10}$$

Diffusion

$$\rho w_x \frac{\partial \rho_{10}}{\partial x} + \rho w_y \frac{\partial \rho_{10}}{\partial y} = \frac{\partial}{\partial y}\left(D\rho \frac{\partial \rho_{10}}{\partial y}\right) + I \tag{11}$$

Heat transfer

$$\rho w_x c_p \frac{\partial t}{\partial x} + \rho w_y c_p \frac{\partial t}{\partial y} = \frac{\partial}{\partial y}\left(k \frac{\partial t}{\partial y}\right) + \rho D(c_{p2} - c_{p1}) \frac{\partial t}{\partial y} \frac{\partial \rho_{10}}{\partial y} + LI \tag{12}$$

where subscript 1 designates vapor and 2, dry air.

It is assumed that the pressure gradient is negligible ($\partial p/\partial x = 0$) and thermal diffusion effects are assumed to be negligibly small.

The system of differential equations (9–12) differs from an ordinary system of equations by the presence of additional terms I (vapor source) and LI (heat sink).

With the help of the methods of the similarity theory from Eq. (12) we find a dimensionless variable K

$$K = \frac{LIl^2}{kT_a} \tag{13}$$

where the length of an evaporation surface l is the characteristic dimension and the absolute air temperature T_a is the determining temperature.

The value LI is equal to the heat necessary for volumetric evaporation. Designate the amount of droplets per unit volume of a boundary

[5] The effect of evaporation on the momentum equation is neglected.

layer through N_v and their mean radius, through $\bar{R}$. Then, it may be written in the following form:

$$LI = 4\pi\bar{R}^2 N_v h\,\Delta t = 4\pi\bar{R}N_v k\,\Delta t \tag{14}$$

where Δt is the difference between the air temperature in a boundary layer $t(x,y)$ and the wet-bulb temperature $t_b[\Delta t = t(x,y) - t_b]$. Consequently, we have

$$K = 4\pi\bar{R}N_v l^2 \frac{\Delta t}{T_a} \tag{15}$$

The value $4\pi\bar{R}N_v l^2$ depends on physical liquid properties and fluid dynamics of a flow. The dimensionless value $\Delta t/T_a$ determines the relative intensity in volumetric evaporation. It changes along x–y coordinates. The maximum value of this quantity is equal to $\mathrm{Gu} = (T_a - T_b)/T_a$.

From this viewpoint the Gukhman number shows whether the humid air may evaporate in volume (evaporation of fine droplets in a boundary layer).

The Gukhman number should be in formulas for Nu_q and Nu_m since it characterizes a vapor source in a boundary layer.

The hypothesis on volumetric evaporation needs to be proven by direct experiments. Such experiments are being conducted at the Heat and Mass Transfer Institute.

One may, however, come to the conclusion that a heat and mass transfer process with liquid evaporation from the free surface differs from that with the injection of an inert gas into a boundary layer.

2. Drying of Capillary-Porous Bodies

As was already mentioned above, two sets of experiments were carried out. For the first set, plates were used at a temperature from 30° to 90°C with relative air humidity from 5 to 80%. Air velocity in the wind tunnel ranged from 3.0 to 15.0 meters per second.

Experiments with dry bodies of porous ceramics and metal bodies were made to compare heat transfer in the presence of drying with that of a dry body. First of all it should be noted that the results of the experiments with the reference standard bodies made of porous ceramics and of sheet steel are similar (see Fig. 9). A rough surface of porous ceramic has therefore no effect on heat transfer.

The solid line in Fig. 9 corresponds to the equation

$$\mathrm{Nu} = 0.037\mathrm{Pr}^{0.33}\mathrm{Re}^{0.8}$$

which correlates the data with a maximum deviation ±6%. All the coefficients entering Nu, Pr, and Re were based on the ambient temperature.

Experimental data on drying of the moist porous plate were correlated in the same way as those on evaporation of water from the free surface.

The temperature of the moist plate was found to be the same at all the points of the surface. The heat transfer coefficients h_e were larger for the moist plate than those for the dry one ($h_e > h_d$). The maximum difference between h_e and h_d ($h_e/h_d = 1.15$) is found with a small relative air humidity φ. With high φ the ratio h_e/h_d approaches unity ($h_e/h_d = 1.05$). Similar ratios h_e/h_d were found in Lebedev's experiments on drying of

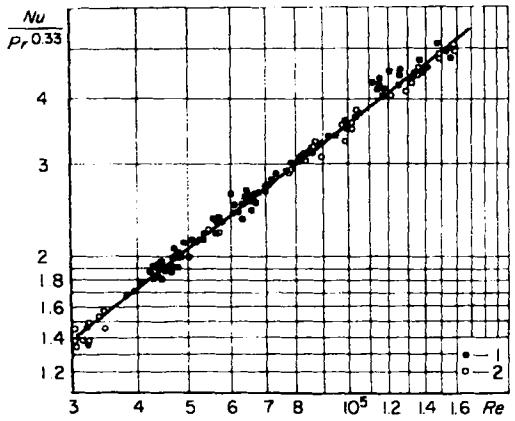

FIG. 9. Plot of $Nu/Pr^{0.33}$ versus Re for: 1—metal plate; 2—dry plate or porous ceramics. Equation $Nu = 0.037Pr^{1/3}Re^{0.8}$ is represented by a solid line.

clay (*1*). Thus, for instance, a decrease in relative air humidity from 60 to 10% caused a 15% increase of h_e.

Comparison of heat and mass transfer Nusselt numbers shows that $Nu_m > Nu_q$ and with an increase in the relative humidity ratio Nu_m/Nu_q approaches unity.

The data were correlated by the following formulas:

$$Nu_q = 0.083Pr^{0.33}Re^{3/4}Gu^{0.10} \tag{16}$$

$$Nu_m = 0.110Sc^{0.33}Re^{3/4}Gu^{0.14} \tag{17}$$

over the range of Reynolds numbers between 2.5×10^5 and 1.6×10^6 and Gukhman number between 0.014 and 0.17 with a maximum deviation of $\pm 7.5\%$.

Comparison of formulas (16) and (17) with similar formulas (5) and (6) shows that an exponent of the Gukhman number with drying is less than that with evaporation from a free surface. Assuming the Gukhman number to characterize the intensity of volumetric evaporation, a conclusion may be drawn on the decrease in droplet evacuation into the

boundary layer with drying of a capillary-porous body (an average pore radius is about 0.5–0.8 μ) in comparison with evaporation from a free surface. This conclusion qualitatively agrees with the physical mechanism of droplet formation in a boundary layer.

The modified Gukhman number $Gu' = T_a/T_b$ may be used instead of Gu. Then formulas (16) and (17) become

$$Nu_q = 0.057Pr^{0.33}Re^{3/4}(T_a/T_b)^{1.5} \tag{18}$$

$$Nu_m = 0.063Sc^{0.33}Re^{3/4}(T_a/T_b)^{2.0} \tag{19}$$

These are more convenient for engineering calculations.

Consider tests on drying of moist porous ceramic bodies of different shapes (sphere, cylinder, disc, cone) carried out by S. S. Chervyakov. To compare heat transfer with drying of moist bodies with that of dry bodies of the same shape, we refer to Shchitnikov's data (*11*). For this research sheet copper models 1.5 mm in thickness were used. Tube spirals were installed inside the bodies, which were of a spherical shape and of a cylindrical shape. Tube grids were inserted into the plate and disc. Holes 0.5 mm in diameter were drilled in these tubes. Cooling water was supplied through a pipe, connected with the spiral or the grid. The amount of heat transferred into the air from a heated body was determined by water rate and by the difference between the inlet and outlet temperatures of the water. The wall temperature of a body was measured by thermocouples at fourteen different positions.

The experiments were carried out in the wind tunnel with the air velocity varying from 2.5 to 18.0 meters per second which made it possible to cover a range of Reynolds numbers from 2×10^4 to 1.5×10^5. The air temperature ranged from 60° to 140°C and the surface temperature was uniformly equal to 32.7° $\pm$ 0.3°C. The experimental data were correlated by a plot $lg\ Nu = f(lg\ Re)$. They also gave the values of constants A and n for $Nu = A\ Re^n$.

The deviation of experimental points from the plot was small, the maximum deviation ϵ being ± 3–6%. The experimental data are summarized in Table IV. Formula $Nu = f(Re)$ may be plotted based on values of A and n for comparison with the similar plot for moist bodies.

It should be noted that the experiments by Shchitnikov were carried out carefully as confirmed by his data for a plate with fairing. The values of A and n are in good agreement with those obtained by the well-established conventional empirical formula $Nu = 0.032\ Re^{0.8}$ for the case of a flat plate in an airflow (*13*, *14*).

In S. S. Chervyakov's experiments, the relative air humidity was unchanged (φ = const). The value of Gu^m was, consequently, almost constant. Experimental data were therefore presented as empirical

TABLE IV

Heat Transfer of Differently Shaped Metal Bodies in a Heated Air Flow

Body shape and orientation to air flow		Size (mm)	Characteristic size, l	A	n	ϵ(%)
		d = 120	$l = d$	0.190	0.64	±4
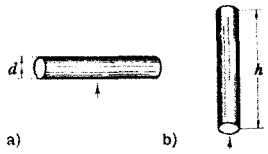 a) b)	a	d = 70	$l = d$	0.118	0.67	±4
	b	h = 170	$l = d$	0.123	0.68	±5
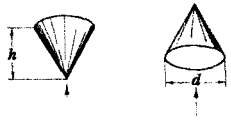 a) b)	a	d = 120 h = 180 l = 190	$l = l$	0.128	0.65	±6
	b	d = 120 h = 180 l = 190	$l = l$	0.057	0.74	±6
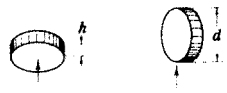 a) b)	a	d = 143.7 h = 27	$l = d$	0.028	0.77	±3
	b	d = 143.7 h = 27	$l = d$	0.017	0.86	±3
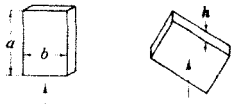 a) b)	a	a = 160 b = 100 h = 25	$l = a$	0.107	0.70	±5
	b	a = 160 b = 100 h = 25	$l = a$	0.290	0.58	±5
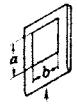		a = 160 b = 100	$l = a$	0.031	0.80	±3

formulas

$$\mathrm{Nu}_q = A\,\mathrm{Re}^n \text{ and } \mathrm{Nu}_m = A'\,\mathrm{Re}^{n'} \tag{20}$$

Constants A, A', n, n' are compiled in Table V. Orientation of the body to the flow is the same as in Table IV.

The heat transfer performance $\mathrm{Nu} = f(\mathrm{Re})$ is plotted in Fig. 10 for heat and mass transfer of a cylinder being dried, and Shchitnikov's data are presented for comparison. Figure 10 shows that Nusselt number Nu_q

TABLE V

HEAT AND MASS TRANSFER WITH DRYING ($2.5 \times 10^4 < \mathrm{Re} < 7.2 \times 10^4$)[a]

Body shape and its orientation to flow	A	n	A'	n'
Cylinder (orientation *a*)	0.167	0.65	0.090	67
Sphere	0.114	0.70	0.132	0.63
Cone (orientation *b*)	0.077	0.80	0.0815	0.76

[a] It should be emphasized that these results were obtained by Chervyakov and that the A' and n' refer to a Nusselt number for mass transfer defined by Eq. (23); that is

$$\mathrm{Nu}_{m'} = A'\mathrm{Re}^{n'}$$

when

$$\mathrm{Nu}_{m'} = \frac{j_d l}{D\Delta\rho_1}$$

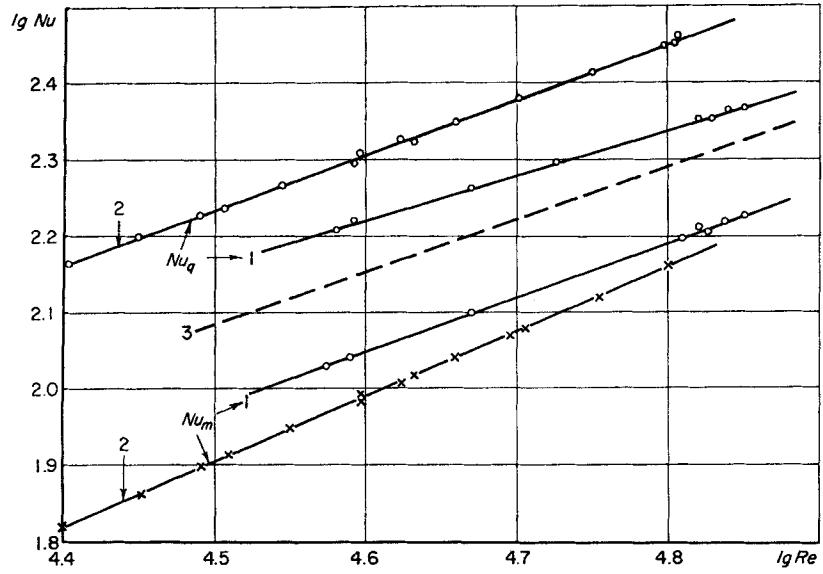

FIG. 10. Plot of Re versus Nu (Nu_q and Nu_m) for cylinder in cross flow with 1—drying, 2—porous cooling, 3—theoretically predicted values for dry heat transfer. (Note that Nu_m for Case 1, drying is actually defined by Eq. (23) and should rigorously be identified as $\mathrm{Nu}_{m'}$)

with drying is about 14% larger than Nu with heat transfer of a metal cylinder over the range of Re from 10^4 to 10^5. In comparison with Sergeyev's data, the mass-transfer Nusselt number is less than the heat-transfer Nusselt number ($Nu_m < Nu_q$). One of the sources of such a divergence is a different method for calculation of the mass-transfer Nusselt number. Sergeyev found Nu_m by the following formula

$$Nu_m = \frac{j_s l}{\Delta p_1 D_p} = \frac{h_m l}{D_p} \tag{21}$$

where D_p is the diffusion coefficient based on the pressure difference (kg/m h mm Hg) and related to the conventional coefficient $D(m^2/h)$ by

$$D_p = \frac{DM}{RT} \tag{22}$$

In this case all the transfer coefficients, including the diffusion coefficient, were determined at the ambient temperature ($T = T_a$).

S. S. Chervyakov obtained mass-transfer Nusselt number by the formula

$$Nu_m' = \frac{j_s l}{D\Delta\rho_1} = \frac{h_m' l}{D} \tag{23}$$

where mass-transfer coefficient $h_m'(m/h)$ is based on the difference of vapor fractions in the air $\Delta\rho_1$. A diffusion coefficient was found at the ambient temperature as well.

Comparing formulas (21) and (23) and keeping in mind formula (22), one can see that $Nu_m > Nu_m'$. As an example, in one of the experimental runs $j_s = 0.5$ kg/m²h, $\Delta p_1 = 9.85$ mm Hg, $\Delta\rho_1 = 0.0108$ kg/m³, then $h_m = 0.051$ kg/m h mm Hg and $h_m' = 46.5$ m/h, $h_m RT/M = 55$ m/h. Hence, ratio $Nu_m/Nu_m' = 1.18$. Thus, Nu_m is about 18% larger than Nu_m'. Besides, in S. S. Chervyakov's experiments temperature head Δt was small. The surface temperature (wet-bulb temperature) was therefore 15°–20°C lower than that of air.

Comparison of Tables IV and V indicates that in all the cases heat-transfer Nusselt number Nu_q with drying is larger than Nusselt number with dry heat transfer. The difference is from 12 to 50%, depending on Re and a body shape.

3. Porous Cooling

Experiments on porous cooling, described in Section II,A point 3, were carried out by Mironov (*12*) with the same relative humidity. Experimental data were therefore correlated by empirical formula (20). Constants A, A', n, and n' are compiled in Table VI. Comparison of Tables

TABLE VI
HEAT AND MASS TRANSFER IN THE PROCESS OF POROUS COOLING
($2.5 \cdot 10^4 < \mathrm{Re} < 7.2 \times 10^4$)

Shape and orientation to flow	Size (mm)	A	n	A'	n'
Sphere	$d = 102$	0.277	0.630	0.020	0.81
Cylinder (orientation a)	$d = 168$	0.073	0.75	0.0142	0.835
	$d = 84$				
Disk (orientation b)	$d = 23$	0.121	0.725	0.0237	0.830
	$d = 135$				
Cone (orientation a)	$d = 178$	0.161	0.67	0.0122	0.84
	$d = 110$				

IV and VI shows that with porous cooling heat-transfer Nusselt number is also larger than Nusselt numbers with pure heat transfer. This difference is even greater than that with drying and in some cases reaches 70% over the range of great Reynolds numbers. The values of $\mathrm{Nu} = f(\mathrm{Re})$ for a cylinder in a cross flow are also plotted in Fig. 10 for comparison (curve 3). Figure 10 shows that Nu_q with porous cooling is larger than that with drying. This difference increases with Reynolds number Re. Mass-transfer Nusselt number Nu_m with porous cooling is smaller than Nu_m with drying. In this case the difference between them decreases with increase of Re.

This trend is caused by the mechanism of heat and mass transfer of moist capillary-porous bodies. With porous cooling evaporation occurs at a body surface or in a layer close to it. With drying of a moist body evaporation takes place at a certain depth even at constant rate of drying. Increase in air velocity is known to move the evaporation zone into the interior of the body.

Since the experiments by Mironov and Chervyakov were carried out with bodies almost equal in size, the air velocity is proportional to Reynolds numbers. With increase in Reynolds numbers mass-transfer mechanism of drying becomes therefore similar to that of porous cooling.

Since the amount of heat spent for evaporation is determined by the amount of moisture evaporated and the water supply with porous cooling is constant (a moisture content of the body is constant below the evaporation zone), a conclusion may be drawn that Nu_q with drying should be smaller than that with porous cooling over the range of great Reynolds numbers.

These experiments indicate that heat and mass transfer between moist capillary-porous bodies and ambient air has its own peculiarities. The orientation and, consequently, the structure of the evaporation zone of

a capillary-porous body are of great importance. Heat required for evaporation is transferred to the evaporation zone not only through a boundary layer at the surface, but also through a very thin layer of the body. This thin layer has a capillary-porous structure through which heat and mass are transferred by conduction and diffusion. This heat and mass transfer through the body layer has a direct effect on distribution of temperature and vapor fraction in a boundary layer of humid air. Smolsky has shown that temperature and concentration profiles in a boundary layer depend on porous structure, with velocity, relative humidity, temperature and, consequently, temperature head being equal. Colloid bodies, for example, produce $t(y)$ and $\rho_1(y)$ profiles different from those for a capillary-porous body. Mel'nikova has found that constants A and A' entering formula (20) depend on porosity and capillary structure of a body. External heat and mass transfer depend, therefore, on heat and mass transfer inside the body (internal heat and mass transfer).

The effect of mass transfer on heat transfer with evaporation of liquid from capillary-porous bodies mainly results in the change of heat and mass transfer mechanism due to the deepening of the evaporation surface into the interior of the body. The present author's experiments (*15*) have shown that mass transfer does not effect the air velocity profiles in a boundary layer.

To analyze a complex problem of heat and mass transfer with transpiration cooling we shall avail ourselves of the Krischer method. The essence of the method is in the following.

If the influence of the mass cross flow is neglected, the differential equation for heat transfer in the boundary layer with a laminar flow over a flat plate may be written as[6]

$$w_x \frac{\partial t}{\partial x} = a \frac{\partial^2 t}{\partial y^2} \tag{24}$$

The boundary conditions are:

$$\text{at } y = 0\colon t(x,0) = t_s; \qquad \text{at } x = 0, \quad t(0,y) = t_a$$
$$\text{at } y \to \infty\colon t(x,\infty) = t_a \tag{25}$$

The flow velocity w_x is the function of coordinates and is determined by solving the equation of motion. The Krischer method assumes w_x to be constant and equal to the average flow velocity in the boundary layer ($w_x = \bar{w}_x$). In actual processes a constant velocity takes place only in a flow of liquid without friction, i.e., when the coefficient of internal friction is very small. In the case of viscous fluid such an assumption

[6] Heat transfer due to vapor diffusion may be neglected as a small value.

($w_x = \bar{w}_x = \text{const}$) allows the solution of the problem of heat transfer in a boundary layer.

In the case of a flow over an infinitely long plate ($l \to \infty$) the solution of the differential Eq. (24) subjected to boundary conditions (25) has the form:

$$\frac{t(x,y) - t_s}{t_a - t_s} = erf\left(\frac{y\sqrt{\bar{w}_x}}{2\sqrt{ax}}\right) \tag{26}$$

The local Nusselt number Nu_x is

$$\mathrm{Nu}_x = \frac{h_x x}{k} = \frac{x}{(t_a - t_s)}\frac{\partial t(x,0)}{\partial y} \tag{27}$$

Differentiating the solution (26) with respect to y and assuming $y = 0$, we obtain

$$\mathrm{Nu}_x = \left(\frac{\bar{w}_x x}{\pi a}\right)^{0.5} = \frac{1}{\sqrt{\pi}}\sqrt{\mathrm{Pe}_x} \tag{28}$$

The average Nusselt number over the surface is

$$\mathrm{Nu} = \frac{1}{l}\int_0^l \frac{l}{x}\mathrm{Nu}_x\, dx = \frac{2}{\sqrt{\pi}}\sqrt{\mathrm{Pe}} \tag{29}$$

In order to compare the obtained results with the known formulas for the Nusselt number with the laminar flow over a plate it is necessary to determine the value of $\bar{w}_x$. If the profile of the velocity $w_x(y)$ is taken for a cubic parabola, the average integral velocity $\bar{w}_x$ will be

$$\bar{w}_x = w_a \frac{1}{\delta}\int_0^\delta w_x(y)\, dy = \frac{5}{\delta} w_a \tag{30}$$

where δ is the boundary-layer thickness. Then for moist air ($\mathrm{Pr} = 0.7$) we shall have

$$\mathrm{Nu} = 0.625\frac{2}{\sqrt{\pi}}\sqrt{\mathrm{Pe}} = 0.74\sqrt{\mathrm{Re}} \tag{31}$$

This result differs from the known analytical solution $\mathrm{Nu} = 0.60\sqrt{\mathrm{Re}}$ only by 23%. Thus, the assumption that the velocity $\bar{w}_x$ is constant when solving a differential equation of the boundary layer is quite justified as the method of solution. It gives satisfactory results.

The present problem on evaporation porous cooling may be stated as follows.

The differential equation for heat transfer remains the same [see Eq. (24)].

The boundary conditions will be as follows:

$$t(0,y) = t_a; \qquad t(x,\infty) = t_a; \qquad t(x,-\xi) = t_b = \text{const} \tag{32}$$

$$-k\frac{\partial t(x,0)}{\partial y} = -k_b\frac{\partial t(x,0)}{\partial y} = \frac{k_b}{\xi}[t(x,0) - t_b] \tag{33}$$

And it is assumed that the temperature on the surface of evaporation is equal to the wet-bulb temperature. Due to the small boundary-layer thickness of the body the distribution of temperature in it proceeds according to the limit law.

In this case the boundary condition (33) may be written as

$$-\frac{\partial t(x,0)}{\partial y} + H[t(x,0) - t_b] = 0 \tag{34}$$

where $H = k_b/k\xi$ is some value similar to the relative coefficient of heat transfer.

The solution of differential Eq. (24) subjected to boundary conditions (32) and (34) has the form

$$\frac{t(x,y) - t_b}{t_a - t_b} = erf\left(\frac{y\sqrt{\bar{w}_x}}{2\sqrt{ax}}\right) + \exp\left(Hy + H^2\frac{ax}{\bar{w}_x}\right) erfc\left(\frac{y}{2}\frac{\sqrt{\bar{w}_x}}{\sqrt{ax}} + H\sqrt{\frac{ax}{\bar{w}_x}}\right) \tag{35}$$

From Eq. (35) we obtain Eq. (26) as a specific case. If evaporation takes place on the surface of a body ($\xi = 0$), the second term of the right-hand side of (35) is equal to zero, as at $\xi \to 0$, then $H \to \infty$.

The temperature on the surface of the body ($y = 0$) will not be constant but will change along the axis x

$$\frac{t(x,0) - t_b}{t_a - t_b} = \exp\left(H^2\frac{ax}{\bar{w}_x}\right) erfc\left(H\sqrt{\frac{ax}{\bar{w}_x}}\right) \tag{36}$$

Near the edge of the plate ($x = 0$) the temperature of the surface of the body $t_s[t_s = t(x,0)]$ is equal to the air temperature $t_s = t_a$, while at a considerable distance ($x \to \infty$) the temperature of the surface is equal to the wet-bulb temperature ($t_s = t_b$). *Hence, the temperature head* Δt ($\Delta t = t_a - t_s$) *changes from zero near the edge of the plate to the constant value* ($t_a - t_b$). It is a very important fact which determines the relationship of heat and mass transfer when the surface of evaporation deepens inside the body. If evaporation takes place on the body surface, then under adiabatic conditions its temperature is constant and equal to the wet-bulb temperature.

It is known from the general theory of heat transfer that if the temperature head Δt increases in the direction of flow, the heat transfer coefficient is higher than that at constant temperature. *Hence, when the surface of evaporation deepens the heat transfer coefficient is higher than that with evaporation on the surface.* If as the first approximation we assume that the heat transfer coefficient with evaporation on the surface of the body is equal to the heat transfer coefficient of a dry body, then *at drying with deepening of the surface of evaporation the heat transfer coefficient will be higher than that of a dry body.* This increase in the heat transfer coefficient should be reflected in calculation formulas $\mathrm{Nu} = f(\mathrm{Re})$ by introducing an additional dimensionless argument. Since Δt is a cause of the change in the heat transfer coefficient, it is natural that Gu or (T_a/T_b) will be the generalized variable. Let us consider it in more detail.

The local Nusselt number will be:

$$\mathrm{Nu}_x = \frac{x}{[t_a - t(x,0)]} \frac{\partial t(x,0)}{\partial y} = \sqrt{\bar{\mathrm{Pe}}_x}\, K \exp K^2 erfc K [1 - \exp K^2 erfc K]^{-1} \tag{37}$$

where the dimensionless variable K is equal to

$$K = \frac{H_x}{\sqrt{\bar{\mathrm{Pe}}_x}} = \frac{k_b}{k\xi} \sqrt{\frac{ax}{\bar{w}_x}} \tag{38}$$

It characterizes the effect of the deepening of the evaporation surface on heat and mass transfer of capillary-porous bodies.

Let us designate

$$f(K) = \sqrt{\pi}\, K \exp K^2 erfc K \tag{39}$$

Then we shall have

$$N = \frac{\sqrt{\pi}\,\mathrm{Nu}_x}{\sqrt{\bar{\mathrm{Pe}}_x}} = f(K) \left[1 - \frac{1}{K\pi} f(K)\right]^{-1} \tag{40}$$

From Eq. (40) we shall obtain Eq. (28). If evaporation takes place on the surface ($K = \infty$), $N = 1$ since $f(K) = 1$, i.e.,

$$\mathrm{Nu}_x = \frac{1}{\sqrt{\pi}} \sqrt{\bar{\mathrm{Pe}}_x}$$

and this finally coincides with Eq. (27). Thus the dimensionless value N characterizes a relative increase in the local Nusselt number with evaporation of moisture from capillary-porous bodies, as compared to moisture evaporation on the surface of the body.

It is seen from equation (39) that the value of N decreases with the increase in K gradually approaching unity.

In the range of values of K from 0.1 to 5 ($0.1 < K < 0.5$) the relation $\mathrm{Nu} = f(K)$ may be approximated by the relation

$$N = 1.31K^{-0.12} \tag{41}$$

It is known from the theory of drying of moist materials that the distance of the evaporation surface from the surface of the body during the constant rate of drying in the first approximation is proportional to the psychrometric difference Δt ($\Delta t = t_a - t_b$). Then the dimensionless variable K will be inversely proportional to $(t_a - t_b)$ and, consequently, to the Gukhman number ($K \sim \mathrm{Gu}^{-1}$). From this it follows that the number N will be proportional to $\mathrm{Gu}^{0.1}$ ($N \sim \mathrm{Gu}^{0.1}$) and this takes place in experiments on heat and mass transfer in the process of drying.

Only during the constant rate of drying the temperature of the evaporation surface $t(x, -\xi)$ is constant. Beginning from the critical moisture content its temperature increases with time of drying gradually approaching the air temperature, which is reached by it at the equilibrium moisture content. From this it follows that the Nusselt number Nu_x during the falling rate of drying will decrease gradually approaching with time the Nusselt number for a dry body.

It is of interest to determine approximately the value of N. For porous ceramics ($k_b = 0.2$ kcal/mh°C) at $\mathrm{Re} = 6.10^4$ and for $x = 20$ mm for the parameter $K = 1.5$ the value $\xi = 0.5$ mm. In this case, according to Eq. (33), the coefficient $N = 1.25$, i.e., the heat transfer coefficient with drying is higher by approximately 25% than the heat transfer coefficient for a dry body if it is considered that heat transfer with evaporation on the body surface is identical with heat transfer of a dry body. For parameter $K = 0.25$ the value $\xi = 3$ mm, and the coefficient $N = 1.55$, i.e., the heat transfer coefficient is approximately by 50% higher with drying as compared to that of a dry body.

It is quite natural that at small values of ξ it is practically impossible to fulfill an exact measurement of the body-surface temperature. Thermocouples imbedded on the "surface" of the body practically show the wet-bulb temperature. Therefore, the heat transfer coefficient is calculated as the ratio of a heat flow to the psychrometric difference $(t_a - t_b)$

$$h_{xb} = \frac{q}{(t_a - t_b)} \tag{42}$$

Then the local Nusselt number will be equal to

$$\mathrm{Nu}_{xb} = \frac{h_{xb}x}{k} = \frac{x}{(t_a - t_b)} \frac{\partial t(x,0)}{\partial y} \tag{43}$$

Upon simple transformations we obtain

$$N_b = \frac{\sqrt{\pi}\,\mathrm{Nu}_{xb}}{\sqrt{\bar{\mathrm{Pe}}_x}} = f(K) \tag{44}$$

where N_b is the coefficient which shows a relative change in the number Nu_{xb} and, consequently, in the coefficient h_{xb} due to the deepening of the evaporation surface. It is seen from Eq. (44) that with increase in K the coefficient N decreases.

Since the dimensionless K is inversely proportional to the psychrometric difference $(t_a - t_b)$, the Nusselt number will decrease with the increase in $(t_a - t_b)$ or in the Gukhman number.

In a small range of K the relation $\mathrm{Nu}_b = f(K)$ may be given in the form of relations

$$N_b = BK^m \tag{45}$$

where B and m are constants $(0 \leq m \leq 1)$.

For example, in the range $(0.3 < K < 1.5)$ the constants B and m are equal to 0.73 and 0.46, respectively, while in the range $(1.5 < K < 5)$ $B = 0.80$ and $m = 0.15$.

Hence, in the range $(0.3 < K < 1.5)$ the coefficient N_b will be proportional to $\mathrm{Gu}^{-0.46}$. A similar relation was observed in a number of works.

Equation (24) is a particular case of Eq. (12) when the transverse velocity is zero $(w_y = 0)$. Equation (12) may be solved if $w_x = \bar{w}_x = \text{const}$ and $w_y = j_s/\rho = \text{const}$ are assumed. The solution of Eq. (12) with boundary conditions (25) is of the form

$$\frac{t(x,y) - t_s}{t_a - t_s} = 1 - \frac{1}{2}\left[erfc\left(\frac{\sqrt{\bar{w}_x}}{2\sqrt{ax}}\,y - \frac{w_y}{2a}\sqrt{\frac{ax}{\bar{w}_x}}\right) + \exp\left(\frac{w_y}{a}\,y\right) erfc\left(\frac{\sqrt{\bar{w}_y}\,y}{2\sqrt{ax}} + \frac{w_y\sqrt{ax}}{2a\sqrt{\bar{w}_x}}\right)\right] \tag{46}$$

From the above solution the local Nusselt number is obtained

$$\mathrm{Nu}_x = \frac{1}{\sqrt{\pi}}\sqrt{\bar{\mathrm{Pe}}_x}\exp\left(-\frac{\mathrm{Pe}_x^{*2}}{4\bar{\mathrm{Pe}}_x}\right) - \frac{1}{2}\,\mathrm{Pe}_x^*\,erfc\,(\tfrac{1}{2}\mathrm{Pe}_x^*/\sqrt{\bar{\mathrm{Pe}}_x}) \tag{47}$$

where $\mathrm{Pe}_x^* = w_y x/a = j_s x/\rho a$ is the local Peclet number for transverse transfer. If the effect of transverse heat transfer along y is neglected $(\mathrm{Pe}_x^* = 0)$, then from Eq. (47) formula (28) is obtained. If the evaporation rate is lower than 20 kg/m²h $(j_s < 20)$, then for a wet plate in a laminar airflow $(\mathrm{Pr} = 0.7)$, when $\mathrm{Re} \leq 8.10^4$ $\mathrm{Pe}_x^* < 25$. Hence the second term of Eq. (47) is less than 5% in relation to the first one, and the value of $\exp(-\mathrm{Pe}_x^{*2}/4\bar{\mathrm{Pe}}_x)$ is practically unity.

The solution of Eq. (12) with boundary conditions (32–33) is of the form

$$\frac{t(x,y)-t_b}{t_a-t_b}=\frac{\left(H-\frac{w_y}{2a}\right)}{\left(H-\frac{w_y}{a}\right)}\exp\left[\left(H^2-\frac{Hw_y}{a}\right)\frac{xa}{\bar{w}_x}\right.$$
$$+Hy\left[erfc\left[\left(H-\frac{w_y}{2a}\right)\sqrt{\frac{xa}{\bar{w}_x}}\right]+\frac{1}{2}erfc\left(\frac{w_y}{2a}\sqrt{\frac{xa}{\bar{w}_x}}-\frac{y\sqrt{\bar{w}_x}}{2\sqrt{ax}}\right)\right.$$
$$\left.-\frac{Hexp\left(\frac{w_y}{a}y\right)}{2\left(H-\frac{w_y}{a}\right)}erfc\left(\frac{w_y}{a}\sqrt{\frac{xa}{\bar{w}_x}}+\frac{y}{2}\sqrt{\frac{\bar{w}_x}{xa}}\right)\right. \quad (48)$$

If we assume $\bar{w}_y = 0$, then from Eq. (48) the solution (35) will be obtained. From Eq. (48) the following formulas are obtained

$$N=\frac{\mathrm{Nu}_x\sqrt{\pi}}{\sqrt{\bar{\mathrm{Pe}}_x}}=\frac{\varphi(K,B)-\frac{1}{2}\sqrt{\pi}\,Berfc\frac{1}{2}B}{\left[\left(1-\frac{B}{K}\right)-\frac{1}{K\sqrt{\pi}}\varphi(K,B)-\frac{1}{2}\frac{B}{K}erfc\frac{1}{2}B\right]} \quad (49)$$

where

$$\varphi(K,B)=\left(1-\frac{1}{2}\frac{B}{K}\right)\sqrt{\pi}\,K\exp(K^2-BK)erfc\left(K-\frac{1}{2}B\right) \quad (50)$$

$$K=\frac{Hx}{\sqrt{\bar{\mathrm{Pe}}_x}},\quad B=\frac{\mathrm{Pe}_x^*}{\sqrt{\bar{\mathrm{Pe}}_x}}=\frac{w_y\sqrt{x}}{\sqrt{a\bar{w}_x}} \quad (51)$$

For N_b

$$N_b=\frac{\sqrt{\pi}\,\mathrm{Nu}_{xb}}{\sqrt{\bar{\mathrm{Pe}}_x}}=\frac{1}{\left(1-\frac{B}{K}\right)}\left[\varphi(K,B)-\frac{1}{2}\sqrt{\pi}\,Berfc\frac{1}{2}B\right] \quad (52)$$

If the effect of transverse mass transfer is neglected ($B = 0$), then from formulas (49) and (52) we obtain formulas (40) and (44), respectively, since

$$\varphi(K,0)=\sqrt{\pi}\,K\exp K^2 erfcK=f(K) \quad (53)$$

With no deepening of the evaporation surface ($\xi = 0$, $K = \infty$) we obtain from formulas (49) and (50)

$$N=N_b=\exp\left(-\frac{B^2}{4}\right)-\frac{1}{2}\sqrt{\pi}\,Berfc\frac{1}{2}B \quad (54)$$

This is Eq. (47), since

$$[\varphi(K,B)]_{K\to\infty}=\exp\left(-\frac{B^2}{4}\right)$$

Over the range $0.5 < K < 5$ and with the above values of Re and evaporation rate j, $1/2(B/K) \leq 0.06$. Thus for approximate calculations which are sufficient for engineering practice, the effect of transverse mass flow may be neglected.

III. External Heat and Mass Transfer with Sublimation

The above experiments do not yield a clear understanding of the complicated process of combined heat and mass transfer in a boundary layer of an evaporating liquid. Therefore, experiments on heat and mass transfer with sublimation of solid materials carried out by Novikov (*16*), Heat and Mass Transfer Institute, Minsk, are of great interest.

The solid material investigated was naphthalene. This substance has great evaporative capacity, its physical constants being known. Air pressure ranged from 760 to 0.07 mm Hg which permitted the study of the pressure effect on heat and mass transfer. To compare the process of naphthalene sublimation with evaporation of moisture from a capillary-porous body, a porous ceramic body soaked with water and a body made of moist gelatine were taken, the latter being chosen for comparison of heat and mass transfer of a typical capillary-porous body (moist ceramics) with a colloid one (gelatine). Sublimation of frozen moisture (ice) occurred only at low air pressures, at slight rarefactions liquid evaporation taking place.

A. EXPERIMENTAL PROCEDURE

Experiments on sublimation in vacuum are usually carried out under free convection. Since the main aim of the present studies was to compare the processes of evaporation with sublimation in forced convection, a special unit was designed for vacuum experiments in both free and forced convection. This was achieved by setting the model in motion. Its velocity changed in a wide range from 0.0 to 50.0 meters per second.

A schematic drawing of the test unit is depicted in Fig. 11. A vacuum chamber (1) was a steel cylindrical vessel 350 mm in height and 415 mm in diameter. The cylinder was provided with steel covers with rubber packings. The chamber was heated by an electrical heater allowing the air temperature in the chamber to range from 20° to 100°C. The chamber was thermally insulated from the outside. There was a glass window 150 mm in diameter in the top cover through which changes in the mass of the body of interest were recorded. This cover was provided with packing sleeves which connected a vacuum pump (18), pressure gauges (23) and (24), a vacuum gauge (19), air line (20), and thermometers (the hole for thermocouple wires). Through a hole in the bottom cover a shaft was inserted rotated by a direct-current motor (7). The shaft

was in bearings connected with the cover by rubber packings. There was a special prechamber for gasketing the shaft lead, covering the bearings. The prechamber was coupled with the vacuum pump, its capacity being 0.7 liter per second (in Fig. 11 it is not shown).

The shaft was a steel rod 7 mm in diameter and 200 mm in length with a holder (2) on it. The holder was a hollow duralumin cylinder 180 mm in length.

A steel spring was inserted inside the holder for measuring the mass of the body. One end of the spring was fixed, the other being connected

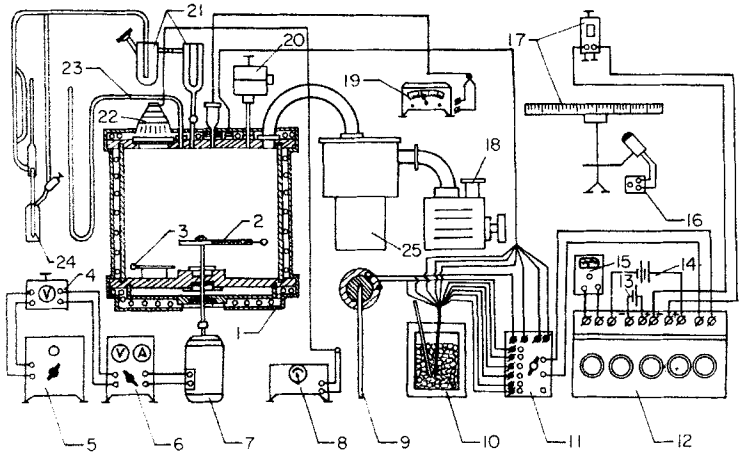

FIG. 11. Schematic drawing of test unit for heat and mass transfer experiments in vacuum (*16*): 1—chamber; 2—steel holder; 3—reference standard body; 4—autotype transformer; 5—voltage stabilizer; 6—rectifier; 7—direct current motor; 8—stroboscope; 9—thermocouple installation in a model; 10—thermostat with melting ice; 11—thermocouple switch; 12—potentiometer; 13—normal element; 14—storage battery; 15—null galvanometer; 16—oil pump; 17—galvanometer; 18—oil pump; 19—thermocouple vacuummeter for pressure range from 1 to 10^{-3} mm Hg; 20—air line with diaphragms; 21—trap; 22—mercury discharge lamp; 23—vacuum gauge for pressure range from 760 mm Hg to 1 mm Hg; 24—compression pressure gauge; 25—cylindrical receiver.

with a body by a rod. When the body rotated, the spring stretched by centrifugal force. This stretch was recorded on the scale adjusted to the same holder. Readings of the scale were made by a stroboscope. A beam was mounted on the other (short) end of the holder which was composed of a set of lead washers and a screw plug. The whole unit was balanced statically and dynamically. The centrifugal force stretching the spring was proportional to the mass. Decrease in mass with evaporation caused, therefore, displacement of the body along the holder, which was registered

by a pointer of the spring balance. The pointer was observed by means of the stroboscope.

There was a set of springs which were used depending on the number of rotations of the body. Relation between the mass of the body and readings of the spring balance was linear. The required vacuum in the chamber was created by the vacuum pump (18) 7 liters per second in capacity.

The vacuum pump was connected with the chamber by a vessel (25) which served as a receiver for pulsation absorption. Pressure in the working chamber was controlled by a special air line (20). Its design allowed the maintenance of a definite air onflow into the working chamber by means of a set of diaphragms made of thin brass foil. A supplementary steam-oil pump 250 liters per minute in capacity was engaged at high rarefaction. Pressure in the chamber was measured by a U-tube with a mercury column (23) over the pressure range from 760 to 1 mm Hg. A compression gauge (24) was used to measure partial pressure of dry air from 1 mm Hg and lower. The pressure gauge was coupled with the working chamber by two traps. One of them was filled with calcium chloride (21), the other, with liquid nitrogen. The total pressure over the range from 1 to 10^{-3} mm Hg was measured by a thermocouple vacuum gauge (19).

Thermocouples (copper-constantan) 0.1 mm in diameter served as thermometers for air in the chamber, the walls and the model. The temperature of the fixed body was measured by a thermocouple with a hot junction adjusted near the surface. The temperature of the rotating body was measured by a special alcohol thermometer, a thin rod with a spherical end. The bulb was covered with melted naphthalene. Then it was placed in the holder and set in rotation. Readings were made on the thermometer scale and through the stroboscope. The thermometer had been calibrated beforehand without naphthalene under the conditions of rotation. These tests allowed a correction for centrifugal force.

Models were prepared in the following way: a textolite sphere 10 mm in diameter was covered by a melted naphthalene. The sphere was submerged into melted naphthalene, and on cooling down, the naphthalene layer was ground and shaped as a concave hemisphere 12.6 mm in diameter. Thus, the textolite sphere was covered with a naphthalene layer 1.3 mm in thickness. A hole was made in the sphere for adjustment to the holder. A thermocouple was inserted in this hole to measure naphthalene temperature.

The second model was a sphere 15 mm in diameter made of the same porous ceramics as in the experiments on porous cooling. Before the experiment this sphere was soaked with water as described above (Section II,A).

The third model was made of moist gelatine which is a typical colloid. It is shaped as a parallelepiped, 10 × 10 × 5 mm. This shape was chosen because of difficulty in manufacturing a spherical body. The experimental procedure and units are described in detail in Novikov's work (*16*).

The experiments were carried out under stationary conditions when the body temperature was constant in time. Therefore the total heat transferred to the body was spent on evaporation. Consequently, heat flux q_s (kcal/m²h°C) is equal to the product of a specific heat of evaporation L (kcal/kg) by evaporation intensity j_s (kg/m²h), i.e., $q_s = Lj_s$. The total heat transfer coefficient h_{eg}, including heat transfer by convection and radiation, was defined by formula

$$h_{eg} = \frac{q_s}{t_a - t_b} = \frac{Lj_s}{t_a - t_s} \tag{55}$$

Radiant heat transfer coefficient h_r is calculated by the conventional formulas and additional experiments were carried out to find emissivity of naphthalene, moist porous ceramics, and gelatine. Convective heat transfer coefficient is defined by formula $h_c = h_{eg} - h_r$, mass transfer coefficient for a viscous region is found by formula

$$h_m = \frac{j}{p_{vs} - p_{va}} \tag{56}$$

and for a molecular-viscous[7] region by formula

$$h_m = \frac{j_s - 0.583 p_{vs}(M/T)^{0.5}}{p_{vs} - p_{va}} \tag{57}$$

where p_{vs} is a partial vapor pressure at the body surface.

B. INTERPRETATION OF THE DATA

The pressure effect on evaporation intensity at various velocities is depicted in Fig. 12 for three models.

In free convection, evaporation for all the bodies increases to a maximum value with pressure decrease and then it decreases. Maximum intensity j_{max} for naphthalene is 0.57 kg/m²h at a pressure of 0.5 mm Hg, for gelatine j_{max} = 0.5 kg/m²h at a pressure of 1 mm Hg ($lg\ p = 0$), and for moist ceramics j_{max} = 0.46 kg/m²h at 0.5 mm Hg.

In forced convection, evaporation intensity varies with material properties. For naphthalene j_s changes with $lg\ p$ in forced convection in a similar way as in free convection. Maximum evaporation intensity for

[7] Here we define molecular, viscous, and molecular-viscous as follows: If (1) $k \gg d$, molecular region; (2) $k \ll d$, viscous region; and (3) $k \sim d$, molecular-viscous region.

naphthalene is found at 1 mm Hg, for porous ceramics it is at 100 mm Hg ($lg\ p = 2$), and for gelatine, at 4 mm Hg. The shape of curves $j_e = f(lg\ p)$ over the pressure range from 500 to 1 mm Hg depends on the body structure. For gelatine evaporation intensity decreases with pressure falling from 500 to 100 mm Hg ($lg\ p = 2$), while with porous ceramics it increases.

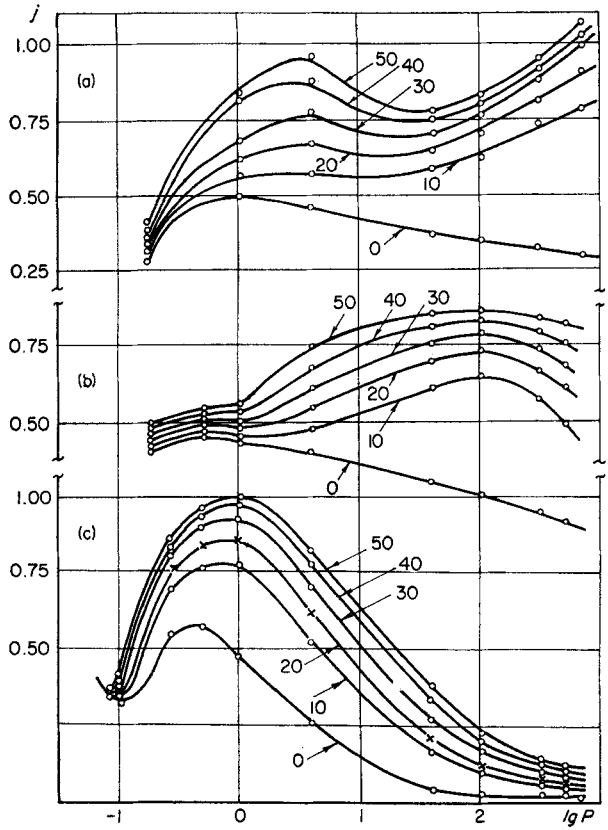

FIG. 12. Effect of pressure p (mm Hg) on evaporation intensity j (kg/m²h) for a) gelatine; b) moist porous ceramics; c) naphthalene.

Thus, the general trend is similar to that with drying of moist bodies at normal barometric pressure. Heat and mass transfer coefficients are summarized in Table VII. The heat transfer coefficient of a colloid body (gelatine) and a typical capillary-porous one (ceramic) are close to each other only at extreme pressures—740 mm Hg and 0.17 mm Hg. In the rest of the pressure range ($740 < p < 0.17$) heat transfer coefficients h_e for gelatine are larger than those for ceramics.

To illustrate this, take the data for a pressure of $p = 100$ mm Hg and

TABLE VII

HEAT AND MASS TRANSFER COEFFICIENTS RELATED TO MEDIUM PRESSURE AND BODY VELOCITY

		Naphthalene		Moist ceramics		Gelatine	
P mm Hg	w m/sec	h_e kcal/m²h°C	h_m kg/m²h mm Hg	h_e kcal/m²h°C	h_m kcal/m²h mm Hg	h_e kcal/m² h°C	h_m kg/m²h mm Hg
742	0	3.0	0.11	—	—	20.6	0.018
	10	23.0	—	—	—	83.5	0.075
	20	32.0	—	—	—	100.6	0.075
	30	45.0	—	—	—	115.6	0.085
	40	54.0	—	—	—	122.6	0.090
	50	67.0	—	—	—	128.6	0.093
500	0	2.0	0.17	11.8	0.014	—	—
	10	18.8	—	42.6	0.043	—	—
	20	25.0	—	55.1	0.056	—	—
	30	31.3	—	62.6	0.063	—	—
	40	39.7	—	69.6	0.070	—	—
	50	43.8	—	74.6	0.075	—	—
300	0	1.6	0.28	9.8	0.022	15.5	0.037
	10	15.1	—	31.2	0.065	40.5	0.083
	20	21.5	—	38.7	0.074	45.5	0.092
	30	27.8	—	43.2	0.082	48.5	0.098
	40	34.0	—	46.2	0.087	50.5	0.100
	50	40.2	—	49.7	0.093	51.5	0.103
100	0	1.1	0.3	6.6	0.050	15.3	0.046
	10	3.1	1.9	20.8	0.130	30.3	0.078
	20	4.8	2.7	23.8	0.146	34.3	0.088
	30	6.4	3.6	25.8	0.157	38.3	0.096
	40	7.6	4.4	27.3	0.168	41.3	0.100
	50	9.1	4.3	28.3	0.175	42.3	0.105
40	0	0.7	0.89	—	—	—	—
	10	5.7	4.0	—	—	—	—
	20	7.6	5.5	—	—	—	—
	30	9.2	7.1	—	—	—	—
	40	10.6	8.8	—	—	—	—
	50	12.6	10.5	—	—	—	—
4	0	4.65	7.8	10.5	0.100	11.7	0.113
	10	9.45	17.3	12.6	0.115	15.4	0.140
	20	10.75	22.2	14.9	0.130	18.4	0.163
	30	11.85	26.0	16.6	0.150	22.0	0.190
	40	12.65	29.4	19.4	0.165	25.4	0.215
	50	13.45	33.0	21.4	0.180	28.3	0.236

TABLE VII (*Continued*)

1	0	5.32	26.0	6.4	0.250	11.2	0.152
	10	8.52	44.5	6.9	0.280	13.3	0.173
	20	8.58	58.0	7.5	0.300	14.8	0.188
	30	8.97	66.0	8.0	0.310	16.8	0.206
	40	9.34	76.0	8.5	0.330	18.8	0.225
	50	9.4	79.5	9.0	0.350	21.8	0.245
0.5	0	6.37	31.7	6.6	0.35	—	—
	10	8.31	43.5	6.9	0.36	—	—
	20	8.57	56.0	7.2	0.38	—	—
	30	8.45	62.0	7.5	0.39	—	—
	40	8.30	70.0	7.8	0.40	—	—
	50	8.40	75.0	8.3	0.42	—	—
0.27	0	4.95	36.6	—	—	—	—
	10	5.88	54.5	—	—	—	—
	20	6.33	60.5	—	—	—	—
	30	6.50	79.0	—	—	—	—
	40	6.65	83.5	—	—	—	—
	50	6.70	86.0	—	—	—	—
0.18	0	—	—	5.2	0.33	3.8	0.130
	10	—	—	5.5	0.35	4.3	0.140
	20	—	—	6.0	0.36	4.7	0.145
	30	—	—	6.4	0.37	5.3	0.155
	40	—	—	6.6	0.39	5.9	0.163
	50	—	—	7.0	0.40	6.4	0.175
0.11	0	1.46	33.2				
	10	1.52	35.4				
	20	1.64	38.7				
	30	1.72	41.6				
	40	1.82	44.3				
	50	1.92	47.1				
0.09	0–50	1.98	40.2				
0.07	0–50	1.98	59.0				

a velocity of $w = 50$ meters per second. Under these conditions evaporation intensity of water from gelatine and ceramics are almost the same (for gelatine $j_s = 0.84$ kg/m²h, and for ceramics $j_s = 0.86$ kg/m²h). However, heat transfer coefficient h_e for gelatine is 42.3 kcal/m²h°C, and $h_e = 28.3$ kcal/m²h°C for ceramics, i.e., heat transfer coefficient for gelatine is 50% larger than that for ceramics. A similar relation is found for other pressures. In natural convection a heat transfer coefficient for

gelatine is 15 kcal/m²h°C, and h_e = 6.5 kcal/m²h°C for ceramics at the same pressure (p = 100 mm Hg). Thus, in the latter case the heat transfer coefficient is as much as 2.3 times that of ceramics. It is interesting to note that the general trend is quite different with mass transfer coefficients. At the same pressure 100 mm Hg mass transfer coefficient for gelatine h_m = 0.105 kg/m²h mm Hg (w = 50 meters per second), and for ceramics h_m = 0.175 kg/m²h mm Hg. Thus, mass transfer coefficient for gelatine is 1.65 times smaller.

The surface temperature for gelatine was 9.5°C, and for ceramics −3.2°C. Since the ambient temperature was uniform (t_a = 20°C, resistance to heat transfer to a ceramic body is large compared with that for gelatine. Assume evaporation of moisture to take place at a certain depth ξ, but not at the surface. Then heat flux q_s and mass flux j_s will be

$$q_s = h_e'\Delta t; \qquad j_s = h_m'\Delta p_1 \tag{58}$$

where heat and mass transfer coefficients h_e' and h_m' will be

$$h_e' = \frac{1}{1/h_e + \xi/k_b}; \qquad h_m' = \frac{1}{1/h_m + \xi/a_{mp}} \tag{59}$$

respectively.

k_b is thermal conductivity of a surface layer, a_{mp} is a moisture diffusion coefficient based on the pressure difference.

Since the layer thickness ξ is small, the distribution of temperature and partial vapor pressure may be assumed linear. The thermal conductivity k_b of the body increases with moisture content. The initial moisture content of the gelatine is considerably greater than that of porous ceramics. The thermal conductivity of the ceramic is, therefore, small compared with gelatine. However, the main difference in thermal resistance (ξ/k_b) of the surface layer is caused by different values of ξ. For a capillary-porous body ξ is considerably greater than that for a colloid body. The thermal resistance (ξ/k_b) of a gelatine surface layer is, therefore, smaller than that for a ceramic one. Thus, the heat transfer coefficient h_e' for gelatine is large compared with porous ceramics. The moisture diffusion coefficient of capillary-porous bodies is as much as 100 times that of colloid bodies. For example, moisture diffusion coefficient a_m for gelatine is 0.03×10^{-5} m²/h, and for capillary-porous bodies it is from 2.10^{-5} to 8.10^{-5} m²/h with 400–800% of moisture content.[8] Therefore, though

[8] The moisture diffusion coefficients for gelatine are reported in Drying Engineering, Proceedings of the Cinema and Photo Institute, Moscow, 1962; while the data for ceramics are from "Transport Phenomena in Capillary Porous Bodies," by Luikov, Gosenergoizdat, 1954.

a boundary layer for a gelatine body is extremely small, its resistance to mass transfer will be larger than that for a ceramic body. As a result mass transfer coefficient h_m' for gelatine is small compared with that for porous ceramics.

In view of the above pattern, heat and mass transfer coefficients acquire the meaning of heat and mass exchange coefficients. A boundary layer consists of vapor-air mixture adjacent to the body surface and of a thin layer of the body itself, ξ in thickness. Thus, external heat and mass transfer is inseparably linked with the internal process since moisture evaporation takes place inside the body.

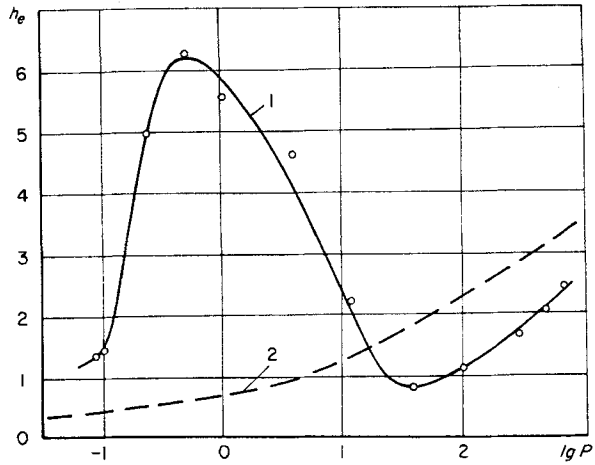

FIG. 13. Effect of pressure p (mm Hg) on heat transfer coefficient h_e (kcal/m²h°C) for naphthalene in free convection according to the data by 1—P. A. Novikov (*16*); 2—theoretically predicted values for dry heat transfer.

Turning to heat transfer with sublimation of naphthalene, the effect of pressure on the heat transfer coefficient h_e in free convection is illustrated in Fig. 13. A pressure drop from 742 to 40 mm Hg ($lgp = 2.6$) causes decrease in h_e from 2.5 to 0.8 kcal/m²h°C. Then h_e increases and reaches a maximum value ($h_e = 6.3$ kcal/m²h°C) at 0.5 mm Hg. As the pressure continues to drop, heat transfer coefficient becomes less and at pressure of 0.1 mm Hg it is 1.4 kcal/m²h°C. Figure 13 illustrates also variation of heat transfer coefficient h represented by

$$\mathrm{Nu} = 1.18(\mathrm{Gr\,Pr})^{0.125} \qquad 1.10^{-3} < \mathrm{Gr\,Pr} < 5.10^{2} \qquad (60)$$

For the case of heat transfer in the absence of mass transfer, coefficient h continuously decreases with decreasing pressure from 3.4 to 0.3 kcal/m²h°C. Thus, h_e is larger than h over the pressure range from 10

to 0.1 mm Hg. At 0.5 mm Hg ratio $h_s/h = 10.6$, i.e., heat transfer coefficient h_s with sublimation is as much as about 11 times h. This increase in h_s can be explained in the following way. As a solid material evaporates into the surrounding medium over the pressure range of about 10–0.1 mm Hg, its volume becomes 10^4–10^6 times larger. The mass of vapor in this vast volume (compared with the model) leaves the surface and penetrates the surrounding medium. Evaporation is nonuniform over the whole surface, but it takes place in the form of jets escaping from numerous discretely located centers of evaporation. The theory of discrete evaporation is confirmed by the fact that with sublimation of ice in vacuum the surface layer of ice becomes porous.

These jets quickly rush into the medium, producing strong turbulence. A very complicated and random movement arises, caused by circulation streams, multiplied by these jet streams. To get an idea of the magnitude of the circulation multiplication factor n, one can use the following approximation.

Assume the total heat required for evaporation of the material, to be transferred by radiation and direct exchange between the medium and the body surface. Then, from the equation of thermal balance we may write

$$Lj_s - q_r = c_p j_s (t_a - t_s)(n + 1) \tag{61}$$

where q_r is a heat flux by radiation. This is about 30 to 50% of the total heat Lj_s required for evaporation. In this case evaporation is assumed to be uniform over the whole surface of the body and heat transfer to be purely turbulent. From formula (61) it follows that at pressure of 0.5 mm Hg $n = 34$ for naphthalene, and $n = 36$ for porous ceramics (for ice, evaporating from porous ceramics).

Thus, the heat transfer is accompanied by a complicated turbulent transfer, caused by discrete evaporation of solid material from the surface which takes place repeatedly.

In the case of ice sublimation vapor pressure p_{vs} at the body surface is larger than the ambient pressure $p (p_{vs} > p)$. According to the experimental data ratio p/p_{vs} is about 0.3–0.4, i.e., it is supercritical.

Under these conditions vapor escapes from discrete evaporation sites with extremely great velocity. The vapor in the form of jets rushes into the surrounding medium and causes ejection of vapor-air mixture between the sites.

Heat transfer rate by convection is proportional to volumetric heat capacity $c_p\rho$. Since the density of the medium decreases with pressure, the convective heat transfer becomes of less significance over the pressure range $p < 0.5$ mm Hg.

In addition, at small pressures at the surface a layer arises close to the wall with a thickness comparable to a mean free molecular path which is inversely proportional to the pressure. In this layer no turbulence occurs and heat is transferred by molecular transfer alone. This results in a decrease of the heat transfer coefficient h_e with pressure. Over the pressure range $0.1 < p < 0.5$ molecular-viscous heat exchange is gradually changed to a purely molecular one.

This conclusion is confirmed by the experimental data on the velocity effect on heat transfer coefficient h_e (Table VII). At a pressure of 1 mm

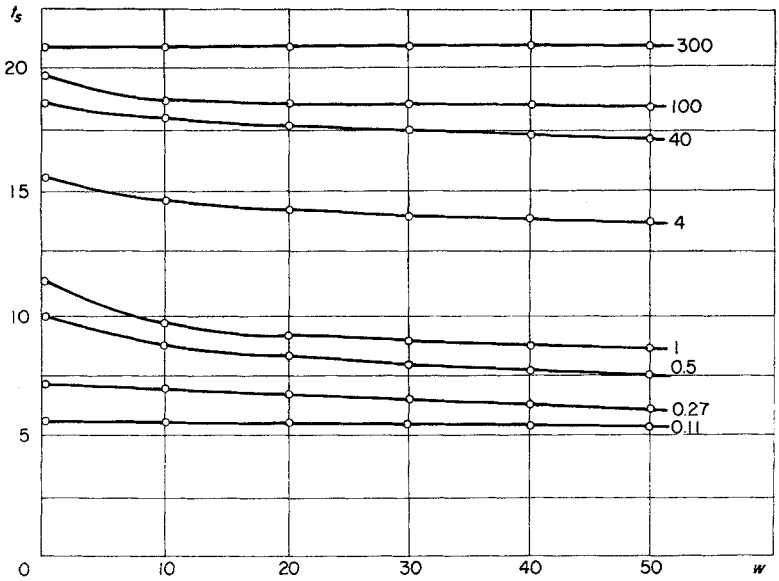

FIG. 14. Effect of velocity w (m/sec) on surface temperature t_s (°C) of naphthalene sphere at air pressure in chamber ranged from 300 mm Hg to 0.11 mm Hg.

Hg, an increase in velocity from 0 m/sec (a motionless body) to 50 m/sec causes an increase in h_e from 5.32 to 9.4 kcal/m²h°C (1.95 times increase), while at a pressure of 0.5 mm Hg this increase is 1.31, and at 0.09 mm Hg, the coefficient h_e is actually independent of velocity.

The above conclusions are confirmed by the analysis of temperature change at the sphere surface made of naphthalene with the velocity at various pressures of the medium (see Fig. 14). At a pressure of 300 mm Hg surface temperature t_s is actually independent of the velocity. At pressures from 100 to 0.5 mm Hg increase in the velocity causes decrease of the body temperature. The value of this temperature change increases with pressure decrease. With further pressure decrease ($p < 0.5$ mm Hg)

the value of t_s change decreases and at 0.11 mm Hg the surface temperature is actually independent of the velocity.

The effect of the body size on evaporation intensity and heat transfer coefficient is of some interest. The data are presented in Fig. 15 for naphthalene spheres with various diameters. As expected, evaporation intensity and heat transfer coefficient become smaller with increase of the body surface (of a sphere diameter).

We have attempted to consider the nature and the effect of evaporation on the process of convective heat transfer under various conditions. The following conclusions may be drawn from the investigations:

Heat transfer with simultaneous mass transfer due to a new gas phase formation involves a great number of phenomena which are inseparably

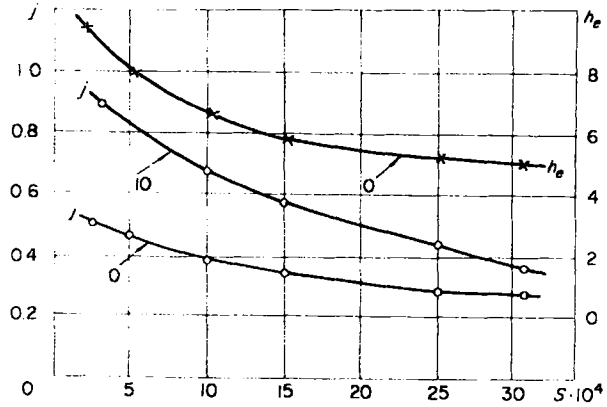

FIG. 15. Effect of surface S (m^2) on evaporation intensity j (kg/m^2h) and heat transfer coefficient h_e ($kcal/m^2h°C$) of a naphthalene sphere in free convection (w = 0 and 10 meters per second).

interconnected. Investigation into this process will be successful only if the process is considered as a whole, as the sum of all the interconnected phenomena involved. It does not appear possible to utilize existing expressions based on a heat transfer-mass transfer analogy. Rather, quantitative relations must be obtained which correspond to the actual physical process.

IV. Internal Heat and Mass Transfer in Capillary-Porous Bodies

Transfer of noncondensing gases, vapor, and liquid may occur in a capillary-porous body. Transfer of vapor and inert gas proceeds in different ways: by diffusion and effusion (molecular transport) and by filtra-

tion under the pressure gradient (molar transport). Transport of a liquid occurs by diffusion, capillary absorption, and by filtration. Consequently, the derivation of mass-transfer relations in capillary-porous bodies on the basis of a molecular and molar transport mechanism involves great difficulties. These relations may serve to analyze a qualitative mass-transfer pattern and to find out the character of a change in transfer coefficients, depending on moisture content and body temperature. Heat and mass transfer coefficients are determined experimentally for various bodies.

A. ANALYTICAL HEAT AND MASS TRANSFER THEORY

Consider a system: a capillary-porous body and a substance bounded within it. At a positive temperature ($t > 0°C$) the bound substance consists of a liquid, vapor, and inert gas. At a negative temperature ($t < 0°C$) it consists of ice, supercooled liquid (water), vapor, and gas. Depending on the energy of binding between the moisture and the body, the freezing temperature of water changes over a wide range. Thus, in most cases there is always some amount of a supercooled liquid in capillary-porous bodies at the negative temperature.

The second peculiarity of mass transfer in capillary-porous bodies is the partial filling of pores and body capillaries with a gas and moisture (vapor, water, or ice) i.e., a part of a capillary is filled with water or ice and the remainder, with a vapor-gas mixture (humid air).

Steamlike moisture (vapor) is designated through 1; water, through 2; moisture in a solid state (ice), through 3, inert gas (dry air), through 4 and a body skeleton, through 0. As a result, a moist capillary-porous body is a multicomponent system containing the bound substance ($k = 1,2,3,4$) and a dry body skeleton ($k = 0$). The volume concentration of the bound substance (dry air, vapor, water, and ice) is equal to the relation of the mass m of this substance to the body volume, V:

$$\omega = \frac{m}{V} = \frac{1}{V}\sum_{k=1}^{4} m_k = \sum_{k=1}^{4} \omega_k \tag{62}$$

where m_k and ω_k are the mass and concentration of the kth component ($k = 1,2,3,4$), respectively. The quantity w_k may be expressed in terms of ρ_k and porosity Π of a body (pore volume per unit of a body volume).

$$\omega_k = \frac{m_k}{V} = \rho_k \Pi b_k \tag{63}$$

where ρ_k is the density of the bound substance (ρ_1 and ρ_4 are fractions

of vapor and dry air in the humid air, respectively; ρ_2 is the density of water; ρ_3 is the density of ice[9]).

In the first approximation the quantity of filling of capillaries b_k is equal to the relation of the volume of the bound substance in the state k to that of capillaries. According to the filtration theory in porous media b_k is referred to as a saturated state. In the present case such a determination of the coefficient b_k is, however, conditional, since moisture may be bounded by adsorptive and osmotic forces not only within the walls of capillaries but also with the internal wall surfaces of a capillary. Equality (63) shows that the volume concentration ω_k depends not only on ρ_k and Π but also on b_k which varies in the process of mass transfer. Consequently, filtration equations in porous media are inapplicable for moisture transfer in capillary-porous bodies since according to the filtration theory the value of b_k is assumed to be unity.

The volume of a moist body depends on moisture content, therefore, instead of the volume concentration it is better to use the relative concentration u_k, determined by the formula:

$$u_k = \frac{m_k}{m_0} = \frac{\omega_k}{\rho_0} \tag{64}$$

where ρ_0 is the density of the body itself.

The relative concentration of the bound body $u = \sum_{k=1}^{4} u_k$ is equal with great accuracy to the sum of relative concentrations of water u_2 and ice $u_3 (u = u_2 + u_3)$, as the mass of vapor and dry air in pores and capillaries of the body is negligibly small, as compared with that of water and ice. According to Posnov's calculations (*17*) at the normal pressure (p = 760 mm Hg) and at t = 20°C for a maximum-porosity body the mass of the humid air in body pores make-up 10^{-3}% of that of water, corresponding to equilibrium moisture-content. And so the relative concentration u is equal to:

$$u = \sum_{k=1}^{4} u_k = u_2 + u_3 \tag{65}$$

and is called moisture content of a body.

In the heat and mass transfer theory for capillary-porous bodies relation (65) is of great importance as it allows to make some simplifications and transformations.

In a capillary-porous body moisture moves slowly. The temperature

[9] With adsorption ρ_2 is the density of adsorbed water.

of water and humid air in body pores and capillaries is practically equal to that of their walls. Vapor in capillaries is in thermodynamic and molecular equilibrium with liquid. The partial vapor pressure in a hygroscopic body state depends on temperature and moisture contents of a body;

$$p_v = f(u,T) \text{ at } 0 < u < u_{sm} \tag{66}$$

where u_{sm} is the maximum moisture content of the body reached by sorption.

In the moist state ($u > u_{sm}$) the partial pressure of vapor is equal to the pressure of a saturated vapor p_s. Consequently, p_v depends only on temperature:

$$p_v = p_s = f(T) \text{ at } u > u_{sm} \tag{67}$$

1. Differential Heat and Mass Transfer Equations

Molecular and molar transport of vapor, air, and water proceed simultaneously in a capillary-porous body. All these types of transfer may be conditionally called diffusion. Here by diffusion is meant molecular diffusion, capillary diffusion (capillary absorption) and convective diffusion (filtration).

If we designate the density of a mass flow of the kth component of a bound substance in the state $k(k = 1,2,3,4)$ through j_k, then the differential mass transfer equation may be written as:

$$\frac{\partial(\rho_0 u_k)}{\partial \tau} = -div j_k + I_k \tag{68}$$

where I_k is the strength of the mass source or sink of the kth component.

Summing Eq. (68) over all the kth components ($k = 1,2,3,4$), we obtain the following differential equation:

$$\frac{\partial(\rho_0 u)}{\partial \tau} = -\sum_{k=1}^{4} div j_k \tag{69}$$

since the sum of all the mass sources and sinks is equal to zero:

$$\sum_{k=1}^{4} I_k = 0 \tag{70}$$

A differential heat transfer equation is obtained from that for enthalpy transfer of the present system. At constant pressure the local derivative of the volumetric enthalpy concentration is equal to the divergence of

an enthalpy flow

$$\frac{\partial}{\partial \tau}\left(h_0\rho_0 + \sum_{k=1}^{4} h_k\,\rho_0 u_k\right) = -div\left(q + \sum_{k=1}^{4} h_k j_k\right) \tag{71}$$

where q is the heat flux; h is the specific enthalpy.

Designate the specific heat capacity at the constant pressure through $c_{pk} = (dh_k/dt)$, then we shall have:

$$\left(c_0\rho_0 + \sum_{k=1}^{4} \rho_0 c_{pk} u_k\right)\frac{\partial t}{\partial \tau} + \sum_{k=1}^{4} h_k \frac{\partial(\rho_0 u_k)}{\partial \tau} = -divq - \sum_{k=1}^{4} c_{pk} j_k \nabla t - \sum_{k=1}^{4} h_k\, div j_k \tag{72}$$

Multiply Eq. (68) by h_k and summarize over k from 1 to 4

$$\sum_{k=1}^{4} h_k \frac{\partial(\rho_0 u_k)}{\partial \tau} = -\sum_{k=1}^{4} h_k div j_k + \sum_{k=1}^{4} h_k I_k \tag{73}$$

Hence from Eqs. (72) and (73) we obtain the differential heat transfer equation:

$$c\rho_0 \frac{\partial t}{\partial \tau} = -divq - \sum_{k=1}^{4} h_k I_k - \sum_{k=1}^{4} c_{pk} j_k \nabla t \tag{74}$$

where c is the total specific heat of a body:

$$c = c_0 + \sum_{k=1}^{4} c_{pk} u_k \tag{75}$$

From Eq. (74) the Fourier-Kirhoff equation for a moving liquid may be obtained as a particular case. Assume $k = 2$

$$c\rho_0 = c_{p2}\rho_0 u_2 = c_{p2}\rho_2; \qquad \vec{j_2} = \rho_2 \vec{w} \tag{76}$$

then we have

$$c_{p2}\rho_2 \frac{\partial t}{\partial \tau} + c_{p2}\rho_2 w \nabla t = -divq \tag{77}$$

We now examine Eq. (74) in more detail. In capillary-porous bodies in the absence of filtration the convective component of heat transfer [168]

is small compared with the conductive one. The term $\sum_{k=1}^{4} c_{pk} j_k \nabla t$ may, therefore, be neglected.

If there are no chemical conversions connected with the formation of a noncondensing gas (dry air), the source I_4 is equal to zero ($I_4 = 0$).

Differential Eq. (74) may be written as follows:

$$c\rho_0 \frac{\partial t}{\partial \tau} = -divq - \sum_{k=1}^{3} h_k I_k \tag{78}$$

Equations (78), (68), and (69) represent a system of differential equations for heat and mass transfer with sources of mass I_k and heat $h_k I_k$, accounted for by phase conversions. In order to complete these equations it is necessary to determine sources I_k and flows of heat and mass.

a. The Mass Sources. If the body temperature is above zero ($t > 0$°C), moisture inside it is composed of two phases (liquid and vapor). In this case we obtain from relation (70)

$$I_2 = -I_1 \tag{79}$$

Since the mass of vapor in capillaries is negligibly small compared with that of liquid ($u_2 \gg u_1$), we may assume $u_1 = 0$. Then it follows from Eq. (68):

$$\frac{\partial(\rho_0 u_1)}{\partial \tau} = -divj_1 + I_1 = 0 \tag{80}$$

Hence the expression for a liquid source is

$$I_2 = -I_1 = -divj_1 \tag{81}$$

If the body temperature is below zero ($t < 0$°C), the moisture inside it is composed of vapor and ice or saturated liquid. No mass transfer of the solid state occurs ($j_3 = 0$). Then for a two-phase system we obtain from Eq. (68)

$$\frac{\partial(\rho_0 u_3)}{\partial \tau} = I_3 \tag{82}$$

Usually, considering dispersed media containing ice, the notion of ice content factor ϵ_{ic} is introduced, which is a ratio of the mass of ice and that of moisture (water and ice). In the present symbols

$$\epsilon_{ic} = \frac{u_3}{u_2 + u_3} = \frac{u_3}{u} \tag{83}$$

If a body does not contain ice ($u_3 = 0$), factor ϵ_{ic} is zero ($\epsilon_{ic} = 0$). When

the whole of water converts into ice ($u_2 = 0$), $\epsilon_{ic} = 1$. In most cases ϵ_{ic} is less than unity ($0 < \epsilon_{ic} < 1$). According to Tsitovich (*18*) the factor ϵ_{ic} is independent of moisture content u, but it depends on the temperature alone. We may, therefore, write

$$du_3 = \epsilon_{ic}\, du \tag{84}$$

Then source I_3 will be

$$I_3 = \frac{\epsilon_{ic}}{1 - \epsilon_{ic}} \frac{\partial u_2}{\partial \tau} \rho_0 = \epsilon_{ic}\rho_0 \frac{\partial u}{\partial \tau} \tag{85}$$

A similar relation may be obtained for the source I_2 at a temperature of the body $t > 0$°C. Changes in the mass of the liquid may be caused by transfer ($d_e u_2$) and phase conversion $d_i u_2$, i.e.,

$$du_2 = d_e u_2 + d_i u_2 \tag{86}$$

Denote relation $d_i u_2 / d_e u_2$ through $\beta_2 (\beta_2 = d_i u_2 / d_e u_2)$. This value ranges from ($\beta = 0$) when no phase conversions occur ($d_i u_2 = 0$), to infinity ($\beta_2 = \infty$), when all the changes of mass are caused by phase conversion alone ($d_e u_2 = 0$). Therefore, introduction of a new value ϵ_2 is advisable,

$$\epsilon_2 = \frac{\beta_2}{1 + \beta_2} \tag{87}$$

which is referred to as a phase conversion coefficient. This coefficient ranges from zero to unity ($0 < \epsilon_2 < 1$). The case $\epsilon_2 = 0$ corresponds to absence of phase conversions ($\beta_2 = 0$), and when $\epsilon_2 = 1 (\beta_2 = \infty)$, no mass transfer occurs.

Then relation (86) may be written as

$$du_2 = (1 + \beta_2)\, d_e u_2 = \frac{1}{1 - \epsilon_2} d_e u_2 \tag{88}$$

Consequently, a diffusion equation of mass transfer will be

$$\rho_0 \frac{\partial u_2}{\partial \tau} = -div j_2 + \epsilon_2 \rho_o \frac{\partial u_2}{\partial \tau} \tag{89}$$

Comparing Eq. (89) with (68), we obtain (since $u_2 = u$ for $t > 0$°C)

$$I_2 = \epsilon_2 \rho_0 \frac{\partial u_2}{\partial \tau} = \epsilon_2 \rho_0 \frac{\partial u}{\partial \tau} \tag{90}$$

The following formula may, therefore, be written for the source $I_k (k = 2,3)$

$$I_k = \epsilon_k \rho_0 \frac{\partial u}{\partial \tau} \tag{91}$$

Thus, ice content factor ϵ_{ic} is a phase conversion coefficient $\epsilon_3 (\epsilon_{ic} = \epsilon_3)$.

The physical meaning of this factor may be explained in the following way.

Allowing for $\partial u_1/\partial \tau = 0$, it follows from Eqs. (68) and (69) at $t > 0°C$, that

$$I_2 = -I_1 = \epsilon_2 \rho_0 \frac{\partial u}{\partial \tau} = -div j_1 = -\epsilon_2 (div j_1 + div j_2) \tag{92}$$

Hence

$$\epsilon_2 = \frac{div j_1}{div j_1 + div j_2} \tag{93}$$

If we assume for approximation $\epsilon_2 = \text{const}$, we get from Eq. (91) for one dimensional problems ($div \equiv \partial/\partial x$), i.e., when vectors j_1 and j_2 are parallel or unparallel

$$\epsilon_2 = \frac{|j_1|}{|j_1| + |j_2|} \tag{94}$$

Consequently, coefficient ϵ_2 determines the amount of vapor transferred in a body in relation to the whole vapor and liquid flow.

b. Calculation of Heat and Mass Flows. Vapor in the interior of a capillary-porous body is transferred by molecular transport.[10] It is in thermodynamic equilibrium with liquid. A mass flow of vapor is

$$j_1 = -\epsilon \rho D \nabla \rho_{10} = -a_{m1} \rho_0 \nabla u - a_{m1}{}^T \rho_0 \nabla t \tag{95}$$

where ϵ is a dimensionless factor characterizing resistance to vapor diffusion in a moist body.

The vapor diffusion coefficient of a moist porous body is equal to

$$a_{m1} = \epsilon D \frac{\rho}{\rho_0} \left(\frac{\partial \rho_{10}}{\partial u} \right)_T \tag{96}$$

and thermal diffusion coefficient $a_{m1}{}^T$ of a moist body is

$$a_{m1}{}^T = \epsilon D \frac{\rho}{\rho_0} \left(\frac{\partial \rho_{10}}{\partial T} \right)_u \tag{97}$$

In the moist state of a body ($u > u_m$) the coefficient a_{m1} is zero, since $(\partial \rho_{10}/\partial u)_T = 0$, and $a_{m1}{}^T$ is

$$a_{m1}{}^T = \epsilon \rho D \rho \frac{M_1}{M} \frac{dp_s}{dT} \tag{98}$$

The liquid transfer in a capillary-porous body may be described in an

[10] Molar transport of water will be considered below.

analogous manner, as functions of moisture content u and body temperature T. We obtain

$$j_2 = -a_{m2}\rho_0\nabla u - a_{m2}{}^T\rho_0\nabla t \tag{99}$$

The diffusion coefficient a_{m2} and the thermal diffusion coefficient $a_{m2}{}^T$ of liquid in a porous body are not constant, but depend on temperature and moisture content of the body.

The heat flux according to Fourier's law is

$$q = -k\nabla t \tag{100}$$

The coefficient of heat conduction k of a moist body depends on both u and T.

Using relations (95), (99) and (100) we get a set of transfer equations

$$\frac{\partial u}{\partial \tau} = div[a_m(\nabla u + \delta\nabla t)] \tag{101}$$

$$c\rho_0\frac{\partial t}{\partial \tau} = div(k\nabla t) + L\epsilon\rho_0\frac{\partial u}{\partial \tau} \tag{102}$$

where a_m is a total moisture diffusion coefficient $a_m = (a_{m1} + a_{m2})$; δ is a thermal gradient coefficient

$$\delta = \frac{a_{m1}{}^T + a_{m2}{}^T}{a_{m1} + a_{m2}} \tag{103}$$

L is a specific heat of phase transition equal to the difference of specific enthalpies $L_{ki} = (h_k - h_i)$.

In the case of liquid evaporation (a moisture sink) or ice melting positive sign in Eq. (102) before $L\epsilon\rho_0\,\partial u/\partial\tau$ should be replaced by a negative sign.

All the transfer coefficients (a_m, k, ϵ, c, δ) are variables. For a short range of Δu and Δt, they may be assumed constant for approximation. Then accounting for relations (81) and (91) Eqs (101) and (102) may be written as

$$\frac{\partial u}{\partial \tau} = \kappa_{11}\nabla^2 u + \kappa_{12}\nabla^2 t \tag{104}$$

$$\frac{\partial t}{\partial \tau} = \kappa_{21}\nabla^2 u + \kappa_{22}\nabla^2 t \tag{105}$$

where the transfer coefficients $\kappa_{ki}(k, i = 1,2)$ are

$$\kappa_{11} = a_m = (a_{m1} + a_{m2}); \qquad \kappa_{12} = a_m\delta = (a_{m1}{}^T + a_{m2}{}^T) \tag{106}$$

$$\kappa_{21} = \frac{L\epsilon}{c}a_m; \qquad \kappa_{22} = a + \frac{\epsilon L}{c}a_m\delta \tag{107}$$

c. Heat and Mass Transfer with Filtration. At intense heating of a moist body above 100°C there appears a pressure gradient due to liquid evaporation. A pressure gradient ($\nabla p \neq 0$) may also take place at temperature less than 100°C due to effusion of the humid air through microcapillaries inside a body. The presence of ∇p inside a capillary-porous body causes filtration of vapor and liquid. This mode of transfer is described by the Darcy law:

$$j_f = -k_f \nabla p \tag{108}$$

where k_f is the total filtration-coefficient.

In this case the system of differential equations for heat and mass transfer in a capillary-porous body is as follows (*19*):

$$\frac{\partial u}{\partial \tau} = \kappa_{11}\nabla^2 u + \kappa_{12}\nabla^2 t + \kappa_{13}\nabla^2 p \tag{109}$$

$$\frac{\partial t}{\partial \tau} = \kappa_{21}\nabla^2 u + \kappa_{22}\nabla^2 t + \kappa_{23}\nabla^2 p \tag{110}$$

$$\frac{\partial p}{\partial \tau} = \kappa_{31}\nabla^2 u + \kappa_{32}\nabla^2 t + \kappa_{33}\nabla^2 p \tag{111}$$

where coefficients

$$\kappa_{13} = a_m \delta_f, \quad \kappa_{23} = \epsilon L \frac{a_m}{c}\delta_p; \qquad \kappa_{33} = \left(a_f - \frac{\epsilon a_m}{C_f}\delta_p\right);$$

$$\kappa_{31} = -\frac{\epsilon a_m}{C_f}; \qquad \kappa_{32} = -\frac{\epsilon a_m \delta}{C_f}\delta,$$

$a_f = k_f/C_f\rho$ and is the coefficient of filtration diffusion, C_f[11] is the body capacity for the humid air with filtration, $\delta_f = k_f/a_m\rho_o$.

2. Boundary Conditions

Space boundary conditions reflect the law of interaction between a body surface and the surrounding medium. This interaction implies transfer of energy and mass. If the transfer of energy and mass occurs

[11] C_f is similar to c_m. It represents the change in vapor concentration in capillaries of a body with specific pressure of humid air. Or it is a capacity of a porous body related to the quantity of vapor in capillaries. C_f is defined by

$$d(u_1 + u_4) = C_f\, dP$$

If we assume humid air is governed by the equation for ideal gases, then from Eqs. (62) and (63)

$$C_f = \frac{RT\rho_o}{\Pi b_k}$$

where R is a gas constant for humid air.

according to the convective transfer law, then at the constant pressure (p = const) boundary conditions may be written in such a way:

$$a_m\rho_0(\nabla u)_s + a_m{}^T(\nabla t)_s + j_s(\tau) = 0 \tag{112}$$

$$-(k + La_{m2}{}^T)(\nabla t)_s - La_{m2}\rho_0(\nabla u)_s + q_s(\tau) = 0 \tag{113}$$

Equation (112) represents a mass balance close to a body surface (subscript s). The moisture amount, supplied to a body surface as a result of thermodynamic forces ∇u and ∇t is equal to that which left the body surface for the surrounding medium $j_s(\tau)$. Equation (113) is the energy (heat) conservation equation. The amount of heat, supplied to the body surface $q_s(\tau)$, is equal to that which penetrated inside a body $(-k\nabla t)_s$ and that, spent for liquid evaporation (subscript 2), the flow of which depends on ∇u and ∇t.

If $j_s(\tau)$ and $q_s(\tau)$ are given as time functions, then Eqs. (112) and (113) are boundary conditions of the second kind. When a moist body interacts with the heated air, flows $j_s(\tau)$ and $q_s(\tau)$ are equal to

$$j_s(\tau) = \beta\rho_0(u_s - u_e) \tag{114}$$

$$q_s(\tau) = h(t_a - t_s) \tag{115}$$

where β is the mass transfer coefficient based on the difference of moisture content and u_e is the equilibrium moisture content.

The mass transfer coefficient h_m in the diffusion Nusselt number, Nu_m, is determined from the relation $h_m = j_s/\Delta\rho_1$.

In the hygroscopic state of a moist body there exists a definite relation between the mass transfer coefficients h_m and β. The vapor fraction in the humid air is a function of the relative humidity φ and of the air temperature T. At an isotherm it follows that the definite moisture content of the body u corresponds to the given value of φ and T. In the moist body state the intensity in liquid evaporation $j_s(\tau)$ will be constant (j_s = const) and Eq. (114) does not apply (is not valid) in this case.

For one-dimensional problems ($\nabla \equiv \partial/\partial x$) the boundary conditions may be written as follows:

$$a_m\rho_0\left(\frac{\partial u}{\partial x}\right)_s + a_m\rho_0\delta(\nabla t)_s + j_s(\tau) = 0 \tag{116}$$

$$-k(\nabla t)_s - (1 - \epsilon)Lj_s(\tau) + q_s(\tau) = 0 \tag{117}$$

3. Dimensionless Heat and Mass Transfer Variables

From the system of differential Eqs. (104) and (105) and boundary conditions (112) and (113) we obtain generalized arguments and functions. [174]

The Fourier numbers for temperature and moisture content fields are determined by the following relations:

$$\mathrm{Fo}_q = \frac{a\tau}{l^2}; \qquad \mathrm{Fo}_m = \frac{a_m\tau}{l^2} \tag{118}$$

Between these dimensionless arguments there exists an interrelation made by the Luikov number, Lu, ($\mathrm{Fo}_m = \mathrm{Fo}_q\mathrm{Lu}$), where Lu is equal to

$$\mathrm{Lu} = \frac{a_m}{a} \tag{119}$$

The Luikov number characterizes the velocity of an equal moisture content surface with respect to the velocity of an isothermal surface. For the majority of moist bodies $\mathrm{Lu} < 1$ since the moisture content field changes slower, as compared with a change in a temperature field.

The Kossovich number, Ko, determined by the relation

$$\mathrm{Ko} = \frac{L\,\Delta u}{c\,\Delta t} \tag{120}$$

is equal to the ratio of heat spent for moisture evaporation ($L\,\Delta u$) to that spent for body heating ($c\,\Delta t$).

The Posnov number, Pn, determines the effect of a temperature field on a moisture content field. It is equal to the relative moisture content drop, caused by the temperature difference:

$$\mathrm{Pn} = \frac{\delta\,\Delta t}{\Delta u} \tag{121}$$

On the basis of the boundary conditions (112) and (113) we obtain two dimensionless arguments, Kirpichev numbers Ki_q and Ki_m.

The Kirpichev heat and mass transfer numbers are equal, respectively to

$$\mathrm{Ki}_q = \frac{q(\tau)l}{k\,\Delta t}; \qquad \mathrm{Ki}_m = \frac{j(\tau)l}{a_m\rho_0\,\Delta u} \tag{122}$$

If flows $q(\tau)$ and $j(\tau)$ are determined by relations (114) and (115), then instead of Ki_q and Ki_m we obtain the heat and mass transfer Biot numbers:

$$\mathrm{Bi}_q = \frac{hl}{k}; \qquad \mathrm{Bi}_m = \frac{\beta l}{a_m} \tag{123}$$

The values of Δt and Δu are chosen in accordance with the conditions of a specific problem.

4. Solutions of Heat and Mass Transfer Equations

Differential equations (104) and (105) with boundary conditions (114) and (115) and (116) and (117) may be solved. These solutions are given in monograph (*19*).

The dimensionless temperature $t^*(t^* = t/t_o)$ and moisture content of a body $u^*(u^* = u/u_o)$ are functions of generalized variables and heat and mass transfer similarity numbers:

$$u^* = F\left(\frac{x}{l}, \mathrm{Fo}_q, \mathrm{Lu}, \mathrm{Bi}_q, \mathrm{Bi}_m, \epsilon, \mathrm{Ko}, \mathrm{Pn}\right) \tag{124}$$

$$t^* = f\left(\frac{x}{l}, \mathrm{Fo}_q, \mathrm{Lu}, \mathrm{Bi}_q, \mathrm{Bi}_m, \epsilon, \mathrm{Ko}, \mathrm{Pn}\right) \tag{125}$$

where u_o is the initial moisture content and t_o is the initial temperature of a body. The analysis of solutions shows that not all the variables equally influence a process. The mass transfer arguments Bi_m and Pn mainly influence a moisture content field, and the heat transfer arguments Bi_q and Ko, a temperature field. It was determined that calculations may be considerably simplified, and the following relations:

$$u^* = F\left(\frac{x}{l}, \mathrm{Fo}_q, \mathrm{Lu}, \frac{\mathrm{Bi}_m}{\mathrm{Pn}}\right) \tag{126}$$

$$t^* = f\left(\frac{x}{l}, \mathrm{Fo}_q, \mathrm{Lu}, \frac{\mathrm{Bi}_q}{\epsilon \mathrm{Ko}}\right) \tag{127}$$

may be used instead of relations (124) and (125). Thus, the complex dimensionless argument $\mathrm{Bi}_q/\epsilon\mathrm{Ko}$ influences heat transfer of a moist body and $\mathrm{Bi}_m/\mathrm{Pn}$, mass transfer.

Under the boundary conditions of the third kind the heating of a dry body is determined by the dimensionless arguments Fo_q and Bi_q. The heating of a moist body will be defined by three arguments: Fo_q, Lu and $\mathrm{Bi}_q/\epsilon\mathrm{Ko}$. From these dimensionless arguments the Luikov number is the parameter of interaction between moisture content and temperature fields. The dimensionless argument $\mathrm{Bi}_q/\epsilon\mathrm{Ko}$ reflects the relation between heat supplied to a body and that spent for internal moisture evaporation.

Consequently, in the presence of heat transfer with simultaneous mass transfer the number of dimensionless arguments increases by one (instead of two arguments we have three).

The solution of the system of differential equations (113–115) under the corresponding boundary conditions are presented in monograph (*19*).

B. EXPERIMENTAL INVESTIGATIONS

Experimental procedure for the study of moisture and heat transfer in moist capillary-porous bodies are described in monographs (*20, 21*). In these monographs experimental methods for determining the moisture transfer coefficients (a_m,δ) and the heat transfer coefficients (k,a) are expounded. Since the moisture transfer coefficients are of great interest, Table VIII illustrates these coefficients for some building materials.

TABLE VIII
MOISTURE TRANSFER COEFFICIENTS

Material	t (°C)	u %	a_m m²/h	$\delta \cdot 10^2$ 1/deg
Autoclave concrete ρ_0 = 400 kg/m m³	20	10	1.9	0.40
		20	2.0	0.80
		30	2.5	0.92
		40	4.0	0.96
Asbestoscement slabs ρ_0 = 390 kg/m³	20	10	1.4	0.54
		20	3.2	1.14
		30	6.2	0.88
		40	7.9	0.42
		50	8.3	0.21
		60	8.3	0.14
Mineral wool ρ_0 = 200–280 kg/m³	20	20	0.9	0.92
		100	3.9	0.92
		140	4.8	—
		180	5.6	—
Diatomic slabs ρ_0 = 500 kg/m³	20	10	1.0	0.50
		20	3.5	0.52
		30	7.0	0.35
		40	9.1	0.25
		50	9.1	0.17
Wood (pine)	40	10	0.18	1.0
		25	0.46	2.0
		30	0.62	2.0
		75	0.62	0.6

For the majority of materials the moisture diffusion coefficient a_m continuously increases with moisture content. In the moist state for some bodies the diffusion coefficient a_m changes negligibly, so it may be considered constant.

The diffusion coefficient a_m increases with the body temperature which is approximately proportional to T^n. For ceramic bodies the exponent $n = 14$ according to Miniovich's (*22*) data and for wood $n = 10$ according to Sergovsky's (*23*) data.

The thermal gradient coefficient δ also depends on moisture content. At first δ increases with moisture content, becomes maximum and then decreases. With the total saturation by water the coefficient δ is equal to zero.

For many thermal insulating materials the change in the coefficient δ, depending on u, is well described by the Dubnitsky formula (*24*)

$$\delta = Au^2 exp\,(-Bu) \tag{128}$$

The constants A and B are determined experimentally.

The coefficient δ depends only slightly on temperature, therefore in engineering calculations it may be considered to be independent of temperature.

For some materials (clay, quartz, sand, peat) Lu is a linear function of moisture content.

Experimental investigations show that the moisture content of the body u is not a potential of moisture transfer. The equality of transfer potentials of contacting bodies in thermodynamic equilibrium is the main property of a transfer potential of any substance. The moisture content does not satisfy this property. For instance, if plates of moist peat and paper are contacted, then in the equilibrium state the moisture content of peat will be 210% and of paper, 50%. Consequently, at the border of their contact there takes place a jump in the moisture content from 50 to 210%. A similar jump of enthalpy (heat content) occurs when two dissimilar metallic plates come into contact. If one plate is made of lead ($c = 0.3$ kcal/grad) and another of iron ($c = 0.11$ kcal/grad), then their contact at the temperature of 50°C enthalpy will be 1.5 kcal/kg for lead plate and 5.5 kcal/kg for the iron plate. As is known, the temperature is potential of heat transfer. The temperature of both plates in the equilibrium state is, therefore, the same and equal to 50°C.

Moisture transfer under isothermal conditions in a uniform body occurs from the great moisture content to the small one. However, when two dissimilar bodies come in contact, a contrary process may take place. For example, if a bed of moist peat ($u = 300\%$) is spread over that of moist quartz sand ($u = 10\%$), then transfer of moisture will occur from sand to peat, i.e., from a body with the small moisture content to that with the great one.

These experimental facts served as a basis for introduction of the moisture transfer potential. At first the moisture transfer potential in a

capillary-porous body was introduced purely empirically. It was determined by the value of the moisture content of a reference standard body. The maximum moisture content for a reference standard body u_{sm}, achieved in the process of sorption of water steam was assumed to be 100 mass transfer degrees (100°M). Then the moisture transfer potential θ of the body of interest was determined by the moisture content value of the reference standard body u_s, being in the thermal dynamic equilibrium with the body investigated

$$\theta = \frac{u_s}{u_{sm}} \cdot 100°M \tag{129}$$

Such a determination of the potential θ resembles an elementary experiment on determining the heat capacity of a body by the calorimetric method. Usually water, the heat capacity of which is approximately equal to unity ($c = 1$), is taken as a calorimetric liquid. In the equilibrium state the temperature of the body of interest and of water is just the same. Since the heat capacity of water is equal to unity, the body temperature is numerically equal to enthalpy (heat content) of water (of reference standard liquid).

After the analogy of this experiment, in the equilibrium state of contacting moist bodies (reference standard and investigated) the moisture transfer potential is the same, i.e., $\theta_1 = \theta_2$, and moisture contents are different, i.e., $u_1 \neq u_2$.

By analogy with the specific heat of a body the concept of the isothermal specific mass capacity c_m was introduced according to the following relation:

$$c_m = \left(\frac{\partial u}{\partial \theta}\right)_T \tag{130}$$

If over some range of the moisture content Δu the mass capacity $\bar{c}_m$ is assumed to be constant, then the relation between the moisture content and moisture transfer potential will correspond to the linear law:

$$u = A + \bar{c}_m \theta \tag{131}$$

where A is a constant and $\bar{c}_m$ is the average specific mass capacity.

If a filter paper is taken as a reference standard body, then in the moist body state ($\theta > 100°M$) for some materials the relation between u and θ is represented by a straight line. For example, for wood (pine at $t = 60°$C)

$$\bar{c}_m = 0.21 \times 10^{-2} \text{ kg/kg°}M, \quad A = 0.042 \text{ and for milling peat}$$

$$\bar{c}_m = 0.51 \times 10^{-2} \text{ kg/kg°}M, \quad A = 0.066$$

In the hygroscopic state the relation between u and θ is also linear. However, with some moisture contents the mass capacity $\bar{c}_m$ of a body changes unevenly. This moisture content corresponds to the moisture of polymolecular adsorption. For instance, for the above wood over the range $0 < \theta < 40°M$ $\bar{c}_m$ is equal to 0.380×10^{-2} kg/kg°M and over the range $40 < \theta < 100°M$ $\bar{c}_m = 0.270 \times 10^{-2}$ kg/kg°M. (See Table IX.)

TABLE IX
ISOTHERMAL SPECIFIC MOISTURE CAPACITY OF MOIST BODIES AT 25°C

Material	$C_m \times 10^2$ [a]		
	$0 < \theta < \theta_a$	$\theta_a < \theta < 100°M$	$\theta > 100°M$
Foam concrete (ρ_0 = 700 kg/m³)	0.110	0.040	—
Peat slabs	0.074	0.052	
Wood (pine)	0.380	0.270	0.210
Fibrolite	0.130	0.090	—
Red clay	0.180	0.180	0.030
Peat	—	1.200	0.510
Red Brick	0.004	0.009	—
Gelatine	—	0.700	—

[a] θ_a is the moisture transfer potential corresponding to polymolecular adsorption. It depends on body properties.

Consequently, the isothermal mass capacity characterizes the binding energy between moisture and a capillary-porous body. This binding energy between moisture and a capillary-porous body is determined by the work of separation of mass unit of moisture in an isothermal reversible process. This work is equal to a change in the free energy E in the isothermal process (T = const).

$$\left(\frac{\partial E}{\partial m}\right)_T = -\frac{RT}{M} ln\varphi \tag{132}$$

In this case the relative air humidity is equal to the ratio of pressure of moisture vapor in a body p_v to that of saturated vapor p_s at the given temperature ($\varphi = p_v/p_s$). In the hygroscopic state the moisture content of any body including the body, chosen as a reference standard, is determined by the relative air humidity and its temperature $u = f(\varphi,T)$. Consequently, the potential of moisture transfer θ thermodynamically is the function of binding energy alone between moisture and a capillary-porous body [$\theta = f(E)$].

Filter paper was chosen as a reference-standard capillary-porous body as it contains all the types of relations between moisture and moist bodies

(adsorption, capillary and osmotic moisture). The main property which establishes the applicability of the filter paper for a reference standard body lies in the fact that its relative moisture content u_{ss}/u_{sm} (the ratio between equilibrium u_{ss} and maximum sorption of moisture content u_{sm}) is independent of temperature over the range from 20° to 80°C.

It is of some interest to compare the potential of moisture transfer θ with that of transfer applied in agrophysics. In the works of American investigators the value of pF, equal to the logarithm of the value of the suction force F, is assumed to be the potential of moisture transfer in grounds. In the hygroscopic state the suction force F is determined by the value of $RTln\varphi$, i.e., it is proportional to free energy of moisture mass unit $(\partial E/\partial m)_T$. Consequently, here potential pF is proportional to the logarithm of the moisture transfer potential $\theta(pF \sim ln\theta)$. In the moist state the suction force F is proportional to capillary pressure determined experimentally. In the moist state ($\theta > 100$°M) the potential pF for a reference standard capillary-porous body (filter paper) was defined by special tests. From these experiments the relation was obtained between pF and θ, which may be presented as the following empirical formula:

$$pF = 3.66 - 1.5 \cdot 10^{-3}\theta \quad \text{at} \quad \theta > 100°M \tag{133}$$

The peculiarity of the moisture transfer potential θ lies in the fact that it characterizes transfer of moisture in a capillary-porous body both as liquid and vapor. It follows from the fact that according to relations (95) and (99) liquid and vapor transfer is determined by two thermodynamic forces (∇u and ∇t). Under isothermal conditions (T = const) the density of a moisture flow is equal to

$$j = -a_m\rho_0 \nabla u = -a_m\rho_0 \left(\frac{\partial u}{\partial \theta}\right)_T \nabla\theta \tag{134}$$

as at a constant temperature $u = f(\theta)$. Since the value $(\partial u/\partial\theta)_T$ is equal to the isothermal specific mass capacity (moisture capacity) then relation (134) may be written as:

$$j = -k_m\nabla\theta \tag{135}$$

where $k_m = a_m\rho_0 c_m$ is the coefficient similar to that of heat conduction ($k = a\rho_0 c$) and it may be referred to as the moisture conduction coefficient (kg/mh°M).

As in the moist body state the specific mass capacity is constant for many moist bodies, the moisture conduction coefficient will change with moisture content of a body just in the same way as the moisture diffusion coefficient changes.

At present there is a number of experimental methods for determining diffusion coefficients of liquid, moisture, moisture transfer potential, and specific moisture capacity in moist bodies (*25*).

The complex of these physical values will be referred to as mass transfer characteristics of capillary-porous bodies. Heat transfer characteristics (coefficients of heat conduction and thermal diffusivity) alongside with mass transfer ones completely determine physical properties of capillary-porous bodies.

The above experimental relations cogently demonstrate the interaction of heat and mass transfer. This interaction for capillary-porous bodies extends over heat and mass transfer between a body surface and surrounding medium and over that inside a capillary-porous body.

In order to describe quantitative relations it is, therefore, necessary to have a method of analysis which makes it possible to consider the interaction of the heat and mass transfer processes. One such method is the thermodynamics of irreversible processes (*26*). The present experimental data well confirm the mathematical theory of thermodynamics of irreversible transfer processes.

NOMENCLATURE

A	constant value in empirical formulas
a	thermal diffusivity (m^2/h)
a_m	diffusion coefficient of moisture in a capillary-porous body (m^2/h)
$a_m{}^T$	thermal moisture diffusivity in a body ($m^2/h°C$)
a_f	coefficient of filtration diffusion in a porous body (m^2/h)
c	specific heat (kcal/kg°C)
c_p	specific isobaric heat of humid air (kcal/kg°C)
c_m	specific isothermal mass capacity (moisture capacity) of a moist body (kg/kg°M)
D	diffusion coefficient of vapor into air (m^2/h)
h	heat transfer coefficient (kcal/m^2h°C) or specific enthalpy (kcal/kg)
h_m	mass transfer coefficient (kg/m^2h, mm Hg)
j	evaporation intensity or moisture-flow density (kg/m^2h)
k	thermal conductivity (kcal/mh°C)
k_f	filtration coefficient (kg/m h mm Hg)
L	specific evaporation heat (kcal/kg)
l	characteristic body dimension (m)
M	molecular weight (kg/mole)
m	mass (kg)
p	pressure in surrounding medium (mm Hg)
p_s	pressure of saturated vapor (mm Hg)
q	specific heat flow (kcal/m^2h)
R	universal gas constant (mmHg m^3/°K mole) or radius (m)
S	surface area (m^2)
t	temperature (°C)
T	absolute temperature (°K) ($T = t + 273.16$)
u	moisture content of a body (kg/kg)
V	volume (m^3)

w air velocity (m/sec)
β mass-transfer coefficient based on moisture-content difference (m/h)
δ thermal gradient coefficient of a moist body (1/°C)
ϵ phase conversion coefficient
ϵ_{ic} ice-content factor
μ dynamic viscosity coefficient (kg/m sec)
ν kinematic viscosity coefficient (m^2/sec)
ρ density (kg/m^3)
ρ_{10} relative vapor concentration ($\rho_{10} = \rho_1/\rho$)
τ time (h)
θ moisture transfer potential (°M)
φ relative air humidity
ω moisture concentration in a body (kg/m^3)

Subscripts

a surrounding medium (humid air)
b state of adiabatic air saturation
c values, corresponding to convection
d dry body
e evaporation or moist body
f filtration characteristics
m mass-transfer characteristics
o relative value or state of absolutely dry body, or initial state
q heat-transfer characteristics
r radiative characteristics
s body surface or saturation state
v vapor
1 vapor
2 liquid
3 ice
4 dry air in pores and capillaries of a body
°M moisture-transfer potential unit in a moist body (mass transfer degree)

Dimensionless Numbers

Nu_q hl/k Nusselt number for heat transfer
Nu_m $h_m l/D_p$ Nusselt number for mass transfer (D_p is a diffusion coefficient based on pressure difference)
Nu_x $h_x x/k$, local Nusselt number
Gu $(T_a - T_b)/T_a$ Gukhman number
Pr ν/α Prandtl number
Sc ν/D Schmidt number
Pe $\frac{wl}{a}$ Peclet number
Pe_x $\frac{w_x x}{a}$ local Peclet number
Fo $a\tau/l^2$ Fourier number
Lu a_m/a Luikov number
Ko $\frac{L\Delta u}{c\Delta t}$ Kossovich number
Pn $\frac{\delta\Delta t}{\Delta u}$ Posnov number

Ki_q $\frac{q(\tau)l}{k\Delta t}$ Kirpichev number for heat transfer

Ki_m $j(\tau)l/a_m\rho_0\Delta u$ Kirpichev number for mass transfer

Bi_q $\frac{hl}{k}$ Biot number for heat transfer

Bi_m $\frac{\beta l}{a_m}$ Biot number for mass transfer

REFERENCES

1. P. D. Lebedev, *Intern. J. Heat Mass Transfer* **1**, 301 (1961).
2. F. M. Polonskaya, *Zh. Tekhn. Fiz.* **23**, 796, 802 (1953).
3. G. T. Sergeev, *Inzh. Fiz. Zh.* No. 2, 77; No. 5, 33; No. 9, 76 (1961).
4. B. M. Smolsky, "External Heat and Mass Transfer in the Process of Convective Drying" (Vneshnii teploi massoobmen v processe konvektivnoi sushki). Belgosuniversitet, Minsk, 1957.
5. A. V. Nesterenko, *Zh. Tekhn. Fiz.* **24**, 729 (1954).
6. E. R. G. Eckert and R. M. Drake, "Heat and Mass Transfer." McGraw-Hill, New York, 1959.
7. N. F. Dokuchaev, *Zh. Tekhn. Fiz.* **26**, 2348 (1956).
8. V. L. Zakharov, "Study of Heat Conduction of Humid Air" (Issledovaniye teploprovodnosti vlazhnogo vozdukha). Minsk, 1961.
9. I. H. de Boer, "The Dynamical Character of Adsorption." Clarendon Press, Oxford, 1953.
10. N. N. Fedyakin, in "Heat and Mass Transfer in Capillary-Porous Bodies" (Teplo- i massoobmen v kapillyarno-poristykh telakh). Gosenergoizdat, Moscow, 1957.
11. V. K. Shchitnikov, *Inzh. Fiz. Zh.* No. 6, 78; No. 7, 73; No. 8, 117 (1961).
12. V. F. Mironov, *Inzh. Fiz. Zh.* **5**, 10 (1962).
13. M. A. Mikheev, "Fundamentals of Heat Transfer" (Osnovy teploperedachi). Gosenergoizdat, Moscow, 1949.
14. B. S. Petukhov, A. A. Detlof and V. V. Kirillov, *Zh. Tekh. Fiz.* **24**, 1761 (1954).
15. A. V. Luikov, *Intern. J. Heat Mass Transfer* **3**, 167 (1961).
16. P. A. Novikov, *Inzh. Fiz. Zh.* **4**, 36 (1961).
17. B. A. Posnov, *Zh. Tekhn. Fiz.* **23**, 865 (1953).
18. N. A. Tsitovich, "Frozen Rock" (Myorzlye gornye porody). Izd. AN SSSR, Moscow, 1961.
19. A. V. Lykov (A. V. Luikov) and Y. A. Mikhaylov, "Theory of Energy and Mass Transfer." Prentice-Hall, New York, 1961.
20. A. W. Lykow (A. V. Luikov), "Experimentalle und Theoretische Grundlagen der Trocknung." Berlin, 1955.
21. A. W. Lykow (A. V. Luikov), "Transporterscheinungen in Kapillarporösen Körpern." Berlin, 1958.
22. Y. M. Miniovich, Addition to the Girsch's book "Drying Procedure." Moscow, 1937.
23. P. S. Sergovsky, "Calculation of Wood Drying and Moistening Processes" (Raschyot protsessov vysykhaniya i uvlazhneniya drevesiny). Goslesbumizdat, 1952.
24. V. N. Dubnitsky, *Izv. Vses. Teplotekhn. Inst.* No. 2, 9 (1952).
25. A. V. Luikov, "Theory of Thermophysics of Structures" (Teoreticheskiye osnovy stroitel'noi teplofiziki). Izd. AN BSSR, Minsk, 1961.
26. S. R. de Groot and P. Mazur, "Non-equilibrium Thermodynamics." North-Holland Publishing Co., Amsterdam, 1962.
27. A. V. Luikov, *Intern. J. Heat Mass Transfer* **6**, 559 (1963).

Boiling

G. LEPPERT and C. C. PITTS

Department of Mechanical Engineering, Stanford University, Stanford, California

I. Introduction

A. History and Applications

When heat is transferred to a liquid which is at or near its saturation temperature, there may be a phase change of some of the liquid into the vapor state. The applications of such boiling heat transfer are many, not only in apparatus whose primary purpose is to vaporize a liquid, such as steam boilers, but also in situations where it is desired to remove heat from a surface at a high rate with the lowest possible surface temperature.

Historically, the engineer's primary interest in the transfer of heat to a boiling liquid has been toward the generation of steam for power produc-

tion, either electrical, propulsive, or both. To this need was added, at a fairly early date, that of the manufacturing chemist, whose production processes required the vaporization of numerous liquids in distillation and other routine operations.

Starting around 1948, extensive research and development directed toward nuclear power generation for ship propulsion got under way. Since the first plant was to be a pressurized water reactor for the submarine *Nautilus*, it was imperative that design criteria in water heat transfer technology be firmly established. To the student of boiling technology, it is interesting to observe the impetus given to research in this field by the development of the pressurized water reactor, which was itself carefully designed to avoid boiling of the coolant. Since that period, of course, reactors have been built in which steam generation takes place in the core, in direct contact with the nuclear fuel elements, and these have proved eminently successful.

Before the feasibility of the boiling reactor principle was demonstrated, however, it was thought that the variations in moderator density caused by vaporization in the core might cause power transients which would threaten the operational stability of the plant. Consequently, the early boiling water research for pressurized water reactors was intended to delineate the permissible range of heat flux and the minimum velocity and subcooling required to insure the presence of the primary coolant in the liquid phase only.

From the standpoint of heat transfer to the boiling liquid, it is almost incidental that the energy source in these reactors comes from nuclear fission. Similar plates, tubes or rods resistively heated by an electrical current would produce much the same heat transfer situation. Quite a different method of steam formation occurs in a homogeneous reactor, however, in which the fissionable material is chemically combined in a salt, such as uranyl sulfate, and carried in aqueous solution. If such a device were permitted to boil, steam formation would take place throughout the fluid volume rather than at a heating surface, as with heterogeneous reactors. Similar vapor formation takes place when a liquid at or slightly above saturation temperature is heated internally by infrared radiation from an outside source, such as a heating lamp.

B. SATURATED BOILING

In many ways, it is advantageous to regard boiling as a special case of convection, either free or forced. To appreciate this similarity, consider a simple heat transfer situation, that of an electrically heated, cylindrical metal tube immersed in a few inches of water. Passage of current through the tube produces thermal energy which raises its temperature, and

convective heating of the water takes place. If quantitative measurements are made when the water just reaches saturation temperature and when the heat input is small, it might be expected that vapor bubbles would form at the heated surface and that these bubbles would rise to the water surface and escape. That this is not the case has been shown by careful measurements (*1*), and, in fact, what happens is that the liquid near the heater reaches a temperature slightly in excess of saturation. This superheated liquid is less dense than the lower-temperature saturated liquid, and it therefore tends to rise to the free surface, where vaporization takes place. In spite of the fact that there is vaporization at the water-air interface, this mechanism is simply natural convection insofar as conditions at the heater are concerned. The temperature driving force at the heater required to produce a certain heat flux is predictable from natural convection correlations.

As the heat flux is increased, the water superheat increases to an amount which permits the formation of vapor bubbles on the heater surface. It will be observed that there are preferred locations where bubbles form, and the bubbles form in columns at these places, which are known as nucleation centers. For low heat flux, relatively few such centers will be observed, but an increase in heat transfer is accommodated by an increase in the number of bubble columns. Since the vapor bubbles so formed detach from the heater and rise in the superheated liquid, and since the vapor is not itself superheated, there is heat transfer to the bubbles from the liquid as they rise to the surface. Experiments have shown that, contrary to intuition, most of the vapor formation in this type of nucleate boiling takes place after the bubble leaves the heating surface. Consequently, most of the heat transferred from the surface during nucleate boiling goes to the superheated liquid adjacent to the heater and not directly to the vapor bubbles which grow on the surface. Figure 1a shows nucleate boiling from a ⅛-inch diameter tube at low heat flux with relatively few nucleation centers.

Figure 2 shows the variation of heat flux with the temperature driving force, which may be taken for present purposes as the heater surface temperature minus bulk liquid temperature, for an electrically heated platinum wire (*2*, *3*). A similar variation has been measured with the apparatus shown in Fig. 1.

At very low heat flux, the curve is a straight line on a log-log plot, which indicates a functional relation of the type

$$q'' = h(t_s - t_o)$$

where the coefficient, h, is simply the convective conductance, and is proportional to the ¼ power of the temperature difference for natural

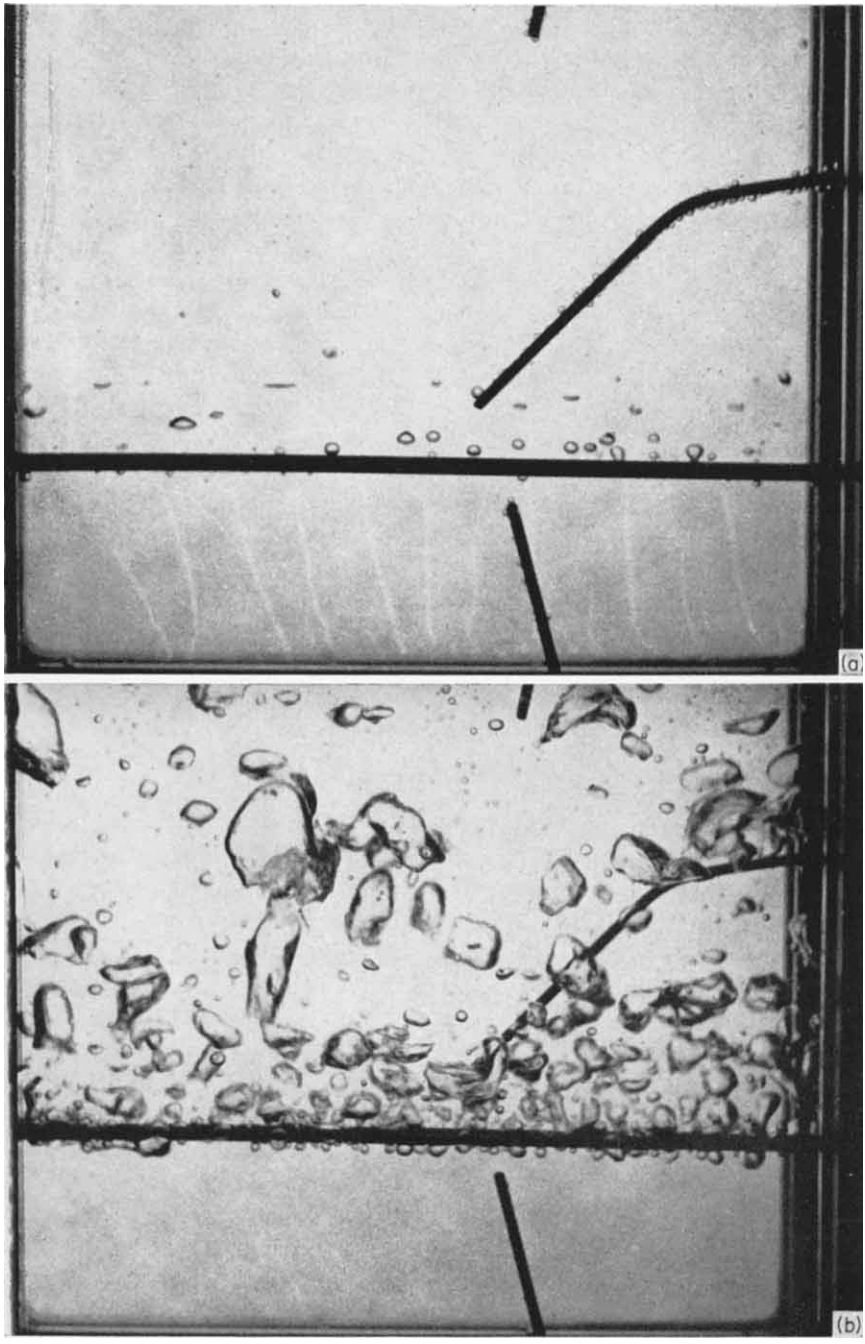

FIG. 1. (For descriptive legend see page 189)

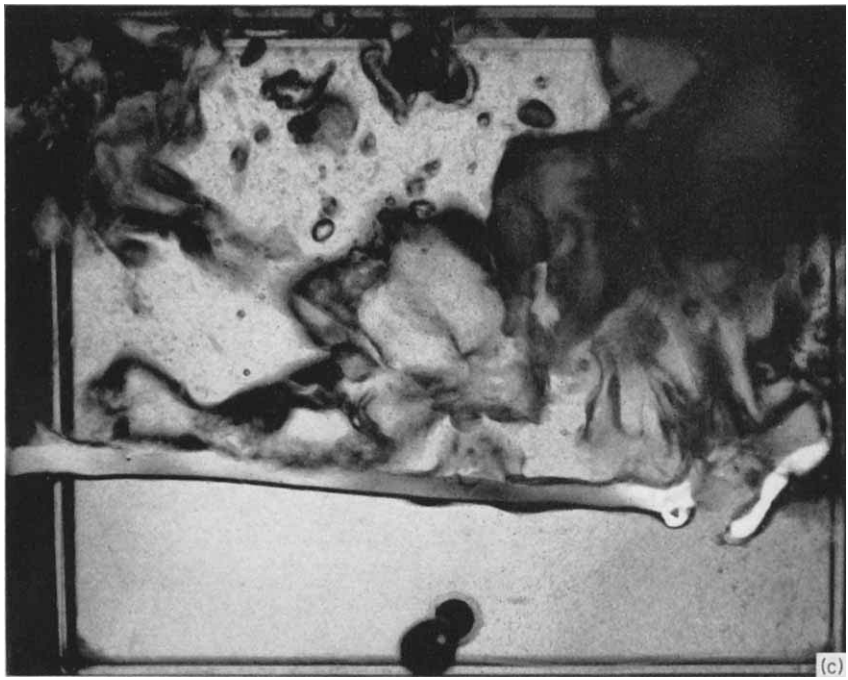

FIG. 1. (a) Pool boiling of water at atmospheric pressure and a heat flux of 15,000 Btu/(hr)(sq ft). The bubbles collapse soon after leaving the heating tube because the bulk temperature is only 208° F. (b) Vigorous nucleate boiling at a heat flux of 171,000 Btu/(hr)(sq ft) and a bulk temperature of 210° F. (c) Transition to film boiling with melting of the heating tube (*4*).

convection in the laminar range. Consequently, the heat flux is proportional to the $\frac{5}{4}$ power of the temperature difference (*1*) in the region $A - B$.

At heat input sufficient to produce bubble formation on the surface, which is the nucleate boiling regime $B - C$ shown in Fig. 2, the rate of increase of q'' with temperature difference is much greater than before, and, as can be deduced from the graph, very large heat transfer rates are possible with a relatively small temperature driving force. This is of great practical advantage in many situations where a cooling problem exists but where the maximum surface temperature is limited by metallurgical or other considerations.

As the heat flux is increased in the nucleate boiling regime, more nucleation centers are activated and there is more and more vapor in the vicinity of the heated surface. At some critical point (C, Fig. 2), the nucleate boiling mechanism can accommodate no additional heat transfer. At this

point, a vapor blanket forms over the entire surface, and the heat transfer mechanism changes completely. Figure 1b shows nucleate boiling at a flux slightly less than that which produces vapor blanketing.

Beyond the peak heat flux just described, the film boiling regime is encountered, as is indicated in Fig. 2. The very large heat transfer rate must be accomplished through a vapor film, which requires a much larger temperature difference than existed at almost the same heat flux in

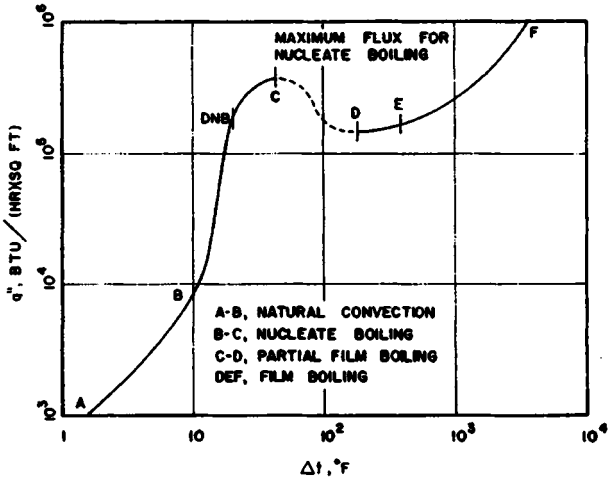

FIG. 2. Boiling of water at 212° F on an electrically heated platinum wire. Data of Nukiyama (*2*) as presented by McAdams (*3*).

nucleate boiling. With water, the required surface temperature is greater than the melting points of the common metals and alloys. Consequently, the phenomenon of a sudden transition from nucleate to film boiling at nearly constant heat flux is frequently called burnout. Figure 1c shows the failure of a stainless steel heating tube when the peak heat flux is reached (*4*).

For certain fluid-surface combinations, it is possible to operate in the film boiling regime without damage to the surface. In such cases, the entire curve in the film boiling region may be obtained experimentally. It can be seen from Fig. 2 that with water, for example, the temperatures are such that radiation from the surface to the liquid, through the film, will play an important part in the film boiling heat transfer mechanism.

There is a fairly wide interval in temperature between the nucleate boiling peak and the minimum stable condition at which film boiling can be sustained. This region is usually termed unstable film boiling and is characterized by the alternate growth and collapse of a vapor film. It can be deduced from the graph that this type of boiling will not occur in a

device which has relatively constant heat input, because an increase through nucleate boiling to the peak heat flux will cause a sudden "jump" (along a horizontal line on the graph) to a corresponding point which is well into the film boiling regime. Similarly, during operation in stable film boiling, a decrease in heat flux below the relative minimum in the curve produces a jump to a point in the nucleate boiling region which is well below the peak heat flux.

With a different kind of heating, however, operation in the unstable film boiling regime becomes quite feasible. If, instead of heating the tube shown in Fig. 1 electrically, it is heated internally by the flow of a hot fluid, then any desired value of surface temperature can be maintained. If the thermal capacity of the heating medium is large enough, its temperature change will be small as it passes through the tube, and the entire outer surface of the tube can be held at practically the same temperature.

C. SUBCOOLED BOILING

Before examining the mechanism of nucleate boiling in greater detail, a distinction needs to be made according to whether the main body of liquid in the vicinity of the heater is at or slightly above saturation temperature, as described above, or at a lower temperature. In the latter case, which is called subcooled boiling or, sometimes, local boiling, vapor bubbles form at a surface because it is substantially above saturation temperature, but the bubbles either collapse without leaving the surface by transfer of heat to the adjacent subcooled liquid, or else they leave the surface and then immediately collapse. In either case, the heat transfer is materially improved over convection without phase change because of the violent agitation of the liquid in the boundary layer by the growing and collapsing bubbles.

Suppose liquid at constant pressure and at temperature t_0 is pumped upward past the heater in Fig. 1 at a constant velocity, V, and that the thermal capacity rate, mc, is sufficiently large that the liquid temperature rise is small. Consider first the forced convection region, where the surface temperature is below t_{sat}. Unlike its situation with natural convection, the heat transfer coefficient is now independent of the temperature difference, and it may be calculated from an equation of the following form if the effects of fluid property variation across the boundary layer are neglected.

$$\frac{hD}{k} = C\left(\frac{DV\rho}{\mu}\right)^a\left(\frac{c\mu}{k}\right)^b$$

Since h is defined as $q''/\Delta t$,

$$q'' = (CkN_{Re}{}^aN_{Pr}{}^b)\Delta t/D$$

where the terms in the parentheses are functions of velocity and bulk temperature only. Figure 3a shows this relationship as a log-log plot of unit slope.

Now consider what happens when the heat flux is increased until the surface temperature exceeds the saturation temperature of the liquid.

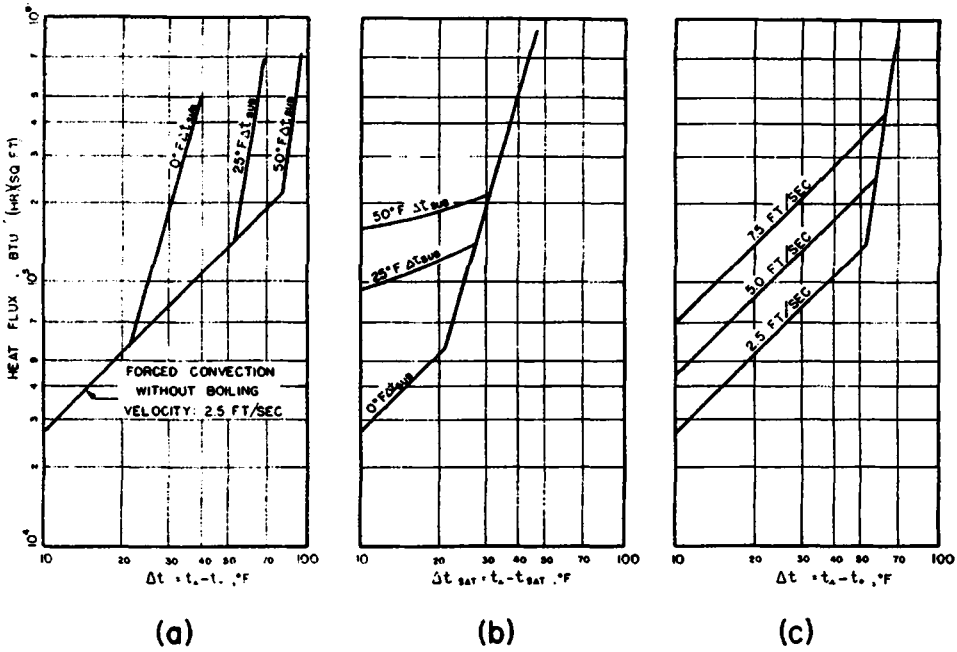

FIG. 3. (a) Variation of heat flux during forced convection and subcooled boiling at different liquid subcoolings and at atmospheric pressure. (b) Variation of heat flux with Δt_{sat} instead of Δt. (c) Variation of heat flux during forced convection and subcooled boiling at different velocities and at atmospheric pressure. The subcooling is 25° F.

As with pool boiling, bubble formation requires a finite positive surface temperature excess, Δt_{sat}. When nucleate boiling first starts, most of the heat is still being transferred by forced convection. However, as the heat flux is increased still further, the nucleate boiling mechanism begins to predominate, and the effect of convection becomes unimportant. Figure 3a shows curves for nucleate boiling at a given velocity with different bulk liquid temperatures and, therefore, different subcoolings.

It has been shown in many experiments that, over most of the nucleate boiling range, the surface temperature excess above saturation is a function of heat flux only, regardless of the subcooling. The nucleate boiling curves in Fig. 3a may be represented quite satisfactorily by a single line

from which the subcooling, and therefore the bulk temperature, has been eliminated, by plotting q'' vs. Δt_{sat} instead of Δt.

Figure 3b shows the curves of Fig. 3a replotted in this manner, from which it can be seen that the new curve has the same coordinates as the zero subcooling curve in Fig. 3a. Since values of bulk temperature below saturation cannot be represented on the logarithmic scale of Δt_{sat}, the forced convection portions of these curves have little meaning and have been included mainly for the sake of completeness. However, they are useful for predicting where boiling starts at various subcoolings with the velocity chosen.

The effect of liquid velocity will next be examined. Figure 3c shows the idealized curve of Fig. 3a for one value of subcooling, to which has been added two additional curves at higher velocities. These curves illustrate the relative independence of nucleate boiling on velocity except near the region of initiation of nucleate boiling.

Two additional remarks need to be made about these curves. In the first place, the transition from forced convection to nucleate boiling does not occur with discontinuous slope, as the straight-line portions of Fig. 3 would suggest, but smoothly, through a transition region where both effects are important. Secondly, velocity and subcooling have a significant effect on the peak heat flux, but this portion of the curve is not shown in the figures.

D. THE MECHANISM OF NUCLEATE BOILING

It was pointed out earlier that in the regime of most practical importance, nucleate boiling, the heat transfer from a surface takes place chiefly by a convective process to the liquid. The high transfer rates can be achieved with fairly small temperature differences because of the very high turbulence level produced in the liquid by the vapor bubbles growing and leaving the surface.

However, the greater complexity of nucleate boiling compared with convection without change of phase may be appreciated by a consideration of the pertinent factors affecting the two mechanisms. Whereas the viscosity, density, thermal conductivity and specific heat of the fluid can be used to describe single-phase heat transfer, in nucleate boiling many additional properties are relevant. The surface tension, latent heat of vaporization, saturation temperature, liquid and vapor densities, and other properties of both phases must be introduced. As with ordinary convection, the configuration of the flow channel and the flow rate must also be considered, but in addition the type of metal, the surface roughness and the presence of adsorbed gas have all been found to affect boiling heat transfer.

A lucid description of the mechanism of nucleate boiling from a submerged heater in a liquid pool was given by the late Max Jakob (*1*). In 1949 Professor Jakob, who, together with co-workers in Germany and, later, in the United States, made many important contributions to the understanding of boiling heat transfer, had this to say about saturated boiling:

"Summarizing our knowledge of the mechanism of nucleate boiling on a clean, smooth or rough, heating surface, it can be said that only a very small part of the heat produced in a heater is directly transferred to the interior of bubbles adhering on the surface. The main part of the energy makes a detour through the liquid. The prerequisite of boiling is formation of a thin, considerably superheated layer of liquid on the heating surface and slight superheating of the bulk of the liquid. Vapor bubbles originate on roughnesses or from gas bubbles which exist at the heating surface. The bubble develops first by evaporation because of the considerable temperature excess of the liquid layer mentioned over the saturation temperature. The bubble breaks off when its volume has grown so much that the buoyancy exceeds the capillary forces which bind it to the heating surface. In the ensuing rise of the bubble through the bulk of the liquid, the excess of liquid temperature and the coefficient of heat transfer on the bubble surface are smaller. However, this surface and the time available for heat transfer are so much greater that the vapor formation is largest during the free rise of the bubble. Vapor bubbles subsequently originating on the same spot form a sort of swaying column; with increasing heating energy and temperature excess spots of smaller roughness satisfy the capillary conditions of bubble formation and start as new sources of vapor columns."

It is to be expected that nucleate boiling from a heater cooled by a subcooled liquid will differ in some important respects from the mechanism just described. In the first place, if there is to be a condition of steady state, some means must be provided to introduce subcooled liquid at an unchanging temperature and to remove heated fluid. Consequently, interest in subcooled boiling is usually confined to forced convection.

In the second place, the vapor bubbles which grow and leave the surface in subcooled boiling immediately find themselves surrounded by liquid colder than themselves. Instead of growing during a buoyant rise through the liquid to a free surface, the bubbles immediately collapse in the stream of subcooled liquid. Whether the vapor bubbles actually become detached from the heater before collapsing, or do so while still attached to the heater, depends upon such conditions as fluid velocity and subcooling.

In spite of these rather significant differences, the mechanism of

nucleate boiling in the vicinity of the heated surface appears to be relatively independent of the bulk fluid temperature. Rohsenow and Clark (*5*) have studied high speed motion pictures of subcooled nucleate boiling in order to estimate the net heat transferred to vapor bubbles compared to the total heat transferred from the surface. They found that only a very small part of the total was represented by the latent heat of the growing and collapsing bubbles. Consequently, the high rate of heat

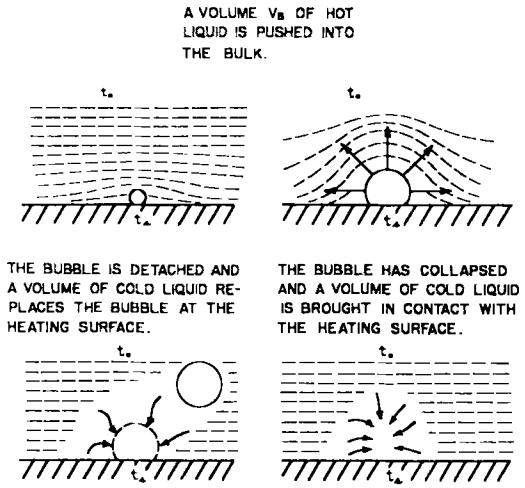

FIG. 4. Schematic diagram of nucleate boiling model of Forster and Greif (*6*). Lower left, vapor bubble leaves surface; lower right, bubble collapses without leaving surface.

transfer associated with subcooled nucleate boiling was attributed by them to violent agitation of the liquid adjacent to the surface.

A significant refinement of this model of nucleate boiling heat transfer is described in a paper by Forster and Greif (*6*), in which they attribute the increased heat transfer to a "pumping action" caused by the growth and collapse of vapor bubbles. Their model, which will be described briefly, appears to yield useful quantitative results and to agree with observations in several important respects. However, it should be regarded as a modification and amplification of the mechanism already presented, since it is in no way contradictory.

Figure 4 shows schematic diagrams of the heat transfer mechanism as conceived by Forster and Greif. After its initiation on the heating surface, which is at temperature t_s, the bubble grows to a volume V_b. As a result of this growth, an equal volume V_b of hot, superheated liquid is forced out of the sublayer into the main stream, which is at a lower

temperature, t_o. When drag and/or buoyant forces cause the bubble to be detached from the wall or to collapse at the wall, its place next to the wall is taken by cold liquid. If the temperature t_o is below saturation, the bubble collapses, and if t_o is above saturation, it grows in the main stream, but in either case its place next to the wall is taken by liquid at temperature near t_o. This model appears to explain the high heat transfer rates which are obtained with nucleate boiling, and it may go a long way toward explaining quantitatively the nearly complete independence of heat transfer rate on main stream velocity and subcooling over a wide range of the boiling regime.

E. FLUID FLOW WITH BOILING

In most design problems where boiling occurs, the determination of the heat transfer coefficient or, what is equivalent, the variation of surface temperature with heat flux, is only part of the information required. Data which may be of even greater importance are the peak heat flux; the static pressure drop in the flow channel; the stability of nucleate boiling and of the flow; and the density of the liquid-vapor mixture. The mixture density is especially important in natural circulation systems, where it controls the flow rate, and in nuclear reactors, where the reactivity may be a sensitive function of the moderator density.

Several different regimes of boiling flow are of interest and can be delineated. Most common, perhaps, is the situation in which either subcooled or saturated liquid is brought under pressure to the entrance of a heated channel. For convenience of discussion, it will be supposed that the channel is a round tube, but the phenomena which will be described are not confined to this configuration.

As the liquid flows through the heated tube, its temperature increases, and, if conditions described earlier are appropriate, nucleate boiling starts. At moderately high heat flux, the surface temperature excess, Δt_{sat}, is sufficient to produce boiling even before the bulk temperature reaches saturation, and subcooled boiling occurs. Static pressure and density variations in subcooled boiling flow are not yet predictable from analysis, nor is there much reliable empirical information. However, it is known that static pressure gradients may be several times as great as with similar subcooled liquid flow without vapor formation.

Further along the length of the heated tube, the bulk liquid temperature may reach saturation, and additional heating will cause the formation of vapor which, unlike that in the situation just discussed, will not condense in the main stream. Consequently, a two-phase mixture of liquid and vapor will flow in the tube from this point until the exit is reached or until all the liquid is vaporized.

It will be appreciated immediately that flow conditions are drastically changed from those prevailing earlier, before boiling began. Because of the usually large (sometimes enormous) specific volume of the vapor phase compared to that of the liquid, flow continuity requires acceleration of the fluid mixture. The magnitude of this acceleration may be quite small with subcooled boiling, especially in channels of at least moderate size, but large increases of momentum must be expected with saturated boiling.

Frictional forces between the fluid and the walls of the channel are naturally quite dependent on the velocity of the flowing mixture. The force which is required to accelerate the fluid and to overcome this increased wall friction is supplied at the expense of static pressure. For a flow channel which is not horizontal, a further change in static pressure occurs because of the change in elevation. In order to predict the magnitude of this effect, the density of the two-phase mixture must be known.

A different application of boiling flow from that in a heated channel is adiabatic flow of a saturated mixture. If liquid at saturation temperature is flowing in an insulated channel, its static pressure tends to decrease because of frictional effects. If heat losses are small, the temperature at first remains constant and the liquid becomes superheated because of the pressure decrease. With sufficient superheating, vapor begins to form. As in the case of boiling flow in a heated channel, acceleration and increased frictional effects must be made up by the continuing decrease of static pressure along the channel. Sometimes called flashing flow, this phenomenon is of practical interest in many engineering applications.

F. BOILING TERMINOLOGY

There is not yet agreement among workers in the field on terminology for various types of boiling heat transfer, but suitable descriptive terms have been used by various authors, and a consistent terminology is evolving. One basic distinction is between surface boiling and volume boiling, i.e., whether vapor bubbles form originally at a heated surface of macroscopic size or whether they form spontaneously in the liquid. Volume boiling, which is relatively uncommon, occurs in pure liquids heated by radiation, and in solution-type nuclear reactors in which heat generation occurs in the bulk of the fluid.

There is no difficulty in distinguishing between nucleate boiling and film boiling. As was pointed out earlier, the mechanisms of heat transfer are completely different in these two regimes, with the most obvious difference being that with nucleate boiling from a surface, most of the heat transfer is to the highly agitated liquid. When film boiling takes place, on the other hand, the heater is blanketed with a layer of super-

heated vapor. Much less is known about unstable film boiling, but its practical importance is limited by its difficulty of achievement except by so-called constant temperature heaters.

When the heat transfer rate is increased to the critical heat flux, nucleate boiling can no longer exist, and the surface becomes covered with an insulating film of vapor. Various other terms have been applied to this heat transfer rate, including burnout, transition heat flux, and peak heat flux. Closely related to these terms is the concept of "departure from nucleate boiling" (DNB) which is defined as the point on the nucleate boiling curve (Fig. 2) at which a noticeable variation from linearity occurs as the critical flux is approached.

The distinction between saturated boiling and subcooled boiling has been made in some detail in the preceding discussion. The most common instance of saturated boiling is pool boiling, which occurs when a heater is immersed in a relatively large quantity of liquid which would be stagnant except for the natural convection currents set up by the heating. After an initial transient period during which the heat added brings the liquid to the boiling point, subsequent heat addition results in saturated boiling. If the liquid, subcooled or saturated, is forced to flow past the heated surface while it is partially or wholly evaporated, forced convection boiling is said to take place.

From the qualitative discussion which has been presented above, it may be seen that the subject of boiling heat transfer may be divided into two general areas: one, which is concerned primarily with conditions at or near the heating surface, includes nucleation, bubble growth, peak heat flux, and film boiling theory; the other, for heated or unheated channels with vapor and liquid in coexistence, is one of two-phase fluid flow and hydrodynamic instability analysis. Various aspects of these subjects will be examined in detail in succeeding sections, and both theoretical analysis and empirical correlations will be presented.

II. Nucleation and Bubble Dynamics

A. Nucleation from a Solid Surface

1. Thermodynamic Equilibrium at a Curved Interface

Although heat transfer does not occur in a system which is in equilibrium, it is possible to derive useful limiting conditions for heat transfer from equilibrium considerations. For example, the physical properties which are utilized in heat transfer calculations are reported for equilibrium conditions, although we apply them with more or less success to highly nonequilibrium systems.

In particular, thermodynamic analysis leads to three criteria for equilibrium between a pure liquid and its vapor (*7*):

(a) The temperature must be uniform throughout both phases.

(b) The chemical potentials (for a pure substance, identical with the Gibbs free energies) of the two phases must be equal.

(c) If the interface is spherical, the pressures in the liquid and in the vapor are related by

$$p_v - p_l = \frac{2\sigma}{r} \tag{1}$$

Equation (1) can also be derived readily from a force balance on a hemispherical segment of a vapor bubble which is in dynamic equilibrium with surrounding liquid. The liquid pressure and the effect of surface tension combine to balance the vapor pressure, which must therefore exceed the liquid pressure.

The saturation states of liquid and vapor which are ordinarily tabulated (e.g., *8*) are for equilibrium at a plane surface. If the interface is curved, as would be the case with a vapor bubble surrounded by liquid, a liquid droplet surrounded by vapor, or a column of liquid in a capillary tube in equilibrium with vapor, Eq. (1) shows that the phases must be at different pressures if they are in equilibrium.

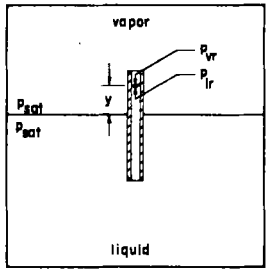

FIG. 5. Liquid rise in a capillary tube due to surface tension.

Perhaps the most graphic demonstration of this situation can be given by considering liquid which has risen in a capillary tube, Fig. 5. When this system reaches equilibrium, its temperature must be uniform throughout according to the criteria we have accepted earlier. The pressures of liquid and vapor at the plane surface must be the same and equal to saturation pressure for the system temperature. From hydrostatics we may write expressions for the vapor and liquid pressures on

either side of the curved interface:

$$p_{vr} = p_{sat} - \frac{\rho_v g y}{g_c}$$

$$p_{lr} = p_{sat} - \frac{\rho_l g y}{g_c}$$

Consequently, at the curved interface both the liquid and the vapor are superheated, since each phase is at a pressure less than the saturation value for the system temperature. The amount of vapor superheat may be negligible compared to that in the liquid, since ordinarily $\rho_l \gg \rho_v$.

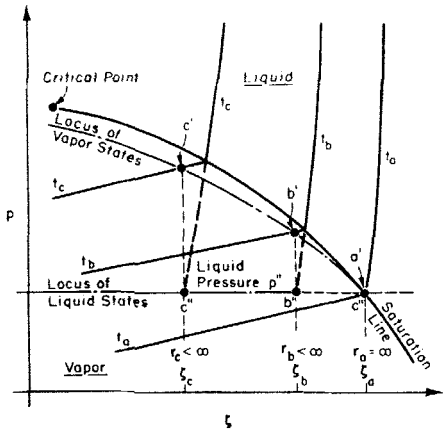

FIG. 6. Variation of pressure with chemical potential for a single-component liquid in equilibrium with its vapor (9).

For a round capillary tube, the interface will be approximated by a portion of a sphere, the radius of which is determined by the surface tension. Consequently, equilibrium thermodynamic states derivable from this illustration will apply to any spherical liquid-vapor boundary, including vapor bubbles and liquid droplets.

Instead of pursuing this example further, however, let us take a more general approach and apply the conditions of equilibrium directly to vapor bubbles (9). Figure 6 shows the variation of pressure with chemical potential (or free energy) for a typical, single-component liquid in equilibrium with its vapor. Isotherms in both vapor and liquid regions have positive slopes, with a discontinuity in slope at the saturation line.

For a fixed liquid pressure p'', all possible liquid states lie along the line $a''c''$ or its extension. Equilibrium at a plane interface ($r \rightarrow \infty$) is represented by the point a'' on the saturation line, while, for a finite radius of curvature, r_b for example, the vapor pressure exceeds p'' by an

amount specified by Eq. (1), which therefore specifies the pressure coordinate of the vapor state b'.

The other coordinate (ζ) of the two phase states b' and b'' is determined by the requirements that they be at the same temperature and at the same free energy. It is again apparent that both phases are superheated, but the locations of b' and b'' on their respective isobars must be found by trial. The superheated liquid point, b'', is on the projection of the isotherm t_b (not yet determined) from the liquid region (*7*, p. 433), while b' must lie on the superheated vapor portion of the same isotherm. Consequently, the conditions of equilibrium and the equation of state of the fluid are sufficient to determine the vapor and liquid states for a bubble of any given radius when the liquid pressure is specified.

To apply these observations to nucleate boiling, suppose a very small vapor bubble exists at a heated surface where it is largely, if not entirely, surrounded by liquid. Merely to avoid collapse, the vapor bubble must be at a higher pressure than the liquid. Since the vapor superheat is usually very small, and since its existence merely strengthens our argument, let us neglect it and assume the vapor to be at saturation temperature for its pressure. The liquid temperature must be at least as great as this or else the bubble size will diminish through condensation at the interface. For nucleate boiling, and therefore bubble growth, to occur, the liquid must be superheated even more than the equilibrium diagram (Fig. 6) would indicate.

One further observation may be made of the nature of Eq. (1): as the radius of a bubble approaches zero, the vapor pressure apparently approaches infinity. Such a situation is meaningless physically, of course, and a consideration of the derivation of the equilibrium criteria, including Eq. (1), will show them to be valid only for bubbles which are large compared to molecular sizes and distances. Nevertheless, the equation predicts, and experiment confirms, that very high liquid superheats can occur if great care is exercised to remove favorable nucleation centers before heating. For example, Kenrick *et al.* (*10*) reported 306° F superheat in water at atmospheric pressure in a capillary tube, which corresponds to a saturation pressure of 800 psia and a calculated bubble radius from Eq. (1) of 0.6×10^{-6} inch.

Since we know from experience that nucleate boiling of water occurs quite readily at superheats of the order of 0.1 of the above value, say 30 to 50° F, we can deduce that much larger nuclei (of the order of 10^{-4} inch) are normally available in engineering systems. The next section will present the results of recent research which demonstrates that minute pits and crevices in a heating surface can entrap gas and vapor, thereby providing nucleation centers of such a size.

2. Surface Variables

For a long time there has been interest in the nature of those preferred locations on heating surfaces at which columns of bubbles form, the nucleation centers. Jakob observed that the temperature difference required between a vapor bubble and the superheated liquid layer next to the surface depends mainly on the radius of the bubble, and that this radius is influenced by the roughness of the heating surface (*1*). He also

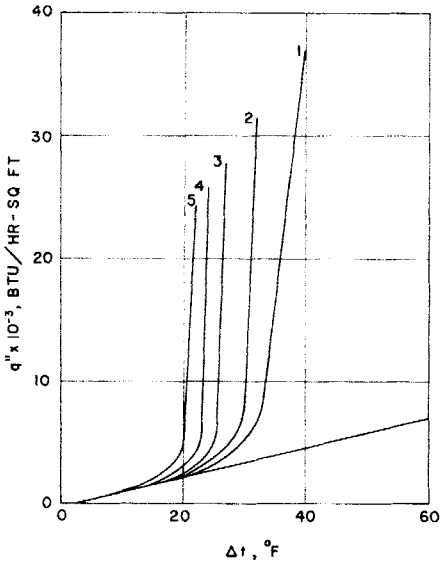

FIG. 7. Nucleate boiling of *n*-pentane on nickel polished with various grades of emery paper; 1. 4/0.–polished nickel; 2. 2/0–polished nickel; 3. 0–polished nickel; 4. 1–polished nickel; 5. 3–polished nickel (*11*).

pointed out that the mean size of the originating bubbles is controlled by a statistical mean of the roughness of the heating surface, an observation which later research has amplified considerably (*11*, *12*).

Corty and Foust have reported the effects of surface roughness and surface aging on the boiling curve (Fig. 2) and on the bubble contact angle for several fluid-surface combinations (*11*). Electron micrographs, photomicrographs, and profilometer roughness measurements were made of the heating surfaces, while bubble shape, size, and population were determined from enlargements of short-exposure (10 μsec) motion pictures. In these experiments, saturated, pool boiling of ethane, normal pentane, and Freon-113 was performed from an upward-facing, horizontal plate which had first been plated with either copper or nickel, then

roughened by rubbing with one of various grades of emery paper (4/0, 2/0, 0, 1, and 3).

Figure 7 shows five curves obtained with *n*-pentane boiling from nickel with different finishes, from which it is evident that successively rougher

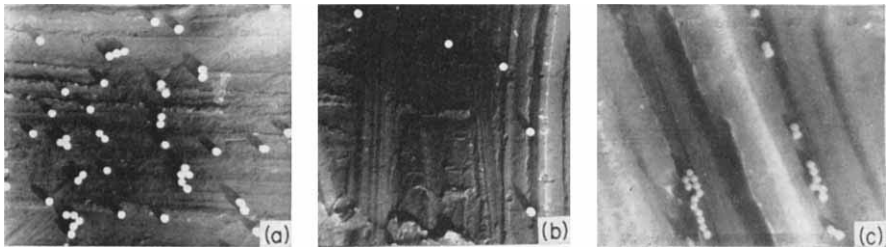

FIG. 8. Electron micrographs of collodian replicas of boiling surfaces. Dow latex yardstick balls are approximately 10-microinch replicas shadow cast at arctan ⅓ (*11*). (a) 4/0–polished nickel. (b) 2/0–polished nickel. (c) 1–polished nickel.

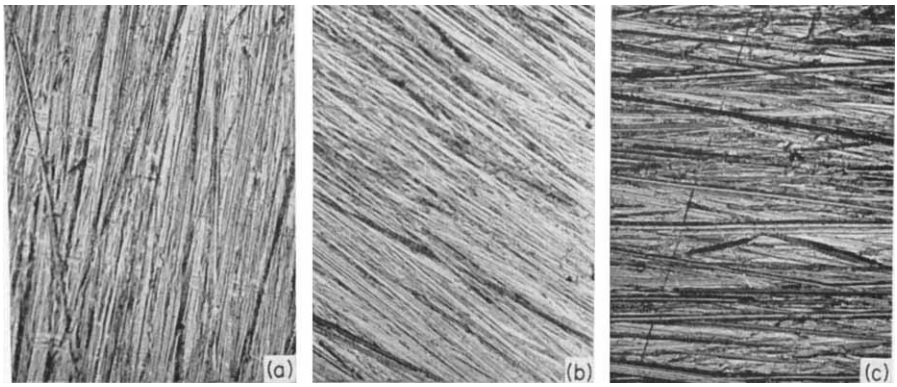

FIG. 9. Photomicrographs of collodian replicas of boiling surfaces (*11*). (a) 0–polished nickel. (b) 1–polished nickel. (c) 3–polished nickel.

finishes required successively smaller temperature differences for a given flux, as one might expect from Eq. (1). Electron micrographs of three of the surfaces are shown in Fig. 8, while photomicrographs are shown in Fig. 9. Observe that Figs. 8c and 9b are of the same surface. The scratch marks left by polishing with emery paper appear from the micrographs to be from 10 to 1,000 microinches wide, while a diamond-tip profilometer gave readings of 2.2 to 23 microinches (rms).

Figure 10 shows an idealized conical cavity which may be used to compare the bubble radius, *r*, predicted by Eq. (1) to the observed rough-

ness, expressed as the cavity radius, R. From the figure we see that

$$r = R/\cos(\phi/2 - \beta)$$

and therefore, from Eq. (1),

$$R = \frac{2\sigma \cos(\phi/2 - \beta)}{p_v - p_l} \tag{2}$$

Corty and Foust arbitrarily assumed a constant value of 120° for the

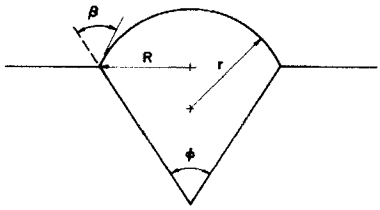

FIG. 10. Idealized conical cavity and vapor bubble.

angle ϕ, since the electron micrographs showed the grooves to be quite flat, while observed values (44 to 60°) of the contact angle, β, were used. Evaluating the pressure difference from the observed surface superheat and the surface tension at saturation temperature, they calculated cavity radii of 3.7 to 9.8 microinches for the 4/0-roughened surfaces.

It might be observed at this point that the very flat grooves which the polishing apparently produced are relatively ineffective in trapping and, especially, in retaining vapor. This aspect of nucleation will be discussed further in reporting Bankoff's work (*13*), but should be born in mind when considering the hysteresis effects observed by Corty and Foust and presented below.

The boiling curves in Fig. 7 illustrate another significant effect of the surface condition in that their slopes vary somewhat with roughness and, particularly for the rougher surfaces, that their slopes are much greater (13 to 25) than is usually found with unprepared surfaces (3 to 5). Apparently the careful roughening of these surfaces replaced the fairly broad size distribution function of the typical "as-received" metallic surface with narrow distributions whose peaks were closely related to the grade of emery paper used.

3. Hysteresis

Some of the most interesting observations made by Corty and Foust had to do with the difference in behavior of nucleation centers under certain conditions depending upon whether the heat flux was increasing

or decreasing. Curve *abe* in Fig. 11 represents the variation of q'' with Δt for free convection in a pool without boiling, while curve *bdc* is the normal nucleate boiling curve which was obtained when the heat flux was decreased from a region where the surface was densely covered with bubble columns. As the flux was reduced, more and more of these bubble columns disappeared, until the free convection curve was reached and no vapor was being produced. If the surface was then kept free of bubbles for at least 10 to 15 minutes, subsequent increase of flux took place along the free convection curve *abe*, with surface superheats of 40 to 50° F

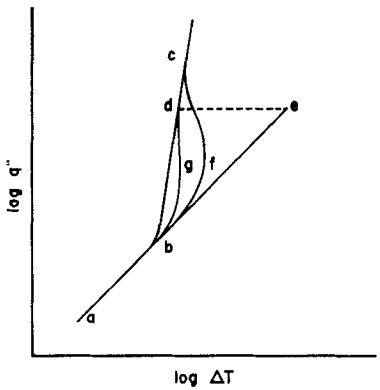

FIG. 11. Hysteresis in nucleate boiling.

being accommodated entirely by free convection and without bubble formation. Finally, at a point such as *e*, vigorous nucleate boiling began suddenly and the superheat dropped to about 25° F at point *d*. Corty and Foust observed that when this occurred, the first bubble formed at some random point on the surface, and nucleation then spread concentrically.

If the heat flux was increased from the point *b* immediately upon the cessation of nucleation, instead of waiting as before, the start of nucleation was not random, but began with the nuclei which had most recently been active. Nucleation spread from these points in patchwise fashion as the heat flux was further increased, until vigorous nucleate boiling was again reached over the entire surface. Curve *bfc* illustrates this condition, while *bgc* shows the case of increasing the heat flux while a few nucleation centers per square inch are still active. Temperature readings taken at three locations, 0.19 inch below the heater surfaces, led to the observation that the surface temperature in the boiling patches was characteristic of the nucleate boiling curve *bdc*, while the bare spots were at a considerably higher temperature such as represented by the point *e*.

Another interesting facet of the hysteresis effect is that the surface

roughness was found to influence the maximum surface superheat which could be obtained by free convection before nucleation started. The point e in Fig. 11 for the smoothest surface (2.2 microinches by profilometer) occurred at a superheat of 35° F, while the roughest surface could sustain 52° F superheat before boiling began. This suggests some of the smaller cavities were more effective in retaining entrapped vapor after boiling has stopped. Furthermore, very large cavities would be unlikely to trap

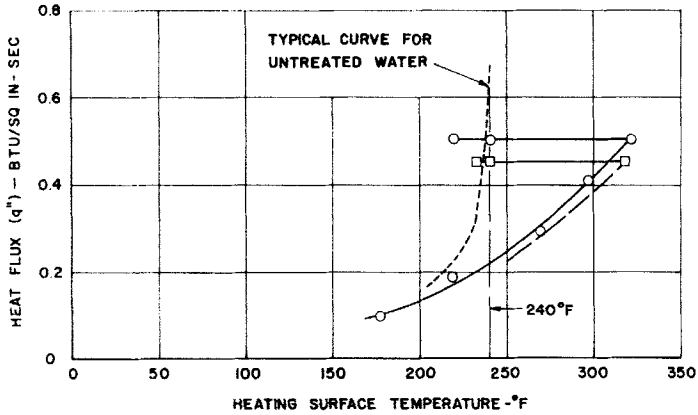

FIG. 12. Influence of prepressurization of water to 15,000 psia on the maximum surface superheat obtained before incipient boiling (*14*).

vapor even when vigorous boiling occurred, since the liquid would tend to penetrate such cavities completely.

Sabersky and Gates (*14*) found an even greater temperature overshoot when heating water which had been prepressurized to 15,000 psia for not less than 15 minutes. Resistance-heated wires of 0.010-inch diameter were used, with typical results as shown in Fig. 12. The very large superheats which they obtained in free convection without bubble formation are of the same order as those which can be obtained with clean water without any foreign surfaces, which indicates that the prepressurization treatment eliminated the more effective nucleation sites, i.e., those of larger diameter. Once the entrapped gas had been dissolved or the vapor condensed at these sites, subsequent reduction of pressure did not cause their reactivation. These results give additional weight to the supposition that the start of nucleation normally occurs at preexisting cavities in which gas or vapor is entrapped.

4. Vapor Trapping

The vapor trapping mechanism has been analyzed in more detail by Bankoff (*13*), who considered the conditions under which gas will be

trapped in a V-shaped groove by a liquid front advancing normal to the groove, as well as the mechanism by which gas would be displaced by such a front. These arguments apply qualitatively to conical, cylindrical and other cavity shapes as well as to grooves. Consider Fig. 13a, from

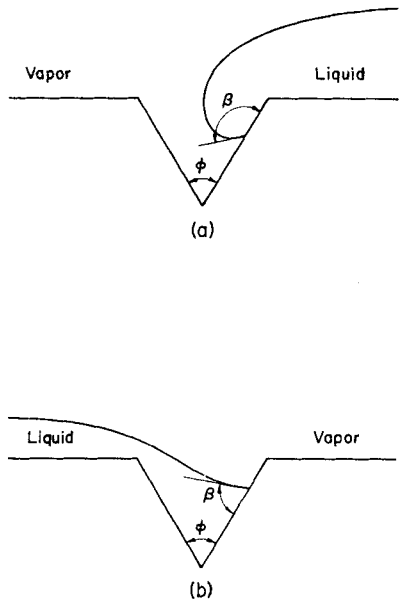

FIG. 13. Idealized vapor trapping model (*13*). (a) Vapor displaced by liquid front advancing normal to V-shaped groove. (b) Liquid displaced by vapor front advancing normal to V-shaped groove.

which it can be seen that no gas will be entrapped if

$$\beta \leq \phi$$

because the liquid will completely fill the bottom of the groove by the time it reaches the opposite wall. If, as Fig. 13a illustrates,

$$\beta > \phi \tag{3}$$

some gas will be trapped in the bottom while the rest of the groove fills with liquid.

Now consider the opposite problem of displacing liquid from the groove by gas, as shown in Fig. 13b. The angle which the gas-liquid interface makes with the solid as it advances down the right-hand wall is β, the contact angle, and this interface will be parallel to the left-hand solid face if

$$\beta = 180 - \phi$$

Consequently, at this or at any smaller value of β the liquid will not be completely displaced before the interface transfers to the left-hand wall, and the criterion that liquid be left in the groove as the gas sweeps over it is

$$\beta < 180 - \phi \tag{4}$$

On the basis of inequalities (3) and (4), Bankoff divides the surface roughnesses in any particular system into four classes:

(a) Those which obey (3) but not (4). These occur when the solid is poorly wet ($\beta \geq 90°$) and the grooves are relatively shallow ($\phi/2 \cong 45°$). Such grooves are stable when completely filled either with vapor or with liquid, and can be refilled with vapor even if they become filled with liquid. Consequently, this class of roughness favors nucleation.

(b) Those which obey (4) but not (3). These occur with good wetting ($\beta \ll 90°$) and when ϕ is not too close to 180°. Liquid can completely fill these grooves, and it will not be displaced later by a vapor front. In both of these first classes of roughness, it is possible to switch from vapor to liquid or from liquid to vapor, which can account for the hysteresis effects discussed earlier.

(c) Those which obey both (3) and (4), when β is not close to zero and $\phi/2 \ll 45°$, are very steep and, once they are filled with either liquid or vapor, cannot be completely purged by the opposite phase.

(d) Those which obey neither (3) nor (4), when β is not close to zero and $\phi/2 \gg 45°$, are very shallow and cannot trap vapor.

Bankoff has also extended the thermodynamic nucleation theory of Volmer (*15*, *16*) and Fisher (*17*) to consider wetted and unwetted surface projections, plane surfaces and cavities (*18*). As we have noted earlier, very large superheats can be sustained by a pure liquid in contact only with smooth, clean, wetted surfaces. Bankoff shows that the superheat required for the formation of a vapor nucleus of critical size (i.e., large enough to grow spontaneously) on a plane surface is a function of fluid properties and of the tendency of the liquid to wet the surface. The poorer the wetting, the lower the required superheat (or excess pressure), but even for water on paraffine, commonly considered nonwetting, the contact angle β is only 95°, and a theoretical pressure of about 800 atmospheres would be required. Since this is far in excess of observed values, it is concluded that nucleation from a plane surface, like nucleation in the pure liquid, is of no importance in surface boiling.

It has long been supposed that surface projections, as well as pits and scratches, serve as nucleation centers (*1*). However, Bankoff's analysis demonstrated that a surface projection is, if anything, inferior to a plane surface in minimizing the work of forming a vapor nucleus. Consequently,

only surface cavities should be of importance as nucleation centers, and even these are effective only if poorly wetted by the liquid or if they contain an incondensable gas. Eventually, the incondensables will diffuse into the liquid phase and the cavity will fill with liquid unless boiling is maintained, in which case such a cavity may continue to nucleate from the entrapped vapor.

Experimental verification of some of these conclusions has been reported by Clark, Strenge and Westwater (*19*). Photographs of the nucleate boiling of diethyl ether and of normal pentane were made through a microscope. Clean, polished heating surfaces of both zinc and aluminum alloy were used. Twenty nucleation sites were observed: 13 were identified as pits in the surfaces: 3 were scratches; 3 occurred at the boundary between the metal heater and a plastic cement used as a sealant against the surrounding packing material; and 1 was on a shifting speck of unidentified material which appeared briefly on one of the surfaces. The active pits were from 0.0003 to 0.0033 inch in diameter and were nearly circular, while the active scratches were about 0.0005 inch wide.

The possibility that grain boundaries might also act as nucleation centers was explored in two ways: by a comparison of the boiling curve obtained from a heating surface of polycrystalline zinc with that obtained from a single crystal, and by direct microscopic observation of nucleation on numerous polycrystalline surfaces. No significant difference could be observed between the boiling curves, nor was any grain boundary seen to be acting as a nucleation center.

5. *Size Range of Cavities and Critical Radius*

Another useful concept, that of the critical radius, can be illustrated with the aid of the equilibrium theory presented earlier and the idealized sketch in Fig. 14a. Suppose vapor to be trapped in the bottom of this cavity, with the liquid-vapor interface initially in the spherical segment labeled r_0 and with a constant contact angle of 90° with the solid. The three equilibrium criteria stated in Section II,A,1 and illustrated in Fig. 6 are assumed to be satisfied, so the system is in a stationary state. In order to disturb this state and to cause the vapor volume to increase, we may either add heat or reduce the pressure level of the entire fluid system, thereby increasing the superheat of both phases. Imagine that we carry out the latter process slowly, so the system temperature remains nearly uniform but changes with time according to the equilibrium requirements and the equation of state. Evaporation will occur at the interface and the vapor mass will increase.

Now consider the variation of the liquid superheat (or, what amounts to the same thing, Δp), as the vapor volume increases. Figure 14b shows

how the reciprocal of the radius, which is just $\Delta p/2\sigma$ at equilibrium, decreases as the amount of vapor increases. After state 1, when the interface reaches the mouth of the cavity, further growth results in a decrease in the radius, and therefore in an increase in the superheat, until the contact angle with the solid surface outside the cavity reaches its characteristic value (assumed 90° for this illustration), after which further growth again increases the radius and therefore decreases the superheat. Observe that there is a minimum radius r^*

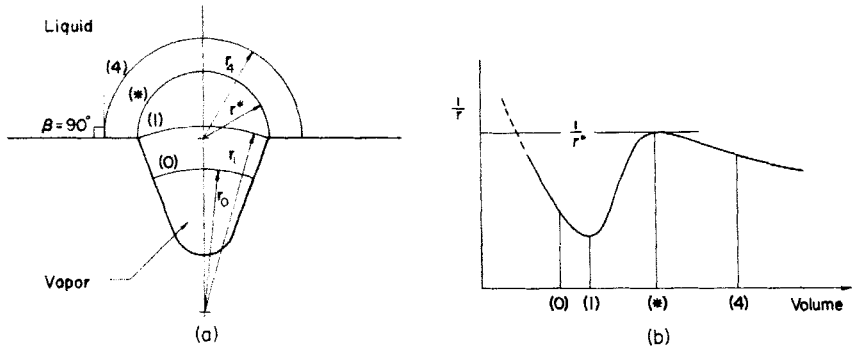

FIG. 14. (a) Idealized conical cavity with a 90° contact angle. (b) Variation of the reciprocal of r with bubble volume. The r^* is the critical value and has associated with it the critical Δt (*12*).

whenever the contact angle is equal to or greater than 90°, and there is a corresponding maximum superheat. This minimum is called the critical radius because, although a smaller bubble can exist and even increase in volume, its growth will be stopped before it reaches this critical size if the liquid superheat is not sufficient to carry it through this stage.

Griffith and Wallis (*12*) have found that the nucleating properties of a conical cavity can be characterized by a single dimension under certain conditions. They also found that boiling would not occur at the desired sites (i.e., they were not stable) if the water had been degassed prior to the test. The degassing of the water apparently resulted in the removal of all gas from the cavities before boiling began. Furthermore, they observed that the conical cavities were not stable for much subcooling and that unwetted cavities were more stable than wetted ones, all of which observations are consistent with the earlier analysis of Bankoff and others.

Instead of examining the Griffith and Wallis results in greater detail, let us now consider a more recent analysis by Hsu (*20*) based on the

nucleate boiling model of Hsu and Graham (*21*). Assume a bubble nucleus exists at the mouth of an active cavity such as is illustrated in Fig. 15a. The previous bubble has just departed and relatively cool liquid at temperature t_0 now occupies the region, as indicated by the temperature profile ($\theta = 0$) shown in Fig. 15b. Also shown is a broken line, $\theta = \theta_b$, from the wall to the extremity of the bubble representing the vapor temperature, which is uniform.

In Hsu's model, it is assumed that a liquid layer of thickness δ is heated by transient conduction from the wall, but that beyond this layer, eddy

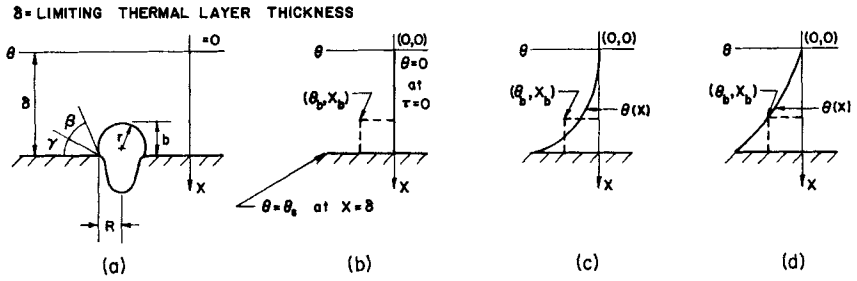

FIG. 15. Model for calculation of the waiting period with typical temperature profiles (*20*). (a) Bubble nucleus at cavity mouth. (b) Temperature profile at $\tau = 0$. At the beginning of the waiting period, $\theta = 0$ at all x except at the wall ($x = \delta$). (c) Temperature profile at $0 < \tau < \tau_w$. During the waiting period, the surrounding liquid is cooler than the bubble interior. (d) End of the waiting period; θ (x) curve reaches point (θ_b, x_b).

diffusivity is controlling and the liquid is at the bulk temperature. In the boundary layer, then, we have a simple transient conduction problem with either a step change in temperature at the wall (constant surface temperature case) or else a sudden start of heating at the wall (constant heat flux case), both solutions being available in the literature (*22*). For the sake of brevity, the present treatment will be confined to the constant surface temperature case, while both cases are treated by Hsu (*20*). Figures 15c and d show schematically how the temperature excess, $\theta(x,\tau) = t(x,\tau) - t_0$, builds up as heating of the boundary layer progresses, until in the latter curve the temperature in the liquid is everywhere equal to or greater than the vapor temperature. This is equivalent to stating that $\theta(x,\tau) = \theta_b$ at $x = \delta - b$ at the end of the waiting period, τ_w. A more complete way to represent the transient solution is shown in Fig. 16, in which the dimensionless liquid temperature group ξ is plotted as a function of the dimensionless distance group η with a dimensionless time group as the parameter.

Also shown in Fig. 16 is a typical curve of ξ vs. η derived from Eq.

(1), in which Δp is replaced by a corresponding temperature difference from the Clapeyron equation, i.e.,

$$\Delta p \cong \frac{\lambda(t_b - t_{sat})}{t_{sat} v_{fg}} \tag{5}$$

Equations (1) and (5) yield

$$t_b - t_{sat} = \theta_b - \theta_{sat} = \frac{2\sigma t_{sat}}{\lambda \rho_v R} \tag{6}$$

where R is the cavity radius and the condition $v_{fg} \cong 1/\rho_v$ is met. Although

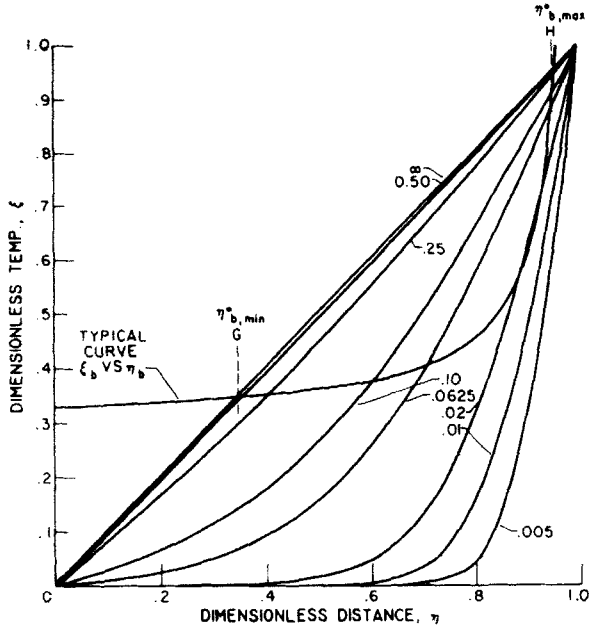

FIG. 16. Dimensionless temperature variation with dimensionless distance for constant surface temperature with the dimensionless time group, $\alpha\tau/\delta^2$, as a parameter (20). $\xi = \theta/\theta_s$, $\eta = x/\delta$.

the contact angle β and the slope of the cavity mouth γ are unknown, a simple but reasonable assumption is that the bubble height, $b = \delta - x_b$, is equal to the cavity diameter, $2R$, which leads to an expression for the bubble radius r in terms of b (20). With this substitution, then, Eq. (6) may be nondimensionalized to give

$$\xi_b = \frac{\theta_b}{\theta_s} = \xi_{sat} + \left(\frac{3.2\sigma t_{sat}}{\lambda \rho_v \delta \theta_s}\right)\left(\frac{1}{1 - \eta_b}\right) \tag{7}$$

Hsu's model requires that this equation, which is plotted in Fig. 16 for typical values of fluid properties and δ, be satisfied at the end of the waiting period. The intersections of this ξ_b vs. η_b curve with the transient conduction curves give the waiting periods for bubbles of various sizes.

It is immediately clear that for a cavity to be effective, its waiting period must be finite. Therefore, the intersections of this infinite time curve ($\xi = \eta$) in Fig. 16 with the typical ξ_b vs. η_b curve provide minimum and maximum values of η_b, as shown, and only cavities within this size range can be effective. Expressed algebraically, these limiting radii are

$$R_{\max} = \frac{\delta}{2C_1}\left[1 - \frac{\theta_{\text{sat}}}{\theta_s} + \sqrt{\left(1 - \frac{\theta_{\text{sat}}}{\theta_s}\right)^2 - \frac{8\sigma C_3 t_{\text{sat}}}{\lambda\,\delta\theta_s\rho_v}}\right] \tag{8a}$$

$$R_{\min} = \frac{\delta}{2C_1}\left[1 - \frac{\theta_{\text{sat}}}{\theta_s} - \sqrt{\left(1 - \frac{\theta_{\text{sat}}}{\theta_s}\right)^2 - \frac{8\sigma C_3 t_{\text{sat}}}{\lambda\,\delta\theta_s\rho_v}}\right] \tag{8b}$$

where C_1 and C_3 are functions of the angle $\beta + \gamma$ (Fig. 15a) and the cavity radius R (*20*).

Not all sites within the limits given by Eqs. (8a) and (8b) are active, since there may be two cavities very close together, of which only the one with the shorter waiting period will be active at a given surface temperature (or heat flux). From these equations it may also be deduced that nucleate boiling is impossible if there are no real roots, i.e., if

$$\left[\left(1 - \frac{\theta_{\text{sat}}}{\theta_s}\right)^2 - \frac{8\sigma C_3 t_{\text{sat}}}{\lambda\rho_v\delta\theta_s}\right] < 0$$

Therefore, the temperature difference of incipient boiling is predicted from this inequality to be

$$\theta_{\text{so}} = \theta_{\text{sat}} + \frac{4\sigma t_{\text{sat}} C_3}{\lambda\rho_v\delta} + 2\sqrt{\left(\theta_{\text{sat}} + \frac{2\sigma t_{\text{sat}} C_3}{\lambda\rho_v\delta}\right)\left(\frac{2\sigma t_{\text{sat}} C_3}{\lambda\rho_v\delta}\right)} \tag{9}$$

This expression is significant because it relates the condition of incipient boiling, which can be estimated in various ways (e.g., Fig. 3), to the boundary layer thickness δ.

Hsu (*20*) has compared the incipient nucleate boiling data reported by McAdams *et al.* (*23*), with the pressure and subcooling dependence predicted by Eq. (9). A reference point was chosen to evaluate δ/C_3 from a measured value of θ_{so}, after which θ_{so} was calculated for a wide range of boiling conditions with the same value of θ/C_3. Equations (8a) and (8b) were also tested against the temperature and cavity size measurements of Clark, Strenge and Westwater (*19*) and of Griffith and

Wallis (*12*). In all cases, the calculated results from the nucleate boiling model of Hsu and Graham were consistent with experimental observations.

B. HOMOGENEOUS NUCLEATION AND RADIATION EFFECTS

Nucleation from a homogeneous liquid phase is relatively rare, because long before the very large liquid superheats which would be needed are attained, heterogeneous nucleation usually occurs. In nearly all engineering systems, there will be gas entrapped in the container walls, gas bubbles in the liquid, or suspended solids, perhaps very small, which provide nucleation sites. However, it is possible in the laboratory, if extreme care is taken, to achieve very high degrees of superheat in liquids before nucleation and bubble growth occur.

The theory of homogeneous nucleation has been reviewed in detail by Westwater (*24*) and will not be discussed here. Classical thermodynamics and the reaction rate theory of Eyring seems capable of explaining some of the main features of this phenomenon, but Westwater concludes that considerably more work needs to be done in this area.

We have referred earlier to a solution-type nuclear reactor as a practical example of homogeneous nucleate boiling, but it is clear that homogeneous nucleation is not likely to occur in such a device. However, this application is interesting to the present discussion because of the high density of ionizing radiation which is likely to be present.

Fast and slow neutrons, gamma rays, beta particles, protons and even fission products can conceivably contribute to nucleation in a superheated liquid, and, in fact, the well-known bubble chamber invented by D. A. Glaser (*25*, *26*) for the detection of nuclear particles depends upon this process for its operation. According to a model proposed by Seitz (*27*), most bubble nuclei formed in a bubble chamber are produced when incident particles (e.g., protons or pions) transfer energy by Rutherford scattering to electrons in the superheated liquid. These electrons rapidly lose this kinetic energy, which is of the order of kilovolts, to the molecules in their path, and this energy reappears chiefly in the form of heat.

In order for such an excited electron to form a nucleus of sufficient size that a macroscopic bubble will be formed, the electron must have a range of the same order of magnitude as the radius demanded by Eq. (1) for the particular values of surface tension and superheat which are used. That is, within a distance approximately equal to $2r = 4\sigma/\Delta p$, the electron must transfer enough energy to produce a bubble of radius r. A static bubble of this size represents an energy investment of

$$E_m = 4\pi r^2\sigma + 4\pi r^3\rho_v\lambda/3 \tag{10}$$

where the first term is the energy required to create the vapor-liquid

surface and the second represents the latent heat. Seitz shows that the static energy demanded by Eq. (10) is exceeded by an order of magnitude by the energy which would be lost within a range of $2r$ by 10 kev electrons, so the process is feasible from this standpoint. This phenomenon which results in a substantial and rapid energy transfer in a very small region is known as a "thermal spike."

It is essential that the nucleus be formed in a period of time which is short compared to the time in which the heat would diffuse through the liquid. This criterion is found to be met by average bubble growth velocities of the order of 0.1 the speed of sound. Seitz further considers in an approximate way the additional energy required to accelerate the liquid and to overcome resistance of viscosity. Although viscous effects are apparently negligible for liquid hydrogen, which has a very low coefficient of viscosity (about 10^{-4} poise), they may be appreciable in propane and similar liquids with viscosities near 10^{-2} poise.

Because of the scarcity of experimental data on bubble production by ionizing radiation, as well as the approximate nature of certain aspects of the analysis, these results must be considered somewhat tentative. Nevertheless, they present a consistent picture of the processes which seem to be taking place and agree with the limited experimental data which are available.

C. BUBBLE DYNAMICS

1. Introduction

Having considered the circumstances which control the nucleation of vapor bubbles at a heated surface or, occasionally, within a bulk liquid phase, we may now turn our attention to the conditions which govern the subsequent growth of these nuclei into vapor bubbles of macroscopic size. The simplest form that this problem can take is that of a spherical bubble growing in a large volume of uniformly superheated liquid. This situation might be approached not only in homogeneous boiling, such as in a bubble chamber or in a homogeneous nuclear reactor, but also in certain surface boiling situations.

In pool boiling, for example, bubbles experience a relatively small fraction of their growth while they are attached to the heated surface. As we have discussed earlier, most of the heat transferred from the heater goes to the liquid in the pool and thence to the vapor bubbles during their ascent to the free surface. Another important instance of a vapor bubble growing in uniformly superheated liquid occurs when the pressure is suddenly reduced in an isothermal liquid system which is at or near its saturation temperature. Nearly uniform superheat can be achieved and bubbles can grow at such nucleation sites as may be present.

Considerably more complex is the problem of bubble growth in a non-uniform temperature field, such as exists in the thermal boundary layer during surface boiling. This is the problem in pool boiling from the time of formation of the nucleus of critical radius until detachment of the bubble from the heated surface. Similar but still more difficult is the analysis of the bubble growth rate during subcooled surface boiling, when the nucleus grows in a superheated layer near the heater, but collapses when it contacts subcooled liquid a short distance away. The bubble may or may not detach and move into the main stream before collapsing. The dynamic analysis of bubble detachment in these various surface boiling situations is, itself, a subject of considerable interest.

Valuable reviews of bubble dynamics have been published by Jakob (*1*), Westwater (*24*), Zuber (*28*) and Hsu and Graham (*21*). Much of the material in the following paragraphs was drawn from these sources.

2. Bubble Growth in a Uniformly Superheated Liquid

According to Bosnjakovic (*29*), the thermal resistance to bubble growth may be considered to be concentrated in a thin layer of liquid next to the growing bubble. The vapor in the bubble, and therefore the surface layer of liquid molecules, is nearly at saturation temperature during most of the bubble growth period. Therefore we denote the conductance of the boundary layer, k/δ, by h, and obtain an energy balance at the interface

$$h(t_0 - t_{sat}) = \lambda \rho_v \, dr/d\tau \tag{11}$$

From measurements of the bubble growth rates obtained from high-speed motion pictures, Jakob and others (*1*) found values of h from Eq. (11). For water in pool boiling at atmospheric pressure, values of h as high as 40,000 Btu/(hr)(sq ft)(F) were observed in the initial transient when the bubbles formed. After 10 millisec, this value decreased to about 4,000 and then to about 3,000 for most of the 200 millisec observation. After about 25 millisec, the average bubble left the surface and began its free ascent through the superheated liquid.

Fritz and Ende (*30*) treated this problem by numerical integration of the heat equation, assuming the newly created vapor-liquid interface acted as a plane wall of temperature t_{sat} bounding a semiinfinite slab of liquid initially at t_0. Formulated mathematically, this partial differential equation for $t = t(x,\tau)$ is

$$\frac{\partial t}{\partial \tau} = \alpha \frac{\partial^2 t}{\partial x^2} \tag{12}$$

subject to the initial and boundary conditions that

$$t(x,0) = t_0$$
$$t(0,\tau) = t_{sat} \text{ for } \tau > 0$$
$$\lim_{x \to \infty} t(x,\tau) = t_0$$

An energy balance at the interface then provides the coefficient h:

$$h(t_0 - t_{sat}) = k\left(\frac{\partial t}{\partial x}\right)_{x=0}$$

where x is measured from the interface into the liquid and where the derivative is obtained from the transient solution. Reasonably good agreement was found between values of h from this calculation and those found from the photographic measurements.

This transient conduction model was later refined by Plesset and Zwick (*31*) and Forster and Zuber (*32*), who combined the equation of motion with the transient heat conduction equation. This approach starts with Rayleigh's equation for the growth of a spherical bubble in an infinite liquid medium

$$r\frac{d^2r}{d\tau^2} + \frac{3}{2}\left(\frac{dr}{d\tau}\right)^2 + \frac{2\sigma g_c}{\rho_l r} = \frac{p_v - p_l}{\rho_l/g_c} \tag{13}$$

The pressure excess which is assumed to produce the bubble growth may be written in terms of the Clapeyron equation

$$p_v - p_l = \frac{\lambda(t_v - t_{sat})}{t_{sat}v_{fg}} \tag{14}$$

where the vapor pressure and temperature are functions of the radius, according to Eq. (1), and therefore of time. Note that temperature t_{sat} is not the temperature of the liquid, but rather is the saturation temperature which corresponds to the liquid pressure. Finally, the energy equation in spherical coordinates is written as

$$\alpha\left(\frac{\partial^2 t}{\partial r^2} + \frac{2}{r}\frac{\partial t}{\partial r}\right) = \frac{\partial t}{\partial \tau} + \frac{\partial t}{\partial r}\frac{dr}{d\tau} \tag{15}$$

At the start of bubble growth ($\tau = 0$), the temperature everywhere in the liquid is constant at some known degree of superheat, and the liquid temperature far from the interface remains at this superheat. These two boundary conditions, together with an instantaneous energy balance at

the liquid-vapor interface, can be expressed as follows:

$$t(r,0) = t_0$$

$$\lim_{r \to \infty} t(r,\tau) = t_0$$

$$k \frac{\partial t}{\partial r} = \lambda \rho_v \frac{dr}{d\tau}$$

The thin thermal boundary layer assumption of Bosnjakovic (*29*) is retained to simplify the integration.

Although somewhat different procedures were followed by the authors of references (*31*) and (*32*) in obtaining solutions to these equations, both found that bubble growth is limited by the rate of heat diffusion to the interface, and that the effects of liquid inertia and surface tension are small and can be neglected. The predicted growth rate is expressed by the asymptotic solution

$$\frac{dr}{d\tau} = \frac{\sqrt{3}\, k(t_0 - t_{sat})}{\lambda \rho_v \sqrt{\pi \alpha \tau}} \tag{16}$$

which is in good agreement with the experimental measurements of Dergarabedian (*33*).

G. Birkoff *et al.* (*34*), obtained an asymptotic solution to Eq. (15) by a similarity assumption which does not require the thin boundary layer approximation. They showed that Eq. (16) is a good approximation whenever the dimensionless group

$$N_{Ja} \equiv \frac{(t_0 - t_{sat})\rho_l c}{\lambda \rho_v} \gg 1$$

A similar observation had been made earlier by Griffith (*35*). First Savic (*36*) and later, Zuber (*28*) have called this dimensionless group the "Jakob number" in honor of the late Professor Max Jakob.[1]

A further contribution to the theory has been made by Scriven (*37*), who solved the equations of continuity, momentum and energy not only for single-component systems but also for binary systems. His results for single-component systems are consistent with those of Plesset and Zwick (*31*) for large values of the Jakob number. While heat diffusion is the limiting process for bubble growth in the single-component case, both heat and mass must diffuse to the vapor-liquid interface in the two-component case. If the more volatile component does not diffuse

[1] In a personal communication Professor S. P. Kezios has informed the authors that Mr. Savic proposed to him that this dimensionless group be named the Jakob number some years prior to the publication of reference (*36*).

with sufficient rapidity to the interface, the boiling temperature increases in that vicinity and bubble growth is inhibited.

From the above discussion it is clear that the theory of bubble growth in an infinite liquid medium at uniform superheat is well advanced, especially in the period after the first instant when surface tension and liquid inertia become unimportant. One circumstance which is not considered by these theories, however, is that there may be turbulence in the liquid which will increase the effective diffusivity of both heat and mass. Much more complex is the problem of bubble growth in a nonisothermal liquid layer, which will we discussed in the next section.

3. Bubble Growth on a Heated Surface

Recognizing the fact that in surface boiling a bubble grows in a liquid which is not uniformly superheated, but of varying temperature, Griffith (*35*) obtained a numerical solution of the transient conduction problem for nonuniform liquid temperature. Utilizing the results cited earlier that surface tension and liquid inertia are negligible during the later and more important stage of bubble growth, he combined Eq. (15) with an energy balance at the liquid-vapor interface and with a velocity expression obtained from the continuity equation. The distinctive feature of this analysis is the use of a linearly varying liquid temperature in the boundary layer next to the heating surface as an initial condition.

Perhaps the most serious limitation of Griffith's analysis is the difficulty of predicting suitable values of the boundary layer thickness. Furthermore, no attempt was made to predict bubble collapse rates in subcooled boiling, presumably because Eq. (15) is written for laminar flow, while a high degree of turbulence is likely in the collapse process. Nevertheless, Griffith's analysis predicts a number of interesting trends:

(a) For increasing pressure and decreasing values of the Jakob number, the growth velocity decreases.

(b) The maximum size attained by bubbles at small Jakob number is independent of the Jakob number and depends only on the thickness of the superheated boundary layer.

(c) The average growth velocity of bubbles with a smaller maximum size is greater than for those with a larger maximum size for the same Jakob number.

Bankoff and Mikesell (*38*) showed that the nearly symmetrical bubble growth and collapse curves which have been obtained experimentally by Gunther (*39*) and Ellion (*40*) with highly subcooled surface boiling would not occur if the limiting process were entirely transient conduction as expressed by Eq. (15). They postulated a turbulent convective mechanism for that part of the bubble which projects into the turbulent core

of subcooled liquid. Thus, evaporation in the laminar flow region near the base of the bubble may continue even while rapid condensation occurs where there is contact with the highly subcooled turbulent core. The use of an empirical expression for the turbulent flow heat transfer resulted in qualitative agreement with experiments in which heat flux, liquid bulk velocity and liquid subcooling were independently varied.

In another paper, the same authors (*41*) extended the laminar flow analysis of Plesset and Zwick (*31*) to the case of a bubble growing in a non-uniform liquid layer of either a linear or an exponential temperature profile. In this model, it is assumed that the bubble initiates in a superheated layer at the surface, but that its growth forces a thin layer of superheated liquid into the main stream (cf. Fig. 4). The results of the computation are expressed parametrically in terms of the volume of the bubble boundary layer, which in turn was obtained empirically from experimental bubble growth data. Agreement with the trends exhibited by bubbles growing in saturated surface boiling is good, but not in subcooled boiling. The authors attribute the latter disagreement to inaccuracy in the assumed temperature distribution or to turbulent heat transfer between the vapor bubble and the subcooled bulk fluid.

Experimental measurements of bubble growth rates in the pool boiling of distilled water and methyl alcohol have been reported by Staniszewski (*42*). Although most of these observations were made with upward-facing horizontal plates, two runs were with a vertical plate. System pressure was varied from 1 atmosphere to 40 psia, the pool depth to as little as 1 inch, and the heat flux from 15 to 80% of the critical value. High-speed movies were analyzed to obtain bubble diameter as a function of time from the instant of first visibility until that of detachment from the surface.

Although the usual statistical variation among growth curves was observed, the growth rate proved to be almost independent of the system pressure. However, both the bubble frequency and departure diameter are smaller at higher pressure. At the highest heat flux, the departure diameter tends to increase, while the bubble frequency correspondingly decreases. Changing the heater orientation from horizontal to vertical had no pronounced effect on the departure diameter, but did result in slower bubble growth.

Staniszewski found that if the growth curves are written in the form

$$r = C\tau^m \tag{17}$$

the exponent m varies from a value of 0.5 to 1 early in the growth period, with a subsequent decrease to a value of about $\frac{1}{3}$. The analysis of Bankoff and Mikesell (*41*) most nearly fits the curves, but suffers from the dis-

advantage of requiring an empirical constant which depends upon experimental conditions. When Griffith's numerical results (*35*) were fitted to an equation of the form of Eq. (17), the exponent varied from about 0.5 in the early growth stage down to 0.22 to 0.35 for larger bubbles. Consequently Griffith's theory underestimates the growth in the early stage, but agrees well in the later part of the period. The constant-superheat theories (*31*, *32*), with their constant exponent of 0.5, do not agree very well with the experimental results.

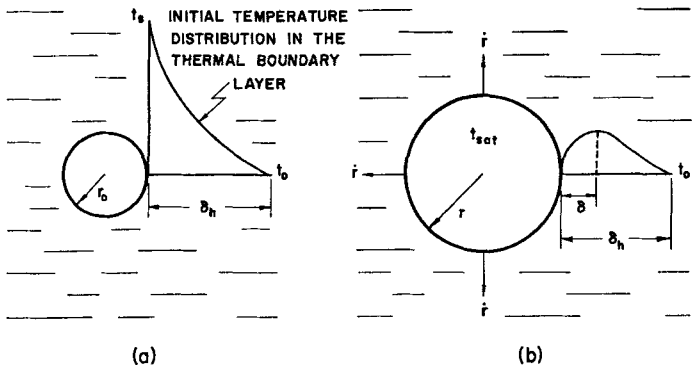

FIG. 17. Jakob's analytical model of a bubble growing in a nonuniform temperature field (*28*). (a) Initial temperature distribution. (b) Temperature distribution for a growing bubble.

The bubble diameter at detachment was compared by Staniszewski with the approximate formula derived by Fritz (*43*) from a balance of buoyant and surface tension forces acting on typically shaped bubbles:

$$D_b = 0.0148\beta \sqrt{\frac{2\sigma g_c}{g(\rho_l - \rho_v)}} \quad (\beta \text{ in degrees})$$

This formula overestimates the mean values of observed data and the scatter is considerable. It was observed that faster growing bubbles attained a larger breakoff diameter, which fact was incorporated into a formula for D_b

$$D_b = 0.0071\beta \sqrt{\frac{2\sigma g_c}{g(\rho_l - \rho_v)}} (1 + 0.073\, dr/d\tau) \tag{18}$$

where $dr/d\tau$ is in ft/sec. Eq. (18) agrees within $\pm 25\%$ with all the experimental observations of D_b which Staniszewski made.

In his dissertation (*28*), Zuber treats the problem of bubble growth in a nonuniform temperature field by extending the Bosnjakovic-Jakob model which we have discussed earlier. Figure 17a shows an idealized

initial temperature distribution in a thermal boundary layer of thickness δ_h, just as a microscopic bubble is formed but before its growth has begun to cool the boundary layer. In Fig. 17b, the bubble has grown and the adjacent temperature distribution has changed as a result of the diffusion of thermal energy toward the interface. Within a layer of thickness δ, the heat flow is from the hotter liquid to the interface, while beyond δ, heat continues to flow toward the bulk liquid. To describe this situation,

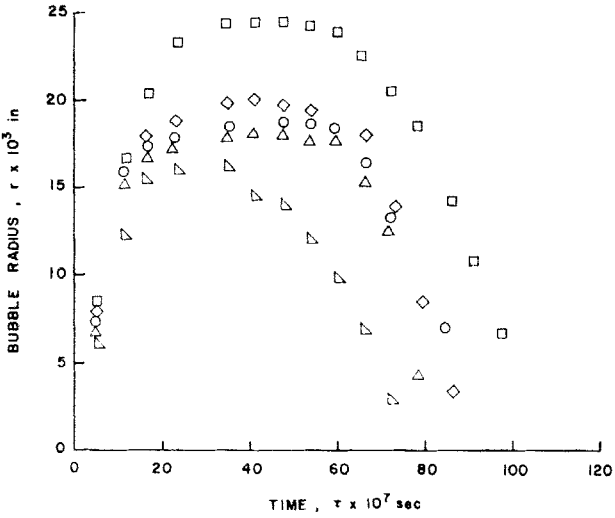

FIG. 18. Ellion's experimental data for bubbles growing and collapsing in subcooled water at atmospheric pressure (*40*). The heat flux is 147 Btu/(sec)(sq ft) and the bulk temperature 135° F.

Zuber modifies Eq. (16), which was obtained for a uniformly superheated liquid, by equating the transient heat transfer rate to the sum of the rates of latent energy increase and heat transfer to the bulk liquid (q''):

$$\lambda\rho_v \frac{dr}{d\tau} + \frac{\pi q''}{2} = \frac{\pi k(t_s - t_{sat})}{2\sqrt{\pi\alpha\tau}} \tag{19}$$

(note that the coefficient $\pi/2$ has been substituted for its near equal, $\sqrt{3}$, which appears in Eq. (16)). The quantity q'' is assumed by Zuber to be equal to the average heat flux from the heating surface on the grounds that the average temperature gradient in this portion of the liquid is not distorted greatly by the appearance and growth of the bubble. The integrated form of Eq. (19) is

$$r(\tau) = \frac{\rho_l c(t_s - t_{sat})\sqrt{\pi\alpha\tau}}{\rho_v\lambda}\left[1 - \frac{q''\sqrt{\pi\alpha\tau}}{2k(t_s - t_{sat})}\right] \tag{20}$$

Zuber found good agreement between the bubble sizes predicted by Eq. (20) and measurements made by Fritz and Ende (*30*) of the diameters of vapor bubbles at the time of departure from a heated surface in pool boiling. A further check was made against experimental bubble growth curves obtained by Zmola (*44*), again with close correspondence.

Zuber also treats the problem of bubble growth and collapse in a subcooled liquid and compares the predictions from the extended Bosnjakovic-Jakob model with Ellion's experimental data (*40*). Figure 18 shows radius-time data obtained by Ellion, while Fig. 19 presents the same data

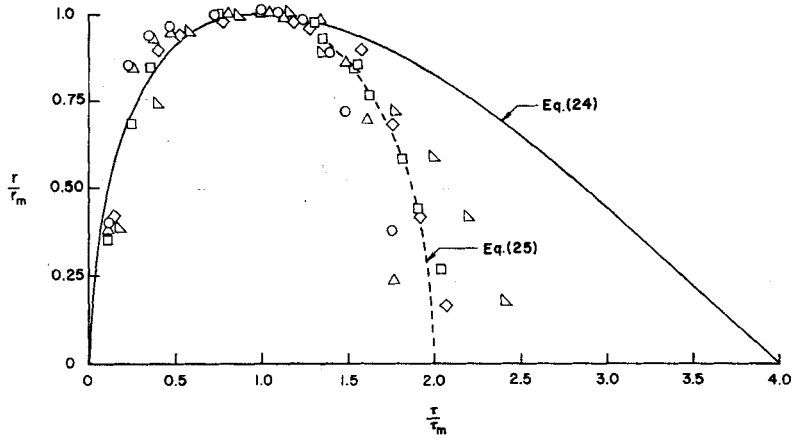

FIG. 19. Comparison of theoretical bubble growth and collapse curves (*28*) with subcooled boiling data of Ellion (*40*).

normalized on the maximum radius r_m and the time at which this radius is reached, τ_m.

From Eq. (19), the maximum bubble radius occurs when $dr/d\tau = 0$, i.e., when

$$\sqrt{\pi\alpha\tau_m} = k(t_s - t_{sat})/q'' \tag{21}$$

Equation (20) may then be written

$$r(\tau) = \frac{\rho_l c(t_s - t_{sat})\sqrt{\pi\alpha\tau}}{\rho_v\lambda}\left(1 - \tfrac{1}{2}\sqrt{\frac{\tau}{\tau_m}}\right) \tag{22}$$

and the maximum radius is

$$r_m = \frac{\rho_l c(t_s - t_{sat})\sqrt{\pi\alpha\tau_m}}{2\rho_v\lambda} \tag{23}$$

Dividing Eq. (22) by Eq. (23) gives an expression for r/r_m:

$$r/r_m = \sqrt{\tau/\tau_m}\,(2 - \sqrt{\tau/\tau_m}) \tag{24}$$

Figure 19 shows that this equation successfully predicts the observed bubble growth, but not the collapse, which occurs much more rapidly than the theory predicts.

Reasoning that the heat transfer mechanism in the liquid near the interface is much more favorable during collapse than during growth because of deformation and motion of the bubble, as well as turbulence, Zuber has obtained a solution to the collapse phase of the problem by assuming isothermal conditions. Unlike the growth phase, inertial effects are now controlling, and the Rayleigh equation becomes

$$r\frac{d^2r}{d\tau^2} + \tfrac{3}{2}\left(\frac{dr}{d\tau}\right)^2 = \frac{p_v - p_l}{\rho_l/g_c}$$

where surface tension effects are again ignored and the right-hand side is constant for the isothermal case. The solution to this equation is (*28*):

$$\frac{\tau}{\tau_c} = 2 - \int_0^{r/r_m} \frac{(r/r_m)^{3/2}d(r/r_m)}{\sqrt{1-(r/r_m)^3}} \Big/ \int_0^1 \frac{(r/r_m)^{3/2}d(r/r_m)}{\sqrt{1-(r/r_m)^3}} \qquad (25)$$

$$\text{for } \tau/\tau_m \geq 1$$

Equation (25) is also shown in Fig. 19 for comparison with Ellion's data.

Hsu and Graham (*21*) have evaluated the terms in Eq. (19) somewhat differently than did Zuber. In the first place, they have calculated the heat transfer rate to the bulk liquid (q'') by means of a solution to the transient equation for heat conduction in a flat plate. The liquid layer temperature is assumed initially to vary linearly from the wall to the bulk liquid at the edge of the thermal boundary layer ($x = \delta_h$). The transient which follows is caused by the sudden drop in temperature from t_s to t_{sat} at the surface of the "liquid slab" which is bounded by the newly formed and growing bubble. These initial and boundary conditions for Eq. (12) can be written as follows:

$$\begin{aligned} t(x,0) &= t_s - q''x/k_l, \quad 0 \leq x \leq \delta_h \\ t(0,\tau) &= t_{sat} \text{ for } \tau > 0 \\ t(\delta_h,\tau) &= t_0 \text{ for } \tau \geq 0 \end{aligned}$$

where x is measured from the wall and q'' is the heat flux from the wall. The transient flux to the bubble, q_s'', can then be found from the solution to Eq. (12) with these boundary conditions, and this flux is analogous to the two corresponding terms in Eq. (19). However, these terms in the latter equation have been multipled by $\pi/2$ to correct for the sphericity of the interface, and a similar correction will be applied to q_s''.

The other refinement which Hsu and Graham applied to Zuber's analysis was to include a term which accounts for heat transfer through the

base of the bubble, which had been ignored. The latter flux is assumed equal to the flux from the heated surface, q'', and a heat balance on the bubble may be written

$$\lambda\rho_v \cdot 4\pi r^2 dr/d\tau = q''A_{ba} + Cq_s''A_s \tag{26}$$

where $C = 1$ for the flat film approximation and $\pi/2$ for a spherical film. The geometrical problem of relating the base area to the bubble wall

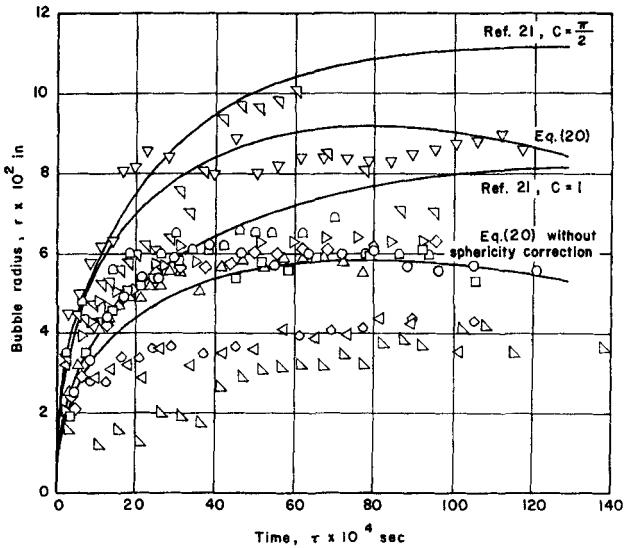

FIG. 20. Comparison of theoretical bubble growth predictions (*21, 28*) with boiling data for water at 18° F subcooling, atmospheric pressure (*21*).

area was resolved by recourse to the calculations of Bashforth and Adams (*45*), from which it was found that for very small bubbles, $A_{ba} \cong A_s$, while for larger bubbles ($r > 1$ mm), $A_{ba} \cong A_s/4$.

Finally, Eq. (26) can be integrated to find the radius as a function of time. This integration is performed in two parts, according to the two ranges of bubble size just mentioned, with the results shown in Fig. 20. Bubble growth curves are shown with and without the sphericity correction for both Zuber's and Hsu and Graham's calculations. The experimental data in the illustration were reported by Hsu and Graham for distilled, degassed water in pool boiling at atmospheric pressure with a subcooling of about 18° F.

An interesting feature of the bubble growth analysis of Hsu and Graham is its dependence on the thickness of the thermal boundary layer (δ_h) which exists in the liquid at the end of the waiting period

(cf. Section II,A,5). Consequently, a larger, faster-growing bubble would be expected after a long waiting period than after a short one, and this behavior was observed experimentally. The nucleation characteristics of the surface influence the waiting period (Section II,A,5) and can therefore be considered in the bubble growth calculations.

III. Nucleate Boiling

The nucleate boiling process is too complex to have yielded to adequate representation by a mathematical model and, therefore, to satisfactory analysis. For saturated pool boiling, Jakob (*1*) showed that only a small fraction of the heat passes from a surface directly to the vapor, while both Gunther and Kreith (*46*) and Rohsenow and Clark (*5*) made similar observations for forced convection, subcooled boiling. Therefore, the primary nucleate boiling mechanism is apparently one of convection from the hot surface to superheated liquid, with vapor bubbles serving to promote mixing of the liquid near the surface. However, the exact mechanism by which the bubble action increases the heat flux is not clearly understood.

A. CONVECTION ANALOGIES

Gunther and Kreith (*46*) have described the nucleate boiling process as "microconvection in the sublayer." They hypothesize that the growth-and-collapse cycling of bubbles introduces subcooled liquid into the sublayer and excites oscillating local velocities. Shadowgraphs which they presented of the convection currents induced by surface boiling tend to support this hypothesis. Using reasonable values for equivalent diameter, local velocity and liquid temperature in the Sieder-Tate equation they showed that the proposed mechanism could accommodate the high heat transfer rates observed in nucleate boiling.

Rohsenow (*47*) proposed a different analogy between nucleate boiling and single-phase forced convection heat transfer based on the common form of nonboiling convection correlations

$$\frac{hD}{k} = \phi\left(\frac{DG}{\mu}, \frac{\mu c}{k}\right) \tag{27}$$

Since the controlling resistance to heat transfer in surface boiling is postulated to be in the liquid, the properties k, μ and c in Eq. (27) are chosen as those of saturated liquid corresponding to the local pressure. The characteristic length, D_b, on the other hand, is related to an average vapor bubble on the heated surface, as is the mass flux, G_b, since it is the bubble growth characteristics which determine the amount of local agitation in the liquid sublayer.

The growing bubbles are not ordinarily spherical, but a characteristic length can be conveniently defined as the diameter of a sphere having the same volume as an actual vapor bubble when it breaks away from the surface. Denoting this length hereafter by D_b, Fritz's formula (cf. Section II,C,3) can be written

$$D_b = C_1\beta\sqrt{\frac{2g_c\sigma}{g(\rho_l - \rho_v)}}; \qquad 0 \leq \beta \leq 140°$$

The bubble diameter is, therefore, a function of saturation pressure only for a given solid-liquid combination.

The volume of an actual vapor bubble is $\pi D_b^3/6$, and the mass rate of vapor leaving per unit heater area is

$$G_b = \rho_v \frac{\pi D_b^3}{6} fn$$

where n = number of nucleation centers per unit area

f = frequency of bubble formation at a nucleation center.

Furthermore, Jakob showed that, for pool boiling, the product fD_b is a constant at a given pressure and at low to moderate heat flux (*1*).

Next consider the rate of heat transfer to the vapor bubbles while they are attached to the surface, i.e.,

$$q_b'' = \lambda G_b = \left[\lambda\rho_v(fD_b)\frac{\pi D_b^2}{6}\right] n \tag{28}$$

All quantities in the brackets are constant or are functions of the saturation pressure only, so q_b'' varies linearly with n at a given pressure. However, Jakob found that the number of nucleation sites on a surface in pool boiling is proportional to the total heat flux, and an increase in the heating rate is accompanied by a proportionate increase in the number of bubble columns. Consequently, at a given pressure the total heat flux is also proportional to n, the nucleation site density, and therefore

$$q'' = C_2 q_b'' \tag{29}$$

where C_2 may be a function of the pressure. Let us now solve Eqs. (28) and (29) for the bubble mass velocity

$$G_b = \frac{q_b''}{\lambda} = \frac{q''}{C_2\lambda}$$

The bubble Reynolds number is, then,

$$N_{\mathrm{Re},b} = \frac{D_b G_b}{\mu_l} = \frac{C_1\beta}{\mu_l}\sqrt{\frac{2g_c\sigma}{g(\rho_l - \rho_v)}}\frac{q''}{C_2\lambda} = \frac{C_3 q''}{\mu_l\lambda}\sqrt{\frac{g_c\sigma}{g(\rho_l - \rho_v)}}$$

where $C_3 = C_1\beta\sqrt{2}/C_2$. The contact angle has been absorbed into the coefficient C_3 because of lack of data on the variation of this quantity with pressure and with surface condition.

Many investigations have shown that the heat flux in nucleate boiling depends upon the excess of surface temperature over local saturation

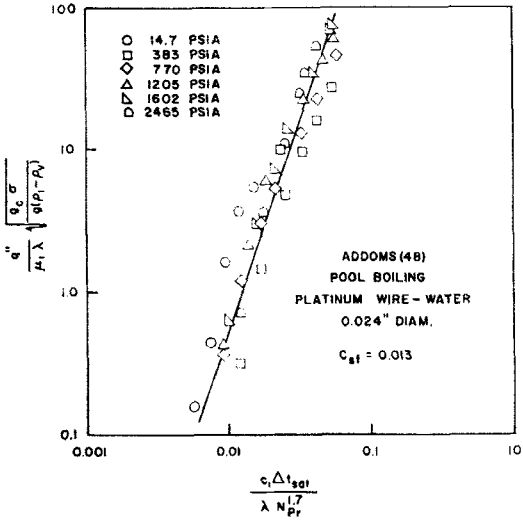

FIG. 21. Rohsenow's correlation (*47*) of Addoms' pool boiling data (*48*).

temperature rather than over a local bulk liquid temperature. Consequently, the bubble Nusselt number is defined as

$$N_{\mathrm{Nu},b} = \frac{q'' D_b}{k_l \Delta t_{\mathrm{sat}}}$$

which will be found to be equally applicable to subcooled nucleate boiling and to saturated boiling.

We now have the three dimensionless groups in Eq. (27) expressed in terms of usually measured variables, and we can try to obtain a correlation of nucleate boiling heat transfer in terms of these groups. Instead of using the bubble Nusselt number as the dependent group, however, it is more convenient to use the group

$$\frac{C_2 N_{\mathrm{Re},b} N_{\mathrm{Pr},l}}{N_{\mathrm{Nu},b}} = \frac{c_l \Delta t_{\mathrm{sat}}}{\lambda}$$

and to seek a correlation of the form

$$\frac{c_l \Delta t_{\mathrm{sat}}}{\lambda} = \phi_2(N_{\mathrm{Re},b},\ N_{\mathrm{Pr},l})$$

The data of Addoms (*48*) were selected for this purpose because of

the wide pressure and heat flux ranges covered. Figure 21 shows Addoms' results at various pressures from 14.7 to 2465 psia, which are correlated by

$$\frac{c_l \Delta t_{sat}}{\lambda} = C_{sf}\left[\frac{q''}{\mu_l \lambda}\left(\frac{g_c \sigma}{g(\rho_l - \rho_v)}\right)^{1/2}\right]^{0.33}\left(\frac{c_l \mu_l}{k_l}\right)^{1.7} \tag{30}$$

where C_{sf} is 0.013, and the data spread by approximately $\pm 20\%$.

The correlation Eq. (30) has also been applied to the data of numerous other experimenters. Values of the coefficient C_{sf} for various fluid-surface combinations are listed in Table I (*47*).

TABLE I

VALUES OF C_{sf} FOR SOME SURFACE-FLUID COMBINATIONS

Surface-fluid combination	C_{sf}
Water-Nickel	0.006
Water-Platinum	0.013
Water-Copper	0.013
Water-Brass	0.006
CCl_4-Copper	0.013
Benzene-Chromium	0.010
n-Pentane-Chromium	0.015
Ethyl alcohol-Chromium	0.0027
Isopropyl alcohol-Copper	0.0025
35% K_2CO_3-Copper	0.0054
50% K_2CO_3-Copper	0.0027
n-Butyl alcohol-Copper	0.0030

Rohsenow found the exponents of 0.33 and 1.7 adequate to correlate a wide range of data for single component liquids boiling on clean surfaces. For dirty surfaces, the 0.33 exponent on the bubble Reynolds number was still adequate for most of the data, but the best Prandtl number exponent varied from 0.8 to 2.0.

Since the contact angle β is seldom known, it is difficult to assess the significance of the absorption of this factor into the coefficient C_{sf}. However, it is presumably this step in the analysis which makes C_{sf} so dependent on the fluid-surface combination.

Another difficulty with this correlation lies in the Prandtl number effect which it predicts. If we write the correlation in the form of Eq. (27) we obtain

$$N_{Nu,b} = \frac{1}{C_{sf}}(N_{Re,b})^{0.67}(N_{Pr,l})^{-0.7}$$

or

$$\frac{C_{sf} q'' D_b}{k_l \Delta t_{sat}} = \left(\frac{D_b G_b}{\mu_l}\right)^{0.67}\left(\frac{k_l}{c_l \mu_l}\right)^{0.7} \tag{31}$$

In no other forced or natural convection correlation does the Nusselt number diminish with increasing Prandtl number. If we examine Eq. (31) we see that the negative exponent merely intensifies the dependence of $q''/\Delta t_{sat}$ on the liquid conductivity, k_l, and on the viscosity, μ_l. The only aspect of the situation which is disturbing is the prediction that $q''/\Delta t_{sat}$ is diminished by an increase in the liquid specific heat, which is contrary to reason and to the prediction of Reynolds analogy.

Rohsenow's correlation has been applied to a variety of liquids covering a wide range of fluid properties and appears to be the most successful correlation which has been developed to date. It permits the calculation of the heat flux which can be accommodated by nucleate boiling for a given temperature difference, Δt_{sat}, at various system pressures, once the coefficient C_{sf} has been found by a suitable experiment.

Forster and Greif (*6*) have used the vapor-liquid exchange model which has been discussed in some detail in Section I,D to derive a correlation for nucleate boiling:

$$q'' = 1.2 \times 10^{-3} \frac{\alpha c \rho_l t_{sat}}{J\lambda\rho_v \sqrt{\sigma}} \left[\frac{c t_{sat} \alpha^{1/2}}{J(\lambda\rho_v)^2}\right]^{1/4} \left(\frac{\rho_l}{\mu_l}\right)^{5/8} \left(\frac{\mu c}{k}\right)^{1/3} (\Delta p)^2$$

This is the same as a correlation derived earlier by Forster and Zuber (*49*), who used a model much the same as Rohsenow's except that the radial bubble growth rate was used as the characteristic velocity in the Reynolds number and a bubble radius obtained from bubble dynamics was used as the characteristic length in the Nusselt number.

B. Effects of Surface Roughness

It has been shown that surface roughness influences not only the intercept of the boiling curve but also its slope (Fig. 7). Rohsenow's correlation permits adjustment of the intercept by proper choice of the constant C_{sf}. However, all of the correlations which have been discussed so far ignore the dependence of the slope of the boiling curve on surface conditions and hence on the size distribution of active nucleation sites. This is undoubtedly due, at least in part, to the difficulty of describing surface roughness mathematically.

Kurihara and Myers (*50*) were the first to attempt to incorporate surface effects quantitatively into a correlation of nucleate pool boiling heat transfer. Their experiments show that the average boiling coefficient, h_m, varies approximately as $n^{1/8}$ for $n > 200$ per sq ft, where n is the concentration of nucleation sites. This type of relationship has since been confirmed by Tien (*51*), who found that the exponent on n varies from 0.3 to 0.5 for data taken with several liquid-solid combinations. For $n < 200$ per sq ft the average boiling coefficient appears to be nearly independent of n.

Using the Reynolds, Nusselt and Prandtl numbers as defined by Rohsenow (*47*), Kurihara and Myers employed dimensional reasoning to arrive at the equation:

$$\frac{h_m}{k} = 820\left(\frac{\rho_v}{\mu_l}\right)^{1/3} n^{1/3} N^{2}_{\mathrm{Pr}}{}^{-0.89} \tag{32}$$

where h_m is in Btu/(hr)(sq ft)(F). They also presented a method for calculating the number of nucleation sites as a function of surface superheat provided that one experimental point of n vs. Δt_{sat} is known. Their predicted relations show reasonably good agreement with the experimental data for $n > 200$ per sq ft.

Tien (*51*) proposed a new model for the nucleate boiling mechanism in which the bubble columns rising from the heated surface induce a flow pattern similar to axisymmetrical stagnation point flow. Solutions for this flow pattern which are available in the literature are used to derive the following relationship for nucleate pool boiling:

$$h_m = 61.3 N_{\mathrm{Pr}}{}^{0.33} k_l n^{-0.5}$$

This equation does not correlate the available data as well as Eq. (32), perhaps, as suggested by Tien, because the properties of the vapor phase have been neglected.

C. THERMAL BOUNDARY LAYER

In their measurements of the temperature distribution over a heater in nucleate boiling, Gunther and Kreith (*46*) observed that there is a thermal boundary layer near the heated surface. The existence of this layer was confirmed by Yamagata *et al.* (*52*) who used an optical method and later by Hsu and Graham (*21*) who used shadowgraph and schlieren photography. Hsu and Graham have discussed the role of this thermal boundary layer in the heat transfer process and have shown that the ebullition cycle consists of three stages:

(a) The development of a thermal layer next to the heated surface.

(b) The growth of the bubble which pushes the surrounding liquid radially outward. The area of influence of each bubble has a diameter about twice that of the bubble.

(c) The destruction of the thermal layer due to the replacement of hot fluid from the bulk liquid.

D. MASS TRANSFER MODEL

Recently Bankoff (*53*) has questioned the generally accepted idea that latent heat transport plays a minor role in nucleate boiling heat transfer at a heated surface. If the high heat fluxes found in nucleate boiling are caused only by the bubble stirring action, similar action should be

accomplished by generating inert gas bubbles at the heating surface. However, experiments by Mixon *et al.* (*54*) show that even with high rates of bubble generation, the resulting heat fluxes are in the range of the lower limit of nucleate boiling. Bankoff suggests therefore that the mechanism of latent heat transport is significant for high heat transfer rates, and that it consists of simultaneous evaporation near the base of the bubbles and condensation at the top.

Bankoff and Mason (*55*) have performed experiments to measure the heat transfer coefficients at the surfaces of single steam bubbles in a turbulent stream of subcooled water. Using these results they calculated that the mechanism of latent heat transport could account for the major fraction of the total heat flow in subcooled boiling and that it is, in fact, the dominant process near the critical heat flux.

IV. Critical Heat Flux

The heat flux at which nucleate boiling fails and at which a heating surface becomes partially or entirely blanketed with vapor is of great practical interest to the engineering designer. Furthermore, the mechanism by which this transition occurs is of considerable theoretical interest. Nevertheless, the complexity of the hydrodynamic and thermodynamic processes which occur at very high nucleate boiling rates are such as to have defied even approximate analysis.

Consider again the boiling curve shown in Fig. 2, in which the heat flux variation with the temperature difference Δt is shown. In most of the nucleate boiling regime, columns of discrete bubbles originate from specific nucleation sites, and a relatively large increase in heat flux is provided by a small increase in the surface temperature. As the flux is increased above the value marked "DNB," however, there is an increasing tendency for bubbles to coalesce near the surface. This tendency may be traced not only to the crowding of more vapor columns into the same area as new sites are activated, but also to the increased likelihood of coalescence of successive bubbles from the same nucleation site as the waiting time diminishes.

Boiling at fluxes between DNB (departure from nucleate boiling) and the peak value is characterized by a pronounced two-phase boundary layer near the surface and by oscillating, nonuniform surface temperatures caused by local insulation by patches of vapor. As long as these patches are unstable, however, there is a tendency toward their immediate replacement by liquid, and nucleate boiling continues. Consequently, the stability of vapor-liquid interfaces is an important consideration in most of the successful theoretical work which has been reported. In succeeding sections we shall consider both theoretical analysis and

experimental correlations of the critical heat fluxes which have been observed in pool boiling, flow inside heated channels, and forced convection normal to heated cylinders.

A. POOL BOILING

1. Dimensional Analysis

Kutateladze (*56*) has treated the failure of nucleate boiling as a purely hydrodynamic problem, hypothesizing that the critical flux is reached when the stability of the two-phase boundary layer, characteristic of the region between DNB and critical heat flux, is destroyed. This layer remains stable as long as the kinetic energy of the vapor leaving the heated surface is low enough that the liquid can penetrate the layer and cool the surface. Near the critical flux the vapor and liquid are in such violent agitation that viscous drag is negligible, and the occurrence of instability is equally probable for any part of a sufficiently large surface. Consequently, the critical heat flux should be independent of heater dimensions except for fine wires, for example, when the heater diameter is of the same order as the bubble sizes.

With this model as a basis, Kutateladze nondimensionalized the equations of motion and the equations of dynamic interaction of the vapor and liquid phases and arrived at the single dimensionless group

$$K = \frac{q_c''}{\lambda \rho_v^{1/2}[\sigma g\, g_c(\rho_l - \rho_v)]^{1/4}}$$

The value of K was found by comparison with data from several sources to vary from 0.095 to 0.20 depending on the surface roughness and the liquid-surface combination. Sterman (*57*) derived this same parameter using the principles of similarity.

Borishanskii (*58*) included the effects of viscosity in his dimensional analysis and arrived at two dimensionless groupings, K and N, where K is the same as Kutateladze's parameter and N is expressed as

$$N = \frac{\rho_l (g_c \sigma)^{3/4}}{\mu^2 [g(\rho_l - \rho_v)]^{1/2}}$$

The following functional relationship was found by comparison with data

$$K = 0.13 + 4N^{-0.4} \tag{33}$$

A somewhat simpler semiempirical correlation has been derived by Rohsenow and Griffith (*59*) using vapor binding of the surface as a

criterion for critical heat flux

$$\frac{q_c''}{\rho_v \lambda} = 143 \left(\frac{\rho_l - \rho_v}{\rho_l} \right)^{0.6} \left(\frac{g}{g_0} \right)^{0.25}$$

where the constant coefficient has the units of ft/hr and the gravity ratio was added (*60*) to encompass the data of Usiskin and Siegel (*61*).

2. Stability of a Liquid-Vapor Interface

An idealized hydrodynamic model of vapor-liquid flow conditions at the peak heat flux has been described and analyzed by Zuber *et al.* (*62*, *63*, *64*). Visualize an agglomerate of vapor bubbles over a heating surface which is submerged in a pool of saturated or slightly superheated liquid and which is operating just below the peak flux. Vapor is fed into the agglomerate, chiefly by the capture of additional bubbles from nearby nucleation sites, while one or more jets of vapor flow upward through the liquid and corresponding jets of liquid flow downward.

For purposes of analysis, the main liquid-vapor interface is at first imagined to be horizontal and nearly plane, with insufficient disturbance to overcome surface tension forces and permit the vapor to pass upward into the more dense liquid. This condition of metastable equilibrium is similar to that in the air-water interface below an inverted tumbler of water covered by gauze. In the idealized boiling model, it is hypothesized that such an interface fails by Taylor instability, and that this results in a definite two-dimensional pattern of vapor jets flowing upward and liquid flowing downward.

Since the upward flow rate of vapor increases with heat flux, and since the downward-flowing liquid must compete with the vapor for the available flow area, it is hypothesized in this second phase of the analysis that the critical condition occurs when the relative velocity of the two phases becomes sufficient to prevent further increase of the heat flux. Known as Helmholtz instability, this condition can also be analyzed in terms of the minimum wave length of a disturbance which will result in the destruction of the vertical interface between the counterflowing vapor and liquid. Both the Taylor and the Helmholtz instabilities are discussed by Lamb (*65*) and will be analyzed in the paragraphs to follow.

Let us first consider the Taylor instability, for which we visualize a horizontal liquid-vapor interface in the plane $y = 0$. For potential flow it can be shown that the velocity potentials are given by

$$\Phi_v = Ce^{my} \cos mx \cos \omega\tau, \quad y < 0 \tag{34a}$$

$$\Phi_l = C'e^{-my} \cos mx \cos \omega\tau, \quad y > 0 \tag{34b}$$

where x is measured in the plane of the interface. These potentials are

solutions of Laplace's equation and satisfy the conditions for simple harmonic deformations of the interface which damp out far from the interface. The corresponding perturbations at $y = 0$ are given by

$$\epsilon = a \cos mx \sin \omega\tau \tag{35}$$

Kinematic conditions which must be satisfied at the interface are

$$\frac{\partial \epsilon}{\partial \tau} = -\frac{\partial \Phi_l}{\partial y} = -\frac{\partial \Phi_v}{\partial y} \tag{36}$$

while a force balance there yields the static relationship

$$p_v - p_l + \sigma \frac{\partial^2 \epsilon}{\partial x^2} = 0 \tag{37}$$

Euler's equation must be satisfied in the liquid and the vapor:

$$g_c \frac{p_v}{\rho_v} = \frac{\partial \Phi_v}{\partial \tau} + g_c Y y - \frac{V_v^2}{2} \tag{38a}$$

$$g_c \frac{p_l}{\rho_l} = \frac{\partial \Phi_l}{\partial \tau} + g_c Y y - \frac{V_l^2}{2} \tag{38b}$$

If the velocity effects are assumed to be small and the body force per unit mass, Y, is set equal to $-g/g_c$, Eqs. (34) through (38) will yield the frequency

$$\omega = \left(\frac{\sigma m^3 g_c}{\rho_l + \rho_v} - \frac{\rho_l - \rho_v}{\rho_l + \rho_v} g m \right)^{1/2} \tag{39}$$

The wave number m is related to the wave length L by

$$L = 2\pi/m \tag{40}$$

The criterion for a stable interface is that ω must be real, since otherwise a disturbance would grow exponentially with time. Therefore the critical wave length is found by setting $\omega = 0$ in Eq. (39) and is given by

$$L_{01} = 2\pi \sqrt{\frac{\sigma g_c}{(\rho_l - \rho_v) g}} \tag{41}$$

The wave length which would give the maximum growth rate is found by maximizing ω with respect to m and is

$$L_{02} = 2\pi \sqrt{\frac{3\sigma g_c}{(\rho_l - \rho_v) g}} \tag{42}$$

Zuber *et al.* term this the most dangerous wave length and assume that there is a spectrum of probable unstable values given by L_0, where

$$L_{01} \leq L_0 \leq L_{02} \tag{43}$$

Because of Taylor instability, therefore, it is postulated that the horizontal liquid-over-vapor interface tends to break up in a square, two-dimensional pattern of side length L_0. From each unit cell of area L_0^2 rises a circular vapor column of diameter $L_0/2$ or of area $\pi L_0^2/16$. This choice of diameter, while somewhat arbitrary, is not unreasonable, since it represents the distance between the inflection points of a two-dimensional sinusoidal disturbance of wave length L_0. Furthermore, this wave length is now seen to be dependent only on the fluid properties (Eqs. (41) and (42)), which are constant at a given pressure for saturated boiling. Consequently, the vapor generation rate at the critical flux, which is limited by the Helmholtz instability condition, will depend only on the maximum permissible frequency of bubble emission, which will next be considered.

Visualize now a plane vertical interface at $y = 0$ (note the previous x, y coordinates have been rotated 90°), which is a considerably simplified representation of the flow pattern already described. Let us again use potential theory, after Lamb (*65*), to find the minimum frequency of a disturbance which will grow with time. If the liquid and vapor velocities away from $y = 0$ are V_l and V_v, the velocity potentials are

$$\Phi_v = -V_v x + \Phi_{1v}, \quad y < 0 \tag{44a}$$

$$\Phi_l = V_l x + \Phi_{1l}, \quad y > 0 \tag{44b}$$

where

$$\Phi_{1v} = Ce^{my+i(\omega\tau-mx)}$$

$$\Phi_{1l} = C'e^{-my+i(\omega\tau-mx)}$$

Corresponding perturbations at the interface are given by

$$\epsilon = ae^{i(\omega\tau-mx)} \tag{45}$$

Kinematic conditions which must be satisfied at $y = 0$ are

$$-\frac{\partial\Phi_v}{\partial y} = \frac{\partial\epsilon}{\partial\tau} + V_v\frac{\partial\epsilon}{\partial x} \tag{46a}$$

$$-\frac{\partial\Phi_l}{\partial y} = \frac{\partial\epsilon}{\partial\tau} - V_l\frac{\partial\epsilon}{\partial x} \tag{46b}$$

Since there are no body forces in the y direction, Eqs. (38) become, with the omission of second order terms,

$$g_c\frac{p_v}{\rho_v} = \frac{\partial\Phi_{1v}}{\partial\tau} + V_v\frac{\partial\Phi_{1v}}{\partial x} \tag{47a}$$

$$g_c\frac{p_l}{\rho_l} = \frac{\partial\Phi_{1l}}{\partial\tau} - V_l\frac{\partial\Phi_{1l}}{\partial x} \tag{47b}$$

Solving Eqs. (37) and (44) through (47) at $y = 0$ yields the expression for the frequency of a disturbance at the interface in terms of the wave number m:

$$\omega = \frac{m(\rho_v V_v - \rho_l V_l)}{(\rho_v + \rho_l)} \pm \left[\frac{g_c \sigma m^3}{(\rho_v + \rho_l)} - \frac{m^2 \rho_v \rho_l (V_v + V_l)^2}{(\rho_v + \rho_l)^2} \right]^{1/2}$$

The condition of stability of the interface is that ω must be real, so the critical condition is

$$\frac{g_c \sigma m^3}{\rho_v + \rho_l} - \frac{m^2 \rho_v \rho_l (V_v + V_l)^2}{(\rho_v + \rho_l)^2} = 0 \tag{48}$$

For the square matrix of vapor columns described earlier, the equation of continuity requires that

$$V_l = \frac{\rho_v V_v}{\rho_l} \frac{A_v}{A_l} = \frac{\rho_v V_v}{\rho_l} \frac{\pi}{(16 - \pi)} \tag{49}$$

Equations (48) and (49) may be solved for the critical vapor velocity

$$V_v = \left(\frac{g_c \sigma m}{\rho_v} \right)^{1/2} \left[\frac{\rho_l (16 - \pi)}{\rho_l (16 - \pi) + \rho_v \pi} \right] \left(\frac{\rho_l + \rho_v}{\rho_l} \right)^{1/2} \tag{50}$$

The product of the last two terms is approximately equal to 1 over the entire pressure range of interest, and these two terms are therefore omitted hereafter from the expression for critical vapor velocity.

Rayleigh's analysis (*66*) of a circular gas jet in a liquid shows that axially symmetric disturbances with wave lengths larger than the circumference of the jet are unstable for all vapor velocities. From Eq. (40) and the assumed jet diameter of $L_0/2$, therefore, we find the wave number, m, to be $4/L_0$, and the critical vapor velocity from Eq. (50) becomes

$$V_v = \sqrt{4 \sigma g_c / \rho_v L_0}$$

The heat flux carried by the vapor in saturated boiling is

$$q'' = \rho_v \lambda A_v V_v / A = \pi \rho_v \lambda V_v / 16$$

Thus, with the spectrum of possible wave lengths given by Eq. (43), the critical heat flux is determined within the limits

$$0.16 \geq \frac{q_c''}{\lambda \rho_v^{1/2} [\sigma g g_c (\rho_l - \rho_v)]^{1/4}} \geq 0.12 \tag{51}$$

This dimensionless group is identical to Kutateladze's parameter K, and the agreement of the range of constants with those found experimentally by Kutateladze is very good. Furthermore, this model and the analysis lead one to expect the critical heat flux to span an uncertainty band,

approximately $\pm 14\%$ with the assumptions just reported. Consequently, the well-known lack of reproducibility of experimental burnout data may well be inherent in the process rather than a sign of inadequate control over the variables (*63*).

Figure 22 shows the variation of K with N as reported by Borishanskii (*58*) for water and 5 organic fluids. In addition to the best-fit curve

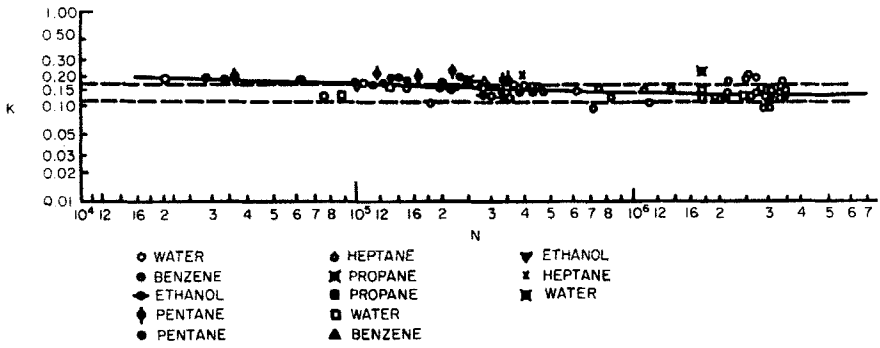

FIG. 22. Correlation of critical heat flux data for various liquids in pool boiling. The solid line is the best fit curve (*58*) represented by Eq. (33) and the range of K predicted by Eq. (51) is shown by the broken lines (*64*).

represented by Eq. (33), the range of K predicted by Eq. (51) is shown by the broken lines. Since some of the assumptions in the analysis are somewhat questionable, this close agreement may be fortuitous, but this model appears nevertheless to represent quite well the general features of the critical heat flux phenomenon in pool boiling.

3. *Pool Boiling Experiments*

Experimental data for the peak flux in pool boiling exhibit wide scatter, even when taken under apparently similar conditions. This may be traced, at least in part, to variations in surface conditions of the heaters, especially for constant heat flux systems. If the heater surface is rough, nucleation sites are plentiful and the boiling process is even and regular. However, if the surface is smooth, high superheat is required to nucleate a bubble, and when a bubble finally does form, a relatively large quantity of the highly superheated liquid can vaporize almost instantaneously (the familiar "bumping" which occurs when liquid boils in a clean glass container) and blanket a local region of the surface with vapor. Since the energy generation rate is a constant the surface may overheat locally and the vapor blanket spread. In a constant temperature system, on the other hand, the surface will recover, since the localized vapor blanket

cannot produce a temperature excursion. Bonilla and Perry (*67*), Kutateladze (*56*), and others have found that surface conditions significantly affect the critical flux in a constant heat flux system, while Berenson's experiments (*68*) show that it is relatively unimportant for constant temperature heaters.

The critical heat flux in pool boiling varies considerably with pressure, tending toward zero both as the pressure approaches zero and as it approaches the thermodynamic critical point, as both Cichelli and Bonilla (*69*) and Kazakova (*70*) have reported. A maximum value occurs at about $\frac{1}{3}$ the critical pressure for water and for several organic liquids. Addoms (*48*) also investigated critical heat flux from platinum wires in boiling water over a wide range of pressures. He found that the peak in the curve of critical heat flux versus pressure occurred at approximately $\frac{1}{2}$ the critical pressure for small diameter wires ($\leq$0.024 inch).

With the advent of space travel and the possibility of using boiling liquids to cool various components of space vehicles, there has been considerable interest recently in the effects of gravity on the boiling process. Usiskin and Siegel (*61*) have investigated critical heat flux in reduced and zero gravity fields using a free-fall apparatus. Although the transients involved in their experimental procedure make the data somewhat difficult to interpret, the $g^{1/4}$ variation of critical flux predicted by Kutateladze (*56*) and Zuber *et al.* (*62*, *63*, *64*) appears to be reasonable.

Costello and Adams (*71*) have investigated the critical flux from a cylindrical heater placed in a centrifuge, with accelerations up to 44 times earth's gravity directed normal to the axis of the cylinder. They found that the critical flux increases slightly with acceleration up to $g/g_0 = 10$, and for higher accelerations varies approximately as $g^{1/4}$. Their experiments indicate, however, that there is a heater size effect, and for larger diameter cylinders higher accelerations would be required to attain the $g^{1/4}$ behavior.

Ivey (*72*) has determined the critical flux in pool boiling in the range $1 < g/g_0 < 160$. His experiments show that the critical flux varies as $g^{0.273}$, which is in reasonably good agreement with the predicted $g^{1/4}$ variation.

Several papers on the critical heat flux in binary mixtures of water and organic liquids have been presented by van Wijk, von Stralen and Vos (*73*, *74*, *75*, *76*, *77*), and by Fastovskii and Artym (*78*). They found that the critical flux with small diameter wires (<0.4 mm) increases with concentration of the organic component to a maximum value and then decreases. In some cases the maximum value was several times the critical flux attained with either pure component. Owens (*79*) has conducted a similar investigation using a $\frac{3}{16}$-inch diameter tube and found that the

addition of organic liquids to water tended to decrease rather than increase the critical flux. Each of these investigators observed that the size of the vapor bubbles was much smaller in the binary mixtures than in either pure component, as did Leppert, Costello and Hoglund (*4*) in forced convection boiling. Although this phenomenon is not clearly understood, it appears that the increase in critical heat flux for small diameter wires in binary mixtures may arise from the fact that in the pure component a relatively large vapor bubble can completely surround the heater and blanket it locally. In the binary mixtures the small bubbles do not lead to this local blanketing and a higher critical heat flux can be attained.

B. INTERNAL FLOW

1. Flow Patterns

Tippets has recently presented the results of a study of critical heat fluxes and flow patterns for high-pressure, steam-water mixtures in heated rectangular channels (*80*, *81*). Photographic observations were made with a high speed moving picture camera sighting across channels of either 0.25- or 0.50-inch thickness which were 2.10 inches in width and 37 inches long. Simultaneous records of power and coolant flow rate were made on an oscillograph, while the critical flux was determined by means of a "burnout detector" which compared the electrical resistance of two 4¼-inches-long sections at the outlet of the heated channel. Since the resistance of the heater element increased with temperature, a tendency toward overheating at the exit could be detected by an imbalance in the resistances of these sections.

Tippets reported the following visual characteristics of the flow at 1000 psia for flow rates of 50 to 400 lb/(sec) (sq ft) and for fluid states at the observation window from 170 Btu/lb subcooled to saturated boiling at a maximum quality of 0.66.

(a) For subcooling greater than 20 Btu/lb, flow rates from 100 to 400 lb/(sec)(sq ft) and heat flux much less than critical, an irregular, frothy layer of growing and collapsing bubbles was observed to slide along the heated surface at a velocity slightly less than the mean channel velocity. Away from the heated surface, the flow was nearly pure liquid.

(b) For low subcooling (up to 20 Btu/lb) and flow rates from 200 to 400 lb/(sec)(sq ft), and for saturated boiling at low qualities (up to 0.10) and a flow rate of 100 lb/(sec)(sq ft), heat fluxes below the critical value produced a frothy mixture of large and small bubbles in a continuous liquid phase. Next to the heated surface was a highly agitated layer of tiny bubbles in liquid, while at a flow of 100 lb/(sec)(sq ft) there were

slight fluctuations in the pattern which suggested a tendency toward slug flow.

(c) At somewhat higher qualities (0.10 to 0.30) and low flow rates (below 100 lb/(sec)(sq ft)), a slug flow pattern developed. This appeared to consist of a finely divided froth of vapor and liquid alternating periodically (0.05 to 0.10 sec) with a thick layer of liquid against the wall and high vapor concentration in the middle of the channel. This pattern was not observed at the higher mass velocities, and it became indistinct and disappeared at the higher qualities even at lower flow rates.

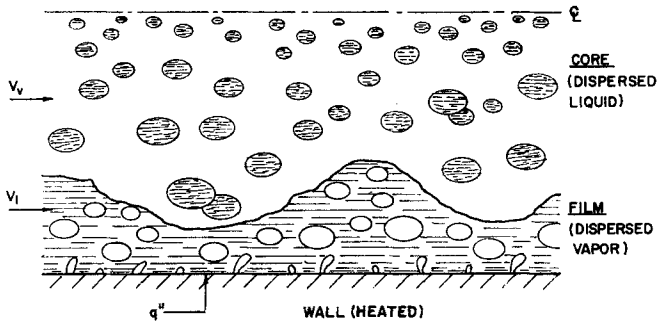

FIG. 23. Simplified representation of flow pattern observed by Tippets (*82*) for saturated boiling in a rectangular channel.

(d) The predominant flow pattern which occurred at all the observed critical flux conditions consisted of an irregular, wavy liquid film along the walls, flowing with the stream, and a dispersion of liquid droplets in a continuous vapor core, or, at the lower qualities, a vapor-liquid emulsion in the core. The liquid film was considerably more agitated at the heated surfaces than at unheated surfaces, with irregular streamers of vapor or bubbles forming at the heater and issuing into the liquid film. This flow pattern was also observed at fluxes less than critical for a flow rate of 400 lb/(sec)(sq ft) at all qualities; for 200 to 400 lb/(sec)(sq ft) at qualities above 0.10; and for 50 to 200 lb/(sec)(sq ft) at qualities above 0.30. Figure 23 is a simplified representation of this flow pattern.

2. General Trends in Saturated Boiling

From his own observations with water at 1000 psia, as well as from those of other investigators who measured the critical flux with high pressure water in forced convection, Tippets presented a summary of major trends:

(a) q_c'' decreases with increasing mass velocity for bulk boiling and increases with increasing mass velocity for subcooled boiling.

(b) q_c'' decreases monotonically with increased steam quality or specific enthalpy for stable, steady flow and may have a maximum with respect to steam quality in conditions of bulk boiling if the flow is unsteady or oscillating.

(c) q_c'' decreases monotonically as pressure is increased above about 600 psia.

(d) q_c'' increases slightly as the characteristic duct size b (the radius of a circular tube, ¼ the hydraulic diameter for annuli and rectangular ducts) increases from 0.024 to 0.084 inch then decreases as the duct size increases further to 0.24 inch.

(e) q_c'' is virtually independent of duct length-to-diameter ratio for ratios greater than about 100, but increases for ducts shorter than this.

(f) q_c'' increases with increasing ratio of heated surface to total surface.

3. Analysis

From the flow pattern which he observed at the critical flux condition, depicted in Fig. 23, Tippets constructed a simplified flow model which could be analyzed (*80*, *82*). The first element in this analysis consists of a potential flow solution to find the maximum liquid film thickness which can remain stable with the dynamic force of the vapor acting against the stabilizing effect of surface tension in the liquid (Helmholtz instability). A critical wave length L_c is thereby obtained which represents the limit beyond which small disturbances will grow exponentially with time. This wave length is

$$L_c = \frac{2\pi\sigma}{\rho_v V_{vl}^2}\left[\coth\,(ml'') + \frac{\rho_v}{\rho_l}\tanh\,(m\delta)\right]$$

where V_{vl} is the effective core to film relative velocity, m is the wave number, δ is the mean thickness of the liquid film and l'' is the half-width of the zone of influence at the interface. Figure 24 shows the idealized system used for this analysis.

In the next step of the analysis, Prandtl's mixing length theory is used to relate l'' to δ and to evaluate the relative velocity V_{vl}. This term is then eliminated through the introduction of the parameter Φ_{TPF} from the two-phase flow correlations of Martinelli *et al.* (*83*) to obtain an equation for the liquid film thickness

$$\delta = \frac{2K_3K_4\sigma\rho_l(1 + \rho_l/\rho_v)}{\Phi_{TPF}f_fG^2(1 + \sqrt{\rho_l/\rho_v})^2}; \qquad 2\pi \leq K_3 \leq 3\pi \tag{52}$$

In this equation, K_3 lies between 2π, for the critical wave length, and 3π, for the wave length of the disturbance with maximum growth rate

(cf. Section IV,A,2). The quantity K_4 is an unknown dimensionless constant and f_f is the Fanning friction factor.

In Tippets' model, therefore, the liquid film thickness varies around the mean value given by Eq. (52) as liquid is exchanged between the film and the vapor core. When the film tends to thicken, unstable disturbances grow more rapidly and increase the liquid entrainment, thereby reducing the film thickness. When the film is thinner than δ, the entrainment diminishes and liquid capture by the interface from the core dominates, thereby increasing the film thickness.

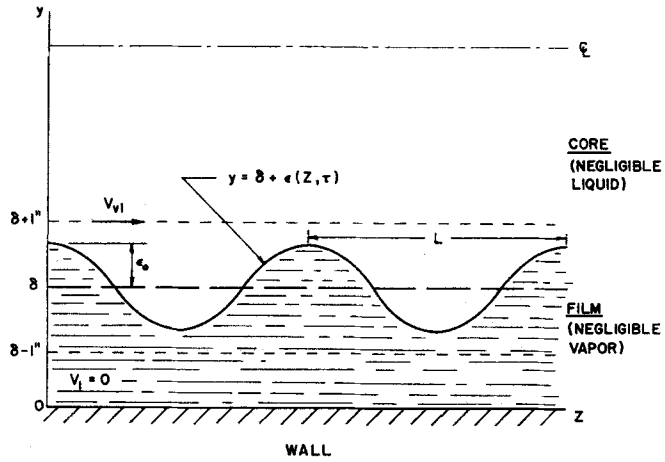

FIG. 24. Idealized system for film stability analysis of critical heat flux (*82*).

The onset of the critical condition is supposed to occur when the liquid vaporization rate in the film exceeds the net liquid supply rate from the core. If all of the heat transferred from the wall is used to vaporize liquid in the film, the net liquid supply rate to the film must be q''/λ at steady state ($q'' < q_c''$). According to Tippets, this liquid flux consists of three components: turbulent diffusion from the core to the interface; liquid carried from the interface region to the core by the vapor current; and entrainment, the liquid torn from the interface by the vapor when the film is unstable. Only the first of these is a supply term, while the last is assumed to be negligible when the critical condition is approached, since the film is then thin and, therefore, stable.

The two liquid diffusion terms are evaluated from mixing length theory, while the average velocity of the vapor near the interface is calculated from a power-law variation, in analogy to single-phase flow. The results

of these calculations give the following working equation for the critical flux:

$$q_c'' = C''\psi^a/\xi \tag{53}$$

where

$$\psi = \frac{\sigma\rho_l(1 + \rho_l/\rho_v)}{\Phi_{TPF}f_f G^2 b(1 + \rho_l/\rho_v)^2}$$

$$\xi = \frac{1 + \left(1 + \dfrac{C'X_e}{1 - X_e}\right)\dfrac{\rho_l}{\rho_v}}{(\rho_l\Phi_{TPF}f_f/\rho_v)^{1/2}G\lambda}$$

The coefficients C', C'' and a are determined by fitting Eq. (53) to experimental data, while b is the characteristic channel dimension mentioned earlier (the radius of a circular tube, ¼ the hydraulic diameter for annuli and rectangular ducts). Reasonably good correlation of a wide range of data was found with

$$a = 0.75$$

$$C' = 1.00 \text{ (fraction of channel heated, 0.80 to 1.0)}$$

$$= 6.5 \text{ (fraction of channel heated, 0.23 to 0.40)}$$

$$C'' = 0.53 \ (b > b_0 = 0.084 \text{ inch})$$

$$= 0.53 \ (b/b_0)^{0.9} (b < b_0 = 0.084 \text{ inch})$$

4. Comparison with Experimental Data

Tippets (*80, 82*) has applied Eq. (53) to 80 of his own data points and to 742 selected experimental points by other investigators. These data were selected, whenever possible, on the basis that the critical heat flux had actually been experienced or else that the detector mentioned earlier had tripped, indicating a marked tendency toward overheating at the end of the channel. Since the region between DNB and the critical flux is characterized by temperature fluctuations which increase in amplitude as the flux is increased, it can be said with certainty that the detector will operate somewhere in this region, but not that it will trip precisely at the peak flux.

Figure 25 shows the variation of the critical flux with quality for various flow rates, heater element widths and thicknesses, and channel equivalent diameters for Tippets' data. Similarly good agreement was found with the measurements of Janssen and Kervinen (*84*) which were taken in an annular duct with the inner walls heated. In this case, however, the coefficient C' in Eq. (53) had a value of 6.5. The data of Aladyev *et al.* (*85*) for flow in a circular tube were well correlated, but the coefficient C'' had to be adjusted to 0.74. Tippets suggests the small length-to-diameter ratio (twenty) of the heated tube as the cause of this adjustment.

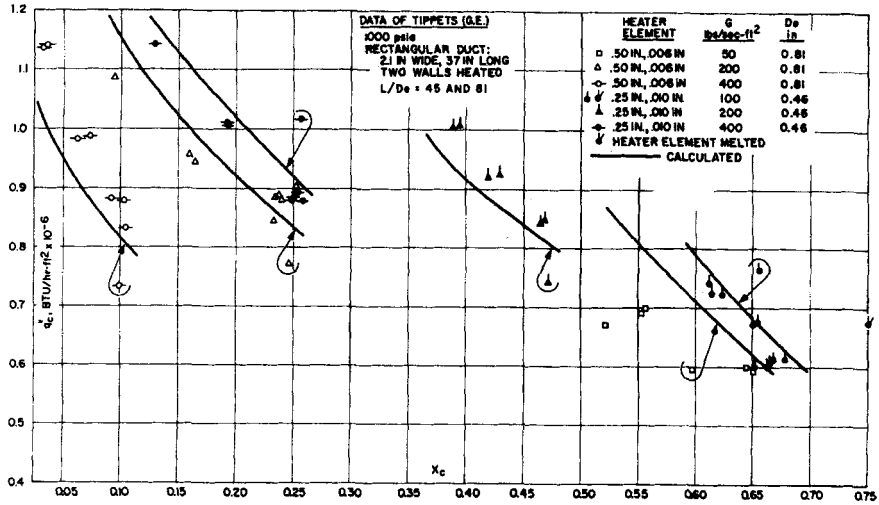

FIG. 25. Comparison of film stability analysis, Eq. (53), with critical heat flux data for water (*82*).

Some of the data of DeBartoli *et al.* (*86*); Bennett *et al.* (*87*); Silvestri (*88*); and Berkowitz *et al.* (*89*) are not as well correlated by Eq. (53), even when the coefficients C' and C'' are determined from the data itself. Some of the deviation may be caused by the fact that two-phase mixtures rather than pure liquids entered the heated channels in some of the latter tests. This might inhibit the attachment of the liquid film to the wall and result in lower peak fluxes (*80*, *82*).

C. EXTERNAL FLOW

1. Flow Patterns

Vliet and Leppert (*90*, *91*) have described the flow conditions for the nucleate boiling of water at atmospheric pressure flowing normal to an electrically heated tube. Figure 26 shows schematically a uniformly heated cylinder with nearly saturated water flowing upward around it. Nucleation starts first on the rear half of the cylinder at seemingly random locations. As the heat flux is increased the density of sites increases and becomes more uniform, and nucleation spreads to the forward half of the cylinder. Bubbles thus initiated on the forward half grow and move around the cylinder as a result of liquid drag and buoyant effects. They then separate individually from the cylinder somewhere downstream of the 90° position, as shown in Fig. 26a. The bubbles tend to grow momentarily while in the superheated liquid near the cylinder, but soon collapse if the liquid above is even slightly subcooled.

With still further increase in the heat flux, the percentage of vapor in the two-phase mixture in the cylinder wake increases to the point that a vapor cavity forms in this region. Initially, the cavity is not continuous along the length of the cylinder, but is broken by liquid which extends down to the cylinder at intervals along its length, as sketched

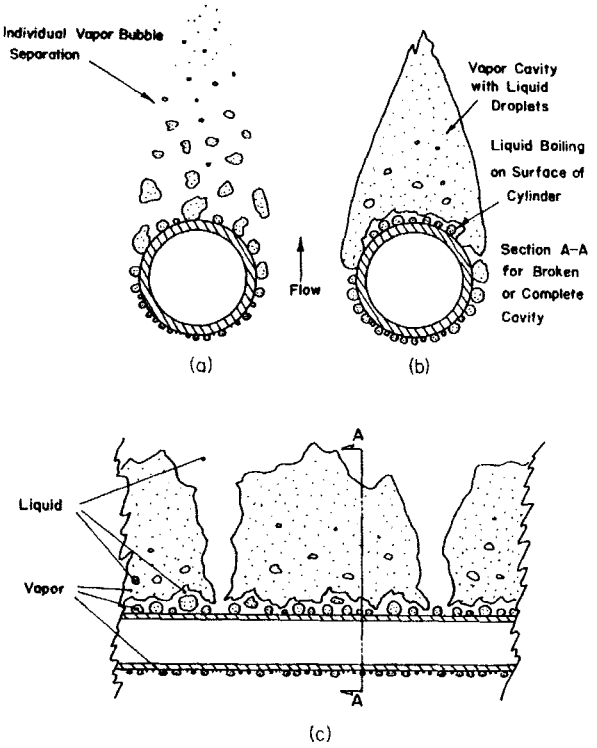

FIG. 26. Schematic diagrams of boiling pattern for nearly saturated water flowing normal to a heated cylinder (*90*). (a) Low heat flux. (b) High heat flux. (c) Broken cavity formation.

in Figs. 26b and 26c. The transition from individual bubble separation to this type of cavity formation takes place gradually. Even though a vapor cavity exists in the wake, liquid continues to be supplied to the back of the cylinder. This liquid apparently flows through the breaks in the cavity and between the bubbles as they move around the cylinder.

The reason for the formation of the cavity may be more fully understood from the following reasoning. For single phase flow about bodies of this type, a separated region (backflow of the fluid) can occur where the fluid encounters a positive pressure gradient which arises from decel-

eration of the flow. For a cylinder, this position varies between 70 and 120° from the forward stagnation point, depending on the cylinder Reynolds number. For nucleate boiling at low heat fluxes, the amount of vapor in the cylinder wake is insufficient to allow the liquid to move past the cylinder without decelerating or causing a backflow region to

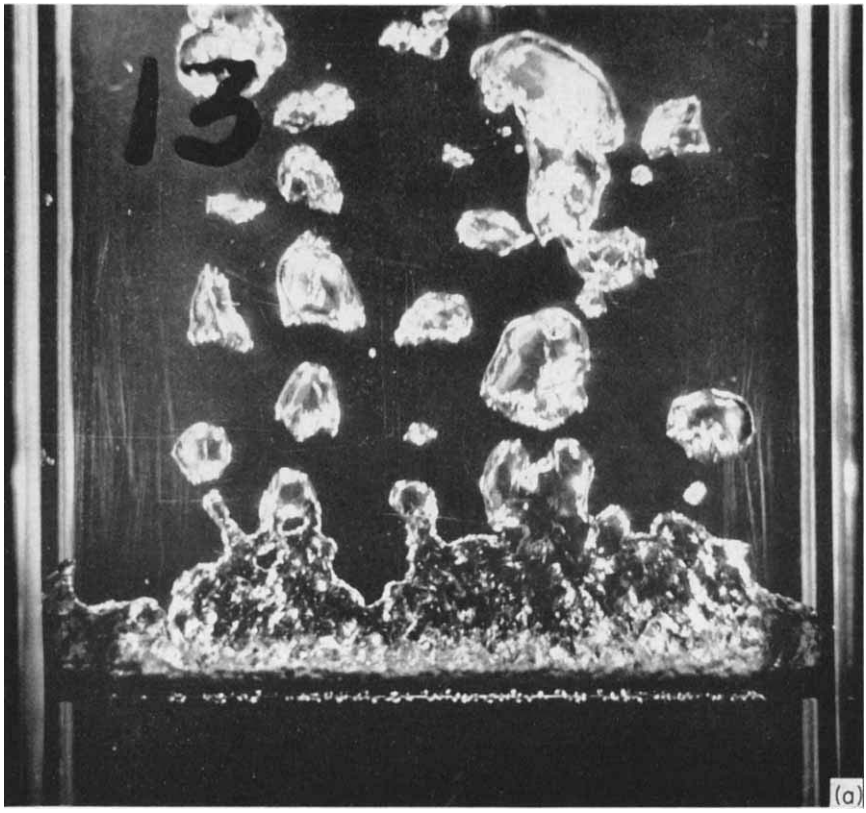

FIG. 27. (a) (For descriptive legend see page 249)

form. However, as the heat flux increases, a condition arises where the amount of vapor is sufficient to allow the liquid to continue in a direction tangential to the 90° position, leaving a separated region of vapor which is similar to the separated region of single phase flow.

There is a further reason for the formation of the cavity. If the liquid-vapor mixture tends to follow the surface, as on the front half, a centrifugal force, arising from the inward centripetal acceleration, is created which acts radially outward on the mixture. Because of the difference

in densities between liquid and vapor, there is a separating tendency which is analogous to the buoyant force of gravity. Near the 90° position the effect is accentuated somewhat by the higher velocity demanded by potential flow. Thus, as the mixture passes the 90° position, the vapor

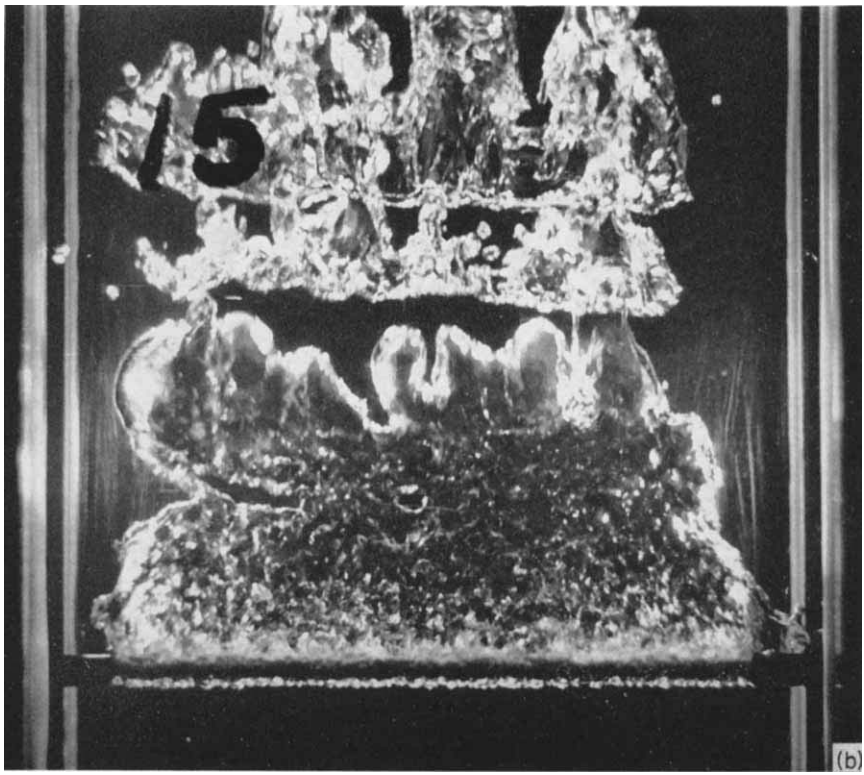

FIG. 27. (b) (For descriptive legend see page 249)

tends to move into the wake region, and the liquid tends to continue in a tangential direction—upward, in this case.

At these heat fluxes the rate of formation of vapor is apparently insufficient to maintain the liquid walls uniformly along the length of the cylinder, and there are intervals where the vapor is pinched off by liquid which therefore extends down to the cylinder. Since all the vapor which is formed either condenses at the cavity walls or leaves as the cavity breaks up above the cylinder, the area of the cavity exposed to the liquid increases as the heat flux increases and the breaks in the cavity become less well-defined. Once the liquid no longer extends down

to the cylinder, the only liquid which enters the cavity is that slower-moving liquid which exists between the vapor bubbles and the heater surface as the bubbles enter the cavity near the 90° position. The rear half of the cylinder is cooled by boiling of this liquid which is in contact

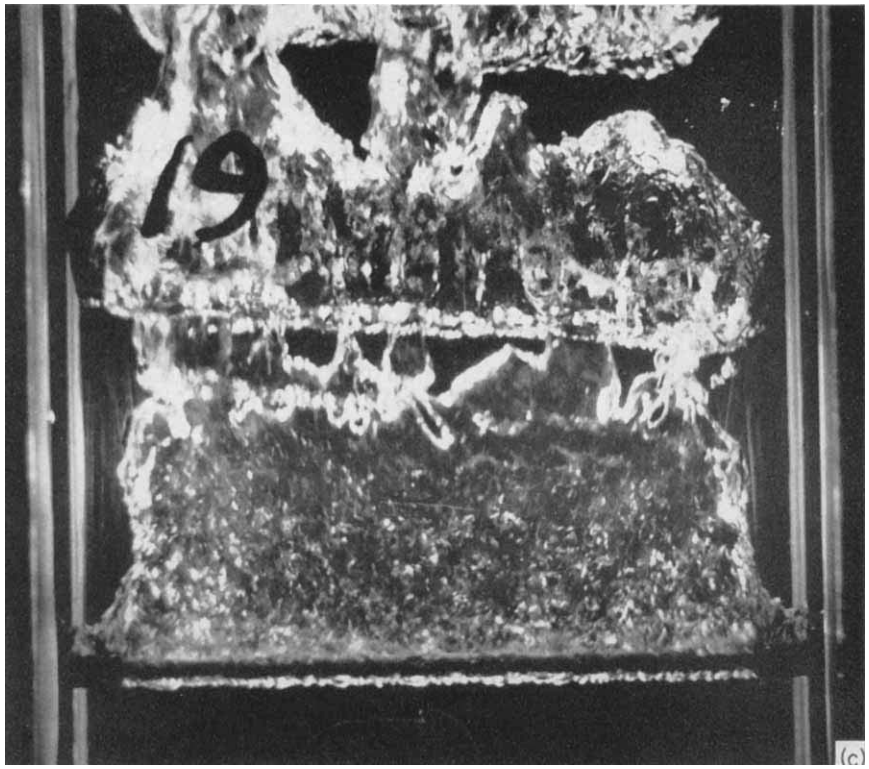

FIG. 27. Effect of heat flux on the boiling pattern of nearly saturated water (4° F subcooling) from a $\frac{3}{16}$-inch tube at 2 ft/sec (*90*). (a) 21% of critical flux. (b) 47% of critical flux. (c) 84% of critical flux.

with it. For heat fluxes below the critical value, more liquid than necessary is carried into the cavity and the excess is lost by entrainment at the cavity walls. Liquid droplets, thrown off by the violent boiling of the liquid on the rear heater surface and from the upward-moving liquid walls, are observed throughout the cavity.

For still further increases in heat flux, there is an abrupt increase in the length of the cavity which results in a very uniform vapor sheet formation. The cavity wall interfaces exhibit criss-cross wave patterns, the angles of which vary with liquid velocity. These angles apparently

depend upon the relative magnitudes of the local liquid velocity and the velocity of propagation of surface waves caused by bubble growth. The shape of the cavity is similar to that illustrated in Fig. 26b for the broken cavity, but it is considerably longer.

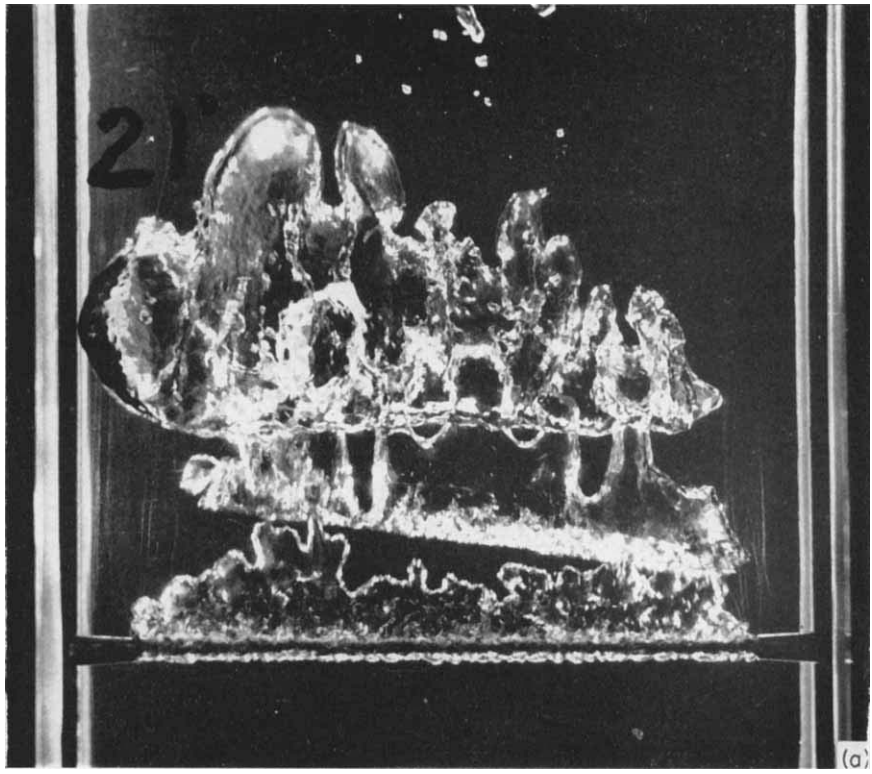

FIG. 28. (a) (For descriptive legend see page 252)

Greater heat flux causes no significant change except for a decrease in the number and size of liquid droplets in the cavity and the amount of liquid on the heated surface. This decrease in the amount of liquid in the region bounded by the cavity walls and the heater is evidence of decrease in the excess liquid carried into the region. Increase in the heat flux causes less liquid to be carried into the cavity because of more closely packed bubbles at the position of separation, while simultaneously requiring more liquid for cooling the rear half of the cylinder. Soon the flux increases to the point where the liquid carried in is insufficient to produce the necessary cooling of the top half of the cylinder. The critical

condition has therefore been reached, starting at the top of the cylinder and, since the surface is electrically heated, rapidly overheating the entire cross section. Once the cavity is formed, so that liquid can enter only along the heated surface, the critical condition is well defined,

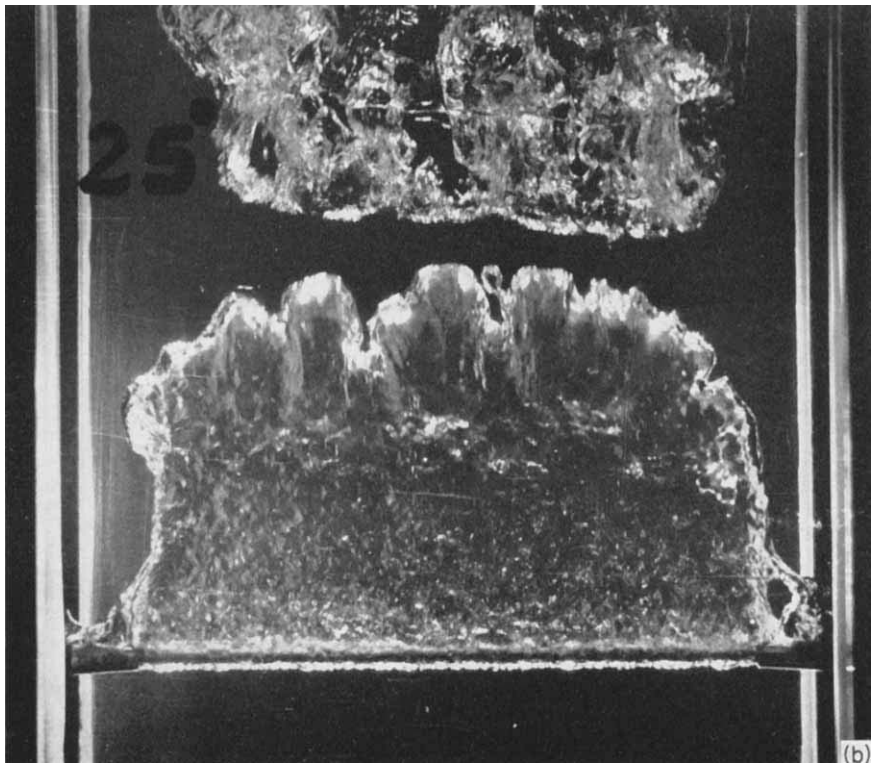

FIG. 28. (b) (For descriptive legend see page 252)

because more liquid is required to produce the necessary cooling on top, but less enters because of the more closely packed vapor bubbles.

Therefore, two factors should govern the magnitude of the critical heat flux for low subcooling: the area per unit length of the rear half of the cylinder and the amount of liquid carried into the cavity along its surface. The first factor is essentially a function only of the cylinder diameter, whereas the second is a function of the diameter, liquid velocity and liquid and vapor thermal properties.

Figure 27 shows a series of photographs indicating the effect on the boiling pattern of increasing heat flux for water with 4° F subcooling

flowing at 2.3 ft/sec. The broken cavity formation is disappearing at 0.21 q_c'' (first photograph) and the last two pictures indicate little effect on cavity shape for $q'' > 0.5\ q_c''$. Figure 28 is a series of photographs near the critical heat flux showing the effect of velocity on the boiling pattern for nearly saturated boiling.

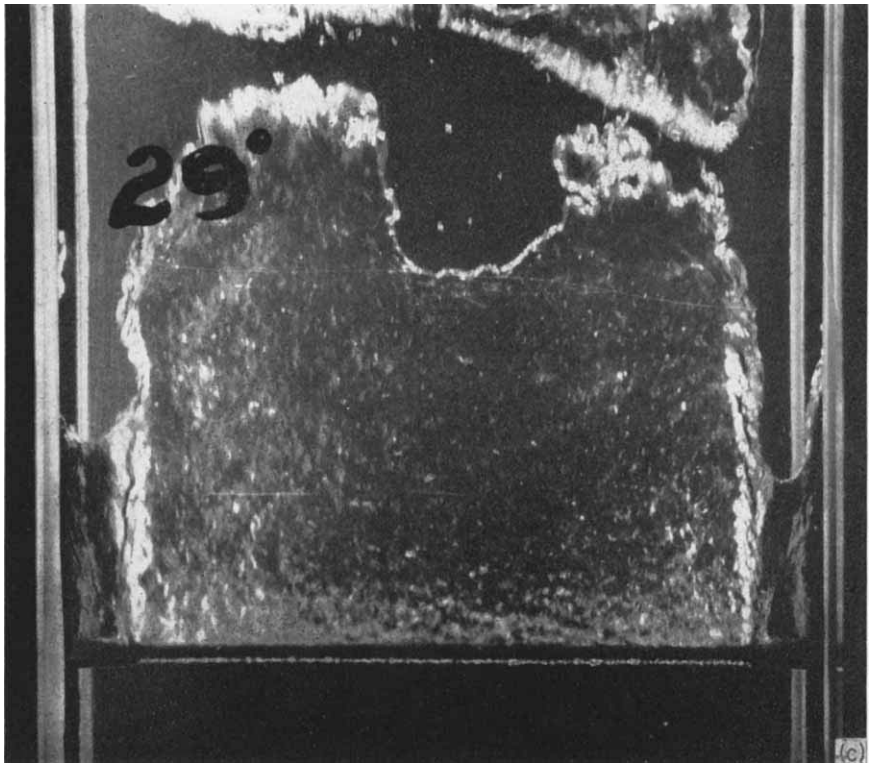

FIG. 28. Effect of velocity on the boiling pattern of nearly saturated water (4° F subcooling) from a ⅛-inch tube at 90% of critical flux. (a) 1.2 ft/sec. (b) 2.4 ft/sec. (c) 4.7 ft/sec.

Observation of the two-phase flow pattern with subcooled boiling at atmospheric pressure (*91*) indicates that the mechanism of failure when the subcooling is approximately 30° F or less is similar to that for saturated boiling. A definite vapor cavity is again formed in the wake of the cylinder when the heat flux is large, and the liquid which cools the rear half of the cylinder enters the cavity between the vapor bubbles in the two-phase boundary layer.

For subcooling greater than about 30° F there is insufficient vapor to form such a cavity because of the rapid condensation which occurs. The two-phase boundary layer on the rear half of the cylinder which is now bounded by liquid rather than vapor, continues around the periphery of the cylinder nearly to the 180° position. An irregular and

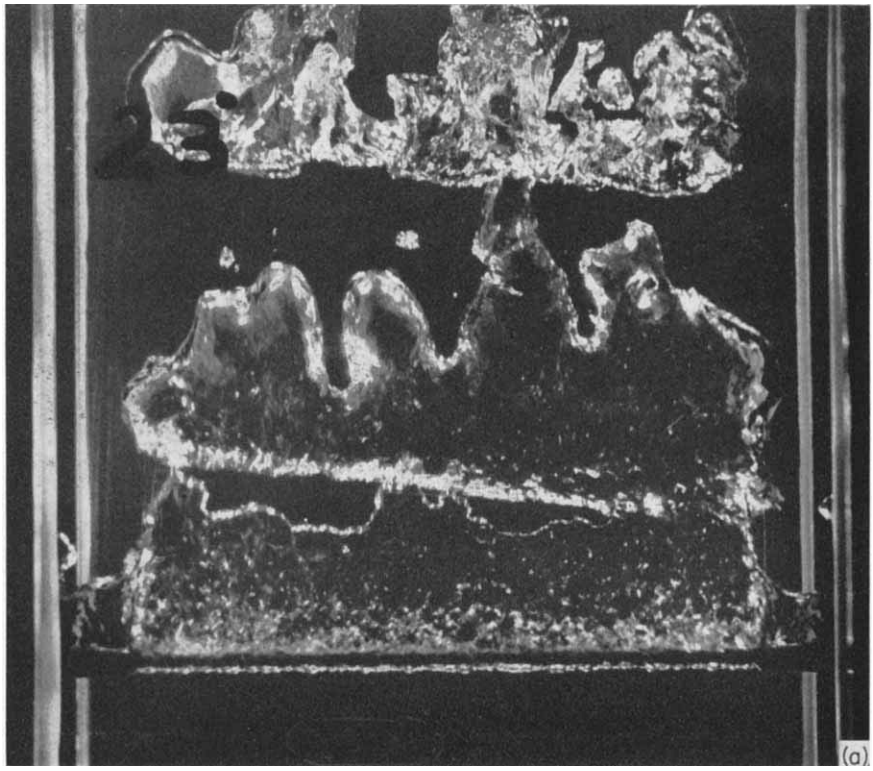

FIG. 29. (a) (For descriptive legend see page 256)

unstable accumulation of vapor in this region leads to the interruption of nucleate boiling. The mechanism of failure is probably similar to the low subcooling case except that the region occupied by vapor is smaller, less well-defined, and appears to be time-variant.

Figure 29 presents a series of photographs which illustrates the effect of increased subcooling on the boiling pattern at a liquid velocity of 2 ft/sec. The vapor cavity clearly exists up to 20° F subcooling, while at 30° F it has almost disappeared. At 50° F subcooling the pattern is reduced to an irregular accumulation of vapor near the 180° position.

2. Analysis

A simplified physical model has been proposed (*90*) of the mechanism of failure of nucleate boiling when a vapor cavity exists behind a cylinder, e.g., when the subcooling of water at atmospheric pressure is less than

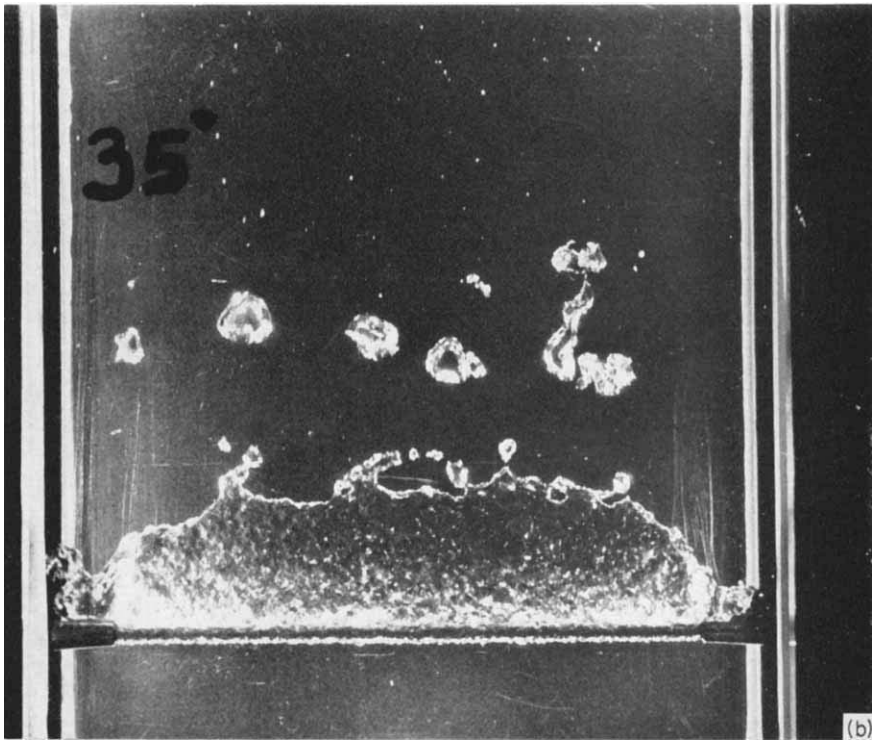

FIG. 29. (b) (For descriptive legend see page 256)

about 30° F. Shown schematically in Fig. 30, this model assumes that the nucleate boiling crisis is caused by a deficiency of liquid entering the cavity between vapor bubbles at the angle θ_s from stagnation. If the liquid enters the cavity at saturation temperature and all of it is vaporized in cooling the top of the cylinder, the critical heat flux is

$$q_c'' = \frac{W_l \lambda \rho_l}{D(\pi - \theta_s)} \tag{54}$$

where W_l is the volumetric inflow of liquid per unit length of cylinder. The analysis consists largely of evaluating this liquid flow rate into the cavity.

The liquid which enters the cavity is assumed to be that liquid in the two-phase boundary layer which flows between a surface through the centers of average sized bubbles and the heater surface as the bubbles pass the angle θ_s. The precise value of θ_s is difficult to determine, but observation of the boiling pattern indicates it is approximately $\pi/2$.

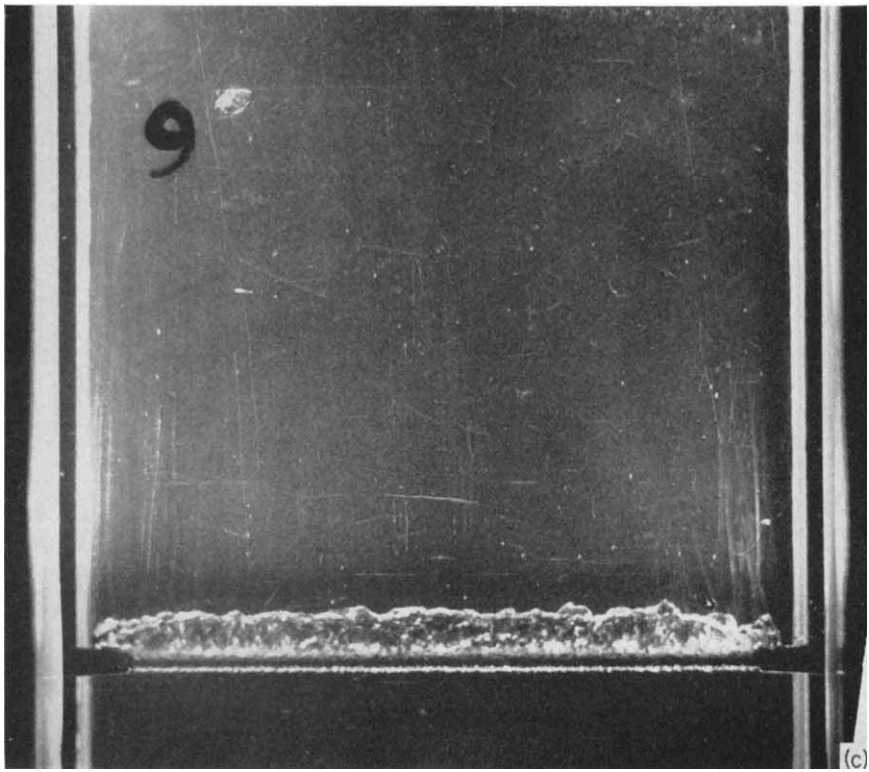

FIG. 29. (c) (For descriptive legend see page 256)

The liquid velocity on the front half of the cylinder just outside the boundary layer can be obtained from potential theory, while a linear velocity profile is assumed for the two-phase boundary layer in that region. It is then possible to approximate the liquid flow rate in the boundary layer at the location θ_s, with the result from Eq. (54)

$$q_c'' = \frac{1.083k\ \Delta t_{sat}}{\bar{f}\sqrt{\bar{\alpha}}} \sqrt{\frac{\overline{V}}{\overline{D}}} \tag{55}$$

The quantity $\bar{f}$ is the integrated average value from the stagnation point

to θ_s of the fraction of the surface heat flux which goes to the production of vapor in the boundary layer. This quantity may be a function of velocity and tube diameter, but would be expected to be dependent chiefly on the fluid properties. It will be retained for the present as an

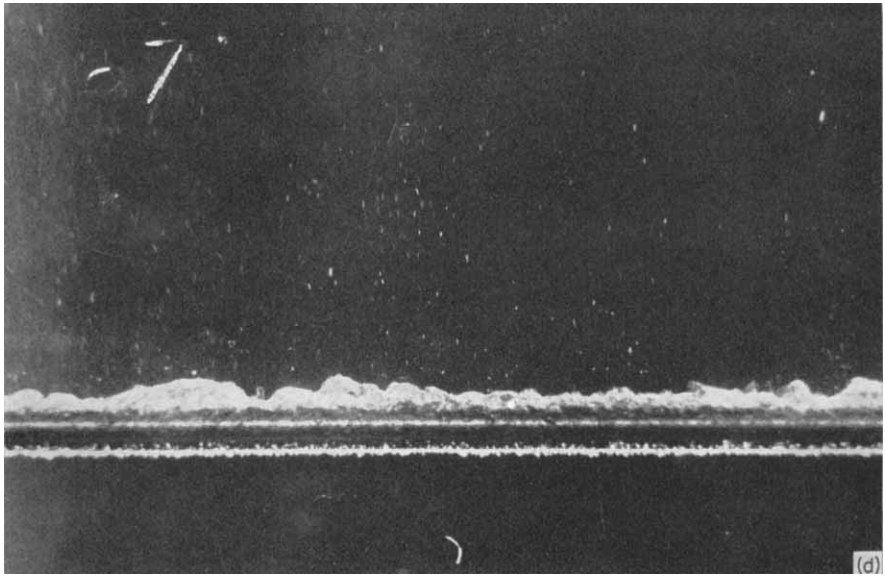

FIG. 29. Effect of subcooling on the boiling pattern for water from a ⅛-inch tube at approximately 80% of critical flux (*91*). The velocity is 2.35 ft/sec. (a) 4° F subcooling and 228 Btu/(sec)(sq ft) heat flux. (b) 20° F subcooling and 255 Btu/(sec)(sq ft) heat flux. (c) 30° F subcooling and 266 Btu/(sec)(sq ft) heat flux. (d) 50° F subcooling and 311 Btu/(sec)(sq ft) heat flux.

unknown parameter to be evaluated from experimental data for the critical flux.

3. Experimental Data

The effect of velocity on the critical flux for water at atmospheric pressure is shown in Fig. 31, which includes three points obtained by Beecher (*92*) for saturated water with 0.024-inch diameter wires and seven points by Vliet and Leppert (*90*) for 3 to 5° F subcooling with 0.125-inch diameter tubes. A dimensional expression for the velocity dependence is

$$q_c'' = 178 V_l^{1/2} \text{ Btu/(sec)(sq ft)} \tag{56}$$

where V_l is the average liquid velocity at the heater in ft/sec (*90*).

Critical flux was also measured for nearly saturated water (3 to 5° F subcooling) over a heater diameter range of 0.010 to 0.189 inch. Figure 32 shows these results, together with saturated boiling data of Beecher (*92*) for a 24-mil wire, from which can be deduced a weak diameter

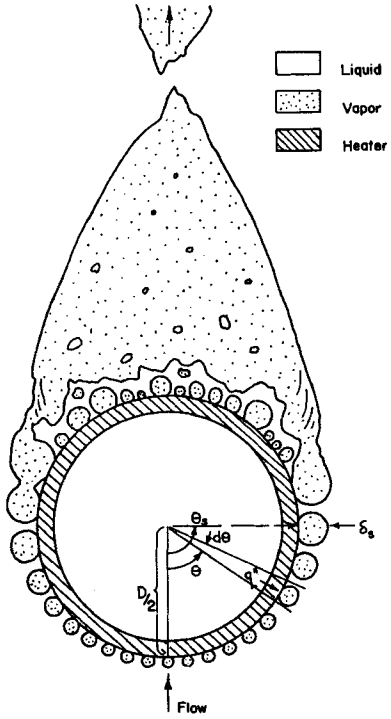

FIG. 30. Proposed model for forced-convection boiling of a saturated liquid from a uniformly heated cylinder (*90*).

dependence of the form

$$q_c'' \sim 1/D^{0.15}$$

for boiling with very low subcooling.

The analytical prediction of the effects of velocity and diameter may be compared with experimental data by inserting the fluid properties, k and α, as well as expressions for the temperature difference Δt_{sat} and the fraction $\bar{f}$ into Eq. (55). Alternatively, since the fraction $\bar{f}$ is unknown and too complex to analyze at present, we can evaluate the other parameters in Eq. (55) and then see whether the required variation and magnitude of $\bar{f}$ is physically reasonable.

The average heater surface temperature was measured at numerous

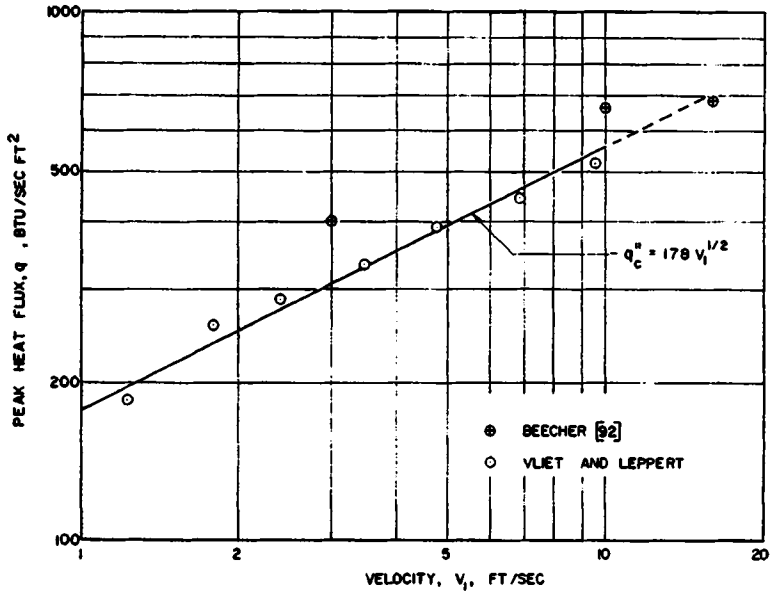

FIG. 31. The variation of critical heat flux with velocity for nearly saturated water flowing normal to a heated tube (*90*).

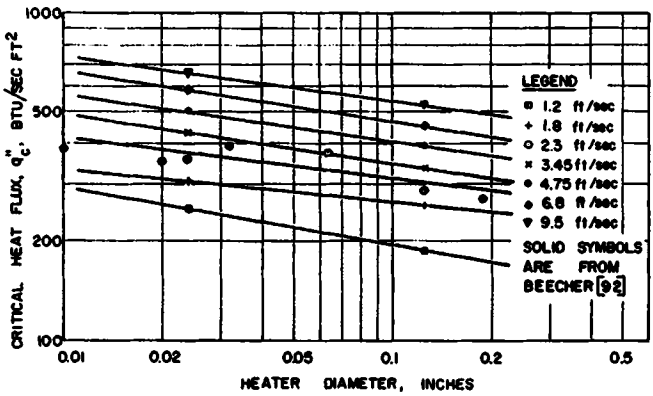

FIG. 32. The variation of critical flux with heater diameter for the forced convection of saturated water at atmospheric pressure (*90*). Seven points shown at 0.024-inch diameter are from Beecher's results (*92*).

values of the nucleate boiling heat flux up to the critical value for a number of velocities. The empirical relationship which fits these data for water at atmospheric pressure is

$$q'' = 0.105(\Delta t_{sat})^{2.0} \text{ Btu/(sec)(sq ft)} \tag{57}$$

This dependence on the temperature difference, though in exact agreement with a prediction of Forster and Greif (*6*) is somewhat weaker than the third-power variation found by Rohsenow (*47*) from the data of Addoms and others. For other boiling situations, values of 4 to 6 for this exponent are not uncommon.

If Eq. (57) is used to eliminate Δt_{sat} in the analytical prediction (Eq. (55)) and if the values 1.1×10^{-4} Btu/(sec)(ft)(°F) and 1.8×10^{-6} ft²/sec are substituted for k and α, (*8*) we obtain

$$q_c'' = \frac{0.075}{\bar{f}^2}\left(\frac{V}{D}\right) \text{Btu/(sec)(sq ft)}$$

For agreement between this result and the ⅛-inch tube experimental data (Eq. (56)), it is necessary that

$$\bar{f} = 0.20V^{1/4}$$

This indicates that $\bar{f}$ varies from 0.20 to 0.36 over the velocity range from 1 to 10 ft/sec.

Jakob (*1*) and Rohsenow and Clark (*5*) reported values below 0.10 at fluxes well below the peak, while the flat plate, pool boiling analyses of Kutateladze (*56*) and Zuber *et al.* (*62*, *63*, *64*) include the assumption that the entire flux evolves as latent heat of vaporization at the critical condition, in which case the fraction is unity. The value of $\bar{f}$ required in the present analysis refers to the front half of the cylinder, while the transition to film boiling invariably occurs in the rear half. Consequently, the front half could sustain a higher flux before transition, and a value of $\bar{f}$ less than unity but greater than 0.10 is to be expected.

The experimental results shown in Fig. 32 indicate a trend of the peak flux to decrease with increasing heater diameter, which is qualitatively consistent with the analysis. However, the dependence predicted by the analysis is much stronger than the experiment seems to indicate. Further consideration of this discrepancy suggests that as the tube diameter becomes smaller, the fraction of surface covered by the bubbles may become larger, since the bubble size is determined by the nature of the surface and by the liquid properties, not by the tube diameter. The fraction of heat transferred to the vapor may therefore become larger, and it is reasonable to suppose that the fraction $\bar{f}$ is a weak inverse function of diameter as well as a function of velocity. It is necessary for the fraction $\bar{f}$ to have a dependence of $\bar{f} \sim D^{-0.42}$ to agree with the empirical results.

The effects of velocity and heater diameter have also been determined for subcooled boiling of water from cylindrical tubes (*91*). Figure 33

shows the results of 60 burnout tests made with 0.125-inch o.d. by 0.10-inch wall, type 347 stainless steel tubes. The curves which have been drawn through these points show that the critical flux varies approximately linearly with subcooling except at the higher velocities, where there is little effect of subcooling below 20 to 30° F. The trends are consistent except for an inversion of the generally positive effect of velocity

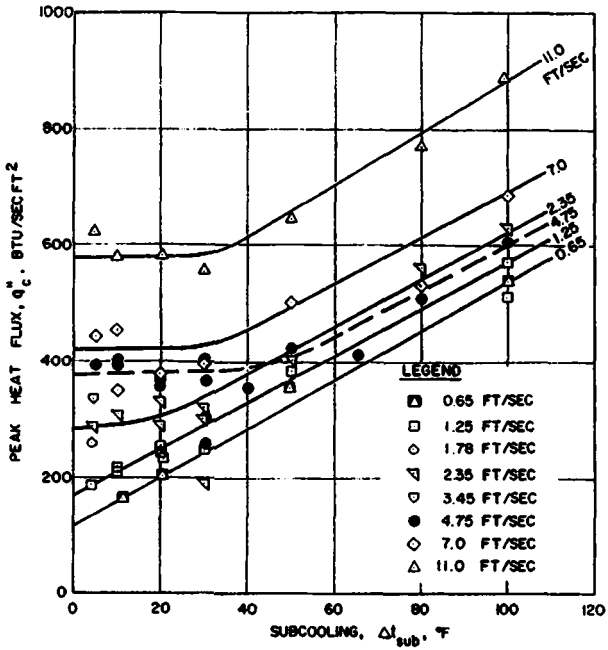

FIG. 33. The variation of critical flux with subcooling and velocity for water flowing upward across ½-inch tubes (*91*).

in the range from 2 to 6 ft/sec. The reason for these anomalously low values obtained at 4.75 ft/sec and high subcooling is not known, but may have been caused by a change in the flow pattern between 2 and 6 ft/sec which was not observable by the methods employed in the investigation.

Kezios and Lo (*93*) have obtained critical heat flux data for 0.125-inch diameter stainless steel rods which show a similar dependence on the subcooling to that in Fig. 33, but only qualitative agreement with the velocity dependence. A possible explanation for the discrepancy may lie in the corrections for channel blockage by the heater tubes, since the tubes occupied a larger fraction of their channel flow area than did the solid rods.

Figure 34 presents all the data of Vliet and Leppert, including not only the 64 tests with 0.125-inch tubes, but also 38 tests with wires and tubes from 0.010 to 0.189-inch o.d. The data, when correlated in this form, can be represented by

$$q_c'' = 140 + 24V_l + 3.9\Delta t_{sub} \text{ Btu/(sec)(sq ft)} \tag{58}$$

with a mean deviation of 12%. The data of Kezios and Lo can be represented by the following equation which differs from Eq. (58) only in

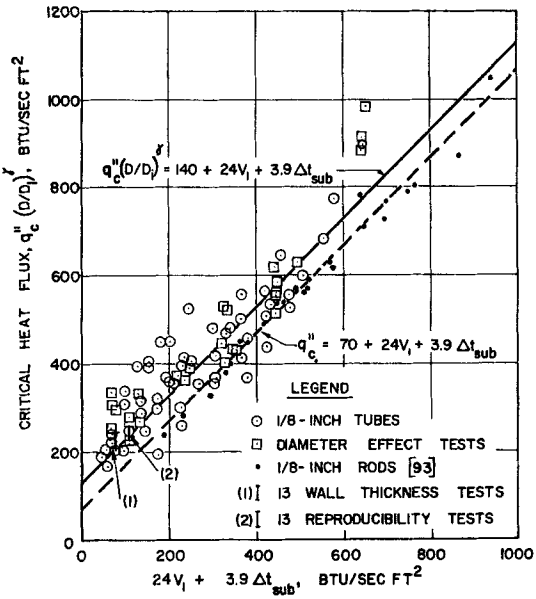

FIG. 34. Correlation of critical heat flux measurements for cylinders at various velocities, subcoolings, heater diameters and wall thicknesses (*91*) including data of Kezios and Lo (*93*).

the constant term

$$q_c'' = 70 + 24V_l + 3.9\Delta t_{sub} \text{ Btu/(sec)(sq ft)}$$

This linear variation of critical heat flux is in agreement with the experiments and analyses of numerous investigators.

Investigation of the effect of heater diameter on the peak heat flux in subcooled boiling was made for several liquid conditions over a range of diameters from 0.010 to 0.189-inch, using type 321 stainless steel tubing of 0.010-inch wall thickness for diameters greater than 0.020-inch and stainless steel wire for diameters less than or equal to 0.020-inch.

In general, the variation can be represented at a given approach velocity and subcooling by

$$q_c'' \sim 1/D^{\gamma} \tag{59}$$

where γ is a positive exponent which depends on the liquid velocity and subcooling. For the nine liquid conditions investigated, the exponent γ is plotted as a function of velocity with subcooling as a parameter in Fig. 35, and the estimated constant subcooling lines are indicated.

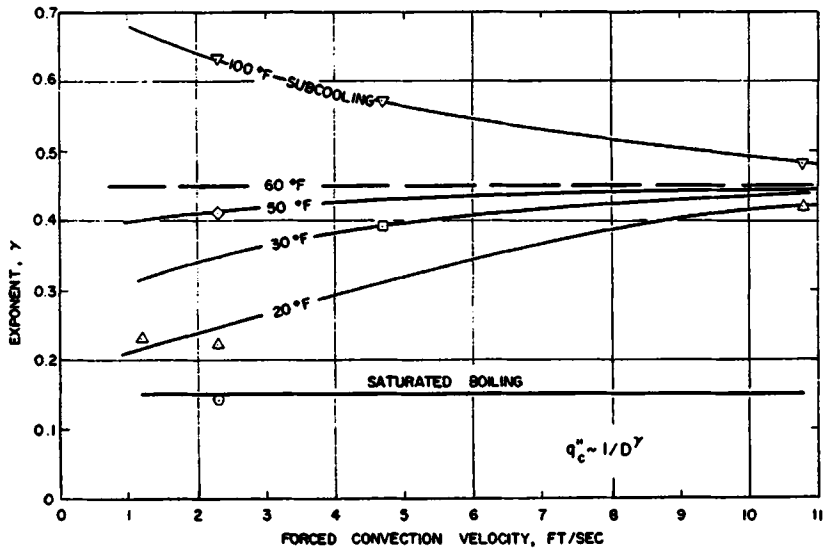

FIG. 35. Variation of the diameter exponent in Eq. (59) with water velocity at various subcoolings (*91*).

The inverse variation of the critical flux with heater diameter at a given liquid approach velocity and subcooling is consistent with the direct dependence of the critical flux on subcooling. For flow across a heated element the effective subcooling varies over the surface in the flow direction, the lowest value occurring at the farthest point downstream. Therefore, the larger the test section the lower is the effective subcooling in the liquid near the element at a given heat flux, and the lower is the critical flux.

The saturated, forced convection boiling data of Beecher (*92*) for 0.024-inch diameter wires, when compared to the results for 0.125-inch o.d. tubes, indicates a diameter exponent of 0.15 over the entire velocity range from 1.2 to 10 ft/sec. This result is also shown in Fig. 35.

ACKNOWLEDGMENT

This work was partially supported by a research grant from the U. S. Army Research Office (Durham).

NOMENCLATURE

A	area
A_{ba}	surface area of the base of a bubble attached to a surface
A_s	surface area of the liquid-vapor interface of a bubble attached to a surface
c	specific heat
D	diameter
D_e	hydraulic diameter
g	acceleration of gravity
g_c	dimensional constant relating force and mass in Newton's law of motion
g_0	standard acceleration of gravity at the earth's surface
G	mass flux
h	convective heat transfer coefficient
h_m	average boiling heat transfer coefficient
J	mechanical equivalent of heat
k	thermal conductivity
L	wave length
m	wave number
N_{Ja}	Jakob number, $(t_0 - t_{\mathrm{sat}})\rho_l c/\lambda\rho_v$
N_{Nu}	Nusselt number, hD/k
N_{Pr}	Prandtl number, $c\mu/k$
N_{Re}	Reynolds number, $DV\rho/\mu$
p	pressure
Δp	pressure difference corresponding to superheat, $t - t_{\mathrm{sat}}$
q''	heat flux
q_c''	critical heat flux
q_s''	heat flux to a bubble across the liquid-vapor interface
r	bubble radius
R	cavity radius
t	temperature
t_s	surface temperature
t_0	bulk liquid temperature
t_{sat}	saturation temperature
Δt	$t_s - t_0$
Δt_{sat}	$t_s - t_{\mathrm{sat}}$
Δt_{sub}	$t_{\mathrm{sat}} - t_0$
v_{fg}	specific volume change by vaporization
V	velocity
X_c	steam quality at critical heat flux
Y	body force per unit mass in the y direction
α	thermal diffusivity
β	contact angle
ζ	chemical potential
λ	latent heat of vaporization
μ	viscosity
ρ	density
σ	surface tension
τ	time
Φ	velocity potential
Φ_{TPF}	two-phase friction multiplier
ω	disturbance frequency

Subscripts

l	liquid
v	vapor

REFERENCES

1. M. Jakob, "Heat Transfer," Vol. I, Chapter 29. Wiley, New York, 1949.
2. S. Nukiyama, *J. Soc. Mech. Engrs. (Japan)* **37,** 367 (1934).
3. W. H. McAdams, "Heat Transmission," third ed., Chapter 14. McGraw-Hill, New York, 1954.
4. G. Leppert, C. P. Costello and B. M. Hoglund, *Trans. A.S.M.E.* **80,** 1935 (1958).
5. W. M. Rohsenow and J. A. Clark, *Trans. A.S.M.E.* **73,** 609 (1951).
6. H. K. E. Forster and R. Greif, *J. Heat Transfer* **81,** 43 (1959).
7. J. H. Keenan, "Thermodynamics," Chapters 25 and 26. Wiley, New York, 1941.

8. J. H. Keenan and F. G. Keyes, "Thermodynamic Properties of Steam." Wiley, New York, 1936.
9. J. A. Clark, Technical Report No. 7, Massachusetts Institute of Technology, 1956.
10. F. B. Kenrick, C. S. Gilbert and K. L. Wismer, *J. Phys. Chem.* **28,** 1297 (1924).
11. C. Corty and A. S. Foust, *Chem. Eng. Progr. Symp. Ser. 17,* **51,** 1 (1955).
12. P. Griffith and J. D. Wallis, *Chem. Eng. Progr. Symp. Ser. 30,* **56,** 49 (1960).
13. S. G. Bankoff, *A.I.Ch.E. J.* **4,** 24 (1958).
14. R. H. Sabersky and C. W. Gates, Jr., *Jet Propulsion* **25,** 67 (1955).
15. M. Volmer, *Z. Elektrochem.* **35,** 555 (1929).
16. M. Volmer, "Kinetik der Phasenbildung," Steinkopf, Leipzig, 1939.
17. J. C. Fisher, *J. Appl. Phys.* **19,** 1062 (1948).
18. S. G. Bankoff, *Trans. A.S.M.E.* **79,** 735 (1957).
19. H. B. Clark, P. S. Strenge and J. W. Westwater, *Chem. Eng. Progr. Symp. Ser. 29,* **55,** 103 (1959).
20. Y. Y. Hsu, *J. Heat Transfer* **84,** 207 (1962).
21. Y. Y. Hsu and R. W. Graham, Report NASA-TN-D-594, National Aeronautics and Space Administration, 1961.
22. H. S. Carslaw and J. C. Jaeger, "Conduction of Heat in Solids," second ed., Oxford Univ. Press, Oxford, 1959.
23. W. H. McAdams, J. N. Addoms and W. E. Kennel, Report ANL-4268, Argonne National Laboratory, 1948.
24. J. W. Westwater, in "Advances in Chemical Engineering." (T. B. Drew and J. W. Hoopes, Jr. eds.), Vol. I. Academic Press, New York, 1956.
25. D. A. Glaser, *Nuovo Cimento Suppl. Ser. 9,* **11,** 361 (1954).
26. D. A. Glaser, *Phys. Rev.* **91,** 762 (1953).
27. F. Seitz, *Phys. Fluids* **1,** 2 (1958).
28. N. Zuber, Ph.D. Thesis in Engineering, Univ. of Calif., Los Angeles, 1959; also Report AECU-4439, U. S. Atomic Energy Commission, 1959.
29. F. Bosnjakovic, *Techn. Mechanik Thermodyn.* **1,** 358 (1930).
30. W. Fritz and W. Ende, *Z. Physik* **37,** 391 (1936).
31. M. S. Plesset and S. A. Zwick, *J. Appl. Phys.* **25,** 493 (1954).
32. H. K. E. Forster and N. Zuber, *J. Appl. Phys.* **25,** 474 (1954).
33. P. Dergarabedian, *J. Appl. Mech.* **20,** 537 (1953).
34. G. Birkhoff, R. S. Margulies and W. A. Horning, *Phys. Fluids* **1,** 201 (1958).
35. P. Griffith, *Trans. A.S.M.E.* **80,** 721 (1958).
36. P. Savic, Report MT-37, National Research Council of Canada, Division of Mech. Eng., 1958.
37. L. E. Scriven, *Chem. Eng. Sci.* **10,** 1 (1959).
38. S. G. Bankoff and R. D. Mikesell, *Chem. Eng. Progr. Symp. Ser. 29,* **55,** 95 (1959).
39. F. C. Gunther, Progress Report 4-75, Jet Propulsion Laboratory, California Institute of Technology, 1950.
40. M. E. Ellion, Progress Report 20-88, Jet Propulsion Laboratory, California Institute of Technology, 1954.
41. S. G. Bankoff and R. D. Mikesell, ASME Paper 58-A-105, New York, 1958.
42. B. E. Staniszewski, Technical Report 16, Massachusetts Institute of Technology, 1959.
43. W. Fritz, *Z. Physik.* **36,** 379 (1935).
44. P. C. Zmola, Ph.D. Thesis, Purdue University, 1950.
45. F. Bashforth and J. C. Adams, "Capillary Action," Cambridge Univ. Press, Cambridge, 1883.

46. F. C. Gunther and F. Kreith, Progress Report 4-120, Jet Propulsion Laboratory, California Institute of Technology, 1950.
47. W. M. Rohsenow, *Trans. A.S.M.E.* **74,** 969 (1952).
48. J. N. Addoms, Sc.D. Thesis in Chemical Engineering, Massachusetts Institute of Technology, 1948.
49. H. K. E. Forster and N. Zuber, *A.I.Ch.E. J.* **1,** 531 (1955).
50. H. M. Kurihara and J. E. Myers, *A.I.Ch.E. J.* **6,** 83 (1960).
51. C. L. Tien, *Intern. J. Heat Mass Transfer* **5,** 533 (1962).
52. K. Yamagata, F. Hirano, K. Nishikawa and H. Matsuoka, *Japan. Sci. Rev.* **2,** 409 (1952).
53. S. G. Bankoff, *A.I.Ch.E. J.* **8,** 63 (1962).
54. F. O. Mixon, Jr., W. Y. Chon and K. O. Beatty, Jr., *Chem. Eng. Prog. Symp. Ser. 30,* **56,** 75 (1960).
55. S. G. Bankoff and J. P. Mason, *A.I.Ch.E. J.* **8,** 30 (1962).
56. S. S. Kutateladze, *Zh. Tekh. Fiz.* **20,** 1389 (1950).
57. L. S. Sterman, *Zh. Tekh. Fiz.* **23,** 341 (1953).
58. V. M. Borishanskii, *Zh. Tekh. Fiz.* **26,** 452 (1956).
59. W. M. Rohsenow and P. Griffith, AIChE-ASME Heat Transfer Symposium, Preprint 9, Louisville, Ky., 1955.
60. W. M. Rohsenow and H. Y. Choi, "Heat, Mass and Momentum Transfer," Prentice-Hall, Englewood Cliffs, N. J. 1961.
61. C. M. Usiskin and R. Siegel, *J. Heat Transfer* **83,** 243 (1961).
62. N. Zuber, *J. Heat Transfer* **80,** 711 (1958).
63. N. Zuber and M. Tribus, Report 58-5, Univ. of California, Los Angeles, 1958.
64. N. Zuber, M. Tribus and J. W. Westwater, International Developments in Heat Transfer, Paper No. 27, Boulder, Colorado, 1961.
65. H. Lamb, "Hydrodynamics," first American ed., Dover, New York, 1945.
66. Lord Rayleigh, "Theory of Sound," Dover, New York, 1945.
67. C. F. Bonilla and C. W. Perry, *Trans. A. I. Ch. E.* **37,** 685 (1941).
68. P. J. Berenson, *Intern. J. Heat Mass Transfer* **5,** 985 (1962).
69. M. T. Cichelli and C. F. Bonilla, *Trans. A. I. Ch. E.* **41,** 755 (1945).
70. E. A. Kazakova, in "Problems of Heat Transfer During a Change of State: A Collection of Articles," (S. S. Kutateladze, ed.), State Power Press, Moscow, 1953; also AEC-tr-3405, U. S. Atomic Energy Commission.
71. C. P. Costello and J. M. Adams, International Developments in Heat Transfer, Paper No. 30, Boulder, Colorado, 1961.
72. H. J. Ivey, The Inst. of Mech. Engrs., Paper PI/63, London, 1962.
73. W. R. van Wijk, A. S. Vos and S. J. D. von Stralen, *Chem. Eng. Sci.* **5,** 68 (1956).
74. A. S. Vos and S. J. D. von Stralen, *Chem. Eng. Sci.* **5,** 50 (1956).
75. W. R. van Wijk, *Dechema Monograph.* **28,** 63 (1956).
76. W. R. van Wijk and S. J. D. von Stralen, *Dechema Monograph.* **32,** 94 (1959).
77. S. J. D. von Stralen, *Brit. Chem. Eng.* **4,** 8 and 78 (1959).
78. V. G. Fastovskii and R. I. Artym, *Teploenerg.* **5,** No. 8, 74 (1958).
79. W. L. Owens, Jr., Ph.D. Thesis in Mechanical Engineering, University of Aberdeen, 1961.
80. F. E. Tippets, Ph.D. Thesis in Mechanical Engineering, Stanford University, 1962; also Report GEAP 3766, General Electric Co., San Jose, Calif., 1962.
81. F. E. Tippets, ASME Paper 62-WA-162, New York, 1962.
82. F. E. Tippets, ASME Paper 62-WA-161, New York 1962.
83. R. C. Martinelli and D. B. Nelson, *Trans. A.S.M.E.* **70,** 695 (1948).
84. E. Janssen and J. A. Kervinen, Report GEAP-3899, General Electric Co., San Jose, Calif., 1962.

85. I. T. Aladyev, Z. L. Miropolsky, V. E. Doroshchuk, and M. A. Styrikovich, International Developments in Heat Transfer, Paper No. 28, Boulder, Colo., 1961.
86. R. A. DeBartoli, S. J. Green, B. W. Letourneau, M. Troy and A. Weiss, Report WAPD-188, Westinghouse Electric Corporation, Pittsburgh, 1958.
87. A. W. Bennett, J. G. Collier and P. M. C. Lacey, Report AERE-R 3804, U. K. Atomic Energy Authority, Harwell, England, 1961.
88. M. Silvestri, International Developments in Heat Transfer, Paper No. 39, Boulder, Colo., 1961.
88. L. Berkowitz, S. Bertoletti, J. Lesage, C. Peterlongo, G. Soldaini and R. Zavattarelli, Report R-27, Centro Informazioni Studi Esperienze, Milan, 148, 1960.
90. G. C. Vliet and G. Leppert, ASME Paper 62-WA-173, New York, 1962.
91. G. C. Vliet and G. Leppert, ASME Paper 62-WA-174, New York, 1962.
92. N. Beecher, M. S. Thesis in Chemical Engineering, Massachusetts Institute of Technology, 1948.
93. S. P. Kezios and R. K. Lo, Report ANL-5822, Argonne National Laboratory, 1958.

The Influence of Electric and Magnetic Fields on Heat Transfer to Electrically Conducting Fluids

MARY F. ROMIG

The Rand Corporation, Santa Monica, California

I. Introduction

Electromagnetic phenomena in rigid conductors have been studied ever since the time of Faraday. It has not been until fairly recent years, however, that the interaction of electromagnetic fields and electrically conducting fluids has attracted much attention. Probably the largest incentive toward an understanding of such phenomena came from the field of astrophysics. It has long been suspected that most of the matter in the universe is in the plasma or highly ionized gaseous state. Much of the basic knowledge in the area of electromagnetic fluid dynamics evolved from these studies.

The field of plasma physics has now grown from these scholarly beginnings to include problems in such widely diverse areas as geophysics and controlled nuclear fusion. Most of the recent impetus toward the establishment of a firm theoretical basis for this discipline has, in fact, been due to the requirements of modern fusion reactor design.

As a branch of plasma physics, the field of magnetohydrodynamics (MHD) consists of the study of a continuous, electrically conducting fluid under the influence of electromagnetic fields. Originally, MHD included only the study of strictly incompressible fluids (hence the "hydro"), but today the terminology is applied to studies of partially ionized gases as well. Other names have been suggested, such as magneto-fluid-mechanics, or magnetoaerodynamics, but the original nomenclature has persisted. The essential requirement for problems to be analyzed under the laws of MHD is that the continuum approach be applicable.

A. MHD AND HEAT TRANSFER

With the advent of hypersonic flight the field of MHD as defined above, which had heretofore been associated largely with liquid-metal pumping and flow velometry, attracted the interest of aerodynamicists. The possibility arose of altering the flow and heat transfer around high-velocity vehicles provided that the air were sufficiently ionized. Furthermore, the invention of high-temperature facilities such as the shock tube and plasma jet provided laboratory sources of flowing, ionized gas, which provided an incentive for the study of plasma accelerators and generators.

As a result of this, many of the classical problems of fluid mechanics were reinvestigated. Some of these analyses arose out of the natural tendency of scientists to investigate a new subject. In this case it was the academic problem of solving the equations of fluid mechanics with a new body force and another source of dissipation in the energy equation. Sometimes there were no practical applications for these results. For example, the natural-convection MHD flows of Section III have been of interest to the engineering community only since the introduction of liquid-metal heat exchangers, although the thermal-instability investigations of Section III are directly applicable to problems in geophysics and astrophysics.

The study of channel-flow heat transfer discussed in Section IV has many applications to the propulsion and power-generation field. The pioneer work in channel flow was done by Hartmann and Lazarus (*1*, *2*) in their studies of liquid-metal pumps. Many of the one-dimensional heat-transfer analyses today are extensions of the early Hartmann flow problem. In reality, however, the assumption of continuum flow is not always justified in flows of partially ionized gases under both electric and magnetic fields. This particular limitation of classical MHD will be discussed further in Section I,B.

But it was in the field of aerodynamic heating that the largest interest was aroused. Rossow (*3*) presented the first paper on this subject in 1957. His results, for incompressible, constant-property flat-plate boundary-layer flow, indicated that the skin friction and heat transfer were reduced substantially when a transverse magnetic field was applied to the fluid. This encouraged a multitude of analyses for every conceivable type of aerodynamic flow; most of the research centered on the stagnation point where, in hypersonic flight, the highest degree of ionization could be expected. The results of these studies were sometimes contradictory as to the amount by which the heat transfer would be reduced. (Some of this was due to misinterpretations and invalid comparisons.) Eventually, however, it was concluded that the field strengths necessary to provide sufficient shielding against high-heat fluxes during atmospheric flight were not competitive (in terms of weight) with other methods of cooling (*4*). However, the invention of new, lightweight, superconducting magnets has recently revived interest in the problem of providing heat protection during the very-high-velocity reentry from orbital and super-orbital flight (*5*).

The present study is divided into several sections, each dealing with a particular classical heat-transfer problem. The simple one-dimensional flows (Poiseuille and Couette) will be discussed at some length in Sections IV and V in order that the behavior in more complex flow problems can be more easily interpreted. In each case the effects of the magnetic and

electric fields will be assessed in the light of analyses available in the published literature.

We shall also be dealing almost exclusively with laminar flow problems. Because of the semiempirical techniques used to analyze the turbulent boundary layer, it is necessary to rely on accurate experimental measurements to obtain certain constants in the skin-friction laws. In ordinary fluid mechanics, Reynolds' analogy can often be used to obtain heat-transfer coefficients from the variation of shear stress. But Reynolds' analogy will not be applicable in MHD flows, and it will therefore be necessary to measure both skin friction and heat transfer to determine the empirical constants. To date, the experiments in MHD turbulent flow have been confined primarily to studies of skin-friction drag and transition from laminar to turbulent flow in insulated channels. As a result, the heat-transfer portion of the theory has not yet been developed to the extent that realistic analyses of turbulent heat transfer are available in the literature (see, e.g., Section IV,B,1.).

This study assesses the effects of externally applied electromagnetic fields on heat transfer to electrically conducting continuous fluids. In order to present a logical exposition of this broad subject, the basic equations are developed first and various classical problems are discussed, such as free convection and heat transfer in channel flow and at a stagnation point. Each of the areas discussed is of practical import in the engineering field of today. The simple one-dimensional flow of Section IV illustrates many of the heating problems associated with some modern generators and accelerators. Similarly, the plane shear flow of Section V serves as a representative example of the more sophisticated flows arising in the study of aerodynamic heating. The limitations of the continuum approach demonstrate the outstanding problems which remain in each of the subject areas discussed.

It is shown that this field of heat transfer contains problems of two general types: those in which the heating is a consequence of electromagnetic fields applied to the fluid for purposes of generating power or pumping, and those in which the electromagnetic fields are used primarily to control the heat transfer (i.e., at the stagnation point of a blunt body or in natural convection flows.)

The extreme heating rates associated with the first area are due primarily to the presence of large electric fields in the fluid and the attendant Joule heating. In the second, the ponderomotive force on the fluid caused by the interaction of the flowing conductor and unapplied magnetic field controls the motion of the fluid and reduces the heat transfer. Although this technique is limited in application by the large magnetic field strengths necessary to affect the flow of naturally ionized air, the develop-

ment of superconducting magnets holds promise for future utilization in the reduction of aerodynamic heating, especially for reentry at super-orbital speeds.

This survey of electromagnetic effects on heat transfer indicates that the most serious lack in this field today is experimental verification of the existing theory.

B. LIMITATIONS IN CLASSIC MHD THEORY

Every mathematical description of a natural phenomenon contains certain approximations. The concept of a continuous fluid is one which serves quite well in determining the gross behavior of a gas, as long as the mean free path is small compared to the characteristic length in the flow. In accordance with this assumption, it is generally specified in MHD analyses that the electronic mean free path is small compared to such characteristic lengths in the problem.

It is also assumed that the fluid will not support any excess of charge—i.e., that it is electrically neutral in a local sense. This condition is easily satisfied when the fluid is a continuum and is unbounded. Near boundaries, where strong concentration gradients exist, it is necessary to examine further the concept of charge neutrality.

1. Wall Effects

The currents in a gas are determined by the motion of the charge carriers relative to the mean velocity of the gas. If we assume either thermal equilibrium or ion generation by the action of externally produced electromagnetic fields, then, because the electrons are much lighter than the ions, their thermal velocities are much higher. In an unbounded gas without concentration gradients, the region of excess of charge in a unit volume is determined by the electron Debye length, which is proportional to the square root of the ratio of electron kinetic energy to the electron density (*6*). In essence, an ion will not "see" an electron over a distance larger than a Debye length. A gas in which the continuum property is upheld, therefore, will not tolerate an extensive space charge, and is said to be quasi-neutral.

To insure quasi-neutrality in the presence of concentration gradients and electromagnetic fields, it is necessary to specify further that the flux of charge into any volume equals the flux of charge out of it. The physical process which regulates the charge density in this case is referred to as ambipolar diffusion (*7*). The ambipolar-diffusion coefficient is so *defined* that the flux and the number density of charges of opposite sign are equal; hence, where it is assumed that ambipolar diffusion occurs the concept of quasi-neutrality is automatically satisfied.

This diffusion process is best described as a limiting situation, in which electrons leaving a volume element will initially diffuse to the walls more rapidly than will the ions. They will set up near the wall, by this motion, a negative space-charge field that repels further electrons and attracts the ions. Outside the space-charge sheath, electrons and ions will diffuse at the same rate and, by definition of the diffusion coefficient, the charge density will be zero. The dimensions of the sheath will again be governed by the electron Debye length. For the case of electrically insulating boundaries in continuum flow, the sheath is of negligible extent and is unimportant as far as the heat transfer is concerned.

In the presence of strong electric-field gradients, such as found near an electrode, conditions at the sheath may seriously affect the heat transfer to the electrode. This problem, which will exist in many low-density MHD generators, has not yet been assessed at any length in the literature (see, e.g., Sections IV,B, and VI,B.).

2. High-Field Effects

Unlike the formation of the sheath, which is due to the high thermal velocity of electrons, another restriction in the application of continuum magnetohydrodynamics to problems involving ionized gases arises because of the directed motion of charged particles in electric and magnetic fields. The former will occur in any bounded system of low-density plasma; the latter will exist at pressures which are normally (in the zero-field case) sufficient to insure the continuum approach. These effects, which can be loosely termed as "high-field" effects, will not be covered at any length here because they occur outside the range of continuum MHD in the strictest sense. They are, however, of sufficient importance to practical engineering problems in modern MHD devices that this brief description is warranted.

a. Hall Currents. In a gas which is sufficiently dense, the electron-atom collision frequency, ν_c, is large enough so that the tendency for free electrons to spiral around the magnetic field lines is suppressed. If the applied field is large or the gas density low so that the cyclotron frequency, $\omega = eB/m$, exceeds the collision frequency, the electron can make a number of cyclotron orbits between collisions and will drift in a direction perpendicular to the direction of the magnetic and electric fields. This drift produces a current (the Hall current), and the gyromotion decreases the electric conductivity of the gas (7). Referring ahead to Ohm's Law [Eq. (9)], we can include the contribution to the current due to the Hall effect, namely

$$\mathbf{j} = \frac{\sigma}{1 + \left(\frac{\omega}{\nu_c}\right)^2}\left[\mathbf{E} + \mathbf{v} \times \mathbf{B} - \frac{\mathbf{j} \times \mathbf{B}}{n_e e}\right] \tag{1}$$

where the conductivity σ is reduced by the factor $(1 + (\omega/\nu_c)^2)$ and where the last term in the brackets is the Hall current, $\mathbf{j}_H$.

By lowering the conductivity, the Hall effect thus reduces the current in the direction of the electric field and causes a current to flow normal to both **E** and **B**. While it is obvious that any DC power generator or accelerator will become inefficient in high field strengths unless it is designed to operate in the Hall mode, the Hall effect also influences the flow, and hence the heat transfer, in a direct manner. It can be shown from Eq. (1) and the discussions of Section II,B, that this current will interact with the applied magnetic field to induce a transverse motion of the fluid. For example, a given two-dimensional flow would become three-dimensional. The Hall effect therefore places a serious restriction on the regime of applicability of many solutions in which partially ionized gases are analyzed using continuum MHD. The limits of validity for solutions of this sort will be noted when appropriate.

b. Ion Slip. When the ratio ω/ν_c becomes very large, the electromagnetic field can force both the ions and electrons to produce a relative drift between them and the neutrals. This drift is called "ion slip" and is of course negligible for highly ionized gases. Brunner (*8*) has investigated both the Hall and ion-slip effect for equilibrium air and concludes that for low-pressure conditions and an applied field of 10^4 gauss (1 weber/m^2) the conductivity is reduced materially by as much as a factor of 10^3 at operating pressures of 10^{-2} atm.

Since both the Hall effect and ion slip will occur in low-pressure, moderately-high-temperature environments, they will affect the heat transfer in both a generator/accelerator and a boundary layer. To the author's knowledge the heat transfer under such conditions has not yet been investigated. It can, however, be predicted that these problems will form the next generation of MHD-heat-transfer studies.

II. The Basic Equations

The governing equations of magnetohydrodynamics result from a combination of two disciplines: electromagnetic theory and fluid mechanics. Extensive derivation of the equations is beyond the scope of this article; instead we will make use of rather general, fundamental laws and refer the reader to the cited literature for a more comprehensive treatment.

A. THE ELECTROMAGNETIC SYSTEM

According to electromagnetic theory (*9*), the forces on a conducting fluid at rest are of the following types: ponderomotive, magnetostrictive, electrostrictive, and electrostatic. The ponderomotive force is the force on a volume distribution of current in a magnetic field. Magnetostriction and electrostriction are both defined, for a nonferromagnetic medium, as

elastic deformation of the fluid under the influence of electromagnetic fields. They are important in a medium where the magnetic permeability and electric susceptibility are functions of the fluid density. The electrostatic force is the usual body force on free-charge carriers in the fluid.

It is usually assumed in MHD that the permeability μ_e and the dielectric constant ϵ are constant; displacement and polarization currents are neglected; and, in accordance with the continuum approach, the net-charge density, ρ_e, is zero. Justification for the neglect of these terms depends, of course, on the physical properties of the gas as well as on the nature of the applied electromagnetic fields. For example, we will be discussing time-independent fields exclusively in this article, so that plasma oscillations, for example, will not be considered and the displacement current can be neglected. The validity of these assumptions depends further on the relative size of the electromagnetic forces compared to the fluid-dynamic forces in a given fluid. Lykoudis (*10*) has pointed out that for electrostatic free-convection problems in polar liquids or gases the electrostrictive force can be on the same order as the buoyant forces (Section III,A). But this situation will be the exception rather than the rule in the MHD problems likely to be encountered, for the ponderomotive force and inertia or shear terms are usually large enough to justify the above assumptions.

This leaves the ponderomotive force as the only remaining electromagnetic force on the system at rest. In order to assess the interaction of the applied fields with a moving fluid, it is convenient to transform the system to the same frame of reference in which the basic thermomechanical laws are used. Maxwell's equations for time-independent fields in a system at rest are

$$\nabla \times \mathbf{H} = \mathbf{j} \tag{2}$$

$$\nabla \times \mathbf{E} = 0 \tag{3}$$

$$\nabla \cdot \mathbf{B} = \nabla \cdot \mathbf{D} = 0 \tag{4}$$

where

$$\mathbf{D} = \epsilon \mathbf{E} \quad \text{and} \quad \mathbf{B} = \mu_e \mathbf{H} \tag{5}$$

and where $\mathbf{H}$ is the magnetic field strength, $\mathbf{j}$, the current density, $\mathbf{B}$, the magnetic induction, and $\mathbf{D}$, the dielectric displacement. The above equations are written in the MKS (m-kg-sec) system of units. Conversion tables between these and the cgs system are given in most textbooks (*9*).

Under a Lorentz transformation for nonrelativistic velocities, Eqs. (2) to (5) still hold in the fluid, but the field vectors $\mathbf{E}$ and $\mathbf{H}$ are replaced by $\mathbf{E}_f = (\mathbf{E} + \mathbf{V} \times \mathbf{B})$ and $\mathbf{H}_f = (\mathbf{H} - \mathbf{V} \times \mathbf{D})$, so that Eqs. (2) and (3) become

$$\nabla \times (\mathbf{H} - \mathbf{V} \times \mathbf{D}) = \mathbf{j} \tag{6}$$

$$\nabla \times (\mathbf{E} + \mathbf{V} \times \mathbf{B}) = 0 \tag{7}$$

where $\mathbf{V}$ is the center-of-mass velocity of a fluid element; $\mathbf{B}$, $\mathbf{D}$, and $\mathbf{j}$ are unchanged, as are the differential operators, when $\mathbf{V}$ is much less than the speed of light and $\rho_e = 0$.

Equation (7) establishes that an electric field will be present in the fluid due to the motion of the current-carrying conductor through the magnetic field. It can be written for a constant-density fluid ($\nabla \cdot \mathbf{V} = 0$) as

$$\nabla \times \mathbf{E} = (\mathbf{B} \cdot \nabla)\mathbf{V} - (\mathbf{V} \cdot \nabla)\mathbf{B} \tag{8}$$

which is often called Faraday's law of induction for a moving medium (*9*). Equation (8) is not valid unless the density of the fluid is constant.

Since this electromagnetic system is now at rest in the fluid, we can apply the phenomenological laws for a medium at rest and obtain Ohm's law

$$\mathbf{j} = \sigma(\mathbf{E} + \mathbf{V} \times \mathbf{B}) \tag{9}$$

and Joule's law

$$Q_j = j^2/\sigma = \sigma(\mathbf{E} + \mathbf{V} \times \mathbf{B})^2 \tag{10}$$

Ohm's law now includes the current induced by the motion of the conducting fluid through the magnetic force lines. The heat due to electrical dissipation in a conductor is given by Joule's heating law. Again, the fluid flow will contribute to the heat through the induced field. The conductivity in Eqs. (9) and (10) is assumed to be scalar, as discussed in Section I,B,2.

B. THE MAGNETOHYDRODYNAMIC EQUATIONS

It is now possible to derive the conservation equations for MHD flow by the usual method of balancing across differential fluid elements. Although these equations are written for generality for time-dependent flows, we shall be considering only the steady state in this study.

The electromagnetic field cannot create mass, and the continuity equation remains unchanged in form:

$$\frac{\partial \rho}{\partial t} + \nabla \cdot (\rho \mathbf{V}) = 0 \tag{11}$$

where ρ is the fluid density and $\mathbf{V}$ is the velocity. For reacting gases, the continuity of each species should be considered.

It is a comparatively simple matter to derive the momentum equation. Starting with Newton's law

$$\rho \frac{d\mathbf{V}}{dt} = \mathbf{F} \tag{12}$$

where $\mathbf{F}$ is the sum of all the forces acting on the fluid, we need only consider which forces arise from the electromagnetic field. The usual

fluid-dynamic forces are

$$\mathbf{F}_m = -\nabla p + \tau_{ij} + \mathbf{f} \tag{13}$$

where τ_{ij} is the viscous stress

$$\frac{\partial}{\partial x_j}\left[\mu\left(\frac{\partial u_i}{\partial x_j} + \frac{\partial u_j}{\partial x_i} - \tfrac{2}{3}\frac{\partial u_l}{\partial x_l}\delta_{ij}\right)\right]$$

and where $\mathbf{f}$ is due to gravitational and buoyancy forces.

The electromagnetic force which acts in Eq. (12) is the usual ponderomotive force discussed earlier, where the fluid is considered a rigid current-carrier moving in a magnetic field; that is,

$$\mathbf{F}_e = \mathbf{j} \times \mathbf{B} = \sigma(\mathbf{E} + \mathbf{V} \times \mathbf{B}) \times \mathbf{B} \tag{14}$$

part of which would exist if the fluid were at rest, and part of which is due to the current induced by the motion through the magnetic field. The force $\sigma\mathbf{E} \times \mathbf{B}$ will accelerate or decelerate the flow, depending on the direction of $\mathbf{E}$, $\mathbf{B}$, and $\mathbf{V}$; the "back" emf $\sigma\mathbf{V} \times \mathbf{B}$ will provide a current whose interaction with $\mathbf{B}$ will always decelerate the flow.

With the forces of Eqs. (13) and (14), the momentum equation becomes

$$\rho \frac{d\mathbf{V}}{dt} = -\nabla p + \tau_{ij} + \mathbf{f} + \sigma(\mathbf{E} + \mathbf{V} \times \mathbf{B}) \times \mathbf{B} \tag{15}$$

where d/dt is the substantial (Eulerian) derivative.

A derivation of an energy equation for MHD should take into account the electromagnetic theory for a moving medium and the thermodynamics of an electrically conducting gas. The most rigorous and complete derivation in the literature is that of Chu (*11*). Other derivations (*12*, *13*), which satisfy the first law of thermodynamics by physical reasoning based on Maxwell's equations at rest, are shown by Chu to be correct (although difficult to interpret) as long as μ_e and ϵ are constant.

The difficulty encountered in writing an energy equation for a gas in which $\epsilon = \epsilon(\rho, T)$ and $\mu_e = \mu_e(\rho, T)$ arises when the constituents of the energy balance given by the first law are separated into mechanical and electromagnetic parts. The reader is referred to (*11*) for a complete treatment of this particular case, since with the exception of Section III,A, we shall not be concerned with problems where the electromagnetic parameters μ_e and ϵ are variable.

From the first law, the energy balance can be written

$$d\mathfrak{U}_t = dW_r + dW_d + dQ \tag{16}$$

where $\mathfrak{U}_t$ is the internal energy per unit mass, W_r the reversible work, W_d the energy dissipated internally, and Q the heat flux. Chu writes the

internal energy and the pressure as the sum of mechanical and electromagnetic components; however, when ϵ and μ_e are constant, these electromagnetic terms are balanced by the electromagnetic contribution to the reversible work; i.e., if

$$\left.\begin{aligned} \mathfrak{U}_t &= C_v T + \left[\frac{1}{2\rho}\left(\frac{D^2}{\epsilon} + \frac{B^2}{\mu_e}\right) + \frac{T}{2\rho}\left(\frac{1}{\epsilon}\frac{\partial \epsilon}{\partial T} + \frac{1}{\mu_e}\frac{\partial \mu_e}{\partial T}\right)\right] \\ p_t &= \rho R T + \tfrac{1}{2}(\mathbf{B}\cdot\mathbf{H} + \mathbf{D}\cdot\mathbf{E}) + \tfrac{1}{2}\rho\left[H^2\frac{\partial \mu_e}{\partial \rho} + E^2\frac{\partial \epsilon}{\partial \rho}\right] \end{aligned}\right\} \tag{17}$$

and

$$dW_r = p_t d\left(\frac{1}{\rho}\right) - \mathbf{H}\cdot d\left(\frac{\mathbf{B}}{\rho}\right) - \mathbf{E}\cdot d\left(\frac{\mathbf{D}}{\rho}\right)$$

then only the mechanical contributions remain in Eq. (16) when ϵ and μ_e are constant. It can also be shown (Section III,A) that this is true even when ϵ and μ_e are variable; however, this result depends on the particular law by which these quantities are related to temperature and density. It should also be specified again that the momentum balance, Eq. (15), is also affected when ϵ and μ_e are variable, because of the entrance of electromagnetostrictive forces.

The remaining terms in Eq. (16) are the dissipative energy given by viscous dissipation and Joule heating, and the heat flux due to diffusion, conduction, and external sources. Using Eq. (10), we can therefore write for the energy equation

$$\rho\left[\frac{d\mathfrak{U}}{dt} + p\frac{d}{dt}\left(\frac{1}{\rho}\right)\right] = -\nabla\cdot\mathfrak{q} + \Phi + Q + \sigma(\mathbf{E} + \mathbf{V}\times\mathbf{B})^2 \tag{18}$$

where now $\mathfrak{U}$ and p are the ordinary state variables given by the first terms in Eq. (17), $\mathfrak{q}$ is the heat flux due to conduction and diffusion, and Φ the viscous dissipation $\tau_{ij}\partial u_j/\partial x_i$. The heat flux will be discussed further in Section II,E,1.

It is convenient at this time to present alternate forms of Eq. (18). For an incompressible fluid, $d\mathfrak{U} = c\,dT$, where c is the specific heat. Then Eq. (18) becomes

$$\rho c\frac{dT}{dt} = -\nabla\cdot\mathfrak{q} + \Phi + Q + j^2/\sigma \tag{19}$$

since the work due to compression is zero.

When the fluid is compressible, $d\mathfrak{U} = dh - d(p/\rho)$ so that Eq. (18) is written in terms of enthalpy as

$$\rho\frac{dh}{dt} = \frac{dp}{dt} - \nabla\cdot\mathfrak{q} + \Phi + Q + j^2/\sigma \tag{20}$$

This form is often useful in a dissociated or ionized gas. If we define the

stagnation enthalpy as $h_s = h + V^2/2$ in the usual manner, and eliminate the pressure term by using the momentum equation, then

$$\rho \frac{dh_s}{dt} = -\nabla \cdot \mathbf{q} + Q + (\Phi + \tau \cdot \mathbf{V}) + \mathbf{j} \cdot \mathbf{E} \tag{21}$$

and the stagnation enthalpy is increased by the power energy addition $\mathbf{j} \cdot \mathbf{E}$. This would be expected, for in the fluid at rest, $\mathbf{j} = \sigma\mathbf{E}$ and the ohmic heating does not vanish. When there is no electric field applied, the stagnation enthalpy is unchanged explicitly by the presence of the magnetic field, although magnetic effects enter implicitly through the viscous term. It is thus convenient to use Eq. (21) for compressible-flow problems when the applied electric field is zero, for example, at the stagnation point of a blunt body (Section VI).

One final equation is needed to complete the system hydrodynamically. This involves the magnetic field which appears in the ponderomotive-force term in Eq. (15) and the Joule heating term in Eq. (18). It is obvious that the magnetic field when applied to the fluid will alter the flow pattern through these coupling terms. In much the same manner, the fluid will react on the applied field through Ohm's law to relieve these forces. Thus the magnetic field which appears in the MHD equations is the resultant, or total magnetic field present in the fluid. Its behavior is determined by Faraday's law of induction, Eq. (2), from the total of currents acting in the system, including those, if any, which generate the applied field. Using Eq. (9), and letting $\mathbf{j}_0$ denote the current in an external solenoid, we can write for $\mathbf{B}$

$$\nabla \times \mathbf{B} = \mu_e \mathbf{j}_0 + \mu_e \sigma(\mathbf{E} + \mathbf{V} \times \mathbf{B}) \tag{21A}$$

where

$$\nabla \times \mathbf{E} = 0 \tag{22}$$

As it stands, Eq. (21A) contains the electric field and is not easy to solve. If, however, the gas is such that σ and ρ are constant, then the continuity equation, along with Eq. (22), may be used to give

$$(\mathbf{V} \cdot \nabla)\mathbf{B} = (B \cdot \nabla)\mathbf{V} + \frac{1}{\mu_e \sigma} \nabla^2 \mathbf{B} \tag{23}$$

where the conductivity of the coil has also been taken as constant.

Equation (23) determines the magnetic field in the fluid when σ and ρ are constant and illustrates the coupling which can exist between the hydrodynamic and electromagnetic fields. Fortunately, it is often possible to linearize the magnetic terms in the system of equations. This will become evident when the magnitude of these terms is discussed in Section II,D.

C. BOUNDARY CONDITIONS

The fluid and thermometric boundary conditions are unchanged by the addition of electromagnetic fields. For continuum flow the tangential and normal velocities vanish at solid boundaries, while the fluid temperature must be continuous.

The electromagnetic equations must be satisfied in the region outside the moving fluid. In this region, say, for example, in the walls of the container, it may be necessary to use the complete Maxwell equations. As we pass from the vacuum to the walls to the fluid, it will be necessary to satisfy the following conditions at the boundaries (*9*): the normal component of **B** is continuous and the tangential component of **E** is continuous. If there is a charge layer on the surface, the discontinuity in **D** is equal to the surface charge density, and if a surface current exists, then the discontinuity of the tangential component of **H** is equal to the current density at the surface. The latter condition of surface currents will not exist if the conductivity of both media are finite, in which case the tangential component of **H** is continuous. In some problems in MHD, however, it is often assumed that the conductivity of the walls is infinite in order to simplify the analysis of the problem. In this case, the first condition must be satisfied. Finally, everywhere in the vacuum, walls, and fluid, the conservation of charge for steady currents, $\nabla \cdot \mathbf{j} = 0$, demands that the lines of current density form closed loops. These loops may be closed outside the fluid by the use of electrodes and wires.

The induced magnetic field is often neglected in MHD flows, so that the boundary conditions for this component are rarely mentioned in the literature. Its value at the fluid boundary can be ascertained by considering the flowing fluid as a carrier of current sheets, each of which will generate a B-field. When the flow is symmetric, the induced magnetic field will be symmetric. It will not necessarily vanish at infinity unless the current acts as a line or point source. It is thus not possible to discuss the boundary conditions on the induced magnetic field without a consideration of the flow problem, which is a further coupling of the equations. For this reason we will present a more complete discussion of the induced field for several flow configurations (Sections IV,A,2, and V,A,1).

D. DIMENSIONLESS PARAMETERS

In ordinary fluid mechanics, dimensionless parameters which delineate flow regimes evolve from the transformation of the basic equations to dimensionless form. The same is true in MHD flows, where the magnitude of the electromagnetic parameters dictates the amount of interaction between the fields and the flow.

We will choose as reference conditions those constants which typify the flow in a designated problem. These will be given the arbitrary subscript o but they will, of course, depend on the particular problem under analysis. With the buoyant force included, the momentum equation becomes

$$\rho^* \frac{d\mathbf{V}^*}{dt} = -\nabla p^* + \frac{\mathrm{Gr}}{\mathrm{Re}^2}\theta + \frac{1}{\mathrm{Re}}\tau_{ij}^* + SK(\sigma\mathbf{E}^* \times \mathbf{B}^*) + S(\sigma\mathbf{V}^* \times \mathbf{B}^* \times \mathbf{B}^*) \quad (24)$$

where the starred quantities are now dimensionless; the pressure, p^*, is as usual referred to the dynamic pressure, $\rho_0 V_0^2$. The dimensionless temperature is

$$\theta = (T - T_1)/(T_2 - T_1) \quad (25)$$

where T_1 and T_2 are arbitrary constant temperatures. The air properties have been taken as variable for generality.

Most of the parameters in Eq. (24) are familiar. These are

$$Re = \frac{\rho_0 V_0 L}{\mu_0} = \text{Reynolds number} = \frac{\text{inertia force}}{\text{viscous force}} \quad (26)$$

$$Gr = \frac{\rho_0^2 g\beta(T_w - T_\infty)}{\mu_0^2} L^3 = \text{Grashof number} = \frac{\text{buoyant force}}{\text{viscous force}} \times \frac{\text{inertia force}}{\text{viscous force}} \quad (27)$$

where β is the coefficient of expansion and L is the characteristic length. The new parameters in Eq. (24) are

$$S = \frac{\sigma_0 B_0^2 L}{\rho_0 V_0} = \text{magnetic-interaction parameter} = \frac{\text{ponderomotive force}}{\text{inertia force}} \quad (28)$$

and

$$K = \frac{E_0}{V_0 B_0} = \text{generator (pump) coefficient} = \frac{\text{applied electric field}}{\text{induced electric field}} \quad (29)$$

The sign of K is determined by the direction of the applied field. It is negative when the applied field is in the opposite direction to the induced field. Both S and K determine the magnitude of the ponderomotive force in the general sense, for one can think of S as determining the induced ponderomotive force due to the interaction of the flow with the field and SK determining the applied force, which would act even if the

system were at rest. As such, in an inviscid flow, if either S or SK is larger than one, the velocity will be affected.

When viscous forces normally predominate, as in a boundary layer, either of the quantities $S\mathrm{Re}$ and $SK\mathrm{Re}$ should be of order one for the flow to be affected by the fields. The product $S\mathrm{Re}$ defines one of the most important parameters in MHD

$$S\mathrm{Re} = \frac{\sigma_0 B_0^2 L^2}{\mu} = \mathrm{M}^2 = \frac{\text{ponderomotive force}}{\text{viscous force}} \tag{30}$$

By convention, M is called the Hartmann number, although M^2 is certainly the more natural parameter (*10*).

Turning now to the energy equation, let us consider the compressible case. Equation (18) becomes, for a perfect nonreacting gas and an isothermal wall,

$$\rho^* \frac{d\theta}{dt} = \frac{-1}{\mathrm{PrRe}} \nabla \cdot (\hat{\mathbf{q}}^*) + \frac{\varepsilon}{\mathrm{Re}} \Phi^* + \varepsilon Q^* + \mathbf{V}^* \cdot \nabla p^* + \varepsilon S\{\sigma(K\mathbf{E} + \mathbf{V}^* \times \mathbf{B}^*)^2\} \tag{31}$$

where $Q^* = QL/\rho_0 V_0^3$ is a dimensionless heat source. The usual parameters in Eq. (31) are

$$\mathrm{Pr} = \frac{\mu_0 C_{p_0}}{k_0} = \text{Prandtl number} = \frac{\text{energy dissipated}}{\text{energy conducted}} \tag{32}$$

$$\varepsilon = \frac{V_0^2}{C_{p_0}(T_2 - T_1)} = \text{Eckert number} = \frac{\text{kinetic energy}}{\text{thermal energy}} \tag{33}$$

The others are defined above.

The Joule dissipation term in Eq. (31) will vanish only if

$$K\mathbf{E}^* = -\mathbf{V}^* \times \mathbf{B}^*$$

i.e., only if the electric field as seen by an observer moving with the velocity $\mathbf{V}^*$ *vanishes.* It is difficult to determine a priori when the Joule dissipation will contribute significantly to the temperature distribution and the heat transfer at the wall. In general, however, when an electric field is applied, the term is not negligible. In fact, even when $K = -1$, which corresponds to the case of electrically insulated walls, the Joule dissipation is not negligible. This is a result of the fact that when $K = -1$, the mean current vanishes, but there remain circulating currents $\sigma^*\mathbf{V}^* \times \mathbf{B}^*$ which can influence the heat transfer (Section IV,A,3).

So far we have not mentioned the influence of the hydrodynamic flow on the magnetic field. In order to determine this, consider Eq. (23), remembering that both σ and ρ are constant. In dimensionless form, this

equation becomes

$$(\mathbf{V}^* \cdot \nabla)\mathbf{B}^* = (\mathbf{B}^* \cdot \nabla)\mathbf{V}^* + \frac{1}{\sigma_0 \mu_e V_0 L} \nabla^2 \mathbf{B}^* \tag{34}$$

Equation (34) indicates the magnitude of the induced field—i.e., the amount of bending of the applied field lines by the flow. The dimensionless parameter in Eq. (34) is

$$\mathrm{Re}_m = V_0 L \sigma_0 \mu_e = \text{magnetic Reynolds number} \tag{35}$$

in which $1/\sigma_0 \mu_e$ can be thought of as a "magnetic kinematic viscosity."

Notice that Eq. (34) is remarkably similar to the vorticity equation. (Imagine that B* is replaced by Ω.) The magnetic Reynolds number acts in the same way a Reynolds number does: when Re_m is zero the field lines are undisturbed by the flow, but when $\mathrm{Re}_m \to \infty$ the lines are frozen into the fluid. The induced magnetic field vanishes when $\mathrm{Re}_m = 0$, and the motion equations can be solved independently from Maxwell's equations. This is a strong assumption to make, but it is useful since first-order influences of magnetic forces still are included.

Let us assume that $\mathrm{Re}_m \ll 1$ so that the induced field $\mathbf{B}_i$ is much less than the applied field **B**. This corresponds to a weak interaction, which is often the case in engineering MHD. Then the ponderomotive-force term in Eq. (15) is determined by $\mathbf{B}_0$ alone, where the current depends only on the applied field. Equation (23) or (34) become superfluous, since the induced field can be determined from Eq. (2) and Ohm's law. It is often useful to find $\mathbf{B}_i$ when $\mathrm{Re}_m \ll 1$ in order to verify that the assumption is justified.

E. TRANSPORT PROPERTIES

In order to determine the heat transfer, suitable assumptions will have to be made to account for the variation of transport properties of the various working fluids. For liquid metals such as mercury or sodium the transport properties are well-established and are tabulated in most handbooks. It is not possible to make such a definitive statement about ionized gases. Only the electrical conductivity has been measured at high temperatures; for the remainder of the transport properties, it is necessary to rely on calculations. It should be mentioned again that when the magnetic field strength is large, the possibility exists that the transport coefficients will be nonisotropic, as discussed in Section I,B, in which the Hall current was defined. We will, however, only be concerned here with cases where the transport properties are scalar.

Since gases other than ionized air will be encountered in this article, we do not have space to present values for the various transport properties.

The literature cited in this section will provide a guide, if not a definitive answer, to the problem of their determination.

1. The Heat-Flux and Thermodynamic Coefficients

The heat flux, $\mathbf{q}$, in Eq. (18) consists of heat conducted through the fluid element and chemical heat transported by diffusion of the reacting species. In accordance with kinetic theory (*14, 15*), we may write

$$\mathbf{q} = -k\nabla T + \sum_{k=1}^{n} \rho_k h_k \mathbf{V}_k \tag{36}$$

where k is the coefficient of thermal conductivity (usually referred to as the "frozen" conductivity) and ρ_k, h_k, and $\mathbf{V}_k$ the density, specific enthalpy, and diffusion velocity of the kth species, in an n-species gas. In writing Eq. (36) we have neglected thermal diffusion and pressure gradients, as is usually done. Evaluation of the second term in Eq. (36) is exceedingly difficult unless the mixture is a simple binary gas.

For a binary nonionized gas, Fick's law gives

$$\rho_k \mathbf{V}_k = -\rho D_{12} \nabla c_k, \quad k = 1, 2 \tag{37}$$

where c_k is the mass-fraction concentration of the kth species and D_{12} is the binary-diffusion coefficient. A Lewis number can be defined as

$$\mathrm{Le} = \frac{\rho D_{12} \overline{C_p}}{k} \tag{38}$$

where $\overline{C_p}$ is the average specific heat. Using the above definition, Eq. (36) can be written

$$\mathbf{q} = -k\nabla T \left\{ \rho D_{12} \left(1 - \frac{1}{\mathrm{Le}} \right) \sum_{k=1}^{2} h_k \nabla c_k \right\} \tag{39}$$

The Lewis number thus determines the amount of heat transported by diffusion. When Le = 1, the heat flux is independent of the diffusing species.

For a multicomponent nonionized mixture one can assume (*14*) that the various D_{kl} are similar and use an average diffusion coefficient. This cannot be done when the gas is ionized or not in thermal equilibrium because the electrons then have a higher diffusion velocity than all the other particles.

The transport coefficients k, μ, and D_{kl} are difficult to determine for a multicomponent, reacting, partially ionized gas. Calculations have been made, using the standard techniques of kinetic theory, but these differ in their results because of various assumptions made as to the collision cross

sections. It is felt that calculations using the low-temperature cross sections, for example, (*14*) or (*15*), are as reliable as any others at the present time. A good summary of all high-temperature transport properties is given in (*16*). One remark should be inserted here about the diffusion coefficients, however.

2. Diffusion in Ionized Gases

In high-temperature air, good agreement between theory and experimental values of heat transfer in the absence of applied fields has been found when the gas is assumed to be a binary mixture such that D_{kl} is the binary-diffusion coefficient. The Lewis number assumes values (*17*) near Le $\sim$ 1.4 for $T \leq 9000°$K. For other mixtures at high temperatures where measurements are not available, a kinetic-theory approach such as that described in (*14*) is adequate.

The theory of (*14*) considers an unbounded medium where the diffusion of electrons and ions takes place independently, i.e., free diffusion. It was pointed out in Section I,B,1, that this is not possible near a boundary where concentration gradients will lead to gross space charge if the ions and electrons move at different velocities. The kinetic theory of a partially ionized three-component gas is given in some detail by Finkelnburg and Maecker (*15*), but it is too lengthy to reproduce here. It can be shown, however, that in the absence of strong normal electric fields the diffusion of charged particles (as a group) to the wall obeys essentially the same law as does the binary gas of Eq. (39). In the presence of strong fields the electrons are accelerated to very high thermal velocities, and the gas is unlikely to be in thermodynamic equilibrium.

3. Electric Conductivity

The electric conductivity, which determines the heat transport in an indirect manner, is one of the best-defined of the transport properties because it is relatively easy to measure.

When Hall effects are not considered, σ is a scalar function of temperature and density. Lamb and Lin (*18*) have measured σ for high-temperature air at various pressures. Among others, Brunner (*8*) has calculated σ for air when Hall effects and ion slip are important; his equations are based on kinetic theory and are hence applicable to other gases. In many cases it is desirable to seed the gas with some low-potential ionizing agent; Brunner's methods also apply in this case and he has calculated σ for air seeded with 1% potassium.

The natural variation of σ with temperature (or degree of ionization) follows an easily remembered pattern. For degrees of ionization less than

0.1%, σ is an exponential function of T, rising rapidly; as the ionization exceeds this value, $\sigma \sim T^{3/2}$.

F. RÉSUMÉ

Before embarking on a survey of the classical MHD heat-transfer problems, let us summarize briefly the following pertinent facts which have emerged from this section.

First, the ponderomotive force $\sigma(\mathbf{V} \times \mathbf{B}) \times \mathbf{B}$ which is caused by the interaction of the magnetic fields and the velocity always acts in a direction which will decelerate the flow. We may therefore expect an increase in drag (considered as, say, "magnetic" drag) whenever the ponderomotive coefficient S is greater than 1. Conversely, the friction drag would decrease because the velocity is lower.

The ponderomotive force due to the applied electric field $\sigma\mathbf{E} \times \mathbf{B}$ will accelerate the flow if $\mathbf{E}$ is opposite in direction to the induced electric field $\sigma\mathbf{V} \times \mathbf{B}$. Otherwise, it will decelerate the flow whenever SK is greater than 1.

The deceleration of the flow will always cause a decrease in heat transfer if the Joule dissipation term is zero. This term vanishes only when $\mathbf{E} = -\mathbf{V} \times \mathbf{B}$, or, equivalently, when $\nabla \times (\mathbf{V} \times \mathbf{B}) = 0$. For an incompressible fluid this reduces to the condition that

$$(\mathbf{B} \cdot \nabla)\mathbf{V} = (\mathbf{V} \cdot \nabla)\mathbf{B}$$

i.e., a condition which depends on the geometric relation of the velocity and field which cannot be determined a priori. When an electric field is applied the Joule heating is, in general, significant.

The magnetic field will have no explicit effect on the stagnation enthalpy when the applied electric field is zero. It will, however, affect the magnitude of the viscous dissipation and should cause a reduction in heat transfer since the friction drag is less, although one would not expect, a priori, Reynolds' analogy to apply in MHD flow.

The magnetic field induced by the current $\mathbf{J} = \sigma(\mathbf{E} + \mathbf{V} \times \mathbf{B})$ will be generally assumed to be zero in most problems discussed here. To be neglected, however, its magnitude should be small in comparison with both the applied field and other forces in the momentum equation.

The parameters of most importance in this analysis are the interaction parameter, S, the Hartmann number, M, and the generator coefficient, K. Other parameters will arise during the course of the investigation, some in conjunction with a special flow configuration. Others, which are pertinent to ordinary heat transfer (Nusselt number, Stanton number), are not changed in definition by the electromagnetic field.

We will henceforth be discussing flows in which the Reynolds number is moderate (laminar flow), and the magnetic Reynolds number is small. Equations (11), (15), (18), and (23), or their dimensionless counterparts, constitute the basic set of equations, along with an equation of state, transport properties, and boundary conditions.

When boundary-layer problems are considered, the above equations, with the exception of the additional MHD terms, will assume their usual forms in the boundary-layer approximation. The methods of solving the MHD boundary-layer equations are straightforward. Techniques involving similar solutions or series expansions are employed just as in the field-free case. Because the reader is assumed to be familiar with such procedures, these solutions are not discussed in detail.

III. Free Convection

Among the classical hydrodynamic flows which already contain a body force are those associated with natural convection. When MHD became a popular subject, it was only normal that these flows be investigated with the additional, ponderomotive, body force as well as the buoyant force. At first glance there seems to be no practical application for these MHD solutions, for most heat exchangers utilize liquids whose conductivity is so small that prohibitively large magnetic fields are necessary to influence the flow. But some nuclear power plants employ heat exchangers with liquid-metal coolants, so the application of moderate magnetic fields to change the convection pattern appears feasible.

Another classical natural convection problem is the thermal instability which occurs in a liquid heated from below. This subject is of natural interest to geophysicists and astrophysicists, although some applications might arise in boiling heat transfer.

Before these topics are discussed, it is worthwhile to mention another free-convection problem in which electric forces, rather than the usual MHD forces, play a significant role.

A. Free Convection in Electrostatic Fields

The ponderomotive force is by no means the most important of the electromagnetic forces in free convection. It was pointed out in Section II,A, that the electrostrictive forces would be neglected in this treatment of MHD flows because they were small. This is not necessarily true in a heated, low-velocity fluid subjected to an electric field. In liquids or gases with polar molecules, for example, the dielectric susceptibility will depend on both the density and the inverse power of temperature, so that the resulting force due to an electric-field gradient behaves much like the buoyancy force in pure convection.

The electrostrictive effect was first noticed by Senftleben and Braun (*19*) in 1936. They were studying the free convection of gases in a horizontal cylinder with a heated wire placed along the cylinder axis. When an electric field was applied between the wire and the cylinder, the heat-transfer rate increased by as much as 50% if the working fluid was paraelectric (i.e., the molecules carry a permanent dipole moment). Theoretical predictions of the Nusselt number, based on similarity arguments, were found to be inadequate when later workers extended the experimental domain. Studies recently made at Purdue University (*20*) determined the Nusselt number semianalytically and found that the increase in Nusselt number due to the electrostrictive force was a function of the Prandtl number, the Grashof number, the Senftleben number, and an empirical constant depending on the ratio of wire to cylinder diameters. The Senftleben number behaves in much the same way as the Grashof number of Eq. (27); if the gravitational force g is replaced by $\gamma E_s^2/d$ one obtains the Senftleben number. Here γ specifies the temperature dependence of the electric susceptibility, E_s is the electric field at the surface of the wire, and d is the wire diameter. The analytic results compare well with the experiments when the product (Senftleben) (Grashof) is small; the comparison is better for gases than in liquids. It is also shown in (*20*) that the energy equation retains its usual form [Eq. (18)] if the electric susceptibility and magnetic permeability are given by the Debye theory.

Other electrostatic effects have been noticed in the natural convection of a liquid in strong electric fields. For example, Schmidt and Leidenfrost (*21*) found that the heat transfer in certain nonconducting oils (paraffin, beeswax, and castor oil) was greatly increased when an electric field was applied. These increases could not be attributed to the electrostrictive effect, but were shown to result from the formation of electrically charged "balls" of fluid which wandered in an irregular manner between the electrodes. An electrohydrodynamic model of this phenomenon does not presently exist, but one would suspect that the oil became charged through friction and that the electrostatic body force contributed to the peculiar convection patterns which evolved.

The essential element in considering these usually neglected forces is their magnitude in comparison to the inertia and shear terms in the momentum equation. In a forced convection flow these forces would be too small in magnitude to ever influence the flow.

B. THERMAL INSTABILITY

Cowling (*22*) attributes to Walén the idea that a magnetic field will inhibit the onset of convection in a liquid heated from below. The

principle, for a high magnetic Reynolds number, is that when convection tends to bend the magnetic-force lines, the associated tension $\mu_e H^2$ leads to a volume force opposing any further bending.

Lehnert and Little (*23*) gave a striking demonstration of the ability of the applied field to arrest the formation of convection cells, a demonstration in which both a pure-conduction region and a cellular-convection region appeared in the same liquid. This was made possible by placing a container of heated liquid mercury on the edge of the magnetic pole piece so that part of the liquid was in a normal field and part was in an oblique field. The liquid subjected to the strong vertical magnetic field remained stable, while the other portion exhibited typical Benard cells.

The theory of thermal stability for a wide variety of configurations was developed by Chandrasekhar (*24*), who showed that the critical Rayleigh number at which convection first occurs is a function only of the boundary conditions at the surface of the heated liquid and the Hartmann number defined as

$$\mathrm{M} = B \cos \theta d \sqrt{\frac{\sigma}{\mu}} \tag{40}$$

where d is the depth of the liquid and θ is the angle of incidence between the magnetic field and the liquid surface. The critical Rayleigh number was found for three cases of a horizontal layer heated from below in a transverse field: (a) both surfaces free, (b) one free, one rigid, (c) both surfaces rigid. In all cases as $\mathrm{M} \to \infty$, $\mathrm{Ra}_c = \pi^2 \mathrm{M}^4$, where the Rayleigh number is defined in the usual sense as $\mathrm{Ra} = (\mathrm{Pr})(\mathrm{Gr})$.

Chandrasekhar's theory was verified for $\mathrm{M} > 10$ and case (c) by Nakagawa, who performed a series of experiments (*25*, *26*, *27*, *28*) with various magnets. Although the upper surface in Nakagawa's experiments was "free," a contaminant film that prevented any motion of the surface formed on the surface of the heated mercury. The data from Nakagawa's experiments are given in Fig. 1 with the theory for rigid boundaries and the asymptotic prediction. Figure 1 shows good agreement over a wide range of Hartmann numbers and liquid-layer depths, although there is some divergence for $d = 0.06$ m.

The region to the left of the curve in Fig. 1 is unstable. For $\mathrm{M} = 0$, $\mathrm{Ra}_c = 1708$, so that an appreciable increase is gained in the maintenance of a pure conduction mode by the application of even moderate magnetic fields. Even after convection is established, the magnetic field influences the transport of heat in a favorable manner. This was predicted and experimentally verified by Nakagawa (*28*, *29*), who established that the convective heat transport is characterized by a linear function of the temperature difference between the upper and lower surfaces, at least for

values of Rayleigh number near Ra_c and for large values of the Hartmann number. This relationship can be written in terms of the Nusselt number as

$$\mathrm{Nu} = 1 \quad (\mathrm{Ra} < \mathrm{Ra}_c)$$

$$\mathrm{Nu} = 1 + C\left(1 - \frac{\mathrm{Ra}_c}{\mathrm{Ra}}\right) \quad (\mathrm{Ra} > \mathrm{Ra}_c) \tag{41}$$

where the Nusselt number for the pure-conduction mode was normalized

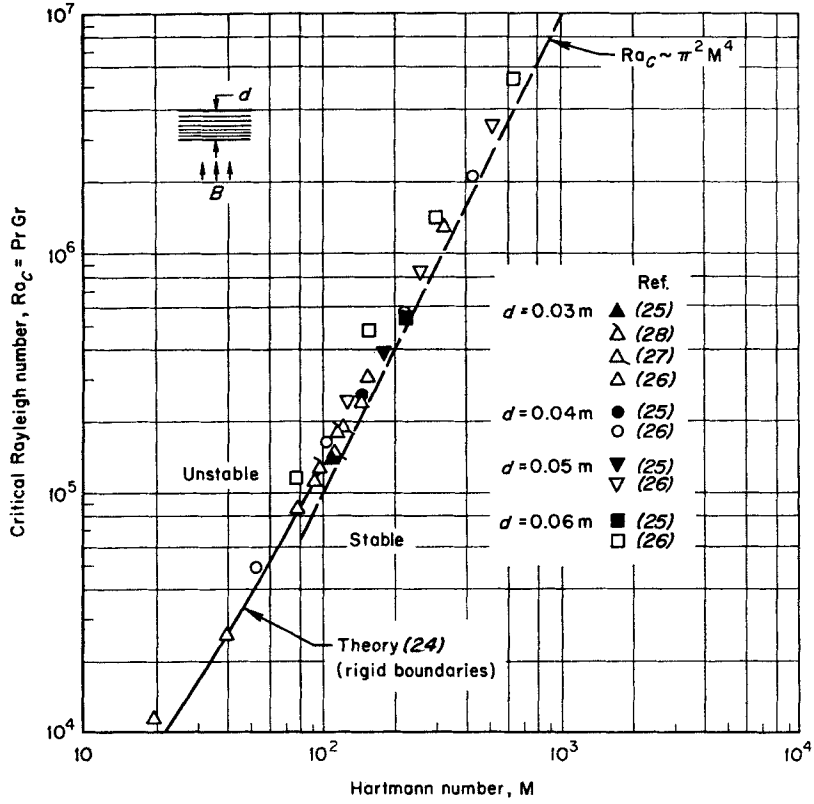

FIG. 1. Variation of critical Rayleigh number with Hartmann number for liquid mercury heated from below.

for convenience by Nakagawa to eliminate the dependency on Rayleigh number. We have plotted the factor C in Fig. 2 as a function of Hartmann number; Figs. 1 and 2 permit Eq. (41) to be evaluated for any given magnetic field.

The experimental agreement with Eq. (41) is best for M > 100; below that value, the observed heat transport is less efficient than the relation indicates. This is attributed by Nakagawa to the fact the the convection cells are larger for small values of M, and that the development of the amplitude of convection might be delayed by frictional effects in the experiment (the liquid layer was only 0.03 m deep). For large values of the Hartmann number, the magnetic field decelerates motion normal to it

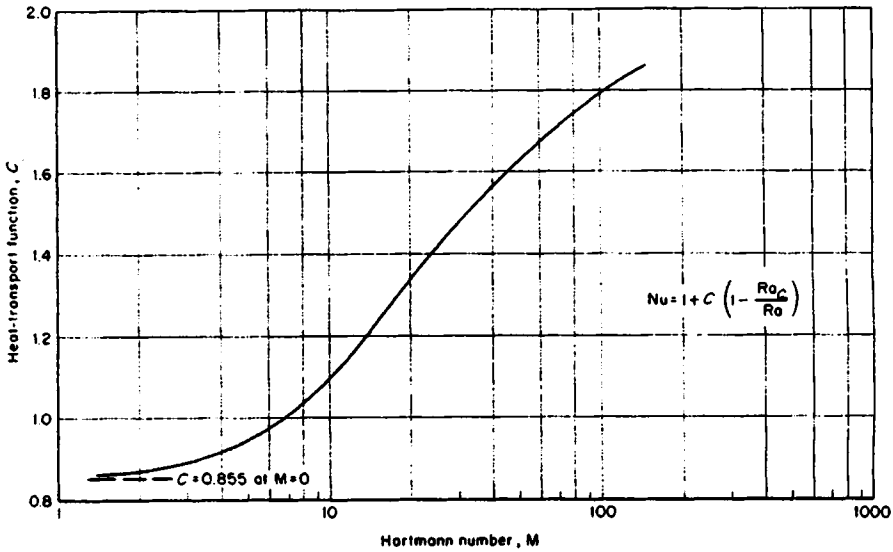

FIG. 2. Theoretical variation of convective-heat-transport function with Hartmann number for a liquid heated from below (*29*).

and stretches out the convection cells longitudinally, hence permitting a more efficient transport of heat in the upward direction.

C. SEVERAL NATURAL CONVECTION FLOWS

1. Heated Vertical Plate

Among the many geometries associated with classical natural convection flows is the heated vertical plate. Here, the heat from the surface is transferred to the fluid, which causes a decrease in the fluid density and a subsequent flow upward due to buoyant forces. When a magnetic field is applied normal to the plate, the ponderomotive force will act in a downward direction to inhibit the flow and to reduce the heat transfer to the fluid.

The basic equations of Section II,B, indicate that this problem is rather formidable if the momentum, energy, and magnetic equations remain coupled. In practice, assumptions are made which facilitate the solution. These are

(a) The magnetic Reynolds number is small
(b) Viscous and Joule dissipation are neglected
(c) The fluid is semiincompressible: the density is constant except in its contribution to the buoyant forces; the fluid thermodynamic properties are constant
(d) The applied electric field is zero

Assumption (a) uncouples the momentum and magnetic equations; assumptions (b) and (c) uncouple the momentum and energy equations; assumption (d) is physically realistic for a single plate.

The assumption that $\mathrm{Re}_m = 0$ is probably more justified in free-convection flow than for any other case discussed in this article. This occurs because the velocity is much lower. Poots (*30*) has shown for the free-convection flow between heated vertical plates that when

$$B_0 = 0.0384 \text{ weber/m}^2 \text{ (384 gauss)}$$

the induced field is less than the value of the earth's magnetic field! Since this field is neglected in all practical MHD problems, it seems justified to ignore the effect of the induced field in the momentum equation even for strong applied fields.

The generalized conditions under which it is possible to neglect viscous and Joule dissipation have already been discussed in Section II,D. For the mean viscous dissipation to be unimportant, the Eckert number must be small. This is certainly true in a low-velocity heated fluid. The mean Joule dissipation is small when $\mathrm{M}^2(K+1)^2 < 1/\varepsilon$. If the system is short-circuited to satisfy the electromagnetic boundary conditions, then $\mathrm{M}^2 < 1/\varepsilon$, which is again true for relatively high magnetic fields. Finally, assumption (c) is generally made for natural-convection flows, and there is no reason to disregard it now that magnetic fields are present.

We should say a word about the boundary conditions in this type of flow. First, the usual thermofluid-dynamic conditions of continuity and no slip will hold. As far as the electromagnetic conditions are concerned, when no electric field is applied only the induced current will be present. It will flow in closed loops transverse and parallel to the plate. Continuity will be established only a infinity, although in practice a short circuit could easily be arranged. The applied magnetic field will have only the normal component, which must satisfy Maxwell's equations.

Under these assumptions, Eqs. (11), (15), and (18) can be written in terms of the plate length and conditions at the edge of the layer as

$$\frac{\partial U}{\partial X} + \frac{\partial V}{\partial Y} = 0 \tag{42}$$

$$U\frac{\partial U}{\partial X} + V\frac{\partial U}{\partial Y} = \frac{\mathrm{Gr}}{\mathrm{Re}^2}\theta + \frac{1}{\mathrm{Re}}\frac{\partial^2 U}{\partial Y^2} - U\left(\frac{B}{B_0}\right)^2 S \tag{43}$$

$$U\frac{\partial \theta}{\partial X} + V\frac{\partial \theta}{\partial Y} = \frac{1}{\mathrm{PrRe}}\frac{\partial^2 \theta}{\partial Y^2} \tag{44}$$

where $X = x/L$ is along the plate and $Y = y/L$ is normal to it. The reference conditions on temperature are the adiabatic temperature and the wall temperature. Equations (42–44) are of the usual thermal-boundary-layer type with the exception of the additional force terms for the electromagnetic fields. Equations of this sort are generally solved by a series expansion when B is constant or by application of the method of similar solutions. In this case $B(x)$ must vary in a manner specified by the similarity transformation. (See Section III,C,1.)

a. Constant Magnetic Field. Sparrow and Cess (*31*) obtained a solution by series expansion in powers of the parameter ΛX^2, when B_0 is constant, where

$$\Lambda = \frac{2\mathrm{M}^2}{\sqrt{\mathrm{Gr}}} = \frac{\text{ponderomotive force}}{[\text{buoyant force} \times \text{inertia force}]^{1/2}} \tag{45}$$

This parameter, which has been called the Lykoudis number, will generally be of order one, depending on the magnetic-field strength, since the Grashof number must be of order (Reynolds number) for the buoyant forces to induce convection.

Their results for heat transfer can be written in terms of the mean Nusselt number over the plate

$$\frac{\overline{\mathrm{Nu}}}{(\mathrm{Gr})^{1/4}} = \frac{\overline{\mathrm{Nu}_0}}{(\mathrm{Gr})^{1/4}} - 0.3145\theta_1'\Lambda \tag{46}$$

where $\overline{\mathrm{Nu}_0} = -0.404\theta_0'\,(\mathrm{Gr})^{1/4}$ is the mean Nusselt number without a magnetic field, and θ' is the temperature gradient at the wall. Solutions were obtained for Pr = 10, 0.72, and 0.02. The first two values correspond to, say, electrolytic solutions and partially ionized air, and the last to liquid metals and highly ionized air. The conductivity for electrolytes (e.g., salt water) is on the order of 10 mho/m, while that for liquid mercury is about 10^6 mho/m. It is evident that very large magnetic fields (on the order of 1 weber/m^2 or 10^4 gauss) would be necessary in the case of salt water if the parameter Λ is to be on the order of one.

We have plotted Eq. (46) in Fig. 3 for Pr = 0.72 and 0.02, along with another solution of this problem, which will be discussed shortly. It is obvious from Fig. 3 that the magnetic field reduces the heat transfer to the fluid and inhibits the growth of convection. In fact, if M is large enough, Nu = 0, which would imply that the magnetic field has effectively stopped convection. The solution for $\Lambda \gg 1$ may be invalid because of the series truncation in Eq. (46).

b. Variable Magnetic Field; Similar Solutions. It is of interest to compare this solution with one in which the field varies along the plate. A variation in B could be imposed arbitrarily, like the experiment by

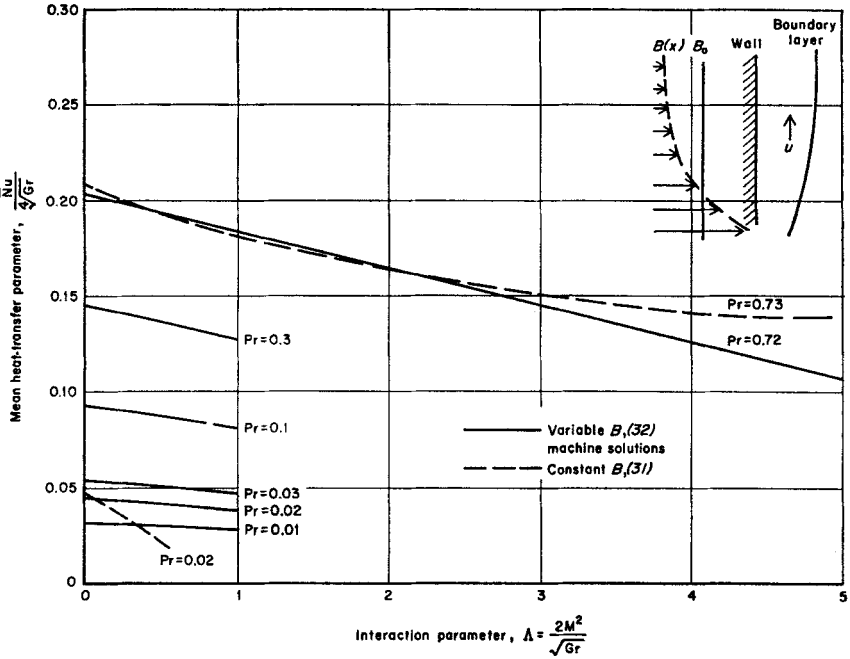

FIG. 3. Variation of the mean heat transfer with magnetic field for a heated vertical plate, showing the effects of Prandtl number and two different field configurations.

Lehnert (*23*) for demonstrating convection patterns. More often, however, the field is made variable because the governing equations cannot be solved in closed form unless $B = B(x)$.

Lykoudis (*32*) derived the conditions on n for $B = B_0(x)^n$ such that Eq. (43) will have similar solutions (i.e., will be independent of x under a similarity transformation). He showed that it is necessary for $n = -\frac{1}{4}$ in order that the free-convection case may become independent of x. Gupta (*33*) obtained a similarity solution using integral methods.

The technique of obtaining similar solutions to the momentum equation is used quite often in ordinary fluid mechanics. Its application to MHD problems follows a tradition of somewhat unfortunate impositions on the boundary conditions which cannot always be simulated in practice. For example, the similar solutions to boundary-layer mass-transfer problems demand that the wall velocity vary as $x^{-\frac{1}{2}}$, which is not successfully met experimentally with a uniformly porous plate except far downstream from the leading edge. When similar solutions are obtained for the MHD case, the applied magnetic field must also vary in a way which may be difficult but not impossible to meet experimentally.

Even more important, the use of similar solutions in MHD, which is also discussed in Sections V and VI, has aroused some criticism because the magnetic field does not satisfy Maxwell's equations. To be sure, Eqs. (2–5) are not satisfied exactly when $B = B(x)$ alone, but neither are they satisfied exactly when the induced field is neglected. By proper design of the magnet the variation in B normal to the plate can be made small and, *in the mean*, it can be said to vanish, which is a valid approximation to Maxwell's equations in the same manner by which an integral method can be used to satisfy the boundary-layer equations. The same comment applies to the neglect of the induced field in the fluid, for that also approximates Maxwell's equations in much the same sense that the boundary-layer equations are an approximation to the Navier-Stokes equations.

Again we will be interested in solutions for low Prandtl numbers. Lykoudis obtained both analytic and machine solutions for the heat transfer when $0.01 \leq \mathrm{Pr} \leq 0.73$. We have shown the results of his machine calculations in Fig. 3. It appears that the mean heat transfer is not reduced so much, or the flow decelerated so effectively, when the magnetic field is variable. This is especially true at low Prandtl numbers and $\Lambda' \leq 1$, which is the region of most validity of the series solution of (*31*).

Sparrow made a comparison of the local heat transfer, $\mathrm{Nu}(x)$, at a given station for these two solutions under the condition that the local magnetic fields were the same at the station under consideration. He found that the local heat-transfer coefficients were in close agreement for all values of ΛX^2 up to and including unity, basing his comparison only on the data available to him for $\mathrm{Pr} = 0.73$. For higher values of ΛX^2, the results of the constant field solution were lower. He attributed this deviation to either upstream influence or, perhaps, to the series approximation made in his solution. Figure 3 indicates that the deviation is most likely due to upstream influence which becomes more important as the Prandtl number decreases, i.e., as the boundary layer becomes more transparent to heat. On a physical basis, this difference might be due to the fact that the large

magnetic field at the leading edge of the plate has little effect on the heat transfer to the fluid because the velocities there are so low. Farther up the plate, where velocities have increased, the magnetic field strength has dropped below the constant value assumed by Sparrow, and the ponderomotive force is again less than it would be for the constant-field case. The upstream heat transfer is therefore greater than that calculated for the constant magnetic field, and the net heat transfer to the fluid is larger.

2. Convection Between Parallel Vertical Plates

A slightly more complex situation arises when the flow between two heated plates is examined, since an additional parameter (the wall-temperature difference) enters. However, this geometry permits a one-dimensional flow problem to be studied. Poots (*30*) has made an exhaustive analysis of this case, including the Joule heating, viscous dissipation, and internal heat sources in the energy equation. Gershuni and Zhukhovitskii (*34*) have treated the situation where the walls were at equal temperatures, but did not include the dissipation terms in their analysis.

In Poots' investigation, the parallel plates are combined with electrically insulated walls to form a channel. The induced current will then flow in closed loops parallel and transverse to the plates as long as an electric field is applied to the walls so that the mean current flow across the plates is zero. This condition implies that the induced magnetic field vanishes at the vertical plates, an implication which is consistent with the boundary conditions discussed in Section II,C. The configuration is identical to that of the Hartmann channel-flow problem discussed in Section IV,A. The heat transfer depends, in his study, on four parameters:

$$\lambda = \frac{T_{w1} - T_\infty}{T_{w2} - T_\infty}, \text{ the plate-temperature-difference ratio}$$

$$Q^* = \frac{Qa^2}{k(T_{w2} - T_\infty)}, \text{ the dimensionless heat source}$$

$$\mathrm{M} = B_0 a \sqrt{\sigma/\mu}, \text{ the Hartmann number}$$

$$\kappa = \mathrm{PrGr}\frac{\beta g a}{C_p}, \text{ a dimensionless heating parameter where } a \text{ is the distance between the plates.}$$

(The difference between these numbers and those of Section II,D, evolves from a different dimensional analysis.) A series expansion was made in powers of κ; for liquid mercury or sodium this is reasonable, for although $\mathrm{Pr} \cdot \mathrm{Gr}$ is generally large, the coefficient $\beta g a/C_p$ is small so that $\kappa \leq 0(1)$.

Poots verified that the trends for M = constant were the same as for the magnetic-free case: an increase in λ or Q^* increased the mass flow and temperature; and the viscous dissipation affected the velocity and temperature; profiles, for as κ increased (λ, Q^* constant), the velocity increased and the heat transfer to the fluid was altered. By letting λ, Q^*, and κ

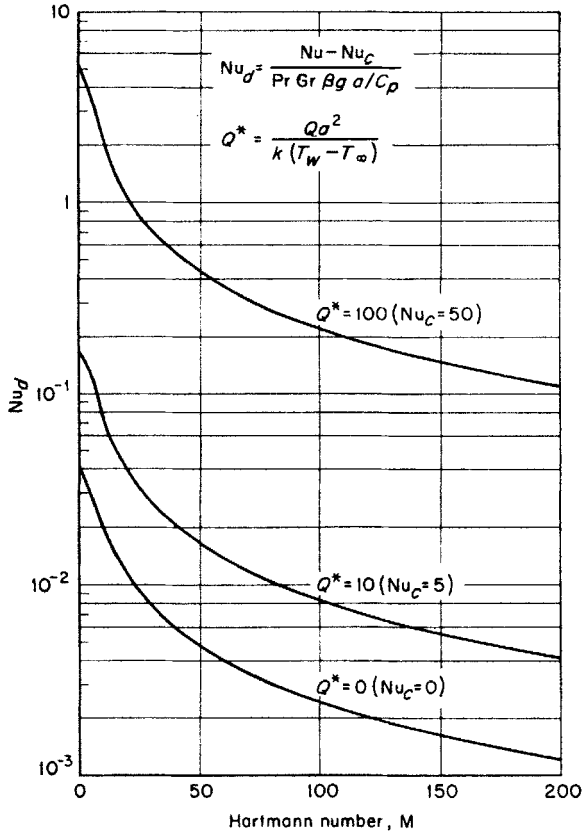

FIG. 4. The reduction in dissipative heat transfer with increase in magnetic fields for plates of equal temperature (*30*).

remain fixed, and by varying M, he showed that the velocity and temperature were reduced, due to the downward ponderomotive force. Numerous tabulated results for heat transfer and mass flow are given in (*30*) for various λ, Q^*, κ, and M. They indicate that for moderate values of κ the dissipative terms in the heat-transfer equation can be neglected, especially as M increases.

This trend is quite apparent in Fig. 4, where we have plotted the dissipative portion of the total heat transfer as a function of Hartmann

number and internal heat load for the case of plates at equal temperatures. The Nusselt number in Poots' analysis

$$\mathrm{Nu} = \mathrm{Nu}_c + \kappa \mathrm{Nu}_d + 0(\kappa^2) \tag{47}$$

consists of that due to pure conduction, $\mathrm{Nu}_c(Q^*, \lambda)$, and that due to dissipation, $\mathrm{Nu}_d(Q^*, \lambda, \mathrm{M})$. Since Nu_c can be quite large ($\mathrm{Nu}_c \sim 50$ for $Q^* = 100$) and κ is on the order of one, the heat transfer is primarily due to conduction, even at $\mathrm{M} = 0$.

It is not possible to make any general comparisons between the solutions of Section III,C,1 and the tabulated values for $\lambda \neq 1$ provided by Poots. This is due to the fact that the solutions of Section III,C,1, assumed that the applied electric field was zero, while Poots' solution is for the insulated case, where $E = -\sigma \bar{u} B_0$, and where $\bar{u}$ is the mean velocity in the channel.

3. Other Solutions

Poots (*30*) also considered a problem which has no classical fluid-dynamic analog; that is, the problem of natural convection in a horizontal tube in which an axial current is flowing (see Fig. 5). The equations

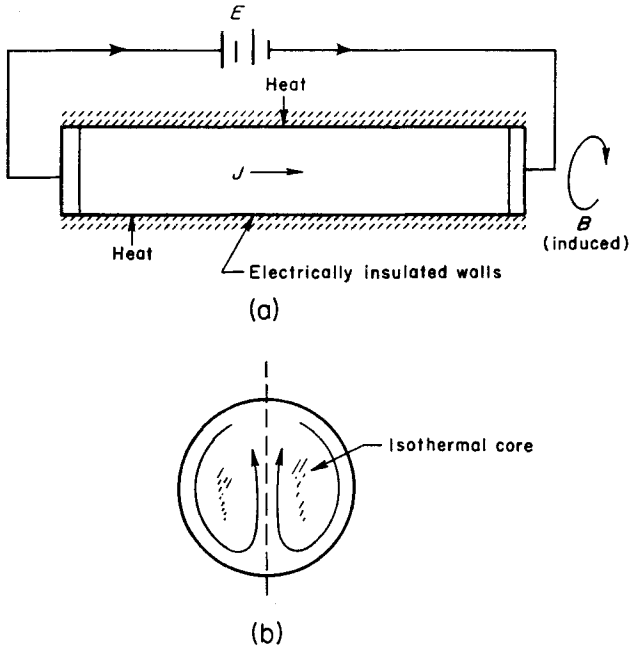

FIG. 5. Free convection in a horizontal tube in an electrostatic field; (*a*), Electromagnetic configuration; (*b*), Convection pattern.

for the central portion of the tube are the same as for the vertical plates with $Q^* = 0$; the electromagnetic field is identical with that for an infinitely long cylindrical current-carrying wire. He again employed a series-expansion technique and found that the 0th order solution gave a temperature distribution and magnetic field identical to the classical Joule heating problem in a long cylindrical wire. But in a fluid the temperature gradients induce a nonuniform motion which modifies the current density and field structure in a manner shown in Fig. 5. These cells would be set up, as κ increases, so that an isothermal core would exist with flow traveling up the center and around the side in a boundary layer. Whether or not this flow is stable was not discussed. It should also be mentioned that in this particular problem the electrostrictive forces may become important (see Section III,A).

Cramer (*35*) has investigated the free-convection flow in a vertical isothermal pipe in a transverse field, but he does not discuss heat transfer explicitly. Lu (*36*) examined free-convection flow past a porous plate with suction; but again the heat transfer is not given in easily accessible form. Reeves (*37*) has inspected qualitatively the combined effects of nonuniform wall temperature and magnetic field on the heated vertical plate. Mori (*38*) also solved the vertical-plate problem, but there appears to be an error in the governing differential equations (*32*).

D. CONSEQUENCES AND IMPLICATIONS

It was shown in this section that the application of a magnetic field normal to a heated wall reduced the heat transfer from the plate to the fluid but also decreased the fluid velocity. This will affect the hydrodynamic stability of the flow. Gershuni and Zhukhovitskii (*39*) have calculated the critical Grashof number for flow between parallel vertical plates and $\mathrm{Pr} = 0.02$. They show that the minimum critical Grashof number increases from 405 to 4500 as M increases from 0 to 10. However, in the case of a single plate, the magnetic field may produce inflection points in the velocity profiles. This destabilizing effect may actually lower the transition point (*10*).

The decrease in fluid velocity is not necessarily beneficial. If these devices are used as heat exchangers in nuclear reactors, it may be expedient to circulate the radioactive metal by other means, possibly by pumping.

Lykoudis (*32*) showed that it was feasible to study free-convection problems in the laboratory by utilizing liquid mercury. This is one of the few MHD heat-transfer problems which adapts itself to a "clean" experiment. Experiments of this type are now in progress at Purdue (*40*).

IV. Heat Transfer in Channel Flow

The analysis of magnetohydrodynamic flow through ducts has received considerable attention. This class of flow has many applications in the design of MHD generators, cross-field accelerators, shock tubes, pumps, and flowmeters. In many cases the flow in these devices will be accompanied by heat, either that dissipated internally through viscous or Joule heating, or that produced by electric currents in the walls.

Internal MHD flows fall naturally into categories which depend on their field configuration. For example, in a typical MHD generator a dc magnetic field is applied normal to the moving fluid. When electrodes are connected to the walls, perpendicular to **B** and **V**, the induced electric field will cause currents to flow through the plasma and an external load. These electrodes serve the same purpose as does a brush in an ordinary generator. Energy is transferred to the load at the expense of kinetic energy of directed motion of the fluid. Such a device would be used in a heat cycle, which would be conventional except for the high temperatures involved. It would take over the functions of both the turbine and the generator in the cycle.

An MHD power generator has no moving parts, other than the fluid. But the temperatures of the working fluid will be high in order to obtain adequate σ; if it is seeded it may be contaminated with alkali metals and be subject to corrosion problems; and, finally, it is difficult to obtain adequate velocities without long entrance lengths. In a generator, the power output per unit volume varies as σu^2, while the heat generated per unit length varies as σu. Thus one or the other will have to be minimized (*41*) for a given reservoir temperature to obtain an optimum output.

The MHD accelerator works in the opposite sense to a generator. By application of an external field opposite to the direction of the induced field, energy is transferred to the gas by Joule heating and the ponderomotive force. Both the generator and the accelerator are limited by high temperatures, the Hall effect, and sheath formation at the electrodes, since operation at low pressures is usually desirable to decrease the heat transfer.

A device which is not plagued by these high-temperature problems is the liquid-metal flowmeter (*42*). It utilizes the voltage induced in the flow by the applied field. The potential difference measured between the electrodes will indicate the flow rate. Heat transfer is not likely to be an outstanding problem here unless the flowmeter is used in heat exchangers. The same remarks can be applied to liquid-metal pumps.

Most research effort has been directed toward one-dimensional incom-

pressible laminar flows with transverse magnetic and normal electric fields. The popularity of this model is due primarily to its mathematical simplicity, since in actual operation the flow will most likely be turbulent, two-dimensional, and, if the working fluid is a gas, compressible. Flows with parallel magnetic fields, such as a circular channel with an axial magnetic field, have found application in shock-tube studies. In a one-dimensional flow, the parallel field does not influence the velocity distribution, but it will in theory delay transition to turbulent flow and tend to prevent the transport of heat and momentum across the field lines. An axisymmetric flow with a normal field, such as a pipe flow in a radial magnetic field (*43*), is difficult to study experimentally.

It is possible, because of the simplicity of the one-dimensional equations, to establish trends with M and K that will apply in a general sense to the more complex situations associated with two-dimensional or compressible flows. Therefore, the classical Hartmann channel-flow problem is discussed in some detail in the next section.

A. ONE-DIMENSIONAL INCOMPRESSIBLE FLOW

The Hartmann problem (*1*, *2*) and extensions of it involve strictly one-dimensional flows between parallel plates of spacing $2a$, as sketched in Fig. 6. A channel is formed by placing the side walls at a distance

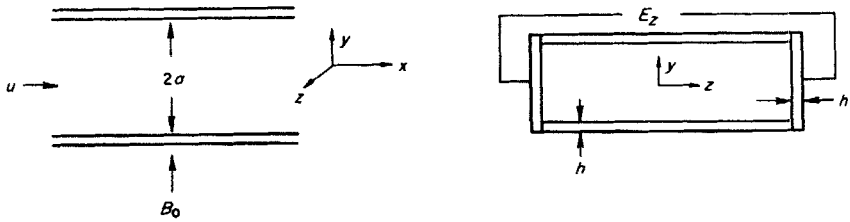

FIG. 6. One-dimensional flow.

$2d \gg 2a$ apart. The channel is long enough that the flow is fully developed and no axial currents exist. A constant magnetic field is applied normal to the plates, and an electric field is applied normal to the side walls. In the following discussion, the plates will not be considered to be electrically conducting. When they are, the problem is exceedingly difficult and can only be solved in special cases (*44*).

1. The Basic Equations

Under the assumption that there is only one velocity component, and that no axial or transverse variation of any parameter is permitted (with

the exception of pressure), the electromagnetic equations can be written

$$\left.\begin{aligned} 0 &= j_x - \sigma E_x = j_y = \sigma E_y \\ j_z &= \sigma(E_z + uB_y) \end{aligned}\right\} \tag{48}$$

$$0 = \frac{\partial E_x}{\partial y} = \frac{\partial E_z}{\partial y} \tag{49}$$

$$\left.\begin{aligned} \frac{\partial B_z}{\partial y} &= \mu_e j_x = 0 \\ 0 &= \mu_e j_y \\ \frac{\partial B_x}{\partial y} &= -\mu_e j_z \end{aligned}\right\} \tag{50}$$

from Eqs. (9), (3), and (2), respectively. It is easily deduced from Eqs. (48) and (49) that $E_x = E_y = 0$ and E_z = constant = E_0 everywhere. For the magnetic field, B_z = constant, from Eq. (50). But $B_z = 0$ outside the fluid so $B_z = 0$ everywhere. Since a normal field B_0 is applied at infinity, $B_y = B_0$ by reasons of continuity. (We shall defer discussion of B_x until Section IV,A,2.)

The MHD equations are now written in dimensionless form, referring all parameters to the reference conditions B_0, E_0, $\bar{u}$ (the mean velocity), and a, the channel radius. The momentum equations are

$$0 = -\frac{\partial p^*}{\partial X} - SK - SU + \frac{1}{\mathrm{Re}}\frac{d^2U}{dY^2} \tag{51}$$

$$0 = -\frac{\partial p^*}{\partial Y} + J_z S B_x^* \tag{52}$$

and

$$J_z = K + U = -\frac{1}{\mathrm{Re}_m}\frac{dB_x^*}{dY} \tag{53}$$

where $j_z = j_z/\sigma\bar{u}B_0$, and where the generator coefficient, K, the ponderomotive coefficient, S, and the two Reynolds numbers were defined in Section II,D. The continuity equation is automatically satisfied for one-dimensional flow, and the energy equation will be deferred until Section IV,A,4. The induced magnetic field B_x does not enter into Eq. (51), since the flow is one-dimensional and B_x does not interact with the fluid to generate a current in the z-direction. If the relation given in Eq. (50) for j_z were used, then the derivative of B_x would be present rather than the applied field B_0. We have therefore not assumed anything about Re_m other than the fact that $B_x \ll B_0$ at infinity.

The solution of Eq. (51) for the usual fluid-dynamic boundary condi-

tions that $U(\pm 1) = 0$ is

$$U = \left\{ - K - \frac{\partial p^*/\partial X}{S} \right\} \left[1 - \frac{\cosh \mathrm{M}Y}{\cosh \mathrm{M}} \right] \tag{54}$$

where M is the Hartmann number of Eq. (30). The average velocity in the channel is written in dimensional form as

$$\bar{u} = \frac{1}{a} \int_0^1 u \, dy = - \left\{ \frac{E_0}{B_0} + \frac{\partial p/\partial x}{\sigma B_0^2} \right\} \left(1 - \frac{\tanh \mathrm{M}}{\mathrm{M}} \right) \tag{55}$$

so that

$$-K - \frac{\partial p^*/\partial X}{S} = \left(1 - \frac{\tanh \mathrm{M}}{\mathrm{M}} \right)^{-1} \tag{56}$$

or

$$U = \frac{\mathrm{M}}{\mathrm{M} - \tanh \mathrm{M}} \left[1 - \frac{\cosh \mathrm{M}Y}{\cosh \mathrm{M}} \right] \tag{57}$$

Both Eqs. (54) and (57) are of interest. Equation (54) shows the effect of changing the pressure head, ponderomotive force, and generator coefficient on the velocity profile for a constant mass flow, while Eq. (57) gives an equivalent relationship in terms of Hartmann number.

The current is obtained from Eqs. (53) and (57). Let $\bar{J}$ be defined as the mean current

$$\bar{J} = \tfrac{1}{2} \int_{-1}^{1} J_z \, dY = K + 1 \tag{58}$$

from Eq. (53). Then the total current can be written as the sum of the mean current and a circulating current, J_c, as

$$J_z = K + U = \bar{J} - (1 - U) = \bar{J} + J_c \tag{59}$$

where $J_c = -(1 - U)$. It is immediately obvious that the mean current vanishes when $K = -1$. This corresponds to a channel in which the walls are electrically insulating (i.e., in which the only currents flowing are circulatory). When $K = 0$, there is no applied electric field and a mean current equal to the electromotive current exists everywhere in the channel. This corresponds to the electrically short-circuited case. The maximum operating condition for a generator occurs when $K = 1$.

Equations (54) to (59) provide the information necessary for assessing the effects of the electromagnetic fields on the flow and heat transfer.

2. The Induced Magnetic Field

While we will not be further concerned with the induced field, we should ascertain the conditions under which it can be neglected. This

particular flow also offers an opportunity for discussing the boundary conditions on the induced field (see Section II,C) in a simple flow problem.

Writing the integral of Eq. (53) in the form

$$B_x^*(\xi) = -\left\{\frac{\mathrm{Re}_m}{2}\int_{-1}^{\xi} J_z\,dY - \frac{\mathrm{Re}_m}{2}\int_{\xi}^{1} J_z\,dY\right\},\quad -1 \le \xi \le 1 \tag{60}$$

we find that

$$B_x^* = -\mathrm{Re}_m\left\{KY + \frac{\mathrm{M}}{\mathrm{M} - \tanh \mathrm{M}}\left(Y - \frac{\sinh \mathrm{M}Y}{\mathrm{M}\cosh \mathrm{M}}\right)\right\} \tag{61}$$

where $B_x^*(0) = 0, B_x^*(1) = -\mathrm{Re}_m(K+1)$, and $B_x^*(-1) = +\mathrm{Re}_m(K+1)$. It is apparent that the boundary conditions on B_x are determined entirely from the mean current across the channel; this is physically realistic when the channel is thought of as a sequence of current sheets, each with its own induced field. This interpretation would imply that the induced magnetic field should vanish at the boundary only when there is no net current interior to the region, i.e., only if $\bar{J} = 0$ or $K = -1$, which is substantiated by Eq. (61). From a consideration of the fields outside the fluid, we see that B_x^* = constant satisfies both

$$\nabla \times \mathbf{B} = \nabla \cdot \mathbf{B} = 0$$

Hence the induced field is given by Eq. (61) inside the fluid, and by the boundary values exterior to the fluid.

The fact that $B_x^*(Y)$ is symmetric with respect to the origin is of importance when the forces in the Y-direction are considered. Since J_z is symmetric about the x-axis, we can immediately conclude that the net ponderomotive force in the Y-direction vanishes, i.e.,

$$\int_{-1}^{1} J_z B_x\,dY = 0 \tag{62}$$

and that the induced field will not impose a net pressure in the Y-direction. Therefore the only importance the induced magnetic field has in one-dimensional channel flow is its influence at infinity; i.e., its magnitude compared to the applied field B_0 must be small.

The magnitude of B_x^* at infinity will be, by continuity, its value at the wall for a two-dimensional current sheet. In absolute units

$$B_x^*(\infty) = |K+1|\,\mathrm{Re}_m \tag{63}$$

When $K = -1$, $B_x^*(\infty)$ vanishes, regardless of the magnitude of Re_m. For other values of K, we must specify that $|K+1|\,\mathrm{Re}_m \ll 1$ for B_x^* not to influence the applied field direction. For liquid mercury

$$|K+1|\,\mathrm{Re}_m = |K+1|\,1.63a\bar{u} \quad (MKS) \tag{64}$$

and for ionized air, it is orders of magnitude less. It appears that under practical operating conditions this condition can be fulfilled easily.

3. Flow Characteristics

The response of the total mass flow to the ponderomotive force and electric field is evident either from Eq. (55) or, in a dimensionless form, from Eq. (56). For a zero electric field and a given pressure head, the flow will decelerate as M increases, due to the ponderomotive force uB_0^2. This deceleration is even more significant when $E_0 > 0$, the generating mode. In the pumping mode, E_0 acts in the opposite direction and power

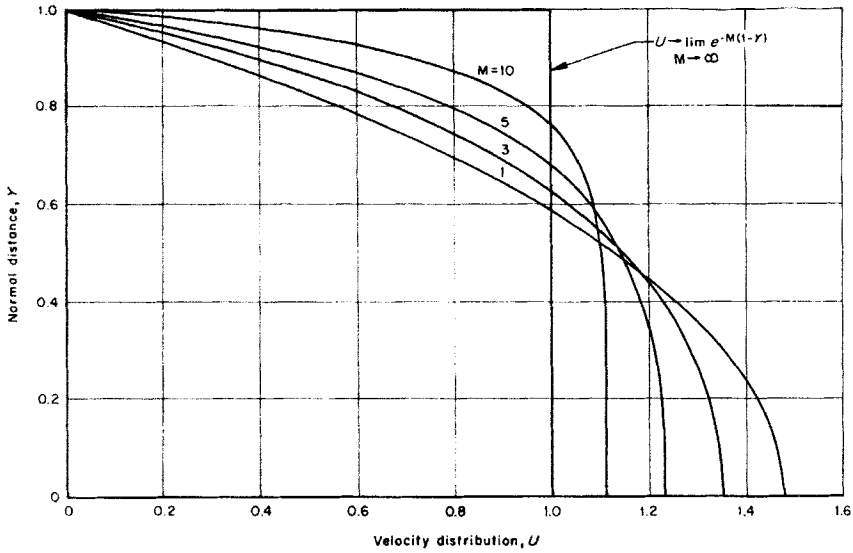

FIG. 7. Velocity distribution in one-dimensional channel flow.

is added to the fluid instead of being extracted. This flow will accelerate in regions where the current is in the same direction as E_0, a condition which is met in the whole channel when K is larger (negatively) than -1.

The shape of the velocity distribution will not change with K since the electric field provides a constant body force on the fluid when the induced magnetic field is neglected. Equation (57) indicates that if the same mass flow is maintained in the channel as M varies, an increase in the magnetic field will increase the ponderomotive force and flatten the velocity profile. We have plotted U for various values of M in Fig. 7. For $M = 0$, the profile reduces to plane Poiseuille flow; for $M \to \infty$, it approaches slug flow. The shape of the profile as M increases will affect

the heat transfer by increasing the convection near the wall and by increasing the viscous dissipation.

The current flow will be unidirectional throughout the entire channel only if $K + U_{max} > 0$, or, since

$$U_{max} = U(0) = \frac{M}{M - \tanh M} \times \left[1 - \frac{1}{\cosh M}\right]$$

the condition on K is

$$K + \frac{M(\cosh M - 1)}{M \cosh M - \sinh M} > 0 \tag{65}$$

In all other cases the current will change direction at some point. As M increases, this location moves closer to the wall, setting up what Hartmann called a "magnetic boundary layer."

The particular Y values where J_z reverses (since J_z is symmetric there are two of them) are given by the points at which $U(Y) = -K$. Since these points move closer to the wall as M increases, we can expect larger gradients to exist in J_z close to the wall, and, as a result, we also expect an increase in Joule heating.

These effects will be seen more clearly if we turn now to the energy equation for this geometry.

4. Heat-Transfer Characteristics

In order to establish trends with M and K it is necessary to define the reference conditions with which any comparison will be made. These are perfectly arbitrary, but the most natural ones for MHD channel flow are the following:

(*a*) Constant mass flow ($\bar{u}$ = constant), which means that the pressure drop is adjusted as M and K vary

(*b*) As M changes, K remains constant; this implies that the applied electric field varies in such a way that the parameter

$$E_0 a \sqrt{\sigma}/\bar{u} M \sqrt{\mu}$$

remains constant as $M \to 0$ or $M \to \infty$. These definitions should be kept in mind throughout the following discussion.

The energy equation for a one-dimensional flow of a constant-density fluid is written from Eq. (18) in dimensionless form (ΔT here is an arbitrary, constant, temperature difference)

$$U \frac{\partial \theta}{\partial X} = \frac{1}{PrRe} \frac{\partial^2 \theta}{\partial Y^2} + \frac{M^2}{Re} \varepsilon J_z^2 + \frac{\varepsilon}{Re} \left(\frac{dU}{dY}\right)^2 \tag{66}$$

when the internal heat source is zero and where $\phi = -k\nabla T$. Since U

and J_z do not vary with axial distance, the internal heat generated at each axial station is identical. A heat balance on the moving fluid gives

$$\frac{\partial \theta}{\partial X} = A = \frac{\dfrac{\varepsilon}{\mathrm{Re}} \displaystyle\int_0^1 \left[\mathrm{M}^2 J_z^2 + \left(\frac{dU}{dY} \right)^2 \right] dY}{\bar{q}} + q^* \tag{67}$$

where $\bar{q} = \rho c \bar{u} \, \Delta T$ and $q^* = q/\bar{q}$ is any heat added externally. Looking at Eqs. (66) and (67), we can list the following items, resulting from the applied fields, which will influence the temperature response and heat transfer to the wall: (*a*) convection: $AU(Y)$; (*b*) internal heat distribution: J_z^2 and $(dU/dY)^2$; and (*c*) total heat input: $\bar{q}A - q^*$. This list does not contain the usual fluid parameters, such as Reynolds and Prandtl numbers, since they will be unaffected by the applied fields when the mean flow is constant.

a. Convection. We have already shown in Fig. 7 that as M increases the convection will be larger close to the wall. If there where no internal heating, the temperature in the fluid would tend to become uniform in response to any external heat load as M increases. This situation could exist in very-low-velocity flows, where both the ohmic and viscous heating are small (*45*). This term vanishes, of course, when the wall temperature is constant.

b. Internal Heat Distribution. The internal heat distribution due to viscous dissipation depends only on M. From Eq. (54), the ratio of viscous dissipation to the mean viscous dissipation in the channel is

$$\left(\frac{dU}{dY} \right)^2 = \frac{\mathrm{M}^4}{(\mathrm{M} - \tanh \mathrm{M})^2} \cdot \frac{\sinh^2 \mathrm{M}Y}{\cosh^2 \mathrm{M}} \tag{68}$$

The viscous dissipation is plotted in Fig. 8 as a function of Y for various magnetic-field strengths. It is at maximum at the wall and increases with M. This will enlarge the heat flux near the wall.

It is more difficult to assess the ohmic heating because it is a function of both M and K. When $K = -1$, however, the net current vanishes and only the circulating current contributes to the heating. Using Eq. (59), the Joule heating for this case (divided by the mean viscous dissipation and M^2) is given in Fig. 9. It appears that this mode of operation (electrically insulated walls) produces internal heat very close to the walls. In fact, for large magnetic-field strengths, the viscous and ohmic dissipation are of the same order of magnitude at the walls:

$$\left[\frac{(dU/dY)^2}{J_z^2} \right]_{Y=\pm 1} \sim \frac{1}{\left(1 - \dfrac{1}{\mathrm{M}} \right)^2} \sim 1 + \frac{2}{\mathrm{M}} \tag{69}$$

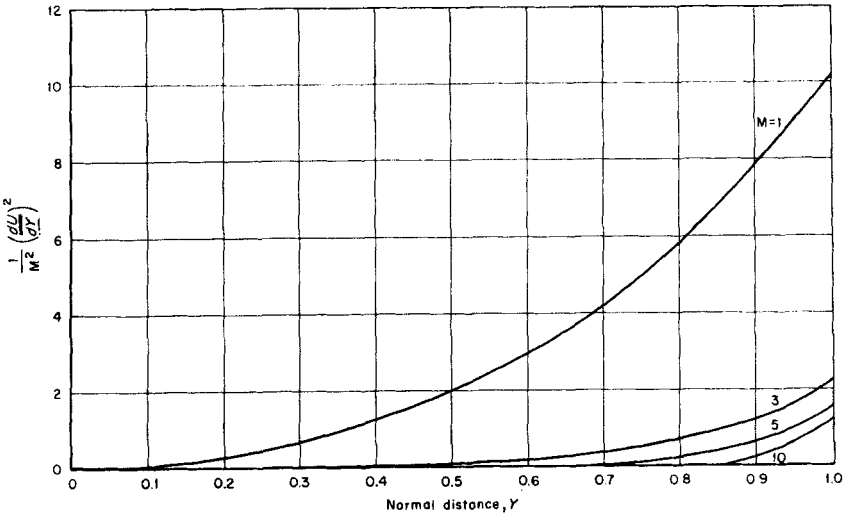

FIG. 8. Comparison of dimensionless viscous dissipation in one-dimensional channel flow with the mean viscous dissipation in the channel.

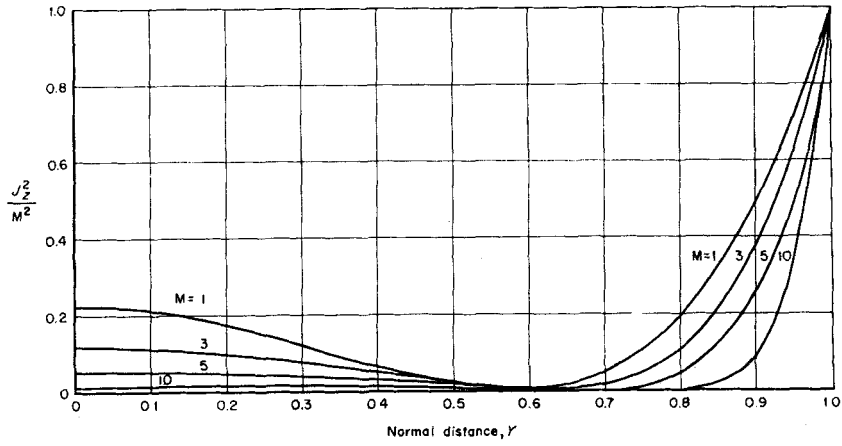

FIG. 9. Ohmic heating for electrically insulated walls in one-dimensional channel flow.

It can be shown, however, that the *maximum* ohmic dissipation is larger than the *mean* viscous dissipation by a factor of M^2, which has prompted some authors to neglect the viscous dissipation in their analyses. Both Alpher (*46*) and Siegel (*47*) solved Eq. (66) for $K = -1$ under this assumption. They found that when M became sufficiently large the ohmic heating could exceed the energy supplied to the fluid by an external

source q^*, and the fluid temperature could surpass the wall temperature (i.e., there was heat conduction *out* of the fluid). Alpher's solution of Eq. (66) gives, in the limit of large M

$$T_w - \bar{T} \sim \frac{1}{3}q\frac{a}{k} - \frac{\bar{u}^2}{6}\frac{\mu}{k}\mathrm{M} \tag{70}$$

where $\bar{T}$ is the bulk temperature. Addition of the viscous heating to this analysis should cause the crossing point to occur for lower values of M.

The current at the wall vanishes only when the device is short-circuited, which is evident from Eq. (61) when $K = 0$. We have plotted the ohmic heating distribution for $K = 0$ in Fig. 10. Most of the heat release is

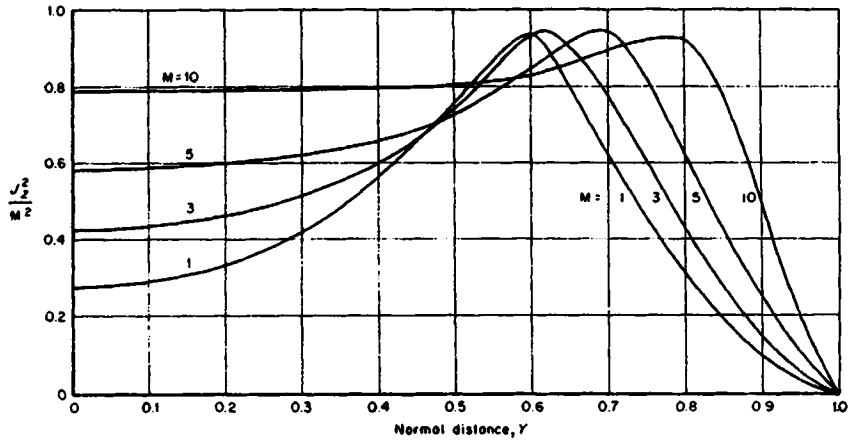

FIG. 10 Ohmic heating for short-circuit mode in one-dimensional channel flow.

in the center of the channel, and as M increases the profile becomes more uniform.

In the short-circuit case, it is possible to neglect the viscous dissipation as long as M is large enough. For large values of the magnetic field, both the maximum viscous and maximum ohmic dissipation approach the same value: $M^2/(1 - 1/M)^2$. However, the ohmic heating occurs throughout a large portion of the channel, while the viscous dissipation is confined in the magnetic boundary layer near the walls. The net result of this combination at high Hartmann numbers is a uniform heat source throughout the channel. This problem has not been solved except in the special case of thermally insulated walls, although the solution could be obtained without too much difficulty. Perlmutter and Siegel (*45*) show that the difference between the wall and bulk temperature is a minimum

when $K = 0$ and the walls are thermally insulated. As M increases, $T_w - T$ approaches zero, as would be expected.

For other values of K the ohmic heating will dominate the viscous heating, and the distribution will depend on the particular value of K. For negative K the bulk of ohmic heating will still take place at the walls, so the conclusions drawn for $K = -1$ still hold. For $K > 0$, the heating will be larger in the center of the channel as $M \to \infty$.

c. Heat Transfer. While it requires considerable algebra to find the mean temperature for the case of variable wall temperature or external heating, we can show the variation in heat transfer when the wall temperature is constant merely by integrating Eq. (67). This yields

$$q = \frac{\mu \bar{u}^2}{a} M^2 \left\{ (K+1)^2 + \frac{M \sinh 2M - \cosh 2M + 1}{2(M \cosh M - \sinh M)^2} \right\} \tag{71}$$

which reduces to $q_0 = 3\mu\bar{u}^2/a$ when $M = K = 0$. We have plotted the ratio q/q_0 in Fig. 11 for various values of K. The dashed lines in Fig. 11 are values of this ratio when the viscous-dissipation term is omitted in Eq. (66), since this is often done in practice (*46*, *47*).

When $M \to \infty$

$$\frac{q}{q_0} \sim (K+1)^2 \frac{M^2}{3} + \frac{M}{12} + 0(1/M) \tag{72}$$

when the viscous dissipation is included. When it is omitted

$$\frac{q}{q_0} \sim (K+1)^2 \frac{M^2}{3} + \frac{M}{24} + 0(1/M) \tag{73}$$

Thus for $K \neq -1$ both solutions approach the same value as M increases. But when the wall is insulated, the heat transfer when viscous dissipation is neglected is lower by a factor of 2. This is evident in Fig. 11, where the behavior at large Hartmann numbers is already evident for $M > 5$. The neglect of viscous dissipation is therefore not justified when the wall is insulated ($K = -1$).

For other values of K, the ohmic heating is quite pronounced, for q/q_0 increases rapidly with M. Notice also in Fig. 11 that the heating in the accelerator mode is equal to that in a generator mode with a lower coefficient; the curves for $K = -3$ and $K = 1$ are equal, for example. This implies that generators with practical efficiencies (say, for $K \sim 0.8$) the heating problem may be as severe as in an accelerator in which considerable energy is deposited by the electric field. The reason for this is that the comparison in Fig. 11 is being made on the basis of constant mass flow, which is unlikely when a generator and an accelerator are being compared.

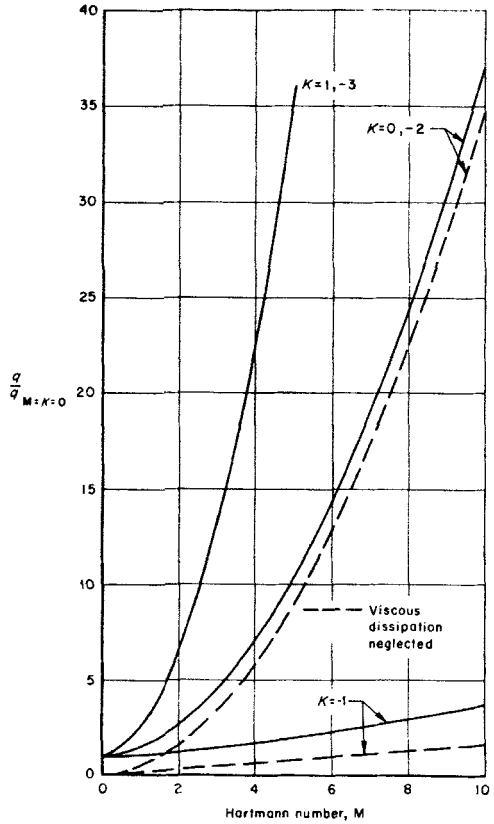

FIG. 11. Convective heat transfer to the walls in one-dimensional MHD channel flow for the case of constant mass flow and constant wall temperature.

5. Other Solutions

Although this has been an extensive discussion of heat-transfer characteristics in one-dimensional MHD flow, we have by no means covered all of the cases treated in the literature. As mentioned previously, Siegel (*47*) and Alpher (*46*) solved the energy equation with a uniform external heat flux for $K = -1$ and no viscous dissipation. [The solution of Eq. (66) is such that it is easy to incur algebraic errors. Alpher points out an error in Siegel's work (*47*) and the author found one in (*46*). It is suggested that any expressions for $T_w - \bar{T}$ be checked independently.]

Alpher's treatment also includes the effects of electrically conducting plates when $K = -1$. (In many cases of interest the plates will heat up during operation and become conductors.) His analysis shows, for large magnetic fields, that a decrease in plate resistance will cause the

mean fluid temperature to approach the wall temperature. However, for very large M, the temperature response becomes independent of the wall conductivity.

Perlmutter and Siegel (*45*), besides solving Eq. (66) for various values of K and M, also investigated the thermal-entrance region for this flow. (The velocity profile was taken as fully developed.) Shohet *et al.* (*48*) considered the entrance problem per se, and obtained solutions for the pressure, velocity, and temperature variation at the channel entrance. They found that an increase in magnetic-field strength decreased the length necessary for the velocity to reach its nominal fully developed value. Subsequently, the temperature distribution would also be independent of axial length sooner than when $M = 0$.

B. Boundary-Layer Effects: Two-Dimensional Channel Flow

In all large rectangular flow devices a boundary layer will form on the channel walls and the flow in the center will be inviscid. The boundary layer is deleterious as far as operating efficiency is concerned, because it changes the effective area, decelerates the flow, and dissipates power to the walls. The thermal behavior of boundary layers will also contribute to losses, either by heating the electrodes or, in a compressible gas, by lowering the temperature (and hence the conductivity) near the wall through heat losses to the wall.

These boundary layers, in comparison to those discussed in Section V, grow in an electrically conducting "free stream," complete with pressure gradient, velocity gradient, and applied electric field. They should not be confused with the magnetic boundary layer, of thickness $\delta < 1/M$, which is the region near the channel walls where the ponderomotive and viscous forces adjust for a given pressure gradient. The magnetic boundary layer is established because of the change in sign of the current [see Eq. (57)] across the channel; unlike a fluid-dynamic boundary layer, it remains one-dimensional.

1. Incompressible Flow

To the author's knowledge, there exists only one analysis expressly for the heat transfer in an incompressible, constant-property MHD channel boundary layer. Moffatt (*49*) discusses boundary-layer phenomena on the electrically insulated (top and bottom) walls of the MHD channel of Fig. 6.

The boundary layer provides a region of velocity deficit where, in generators, a current reversal similar to that of the one-dimensional case can occur. For the generator boundary layer, the current reversal should cause a relative acceleration of the flow by its changing the sign of the

ponderomotive force. This would increase the viscous dissipation (an effect which was masked in the preceding discussion where the mass flow was assumed constant) and subsequently the heat transfer. In the accelerator boundary layer, the current flows more freely near the insulated walls, a condition which would also tend to increase the heat flux.

Several assumptions in the analysis of (*49*) detract from the significance of the calculations. This is unfortunate, because the author is unaware of any other treatments of the heating problem in two-dimensional channel flow. These assumptions and their consequences will be discussed here because the integral technique used by Moffatt is a convenient way to obtain results; perhaps the same method could be used under somewhat modified conditions to obtain more realistic solutions.

First, the existence of similar solutions to the boundary-layer equations was assumed when the applied magnetic field is constant. It can be shown (Section V,B,2) that similar solutions exist only when the magnetic field varies as some power of x. Secondly, in using the integral technique for shear and heat transfer, Moffatt assumed that the velocity profiles for laminar and turbulent flow were given by their nonmagnetic values (i.e., parabolic for laminar and seventh-power for turbulent), so that they are invariant with Hartmann number. This is not true in laminar flow in a constant magnetic field (*3*). The effect of this assumption on skin friction is reflected in the result given by Moffatt that the friction coefficient is independent of Reynolds number when plotted versus M/Re and does not follow the trend established by experiment, which also shows a Reynolds-number dependence. It is difficult to determine the effect of these assumptions on the heat transfer but one would suspect that the values given in (*49*) would be too low.

2. Compressible Flow

Another problem indigenous to generators or accelerators is that of the growth of boundary layers on the electrodes. In this geometry the magnetic field is transverse to the flow and the electric field is normal to it. The significant forces are sketched in Fig. 12. (Note that the coordinate axes have been changed from those of Fig. 6 in order to adhere to the usual boundary-layer nomenclature.) Heat transfer in these boundary layers will be larger than usual because of the tendency, in the accelerator mode, for the currents to be highest near the wall. For a gas, the decrease in temperature near a cooled electrode will diminish the electrical conductivity and hence increase the Joule dissipation. This flux near the wall will lead to a higher temperature gradient and hence an increase in heat transfer for a given wall temperature.

Kerrebrock (*50*) suggests seeding the gas with an alkali metal so that

the conductivity will be high at low temperatures. His analysis of the compressible boundary layer is thus for a gas in which $\sigma \sim e^{-1/T}$ as a result of seeding. The inviscid flow was taken as quasi-one-dimensional and the magnetic field varies as a power of x. The magnetic Reynolds number was assumed to be small, and similar solutions of the boundary layer were obtained. In his analysis, Kerrebrock added a term to the energy equation to account for the transport of heat by the electrons in the current stream. Because this is an unusual configuration, it is

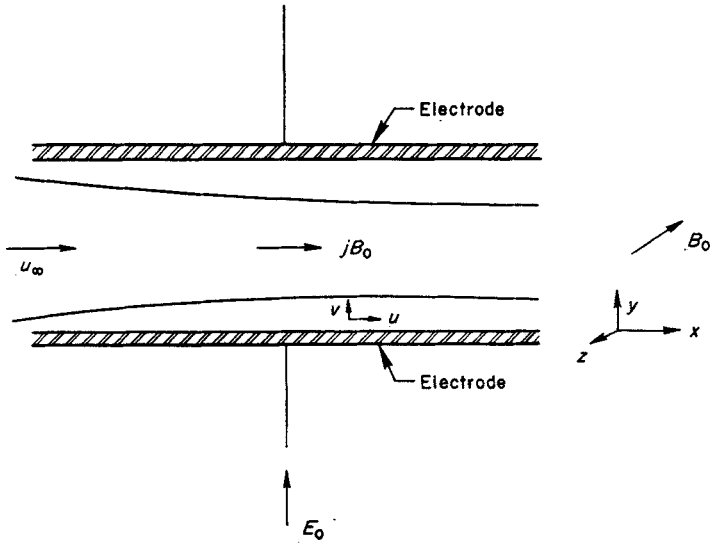

FIG. 12. Electrode boundary-layer problem (shown in the pumping mode).

worth considering briefly the particular mechanisms of heat transfer in this problem. The term added to Eq. (18) was the following:

$$\frac{\partial}{\partial y}\left(\frac{5kT}{2e}j\right) \tag{74}$$

This can be broken into the constituents

$$\frac{5}{2}\frac{kT}{e}j = \frac{5}{2}kTn_e v_d = h_1\rho_1 v_1 \tag{75}$$

where h_1 is the enthalpy of the electrons considered as a monatomic gas at the parent gas temperature; ρ_1, the electron density; and v_1, the drift velocity due to the electric fields $\sigma(E - uB)$. By comparing Eq. (75) with Eq. (36) in Section II,E,1, it is clear that this is the flux of energy carried by the electron-drift velocity. This flux will be much larger than

any other diffusive transport mechanisms because, near an electrode, the current is essentially "one-way." Because this is true, the gas is no longer neutral and the heat transfer in this region will be affected by the energy gain (or loss) of the charged particles in the potential sheath at the electrodes (see Section VI,B,3). However, Kerrebrock assumed that the energy due to electron-ion recombination was negligible because of the low charge concentration. Another phenomenon peculiar to this problem is that the electrons in a strong field will tend to be at a higher kinetic temperature than that of the ions or neutrals, The enthalpy in Eq. (75) would then be that associated with the electron temperature. This effect, which was not considered by Kerrebrock, would increase the heat transfer at one electrode and decrease it at the electrode of opposite polarity.

Kerrebrock found that the largest effects of Joule heating occurred for low Mach numbers and highly accelerated flows, and that Joule heating tended to thin the thermal boundary layer and prevent the heat generated by viscous dissipation from reaching the walls. As a result, a considerable temperature excess developed in the boundary layer. The heat-transfer rates increased by an order of magnitude in constant area flow as the Mach number increased; part of this was due to the temperature excess, and part to the free-stream acceleration. It is not possible to assess his results in terms of Hartmann number because the magnetic field is variable. The expected increase in heat transfer exists, but its rate of growth with Mach number is dependent on the conductivity model assumed and also on the mechanism for heat conduction at the electrode.

C. AXISYMMETRIC FLOW

The shock tube and plasma jet, which have provided significant information on high-temperature aerodynamic heating, are also being used to study MHD flows experimentally. One suggested configuration is sketched in Fig. 13. The ponderomotive force due to B_r and B_z will interact with the velocity components u and v in that order; most of the interaction will be near the wall where v and B_r are relatively large. When a solenoid is used and end-effects can be neglected, the ponderomotive force will appear only in the radial-momentum equation, and will inhibit the flow toward the wall. One could therefore expect a reduction in heat transfer to the wall.

Hains and Yoler (*51*) have studied both the viscous and inviscid flow for the model in Fig. 13, using a donut (single-turn) coil in which an extensive radial field will exist. In their analysis, the parameter S of Eq. (30) was taken as small, so that the magnetic field caused a perturba-

tion, rather than a large change, in the inviscid flow. For subsonic flow, the magnetic interaction caused the streamlines to converge toward the channel axis and the mean velocity to increase during passage through the field. For supersonic flow, the interactions at the wall where the field curvature is large propagated inward, coalesced, and formed shocks downstream of the coil The boundary layer in supersonic flow was found to be thickened somewhat by the magnetic field, but over-all effects were small. Heat transfer was reduced slightly by the soil and increased somewhat downstream. This effect would be more pronounced if the ponderomotive force were larger than the inertia force.

An experimental investigation of the same configuration as Fig. 13, using a solenoid rather than a donut coil, was made by Raelson and Dickerman (*52*), who used a water-cooled arc plasma generator to obtain

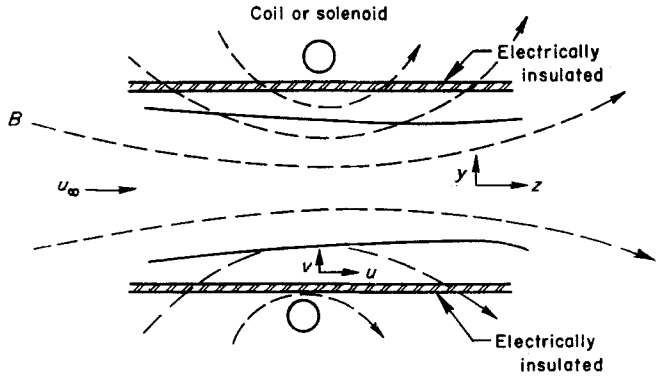

FIG. 13. Axisymmetric MHD flow.

the conducting fluid, in which $T \sim 5000°$–$6000°$K, $p = 1$ atm, and $u = 2.8 \times 10^2$ m/sec. The Hartmann number reached a maximum on the order of $M \sim 10^4$, so that the magnetic forces dominated the viscous forces. Re_m was estimated to be about 0.1 and the Reynolds number was about 10^6. The heat transfer to the wall was measured by calorimeter methods. In the parallel mode (B in the same direction as the flow), the magnetic field evidently provided a shielding against the transfer of heat, for the convective heat transfer was reduced 15% below its value when $B = 0$. In the antiparallel or opposite direction, the field was ineffective in reducing heat transfer. This effect cannot be explained. Theoretically, there should be no difference in the mode of operation as far as the forces on the fluid are concerned, even when the induced magnetic field is included, unless one were to consider Hall currents. But the operating conditions of this experiment are such that the Hall effect should be small.

The theory of (*51*) would tend to predict the measured decrease in heat transfer, although it would not be justified to extrapolate the theory for $S \sim 1$ to the experiments of (*52*).

D. AN ASSESSMENT OF HEAT TRANSFER IN MHD CHANNEL FLOW

The discussion of the various channel-flow problems in this section has not emphasized the problems which remain unsolved in the determination of heat transfer in crossed-field generators and accelerators. These will be summarized briefly in this section.

We can conclude that constant-property, one-dimensional channel flows are well understood qualitatively. Even the inclusion of Hall currents in the determination of heat transfer could be carried out without difficulty, since the velocity field has already been analyzed (*53*). Compressible fully developed channel flow has not been investigated, which is not unusual since the field-free case is not yet well understood.

However, when the conductivity varies with temperature, the heat-transfer rates can be severe (*54*, *55*). The validity of a theoretical analysis for the gas behavior is restricted by the difficulty in assuming a reasonable model for the partially ionized, sometimes nonequilibrium gas. Oates (*54*) has suggested several experiments which can be carried out to determine the nature of the actual gas flow as compared to the predicted one.

Of the several solutions for the free stream in a channel, those which correspond to a constant-area one-dimensional flow are: constant B and E, constant temperature and E, and constant temperature and B. These could be compared with measurements; those which indicate an asymmetry of heat transfer between anode and cathode, for instance, would give evidence for an elevated electron temperature; measurements of the pressure gradients across the channel would give an indication of the magnitude of the Hall current.

It was pointed out earlier that it is necessary to have high velocities in MHD power generators. If the gas is in equilibrium, nozzle-driven generators become exceedingly long at high-inlet Mach numbers because the conductivity depends on gas temperature. If the flow is expanded to supersonic Mach numbers before entering the MHD duct, nonequilibrium ionization will occur; i.e., an overabundance of electrons will exist in an expanding preionized flow because the relaxation to ionization equilibrium is slower than the flow velocity. (This phenomenon is called freezing, and is also found in high-energy flow about blunt bodies.)

Eschenroeder (*55*) discusses these effects and shows that the conductivity due to freezing increases significantly above the equilibrium value at that pressure. The effects of this on MHD channel heat transfer would be important. At the low operating pressures, the heat transfer would be

less. The expansion with nonequilibrium ionization also implies that the static temperature is lower. (The potential energy has been converted to kinetic energy without a loss in conductivity *before* the gas enters the generator.) Hence, the problem of hot exhaust gases is alleviated. However, the theoretical analysis of heat transfer in such a flow would be difficult.

V. Flat-Plate Boundary-Layer Heat Transfer

In high-velocity flow past a thin wing, the air in the boundary layer will become heated due to viscous dissipation. If the velocity is large enough, a small degree of ionization is produced, and the air will become an electrical conductor. A magnetic field of sufficient intensity, applied normal to the wall, will interact with the boundary-layer flow to cause a reduction in the velocity and a decrease in skin-friction drag. The effect of such a flow on the heat transfer to the wall will be discussed in this section.

The two-dimensional boundary-layer equations are in themselves difficult; the addition of a variable conductivity and the ponderomotive force increases the complexity to the extent that the problem is often intractable without unrealistic assumptions (see Section V,B,2). Therefore, we will try to gain insight into the boundary-layer problem by considering first a simple one-dimensional shear flow, much as was done in Section IV with the channel problem.

A. COUETTE FLOW

Couette flow is produced when a viscous fluid between two infinite plates is set into motion by the relative velocity of one of the walls. It can be studied experimentally as the flow between two concentric cylinders in relative angular motion when the spacing between the cylinders is small compared to their radii (see Fig. 14*a*). Analyses of MHD Couette flow have been made by Bleviss (*56*) and Leadon (*57*).

1. Incompressible Couette Flow

Mathematically, this problem is the same as the one-dimensional channel flow of Section IV, with one important exception: The boundary conditions of the fluid are different. Consider the semiinfinite channel of Fig. 14*b* with the magnetic field normal to the lower, stationary plate. These walls are assumed to be electrically insulated. The upper wall moves with uniform velocity, u_∞, in the axial direction. When the magnetic field is not present, the velocity profile is linear.

In order to simulate a boundary-layer flow, let us assume that the axial pressure gradient is zero and that there is no applied electric field.

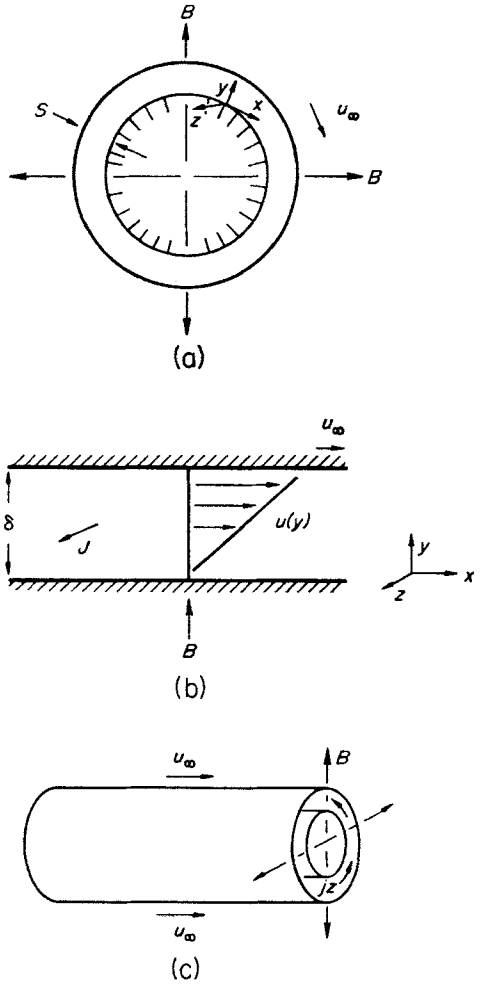

FIG. 14. Various interpretations of MHD Couette flow; (a), flow between concentric cylinders in relative angular motion, in which the induced current is in the Z direction; (b), shear flow between infinite parallel plates; (c), sliding concentric cylinders (*56*), in which the current circulates.

Since $K = 0$, we must provide some shorting arrangement for the currents. Bleviss (*56*) suggested a configuration shown in Fig. 14*c*. This has some limitations, just as a "shorted" Couette flow would. For example, a radial field such as indicated in Fig. 14*c* would not satisfy $\nabla \cdot B = 0$ if B_0 were constant, as is usually assumed. But the problem of providing a shorting mechanism at the open ends of a concentric rotating cylinder would also be difficult.

Under the assumption that $K = \partial p^*/\partial X = 0$, Eqs. (51) to (53) become

$$\frac{d^2U}{dY^2} - \mathrm{M}^2U = 0 \tag{76}$$

$$J_z S B_x^* = \frac{\partial p^*}{\partial Y} \tag{77}$$

and

$$J_z = U = -\frac{1}{\mathrm{Re}_m}\frac{dB_x^*}{dY} \tag{78}$$

where now all quantities are referred to the upper wall in terms of distance δ from the lower, stationary wall, and where $u(\delta) = u_\infty$. The boundary conditions on U are thus $U(0) = 0$, $U(1) = 1$. Equation (76) can be integrated immediately to obtain

$$U = \frac{\sinh \mathrm{M}Y}{\sinh \mathrm{M}} \tag{79}$$

The variation of U and J_z with M is shown in Fig. 15. As M increases, $U \to \exp \mathrm{M}\ (Y - 1)$.

a. Induced Magnetic Field. If we again visualize B_x^* as the field induced by a current sheet of mean density $\bar{J}$, then B_x^* will be antisymmetric at the walls, obtaining equal and opposite values there. Since J_z is also given by Eq. (78), then

$$B_x^* = +\frac{\mathrm{Re}_m}{2}\left\{\frac{1 + \cosh \mathrm{M} - 2\cosh \mathrm{M}Y}{\mathrm{M}\sinh \mathrm{M}}\right\} \tag{80}$$

At the point η determined by $\int_0^\eta J_z\,dY = \int_\eta^1 J_z\,dY$ the field is zero; the mean current below that layer is equal to the mean current above it. This integral condition gives η in the terms of the hyperbolic functions

$$\cosh \mathrm{M}n = \frac{\cosh \mathrm{M} + 1}{2} \tag{81}$$

which agrees with Eq. (80). The null point η for the channel flow of Section IV,A,2, was always at the center because of the symmetry of J_z. Here, as M increases and the current density becomes confined to a thin layer near the wall, the point η moves closer to the wall.

Bleviss (*56*), who included the incompressible case in his treatment of hypersonic Couette flow, discussed the boundary conditions on B_x^*. He assumed that B_x^* was induced by a multilayer solenoid of infinite length. In a short solenoid, the magnetic field induced by the current loops will be axial. It will approach a uniform maximum value in the center and fall off as the inverse distance exterior to the coil. The Couette

flow described by Eqs. (79) and (80) will not yield this condition because it is strictly two-dimensional. However, as M increases, especially for $M > 10$, the current sheet is nearly all confined to a thin layer near the upper wall (see Fig. 14). Therefore, if we were to bend this two-dimensional configuration into a solenoid, the induction would approach a maximum in the center, go through a null near the wall, and be opposite in direction outside the current loop. Then, to satisfy the condition that

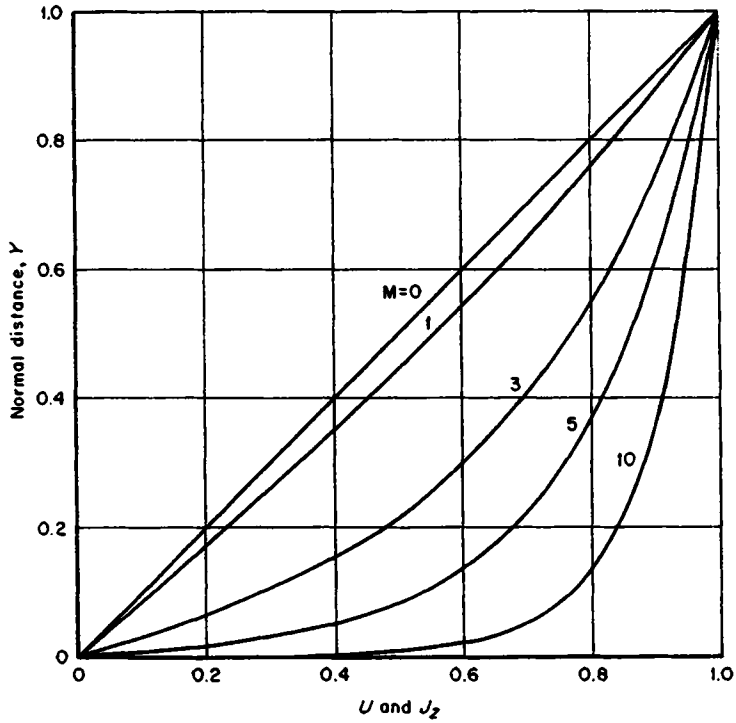

FIG. 15. Variation of velocity and current density with Hartmann number for incompressible Couette flow.

the divergence vanishes for cylindrical coordinates, B_x^* will drop off to zero as the inverse distance as $r \to \infty$. So the boundary conditions on B_x^* in the fluid are the same as in the two-dimensional case, and B_x^* does not vanish externally, as it would if the solenoid were infinite. The exact form of B_x^* is, however, unimportant; it is the magnitude of B_x^* which is of interest.

As far as the effect of B_x^* on the equations of motion, B_x^* enters only into Eq. (79) and does not affect the flow. But because $J_z B_x^*$ is not

symmetric, as in the channel-flow problem, a hydrostatic pressure will be induced by the ponderomotive force. Defining $\Delta p^* = p^*(1) - p^*(0)$, Eq. (62) yields

$$\Delta p^* = \frac{\mathrm{Re}_m}{\mathrm{Re}} \left\{ \frac{\cosh \mathrm{M} - 1}{2 \sinh^2 \mathrm{M}} \right\} \tag{82}$$

which is negligible in most instances since $\mathrm{Re}_m \ll \mathrm{Re}$. For liquid mercury at room temperature, for example, this ratio is on the order of 10^{-6}. In a compressible fluid where the local dynamic pressures are low, this term could, however, become significant.

The fact that an axial field will exert a force on the upper wall in an asymmetric flow is substantiated by the discussion in Section IV,C where it was shown that an axial field increased the boundary-layer thickness slightly. However, in that case the axial field was much larger than this induced field and the flow was two-dimensional, so that the forces were not infinitesimal.

b. Heat Transfer. Both Bleviss and Leadon showed that the heat transfer to the lower wall was not changed by the addition of a magnetic field. Writing Eq. (67) in terms of $\theta = (T - T_w)(T_\infty - T_w)$, where T_w is the temperature of the lower wall,

$$\frac{d^2\theta}{dY^2} = -\mathrm{Pr} \cdot \mathcal{E} \left[\mathrm{M}^2 U^2 + \left(\frac{dU}{dY} \right)^2 \right] \tag{83}$$

Integrating Eq. (83) twice and applying the boundary conditions on θ, we obtain

$$\theta = Y + \frac{\mathrm{Pr} \cdot \mathcal{E}}{2} \left\{ Y - \frac{\sinh^2 \mathrm{M}Y}{\sinh^2 \mathrm{M}} \right\} \tag{84}$$

which reduces to the result

$$\theta_0 = Y + \frac{\mathrm{Pr} \cdot \mathcal{E}}{2} \{ Y - Y^2 \} \tag{85}$$

when $\mathrm{M} \to 0$. Defining $q = k(dT/dy)$ in the usual way

$$q_w = \frac{\Delta T k}{\delta} + \frac{\mu u_\infty^2}{2\delta} \tag{86}$$

for both Eqs. (84) and (85). So the heat transfer to the lower wall is unaffected by the magnetic field.

At the upper wall, which was not treated by Bleviss in the incompressible case,

$$q_\infty = \frac{\mu u_\infty^2}{\delta} \left(\frac{2\mathrm{M}}{\tanh \mathrm{M}} - 1 \right) - \frac{k \Delta T}{\delta} \tag{87}$$

Heat will flow from the fluid to the upper wall when

$$\Pr \cdot \mathcal{E} > \frac{2}{\left(\frac{2M}{\tanh M} - 1\right)} \geq 2 \tag{88}$$

where $\Pr \cdot \mathcal{E} > 2$ for heat to be transferred to the wall when $M = 0$. Therefore the magnetic field effectively increases the heat transfer at the upper wall. The difference between the heat transfer with and without a magnetic field is

$$q_\infty - q_{\infty(M=0)} = \frac{\mu u_\infty^2}{\delta}\left[\frac{2M}{\tanh M} - 1\right] \approx \frac{\mu u_\infty^2}{\delta}(2M - 1) \tag{89}$$

for $M > 5$, so that the increase in heat transfer due to the field is linear in M as M increases.

In a boundary layer the "upper wall" is not fixed; one would suspect that the change in heat transfer in Eq. (89) would be reflected in a growth of the thermal boundary layer and a reduction in heat transfer to the lower wall.

c. Drag and Reynolds' Analogy. Bleviss also investigated the friction drag for incompressible Couette flow and found, as Rossow (*3*) did, that the magnetic field increased the skin-friction coefficient but increased the total drag by the action of the ponderomotive force on the fluid. This result is also evident in the simple channel flow of Section IV,A,3. In that case the pressure drop had to be increased as M grew larger in order to keep the same mass flow.

Since q_w is independent of the magnetic field, then the heat-transfer coefficient, $C_H = q_w/\rho c u_\infty \Delta T$, will also be independent of M if ΔT is not affected greatly by the magnetic field. Bleviss showed that when the "recovery" temperature $T_r = T_\infty + \Pr u_\infty^2/2cT_\infty$ was used (considering that this is incompressible flow), $C_H = 1/\mathrm{PrRe}$ and that the ratio

$$\frac{C_f}{C_H} = \frac{2 \Pr M}{\sinh M} \tag{90}$$

The fact that Reynolds' analogy is invalid in MHD will make experimental verification of much of the theory difficult.

2. Hypersonic Couette Flow

The exact calculation of magnetic effects in a compressible boundary layer is quite difficult, so Bleviss (*56*) studied the simpler geometry of Couette flow, allowing the gas to be ionized and compressible. Even so, suitable transport properties must be chosen in order to simulate properly the behavior of a high-temperature gas. In accordance with the conclu-

sions of Section II,E, Bleviss assumed that the Prandtl number was constant, the electric conductivity was obtained from (*18*), and the viscosity was calculated by using the Sutherland formula. The gas was taken in thermodynamic equilibrium and the Lewis number was assumed to be unity, so that chemical heat flux was not considered.

It was demonstrated in the preceding section that Bleviss used different boundary conditions on B_x^*, the induced magnetic field. His calculations for the compressible case show that the magnetic pressure $[B_x(\max)]^2/2\mu_e$ was less than 10^{-2} atm; hence his results apply for free-stream pressures as low as 10^{-3} atm before the flow will separate from the lower wall. If the other boundary conditions had been used, the restriction on p_∞ would be slightly less stringent, although considerations of the Hall current would also restrict the regions of validity of the solution to pressures higher than these.

One of the most important results of Bleviss' calculations was the showing of the effect on the various aerodynamic coefficients of variable air properties, in particular, the electrical conductivity. He found a peculiar hysteresis effect (see, e.g., Fig. 17) for certain temperature levels in the boundary layer such that the heat transfer and skin friction became multivalued functions of B_0, the applied field strength. This was traced to the variation of electric conductivity with enthalpy in the boundary layer. Since this effect also appears in the compressible boundary layer, we will discuss it further in Section V,B,2.

Another effect of the hysteresis property enabled relatively weak magnetic fields to produce large reductions in skin friction and correspondingly large increases in magnetic drag. The heat transfer to the lower wall is slightly increased by the magnetic field. This is due primarily to the fact that the Couette flow, unlike a boundary layer, is not free to grow in the normal direction.

Bleviss, as did Rossow (*3*), also studied the case where the magnetic field is attached to the moving wall. This will not be discussed further here, as it has no practical significance in boundary-layer flows.

B. FLAT-PLATE SOLUTIONS

1. Incompressible Flow

A pioneer paper by Rossow (*3*) provided the basis for many later studies in the field of magneto-fluid-mechanics. The assumption of a small magnetic Reynolds number was made so that the induced magnetic field did not enter into the equations of motion. The fluid was assumed to be incompressible, and both the case of impulsive motion (the Rayleigh problem) and the boundary-layer problem were analyzed for transverse

constant magnetic fields fixed either to the wall or to the fluid. In all solutions, the electric field was zero and the currents were assumed to be shorted at infinity. In one case, the free stream was taken to be electrically conducting, so that the free-stream velocity was also retarded by the magnetic field.

It is not possible under these conditions to obtain similar solutions to the boundary-layer equations. These were solved by a series-expansion technique in powers of $\sqrt{SX}$, where $X = x/\delta$, for example; terms higher than $(SX)^2$ were neglected. The free-stream velocity varied as $\partial u/\partial x = -\sigma B_0^2/\rho$, a decelerating flow. Rossow found that the skin friction decreased as S increased. The heat transfer, for the case $T_w = T_\infty$, was found to vary as

$$\frac{\mathrm{Nu}}{\mathrm{Pr}\sqrt{\mathrm{Re}_x}} = 0.332 - 0.342SX - \cdots \tag{91}$$

where both the Reynolds number and S are based on the variable free-stream velocity. Equation (89) indicates that the decrease in heat transfer for $(SX) < 0.5$ is not exceptionally large, but it also indicates that the growth of the boundary layer permits a reduction in heating, something which the Couette-flow configuration did not permit. The displacement thickness, in fact, increases as

$$\frac{\delta^*}{x}\sqrt{\mathrm{Re}_x} = SY\sqrt{\mathrm{Re}_x} + (1.73 + 0.54SX) \tag{92}$$

Rossow found that the recovery temperature was not affected by the magnetic field, which is to be expected, since the stagnation enthalpy is unchanged by the presence of B_0 (see Section II,B,3).

Rossow also investigated the case in which σ was assumed to vary throughout the boundary layer. He chose a linear variation of σ with velocity decrement, i.e.

$$\sigma = \sigma_0\left(\frac{u_\infty - u}{u_\infty}\right) \tag{93}$$

so that u_∞ is not affected by the magnetic field. The heat transfer in this case is now

$$\frac{\mathrm{Nu}}{\mathrm{Pr}\sqrt{\mathrm{Re}_x}} = 0.332 - 0.103SX - \cdots \tag{94}$$

which is a reduction of significantly less magnitude than that of Eq. (91). The displacement thickness and skin friction also showed less decrease with the applied field.

In a later paper (*58*) Rossow used an empirical value for $\sigma \sim$

exp $[T - \text{const}]^{1/2}$ and chose the Blasius cold-wall temperature distribution to relate σ with velocity. The heat transfer in this case is

$$\frac{\text{Nu}}{\text{Pr}\sqrt{\text{Re}_x}} = 0.332 - 1.216SX \tag{95}$$

Comparing Eqs. (91), (94), and (95) on the basis of the same kinetic energy in the stream indicates the effect of the different variations in conductivity on the heat transfer. Figure 16 shows that the reduction is most pronounced when Eq. (95) is used.

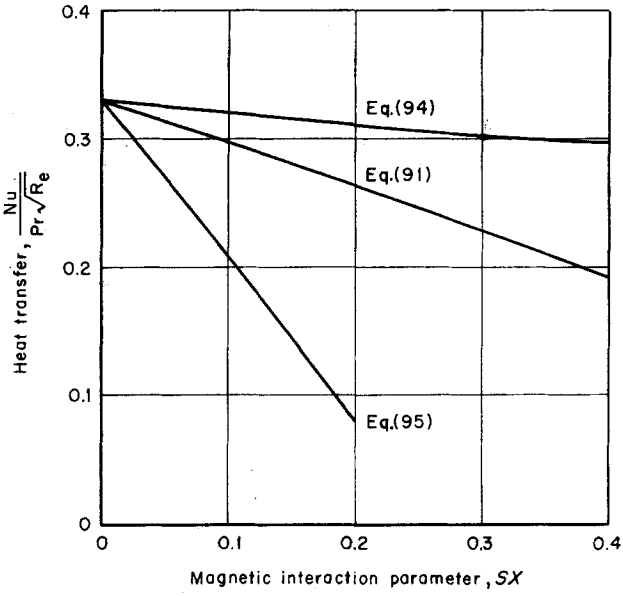

FIG. 16. Effect of variable conductivity on the incompressible-boundary-layer heat transfer (*3*, *58*).

It can be seen that neither of the variable-conductivity solutions by Rossow showed any evidence of hysteresis effects. This is due to the rather arbitrary relationship assumed among conductivity, temperature, and velocity, and it introduces the interesting possibility that a properly seeded gas at relatively low velocities might produce the kind of heat-transfer reductions which were predicted by Rossow.

2. Compressible Flow

The preceding discussions on hypersonic Couette flow and the variable-conductivity solutions by Rossow indicate that the behavior of heat transfer is very different when the air properties—especially the electric

conductivity—are allowed to vary. The manner in which σ varies with T and T varies with u is especially important, as was just pointed out. Bush (*59*) solved the compressible-boundary-layer equations and found the same hysteresis behavior for skin friction and heat transfer as did Bleviss, using a variation of σ with T similar to that of (*18*). This effect occurred even though the magnetic-field configurations were different; the field used by Bush varied along the plate, whereas Bleviss used a constant field. However, there were important differences in the heat transfer, the same as those found by Rossow: The growth of the boundary layer permitted the heat transfer to be reduced, which the Couette flow did not.

Bush assumed that the boundary-layer air was in thermodynamic equilibrium and that the Lewis number was unity. The induced magnetic field was neglected, so the equations were linear in B. A similarity transformation applied to the equations indicated that $B_0 \sim 1/\sqrt{x}$ for similar solutions might exist. [This was also independently determined by Lykoudis (*60*)]. In the hypersonic boundary layer, the most natural thermodynamic-state variables are enthalpy and pressure [see Eq. (20)], so the air and transport properties are usually expressed in terms of these functions. The natural parametric combinations of transport properties which arise in this type of compressible boundary layer under an Hantzsche-Wendt transformation are

$$\bar{\alpha} = \frac{\rho\mu}{\rho_0\mu_0} \sim \left(\frac{h}{h_0}\right)^{-0.35} \tag{96}$$

and

$$\left.\begin{aligned} \bar{\beta} = \frac{\sigma\mu}{\sigma_T\mu_0} &\sim \bar{\beta}_0\left(\frac{h}{h_0}\right)^{4.79} && \text{for } T > 1000°\text{K} \\ &\sim 0 && \text{for } T < 1000°\text{K} \end{aligned}\right\} \tag{97}$$

where the subscript 0 denotes reference conditions at $T = 222°$K, and $\sigma_T = 100$ mho/m is arbitrary. The power-law variation given above holds for a wide range of pressures by adjustment of $\bar{\beta}_0$. The parameter $\bar{\beta}$ determines part of the magnetic interaction through $S\bar{\beta}$, where $S = 2\sigma_T B_0^2 L/\rho_0\sqrt{h_0}$ (in the Hantzsche-Wendt transformation $u_0 = \sqrt{h_0} = 472$ m/sec).

Under these conditions Bush found the same hysteresis behavior in the skin friction and heat transfer as did Bleviss. Both τ and q are plotted schematically in Fig. 17 versus velocity for various values of S. (The actual behavior is a function of h_w, h_∞, and pressure.) Notice that as u_∞ increases for a fixed S the skin friction or heat transfer at first increases. This occurs because the temperatures in the boundary layer are so low that the fluid is a nonconductor. As the velocity increases, magnetic

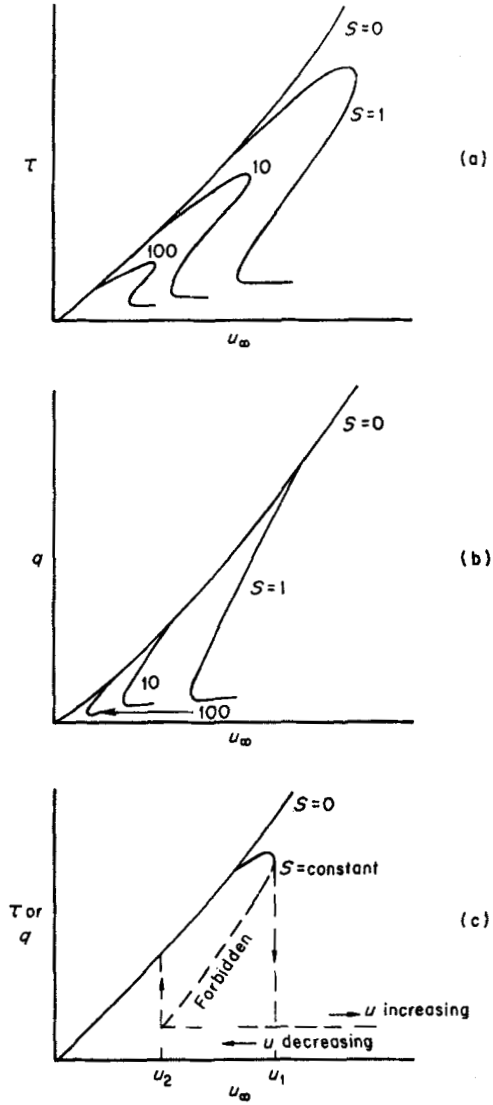

FIG. 17. Schematic behavior of skin friction and heat transfer in compressible-boundary-layer flow (*59*).

effects begin to occur and the skin friction begins to descend below its nonmagnetic value until a point (at the vertical tangent) where a further increase in velocity above, say, u_1 causes a discontinuous drop in τ or q to the lower branch of the curve, as shown in Fig. 17. If the velocity is then decreased, these functions will trace along the lower curve until

the lower vertical tangent is reached at u_2 and will then jump up to the upper curve and join the nonmagnetic curve as the velocity approaches zero. The regions between the two vertical tangents are unstable and would not be attained in practice.

a. Hysteresis Effect. The reasons for the discontinuous drop (or hysteresis behavior) of skin friction and heat transfer were discussed by Bleviss (*56*) and were traced to the rapid variation of σ with enthalpy as the gas first begins to ionize. In his conductivity model [taken from (*18*)], $\sigma(h,p)$ rises exponentially with h until $h \sim 32h_0$ (2600 cal/gm), at which point the temperatures are roughly between 4000° and 5500°K, depending on the pressure. The ion production up to this time has been primarily from the reaction $N + 0 \rightleftarrows NO^+ + e$. Above this point the NO production decreases, as most of the energy is taken up by the remainder of nitrogen dissociation. Hence for enthalpies between around 2600 and 9400 cal/gm, the variation of temperature with enthalpy, and hence conductivity with enthalpy, is relatively slow. Above $h \sim 9400$ cal/gm, both oxygen and nitrogen start to ionize, and the conductivity will again increase. By this time, however, the energy content of the gas is considerably higher than that which would be expected in normal hypersonic flight (i.e., $M_\infty > 40$).

Bleviss believed that the "flat spot" or abrupt change in slope of the conductivity caused the hysteresis behavior. In the boundary layer, the enthalpy level may pass through the point $h = 32h_0$ so that the magnetic effects in the boundary layer change abruptly (i.e., small magnetic fields would give large effects if σ were increasing rapidly). But then as h increases, the variation in σ is small and little effect of the magnetic field would be seen.

The author believes the same explanation applies to the solutions of (*59*), although the true behavior of σ has been masked by the parameter $\bar{\beta}$, which exhibits no such slope change. The fact that Bush found that the hysteresis does not disappear until higher Mach numbers is perhaps due to the differences between Couette and boundary-layer flow. Since the boundary layer remains cooler than Couette flow at higher Mach numbers, because of its ability to grow, the low-enthalpy behavior is retained over a larger range of velocities.

Bush presents the results of calculations for $p = 10^{-3}$ atm, $h_w/h_0 = h_\infty/h_0 = 10$ ($T \sim 2200$°K), and $h_w/h_0 = 10$, $h_\infty/h_0 = 1$. The first case would compared to a very slightly conducting free stream ($\bar{\beta} \sim 10^{-3}$), and the second to a hot wall and nonconducting free stream. In the former case the effects of finite conductivity on the inviscid flow are negligible. We do not have space to reproduce the results of (*59*), but several significant points about the heat transfer can be established.

b. An Assessment of the Results. The calculations by Bush indicated that reductions in heat transfer by as much as 80% would be achieved with moderate field strengths. The field strength, however, is limited in all flow problems by low-pressure effects, such as Hall currents (see Section I,B,2), which would invalidate the concept of a scalar conductivity and a two-dimensional flow. Bush estimated that when $p_\infty = 10^{-3}$ atm and the reference length = 1 m, it would require the interaction parameter $S \leq 0.1$ for $\omega/\nu_c \leq 0.1$. He did not present any curves for this low value of S, but some indications of heat-transfer behavior for low S can be obtained from the curves for $S = 1$.

Referring to Fig. 17*c*, when $h_w/h_0 = h_\infty/h_0 = 10$, the stable solutions are bracketed by $0 < u_1 < 15{,}000$ (m/sec) for increasing velocities and $10{,}850 < u_2 < \infty$ for decreasing velocities. That is, during a flight in which the velocities are always larger than 10,850 m/sec the heat transfer would be reduced substantially. Below those velocities there would be no reduction in heat transfer, since the magnetic interaction is too small. During an accelerating flight to $u_1 = 15{,}000$ m/sec there would be little reduction in heat transfer, and the calculations by Bush indicate there will be only a 10 to 15% reduction in skin friction. The range of velocities in this situation is presently much higher than any which have been achieved for thin-winged vehicles; therefore we must conclude that under normal circumstances at these altitudes the heat transfer would be unaffected. The curves for the heated wall are less restrictive at the lower end in their velocity requirements. That is, the stable solutions are given by $0 \leq u_1 \leq 13{,}700$ and $10{,}850 \leq u_1 \leq \infty$. We should also mention that at these low pressures the induced magnetic field would also become important (see Section V,A,2).

The restriction on field strength due to Hall effects would disappear as the pressure increases. For $p_\infty = 1$ atm, Bush estimated that $S \leq 100$ would satisfy the requirement for small Hall effects. However, even though the limiting velocities decrease when S increases, so does the necessary field strength increase to produce a given S, especially at higher pressures. Bush estimates that for an S of 100, at atmospheric pressure and a length of 1 m, the field strength $B_0 = 200{,}000$ gauss!

It is evident that there is an optimum value for S such that Hall effects are minimal and field strengths are reasonable. This, of course, depends on the velocities during flight and on the heat-flux reductions which would be necessary. The analysis by Bush indicates that even with large magnets ($S = 100$) the velocities must be at least as large as about 6000 m/sec to achieve any reductions in heat transfer.

c. Some Remarks Concerning the Assumptions. Several assumptions are made by Bush and other workers in hypersonic-boundary-layer theory

in order to facilitate the solution of the equations. Besides the neglect of Hall currents and ion slip these include assuming that the induced field is negligible, the gas is in thermodynamic and chemical equilibrium, and the Lewis number is unity (diffusion transport of heat is neglected).

We have already remarked on the first assumption in Section V,A,2. It was shown for the Couette-flow case that the pressure due to the induced field could cause flow separation at ambient pressures lower than roughly $p_\infty \sim 10^{-3}$ atm. [This will not occur if $B \sim 1/\sqrt{x}$, according to (*60*)]. In a boundary layer the induced field would probably contribute to the boundary-layer growth and decrease the heat transfer. However, the induced field becomes important only at those pressures where Hall currents become important. Therefore the assumption that $\mathrm{Re}_m \sim 0$ seems justified in this case where the solution is limited by Hall effects.

The assumption of chemical and thermodynamic equilibrium implies that reaction times are short compared with the time it takes an air particle to enter the boundary layer, become heated, and traverse the length of the body. It also implies that particles which diffuse across the boundary layer adjust instantaneously to the temperature of the gas. If the time for ionization is much larger than the traverse time the gas will never ionize and the magnetic field will have no effect. If the ionization time is equal to or greater than the dissociation time, then the case of equilibrium will indicate maximum magnetic effects, unless the ionization time is less than the dissociation or traverse time. In this instance an equilibrium solution would underestimate the magnetic interaction.

Little is known of ionization rates in gases except those at the relatively high pressures existing behind normal shocks. Because the forward two-body process of dissociation and ionization is fast compared to recombination, a three-body process, it is likely that at the pressures considered in these studies the gas will be in equilibrium—at least in the regions of highest temperatures in the boundary layer.

This conclusion is based partially on a study by Chung and Anderson (*61*) of nonequilibrium effects due to dissociation of pure oxygen in a flat-plate boundary layer. They showed that at 30,000 m ($p_\infty \sim 10^{-2}$ atm) and M = 20, the oxygen was 80% in equilibrium one meter aft of the leading edge. An extrapolation of their results to the ionization equilibrium of NO^+ is certainly not warranted, since the reaction rates are different, but since atomic oxygen is necessary for the ionization reaction, we can conclude that at higher Mach numbers there will probably be sufficient atomic oxygen to cause the ionization to exist.

It should be pointed out that this study was for the adiabatic wall. This is the most favorable situation for equilibrium, since recombination

takes place only in the particles diffusing away from the wall; further, the flow time near the wall is lowest, enabling the gas to spend more time in a particular environment. At higher altitudes, the equilibrating process takes longer.

In actual hypersonic flight the diffusion of heat from the reacting gas can contribute considerably to the heat transfer. The heat released by the recombination of electrons and ions at the wall will not be significant at low degrees of ionization. But the effect of catalytic walls on heat transfer can be severe due to the interaction of the magnetic field with the atom-concentration gradient (see Section VI,B,2).

C. RÉSUMÉ: FLAT-PLATE BOUNDARY-LAYER HEAT TRANSFER

It has become clear in the preceding discussion that the assumed variations of conductivity with temperature and of temperature with enthalpy have a significant effect on the behavior of boundary-layer heat transfer with magnetic fields present. When either nonequilibrium effects or diffusion transport is included, the problem of determining the magnetic interaction can be formidable. Hall-current considerations appear to limit these solutions to relatively low altitudes ($p_\infty \sim 10^{-3}$ atm corresponds approximately to 40,000 m altitude).

On the basis of the discussion in Section, IV,D, it would be of interest to ascertain the effects of seeding both a nonequilibrium (high-temperature "frozen" flow) and an equilibrium gas with a contaminant such as cesium, potassium, or sodium, all of which are easily ionized. The conductivity here would display a more regular behavior and the hysteresis properties of τ and q could be avoided; i.e., more efficient cooling could take place at lower temperatures if the conductivity were high. Of course, seeding would also increase the total drag and would probably contribute to the heat deposition in the wake.

However, it is clear from the analyses reviewed in this section that the reduction of flat-plate aerodynamic heating by magnetic means is not promising for naturally ionized air. But there still remain refinements to these solutions which may indicate further effects on heat transfer which are as yet undetermined. Further, the purely aerodynamic utilization of the magnetic forces as flow-control mechanisms should not be dismissed, for the influence of a magnetic field on drag is much larger than on the heat transfer.

VI. Heat Transfer to Blunt Bodies

It was mentioned in the Introduction that a large portion of the early interest in engineering MHD stemmed from the aerodynamic-heating problems associated with hypersonic flight in the atmosphere. One of

the most critical heating areas is at the stagnation point of a blunt body, where the incoming hypersonic airstream is brought to rest by a strong normal shock and adiabatic compression. For a typical earth-satellite reentry at velocities of about 8000 m/sec, the maximum heating rate to a 1-m body is 7850 w/m^2 (80 Btu/ft^2 sec). For reentry from near space, where the reentry velocity is closer to 11,000 m/sec the maximum heating rate is higher by a factor of 3.

This section will review the numerous analyses presented in the literature during the past 5 years. In retrospect it must be conceded that many of the early estimates of heat-transfer reductions using magnetic techniques were optimistic because the entire flow problem was not completely analyzed. Again, other studies were more pessimistic because the shock strengths considered were those associated with ballistic reentry rather than reentry of a planetary probe. It is hoped that this review will contribute to the clarification of what has been a highly controversial subject. We have tried to present the results in such a form that all comparisons between heating rates and methods of solution are based on bodies of similar shape flying at the same altitude and velocity.

A. STAGNATION-POINT HEAT TRANSFER WITH APPLIED MAGNETIC FIELDS

When a blunt body moves at hypersonic speeds, a large percentage of the kinetic energy of the airstream is converted into heat by the compression of the normal shock at the nose of the vehicle. This heating of the air behind the shock will cause dissociation and, at high enough velocities, will cause ionization to such an extent that the air is capable of being influenced by a magnetic field.

Consider the blunt body of Fig. 18*a*. If there is no applied electric field, and a magnetic field is affixed so that it acts perpendicularly to the oncoming flow, the ponderomotive force acts in a direction to decelerate the tangential velocity, u, since the current, j, flows in loops as shown in Fig. 18*b*. Without a detailed examination of the equations, we can qualitatively state that the magnetic interaction will cause

(*a*) The shockwave standoff distance to increase, since a larger volume is needed for the passage of the air between the shockwave and the nose

(*b*) The coefficients of heat transfer and skin friction to decrease because the local velocity is lower

(*c*) The pressure at the stagnation point, which is determined principally by the normal momentum, to change little

(*d*) The total drag of the body to increase.

It is obvious that the problem of determining the heat transfer near the stagnation point demands a solution of the entire flow field from the

shock to the body both since the inviscid and viscous regimes are conducting. Some of the early papers on this subject (*60, 62, 63, 64*), did not include the effects of the magnetic interaction on the inviscid flow. These solutions could be considered as incomplete in the sense that a viscous problem was solved for an unknown inviscid, or controlling, flow. Neither do

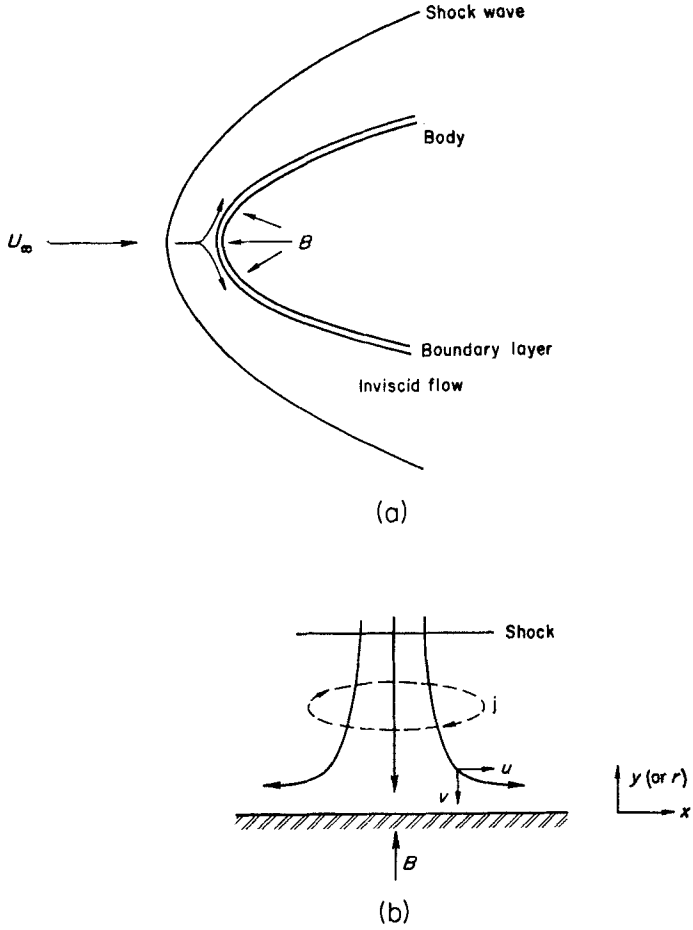

FIG. 18. Schematic diagram of a hypersonic stagnation flow with an applied magnetic field; (a), a typical blunt body; (b), detail of stagnation point.

these solutions include any discussion of the influence of the magnetic field on the pressure distribution around the stagnation point. But Lykoudis (*65*) showed that it was possible to match the viscous solutions with an inviscid flow by choosing an average magnetic-field intensity in that region to adjust the velocity and pressure for the magnetic interaction. This procedure implicitly assumes that the electrical conduc-

tivity and density are constant in the inviscid layer, which is an excellent approximation at hypersonic velocities and altitudes below 60,000 m.

For the purpose of this section, however, it is most convenient to discuss the complete stagnation region, starting with the inviscid flow; after this, the viscous regime can be easily determined by using standard boundary-layer techniques. As in any stagnation-point flow, the heat transfer is proportional to the temperature or enthalpy gradient at the wall and the square root of the tangential velocity gradient at the edge of the boundary layer [see Eq. (104)]. For a constant-property boundary layer, the latter accounts for the largest portion of magnetic influence on the heat transfer. We shall therefore restrict our discussion of the inviscid solution to the determination of the velocity gradient.

1. The Velocity Gradient

The inviscid flow field in the vicinity of the stagnation point is described in a fluid-dynamic sense as the conversion of a unidirectional, high-velocity stream by a normal shockwave into a high-temperature subsonic layer, which is taken to be inviscid and incompressible, both of which are good approximations at high velocities and Reynolds numbers. The second qualification is necessary to insure that the boundary layer and inviscid flow are distinct; for a further discussion of "viscous-layer" effects the reader is referred to Hayes and Probstein (*66*) or Wu (*67*).

The properties directly behind the normal shock are determined by the Rankine-Hugoniot conservation equations; if the gas becomes dissociated or ionized there are numerous charts which describe the gas properties in this region [see, e.g., (*68*)].

There are essentially two mathematical approaches towards the flow problem, both of which have been successfully employed in the non-magnetic case and which are described more fully in (*66*). The first consists of utilizing the Newtonian approximation.

a Newtonian Flow. In the Newtonian approximation, the shockwave is assumed to be either spherical or cylindrical (depending on the body shape at the nose) in the vicinity of the stagnation point. The density is constant in the region between the shock and body. Immediately after passing through the shock, the fluid is assumed to give up all of its normal momentum into pressure; i.e., the flow turns immediately so that the velocity after incidence remains tangent to the wall. Lykoudis made the remark in (*69*) that since the normal velocity, which determines the pressure in this approximation, is parallel to and unaffected by a radial applied field, there will be no magnetic interaction which can affect the pressure. The pressures determined by this approach will become less accurate as the shock detachment distance increases or if

an extensive induced field exists. The velocity gradients obtained by the Newtonian solutions are compared in (*69*) with more exact calculations by Kemp (*70*). It is shown that the agreement is within 8% for reasonable values of the magnetic interaction. These data will be presented after the other flow calculations are discussed.

It should be mentioned here that one of the benefits of the Newtonian approximation is that it permits closed-form solutions to be obtained for all the flow characteristics. This is particularly useful when trends are investigated.

b. Similarity Solutions. The similarity solutions discussed by Hayes and Probstein (*66*) also assume a shock with the same shape as the body, with an incompressible inviscid flow behind it. For a given shock radius, free-stream velocity, and density ratio across the shock, the body surface is found where the normal component of velocity vanishes. As such, these solutions are more refined than the Newtonian approximation, although neither takes into account the finite compressibility that exists between the shock and the body. However, this method will allow for variations in the pressure distribution, due to the magnetic-field interaction, and it need not be restricted to small magnetic Reynolds numbers. However, the shock layer must still be thin enough that the curvature is constant and incompressibility exists.

Kemp (*70*) investigated analytically the extension of this method for spherical flow and the case of small magnetic Reynolds number, in which situation only the component of the applied field at the body need be specified. (Of course, the applied field would still have to satisfy Maxwell's equations for that particular body.) Bush (*71*, *72*) solved numerically the inviscid-spherical flow field for a magnetic field which acted as a dipole in the free stream. Here the boundary conditions were specified at the shock rather than on the body. In this way he was able to consider a nonvanishing magnetic Reynolds number and still solve a relatively simple set of differential equations. Wu (*67*) utilized the same scheme but also considered low-Reynolds-number effects (large viscous layers) as well. He solved both the two- and three-dimensional cases. Meyer (*73*) presented one of the first analyses of the two-dimensional stagnation problem in which the inviscid flow was determined for large magnetic Reynolds number.

c. Comparison of the Various Solutions. In order to compare the results of these various solutions it will be necessary to specify some form of the magnetic-interaction parameter, S [see Eq. (28)], which contains arbitrary lengths and velocities. On the basis of the preceding discussion it would seem that the most logical form for S would be that one which contains all of the "knowns" or starting conditions in the solution: density

ratio, free-stream velocity, shock radius, and magnetic field at the shock. In fact, Lykoudis (*69*) showed through the analytic Newtonian solution that this indeed is the most natural parameter for the inviscid flow. If

$$S_s \sqrt{\frac{\rho_\infty}{\rho}} = S_s^* = \frac{\sigma B_s^2 R_s}{\rho_\infty u_\infty} \sqrt{\frac{\rho_\infty}{\rho}} \tag{98}$$

is used, then all flow parameters in the three-dimensional Newtonian analysis are functions of S_s^* and body type alone; the two-dimensional parameters are weak functions of the density ratio. Here R_s is the shock radius and B_s is the value of the magnetic field at the shock.

But Eq. (98) is inconvenient to use because in most practical problems the body radius, not the shock radius, is known, and the body field rather than its value at the shock will be specified. Kemp (*70*) suggests the parameter

$$S_b = \frac{\sigma B_b^2 R_b}{\rho_\infty u_\infty} \tag{99}$$

to describe the magnetic effects; here B_b is the magnetic field at the body and R_b is the body radius.

To indicate the order of magnitude of S_b, let us consider a body of 1-m radius flying at velocities on the order of Mach 25 ($u_\infty \sim 7800$ m/sec). Let us take an average value of conductivity of 100 mho/m for these velocities and densities. (This is within a factor of 3 of the actual conductivity.) At 30,000 m altitude the density is about 3×10^{-2} kg/m^3. Therefore, for a field strength of 1 weber/m^2

$$S_b \sim 0.5$$

At 60,000 m and at the same velocity, $S_b \sim 30$. Therefore one could consider that $0 \leq S_b \leq 30$ would bracket most practical cases for stagnation flow. The field strength chosen here ($B_b \sim 10{,}000$ gauss) is just about the maximum value for practical application; therefore values of S_b much lower than the above would probably be encountered in reality, even if the velocity reaches 10,000 m/sec.

The flow characteristics when Eq. (99) is used will be functions of the density ratio, ρ_∞/ρ, and S_b, as well as of body type, although Bush (*72*) indicates that the velocity ratio is insensitive to values of ρ_∞/ρ at least for $0.115 \leq \rho_\infty/\rho \leq 0.140$. These are typical density ratios for hypersonic normal shocks (*68*).

It is evident from Eqs. (98) and (99) that

$$S_b = S_s \left(\frac{B_b}{B_s}\right)^2 \left(\frac{R_b}{R_s}\right) \tag{100}$$

so that a transformation between the parameters demands a knowledge

of the magnetic-field configuration and the shock radius (or standoff distance) which is a function of the parameter S_b or S_s. It is well to keep this in mind when comparisons are made between various investigations.

The two-dimensional case has been studied by Lykoudis (*69*), Wu (*67*), and Meyer (*73*), although Wu did not present any numerical calculations. Meyer's solution was for the case of a large magnetic Reynolds number, and, unfortunately, it is not possible to convert from the parameters given in (*73*) to the body parameter S_b, since the standoff distance necessary for the conversion [Eq. (106)] is not given.

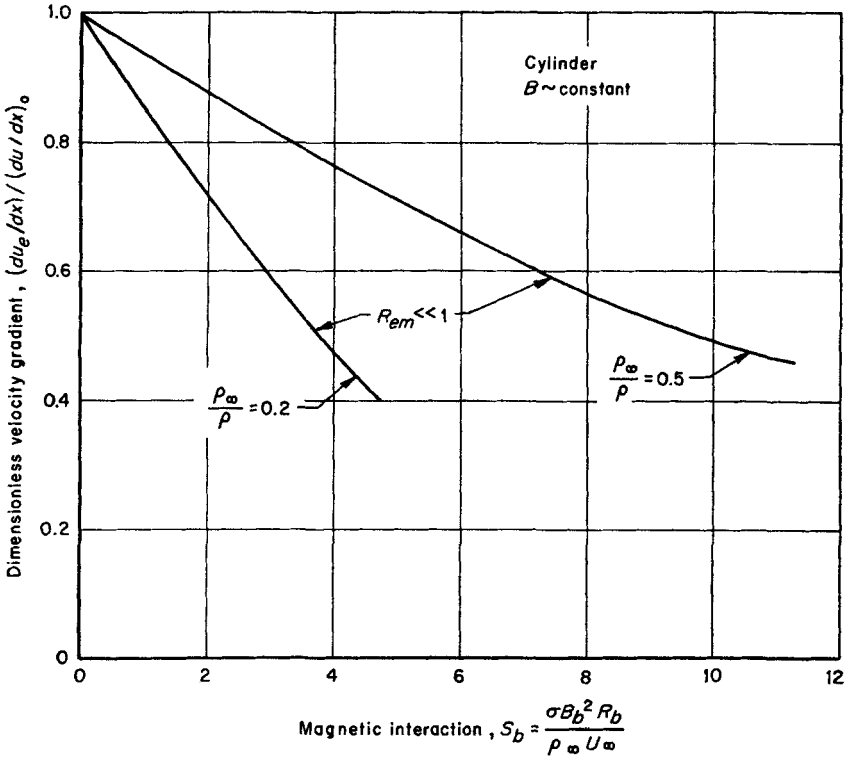

FIG. 19. Velocity gradient compared to the field-free case for two-dimensional stagnation flow (*69*).

We have plotted in Fig. 19 values from the Newtonian analysis of Lykoudis in which B was assumed constant; his results, for $\mathrm{Re}_m \ll 1$, are only slight functions of density ratio when plotted versus $S_s \sqrt{\rho_\infty/\rho}$. The values of ρ_∞/ρ shown in Fig. 19 embrace the entire hypersonic regime. These curves will be utilized more fully in the section on heat transfer.

Bush (*72*), Lykoudis (*69*), Kemp (*70*), and Wu (*67*), have calculated the velocity gradient for the sphere. We show these results in Fig. 20. again as a function of S_b, where the density ratio $\rho_\infty/\rho \sim 0.1$. The curve from (*67*) is for a Reynolds number of 1000 based on shock radius (compared to the other solutions, where $\mathrm{Re}_s \to \infty$). The thick viscous layer in this case is reflected by the rapid decrease in velocity gradient as the magnetic field increases slightly.

Figure 20 indicates that the agreement between various computations for the velocity gradient is quite good even though a different magnetic-field configuration is used in three of the calculations. (Wu used the

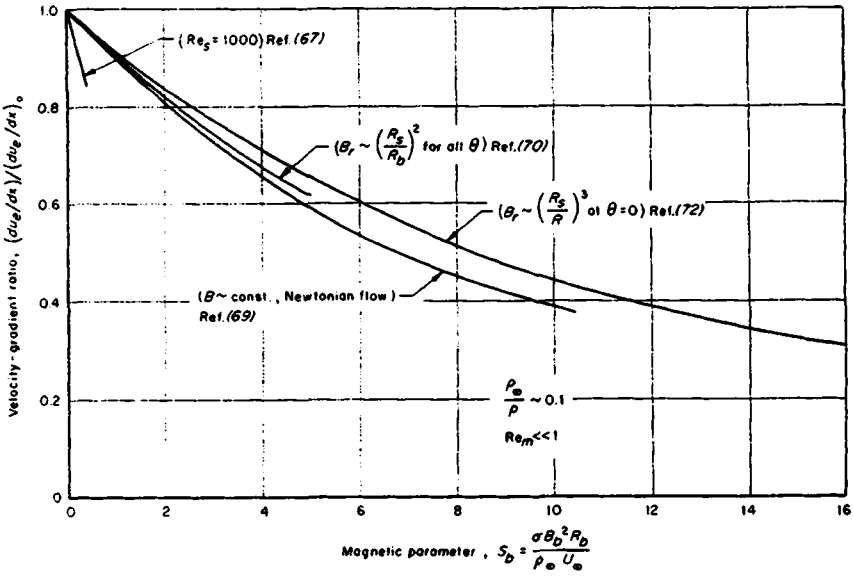

FIG. 20. Comparison of stagnation-point velocity gradients with the field-free case for hypersonic flow around a sphere and various magnetic-field configurations.

dipole field that was employed by Bush.) This is contrary to the comparison made by Lykoudis (*69*), who indicated that his Newtonian solution was about 8.5% lower than the similarity solution at $S_b = 5$. He attributed this disagreement to the change in pressure due to the magnetic field. However, Lykoudis made his comparison with S_s as the interaction parameter; evidently when the shock radius is removed [Eq. (100)], the disparity is eliminated to a great extent.

One important conclusion can be drawn from Fig. 19. Namely, when Eq. (99) is used for the interaction parameter, or when the same bodies under identical flight conditions are compared, the particular form of

the magnetic field along the stagnation axis is relatively unimportant in determining the reduction in the velocity gradient. Even if Maxwell's equations are not satisfied (for example, if B = constant) the velocity gradient is determined largely by the value of B at the body, at least for $S_b < 5$. For higher values of the interaction parameter, the dimensions of the flow field are larger and the influence on the structure of the outer flow of the variable magnetic field is reflected by the divergence of values illustrated in Fig. 20 for $S_b \geq 10$.

Although Fig. 20 shows results for $\mathrm{Re}_m \ll 1$, we can infer from the calculations of Bush (*71*) that as long as $\mathrm{Re}_m \leq 1$ and $S_s < 3$, there is slight effect of the induced field on the velocity gradient. A conversion of S_s to S_b is not possible here since the value of the magnetic field at the body cannot be obtained from the data presented in (*71*). However, on the assumption that the induced field at the body is small, $S_b \sim 35$ when $S_s = 3$; so for the values of interest in hypersonic flight, the induced field is unimportant as long as $\mathrm{Re}_m \leq 1$. For flight at Mach 25 and an altitude of 30,000 m, $\mathrm{Re}_m \sim 0.01$ (taking $\sigma \sim 100$ mho/m). Therefore, the small-magnetic-Reynolds-number approximation is valid in hypersonic flow.

2. The Enthalpy Gradient

The second factor in the stagnation-point heat transfer to be affected by the magnetic field is the enthalpy gradient at the wall. This is determined by the shape of the velocity profile in the boundary layer and by the variation of air properties with temperature. The radial magnetic field will lead to fuller profiles (see, e.g., Section IV,A,3) and as a result will enlarge that portion of the heat transfer due to the enthalpy gradient. However this increase is not likely to be as large as the reduction afforded by the velocity gradient, at least when the electrical conductivity is assumed to be constant across the layer.

The boundary-layer equations for a stagnation flow fall into the class of "wedge" flows for which $U_e = Cx^m$ [see, e.g., (*60*)]. For the axisymmetric case, $m = \frac{1}{3}$. This form of velocity, which in turn dictates the pressure gradient, demands that the magnetic field tangent to the body vary as a power of x; i.e., similar solutions are possible only if

$$B_x \sim x^{m-\frac{1}{2}} \tag{101}$$

At the stagnation point B reduces to a constant and does not vary across the layer. None of the cases analyzed in the literature considered the matching of the inviscid and viscous *magnetic-field* configurations. (Note here that when the velocity is constant $m = 0$ and the flat-plate variation of Section V,B,2, is obtained.)

Many analyses have been made for the viscous two- and three-dimensional stagnation-point heat transfer. Both incompressible and compressible flows have been treated. A survey of these papers brings forth the interesting result pointed out by Kemp (*74*) that the effects of compressibility and body dimension are relatively small in the determination of the enthalpy gradients as long as the electric conductivity is constant. This can be seen in Fig. 21, where we have plotted data from Neuringer

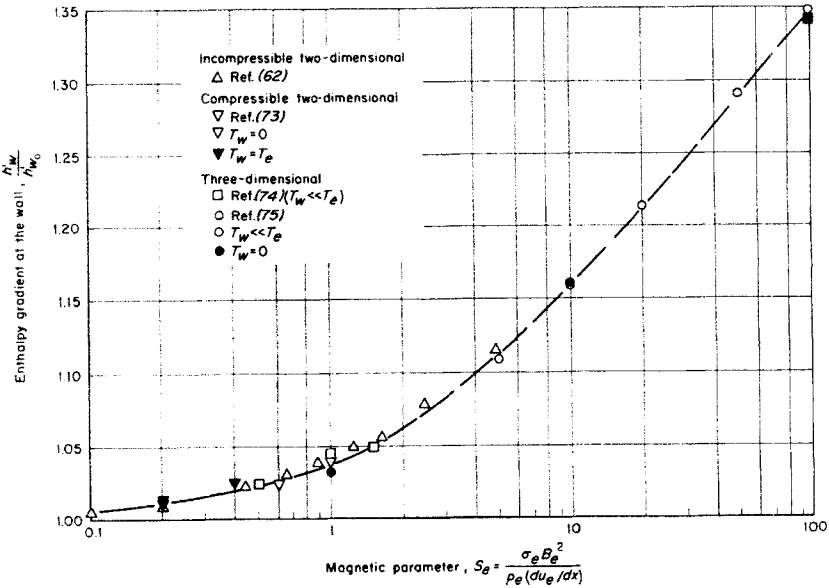

FIG. 21. Invariance of viscous contribution to stagnation-point heat transfer for constant conductivity solutions.

and McIlroy (*62*), Meyer (*73*), Kemp (*74*), and Bush (*75*); only the latter two calculations are for the same body shape and gas assumption, although the field configurations were slightly different.

The data of Fig. 21 are plotted as a function of the parameter

$$S_e = \frac{\sigma_e B_b^2}{\rho_e \left(\frac{du_e}{dx}\right)} \tag{102}$$

which arises naturally from the boundary-layer equations when account is taken of the pressure gradient as determined from the inviscid flow:

$$\rho u \frac{\partial u}{\partial x} + \rho v \frac{\partial u}{\partial y} = \rho_e u_e \frac{du_e}{dx} + (u_e - u)\sigma_e B_b^2 + \frac{\partial}{\partial y}\left(\mu \frac{\partial u}{\partial y}\right) \tag{103}$$

where e denotes conditions at the edge of the boundary layer. It is necessary in this analysis to assume that the magnetic field B_b is constant across the boundary layer, which is not unreasonable unless the viscous layer is very thick, as in the case studied by Wu (*67*).

When the conductivity is allowed to vary as some power of enthalpy, the viscous contribution to the heat transfer can be significant, as shown by Bush (*75*). We have plotted the enthalpy gradients for this case in Fig. 22, where the broken line denotes the average values for σ = constant, taken from Fig. 21.

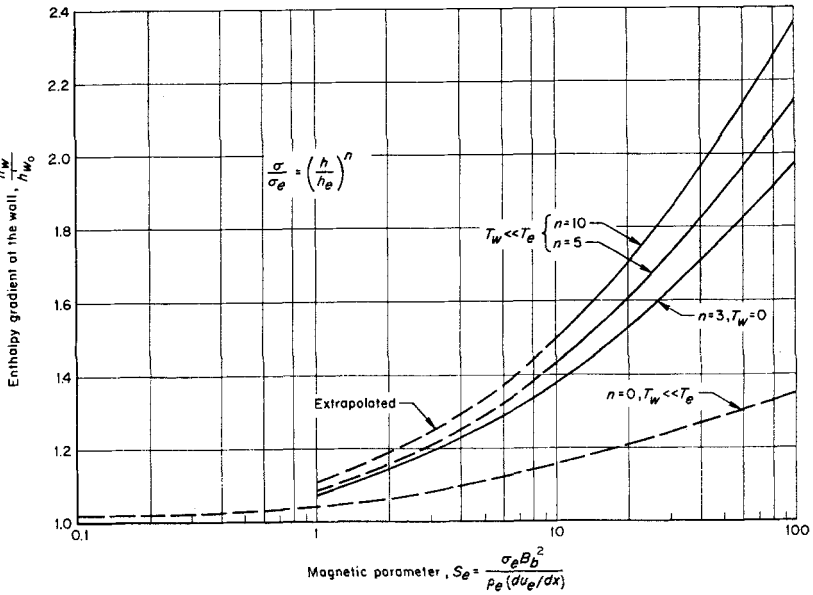

FIG. 22. Effect of variable conductivity on the enthalpy gradient, compared to the field-free case (*75*).

However, to assess the full effect of both the enthalpy gradient and velocity gradient on stagnation-point heating, we should now look at the heat transfer itself.

3. *Stagnation Heating*

As mentioned previously, the stagnation-point heat transfer is a function of velocity gradient, enthalpy gradient, and various air properties, viz.

$$q = \left(k \frac{\partial T}{\partial y}\right)_w = f(\rho, \mu, h)_{\text{stag.}} \left(\frac{du_e}{dx}\right)^{1/2} h_w' \tag{104}$$

[A complete derivation of Eq. (104) can be found in (*66*).] If q is com-

pared to a field-free case with the same stagnation conditions, or, equivalently, the same flight velocity and altitude, the air properties cancel, leaving

$$\frac{q}{q_0} = \left[\frac{(du_e/dx)}{(du_e/dx)_0}\right]^{1/2} \frac{h_w'}{h_{w_e}'} \tag{105}$$

It is apparent that we can either use S_b, which is based on flight conditions and body radius, as the interaction parameter for a comparison;

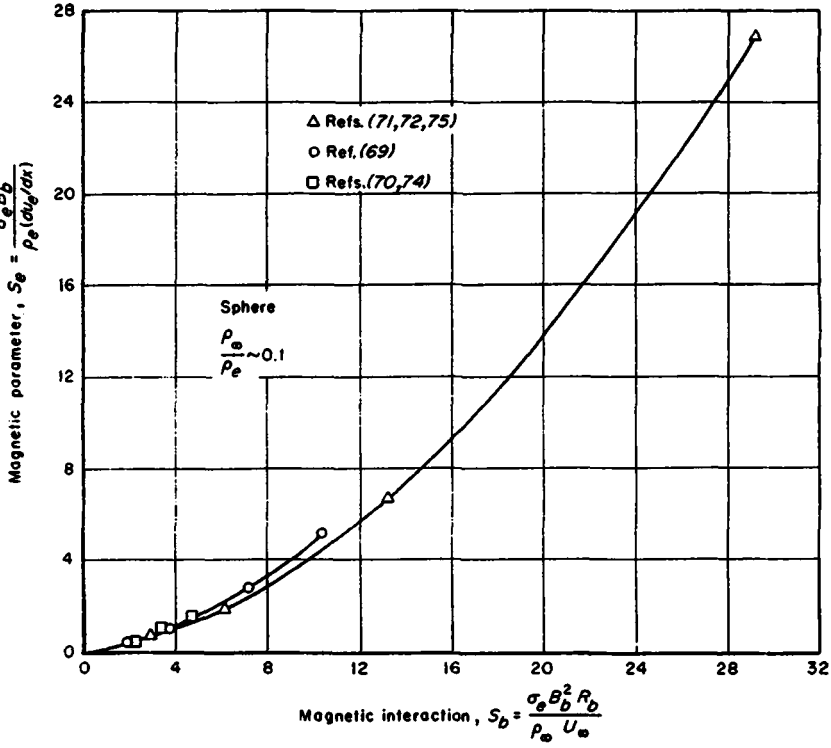

FIG. 23. Transformation between boundary-layer interaction parameter and body parameter for the sphere in hypersonic flight.

or we can use S_s, which would be a comparison of two bodies having the same drag. For the purposes of this section it is more convenient to use the body parameter S_b.

In either case, it is necessary to convert from S_e to S_b in order to combine the results of Figs. 19–22. By use of Eqs. (100) and (102)

$$S_e = S_b \left(\frac{\rho_\infty}{\rho_e}\right) \frac{(du_e/dx)}{(du_e/dx)_0} \left[\frac{R_b(du_e/dx)_0}{u_\infty}\right] \tag{106}$$

The term in brackets can be obtained from a field-free solution of the

flow; for example, one could use the Newtonian values given in (*69*):

$$\left.\begin{aligned} \frac{\left(\frac{du_e}{dx}\right)_0 R_{s_0}}{u_\infty} &= \sqrt{3\rho_\infty/\rho_e} \\ \frac{R_b}{R_{s_0}} &= 1 + \frac{\rho_\infty/\rho_e}{\sqrt{1 - 3\rho_\infty/\rho_e}} \cosh^{-1}\left[\frac{1}{\sqrt{3\rho_\infty/\rho_e}}\right] \end{aligned}\right\} \text{cylinder} \qquad (107)$$

$$\left.\begin{aligned} \frac{\left(\frac{du_e}{dx}\right)_0 R_{s_0}}{u_\infty} &= \sqrt{\frac{8\rho_\infty}{3\rho_e}} \\ \frac{R_b}{R_{s_0}} &= 1 + \frac{\rho_\infty/\rho_e}{1 + \sqrt{\frac{8\rho_\infty}{3\rho_e}}} \end{aligned}\right\} \text{sphere} \qquad (108)$$

a. Heat Transfer to Spheres. This has been done for the sphere and a density ratio of $\rho_\infty/\rho_e \sim 0.1$; the relation between S_e and S_b is given in

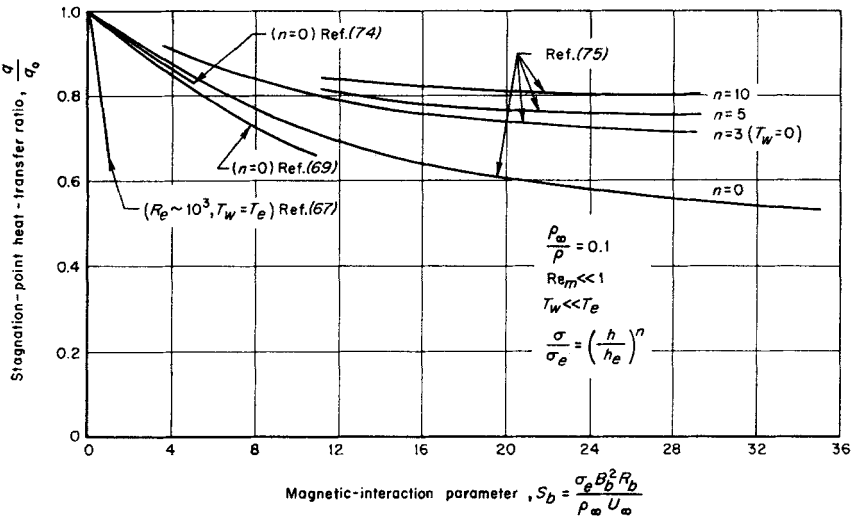

FIG. 24. Comparison of stagnation-point heat transfer with the field-free case for a sphere in hypersonic flow.

Fig. 23 for the solutions of Kemp, Lykoudis, and Bush. The points due to Kemp were taken from (*74*), where the field-free similarity solution gives $R_b(du_e/dx)_0/u_\infty \sim 0.517$ compared to the Newtonian value of 0.549. The agreement for $S_b < 5$ is such that either solution is valid for conversion.

We have plotted q/q_0 on Fig. 24 for the calculations of Bush and Kemp discussed previously, using the data of Figs. 20, 22, and 23. For

$n = 0$ (σ = constant), the two solutions are in agreement for $S_b \leq 5$, to which value Kemp computed heat transfer. The curves given by Bush in (*75*) for all values of the conductivity exponent extend to values of S_e much higher than presented here ($S_e \leq 100$) but these were not plotted in Fig. 24 because $S_b \leq 30$ should be close to the maximum value encountered with unseeded air and practical magnetic-field strengths, at least for altitudes below 60,000 m. It can be seen from Fig. 24 that when $n > 5$, an upper limit of sorts exists on S_b such that an increase in S_b does not decrease the heat transfer further. From the calculations made by Bush on the hypersonic boundary layer (Section V,B,2), we find that the $\sigma/\sigma_e \sim (h/h_e)^{5.44}$ fits the experimental data and the assumption made in (*75*) that $\rho\mu \sim \rho_e\mu_e$ (true when $h_e \gg h_w$). Therefore, in actual flight, the curve marked $n = 5$ is likely to be encountered. Reductions of 20 per cent in stagnation heating can be obtained if S_b is high enough.

The curve in Fig. 24 attributed to Lykoudis (*69*) is the Newtonian solution for the heat-transfer ratio at $n = 0$. This curve can be obtained by using Figs. 20, 21, and 23, or from the simple approximation

$$\frac{q}{q_0} = \left[\frac{du_e/dx}{(du_e/dx)_0}\right]^{0.4} \tag{109}$$

both of which yield the same values. Equation (109) was first used by Lykoudis (*60*), where the exponent was introduced from results of nonmagnetic studies in hypersonic-stagnation heating (*17*). This approximation overestimates the reduction in heat transfer, which can be traced to the lower values of velocity gradient exhibited in Fig. 20 for the Newtonian solution, although the agreement for $S_b < 5$ is within 3% of the calculations made by Bush. Therefore the simple formula of Eq. (109) affords an excellent approximation for stagnation-point heat transfer. The error does not exceed 10%, which is within reason, considering the approximations made in all these solutions, until $S_b \gg 10$. The difference would be even less if an average magnetic field were used, as suggested by Lykoudis (*65*).

Before leaving the case of spherical flow, it is of interest to indicate the effects of large viscous layers on the heat transfer. From Fig. 20 it is evident that Wu's calculations for a shock Reynolds number of 1000 show an extensive decrease in velocity gradient. This is reflected in the heat transfer shown in Fig. 24, where we have multiplied the values given in (*67*) by R_e/R_b to account for changes in the shock Reynolds number as S_b increases.

b. Heat Transfer to Cylinders. With the exception of Meyer's solution for $\mathrm{Re}_m \gg 1$, the literature does not contain any complete solutions for

the cylindrical case. We suggest, on the basis of Fig. 24, that the empirical relationship of Eq. (107) be used for cylindrical flow, where the velocity-gradient ratio is given in Fig. 19. These values will probably overestimate the reduction in heat transfer in the same manner, as evinced by Fig. 24.

To conclude, we have seen that it is possible to obtain significant reductions in stagnation-point heat transfer during ballistic reentry only by the application of very large magnetic fields. In a practical sense, the weight of magnets large enough to produce fields larger than 10,000 gauss would prohibit their use in present-day systems; other methods of cooling are more feasible at the present. For future applications, such as reentry from near space, where significant heating takes place at high velocities and altitudes, this method of cooling might be worth considering, especially if magnet technology produces lighter and more efficient magnets.

B. OTHER STAGNATION-POINT EFFECTS

1. Radiative Heat Transfer

While it was stipulated in the Introduction that we would be studying convective heat transfer only, the peculiar nature of stagnation flow demands that radiation effects be included. Goulard (*76*) has shown in an order-of-magnitude analysis, using the formula due to Lykoudis [Eq. (109)], that an optimum field exists for reduction in total heat transfer. At the time (*76*) was written an analytic expression for the shock-layer thickness did not exist. The analysis made by Goulard can be improved[1] if we use the analytic expressions for the standoff distance given in (*69*). It was shown in (*69*) that the shock-standoff distance is proportional to $(du_e/dx)^{-m}$, where the exponent $m = \frac{3}{4}$ for cylindrical flow and $m = \frac{1}{2}$ for axisymmetric flow. (Goulard used the value $m = 1$.) The energy radiated by the hot gas is thus written on the basis of continuity as

$$\frac{q_R}{q_{R_0}} = \left[\frac{(du_e/dx)_0}{(du_e/dx)}\right]^m \tag{110}$$

Using Eq. (109), the total heat can be written

$$q_{\text{tot}} = q + q_R = q_0\left[\frac{(du_e/dx)}{(du_e/dx)_0}\right]^{0.4} + q_{R_0}\left[\frac{du_e/dx}{(du_e/dx)_0}\right]^{-m} \tag{111}$$

The optimum value for the velocity-gradient ratio occurs when the derivative of Eq. (111) with respect to that ratio is zero:

$$\frac{du_e/dx}{(du_e/dx)_0} = \left(\frac{mq_{R_0}}{0.4q_0}\right)^{1/(m+0.4)} \tag{112}$$

[1]This refinement was suggested by P. S. Lykoudis (*40*).

Now Eq. (112) and the fact that $du_e/dx < (du_e/dx)_0$ implies that $q_{R_0}/q_0 < 0.4/m$ for a reduction in total heat to exist when a magnetic field is applied at the stagnation point. Since

$$q_0 \sim \text{const} \left(\frac{\rho_\infty}{R_b}\right)^{1/2} u_\infty{}^3 \tag{113}$$

and

$$q_{R_0} \sim \text{const}\ \alpha_w(\rho_\infty)^{3/2} R_b u_\infty{}^{10}$$

The heat-transfer ratio becomes

$$\frac{q_{R_0}}{q_0} = \text{const}\ \alpha_w \rho_\infty (R_b)^{3/2} u_\infty{}^7 < \frac{0.4}{m} \tag{114}$$

For a cylinder, the inequality is $q_{R_0}/q_0 < 0.533$, and for a sphere, $q_{R_0}/q_0 < 0.8$. [Notice that if $m = 1$, as in (*76*), then the inequality is $q_{R_0}/q_0 < 0.4$ in all cases.]

It can be deduced from Eq. (113) that the radius for minimum convective heat transfer ($\partial q_0/\partial R_b = 0$) is such that the heat-transfer ratio becomes

$$q_{R_0}/q_0 = 0.5 \tag{115}$$

Therefore if the body shape is designed so that convective heating without a magnetic field is at a minimum, the application of a magnetic field will not increase the total heat transfer, since Eq. (114) is satisfied for either value of m under consideration. Goulard (*76*) found, that the radius would have to be *less* than its optimum value, since the inequality demanded that the heat-transfer ratio be less than 0.4.

It is still unlikely, however, that the inequality of Eq. (114) can be satisfied at very high velocities when the wall absorptivity, α_w, is large (i.e., when the surface is very "black"). Radiative heat transfer will definitely become important at the higher altitudes and velocities associated with reentry from space; and any analysis of stagnation heating with magnetic fields should include the radiative effects. To the author's knowledge, however, a refined analysis has not been made.

2. Effects of Chemical Reactions

Lykoudis (*60*) discussed the effects of diffusion and wall recombination briefly in his analysis of the viscous layer. By utilizing the results of magnetic-free heat-transfer calculations (*17*), he showed that the term governing recombination at the wall is unfavorably influenced by the magnetic field, thus increasing the heat transfer due to diffusion and recombination. If wall effects had been included in the heat-flux balance of Section II,E, the catalytic term would multiply the Lewis number in Eq. (39), thus causing an increase in the heat transfer to the wall. When

a magnetic field is applied, this term is further increased. A more complete discussion is given in (*60*).

3. Stagnation Point with Electric Field

The Langmuir probe is a small electrode to which various potentials are applied and from which currents are measured. It has been used extensively in gaseous discharges and static-plasma investigations. Talbot (*77*) suggests utilization of the Langmuir probe at the stagnation point and has developed the theory for its use in determination of hypersonic ion concentrations and temperatures.

Because of the electric field applied to the probe, a space-charge sheath will exist in the viscous region around it. The gas external to the sheath is taken by Talbot to be chemically frozen, with ambipolar diffusion determining the motion of ions and electrons to the wall. The heat transfer to the wall in this presence of the sheath was determined; this includes the effects of ordinary conduction, ion-electron recombination heating, and the release of kinetic energy gained in the fall of charges through the sheath. An example was calculated for slightly ionized argon at $u_\infty = 2090$ m/sec, $\rho_\infty = 8.1 \times 10^{-5}$ kg/m^3, and $T_\infty = 790$°K. For a flat-ended cylinder of 1-cm radius, he found that the total heat transfer for the probe at negative potential with respect to the plasma was largely conductive ($q = 10^5 w/m^2$) while the other contributions were on the order of a few hundred w/m^2. If the probe were positive, both the electron-kinetic-energy release and work-function contributions to the heat transfer become on the order of 2×10^4 w/m^2; hence, a substantial variation of heat transfer with probe potential is expected. This effect will also be important in the analysis of heat transfer to electrodes (see Section IV,B,2) although it has not as yet been assessed,

C. STAGNATION-POINT HEAT-TRANSFER IN RETROSPECT

The data presented in this section would imply that certain high-velocity reentry missions would benefit from the use of magnetic methods to reduce heat transfer. Before such a conclusion is acceptable, however, it should be pointed out that the analyses discussed here are only crude approximations to the complex problem of MHD stagnation-point flow.

Several factors, some of which have been mentioned here, should be investigated more thoroughly before the problem can be considered in a definitive state. The first is the effect of radiation-heat transfer, which was briefly discussed in Section VI,B,1. Secondly, at high altitudes the relaxation to equilibrium behind the shock takes a finite time, and the conductivity (among other things) is not likely to be uniform across the shock layer.

We should also point out that a particular magnetic-field configuration which reduces stagnation-point heat transfer could actually increase the heating away from the stagnation point. The heat transfer away from the stagnation point was investigated by Wu (*67*), but only in the case where the viscous layer was large ($Re_s = 1000$).

The comparisons made in this section have indicated that the Newtonian approximation sufficiently accounts for magnetic effects when the electrical conductivity is constant. In fact, one could follow Lykoudis' suggestion and use an average magnetic field in the parameter S which would account for the variation of B between the shock and body (and hence its influence on the velocity gradient and detachment distance); the Newtonian formulation for heat transfer would probably agree more closely with the exact solution for values of S_b larger than 10.

The assumption of constant conductivity is not a serious shortcoming in the analyses presented here, for seeding the boundary layer at the stagnation point might permit σ to remain constant in the critical layers near the cool wall where magnetic effects are minimal. This layer, incidentally, causes the phenomenon of velocity overshoot ($u > U_e$) to occur in the boundary layer. This phenomenon, which is due to the variation of conductivity with enthalpy (much like the hysteresis effect in Section V), is discussed in (*78*).

Finally, it appears that the viscous contributions to the heat transfer can be incorporated, for constant conductivity, into a power-law variation of the velocity gradient as in Eq. (109). The consistency of this method is demonstrated in Fig. 24, where the curve attributed to Lykoudis is obtained either from Eq. (109) or from Eq. (105) and the appropriate values given in Figs. 20 and 21.

VII. Concluding Remarks

Each of the preceding sections has contained, more or less, its own conclusions, in order that the independence of each problem area could be maintained. However, there remain certain outstanding conclusions which pertain to the whole field of MHD heat transfer. These will be discussed at this time.

It is apparent, in retrospect, that the field of MHD heat transfer can be divided arbitrarily into two sections: one contains problems in which the heating is an incidental byproduct of the electromagnetic fields, and the second consists of problems in which the primary use of electromagnetic fields is to control the heat transfer. The first section contains such MHD devices as generators and accelerators, and, to a lesser degree, pumps and flowmeters. The second includes the natural convection flows and aerodynamic heating. Both of these areas have several problems in common, among them the lack of experimental verification of the exist-

ing theory. Even more serious is the complete absence of reliable theory for turbulent heat transfer. However, to delineate more clearly the heat-transfer problems which remain in these fields, we shall discuss them separately.

A. HEAT GENERATION BY ELECTROMAGNETIC FIELDS

It is evident from the energy equation and Section IV that when electric fields are present in the gas substantial heat will be generated in the gas by Joule and viscous dissipation. In a generator, the gas must be at a relatively high temperature in order for it to be electrically conducting. The efficiency of a generator will depend on how much of the generated power is delivered to the external load, and how much is dissipated in internal resistance. Other losses in a generator occur through wall heating, electrode heating, and (external) Joule heating in maintaining the magnetic field. (We should also include here such problems as Hall currents, voltage drops at the electrode, and end effects, which also diminish the efficiency.) Accelerators utilizing the ponderomotive or $\mathbf{J} \times \mathbf{B}$ mode will have many of the same practical problems, except that the power levels here are high enough to make the heating problem more severe.

The state of the art of generator and accelerator design is at the point where experiments are now being made to investigate these sources of power loss. For example, Rosa (*41*) discusses an experimental 10-kw MHD generator, in which the performance is assessed in the light of observed Hall effects. The gas was seeded so that high conductivities were obtained without the attendant high temperatures, although the supply gas was generated by an arc heater. Heat-transfer measurements were, however, not made. Other proposed experiments which specifically include heat transfer are discussed in (*54*). Fay and Hogan (*79*) made measurements of the heat transfer to wire electrodes in a shock-heated, seeded gas. A potential was applied to the electrodes and the asymmetry and increase of heating due to the electrical processes at the particular electrode occurred as described in Section IV,D.

It is expected that future generator or crossed-field accelerator design will include studies of the most suitable driver gas, electrode construction and cooling, geometric configuration of the device (*55*) and various seeding materials. However, in many of these studies the primary emphasis will be on reduction of heating losses in order to increase the efficiency.

B. AERODYNAMIC HEATING

The second area, that of heat-transfer reduction by flow control, has proved to be less promising than when it was first considered in 1957. Even so, the primary obstacle to the use of electromagnetic means for

heat-transfer reduction was the weight and Joule heat losses of the magnet and associated power supply. Now, with superconducting coils in the developmental stage, some promise is held in this technique, although it is entirely likely that the superconducting magnet will weigh more than a conventional heat shield because of the necessary cooling equipment. However, it appears (Section VI) that this method will be applicable only at the stagnation point of blunt bodies.

Because of the difficulty in obtaining a suitable supply of uncontaminated high-velocity air, magneto-aerodynamic heating experiments are not prevalent in the literature. Ziemer (*80*) has conducted experiments on the shock standoff distance of a hemisphere-cylinder, in which the data agree in trend, if not quantitatively, with the theory of Bush (*71*). The measured standoff distance was larger by about 20 per cent than that predicted by the theory, which indicates that the heat-transfer reduction would be about 10% more than predicted in Fig. 2, for $S_b < 5$. (The magnetic-field configuration differed from that assumed in (*71*), and the high upstream temperature prohibited the hypersonic-flow assumption to be fulfilled by the experiment.) Another experiment, briefly reported (*81*) at the Third Symposium on Engineering Aspects of Magnetohydrodynamics, was one in which measured heat-transfer rates were found to be in agreement with the theory.

In this particular area of MHD heat transfer it appears that experimental work has suffered somewhat from the apparent lack of a practical goal; early predictions which indicated that this method would never be competitive with convectional heat-protection schemes have evidently prevented experiments, which are necessarily expensive and difficult to run, from being made. However, there remain several areas in the field of hypersonic aerodynamics in which MHD techniques may prove feasible. One is the heat-protection problem associated with superorbital re-entry (Section VI,C) and the attendant problem of radio propagation through the plasma sheath; the other involves use of MHD devices to supplant conventional control surfaces or jets on lifting configurations in hypersonic flight.

C. OUTSTANDING PROBLEMS

Aside from the problems discussed in the various sections of this article, there remain several basic problems which retard the progress of an orderly investigation of the field of MHD heat transfer. It is not likely that solutions to these problems will be available without extensive experimental work.

This conclusion is especially valid in the case of turbulent flow, which we have studiously avoided during this article. Except for the book by

Harris (*82*) the author knows of no detailed experiments on the fluid-dynamic structure of turbulent flow, with the exception of work in progress at Purdue (*40*) in which velocity profiles will be obtained in the channel flow of liquid mercury in the presence of a transverse field. The Purdue group also plans to obtain bulk heat-transfer rates in the pipe flow of mercury, also with a transverse field. The velocity profiles will be exceptionally valuable for the determination of the empirical constants in an MHD turbulent theory based on mixing length, for example.

Another area which is important to all of gasdynamics is the determination of transport properties of slightly ionized gases—in particular, air. It is really not necessary to iterate any further the need for these properties, since it is still a moot question as to the magnitude of ordinary heat transfer at velocities exceeding 8500 m/sec.

Although it was mentioned that almost all the classical problems have been attacked, there still remain many heat-transfer problems which have not been fully investigated within the classical framework. If we combine these straightforward, well-defined problems with those of the next generation, problems which will include Hall effects and other high-field phenomena, the area of MHD heat transfer could be said to have a rich future before it.

ACKNOWLEDGMENTS

Since this is in part a review paper, the author has leaned heavily on the published literature. If an article has been omitted, it is entirely by oversight and not by intention. The author would like to thank Professor Paul Lykoudis, a Rand Consultant, of the Purdue University School of Aeronautical and Engineering Sciences for his many suggestions and valuable comments.

SYMBOLS

The meter-kilogram-second (MKS) system of units is used throughout. The following list contains the symbols used most frequently; others, which are used infrequently, are defined when they occur.

a	unit of length	$\mathbf{D}$	electric displacement
$\mathbf{B}$	magnetic induction	e	unit of electric charge
c	specific heat	$\mathbf{E}$	electric field intensity
c_k	species concentration	$\mathcal{E}$	Eckert number, Eq. (33)
C	parameter, Eq. (41)	$\mathbf{f}$, $\mathbf{F}$	arbitrary forces
C_f	skin-friction coefficient, $2\tau/\rho V^2$	g	acceleration due to gravity
C_H	heat-transfer coefficient, $q/\rho C_p V\,\Delta T$	Gr	Grashof number, Eq. (27)
		h	enthalpy
C_p	specific heat at constant pressure	h_s	stagnation enthalpy
d	unit of length	$\mathbf{H}$	magnetic-field intensity
D	diffusion coefficient	$\mathbf{j}$	current (J, dimensionless)

j_H	Hall current, Eq. (1)
k	coefficient of thermal conductivity or Boltzmann's constant
K	generator coefficient, Eq. (29)
L	unit of length
Le	Lewis number, Eq. (38)
m	mass
M	Hartmann number, Eq. (30)
n	number density
Nu	Nusselt number, $qL/k\,\Delta T$
p	pressure
Pr	Prandtl number, Eq. (32)
q	heat flux
Q	arbitrary heat source
r, R	radial coordinate
Ra	Rayleigh number, Ra = (Pr)(Gr)
Re	Reynolds number, Eq. (26)
Re_m	magnetic Reynolds number, Eq. (35)
S	magnetic interaction parameter, Eq. (28)
t	time
T	temperature, °K
u, v	velocity components (U, V, dimensionless)
U	internal energy
V	velocity
V_k	diffusion velocity of kth species
W	work
x, y, z	coordinates (X, Y, Z, dimensionless)
α	thermal absorptivity
$\bar{\alpha}$	parameter, Eq. (96)
β	coefficient of thermal expansion
$\bar{\beta}$	parameter, Eq. (97)
δ	boundary-layer thickness
δ^*	boundary-layer-displacement thickness
δ_{ij}	Kronecker delta ($\delta_{ij} = 1$, $i = j$; $\delta_{ij} = 0$, $i \neq j$)
Δ	difference
ϵ	dielectric constant
η	length defined in Eq. (81)
θ	dimensionless temperature, Eq. (25) or angular measure
κ	parameter, Section III,C,2
λ	parameter, Section III,C,2
Λ	Lykoudis number, Eq. (45)
μ	viscosity
μ_e	magnetic permeability
ν_c	collision frequency
ξ	dummy variable
ρ	density
ρ_e	charge density
σ	electric conductivity
τ	shear stress
τ_{ij}	shear-stress tensor
$\vec{q}$	heat-flux vector, Eq. (36)
Φ	viscous dissipation
ω	cyclotron frequency
Ω	vorticity

Subscripts

0	reference conditions and conditions without electromagnetic fields present
∞	free stream or adiabatic conditions
b	body
e	edge of boundary layer
s	shock
w	wall

Superscripts

*	dimensionless
-	mean value

REFERENCES

1. J. Hartmann, *Kgl. Danske Videnskab. Sleskab, Mat.-Fys. Medd.* **15,** 6 (1937).
2. J. Hartmann and F. Lazarus, *Kgl. Danske Videnskab. Selskab, Mat.-Fys. Medd.* **15,** 7 (1937).
3. V. J. Rossow, "On the Flow of Electrically Conducting Fluids Over a Flat Plate In the Presence of a Transverse Magnetic Field," NACA TN 3971, May 1957.
4. G. W. Sutton and P. Gloersen, *Phys. Today* **14,** 18 (1961).
5. R. H. Levy and H. E. Petschek, IAS Paper No. 62-100, Los Angeles, California, June 19-22, 1962.
6. L. Spitzer, "Physics of Fully Ionized Gases." Wiley (Interscience), New York, 1956.

7. L. B. Loeb, "Basic Processes of Gaseous Electronics." Univ. of California Press, Berkeley, California, 1960.
8. M. J. Brunner, *Trans. ASME, Series C*, **84,** 177 (1962).
9. J. A. Stratton, "Electromagnetic Theory." McGraw-Hill, New York, 1941.
10. P. S. Lykoudis, *in* "Magnetohydrodynamics" (A. B. Cambel, *et al.*, eds.) pp. 3–19. Northwestern Univ. Press, Evanston, Illinois, 1962.
11. B. -T. Chu, *Phys. Fluids* **2,** 473 (1959).
12. S. I. Pai, *Phys. Rev.* **10,** 1424 (1957).
13. J. A. Stetekee, University of Toronto, Institute of Aerophysics, Reviews No. 9 (1957).
14. P. S. Greifinger, "Transport Coefficients of Dissociating and Slightly Ionizing Air," The Rand Corporation, RM-1794, April 9, 1957.
15. W. Finkelnburg and H. Maecker, *in* "Handbuch der Physik," (S. Flugge, ed.) Vol. XXII, pp. 254–440. Springer, Berlin, 1956.
16. Boris Ragent and C. E. Noble, Jr., "High Temperature Transport Coefficients of Selected Gases," VIDYA Report No. 52, Sept. 1961.
17. J. A. Fay and F. R. Riddell, *J. Aerospace Sci.* **25,** 73 (1958).
18. L. Lamb and S. C. Lin, *J. Appl. Phys.* **28,** 754 (1957).
19. H. Senftleben and W. Braun, *Z. Physik* **102,** 480 (1936).
20. P. S. Lykoudis and C. P. Yu, "The Influence of Electrostrictive Forces in Natural Thermal Convection," School of Aeronautical and Engineering Sciences, Purdue Univ., Report No. 62-7, 1962.
21. E. Schmidt and W. Leidenfrost, *Forsch. Gebiete Ingenieurw. 19,* 65 (1953).
22. T. G. Cowling, "Magnetohydrodynamics," Wiley (Interscience), New York, 1957.
23. B. Lehnert and N. C. Little, *Tellus* **9,** 97 (1957).
24. S. Chandrasekhar, "Hydrodynamic and Hydromagnetic Stability," Oxford Univ. Press, (Clarendon), London, 1961.
25. Y. Nakagawa, *Nature* **175,** 417 (1955).
26. Y. Nakagawa, *Proc. Roy. Soc. Ser. A*, **240,** 108 (1957).
27. Y. Nakagawa, *Rev. Mod. Phys.* **32,** 916 (1960).
28. Y. Nakagawa and I. R. Goroff, *Phys. Fluids* **4,** 349 (1961).
29. Y. Nakagawa, *Phys. Fluids* **3,** 87 (1960).
30. G. Poots, *Intern. J. Heat Mass Transfer* **3,** 1, (1961).
31. E. M. Sparrow and R. D. Cess, *Intern. J. Heat Mass Transfer* **3,** 267 (1961).
32. P. L. Lykoudis, *Intern. J. Heat Mass Transfer* **5,** 23 (1962).
33. A. S. Gupta, *Appl. Sci. Res. Sect. A* **9,** 319 (1960).
34. G. Z Gershuni and E. M. Zhukhovitskii, *Soviet Physics JETP* **34** (7), 461 (1958).
35. K. R. Cramer, *J. Aerospace Sci.* **28,** 736 (1961).
36. P. C. Lu, *J. Aerospace Sci.* **28,** 346 (1961). (See also *J. Aerospace Sci.* **29,** 109, 1962).
37. B. L. Reeves, *ARS J.* **31,** 557 (1961).
38. Y. Mori, *Trans. Japan Soc. Aerospace Sci.* **2,** 22 (1959).
39. G. Z. Gershuni and E. M. Zhukhovitskii, *Soviet Phys. JETP* **34,** (7), 465 (1958).
40. P. S. Lykoudis, private communication, August, 1962.
41. R. J. Rosa, *Phys. Fluids* **4,** 182 (1961).
42. J. A. Shercliff, *Proc. Roy. Soc. Ser. A*, **233,** 396 (1955).
43. S. I. Pai, *J. Appl. Phys.* **25,** 1205 (1954).
44. C. C. Chang and T. S. Lundgren, "The Flow of An Electrically Conducting Fluid Through a Duct With Transverse Magnetic Field," Proc. Heat Transfer and Fluid Mech. Institute, Stanford Univ. Press, Stanford, California, 1959.

45. M. Perlmutter and R. Siegel, "Heat Transfer to An Electrically Conducting Fluid Flowing in a Channel With a Transverse Magnetic Field," NASA TN-D-875, August 1961.
46. R. A. Alpher, *Intern. J. Heat Mass Transfer* **3**, 108 (1961).
47. R. Siegel, *J. Appl. Mech.* **25**, 415 (1958).
48. J. L. Shohet, *et al.*, *Phys. Fluids* **5**, 545 (1962).
49. W. C. Moffatt, "Boundary Layer Effects in Magnetohydrodynamic Flow," Magnetogasdynamics Laboratory Report 61-4, MIT, May 1961.
50. J. S. Kerrebrock, *J. Aerospace Sci.* **28**, 631 (1961).
51. F. D. Hains and Y. A. Yoler, *J. Aerospace Sci.* **29**, 143 (1962).
52. V. J. Raelson and P. J. Dickerman, *Trans. ASME, Series C*, **84**, 169 (1962).
53. A. Sherman and G. W. Sutton, *in* "Magnetohydrodynamics" (A. B. Cambel, *et al.*, eds.), pp. 173–185. Northwestern Univ. Press, Evanston, Illinois, 1962.
54. G. Oates, *et al.*, *in* "Magnetohydrodynamics" (A. B. Cambel, *et al.*, eds.), pp. 207–231, Northwestern Univ. Press, Evanston, Illinois, 1962.
55. A. Q. Eschenroeder, *ARS J.* **32**, 196 (1962).
56. Z. O. Bleviss, *J. Aerospace Sci.* **25**, 601 (1958).
57. B. M. Leadon, "Plane Couette Flow of a Conducting Gas Through a Transverse Magnetic Field," Convair Scientific Research Laboratory RN 13, December 1957.
58. V. J. Rossow, *ZAMP 96*, Fasc. 5/6, 519 (1958).
59. W. B. Bush, *J. Aerospace Sci.* **27**, 49 (1960).
60. P. S. Lykoudis, "On a Class of Compressible Laminar Boundary Layers With Pressure Gradient for an Electrically Conducting Fluid in the Presence of a Magnetic Field," Proc. of the 9th Int. Congress of the Int. Astro. Federation, Amsterdam, Aug. 25–30, 1958.
61. P. M. Chung and A. D. Anderson, "Dissociative Relaxation of Oxygen Over an Adiabatic Flat Plate at Hypersonic Mach Numbers," NASA TN-D-140, April 1960.
62. J. L. Neuringer and W. McIlroy, *J. Aerospace Sci.* **25**, 194 (1958). (See also *J. Aerospace Sci.* **25**, 332, 1958.)
63. R. X. Meyer, *ARS J.* **29**, 187 (1959).
64. V. J. Rossow, *J. Aerospace Sci.* **25**, 334 (1958).
65. P. S. Lykoudis, *J. Aerospace Sci.* **26**, 315 (1959).
66. W. D. Hayes and R. F. Probstein, "Hypersonic Flow Theory," Academic Press, New York, 1959.
67. C. -S. Wu, *J. Aerospace Sci.* **27**, 882, (1960).
68. A. R. Hochstim, "Gas Properties Behind Shocks at Hypersonic Velocities, I. Normal Shocks in Air," Convair (San Diego) Report ZPh(GP)-002, January 1957.
69. P. S. Lykoudis, *J. Aerospace Sci.* **28**, 541 (1961).
70. N. Kemp, *J. Aerospace Sci.* **26**, 672 (1959).
71. W. B. Bush, *J. Aerospace Sci.* **25**, 685 (1958).
72. W. B. Bush, *J. Aerospace Sci.* **26**, 536 (1959).
73. R. C. Meyer, *J. Aerospace Sci.* **25**, 561 (1958).
74. N. Kemp, *J. Aerospace Sci.* **27**, 553 (1960).
75. W. B. Bush, *J. Aerospace Sci.* **28**, 610 (1961).
76. R. Goulard, *ARS J.* **29**, 604 (1959).
77. L. Talbot, *Phys. Fluids* **3**, 289 (1960).
78. P. S. Lykoudis, *J. Aerospace Sci.* **28**, 896 (1961).
79. J. A. Fay and W. T. Hogan, *Phys. Fluids* **5**, 885 (1962).
80. R. W. Ziemer, *ARS J.* **29**, 642 (1959).
81. R. B. Thomas, Jr., *Phys. Today* **15**, 38 (1962).
82. L. P. Harris, "Hydromagnetic Channel Flows," Wiley, New York, (1960).

Fluid Mechanics and Heat Transfer of Two-Phase Annular-Dispersed Flow

MARIO SILVESTRI

Centro Informazioni Studi Experienze, Milano, Italy

I. General Considerations

A. Flow Patterns of Two-Phase Flow

1. Definition of Annular-Dispersed Flow

Annular-dispersed flow is just one of the many flow patterns which may occur, when a liquid and a gas flow in a duct at the same time. This kind of flow is termed in the literature in different ways, all with approximately the same meaning. The commonest ones are: spray flow, fog flow, dispersed flow, etc.

From a physical point of view annular-dispersed flow is identified by

the presence of a continuous gaseous phase, and a discontinuous liquid phase. The liquid phase distributes itself in an annulus around the solid boundary of the duct and as droplets in the gaseous core. Obviously such an arrangement can persist in dynamic conditions only. When droplets in the gas are practically absent, the flow pattern is almost purely annular; when the liquid film does not exist or is disrupted, the liquid deficient region is entered (to which the term "mist flow" is often associated).

Pure annular flow and "mist" flow might be considered the physical limits of annular-dispersed flow, as represented in Fig. 1.

A full description of this flow, as of any two-phase flow, would be quite complicated and impractical for many purposes. One would have to pretend to know the point distribution of the three components of the gas velocity, the point distribution of the components of the liquid

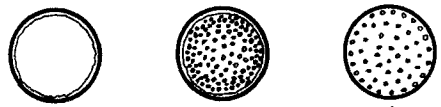

FIG. 1. Annular-dispersed flow pattern. (a), pure annular; (b), annular-dispersed; (c), pure dispersed (mist).

velocity in the annulus, the concentration of the liquid droplets in the core, their size spectrum, their velocities and so on. In comparison with single phase flow the difficulties in the instrumentation and interpretation of data are greater orders of magnitude. But to gain even a knowledge of average quantities (time and space average gas velocity, average liquid velocity, average void fraction, thickness of the liquid annulus) is not a simple task to perform.

2. Independent Variables of Importance

The primary variables upon which the physical situation depends are quite numerous. They are:

(*a*) geometrical variables (the duct diameter for a tube, two diameters for an annulus, a rod diameter and a lattice pitch for an infinitely wide cluster). The use of a single linear dimension—the equivalent diameter—in the latter cases is highly controversial, and is mostly used as an empirical tool to simplify correlations of experimental data, when possible. In some cases even the "roughness" of the solid boundary must be taken into account.

(*b*) physical properties of phases (viscosity, density, surface tension of the liquid in the presence of the gas, contact angle of the liquid with

the solid surface). When heat transfer is present, thermal properties are also important to determine the two phase flow behaviour.

(*c*) kinematic variables (linear velocities).

(*d*) external fields (the gravitational field, centrifugal fields eventually impressed etc.). This shows as a consequence that physical situations are different—all other things being equal—for upward flow or downward flow or flow in an inclined tube.

In addition, to study the phenomenon in fully developed conditions one must be far from any inlet and outlet disturbance.

Steam-water and air-water mixtures are the most common examples of two-phase mixtures, and they are the most studied. In the former case, assuming both phases to be in thermodynamic equilibrium, their physical properties are all single-valued functions of a single variable: pressure (or temperature). Thus, at a constant system pressure, neglecting small variations due to pressure drops, the number of independent variables decreases substantially.

3. Review of Two-Phase Flow Patterns

One of the first tasks to accomplish, in studying annular-dispersed flow, is to determine the range of variables, under which it can exist. Since gravity has an effect, the boundaries between different flow patterns will depend on the inclination of the duct. In any two-phase flow pattern chart this fact must be specified. Unfortunately, in the past, flow pattern charts were traced starting mostly from qualitative visual inspections (by eye or by photographic techniques), which are difficult to translate in quantitative terms.

Words, used for a long time, such as bubbles, dispersions, slugs etc. reflect this situation. Martinelli *et al.* (*1*) were the first to introduce a quantitative, although arbitrary, definition of two-phase flow regimes. Depending on the value of the Reynolds number for each phase, they defined four types of flow: turbulent-turbulent, viscous-turbulent, turbulent-viscous and viscous-viscous, usually abbreviated as *tt*, *vt*, *tv* and *vv*. The Reynolds number was defined in the usual way as GD/μ, supposing that each phase flows alone in the duct. They did not distinguish between upward, downward, and inclined flow. These flow regimes did not coincide with known flow patterns; the annular-dispersed flow, for instance, as defined by many flow pattern charts, is placed across the viscous-(liquid)-turbulent and turbulent-turbulent region.

More recently Baker (*2*) drew a chart of flow patterns for horizontal flow. This chart was slightly modified by Isbin (*3*). A flow pattern chart was also presented by Krasjakova (*4*) and by Alves (*5*) for horizontal tubes. Ambrose (*6*) made a literature survey of flow patterns in horizontal

tubes, from which the following list was laid down (starting from pure liquid and increasing the gas flowrate):

(a) pure liquid
(b) bubble flow
(c) plug flow (alternate plugs of gas and liquid)
(d) stratified flow
(e) wavy flow (gas above a wavy liquid surface)
(f) slug flow (periodic frothy slugs pass through the pipe at a greater velocity than the average liquid velocity)
(g) annular flow (no droplet entrainment)
(h) mist or spray flow (droplets entrained in a pipe with wetted wall)
(f) pure gas

This list—and all two-phase flow pattern lists—contains a subjective component. Annular-dispersed flow would correspond to items (g) and (h), where "mist" has a different meaning from that previously used. The liquid deficient region is not mentioned.

In vertical upward flow some of the flow patterns existing in horizontal flow do not occur.

Galegar (*7*) proposed a flow-pattern plot for vertical flow at atmospheric pressure. These plots, however, are not general; that is, they are different for different fluids.

Koslov (*8*), by photographic techniques, studied vertical upflow of air-water mixtures at atmospheric pressures and divided flow patterns in the following sequence, starting from pure liquid and increasing the gas flow rate (at constant liquid flow rate):

(a) bubble flow
(b) slug flow
(c) slug to emulsified flow
(d) emulsified flow
(e) annular-emulsified (with wavy film)
(f) mist (with wetted walls)

He gives the flow pattern boundaries as relationships between volume flow rate quality, superficial mass velocity, tube diameter, fluid densities. Annular-dispersed flow should correspond to items (d) to (f).

One of the most recent literature surveys of flow patterns was made by Vohr (*9*), who summarizes the basic vertical flow patterns in the following sequence:

(a) bubble flow
(b) piston (or slug) flow

(c) semiannular flow
(d) annular flow
(e) spray-flow

Annular-dispersed flow would correspond to items (c) to (e).

For inclined tubes the flow patterns have not been systematically studied. Because of its importance, upward flow will be mostly discussed in this chapter except when otherwise stated.

B. ANNULAR-DISPERSED FLOW PATTERN BOUNDARIES

1. Transition from Slug Flow to Annular-Dispersed Flow

As seen in the preceding paragraph, most of the annular-dispersed flow pattern boundaries are constructed from visual inspection of what happens in a duct. This is certainly not a satisfying criterion. It would be much better if a quantitative description of the transition between one flow pattern and another could be based on the step variation of a physical quantity, whose measurement could be feasible. It is well known that in single phase flow one can distinguish laminar from turbulent flow through the sudden variation of the law governing frictional pressure drops. But other parameters can be selected: for instance, the variation of the velocity profile or the persistence of a colored wake in the stream.

One of the most important boundaries is that separating annular-dispersed flow from slug and bubble flow. Griffith and Wallis (*10*) started from the consideration that, in vertical upward flow, annular flow is the physical limit of slug flow, when the length of a gas slug goes to infinity. Since the slug length is expressed in their mathematical development by a fraction, the above condition is satisfied when the denominator goes to zero, that is:

$$m(Q_g + Q_l + V_b A) = Q_g \tag{1}$$

where V_b is the slug velocity $= \sqrt{gD}$.

Rearranging terms one has:

$$\frac{Q_g}{A}\left(1 - \frac{1}{m}\right) + \frac{Q_l}{A} = K\sqrt{gD} \tag{2}$$

which means that the sum of the superficial liquid velocity and a fraction of the superficial gas velocity is a constant (at constant diameter) for the slug-annular boundary. The authors admit that the boundary equation is certainly more complicated and depends on other characteristics of the flowing phases.

The general diagram they plot is shown in Fig. 2. Transforming the coordinates adopted by them, one has:

$$\frac{Q_g}{Q_g + \bar{Q}_l} = X_v$$

$$\left(\frac{Q_l + Q_g}{A}\right)^2 \Big/ gD = \frac{\bar{U}^{*2}}{gD} \tag{3}$$

so that the boundary equation is:

$$X_v = f\left(\frac{\bar{U}^*}{\sqrt{gD}}\right) \tag{4}$$

It is interesting to note from Fig. 2 that, above a certain over-all superficial mass velocity, there is a direct transition from bubble flow to dispersed flow, while the slug flow pattern in between appears only below a certain critical mass velocity.

Similar considerations are made by Nicklin and Davidson (*11*). They admit the existence of a semiannular flow, a flow in which very long slugs

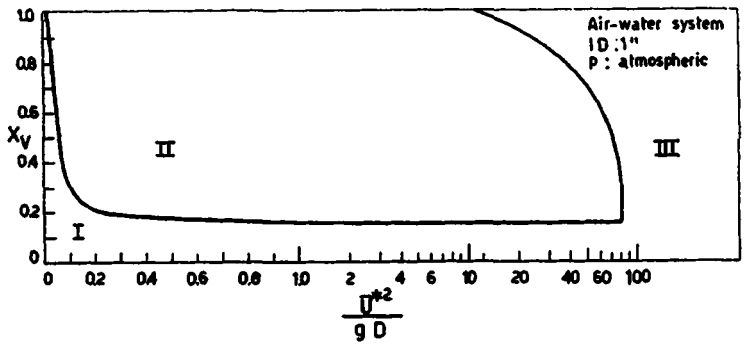

FIG. 2. Flow pattern map for a vertical pipe in fully developed flow following Griffith and Wallis. I (bubble); II (slug); III (annular and mist).

are interrupted by short liquid bridges. This flow pattern in vertical upward flow would be intermediate between slug flow and annular flow. By a direct measurement of some parameters, they arrive at the conclusion that for low Q_l the transition between slug and semiannular flow appears at a constant value of $(Q_l + Q_g)/A = \bar{U}^*$, while at higher Q_l values higher $(Q_l + Q_g)/A$ values are needed.

Another completely different approach is suggested by some experiments carried out at Harwell. These experiments were performed by tracing with silica water in a water-steam system heated with condensing steam, to verify if there were a preferential deposition of solid matter in certain flow patterns. A difference in deposition, if any, would furnish the necessary evidence. In fact this happened and three regions of different

amounts of deposition were identified, corresponding in the opinion of the authors to bubble (and slug) flow, annular-dispersed flow and liquid-deficient flow. These conclusions, of course, are only valid for this particular system (low pressure steam-water system) and under heated conditions, which certainly affect the boundary between annular-dispersed flow and the liquid deficient region, although probably to a much lesser degree the transition between bubble (or slug) and dispersed flow.

The change in the behavior of pressure drops was used by Wallis (*12*) as a criterion to differentiate between flow patterns. At CISE (*13*), (*14*) both this criterion and the interpretation of burnout curves were used to determine boundary lines. With the steam-water system at 70 kg/cm^2 in vertical upward flow, careful measurements of pressure losses were carried out at constant mass velocity for different steam qualities in a tube. Irreversible pressure drops (or pressure losses) per unit length $(\Delta p_f/L)$ deduced from total pressure drops, correcting for the gravity term and for expansion losses (very small corrections indeed), divided by V^{*n}, were plotted as a function of X. The exponent, n, which is different for different G's, is capable of flattening the central portion of the diagram, to better emphasize the change in flow pattern. Two examples of these diagrams are shown in Fig. 3. In Fig. 3a (low mass velocity) three flow patterns (bubble, slug, and annular-dispersed) can be distinguished while in Fig. 3b (high mass velocity) only two flow patterns (bubble, and annular-dispersed) exist. This is in general agreement with the conclusions reached by Griffith and Wallis (*10*), although the numerical results are different. Moreover, inspection of critical heat flux curves against inlet (or outlet) quality shows a maximum for low flow rates, while the maximum does not exist with high flowrates. The value of G for which the maximum clearly disappears, for these experimental conditions, is between 200 and 250 gm/cm^2 second.

At CISE laboratories a rough but useful rule was found to match experimental results quite well: above a mean linear velocity of 500–600 cm/second slug flow does not exist for the steam-water mixture in a wide range of diameters. The mean mixture velocity is defined in the following way:

$$\bar{U} = \bar{U}_l(1 - \bar{\alpha}) + \bar{U}_g\bar{\alpha} = GV_{gl}(X + a) \tag{5}$$

since

$$\begin{cases} G(1 - X) = \bar{U}_l\rho_l(1 - \bar{\alpha}) \\ GX = \bar{U}_g\rho_g\bar{\alpha} \end{cases} \tag{6}$$

Thus the boundary equation between slug and annular-dispersed flow would be:

$$GV_{gl}(X + a) = \text{const} \tag{7}$$

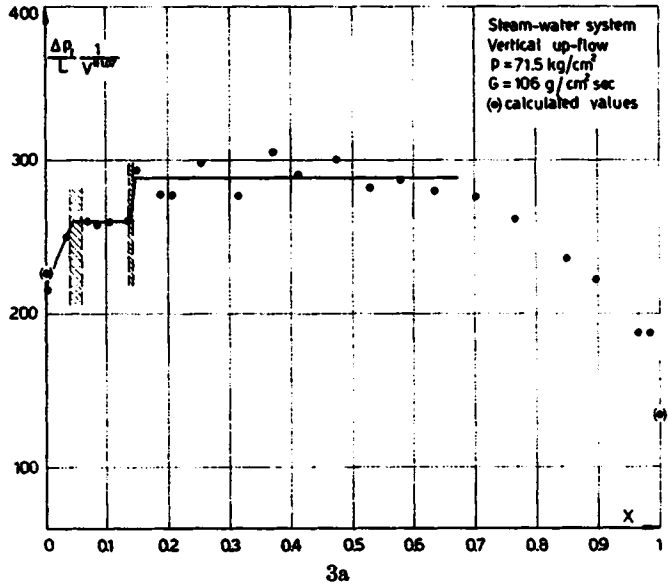

3a

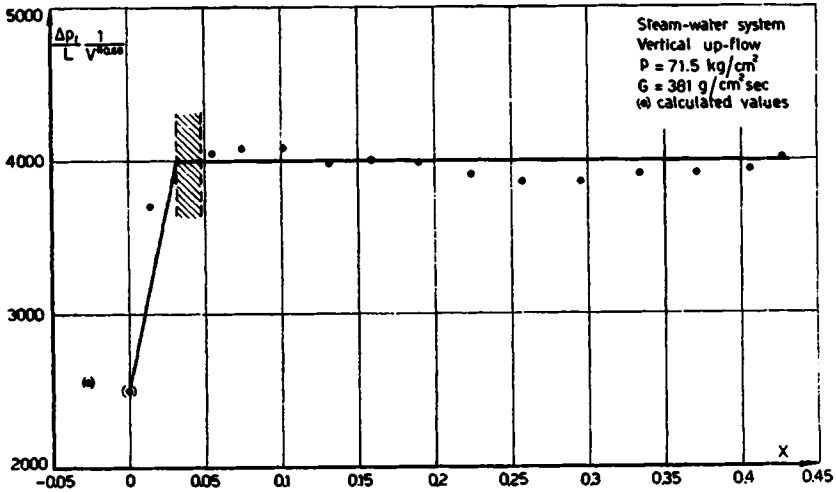

3b

FIG. 3. Individuation of flow patterns through variation of pressure loss gradient with quality. (a), low mass velocity; (b), high mass velocity.

which can be written:

$$\frac{Q_g}{A} + \frac{Q_l}{A} = \text{const} \tag{8}$$

This form is similar to (2) apart from the dependence on the duct diameter. It also resembles the conclusions reached in (*11*), if semiannular flow is included in annular flow.

Since in these experimental conditions bubble flow persisted from zero quality up to about 3–4 % quality (with $\bar{S} = 1$, the void fraction is 0.5 at 3.7% quality), one can see, by introducing this limitation in (8), that slug flow is impossible above 200–250 gm/cm² second.

2. Transition from Annular-Dispersed to Slug Flow

An explanation of the slug-annular transition was proposed at CISE (*13*) starting from a point of view opposite to that of Griffith and Wallis. While they consider annular-dispersed flow as a physical limit of slug flow (with very long slugs), at CISE slug flow was considered the physical limit of annular-dispersed flow. This flow is characterized by the presence of liquid droplets carried into the core. When the gas velocity is not high enough to sustain the droplets, they slip down and coalesce to form slugs. For a spherical liquid droplet in a stagnant gas, the settling velocity is given by (*15*):

$$U_d = \sqrt{\frac{4gD_p(\rho_s - \rho_g)}{3\rho_g C}} \text{ cm/second} \tag{9}$$

where C, the drag coefficient, is a function of the droplet Reynolds number $(N_{\text{Re}})_d$

$$C = C(N_{\text{Re}})_d = C\left(\frac{\rho_g U_d D_p}{\mu g}\right) \tag{10}$$

The size of droplets depends on the mechanism of formation. In fully-developed flow, the only source of droplets is the liquid (wavy) annulus flowing along the solid boundary. Here, only rough hypotheses are possible. Hinse (*16*) suggested the use of a critical Weber number:

$$\text{We}_c = \frac{(U_g - U_l')^2 \rho_g D_p}{\gamma} = \frac{K^2 U_g^2 \rho_g D_p}{\gamma} \tag{11}$$

U_l' here being the absolute value of the velocity of the surface of the liquid film at the instant of droplet formation and $1 - K = U_l'/U_g$. Combining Eqs. (9), (10), and (11), and postulating a value for K, the settling ratio U_d/U_g can be determined. This is the ratio of the free falling velocity of the droplet relative to the gas stream, divided by the gas velocity. When this ratio is close to 1, the droplets would be at rest, and

of course should coalesce with other droplets to form slugs. Rough assumptions are included in this picture: negligible effect of the droplets' transverse velocity, no interaction between droplets, negligible effect of the pressure gradient etc. The agreement, however, with experiments is satisfactory. For instance, putting $K = 0.5$ (and $U_d/U_g = 1$) one has $U_g = 625$ cm/second for the steam-water system at 70 kg/cm^2. This corresponds roughly to the empirical equation (7). In fact, rearranging terms, one has:

$$GV_{gl}(X + a) = \frac{400}{1 + \dfrac{\Delta S}{1 + \dfrac{X}{1 - X}\dfrac{\rho_l}{\rho_g}}} \tag{12}$$

Since $\rho_l/\rho_g \gg 1$, even at low quality and high ΔS, the denominator is higher but close to unity.

3. General Remarks

One must take into account that all indirect methods of detecting flow-pattern boundaries are inductive in nature and, for instance, the sentence that the change in the pressure loss law corresponds to a different visual picture still requires confirmation.

A provisional conclusion which can be reached now, at least for upward vertical flow, is that at constant G (within a certain G range) and starting from pure liquid, the first flow pattern to be encountered is bubble flow. Beyond it annular-dispersed flow can be reached either directly or by passing through slug flow if the flowrate is low enough.

What happens when the quality is increased is even more doubtful. Annular dispersed flow might transform into pure annular flow, as a preliminary to pure gas flow; or a certain amount of droplets might always remain in the gaseous core, giving to the flow the character of a "mist" flow pattern. Absolute values depend, of course, on the properties of the system.

The situation is therefore still somewhat confused, but the time seems near when a systematic description of the flow patterns can be successfully achieved.

C. PHYSICAL QUANTITIES OF INTEREST IN ANNULAR DISPERSED FLOW

1. Void Fraction and Slip Ratio

As pointed out elsewhere, in single phase flow the average velocity U is known, once the volumetric flowrate and the channel cross section are known. The average mass velocity is then $G = \rho U$. On the contrary, in

two-phase flow, knowledge of flowrates and geometry is not sufficient to determine the average linear and mass velocities since the mixture density is an unknown quantity. The known quantities are the apparent (or superficial) mass velocities $\bar{G}^*_g$ and $\bar{G}^*_l$ defined as the gas or liquid flowrate per unit area, supposing that each phase fills the entire cross section: $\bar{G}^*_g = \Gamma_g/A$; $\bar{G}^*_l = \Gamma_l/A$. Also known are the corresponding superficial velocities.

An additional key quantity of interest is the over-all gas volume fraction $\bar{\alpha}$ (or "void fraction") defined as the fraction of the duct cross section (or of the volume per unit length) filled by the gas phase.

The interrelation between this and other quantities is the following:

(a) liquid volume fraction (or "liquid holdup") $\bar{h} = 1 - \bar{\alpha}$; $\bar{h} + \bar{\alpha} = 1$

(b) density of the mixture: $\bar{\rho} = \bar{\alpha}\rho_g + (1 - \bar{\alpha})\rho_l$

The true average mass (and linear) velocities are:

$$\begin{aligned} \bar{G}_g &= \bar{G}^*_g/\bar{\alpha}; & \bar{U}_g &= \bar{G}^*_g/\bar{\alpha}\rho_g \\ \bar{G}_l &= \bar{G}^*_l/(1 - \bar{\alpha}); & \bar{U}_l &= \bar{G}^*_l/(1 - \bar{\alpha})\rho_l \end{aligned} \tag{13}$$

The value of $\bar{\alpha}$ is not equal to that of the volume flowrate quality X_v, because the average linear velocities $\bar{U}_g$ and $\bar{U}_l$ are different. They will only be equal in an idealized homogeneous model. By defining a quantity $\bar{S}$ (over-all slip ratio) as the ratio $\bar{U}_g/\bar{U}_l$, one has:

$$\begin{aligned} \frac{\bar{U}_g}{\bar{U}_l} = \bar{S} &= \frac{\bar{G}_g^+}{\bar{G}_l^+}\frac{1 - \bar{\alpha}}{\bar{\alpha}}\frac{\rho_l}{\rho_g} = \frac{X}{1 - X}\frac{1 - \bar{\alpha}}{\bar{\alpha}}\frac{\rho_l}{\rho_g} \\ &= \frac{X_v}{1 - X_v}\frac{1 - \bar{\alpha}}{\bar{\alpha}} \end{aligned} \tag{14}$$

In the special case $\bar{S} = 1$, $X_v = \bar{\alpha}$; while in general:

$$\bar{\alpha} = \frac{X_v}{1 + \Delta\bar{S}(1 - X_v)} \tag{15}$$

From the above formulas one can see that $\bar{\alpha}$ or $\bar{S}$ are dependent on each other. Neither of them can be easily determined through experiments and this is the chief reason for discrepancies in their values found in literature. In addition to an average value, a point value α can be defined. Its knowledge permits the phase distribution in a duct to be known.

Other formulas of interest, derived from (13) and (14) are:

$$X = \frac{\bar{S}}{\bar{S} + \dfrac{1 - \bar{\alpha}}{\bar{\alpha}}\dfrac{\rho_l}{\rho_g}}; \qquad 1 - X = \frac{\dfrac{1 - \bar{\alpha}}{\bar{\alpha}}\dfrac{\rho_l}{\rho_g}}{\bar{S} + \dfrac{1 - \bar{\alpha}}{\bar{\alpha}}\dfrac{\rho_l}{\rho_g}} \tag{16a}$$

$$\bar{\alpha} = \frac{\dfrac{X}{1-X}\dfrac{\rho_l}{\rho_g}}{\bar{S} + \dfrac{X}{1-X}\dfrac{\rho_l}{\rho_g}}; \qquad 1 - \bar{\alpha} = \frac{\bar{S}}{\bar{S} + \dfrac{X}{1-X}\dfrac{\rho_l}{\rho_g}} \tag{16b}$$

2. Void Fraction and Slip Ratio in Annular-Dispersed Flow

Annular dispersed flow is characterized by having two distinct regions: the former in which $1 - \alpha$ is unity (the liquid annulus), the latter in which $1 - \alpha$ varies from the wall to the axis. Evidently, $\bar{\alpha}$ and $\bar{S}$ can be supposed symmetrical with respect to the flow direction only in vertical flow. We will refer to this case when upward motion is discussed. $\bar{S}$ and $\bar{\alpha}$ are functions of all the variables reported in Section I. For the special case of steam-water at constant pressure and geometry, $\bar{S}$ and $\bar{\alpha}$ will be functions of flowrates only (or G and X). In addition, however, they will be functions of the heat input when heat transfer is taking place. In fact, in annular-dispersed flow, the total cross-sectional area occupied by the liquid phase A_l, is divided in two portions A_f and A_c, respectively occupied by water in the liquid film, flowing at an average velocity $\bar{U}_f$, and water in the core, flowing at $\bar{U}_c$. Thus:

$$A_l\bar{U}_l = A_f\bar{U}_f + A_c\bar{U}_c \tag{17a}$$

whence:

$$\frac{1}{\bar{S}} = \frac{y_c}{\bar{S}} + \frac{y_f}{\bar{S}_f}; \qquad \bar{S} = \bar{S}_c\frac{\bar{S}_f}{\bar{S}_f - y_f(\bar{S}_f - \bar{S}_c)} \tag{17b}$$

where

$$y_f = A_f/A_l; \qquad y_c = A_c/A_l$$
$$\bar{S}_l = \bar{U}_g/\bar{U}_f; \qquad \bar{S}_c = \bar{U}_g/\bar{U}_c$$

Usually in upward vertical motion $\bar{S}_c$ is higher but close to unity. At burnout y_f should go to zero and y_c to unity so that $\bar{S} \to \bar{S}_c \to 1$. In adiabatic flow, due to the often very high value of $\bar{S}_f$, the value of $\bar{S}$ can be much higher than unity.

3. Energy and Momentum Balance in Two-Phase Flow

One important point in two-phase flow is that the energy balance equation and the momentum balance equation do not give the same results for pressure losses. In single phase flow in a constant diameter duct, for flow of noncompressible fluids and fully developed flow (for the sake of simplicity), one has:

(a) mechanical energy dissipated as heat per unit-time per unit-length of duct and per unit-flowrate (from the energy balance):

$$E = \frac{\Delta p_f}{\Delta z} = \left(\frac{\Delta p}{\Delta z} - \rho g\right) \tag{18a}$$

(b) shear stress at the walls (from the momentum balance):

$$\zeta_w = \left(\frac{\Delta p}{\Delta z} - \rho g\right)\frac{D}{4} = \frac{\Delta p_f}{\Delta z}\cdot\frac{D}{4} \tag{18b}$$

On the contrary, in two-phase flow, still for incompressible fluids one has (*9*, *17*, *18*):

$$\frac{\Delta p_f}{\Delta z} = E = \frac{\Delta p}{\Delta z} - \rho^* g \tag{19a}$$

where $\rho^* = \rho_g X_v + \rho_l(1 - X_v)$ is the flowrate density, that is the density of the mixture averaged on the flowrate quality;

$$\tau_w = \left(\frac{\Delta p}{\Delta z} - \bar{\rho} g\right)\frac{D}{4} \tag{19b}$$

where $\bar{\rho}$ is the true density of the mixture.

Since $X_v \neq \bar{\alpha}$ (for $\bar{S} \neq 1$), $\tau_w \neq D/4\ \Delta p_f/\Delta z$. Thus the "head term" in the pressure drop equation has two distinct expressions, following the energy balance or the momentum balance. $\Delta p/\Delta z - \bar{\rho} g = \Delta p_f'/\Delta z$ may be defined as the pressure gradient due to the momentum exchange with the wall of the conduit and is proportional to shear stress at the wall τ_w. In single phase flow, for an incompressible fluid flowing in a conduit of uniform cross section, Δp_f and $\Delta p_f'$ coincide. The same holds for horizontal two-phase flow, if a mean value of τ_w over the whole surface area of the wall is considered. On the other hand, in a two-phase vertical flow the value of τ_w is not strictly related to that of Δp_f; in fact we have:

$$\tau_w = \frac{\Delta p_f}{\Delta z} - (\bar{\rho} - \rho^*) g \frac{D}{4} \tag{20}$$

where

$$\bar{\rho} - \rho^* = (\rho_l - \rho_g) X_v (1 - X_v) \frac{\Delta S}{1 + \Delta S(1 - X_v)} \tag{21}$$

Therefore Δp_f and τ_w do not refer to the same quantity. The expression "pressure loss," which refers to the mechanical energy dissipated as heat, should be restricted to indicate the value of Δp_f.

Since in horizontal flow the pressure loss is known, being directly measured, a question may arise as to which of the two quantities (Δp_f or $\Delta' p_f$) in vertical flow has to be compared with the horizontal pressure drop.

The quantity of interest from the energetic point of view is obviously Δp_f. However, if a comparison is made with the purpose of verifying the coincidence of the values in horizontal and vertical flow (that is, for example, checking an existing correlation of data obtained with horizontal flow), then neither Δp_f nor $\Delta p_f'$ should, strictly speaking, be used.

In fact, they would generally be different in horizontal and vertical

flows because of the inherently different shear stress distribution to which the phase and velocity distribution are related, in vertical and horizontal conduits. The difference, illustrated in Fig. 4 with reference to annular flow (where the asymmetry inherent to horizontal flow is not apparent), makes a possible coincidence purely fortuitous. In some

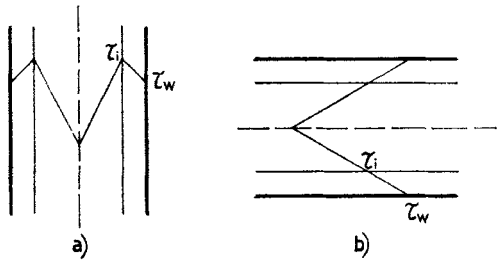

FIG. 4. Shear stress distribution in annular flow. (a) vertical upward flow; (b) horizontal flow.

instances, however, such as in the case of a highly dispersed flow, the difference might not be important from a quantitative point of view, but this is difficult to know a priori with any certainty.

II. Fluid Mechanics

A. TWO-PHASE PRESSURE DROP

1. General Remarks

The pressure drop has been the most investigated item in two-phase flow from both the experimental and theoretical viewpoint. However, a pressure drop correlation has not so far been established which can be considered reliable enough, even for a given flow pattern, for instance, the annular-dispersed regime. Several reasons are responsible for this fact: the incomplete understanding of the basic phenomena involved in two-phase flow, which hinders the right approach to the problem, the influence of many variables which are quite difficult to evaluate, such as, for instance, the entrance conditions, the different interpretation of the experimental data with regard to the contribution of the various terms to the total pressure drop.

As in single-phase flow, the measured total pressure drop is given by the sum of three different terms corresponding respectively to the frictional resistance experienced by the fluid in its motion, to the gravity field and to the velocity variation along the flow direction. In two-phase flow, however, due to the different velocities of phases, the pressure drop equation is different when derived from a momentum balance or, instead, from an energy balance (see also Section I,C,3). The two equations, in

the simple case of incompressible fluids, constant conduit cross section and adiabatic flow, are:

	Total pressure drop		Resistance term		Head (or gravity) term
Energy equation	Δp	=	Δp_f	+	$\rho^* g\,\Delta z$

$$+\left[\frac{\rho_g X_v}{2}(\bar{U}_{2g}^2 - \bar{U}_{1g}^2) + \frac{\rho_l(1-X_v)}{2}(\bar{U}_{2l}^2 - \bar{U}_{1l}^2)\right] \quad (22)$$

	Total pressure drop		Resistance term		Head (or gravity) term
Momentum equation	Δp	=	$\Delta p_f'$	+	$\bar{\rho} g\,\Delta z$

$$+ [\rho_g(\alpha_2 \bar{U}_{2g}^2 - \alpha_1 \bar{U}_{1g}^2) + \rho_l\{(1-\alpha_2)\bar{U}_{2l}^2 - (1-\alpha_1)\bar{U}_{1l}^2\}] \quad (23)$$

The indexes 1 and 2 refer to sections 1 (upward) and 2 (downward) of the conduit.

The resistance term is generally called frictional pressure drop or irreversibility term. (The second expression, or the equivalent one: pressure loss, should be reserved to Δp_f, that is to the resistance term in the energy equation.) A comparison among the various experimental results should always be made on the basis of the same pressure drop equation.

It can be noted that in two-phase flow, even under the above assumptions, the acceleration term is different from zero when the phase distribution, that is the value of $\bar{\alpha}$, varies along the flow direction. This fact, not always taken into account, contributes another source of uncertainty in comparison with the various experimental results. The contribution of the acceleration term under adiabatic conditions, as it was emphasized by Dukler (*19*), can be a substantial fraction of the total pressure drop, especially in the case of low pressure systems, where the gas density varies considerably along the flow direction because of the relatively high variation of the line pressure.

2. The Homogeneous Model Correlation

The simplest approach for the prediction of the two-phase pressure drop is represented by the homogeneous model, in which the two phases are supposed to flow with identical velocity and with a uniform distribution in the test section. According to this visualization of two-phase flow the acceleration term is zero in both Eqs. (22) and (23) and the head terms are equal, so that, with the above assumptions, it is $\Delta p_f = \Delta' p_f$.

The prediction of the pressure loss is made through the well known relationship valid in single-phase flow:

$$\Delta p_f = \frac{2f}{D}\frac{C^2}{\rho^*} \tag{24}$$

However, the expression of a two-phase viscosity to be put in the friction factor, is a quite arbitrary average of the viscosities of the two phases. The following expressions have been assumed alternatively:

$$\frac{1}{\bar{\mu}} = \frac{1}{\mu_g} X + \frac{1}{\mu_l}(1 - X) \tag{25a}$$

$$\bar{\mu} = \mu_g X_M + \mu_l(1 - X_M) \tag{25b}$$

$$\bar{\mu} = \mu_l \tag{25c}$$

Rarely can the homogeneous model predict the pressure drop with an acceptable approximation.

3. Lockhart-Martinelli and Martinelli-Nelson Correlations

The best known pressure drop correlation for isothermal two-phase flow is that proposed since 1949 by Lockhart and Martinelli (*20*). This correlation was based on experiments performed with air and various liquids (water, kerosene, etc.) at room temperature and at pressures varying between 16 and 52 psia. The pipe sizes ranged from capillaries to 1 inch I.D., and the superficial Reynolds numbers between 1 and 124.000 (liquid), 7 and 86.000 (gas). In all runs for which the pipe was not horizontal, "frictional" pressure drops were deduced from total pressure drops, by subtracting the head term according to the momentum equation. The momentum contribution due to change in phase and velocity distributions was neglected.

As mentioned in Section I,A,3, Lockhart and Martinelli distinguish four flow regimes depending on the Reynolds number of the two phases supposed flowing alone in the conduit. For any one of these regimes the correlation, given in the graphical form (Fig. 5), provides a unique value of the parameter

$$\phi_l = \sqrt{\frac{(\Delta p_f')_{TP}}{(\Delta p_f)_l}} \left(\text{or } \phi_g = \sqrt{\frac{(\Delta p_f')_{TP}}{(\Delta p_f)_g}} \right) \tag{26}$$

versus the value of the parameter

$$X^1 = \sqrt{\frac{(\Delta p_f)_l}{(\Delta p_f)_g}} \tag{27}$$

[1] X and ϕ have two subscripts (tt, tv etc.) depending on the flow regimes defined in Section I,A,3. (t = turbulent; v = viscous).

where $(\Delta p_f)_l$ and $(\Delta p_f)_g$ and the frictional pressure drop of the liquid and the gas phase, respectively, supposedly flowing alone in the conduit. The authors used the well-known formula:

$$\frac{\Delta p_f}{\Delta z} = \frac{2f}{D}\frac{G^2}{\rho} \tag{28}$$

where

$$f = \frac{0.046}{N_{\mathrm{Re}}{}^{0.2}} \text{ when } N_{\mathrm{Re}} \geq 2000 \tag{29a}$$

and

$$f = \frac{16}{N_{\mathrm{Re}}} \text{ when } N_{\mathrm{Re}} \leq 1000 \tag{29b}$$

The proposed correlation, in terms of ϕ_1, represents the experimental results used to determine the correlation itself within 30%. The values of the pressure drop suffer of course from a greater deviation.

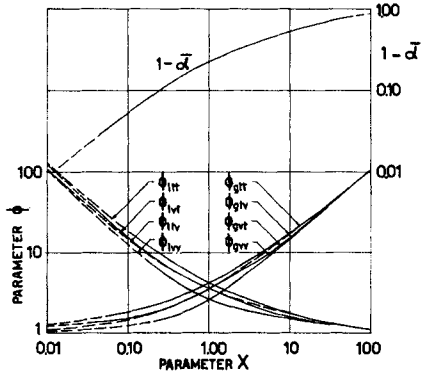

FIG. 5. Martinelli-Lockhart graphical correlations for two-phase friction pressure drops and liquid volume fraction.

It can be observed that the criterion selected for the specification of the flow regimes is not realistic. Furthermore Lockhart and Martinelli did not take into account the role of the surface tension with regard to the energy dissipation, so that this property does not enter the correlation. Other physical properties of the fluids are introduced only through the calculated single-phase pressure losses.

At least it should be pointed out that, considering the postulates taken as a basis for the correlation, it may be inferred that the correlation would be particularly applicable to the annular-dispersed regime.

The Lockhart-Martinelli correlation [or, better, a correlation obtained by Martinelli *et al.* (*1*) with a parameter slightly different from X] was

extended to the flow of saturated steam-water mixtures in turbulent-turbulent flow by Martinelli and Nelson (*21*). In this case, however, the value of the saturation pressure had to be taken into account as a further independent parameter. This shows that the influence of the physical

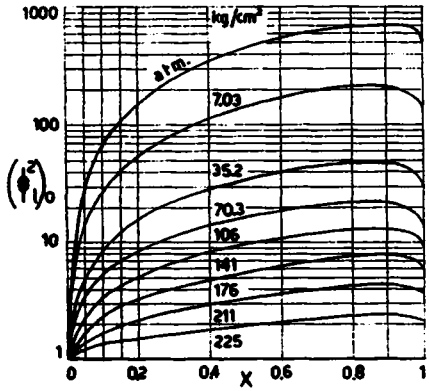

FIG. 6. Martinelli-Nelson correlation for two-phase frictional pressure drops with quality steam (adiabatic flow).

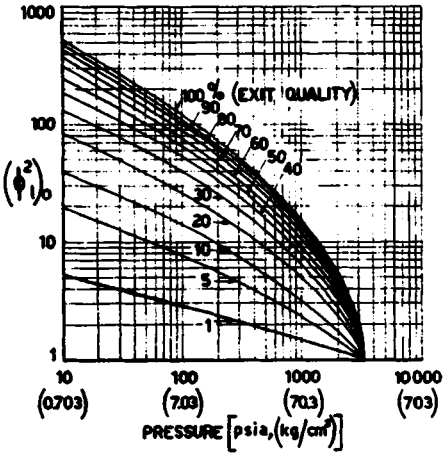

FIG. 7. Martinelli-Nelson correlation for two-phase frictional pressure drops (with linear quality variation).

properties of phases is not adequately represented through single phase pressure losses. The (ϕ_l^2, X_{tt}) curve corresponding to atmospheric pressure was assumed to be coincident with the above mentioned correlation, while the curve corresponding to the critical pressure was derived theoretically taking into account that in this condition the physical properties of the

two phases approach a common value. The intermediate curves were determined on the basis of experiments performed in horizontal flow with pressures varying between 35 and 230 kg/cm^2 under heat transfer condition. These data were corrected for the momentum contribution due to the quality change along the flow direction.

The Martinelli-Nelson correlation for constant quality (or for local values in the case of a quality variation along the flow direction) is represented in Fig. 6, in which the ordinate represents the ratio between the two-phase friction pressure drop and the pressure loss of the liquid phase $(\Delta P_f)_{lo}$ assumed to be flowing at the total mass flowrate.

In Fig. 7 the integrated correlation is represented as a function of the outlet quality X_o in the case of a linear quality variation along the flow direction.

3. Other Results on Pressure Drops in Horizontal Conduits

Alves (*5*) carried out experiments in a pipeline gas-liquid contactor, 1 inch I.D., consisting of four horizontal passes connected between one another by three upflow return bends of 7-inch radius. The fluids were: air at low pressure, water, and oil.

The pressure drop in the horizontal passes agreed fairly well (+20–30%) with the Lockhart-Martinelli correlation. The pressure drop results for the return bonds were remarkably higher than those predicted. The pressure drops in the Tee mixer (water on the run side) were found to be almost equal for both the gas and the water side: they increased with increasing gas flowrate and reached values as high as those in a horizontal section having $L/D = 50$, when $N_{(\mathrm{Re})_g} = 10^4$.

The pressure drop measurements performed by Baker (*2*) with gas-oil (hydrocarbons) mixtures in horizontal pipelines (4 to 10 inches) can be considered as fully developed flow experiments (very long lines, 2 to 3 miles; very high line pressure, 1000 psi). On the basis of these and other experiments carried out by some other authors in very different flow conditions, Baker suggested a new relationship between Martinelli's parameters ϕ_g and X in the case of annular dispersed flow (as indicated by the flow pattern region plot proposed by the author himself) that is:

$$(\phi_g)_{tt} = (4.8 - 0.3125D)X^{0.343-0.021D} (D \text{ in inches}) \qquad (30)$$

This correlation points out a dependence of the ratio $(\Delta p_f)_{TP}/(\Delta p_f)_g$ on the pipe diameter. For other flow regimes a further dependence on the mass flowrate (besides that included in the expression of ϕ_g) is also demonstrated.

Chenowheth and Martin (*22*) carried out experiments with air-water mixtures in horizontal pipes (1.5 and 3 inches) at two different average

pressures (18 and 100 psi). Good agreement was found with the Lockhart-Martinelli correlation for performance at low pressure.

On the other hand, the pressure drops obtained at 100 psi, especially in the case of the largest diameter, were remarkably lower than those predicted by that correlation (up to 2.5 times). On the basis of their own results the authors developed a new empirical correlation for the frictional pressure drop in turbulent two-phase flow $[(N_{Re})_{lo} = GD/\mu_l > 2000]$, which gives the value of $(\Delta p_f)_{TP}/(\Delta p_f)_{lo}$ as a function of the liquid

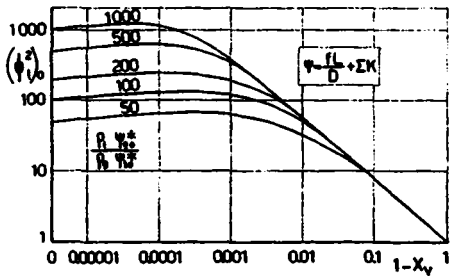

FIG. 8. Chenoweth-Martin correlation for turbulent two-phase frictional pressure drops in horizontal ducts.

volume flow rate quality $(1 - X_v)$, having the ratio $(\Delta p_f)_{go}/(\Delta p_f)_{lo}$ as a parameter (Fig. 8). The terms $(\Delta p_f)_{go}$ and $(\Delta p_f)_{go}/(\Delta p_f)_{lo}$ include the fitting pressure drops (ΣK):

$$\frac{(\Delta p_f)_{go}}{(\Delta p_f)_{lo}} = \frac{\dfrac{f_{go}L}{D} + \Sigma K}{\dfrac{f_{lo}L}{D} + \Sigma K} \cdot \frac{\rho_l}{\rho_g} = \frac{\psi_{go}}{\psi_{lo}} \cdot \frac{\rho_l}{\rho_g} \tag{31}$$

This correlation represents 92% of the data within 35%. The data of other investigators (including those used to develop the Lockhart-Martinelli correlation) correlate equally well. The results obtained with three typical 3-inch fittings do correlate as well.

Isbin *et al.* (*3*) investigated the adiabatic pressure drop in horizontal pipe (0.484 and 1.062 inches I.D.) with saturated steam-water mixtures from 25 to 1415 psi (total flowrate: 454–4350 lb/*h*; mass quality: 0.03 ÷ 0.98). Care was taken to avoid any entrance and exit effect.

The frictional pressure drops were computed by subtracting from those measured the pressure drops due to the momentum variation (these being noticeable only at low pressure). The authors compared the experimental data with the Martinelli-Nelson correlation in terms of parameter $(\phi_g)_o$ which minimizes the effect of pressure. The agreement is not very good and the experimental values of $(\phi_g)_o$ show a dependence of the steam

flow rate. A new empirical correlation is then proposed (Fig. 9) between $(\phi_g)_o^2$ and the quantity $1 - X/X(N)_{go}$, where $(N_{Re})_{go}$ is the Reynolds number based upon total flow as gas. For the highest values of the steam flow rate, the experimental data correlate fairly well with the homogeneous model ($1/\bar{U} = 1/\mu_g X + 1/\mu_l(1 - X)$). The experimental curves of $(\phi_g)_o^2$ versus the mass quality exhibit a maximum in the high quality region ($X > 0.5$).

In 1946 Armand (*23*) developed analytically a relationship between the parameter ϕ_l^2 and the liquid volume fraction $(1 - \bar{\alpha})$ in the case of

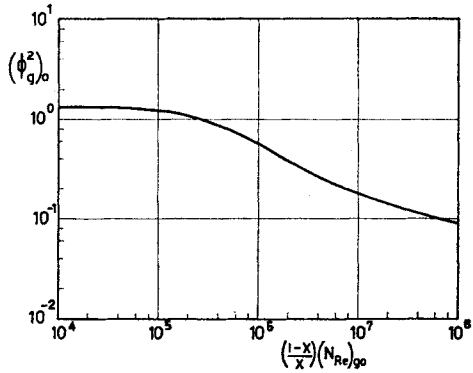

FIG. 9. Two-phase frictional pressure drop correlation presented by Isbin *et al.* (*3*) for steam-water system in adiabatic horizontal flow.

an annular regime and extended it, rather arbitrarily, to other flow regimes:

$$\phi_l^2 = \frac{K}{(1 - \bar{\alpha})^n} \tag{32}$$

where the values of K and n were determined experimentally (air-water mixtures at room temperature and atmospheric pressure in a horizontal copper tube, 26 mm I.D.—Mass quality: $0 \div 95\%$) and depend on that of $(1 - \bar{\alpha})$. A correlation between $\bar{\alpha}$ and the basic variable X_v is also given. The proposed correlation represents fairly well the data obtained by other authors under different experimental conditions.

The author of this article, together with Treshchev (*24*), on the basis of experiments performed with steam-water mixtures in horizontal flow (diameter: 57 mm I.D.; pressure: 10 + 90 atm; $X = 0 + 90\%$) with and without heat transfer, proposed a simplified correlation (valid for $X_v > 0.90$) which accounts for the influence of the static pressure:

$$\phi_l^2 = \frac{0.0025p + 0.005}{(1 - X_v)^{1.75}} \quad (p \text{ in kg/cm}^2) \tag{33}$$

McManus (*25*) carried out experiments at atmospheric pressure in horizontal pipes (1, 2, and 3 inches) with mixtures in annular-dispersed flow. The fluids were air, water, and glycerine solutions. The total pressure drop was corrected for the acceleration term (Δp_a), according to the momentum equation and the experimental variations of the liquid volume fraction along the flow direction. This correction was found to depend substantially only on the gas Reynolds number; the Δp_a fraction due to the liquid phase, however, depends on the liquid Reynolds number. The author found better agreement of his experimental results with the Chenoweth-Martin correlation rather than with the Lockhart-Martinelli one. With the smallest diameter, however, even the first correlation predicts values of the frictional pressure drop (Δp_f) lower than those measured.

McManus observed a large increase in pressure drop when the liquid viscosity is increased, the liquid Reynolds number being the same. At the same time the film waves (see Section II,B,3) are damped and the author suggests that the energy lost is expended in viscous shear stress rather than wave formation.

The influence of the type of entrance and of the liquid properties (viscosity and surface tension) was investigated by Dukler *et al.* (*19*, *26*) in an horizontal apparatus (pipe diameter: 1 and 3 inches) at room temperature and pressure. The pressure gradient was found to be higher, all other things being equal, when the gas enters the Tee mixer side. In this case (see Section II,B,4b) the entrainment is lower, so that it is suggested by the authors that more energy is required to transport a given liquid flowrate in the film adhering to the wall rather than in the core in form of small droplets. A liquid viscosity variation from 1 to 17 cp produced small but measurable pressure drop variations. The influence of this parameter seems to be quite complicated in nature because its influence on pressure drops goes through a minimum and depends on the value of the liquid flowrate. On the other hand, the surface tension influence was found to be negligible. The acceleration (or expansion) pressure drop, according to the momentum equation, was shown to be as high as 50% of the total pressure drop and the authors suggested that many discrepancies among the various authors may be due to a different influence of this term not always taken into account.

4. Results on Pressure Drops in Vertical Conduits

Govier *et al.* (*27*, *28*, *29*), investigated the flow of air-water mixtures in vertical pipes, the gas density and the pipe diameter being taken as additional variables. They related the different trend of the total pressure drop versus the ratio $X_v/1 - X_v$ at constant liquid flowrate to the exist-

ence of different flow regimes. A graphical correlation is proposed for the pressure loss, computed according to the energy equation, in terms of a friction factor defined as:

$$f_l = \frac{D}{2\rho \bar{U}^*_l{}^2} \frac{\Delta p_f}{\Delta z} \tag{34}$$

where $\bar{U}^*_l$ is the superficial linear velocity of the liquid phase.

The values of f_l were found to be nearly independent of the gas density and to increase with increasing pipe diameter.

The prediction of the pressure gradient in annular vertical flow was approached by Anderson and Mantzouranis (*30*), by evaluating the friction factor of the gas phase considered as flowing alone in contact with a liquid rough surface. They suggested that the ripples on the film surface have a marked effect on the value of the friction factor. Due to the difficulty in defining the film surface condition versus the basic flow variables the influence of the liquid phase is tentatively taken into account through the parameter $Q^* = q_l/\pi Ds \sqrt{\rho e/\tau_w}$. The experimental data obtained by the authors themselves with air-water mixtures in a ½-inch test section were correlated in terms of $\tau_i/\rho_g \bar{U}^*_g{}^2$ versus the gas Reynolds number with Q as a parameter. By comparison with other experimental data, it was found that Q is unable to describe the influence of the geometry and liquid properties.

Hewitt *et al.* (*31*) compared the experimental data obtained in a vertical channel (1¼-inch I.D.) with air-water at room conditions with the Lockhart-Martinelli and the homogeneous flow correlation. In the first case the momentum head term was accounted for; in the second one both the liquid viscosity and the mean fluidity were used. Satisfactory agreement was found only with the first correlation.

Hughmark and Pressburg (*18*) investigated the influence of the liquid properties in vertical flow. The test section was a 1-inch I.D. pipe at atmospheric pressure and the fluids were air and six different liquids.

They suggested that the pressure loss, defined according to the energy equation, is related to the difference between the linear mean velocity of the two phases and gave, in graphical form, a series of curves representing $(\Delta p_f)_{TP} - (\Delta p_f)_{lo}/\Delta z$ versus $(\bar{U}_g - \bar{U}_l)$ having as a parameter the value of[2]

$$\psi = \frac{1}{G_{tot}{}^{0.7} \mu_l{}^{0.147} \gamma^{0.194}} \left(\frac{D}{0.0873}\right)^{0.5} \tag{35}$$

However, the value of the liquid volume fraction, that is the value of

[2] Units to be used: G = [lb. mass/sq. ft. sec]; μ = [cp]; ρ = lb. mass/cu. ft; γ = [dynes/cm]; D = [ft].

$(\bar{U}_g - \bar{U}_l)$, depends itself on physical properties and flowrates so that the influence of these variables is more complicated than that shown by (35). In particular the pressure loss will depend also on the physical properties of the gas phase.

A semi-theoretical approach was proposed by Bankoff (*32*) for the bubble flow regime visualizing a smooth phase distribution, the wall being wetted by the liquid and the gas concentration reaching a maximum at the axis, with a local slip ratio equal to unity. If a power law distribution is assumed for both the velocity and the void fraction the ratio between the over-all gas volume fraction and the volume flowrate quality ($K = \bar{\alpha}/X_v$) will depend only on the value of the exponents. On this basis and defining

$$f_{TP} = \frac{\tau_{TP}}{\frac{1}{2}\bar{\rho}\bar{U}^2} = \frac{C}{\left(\frac{D\bar{\rho}\bar{U}}{\bar{\mu}}\right)^{1/4}} \text{ (where } \bar{\mu} \simeq \mu_l\text{)}, \tag{36}$$

a correlation is derived between the shear stress on the wall in two-phase flow and that in single (liquid)-phase flow in which mass and volume quality, gas to liquid density ratio and K are involved. The comparison with experimental results and other correlations for steam-water mixtures seems to indicate that the correlation is reasonably accurate if K is assumed to be a given function at the static pressure. Due to the procedure followed neither the gas viscosity nor the surface tension are included.

A similar approach was tried at CISE by Bertoletti *et al.* (*13*) for annular-dispersed flow. A velocity distribution and a void fraction of the following form were assumed:

$$U' = \frac{U_g}{U_{g\max}} = \frac{U_l}{U_{l\max}} = \epsilon\frac{1}{m} \tag{37a}$$

$$\alpha' = \frac{\alpha}{\alpha_{\max}} = \epsilon\frac{1}{n} \tag{37b}$$

where the subscript "max" refers to the maximum value (on the axis).

The correlation derived for pressure drops was compared with experimental results, and the agreement was poor (not better than using far less complicated correlations). In any case, even if the agreement could be improved through a better knowledge of velocity and void fraction distribution, the main difficulties are not bypassed, since a correlation for velocity profiles and void void fractions would be necessary. It is not demonstrated that this would be an easier task than correlating directly an integral parameter such as friction pressure losses.

5. Results of Investigations Performed at CISE Laboratories

The pressure drop investigation in two-phase adiabatic flow accomplished at CISE (*33, 34, 35, 36, 37, 38*) was mainly devoted to the dispersed region (according to the visual observation as well as to the Baker plot). (See Section I,A,3 and reference (*2*).) The experiments were carried out in a pressurized system (up to 22 kg/cm² abs) at room temperature with a thick wall transparent plastic test section mounted vertically.

Most of the runs performed with argon-water mixtures at full pressure in a 25 mm I.D. circular conduit ($G = 30 \div 300$ gm/cm² second, $X = 7 \div 80\%$). The measured values of the pressure drop were not too far from those predicted by the Lockhart-Martinelli correlation and, at the highest mass flowrate, by the homogeneous model

$$(\bar{\mu} = \mu_g X_M + \mu_l(1 - X_M))$$

which always gave lower figures. The trend of pressure drop against mass flowrate is, however, quite different: the dependence of the pressure loss on specific total mass flowrate can be represented to a first approximation by the exponent 1.4, instead of 1.8 as given by both correlations. The dependence on quality was found to be represented with reasonable accuracy by the flowrate density; the dependence on ρ^* can be expressed approximately by the exponent -0.75. With qualities higher than 0.5 the two-phase pressure loss was always greater than those corresponding to the total flow of gas and at low mass flowrates this happened even with lower qualities.

The influence of the entrance conditions was investigated by varying the aperture of the annular slot of the Tee mixer (gas on the run side). The pressure drop decreased with decreasing aperture size, that is with approach to jet injection to which a higher initial liquid dispersion corresponds.

Other experiments were carried out under different experimental conditions to investigate the influence of the physical and geometrical parameters.

The liquid viscosity was varied between 0.67 and 1.12 cp allowing the operating temperature to vary between 16° and 37 °C. Within this range, no significant influence of this parameter was observed. The same can be said about the influence of the gas viscosity ,which was varied by using nitrogen in place of argon ($1.8\ 10^{-4}$ against $2.2\ 10^{-4}$ poise).

The influence of the gas density, investigated by lowering the line pressure do ~6 kg/cm² abs and operating at constant volume flowrate, was found to depend strongly on both flowrate and quality. At the highest flowrates it was, roughly, $\Delta p \equiv \rho_g^{1/2}$, while at lower flowrates the

exponent is also lower. Furthermore, it was found that even the dependence on ρ_g, together with that on quality, can be represented by the flowrate density.

The influence of the liquid density, on the other hand, was not investigated.

An interesting result is that concerning the influence of the surface tension, which was investigated by using an alcohol-water solution (90 W.% of ethyl alcohol, $\gamma = \sim 24$ dyne/cm) in place of pure water. Figure 10 shows that, while at low flowrate and quality the influence of

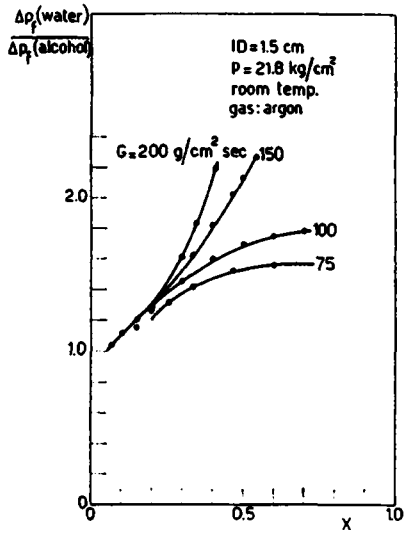

FIG. 10. Comparison of frictional pressure drop with argon-water and argon/alcohol systems in upflow (CISE's results).

this parameter is not significant, according to what was found by other authors (*19*), with higher values of G and X the pressure drop decreases considerably as the surface tension is lowered, as if the interaction between phases played a role of increasing importance in the energy dissipation, when G and X are increased.

Finally, operating with conduits of different size and shape (round conduit 15 mm I.D.; annuli: $^{15}/_{25}$ mm and $^{10}/_{25}$ mm) it was found that in any case the dependence of the pressure drop on the equivalent diameter (defined as $D = 4A/p$) is represented with reasonable accuracy by the exponent -1.2 as in single-phase flow and according also to the Martinelli-Lockhart correlation.

Other experiments in vertical upflow were carried out in a hot loop with steam-water at 70 kg/cm² both in adiabatic and in heat transfer condi-

tions *13*, *39*, *40*, *41*. A fairly simple expression correlated experimental results over a wide range of flowrates and qualities reasonably well:

$$\frac{\Delta p_f}{\Delta z} = \frac{2f^+}{D}\frac{G^2}{\rho} \tag{38}$$

where

$$f^* = \frac{0.046}{\left\{\frac{GD}{\bar{\mu}}\left(\frac{G}{240}\right)^2\right\}^{0.2}} \quad (G \text{ in gm/cm}^2 \text{ second}) \tag{39}$$

and $\bar{\mu}$ is given by (25b).

This correlation was found to apply with some loss in accuracy, even in the results for the argon-water system, previously mentioned. Also pressure losses in the presence of heat transfer, measured in the same loop, could be correlated provided that the proper correction was made for the acceleration term (computed according to the homogeneous model), which is often predominant in the case of steam generation.

B. PHASE AND VELOCITY DISTRIBUTION

1. General Remarks

The studies carried out on phase and velocity distribution in two-phase flow may be conveniently distinguished into two major items:

(a) the investigation of the overall values of the variables averaged over the conduit cross section. Due to the relationships existing between them, only one variable has to be determined experimentally;

(b) the investigation of the local values of the variables. The local values of the specific mass flowrates are not known a priori so that, in this case, three independent measurements have to be made. Referring to the annular-dispersed regime, however, we can further distinguish between the region adjacent to the conduit wall, occupied by the liquid film, in which the number of unknowns is reduced, and the region in the core of the conduit, occupied by the liquid-gas dispersion.

2. Over-all Properties

Apart from the density measurements performed with radiation, described elsewhere (Section II,C) in this chapter, the quantity that generally has been directly measured is the liquid volume fraction (or "liquid holdup") $1 - \bar{\alpha}$. The value of the liquid volume fraction being known, the mean density of the mixture and the mean velocity of both phases, hence the over-all slip ratio ($\bar{S}$), can be easily evaluated using the relationships given in Section I,C,1. In the case of a purely annular

regime, without any appreciable amount of spray in the core, the mean film thickness, too, can be immediately derived from the liquid volume fraction.

a. Measurement Methods. The most used method to measure the overall volume fraction of the liquid phase is that of the "quick closing valve," by which the amount of liquid contained over a length of the conduit is trapped and then weighed. Errors may arise from the following main sources: the nonsimultaneous closing of the valves and the noncomplete recovery of the liquid to be weighed.

An interesting method for the direct measurement of the mean density in horizontal pipes is that used by Armand (*23*) who weighed a portion of the conduit under operation.

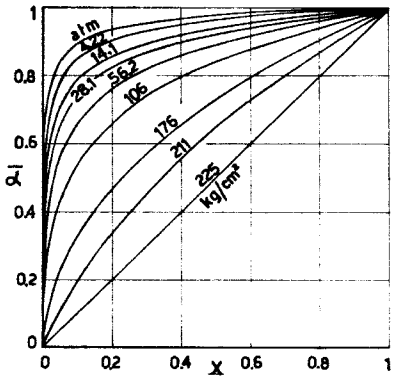

FIG. 11. Martinelli-Nelson correlation for void fraction vs. quality steam at different pressures.

b. Results and Correlations. Lockhart and Martinelli (*20*), on the basis of the already mentioned experiments performed with gas-liquid systems at low pressure, proposed a correlation between the liquid volume fraction and the parameter X which is still extensively used. The correlation, as shown in Fig. 5, is given in graphical form with a single curve valid for any flow regime. For the same reasons, stated in connection with the pressure drop correlation, the holdup correlation should not be generalized to systems having too different properties.

Following a procedure similar to that used for the pressure drop correlation, Martinelli and Nelson (*21*) derived a void fraction correlation for steam-water systems with the saturation pressure as a further parameter (Fig. 11). The curves given, however, are more arbitrary than in the other case due to the lack of experimental data.

Many other authors (*2*, *5*, *23*, *42*, *43*, *44*, *45*) have carried out holdup

measurements under different experimental conditions. The results and the proposed correlations are rarely in mutual agreement. A comparison among a number of published data is made in (*46*).

The correlation recently proposed by Hughmark and Pressburg (*18*) accounts for the influence of all the physical properties. A single holdup curve is given using the following parameter[3]:

$$\chi = \left(\frac{1 - X}{X}\right)^{0.9} \frac{\mu_l^{0.19} \gamma^{0.205} \rho_g^{0.70} \mu_g^{2.75}}{G^{0.435} \rho_l^{0.72}} \tag{40}$$

where G has a maximum value of 24.4 gm/cm² second (50 lb/ft² second). According to this correlation the influence of the diameter of the conduit is not appreciable, while that of the gas viscosity is quite strong.

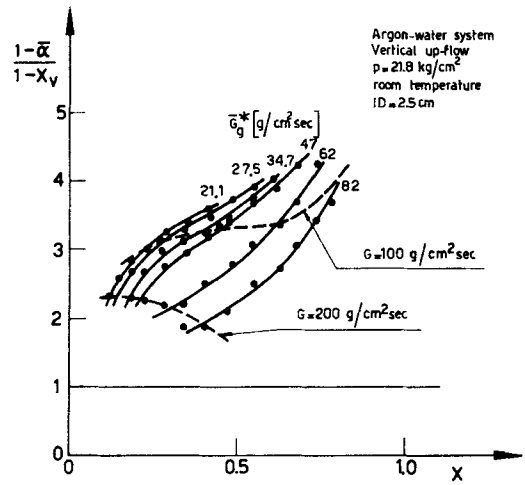

FIG. 12. Ratio $(1 - \bar{\alpha})/(1 - X_v)$ vs. mass quality. Gas and total mass flowrate as parameters (CISE's results).

The over-all liquid holdup was not directly measured at CISE, but the values of this parameter were calculated from the data on the local values in the core and the mean film thickness and from the mean density values obtained with the β-ray method. The figures obtained in the two ways were in reasonable agreement (see Table II in Section II,C,6) and therefore some remarks can be made about the over-all properties of pressurized gas-liquid mixtures in vertical dispersed flow.

With pure water as the liquid phase and argon at full pressure (22 kg/cm²), the values of $1 - \bar{\alpha}$ are always considerably higher than those of $1 - X_v$, but the ratio $1 - \bar{\alpha}/1 - X_v$ depends on both flowrate

[3] Units are the same as in formula (35).

and quality (Fig. 12). Consequently the values of the over-all slip ratio and of the ratio between the true density and the flowrate density is substantially higher than unity. Apart from this dependence, these data agree not too badly with the Lockhart-Martinelli correlation, in spite of the high gas density.

According to experimental results on the influence of the physical properties on the thickness of the liquid film (see Section II, B, 3), liquid and gas viscosity, in contrast with the Hughmark-Pressburg correlation, should not appreciably influence the liquid holdup, at least within the narrow ranges investigated. The surface tension, instead, with sufficiently high values of the flowrate and quality, would play an important role: the lower the surface tension, the lower the liquid holdup.

On the other hand, Larson (*47*) during experiments with steam-water mixtures in adiabatic flow at 70 kg/cm^2 (1000 psi), that is with a surface tension five times lower than that of cold water, found values of $\bar{S}$ rather high (between 1.4 and 4.3), although operating with mass flow rates and qualities similar to those used in CISE experiments. In this case, however, the values of the other physical properties, especially of the liquid viscosity, are too far from the ranges explored with gas-liquid systems.

With regard to the operation with heat transfer, mention can be made of the experiments carried out by Egen *et al.* (*48*) at 140 kg/cm^2 (2000 psi) within the dispersed regime: the values of $\bar{S}$ were found to be very close to unity.

3. The Liquid Film

From the experimental viewpoint, the region adjacent to the wall of the conduit, occupied by the liquid film, has been investigated mainly in terms of film thickness measurements. Some authors (*49*, *50*), however, attempted to measure directly the film flowrate, while Krasiakova (*4*) investigated the velocity distribution.

With regard to the characteristics of the film surface, such as amplitude and frequency of ripples and waves, experiments carried out at Harwell (*51*) provided quantitative data mostly for pure annular flow. Anyway the study of the detailed configuration of the liquid film surface and structure in dispersed flow is just beginning.

In the following, only the experimental data on average film thickness and film flowrate will be reviewed. Theoretical approaches to velocity distribution will also be mentioned.

a. Measurement Methods. The most commonly used methods to measure the liquid film thickness are based upon electrical conductivity, increased, if necessary, by the addition of small amounts of electrolytes, while the two-phase suspension flowing in the core acts as an insulator.

Provided that the wall of the conduit is made of an insulating material, the electrical resistance of the film can be measured either parallel or perpendicular to the flow direction. One can distinguish:

(a) measurements performed with electrodes placed on the wall at a large distance with respect to the film thickness (*34*). In this case the average film thicknesses can be computed by the measured values of the resistance R and the resistivity ρ through the simple relationship:

$$s(D - s) = \frac{1}{\pi} \frac{\rho}{R} \tag{41}$$

Due to the disturbed nature of the film-core interface, the electrical mean thickness does not coincide with the true geometrical mean thickness. For example, if along the circumference there is an interruption in the liquid film the electrical resistance would become infinite while the geometric mean thickness would remain finite.

(b) The electrodes are placed at a short distance (*51*) from each other but on the wall. In this case the relationship between the electrical resistance and the mean film thickness has to be established by calibration. Furthermore, the reading varies continuously following the vicissitudes of the film surface. In principle it would be possible to investigate the amplitude and the frequency of the surface waves.

(c) Measurements of the electrical resistance perpendicularly to the flow direction by means of a fixed electrode on the wall and of a movable inside the duct (*25*). This method provides the maximum and the minimum values of the film thickness and can be used to investigate the frequency of the waves.

For other methods which have been used to investigate the thickness of the liquid film one can see (*49*, *52*, *53*).

The direct measurement of the film flowrate has been performed by measuring the liquid flowing through an annular slot in the test section, having a variable aperture (*49*), or collected in a film separator at the end of the conduit (*31*).

b. Results and Correlations. The first of the above cited methods was adopted at CISE (*34*) to measure the liquid film thickness. The data obtained with argon-water mixtures at room temperature and full pressure in the round conduit 25 mm I.D. are shown in Fig. 13. Under these experimental conditions the film thickness ranges between 0.1 and 2 mm. As would be expected, a variation of the same sign of the gas or liquid flowrate has an opposite effect; that is, an increase in the gas flowrate reduces the film thickness while an increase in the liquid flowrate increases the film thickness. The reduction due to a gas flowrate increase prevails as shown by the curves at constant quality.

The influence of the physical properties was investigated in the same way as for the pressure drop. In this case, too, the influence of the gas and liquid viscosity, within the narrow ranges explored, was not appreciable, while the influence of the surface tension becomes remarkable at increasing quality and flowrate (Fig. 14). Film thickness and pressure drop

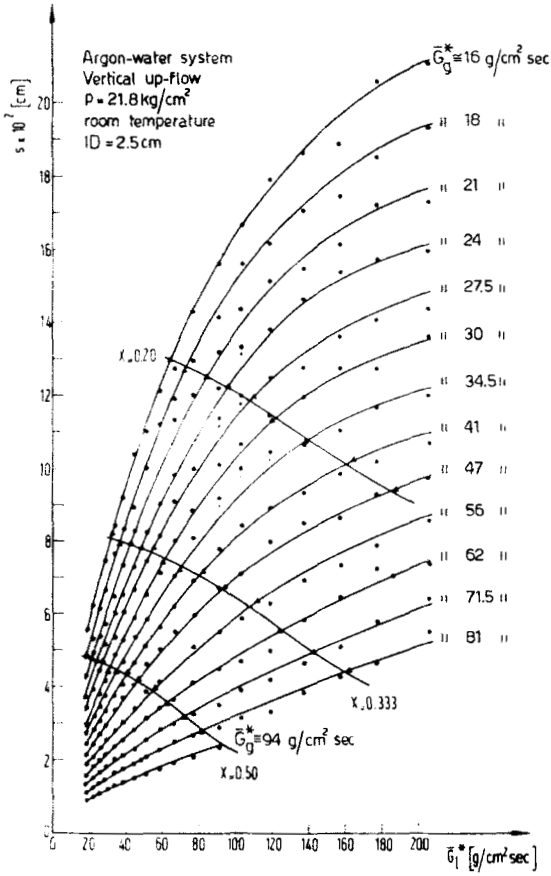

FIG. 13. Film thickness vs. liquid mass velocity, with the gas mass velocity as a parameter (CISE's results).

vary in the same direction as the surface tension. At least, when the gas density is varied, the film thickness undergoes such variations that it can be said, roughly, to be the inverse of the corresponding pressure drop variations.

All physical properties being the same, the pressure drop and film thickness vary in the same direction, as it was revealed by the runs

carried out with different entrance conditions, according to what was found by Dukler (*19*, *26*). (See also Section II,A,4.)

From the comparison of the data obtained in two circular conduits of different size (25 and 15 mm I.D.), one can see that the ratio s/D decreases slightly with increasing diameter (*37*). In annular conduits (*37*), the film on the outer surface is generally thicker than that on the inner surface, but at the same time it is thinner than the film which forms at the same specific mass flowrate on the wall of a round conduit having the same external diameter.

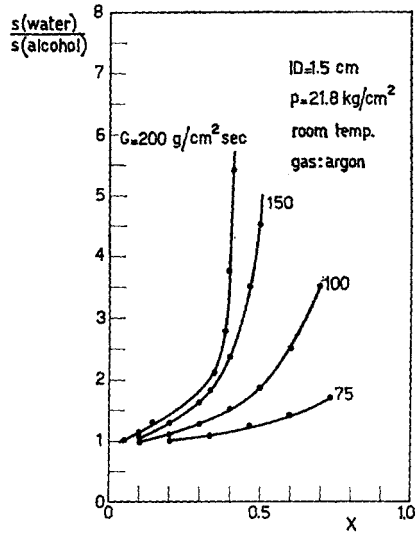

FIG. 14. Comparison of liquid film thickness with argon-water and argon-alcohol systems in upflow (CISE's results).

An important parameter should be the inclination of the conduit especially when passing from vertical to horizontal pipes. This effect was not investigated at CISE and a comparison with other author's data cannot be made because of the very different experimental conditions.

Film thickness measurements were performed at Harwell by Gill and Hewitt (*31*), through the technique of the short distance electrodes, in an air-water system at low pressure. The trend of s against gas and water flowrate is similar to that found at CISE, but the values are not comparable due to the different conditions. The experiments were carried out with two different modes of water injection in the mixer: annular and multijet injection. In the first case, all other things being equal, the film thickness is generally substantially higher than in the second case; the pressure drop, according to the CISE results, shows the same behavior.

Furthermore, for a multijet injection, at high gas flowrates the film thickness tends to level out with increasing liquid rate whereas with the annular slot the thickness continues to increase markedly.

During the same experiments, the film flowrate was also measured by means of the above mentioned technique. As with the thickness, the film flowrate increases at constant gas flowrate with increasing liquid flowrate, but, in the case of the annular injection, at high liquid rates it becomes relatively insensitive to further increases, as if the fully dispersed flow were approached.

McManus (*25*) used the movable method to perform film thickness measurements in horizontal flow with air-liquid (water and glycerine solutions) mixtures. The circumferential profiles at various stations along the test section were investigated. As would be expected, the film is always somewhat thicker in the bottom. The profiles were found to vary along the flow direction and to depend on both flowrate and quality. In most runs the entrainment was negligible so that the over-all liquid holdup could be derived from the film profiles. On the basis of these data, the author proposed the following holdup correlation:

$$1 - \bar{\alpha} = K \frac{(N_{\mathrm{Re}})_l^a}{(N_{\mathrm{Re}})_g^b} \left(\frac{\rho_g}{\rho_l}\right)^c \left(\frac{\mu_l}{\mu_g}\right)^d \tag{42}$$

where K and the various exponents have different values for $(N_{\mathrm{Re}})_l > 2100$ and $(N_{\mathrm{Re}})_l < 1800$.

The experimental investigation of the region occupied by the liquid film was performed by several other authors also with different techniques. Data and discussions are reported in (*4*, *49*, *52*, *53*).

The film region has been investigated theoretically with the aim of finding a correlation between the film thickness and the film flowrate. For this purpose, the velocity profile in the film can be determined if a relationship between the shear stress and the velocity at any point is given. In the case of a purely annular flow, the shear stress distribution can be obtained through a momentum balance provided that the total pressure drop is known: in dispersed flow a further variable is the mean density (or the density of the core region). In practice, the exact shear stress distribution has never been used because the analytical procedure would be too cumbersome. Apart from this question, one can obtain in general a correlation involving the three variables: film thickness, film flowrate and total pressure drop, the reliability of which depends mainly on the selected relationship between velocity and shear stress. Two of these variables being known, the third can be calculated.

Dukler and Bergelin (*52*) assumed a velocity profile equal to that given by Nikuradze for single-phase flow and found good agreement with the

experimental data obtained with a falling film upon a vertical flat plate. Successively Dukler (*54*) developed a correlation on the basis of two different expressions of the eddy viscosity (depending on the adimensional wall distance y^+). Hewitt (*55*) adapted this theory to upward cocurrent flow and found a satisfactory agreement with the experimental data cited above (*31*). Other correlations were developed by Calvert and Williams (*56*) and Anderson and Mantzouranis (*30*).

A relationship between film thickness and the interfacial shear stress τ_i was developed by Silvestri (*57*).

4. The Core Region

The region in the core of the conduit has only been investigated in a partial way, because of the difficulty, from both the conceptual and the experimental point of view, in handling all the three basic variables: gas and liquid velocity and gas (or liquid) volume fraction. The local and the over-all values of the entrainment were more frequently measured due to the fact that the droplet capture efficiency is relatively insensitive to the extraction conditions. The gas extraction, instead, requires special precautions.

The microscopic structure of the core (average droplet size, droplet size spectum, transverse liquid flow rate etc.) is very difficult to investigate and only very recently have some attempts been made to do this.

a. Measurement Methods. The devices for the investigation of the core, apart from the radiation sources, can be divided into two main categories: extraction and impact pressure devices. The major problems related to the use of these devices are, respectively, (a) fulfilment of the isokinetic conditions (where the sampled gas and liquid flowrate are in effect those corresponding to the unperturbed flow, and (b) establishment of a relationship between the impact pressure and the basic variables involved.

A question arises about the optimum size of an extraction probe: a small probe allows a more detailed investigation but the droplet size and/or the probe flooding set a lower limit.

The phase and velocity distribution in the core was investigated at CISE by means of extraction probes ($\sim$1.6 mm I.D.) used also as Pitot tubes (*34*, *36*).

Preliminary runs confirmed the expected different behavior of the two phases: in front of the probe, while the gas stream is very sensitive to the value of the back pressure given by the probe itself, the liquid droplets tend in any case to keep their own direction.

The CISE method has two bases:

(a) the criterion to determine the isokinetic condition: this condition is established when the pressure at the probe inlet is equal to the static pressure in the conduit. The sampled flowrates are related to the basic

variables by the simple relationship:

$$\Gamma_{g_s} = \alpha\sigma\rho_g U_g; \qquad \Gamma_{l_s} = (1 - \alpha)\sigma\rho_l U_l \tag{43}$$

where σ is the sampling area.

(b) the impact pressure relationship. This was derived through a momentum balance in correspondence with the probe inlet taking into account the different behavior of the two phases:

$$\Delta p_p = \tfrac{1}{2}\alpha^2\rho_g U_g + \frac{1 + \alpha}{2}(1 - \alpha)\rho_l U_l^2 \tag{44}$$

Since the value of α is usually not too far from unity, this relationship shows that while the gas momentum is half lost, as in single phase flow, the liquid momentum is almost entirely contributed to the probe. Due to the many simplifying assumptions made, this relationship is affected by an inherent unknown degree of inaccuracy.

In this way, having three independent equations to determine three unknowns, the problem of determining the phase and velocity distribution is in principle solved.

Several authors (*16*, *19*, *24*, *26*, *57*) carried out sampling probe experiments without controlling the isokinetic conditions just to investigate the entrainment distribution or to measure the total entrainment. Krasiakova (*4*) operated under isokinetic conditions, but measured only the liquid flow rate. In some cases the impact pressure was also taken (*4*, *16*, *58*); having two independent measurements, the velocity and phase distribution may be determined, if the value of the local slip ratio, or of an equivalent quantity, is assumed to be known.

The entrainment distribution has been investigated with different sampling devices. An example is a movable knife parallel to the flow direction and placed at the end of the test section. A differentiating process is required in this case to determine the local values of the flowrate (*23*, *59*).

b. Results and Correlations. The experimental data obtained at CISE (*34*, *36*) may be represented by the typical examples of Fig. 15a and b, where the measured quantities and those derived through the above mentioned equations are reported. The corresponding mean film thickness is also indicated.

The local values of the slip ratio are slightly greater than unity throughout the core, so that the much higher values of the over-all slip ratio previously indicated (Section II,B,2b) should be attributed to the higher concentration of liquid into the low velocity regions, close to the film surface and the film region itself.

The local entrainment and therefore the liquid volume fraction (*36*), is always minimum in coincidence with the conduit axis (or near the axis

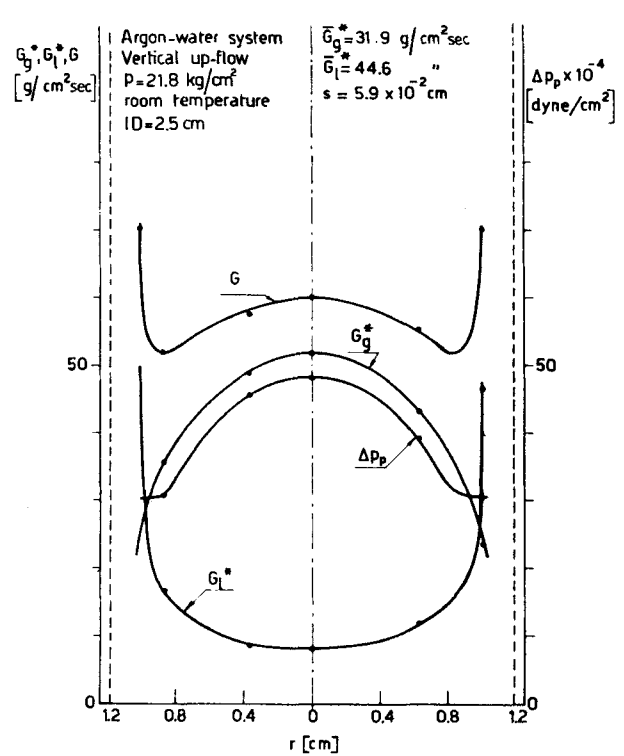

15a

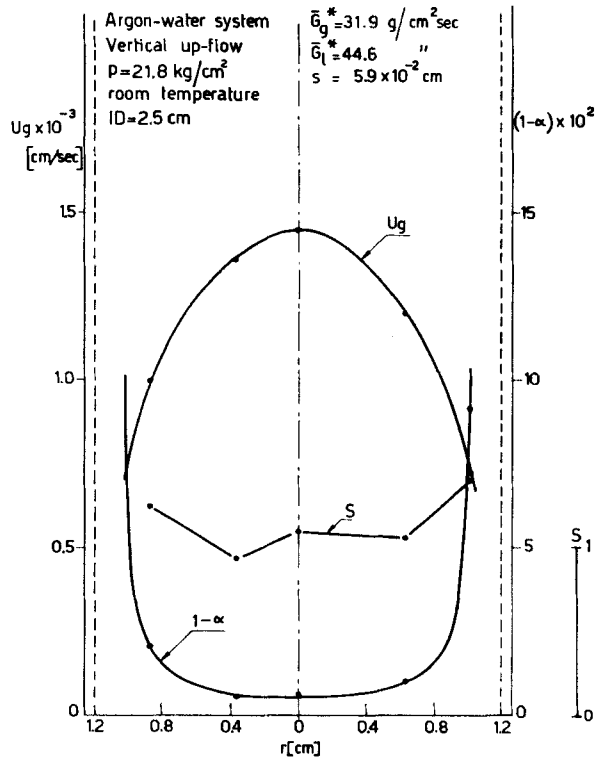

15b

FIG. 15. A typical distribution of quantities as resulting from extraction probe experiments (CISE's data). (a), measured quantities (G^*_l, G^*_g, G, Δp_p); (b), calculated quantities (U_g, $1 - \alpha$, S).

when the volume fraction distribution is not symmetrical). The liquid volume fraction can be as low as less than 1% in the center but reaches much higher values in proximity to the film surface; the measurements near the wall, however, might be affected by the film wave interface.

The gas velocity profiles are always less flattened than single phase flow, the gas Reynolds number being equal: the ratio between the linear velocity in the center and the mean linear velocity, which accounts for the actual area occupied by the gaseous phase, is in the range between 1.30 and 1.38 instead of between 1.15 and 1.18.

The distribution of the local values of the gas and liquid flowrate was also investigated at Ansaldo Co. (Italy) (*60*) by means of an isokinetic probe. The experimental conditions were: round vertical conduit 42 mm I.D., steam-water mixtures at 50 kg/cm^2 in upward dispersed flow. The entrainment distribution was found to have the same trend revealed by the experiments performed at CISE and to be substantially unperturbed passing from a distance of 25 to 50 diameters from the mixer.

An entrainment distribution with a minimum in the center of the conduit was also found by Wallis and Griffith (*59*), who simulated the flow of an evaporating mixture with an air-water low pressure downflow system by injecting air through the porous wall of the test section.

On the other hand, an entrainment distribution variable along the flow direction was found during experiments carried out at Harwell in a very long vertical conduit (19 feet length, 1¼ inch I.D.) (*58*). The entrainment profile in proximity to the mixer (porous wall injection of water) is similar to those just described, while near the end of the conduit the trend is nearly reversed. This result, however, was obtained in a low pressure system, with a substantial variation of the gas density along the conduit.

An entrainment distribution nearly constant throughout the core was found by Anderson and Mantzouranis (*16*): the high values near the wall were attributed to a probe interference with the wavy film surface. The over-all entrainment was found to increase along the flow direction, but in this case the relative variation of the density along the conduit was also remarkable. The entrainment increases with increasing gas and/or liquid flowrate, but the influence of the gas flowrate is greater. The experiments were carried out with a nonisokinetic probe; the authors, however, assuming a gas velocity profile equal to that which would exist in single phase flow and on the basis of an impact pressure relationship similar to that used at CISE, attempted to investigate the phase distribution.

Wicks and Dukler (*26*) carried out entrainment measurements by means of a 0.27 inch I.D. probe placed in the center of horizontal conduits (1 and 3 inch I.D.). They found a remarkable influence on entrainment of

the entrance section; the entrance type that gives higher entrainments also gives lower pressure drops, at least at low liquid rates. The over-all entrainment was evaluated on the basis of the central measurement assuming a uniform distribution throughout the conduit cross-section: values from less than 5 to 100% of the total liquid flowrate were found. The authors developed an entrainment correlation assuming that the similarities in the mechanism for mass and momentum transfer which have been shown to exist in single-phase flow also apply in two-phase flow. The correlation gives, in the graphical form, the Martinelli parameter X against the entrainment parameter

$$R = \frac{\dfrac{1 - X_v}{X_v}(N_{We})_c \Gamma_E}{\left(\dfrac{\Delta p_f}{\Delta z}\right)_g} \tag{45}$$

where $(N_{We})_c$ is the critical Weber number, to which different values have to be assigned depending on the entrance conditions.

Majiros and Dukler (*19*), using a 0.427 inch I.D. probe in long horizontal conduits (20 feet length, 1 and 3 inches I.D.), carried out the entrainment measurements by investigating five different zones of the conduit cross section. From their experimental data one can see, along a horizontal diameter, an inversion of the entrainment profile going along the conduit from a station at ~170 diameters to the last station (~200 diameters). This effect is not detectable along the vertical diameter. They operated with different liquids to investigate the influence of liquid viscosity and surface tension. The liquid viscosity was varied between 1 and 17 cp: the effects of viscosity variation depend on flow rates and on the viscosity itself, the entrainment going through a maximum as the viscosity is increased. The experiments performed by varying the surface tension between 49 and 66 dyne/cm indicate that the entrainment increases with increasing surface tension. It may be noted that, although at CISE the surface tension influence on entrainment was not directly investigated, an opposite conclusion can be derived from the experimental data obtained on the influence of surface tension on film thickness and pressure drop (*36*). The correlation proposed by Wicks and Dukler was found not to handle the liquid viscosity effects correctly.

A theoretical investigation of the phase distribution was performed by Levy (*61*), who, visualizing a smooth variation of the phase and velocity distribution throughout the conduit cross section, extended the mixing length theory to two-phase flow. As a result, the density profile has a minimum in correspondence with the axis of the conduit.

C. DENSITY MEASUREMENT BY RADIATION

1. General Remarks

Absorption of penetrating electromagnetic radiation—γ- or X-rays—or of β-rays has been frequently used for measuring the density of liquid-gas mixtures flowing in a channel. In fact the attenuation of a radiation beam crossing the channel is essentially a function of the density of the fluid flowing inside, although some other factors—like the flow distribution and the chemical composition of the mixture—have to be taken into account.

γ-Rays, being more penetrating, can be successfully employed (*48*, *62*, *63*, *64*, *65*, *66*, *67*, *68*) to traverse relatively thick channels or channels made of "opaque" materials, such as, for instance, stainless steel. On the other hand, the high penetrating power lowers the sensitivity in the case of low density mixtures. β-Rays, due to their stronger attenuation, allow a higher sensitivity, but their use is limited by their relatively short range. To a certain extent range limitations can be avoided by reducing as much as possible the channel thickness in correspondence with the traversing β-ray beam (*69*, *70*, *71*, *72*, *73*).

The use of X-ray techniques is less handy, because it generally requires more elaborate radiation sources instead of simple radioisotope capsules. Application of X-ray absorption technique was reported for gas-fluidized-solid systems (*74*).

2. Sensitivity

It is well known that the absorption of a beam of monochromatic electromagnetic radiation obeys an exponential law, say:

$$I = I_o \exp(-\mu s) = I_o \exp(-\mu' m) \tag{46}$$

where I and I_o are the intensities respectively of the incident and of the emerging beam, μ is the absorption coefficient (cm^{-1}), s the thickness (cm) of the absorbing medium, $\mu' = \mu/\rho[cm^2/g]$ and $m = \rho s[g/cm^2]$.

A collimated beam of beta particles obeys the same exponential law over part of their range, due to the particular shape of the β-spectrum. The mass absorption coefficient depends on the maximum energy of the β-spectrum and on the electron density in the absorbing medium, i.e., on Z/A if the absorber is a pure element.

The sensitivity S of an attenuation method for density measurements may be defined (*75*) as

$$S = \frac{-dI/I}{dm/m} \tag{47}$$

that is, the relative variation of the counting rate referring to the relative variation of m.

In the case of exponential attenuation, taking into account equation (47), sensitivity may be written as

$$S = \mu' m \tag{48}$$

This means that for a given absorbing medium (fixed m) sensitivity is proportional to the mass absorption coefficient and is therefore higher for β-rays than for γ-rays.

Considering the absorption in the duct walls, the exponent of Eq. (46) may be specified as follows:

$$-(2\mu_w' m_w + \mu_f' m_f) \tag{49}$$

where μ_w and μ_f are the absorption coefficients in the walls and in the flowing medium respectively, while m_w and m_f are the corresponding thickness (which are assumed to be the same for both the walls), expressed in mass per unit area.

Varying the density of the flowing medium the second term of the exponent of Eq. (49) varies, while the first term is constant. It is therefore easy to see that sensitivity, as defined by Eq. (47), is independent of wall thickness.

3. Absorption Data Reduction

Traversing a channel with a well-collimated beam and assuming the two-phase mixture has a gas volume fraction α along the beam path, the absorption coefficient of the mixture can be written as

$$\mu = \alpha\mu_g + (1 - \alpha)\mu_l \tag{50}$$

In a channel, with a distance D between two parallel walls, filled subsequently with the gaseous component only and with the mixture of unknown density, attenuation is given respectively by the following equations:

$$\begin{aligned} I_g &= I_o \exp(-\mu_g D) \\ I &= I_o \exp\{-[\alpha\mu_g + (1 - \alpha)\mu_l]D\} \end{aligned} \tag{51}$$

with the same meaning of the subscripts. From these equations one can derive

$$\alpha = 1 + \frac{1}{D(\mu_l - \mu_g)} \ln \frac{I}{I_g} \tag{52}$$

from which the mean density along the beam direction can be calculated

through measurements of I and I_ϱ. Measuring the corresponding counting rates through a detector, background counting has to be considered.

The value of ρ obtained in this way is an average along the beam path, and generally it varies traversing the channel in different positions, since the flow is not uniform. Values of $\bar{\rho}$ averaged on the whole cross section can be obtained through a simple integration.

This treatment is exact only in the case of channel walls perpendicular to the traversing beam. With round tubes the situation is slightly more complicated since the nonnegligible width of the beam affects the intensity of the emerging beam. Calculations show (*76*) that the mean chordal length of the traversing beam can often be satisfactorily substituted for the above mentioned distance D, except for vanishing values of the former.

4. Calibration and Detectors Used

Some attenuation methods must rely entirely on the calibration of the particular device used, since the simple exponential absorption low does not hold. This is mainly a consequence of the following factors: energetic composition of the radiation, geometry, and diffusion. Let us consider each of these factors separately.

a. Energetic composition of the radiation. In the case of electromagnetic radiation an absorption coefficient μ can be defined, strictly speaking, only if the radiation is monochromatic. Otherwise, calibration is the only mean to obtain absorption curves. However, if the emitted energies are sufficiently close, a mean value of μ can be calculated and used.

Another method to overcome the difficulties connected with a complex energetic structure consists in selecting the pulse amplitudes through the use of a proportional detector.

Similar considerations can be made for composed β-spectra, each spectrum behaving—as for absorption—like a monochromatic γ or X line. In the case of β-rays, however, parasitic absorption in the channel walls often helps in cutting off the low energy spectra.

b. Geometry. The exponential absorption law is valid only when the collimation holes are small with respect to the distance of the radiation source from the detector. If the flow distribution of the two-phase mixture is not uniform inside the channel, a further requirement for the exponential law to be obeyed and for the average density to be measured is that the channel width (or diameter) has to be substantially smaller than the distance source-detector.

This fact is connected with the diffusion effect, mentioned here below.

c. Diffusion. Let us call σ the area of the collimation hole near the detector and r the distance of the latter from a point source. The detector,

in addition to the direct radiation comprised in the solid angle $\sigma/4\pi r^2$, receives a portion of scattered radiation coming from the absorption medium outside that solid angle. Diffusion accounts also for the fact that smaller attenuations are measured with the same absorber when placed farther from the collimation hole. When attenuation is measured in nonuniform two-phase mixtures, this effect has to be taken into account if required by geometrical conditions.

Calibration of attenuation devices often requires the use, as absorbers of known density, of substances chemically different from the components of the two-phase mixture studied. In this case the results have to be normalized introducing a correction for the effect of electron density (*75*, *77*), if use is made of β-rays.

The detectors commonly applied in the attenuation measurements are: ionization chambers, GM counters, scintillation crystals and photomultipliers.

The counting rate is one of the determining factors for the choice of the detector: the GM counter is limited to about 1000 counts per second, the scintillation counter to about 10^5 counts per second, while the ionization chamber has practically no limitations.

5. Radioactive Sources

The main factors to be considered in the choice of a radioactive source for density measurements are the following: half-life, intensity, and radiation energy.

Half life has to be sufficiently long in order to avoid calculated corrections or recalibrations.

Intensity will be determined so as to have a radiation flux reaching the detector of sufficient energy, thus obtaining a satisfactory accuracy in a conveniently short time. Since, in practice, accuracy is determined by the signal given by the detector, the efficiency of the latter also plays a role in this matter.

In single pulse counting the probable error of a count is $\epsilon = 0.675\sqrt{nt}$. where n is the counting rate (sec^{-1}) and t the duration of the run (sec). Fixing ϵ and t, the source intensity $I_s(mC)$ can be easily determined in the case of exponential attenuation:

$$I_s = \frac{1.55 \times 10^{-7} \times r^2}{\nu\eta\sigma\epsilon^2 t} \exp(\epsilon\mu s), \tag{53}$$

where ν is the number of particles emitted per disintegration in the active substance, η is the detector efficiency, the terms of the sum $\epsilon\mu s$ refer to the various absorbers traversed by the beam, while the other symbols were defined above.

Radiation energy (of monochromatic γ- or X-rays or simple-spectrum betas) unequivocally determines the values of μ. As far as sensitivity is concerned it is clear from Eq. (48) that radiation energy should be selected as low as possible, in order to obtain the maximum μ'. This choice is not always the best with respect to accuracy, for which the detection system has to be considered (*75*). While for ionization chambers sensitivity and accuracy make opposing demands on the choice of μ' so that a compromise is needed, in the case of GM and scintillation counters a value of μ' as high as possible is the best choice. For beta

TABLE I
RADIOACTIVE SOURCES USED FOR DENSITY MEASUREMENT OF TWO-PHASE MIXTURES

Radioisotope[a]	Type of rad.	Energies (MeV)	Half-life	μ in water (cm^{-1})	Reference
Co^{60}	γ	1.17–1.33	5.25 *y*	0.064	*76*
Cs^{137}	γ	0.66	30 *y*	0.086	*78*
Sn^{113}	γ	0.39	118 *d*	0.088	*79*
Cr^{51}	γ	0.32	27.8 *d*	0.117	*81*
Tm^{170}	γ	0.084	127 *d*	0.221	*48, 62, 63, 64, 65, 67*
Ir^{192}	γ	0.30–0.61 (several lines)	74.4 *d*	—	*66*
Se^{75}	γ	0.024–0.40 (several lines)	126 *d*	—	*68*
Ce^{144}–Pr^{144+}	β	3.12	285 *d*	5.6^{+}	*70, 72*
Sr^{90}–Y^{90+}	β	2.26	27 *y*	8.6^{+}	*69, 71, 79*

[a] + Daughter

however μ' cannot exceed about $7/m$ (where m is calculated including parasitic absorbers), because, as said above, the absorption curve is flattened by straggling at the end of the range (*75*).

Table I shows a list of the radioisotopes more commonly used in attenuation techniques for density measurements of gas-liquid mixtures (*75, 78*). It has to be pointed out that the flow patterns investigated by means of γ-rays in the cited literature do not always include the annular-dispersed flow. γ-Rays can be applied also in this regime provided the channel width or diameter is sufficiently large, so that in Eq. (48) the low value of μ' is compensated for by a larger value of m.

6. Experimental Procedures

As for the experimental procedures the attenuation methods can be divided into two main categories: "one-shot" methods and "traversing" methods (*62*).

In the "one-shot" methods the channel is crossed by a blade-shaped radiation beam, the width of which practically equals the internal diameter of the duct. The collimation hole before the detector is usually a window slightly wider than the test section channel, to facilitate alignment of the source, test section, and detector assembly.

Density measurements performed by this method (based on calibration with homogeneous media) can be in considerable error with respect to actual densities, due to preferential phase distributions inside the channel. Cook (*65*) conducted a series of tests on Lucite mock-ups, finding that the error increased as the channel spacing was increased and as the distance between the radioactive source and the channel was decreased. Errors of up to 93% were obtained, although this value represents an upper limit encountered in pure annular flow.

Better results can be obtained with flow patterns in which the phase distribution is practically uniform. In fully dispersed flow, with $\mu D \leq 0.7$ (D is diameter of the duct), Kosterin *et al.* (*80*) calculated the gas volume fraction through an analytical relationship, which avoided the need for calibration.

The "traversing" methods are generally more precise than "one-shot" methods when the effect of flow distribution is not negligible. As previously mentioned, they consist in crossing the channel by means of a thin radiation beam along different chords. The single measurements so obtained yield linear mean values of the density. From these values, plotted against the coordinate in the direction perpendicular to the beam, one can derive, through a simple integration, the mean cross-sectional values.

Usually the experimental procedure consists in moving the source and the detector, rigidly connected one to the other, in the direction normal to the beam, so that the latter explores the whole duct diameter (or width). There are however some variants. Styrikovic *et al.* (*80*) measured the void fractions of steam-water mixtures at pressures up to 95 kg/cm^2 in a duct 238 mm I.D., using the γ-ray technique illustrated in Fig. 16. As shown in this scheme, the source is uncollimated, and five different beams are collimated through holes placed before five different GM counters. The beams traverse the channel along a diameter and along two chords on each side, forming different angles with the diameter. This technique does not require the source to be moved. If the pulses coming from the GM-counters are all conveyed to the same counting system, this method can be also included in the "one-shot" category.

At CISE (*73*) a small movable β-source, introduced inside the channel for density measurements of argon-water mixtures at room temperature and high pressure, was used. The setup is illustrated in Fig. 17. This is one of the very few examples in which measurements in actual annular-dispersed flow were performed with radiation.

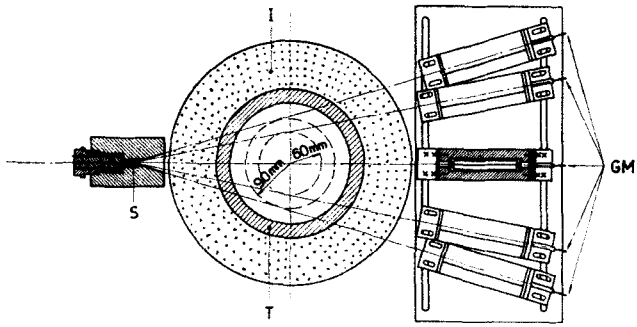

FIG. 16. Experimental arrangement used by Styrikovič *et al.* (cross section): S—uncollimated gamma source; I—thermal insulation; T—pressure tube 23.8 cm I.D., —shielded Geiger-Müller counters.

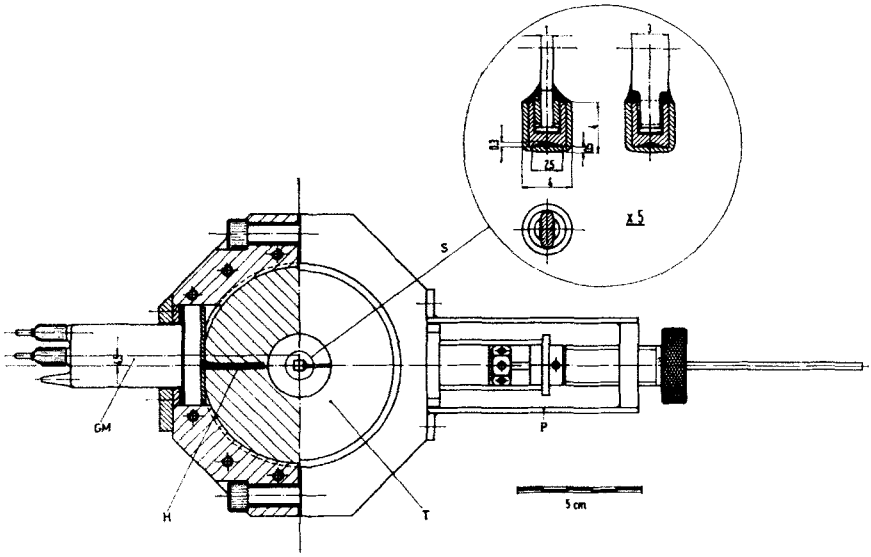

FIG. 17. Experimental arrangement used at CISE (cross section): S—movable beta source in a Lucite capsule (see detail enlarged 5 times a side, dimensions in millimeters); P—positioning device; T—Lucite duct 2.5 cm I.D.; H—collimation hole; GM—Geiger-Müller counter.

The position of the source was varied along the channel diameter and the corresponding attenuation measured. The device had to be calibrated. In spite of the fact that a slight flow disturbance could not be avoided, which probably resulted in the formation of a thin liquid film on the β-source itself, the results proved to be in satisfactory agreement with density data obtained through an extraction technique and reproduci-

bility was within the experimental errors (from 5 to 12% depending on the source position). A comparison between density measured with the β-source and obtained with other methods (*34*) is reported in Table II.

TABLE II

RESULTS FROM β-RAY ATTENUATION EXPERIMENTS IN ARGON-WATER MIXTURES FLOWING UPWARD IN A 2.5 CM I.D. DUCT AT A PRESSURE OF 22 KG/CM^2 AND ROOM TEMPERATURE[a,b]

		$\bar{\rho}_{lin}$					
$\bar{G}_g^+$	G_l^+	A	B	C	D	$\bar{\rho}$ gm/cm^3	$\frac{\bar{\rho}}{\bar{\rho}'}$
gm/cm^2 second		gm/cm^3					
24.4	25.7	0.307	0.167	0.118	0.087	0.141	0.78
24.4	44.6	0.453	0.212	0.153	0.115	0.187	0.82
24.4	77	0.587	0.317	0.206	0.159	0.256	0.80
24.4	134	0.593	0.347	0.215	0.166	0.292	0.73
31.9	25.7	0.282	0.145	0.105	0.083	0.130	0.84
31.9	44.6	0.367	0.191	0.131	0.100	0.162	0.84
31.9	77	0.505	0.265	0.174	0.137	0.222	0.86
54.1	25.7	0.200	0.109	0.083	0.070	0.097	1.00
54.1	44.6	0.247	0.139	0.096	0.080	0.118	0.94
54.2	77	0.253	0.150	0.110	0.089	0.133	0.87
54.4	134	0.417	0.247	0.164	0.132	0.203	0.77
72	25.7	0.139	0.089	0.068	0.064	0.078	1.04
72	44.6	0.164	0.098	0.078	0.069	0.090	0.90
72	77	0.183	0.126	0.090	0.080	0.109	0.94
72.5	134	0.332	0.210	0.154	0.126	0.180	0.93

[a] In the table $\bar{\rho}_{lin}$ is the linear mean density; $\bar{\rho}$ the cross-sectional mean density and $\bar{\rho}'$, the same quantity obtained by isokinetic extraction and film thickness measurements [see (*34*)].

[b] Distance of the source from the axis in different positions (A) $r = 1.05$ cm; (B) $r = 0.70$ cm; (C) $r = 0.34$ cm; (D) $r = 0$.

7. *Other Methods Involving Radioactive Sources*

Compton scattering instead of traversing beam attenuation can also be used for density measurements. Initial tests were performed by Bayly (*81*) aimed at the density measurement of steam-water mixtures through the detection of scattered γ-radiation at an angle of 90°. A source of Cr^{51} was employed and collimated with an opening of 1 × 6 cm both on the side of the source and of the detector (a crystal), for density measurements of fog simulating media in the range 0.03 to 0.3 gm/cm^3. A differ-

ence of 11.7% in exit signal was found at 0.03 gm/cm^3 with respect to an empty duct. The above-mentioned author is developing the method aiming at an accuracy of 0.001 in specific gravity.

III. Heat Transfer

A. GENERAL CONSIDERATIONS

1. Critical Heat Flux

The transfer of heat by an evaporative process is as a rule characterized by the rapid increase of wall temperature when the heat flux exceeds a certain critical value. This is also true in the case of annular dispersed flow. A well-established definition of the critical heat flux does not, however, exist. In the case of boiling water the heat transfer crisis results in a discontinuity of the wall liquid temperature difference as a function of the heat flux, as established by Nukiyama. Thus, at an earlier time, it was not considered very important to discuss the way in which "burnout" was detected or defined.

On the other hand, data on the heat transfer crisis in the case of dispersed flow was for a long time a by-product of boiling studies (which correspond mainly to bubble flow) in the range of higher qualities. It was assumed that no fundamental differences did exist between the two phenomena.

Later on, however, several authors indicated that in a given range of mass velocities and qualities the heat transfer crisis was characterized by a gradual, even if steep, increase in the wall-liquid temperature difference by increasing heat flux. This is illustrated by Figs. 18 and 19. Figure 18 reported from Silvestri (*82*) shows the evolution of the wall liquid temperature difference with heat flux at the outlet of an heated tube.

Figure 19 shows a temperature profile along a heated tube in the last section of which (section B-C) the crisis has been reached, reported from Schrock *et al.* (*83*).

Another well-established fact is that the wall-liquid temperature difference, which is quite constant with time below the critical heat flux, shows random oscillations in coincidence with the incipient crisis. These oscillations first increase in amplitude, as the heat flux increases, and then gradually die out, when the heat flux becomes much higher than critical. The magnitude and location of these oscillations are also reported in Fig. 18 for that particular case.

Afterward it was recognized that in the case of dispersed flow no sharp transition existed between the slow crisis just described and the fast crisis (eventually resulting in burnout) observed at lower quality. In fact, it would seem that when going to lower qualities the rise in average

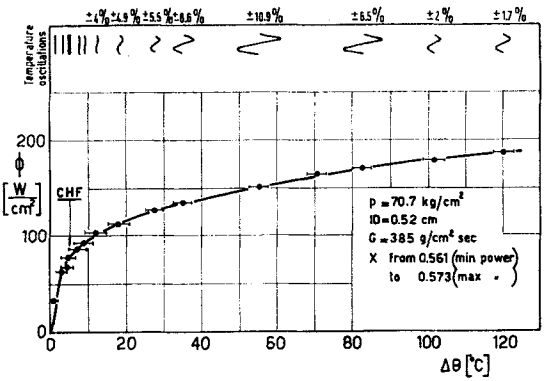

FIG. 18. Temperature difference vs. heat flux below and beyond CHF in annular-dispersed flow (CISE's results).

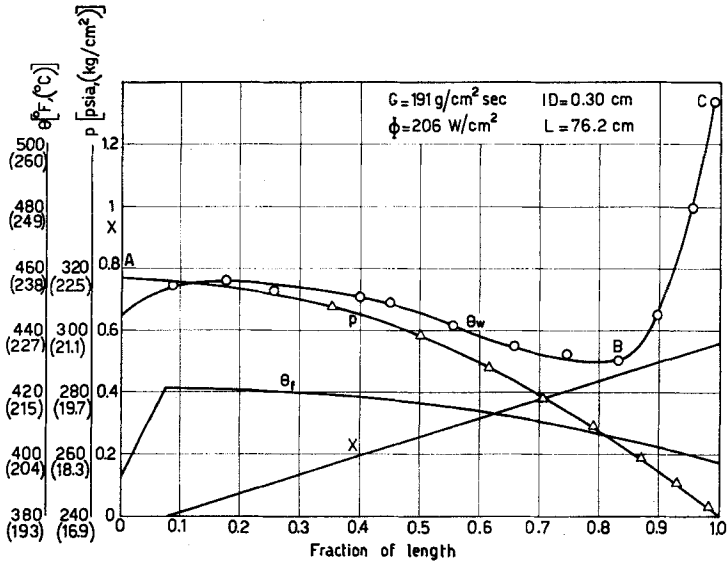

FIG. 19. Profiles of wall and fluid temperature, pressure and quality along the heated length of a vertical duct with steam-water system in upflow.

temperature, after the crisis corresponding to a given increase in heat flux, becomes sharper, and at the same time the amplitude of the oscillations around the average becomes much higher, so that the wall temperature may reach a very high peak value. The mechanism of the crisis in the case of dispersed flow might, however, be very different from the classical burnout observed with boiling water.

These considerations point out why most of the work in heat transfer with dispersed flow has been concentrated in the investigation of the crisis.

Experiments have been made on cylindrical ducts with round, rectangular or annular cross sections. For practical reasons the investigation concerned mainly steam-water mixtures. Upward flow has been more investigated than downward flow or horizontal flow. Electrical heating is most commonly used. Condensing steam is also used as an approximately constant temperature boundary condition.

2. Qualitative Description of the Crisis and Definitions

A number of definitions have been proposed for the critical heat flux. These refer either to a particular character of the phenomenon or to a particular method of detection.

Since the crisis observed in the case of dispersed flow has generally a progressive character, it is felt necessary to give here an accurate description of the successive steps of the crisis. We shall then review the various definitions which have been proposed.

There is hardly evidence that the crisis can occur with dispersed flow anywhere but in the immediate vicinity of the outlet of the heated section, at least in the case of a uniform heat flux distribution along the heated length (see also Section III). Moreover various authors (*83*) (*84*) have found that, by increasing the heat flux progressively, the crisis first appears at the outlet and then propagates upstream.

In this way along the corresponding zone of the heated section it was possible to observe at a given heat flux the successive stages or aspects of the crisis.

It is equally possible to study the successive stages at a given point by progressively increasing the heat flux and recording the output of a thermocouple.

When this is done in a typical case (G = 150 gm/cm² sec; D = 0.5 cm; L = 80 cm; X_i = 0.20) it is possible to draw the curve of ϕ versus $\Delta\theta$ (Fig. 20). It can be seen that after a parabolic segment O–b point b is reached where $\Delta\theta$ suddenly decreases (segment b–c). This decrease has been found systematically at CISE and it seems that also Perroud (*84*) found the same. It has been recently ascertained that whereas the discontinuity b–c was always encountered, point b could shift to b' along the curve O–b to any position corresponding to values of ϕ within a narrow margin. In some cases this decrease could even happen in two or three steps the ultimate value of the discontinuity b–c or b'–c' remaining practically unchanged. From c (or c') onwards $\Delta\theta$ again regularly increases with ϕ until soon enough a point d is reached where $\Delta\theta$ begins to be unstable, showing random fluctuations around the average value. Simultaneously from d downwards $\Delta\theta$ increases with ϕ but at a much faster

rate than along a–b of c–d and h is progressively reduced until its value comes to be of the order of magnitude which corresponds to convective heat transfer for the steam flowing alone.

Further, it must be mentioned that when point c has been reached, if ϕ is decreased, instead of increased, $\Delta\theta$ does not jump back to curve a–b but follows a curve c–O. It would seem, therefore, that in the whole range of ϕ up to very near the crisis there exist two modes of heat transfer: mode O–b would be stable, when ϕ starts from zero, until near enough to the critical heat flux; there would be an abrupt change to mode c, which in its turn is stable down to O; moreover, any intermediate situation

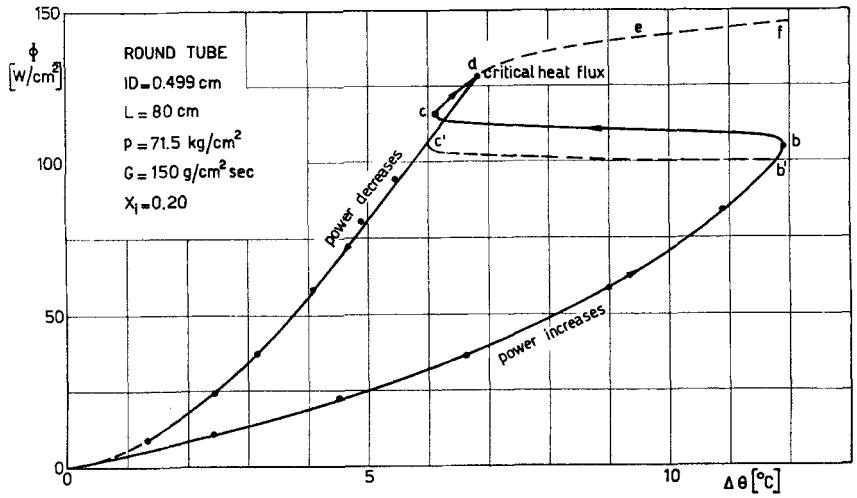

FIG. 20. "Hysterisis" effect in the heat transfer coefficient below CHF.

between the two curves O–b abd O–c, below the critical heat flux, seems to be possible in principle.

This summary description of the succession of events in a typical case shows that confusion may arise in characterizing the crisis by the critical heat flux.

In the case of boiling (bubble flow) it is known that the curve implies the existence of a "burnout" heat flux: this heat flux would adequately characterize the crisis in the case of boiling, but it does not apply to dispersed flow. It is, at any rate, generally impossible to reach this heat flux without destroying the test element (at least in experiments conducted with electrical heating).

For this reason the so-called DNB (departure from nucleate boiling) has been proposed. This point is inferred by a change of trend in the curve ϕ versus $\Delta\theta$ (*85*).

In our case this definition could be taken into account only if applied to curve *a–c–d*. But since it is by no means certain that boiling occurs with dispersed flow the expression "DNB" may not be adequate. Moreover, this definition is not easy to translate into a method of detection.

Another definition, proposed by Griffith (*87*), takes into account the heat flux corresponding to the point where the heat transfer coefficient ($\phi/\Delta\theta$) reaches its maximum value. This definition is adequate in our case but here, too, it is not easy to conceive a convenient method of detection.

In many cases the definitions proposed for the critical heat flux were purely operational. They were mainly based on the detection of a local sharp rise of temperature. In many cases the detection was done by comparing the electrical resistance of the region of the heated section where the crisis occurs to the resistance of another region where it does not.

Other rough detection methods were based on the determination of the flux for which the temperature of the heated wall reached a prefixed value (much higher than the temperature of the coolant bulk); under this category can be mentioned the red-hot spot method used by the Russians (*86*) in many early experiments.

All these methods may be used in the case of dispersed flow but they give values of the heat flux which lie above the value corresponding to the incipient crisis. This may be acceptable in the cases where the slope of *d–e–f* (Fig. 20) is very small (low qualities, low mass velocities), but it becomes very inadequate in the high and medium quality range, above all for high mass velocites where the slope of *d–e–f* is relatively high. In these cases the flow which may be detected does not have any connection with the critical heat flux.

Methods of this kind consist generally in using the sensing element to trip the power supply and may be kept in any case as a safety device.

The most straightforward method is still to use a fast response thermocouple in good thermal contact with the heated wall in the region where burnout is expected to occur. Of course, this method, valuable in annular-dispersed flow, is inadequate in bubble flow or in subcooled boiling.

The output of this thermocouple can be recorded. In the case where the heat flux increment is proportional to time, the recording would give an image of the curve ϕ versus $\Delta\theta$ directly. But this is not generally the case and even if it were, the direct interpretation of such a recording in terms of ϕ versus $\Delta\theta$ is not very easy. However, in the case of dispersed flow, whatever the rate of increase of ϕ, the stage of the crisis, corresponding to point *d* is always easy to distinguish directly: that is the onset of random fluctuations of the wall temperature. Here it should be noted

that the study of these oscillations might be very difficult, since it would have to take into account the attenuation effect of the thermal capacity of the wall, and of the thermocouple itself, and the time delay introduced in the transmission of these fluctuations to the thermocouple; but here we have none of these difficulties since we only need to tell if they are there or not.

This stage of the crisis is always present, reproducible, and is easy to detect. Thus it is proposed to define the critical heat flux as the flux corresponding to the onset of fluctuations of the wall temperature. For sake of simplicity the term CHF (critical heat flux) will be used throughout.

This definition is adequate in the whole range of qualities and mass velocities where the amplitude of the oscillations remain compatible with the safety of the test section. For very low qualities, however, as mentioned before, one has to rely essentially on a device of the type previously described (prefixed temperature detector). It is impossible at the present stage to say if and where in this range the crisis of the type we have described goes to the type of crisis which is found with boiling water, characterized by a discontinuous increase of $\Delta\theta$ versus ϕ, so-called burnout, corresponding to the onset of film boiling.

B. CRITICAL HEAT FLUX CORRELATIONS

1. Variables on Which the Critical Heat Flux Depends

A systematic search for a correlation of CHF in annular-dispersed flow must take into account all the independent quantities involved. Such a search was not made for horizontal or inclined tubes, but only for vertical upward motion. The water-steam system was, of course, the most studied.

The critical heat flux with subcooled water in upward motion is a function of the following variables (*87*):

$$G, D, \frac{L}{D}, \rho_l, \rho_g, \mu_l, \mu_g, K_l, \gamma, \lambda, \theta_s - \theta_i, \beta.$$

When the fluid at the inlet is in the quality region, the term $\theta_s - \theta_i$, disappears and the quality X takes its place. Moreover, if the water-steam mixture is supposed to be in thermodynamic equilibrium, the terms, μ_l, μ_g, ρ_l, ρ_g, K_l, γ, λ are functions of the pressure (or saturation temperature) only. If, in addition, the tube wall is always wetted, we have:

$$\phi_{cr} = f\left(\frac{L}{D}, G, D, p, X\right) \tag{54}$$

where X is intended at the point where the critical heat flux is reached. When this form is adopted, it is difficult and quite unnatural to introduce the inlet quality X_i as an independent variable. Of course X_i is bound to X, by an energy balance equation:

$$X = X_i + \frac{4\int_0^L \phi(z)\,dz}{DC\lambda}$$
$$X = X_i + 4\frac{L}{D}\frac{\phi_{cr}}{G} \text{ (for uniform heat flux)} \tag{55}$$

Introducing this expression for X, an implicit function of ϕ_{cr} is usually obtained. If, however, we take into consideration instead of ϕ_{cr} the total power input $W_{cr} = \pi D \int_0^L \phi(z)\,dz$, to the heated tube for which the critical heat occurs at one point, there are no reasons to prefer X to X_i. In this case we can write:

$$W_{cr} = f\left(\frac{L}{D}, G, X_i, p, D\right) \tag{56}$$

To prefer one presentation to the other is a matter of personal preference. It must be kept in mind, however, that for any correlation the simpler the better.

The following points must also be taken into account before discussing the proposed correlations for CHF:

(a) The phenomena responsible for the crisis in subcooled boiling and in annular-dispersed flow (a special case of quality crisis) may be substantially different. For this reason, at Westinghouse, the notions of q-burnout and H-burnout are being introduced (*88*): the first representing the crisis for excessive local heat flux, the second for "deficiency of water" (high mixture enthalpy). In consequence, it is very unlikely that the same relationship should hold for these two different flow patterns. Correlations valid from the whole quality range, from negative quality (subcooled water) to unity, proved to be quite unsuccessful.

(b) The use of different definitions and different detection systems brought to experimental data which are not strictly comparable. This is mostly valid at high quality, where detection of the crisis is very difficult.

(c) The distribution of phases at the inlet of heated elements is greatly influenced by the characteristics of the mixture generating plant. In particular, the geometry of inlet mixers or of feed circuits (for the case of separate generation of steam and water) has a fundamental influence on results.

(d) The experimental procedure may put in evidence or obscure some functional relationships: for instance, operating at constant total mass

velocity (and changing quality) or at constant mass velocity of one of the two phases (and changing the other).

All these facts together have, as a consequence, a disagreement of unknown extent between results obtained in different laboratories.

2. Older Correlations

From a chronological point of view, the first group of correlations had developed since 1943, on the basis mainly of results in subcooled boiling. The subcooling $\Delta\theta_{sub}$, difference between the inlet temperature and the saturation temperature at the operating pressure, was the fundamental parameter. These correlations are not of direct interest here, even if they were extended to the quality region, see, for instance, (*89*). In what follows we will discuss correlations developed later and more related to annular-dispersed flow. For a wider bibliography see (*90*) and (*91*).

Reynolds (*92*) was one of the first to study the field of $X_o > 0$, using data collected at MIT. Two physical quantities are considered important by him: the liquid film thickness (calculated as if all the liquid would be concentrated on the wall boundaries) and the average mixture velocity (supposing $\bar{S} = 1$). The phenomenon is considered a purely local one. The correlation is of the following form:

$$\phi_{cr} = G^{-0.5} D^{-1.5} f(X, p) \tag{57}$$

The range of the variables is the following:

$L/D = 50$ and 76 $\quad D = 4.6$ cm
$G = 90 \div 490$ gm/cm² sec
$p = 35 \div 141$ kg/cm²
$X_o = 0.01 \div 0.60$
$\phi_{cr} = 190 \div 880$ W/cm²

The CHF is a decreasing function of pressure.

For the first time an inverse relationship between ϕ_{cr} and G is presented. This is just the contrary of what happens in subcooled boiling.

In 1958 Westinghouse presented (*85*) the analysis of hundreds of burnout data collected in different USA laboratories. The "prediction" equation is the following:

$$\phi_{cr} = a H_{cr}^{-2.5} \left(1 + \frac{G}{G_o}\right)^2 \exp\left(-0.0012 \frac{L}{D}\right) \tag{58}$$

The range of variables is:

$G = 3 \div 650$ gm/cm² sec
$\phi = 40 \div 720$ W/cm²
X_{cr} = from subcooled to unity
geometry = circular or rectangular ducts
pressure up to $p = 140$ kg/cm²

The constants a, G_o depend on geometry; for a plane geometry D is replaced by the width of the channel. Equation (58) put in evidence an L/D effect, while ϕ_{cr} is an increasing function of G. Moreover for $X \to 1$, ϕ_{cr} does not go to zero. The dispersion of data correlated by this formula is $\pm 35\%$, so that for design purposes a "design equation" is suggested in which the ϕ_{cr} value is multiplied by 0.65.

The same data collected by Westinghouse were worked on by many authors:

(a) Longo (*93*) presented a correlation identical with (*58*), but with different values for a and G_o.

(b) Isbin *et al.* (*94*) started from a model of "quality burnout," in which the crisis is attributed to the disappearance of the liquid film, for lack of transverse flow of water. The correlation is quite complex and requires the determination of six constants. This model introduces an inverse dependence of ϕ_{cr} on G.

(c) Bell (*95*) proposed an empirical correlation (for $p = 140$ kg/cm^2):

$$\phi_{cr} = a(b + G)^c \left(\frac{H_{sat} - H_{cr}}{H_o}\right) dG^e \,. \tag{59}$$

where a, b, c, d, e, are empirical constants (and H_o is 1000 BTU/lb). Coefficients d and e are such that, for equal H_{cr}, the dependence of ϕ_{cr} is inverse of G. No L/D effect is present. The range or validity is the same as that of (*58*), except that X is always positive.

(d) CISE (*96*) correlated the same data (plus a few points at lower pressure) with an expression of the type:

$$\phi_{cr} = aD^{-0.25}G^{-n}y \tag{60}$$

where $y = 1 - X/X + a$ is a quantity proportional (for $\bar{S} = 1$) to the average liquid concentration in the duct. a and n ($n > 0$) are constant at constant pressure. Also, this correlation is based on a model in which it is assumed that the water cross flow from the main stream to the heated walls has a predominant role in determining the crisis.

(e) Jacobs and Merril (*97*) presented a statistical correlation with 24 empirical constants, which seems really too much. They verified that correlations based on independent system quantities (input quantities known a priori, for which an energy balance is not necessary) correlate experimental results better than correlations based on local values (like H_{cr}, X, etc.).

(f) Also Macbeth (*98*) prefers the use of independent quantities, but, to improve the correlation, he uses one variable more than needed (X and X_i) so that his correlation is incompatible with the heat balance equation. This correlation has eight empirical constants, which are functions of pressure and geometry.

The experimental basis of all of this group of correlations is reference (*85*). Only correlations presented under (b) and (d) try to start from an elementary physical description of the phenomenon. In addition, Goldman *et al.* (*99*) tried a physical interpretation of the crisis and they considered the diffusion of liquid droplets from the core to the heated wall through the vapor layer adjacent to the walls in critical conditions as a slow process. To correlate data, however, knowledge of the average axial slip and of the local slip (average value of slip in a cross section) is necessary.

3. More Recent Correlations

It was evident, at this point, that experimental data collected up to 1958 were not enough and that further data were needed to better understand the influence of the different parameters.

Perroud (*84*), using a number of experimental data collected at 50 and 60 kg/cm², confirms the inverse dependence of ϕ_{cr} on G and proposed for y (or alternatively for $1 - X/X$) a higher exponent than proposed for CISE ($\sim$2 in place of 1).

A wide experimental program was carried by CISE between 1960 and 1961 (*13*, *39*, *40*, *41*) on circular ducts and annuli mostly at 70 kg/cm². The correlation (60) proposed before was modified in the following way:

$$y = \frac{1}{K} G^n \phi_{cr}^m \qquad (61)$$

$$(n, m > 0)$$

where K and m are functions of pressure; in addition K a is function of the L/D ratio. The inverse dependence of ϕ_{cr} on G is still confirmed on most of the quality range. The L/D effect is quite important. The correlation, only valid for annular-dispersed flow, was deduced from experiments in the following range:

$p = 40 \div 85$ kg/cm²
$D = 0.3 \div 1$ cm
$L = 10 \div 80$ cm
$G = 100 \div 400$ gm/cm² sec
$X = 0 \div 0.8$

Quite recently, Westinghouse (*88*) proposed a new correlation, based mostly on experimental data presented in (*85*) and (*13*). As previously mentioned, the possible existence of two critical heat fluxes of different nature is discussed. The correlation valid for the quality region is:

$$H_{cr} - H_i = a_1(H_{sat} - H_i) + [a_2 + a_3 \exp(-a_4 D)] H_{gl} \exp(-a_5 G) + a_6 H_{gl} \exp\left(-a_7 \frac{L}{D}\right) + a_8 H_{gl} \frac{\rho_g}{\rho_l} + a_9 H_{gl} \qquad (62)$$

The range of validity is:

geometries:	circular tube–rectangular channel–annular channel–rod bundle
G:	$27 \div 550$ g/cm² sec
p:	$55 \div 190$ kg/cm²
L/D:	$21 \div 656$
inlet subcooling:	$0 \div 170$ kcal/kg
X_{cr}:	$0 \div 0.9$
ϕ:	$30 \div 550$ W/cm², with uniform and nonuniform axial distribution

Nine empirical constants are necessary in this case; 95% of data are correlated better than 25%. The dependence of ϕ_{cr} on G is direct at low quality and inverse at higher quality.

Mention must be made of a number of correlations used by Russian workers. In these correlations, the physical conditions of the system are introduced through dimensionless groups, introduced by Kutateladze and Styrikovič (*100*) to study the process of nucleate boiling.

One of the most recent correlations, presented by Ivaškevič (*101*, *102*), has the following form, when the mixture enters with a finite quality into the heated section:

$$f_1(p)\phi_{cr} = \frac{aG(V_1 + XV_{gl})f_2(p,D)[1 - X]}{1 + b\frac{\Phi}{\phi}\left(f_3(p)L + \frac{L}{D}\right)G(V_1 + XV_{gl})f_2(p,D)} \tag{63}$$

where a and b are constants and $f_1(p)$, $f_2(p,D)$, $f_3(p)$ are known functions of pressure and diameter. This correlation which is a particular form of a more general relationship, which holds, in the opinion of this author, in a very wide range from subcooled water to 0.9 quality, gives however for annular-dispersed flow a direct relationship between ϕ_{cr} and G. Formula (*63*) also takes into account uneven power distributions, through the term Φ/ϕ, where $\bar{\phi}$ is both axial and transversal average heat flux. The author claims correlating data from different sources better than $\pm 30\%$. The occurrence of the crisis is characterized both by its location (which does not always coincide with the outlet) and by the value of the critical heat flux.

Another correlation for upward flow developed by Miropl'skij and Šicman (*103*) makes a distinction between pulsating flow (when the heated section is preceded by a large free volume) and nonpulsating flow (when, through orifices or other means, the heated section is decoupled from the mixture generating system). The critical heat flux is different for these two cases only when:

$$K_W = \frac{G\mu_l}{\gamma\rho_l}\left(\frac{\rho_l}{\rho_g}\right)^{0.2} < 2.10^{-2} \tag{64}$$

The general formulation is the following, for the case $X > 0$:

(a) nonpulsating flow:

$$\frac{\phi_{cr}\mu_l}{\gamma\rho_l\lambda} = a_1\left(\frac{c_1\theta_s}{\lambda}\right)^{0,8} K_W{}^{0,4}(1 - X)^n \tag{65}$$

where a is a constant (different for different geometries) and n is an exponent, the values of which depend on that of K_W;

(b) pulsating flow (only for $K_W < 2.10^{-2}$): for higher K_W values formula (65) holds:

$$\frac{\phi_{cr}\mu_1}{\gamma\rho_l\lambda} = a_2\left(\frac{c_1\theta_s}{\lambda}\right)^{0.8} K_W(1 - X)(1 + 4X) \tag{66}$$

The validity of these correlations is the following:

geometries: round tubes–annuli–rectangular channels.

$D > 0.4$ cm

$D_e - D_i > 0.2$ cm

$D > 0.13$ cm

$L/D > 100$

$X < 0.9$ for $p = 20$ kg/cm^2; $X < 0.6$ for $p = 100$ kg/cm^2;

$X < 0.4$ for $p = 180$ kg/cm^2; $X < 0.25$ for $p < 200$ kg/cm^2.

The authors claim to correlate a number of results better than $\pm 30\%$.

C. PECULIARITIES OF CRITICAL HEAT FLUX

1. Critical Heat Flux with Constant Power Distribution

Once a particular definition of the CHF is accepted, it is better to study the influence of the different parameters of importance, and to rely on experiments in which the same criteria are used throughout. Thus, we shall refer mostly to experiments carried at CISE following the definition given at the end of Section III,A,2 (*13*, *39*, *40*, *41*).

In this paragraph only constant heat flux (along the channel length) will be considered. The phase distribution at the inlet of the heated section plays an important role in determining the value of the CHF. Thus we shall distinguish between CHF in fully developed flow (when the heated section is preceded by a very long unheated section—or mixing length—of hundreds of diameters), in which the flow pattern peculiar of the specific flowrate and quality can freely develop, and CHF in tubes, in which special injection systems are used.

Results will be presented in graphs where the CHF is plotted as a function of the inlet quality, for constant pressure, flow rate, heated length and diameter. A family of curves will be drawn having one of the above mentioned quantities as a parameter.

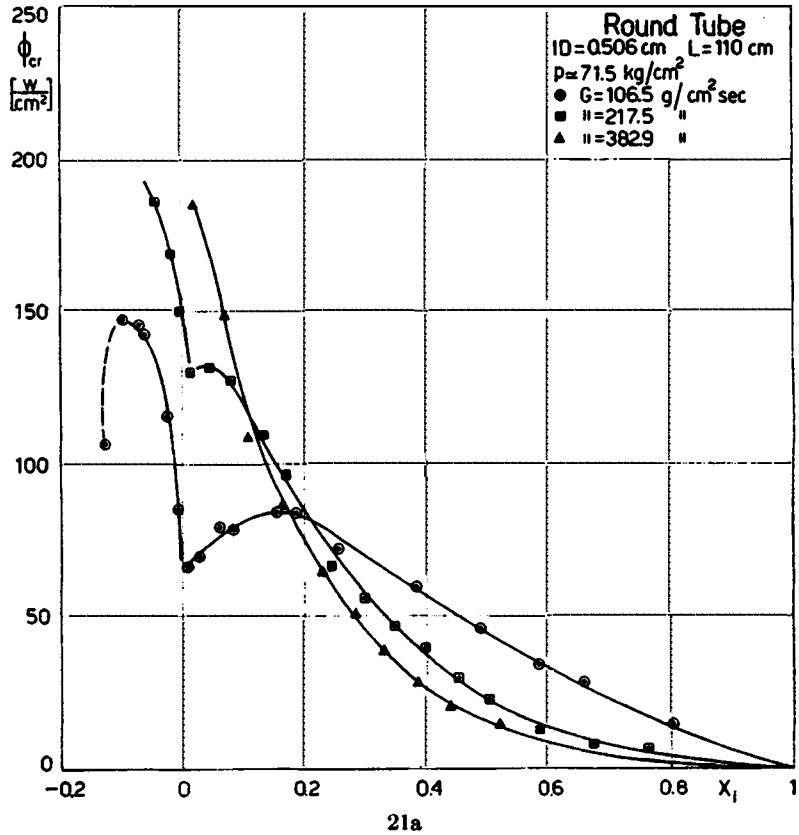

FIG. 21. CHF as a function of quality, with mass velocity as a parameter. (a): Inlet quality as abscissa.

Usually plots of the CHF have exit quality as abscissa. Some of these plots will also be presented here. As seen in Section III,B, it is equivalent to choose X_i or X_o from a logical point of view. From a practical point of view, however, we must make the following points;

(a) X_i is an input independent variable; X_o on the contrary must be deduced through a heat energy balance. This increases the overall errors.

(b) Comparison between plots with X_i or X_o as abscissa shows that X_i-plots can be much more easily interpreted than X_o-plots.

Results presented here refer to steam-water mixtures at pressures around 70 kg/cm², in upward flow. It is evident that, by increasing pressure, any peculiar feature smoothes down.[4] It is also true that in

[4] The behavior of supercritical mixtures is quite complicated, due to the rapid, if not sudden, variation of many properties across the so-called pseudocritical temperature (temperature at which heat capacity reaches a maximum). See, for instance. (104) and (105).

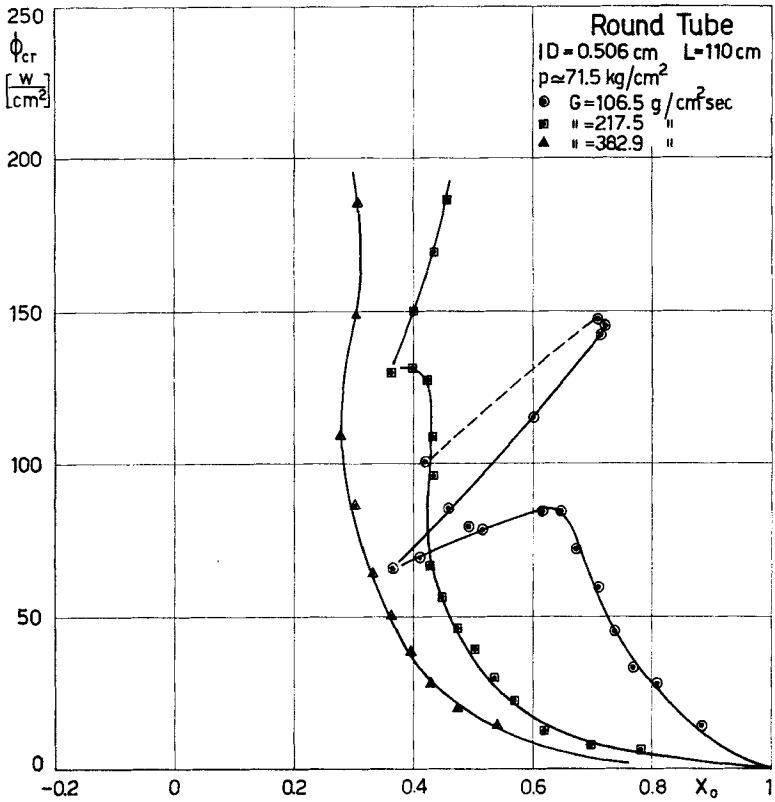

Fig. 21. (b): Outlet quality as abscissa.

horizontal or downward flow, results, although probably not qualitatively different, will differ from a quantitative point of view.

a. CHF in Fully Developed Flow. Results for fully developed flow will be presented first. In this case starting from saturated steam (at the inlet) the critical heat flux goes up with decreasing quality. For low mass velocities it reaches a maximum (when the flow pattern at the inlet is slug flow) and then goes down again. For high mass velocities no maxima occur, but there is a certain inflection in the curve. See Fig. 21a. From the comparison of plots reported in Fig. 21a and b it is seen how the interpretation of results is much more difficult when X_o is in abscissa. With X_i as an independent variable there is only a single value of ϕ_{cr}, while ϕ_{cr} is a multivalued function of X_o.

The main aspects are the followings:

(a) in annular-dispersed flow, ϕ_{cr} has an inverse relationship with G, while the contrary is true at lower qualities (that is for bubble or slug

flow). We will come to the controversial point of maxima later. This relationship:

$$\phi_{cr} \equiv G^{-n}(n > 0)$$

(where n is certainly a function of pressure) was not recognized at first in the Westinghouse correlation, but afterwards an examination of the same data by many authors showed that this was the case (see Section III,B). In addition, a number of Russian works (*106*, *107*, *108*) support this idea, as well as recent experiments carried at the G. E. Vallecitos Laboratories (*109*, *110*).

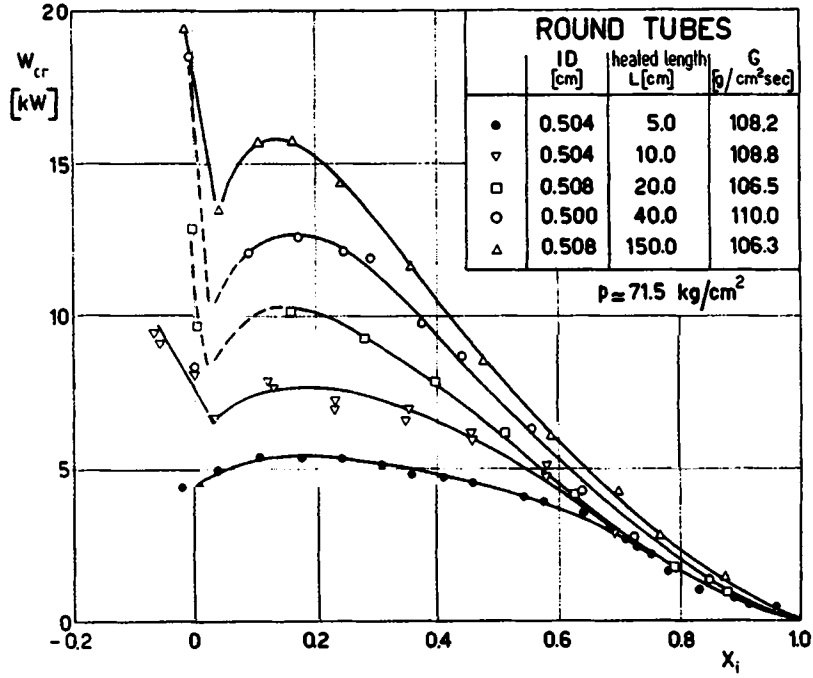

FIG. 22. Critical power at constant mass velocity as a function of inlet quality (L/D as a parameter).

(b) there is a strong L/D effect. In Fig. 22 a family of curves is reported for constant G (and p) and different L/D values. The total power $\pi DL\phi_{cr} = W_{cr}$ is reported on the ordinate. It can be seen that an enormous increase in length (at constant diameter) brings only a very moderated increase in W_{cr}. This means that ϕ_{cr} goes down tremendously with increasing length. Plotting W_{cr} in place of ϕ_{cr} seems a better way of taking into account the L/D effect, to which W_{cr} is much less sensitive than ϕ_{cr}. [416]

This phenomenon ("hystory effect") could possibly be explained by visualizing the water flowrate as divided in two components: the former flowing along the wall as a water film, the latter as droplets in the bulk. The first components could be evaporated in any tube length, giving something like a constant base load power, the second would be partially evaporated as soon as it becomes deposited on the duct wall.

(c) The pressure effect is not a strong one in this range.

b. CHF in Developing Flow. If the L/D effect is difficult to explain in physical terms, much more controversial is the question of maxima. At CISE (where experiments were always carried out with a very long mixing length) maxima were always found (for low mass velocities). Russian researchers found (*107*, *108*) that by throttling the flow injection valve to the heated element maxima disappear. In certain experiments they inserted in a dead end (in respect to the heated duct) a geometric volume which was filled at times with cold water or with nitrogen (or superheated steam). In this latter case, maxima occurred (accompanied by strong pressure oscillations) while, in the first case, maxima did not occur. The reason for this was attributed to the presence of an elastic (gas), or fairly rigid (water), medium hydrodynamically coupled with the heated duct.

To clarify this point three experiments were carried out at CISE, (see Fig. 23) at constant pressure, geometry and flowrate selecting a flowrate for which maxima occurred:

(a) In the first experiment subcooled water or a steam-water mixture was injected into the mixing length ($L/D = 600$), and then freely passed to the heated length. A maximum is clearly seen.

(b) In a second experiment, a very high localized pressure drop (a number of orifices in series) was put between the mixing length and the heated length (flashing occurred in a certain quality range). No maximum occurred.

(c) In a third run, a smaller pressure drop was located as before. The plot of ϕ_{cr} looks intermediate between that of (a) and (b).

Additional experiments were performed with orifices at the bottom of the mixing length and results were in agreement with those obtained without orificing.

Thus it seems reasonable, for the time being, to conclude that in experiment (a) any flow pattern could fully develop, while in experiment (b) the injection in the test section of a high kinetic energy input prevented formation of slug flow. This energy is more or less dissipated in artificial turbulence, which alters the flow pattern even in the low quality region. In condition (c) the behavior was in between. This is all the more true, without bringing into the picture the elastic character of one of the media (steam), since at high mass velocity the maxima disappear,

although the volume of the gas phase in the same quality range should be more or less the same. In addition, even without throttling, maxima disappear in conditions which are coincident, or at least very close, to those for which slug flow disappears (see Section I,B). When subcooled

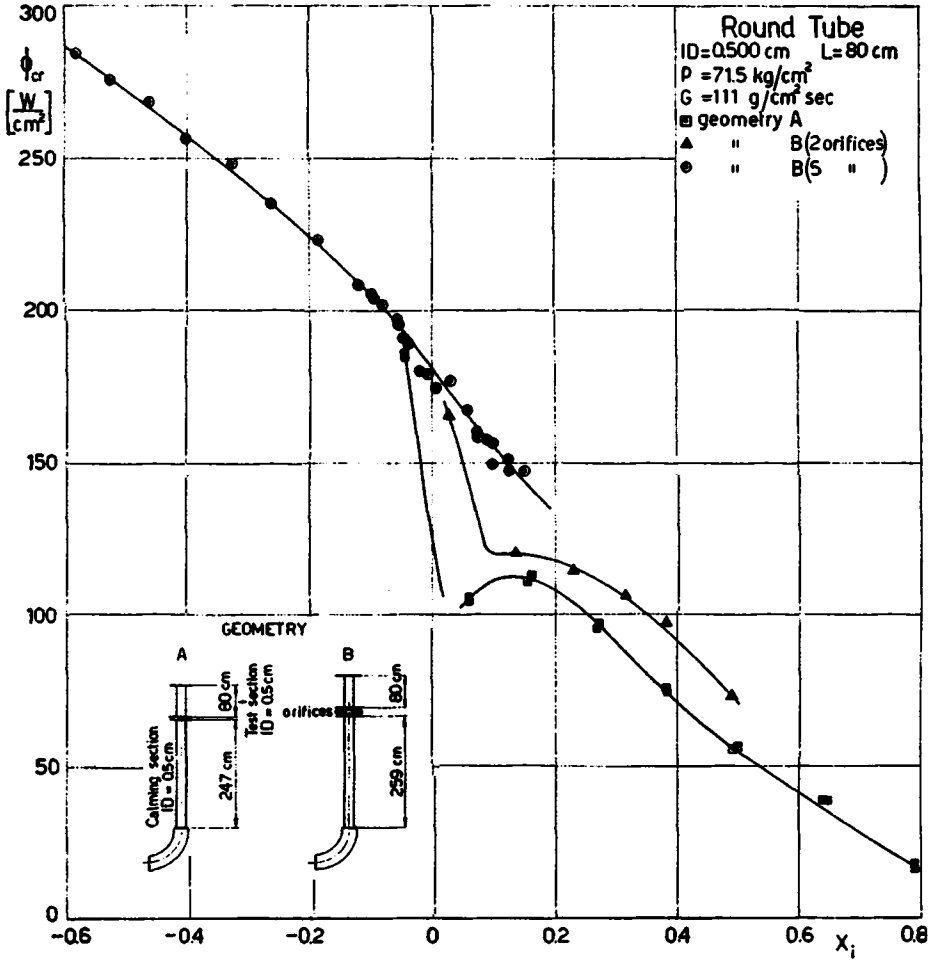

FIG. 23. The influence of inlet conditions on the CHF.

water is injected in a tube, one must take into account that the pressure drop increases (mainly due to the acceleration term), in comparison with adiabatic flow at the same average quality. Thus no flow pattern, including slug flow—which is possible only in a quite narrow quality range—can fully develop and the CHF curve would resemble the one with orifices more than the one in fully developed flow.

2. CHF with Uneven Power Distribution

No systematic study has been made up to now of this aspect of the phenomenon, although a correlation (63) takes into account a form factor for the heat flux distribution and another correlation (62) is also considered valid by the authors for uneven power distribution.

The limited number of experimental results is sufficient to show that a more careful insight would be of great importance for understanding the crisis. Were the crisis a local phenomenon, it would take place at the point where local quality reaches the critical value. But this is far from being the case.

Heat flux shapes frequently used are: hot patches in a uniform heat flux, intervals of constant heat flux and unheated lengths, linearly varying

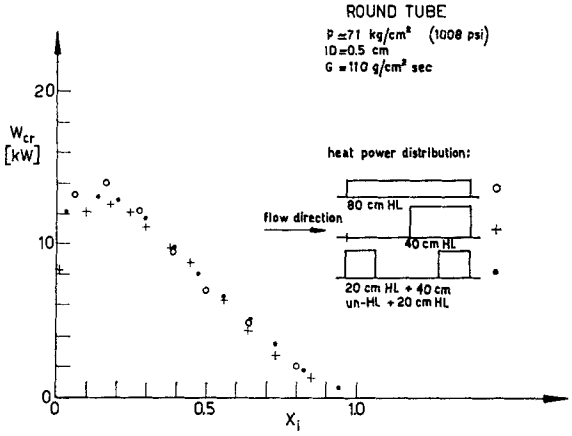

FIG. 24. Critical power for three different heat input distributions.

heat flux (or linearly varying tube thickness, which gives an hyperbolic variation for $s \ll D_i$), cosine-shaped heat flux.

The strong L/D effect on the critical heat flux (which is to be compared with the weak L/D effect on the total power) is evidence that the total heat flux is quite insensitive to the heat flux shape: in fact, a short tube can be considered a small portion of a longer tube with uneven power distribution.

Even more striking are results obtained at CISE (*111*), an example of which is reported in Fig. 24. Here the total critical power as a function of inlet quality is reported for three different cases: an electrically heated length of 80 cm at constant heat flux, the same geometrical length but with a central portion of 40 cm short-circuited (rectangular-shaped flux) and a heated length of 40 cm. Even though small differences may exist

between these three curves, there is no comparison with the very large differences, in the heat flux distribution. It is only close to the maximum (where the annular-dispersed flow pattern tends to disappear) that there is an appreciable differentiation between the three curves.

Similar results were obtained by other authors. At the General Electric Laboratories at San Jose (California, USA) experiments were carried out in an internally heated annulus (*112*), with a high pressure steam-water mixture with a power distribution of the form:

$$\phi = \phi_{max} \cos \frac{\pi y}{139}; \qquad -54 < y < 54$$

where y is the axial coordinate from the midpoint of the heated section, so that the ratio ϕ_{min}/ϕ_{max} was 0.34. Total critical power, at constant heated length, could not be distinguished from data taken with constant heat flux.

Experiments were carried out recently in USSR with linearly varying tube thickness (*113*) and far from the maximum (that is in a region of fully developed annular-dispersed flow). The CHF (the crisis always arising at the outlet of the heated section for $X_i > 0$) was about twice (for increasing heat flux) or one-half (for decreasing heat flux) of the CHF with constant distribution. Since $\phi_{max}/\phi_{min} = 4.9$ and $\phi_{max}/\bar{\phi} = 2.3$ for the tested element, this showed that total critical power was more or less insensitive to power distribution even reversing the tube itself.

The uneven distribution of heat flux in the radial direction was also tested in USSR (114). The (radial) $\phi_{max}/\bar{\phi}$ ratio was 1.8 and maximum CHF's were about 1.6–1.8 times higher than CHF's with uniform (radial) heating. The conclusion reached by the authors was that in these tests the heat flux $\bar{\phi}$, taken as an average over the entire circumference, had, at the moment when the crisis occurred, about the same value as in uniformly heated tubes.

These experiments thus support the idea that the maximum power which can be extracted from a vertical tube in critical conditions is sensitive to the integral of the power distribution and not to local values. Much work is necessary, however, to better clarify the situation, mainly in connection with the criteria for the design of a steam generating tube. The usual design criteria (hot spot factors, hot channel factors, point at which the crisis would occur and so on) would have to be deeply revised.

3. CHF in More Complicated Geometries

Critical flux in geometries more complicated than round tubes or rectangular channels were investigated in a less systematic way.

A certain amount of work was done on annuli, externally, internally

or bilaterally heated. Results of experiments at 70 kg/cm² carried out at CISE (*13*, *40*, *41*, *82*) showed that for annuli externally heated the same correlations holds as those valid for round tubes (for the same conditions and same G's), without changing the value of the numerical constants, provided that for D the "heated diameter" D_h would be introduced. D_h is defined as:

$$D_h = D_e\left(1 - \left[\frac{D_i}{D_e}\right]^2\right) \tag{67}$$

For internally heated annuli, the trend of ϕ_{cr} is more or less the same, but its absolute value is smaller than for externally heated annuli. It is to be noted, in connection with this, that measurements carried on in adiabatic flow, showed that the liquid film thickness of the internal wall of an annulus, is generally thinner than that on the external wall.

With bilateral heating, an interesting conclusion drawn from experiments is that the two heated surfaces have a negligible influence on each other. In Fig. 25 this fact is clearly illustrated. Here plots of ϕ_{cr} in the inner tube (for two G's) as function of inlet quality are reported for different heat fluxes in the outer tube. The data just superimpose (at constant G). This means however that the crisis (in a point of the heated surfaces) is reached for lower outlet qualities, when only one surface is heated, while, with both surfaces heated, the crisis is reached at higher outlet qualities. Thus any unheated surface acts as a "water sink," increasing the water "holdup" for a given critical power W_{cr}.

At Harwell (*58*, *115*) similar results were obtained: in Fig. 26 results obtained at CISE and at Harwell are compared for similar conditions. For other experiments carried out at San José Laboratory of General Electric see (*109*, *110*).

The results for rod bundles are more difficult to interpret because it is more difficult to define and to assure the phase distribution at the inlet. Results recently published by Green *et al.* (*116*) for upflow of water-steam mixtures in bundles of nine rods (0.413′ O.D. in a 0.468′ pitch) at 141 kg/cm² (2000 psia), show that the CHF has the same order of magnitude as that in parallel channels of similar length. Other experiments (*117*) carried at General Electric at low pressure (~2 kg/cm²) in four rod bundles hardly enter the dispersed region.

For the development of the Plutonium Recycle Test Reactor (PRTR) experiments were carried out at Hanford by General Electric (*118*) on an electrically heated mock-up of the fuel element assembly. The test section consisted of 19 rods, 0,564′ (1.43 cm) O.D., 7.3 feet (223 cm) long in a 3.25′ (8.26 cm) I.D. process tube. Power (up to 2000 kW) was applied at 70 kg/cm² and different exit qualities were reached, some of them cor-

responding to annular-dispersed conditions. However critical conditions were never reached, so as not to destroy such an expensive mock-up.

Multirod (7 and 19) cluster behavior in steam-water upflow, with power, is also being studied at Columbia University (*119*) in the range of

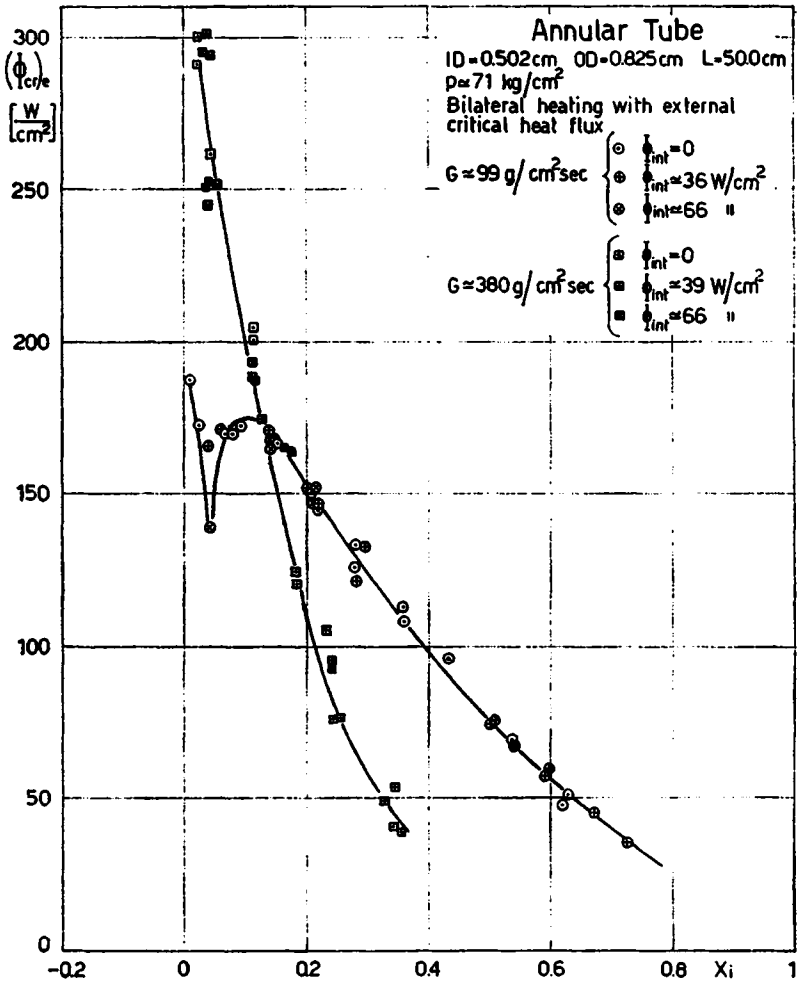

FIG. 25. CHF in an annulus as a function of inlet quality with mass velocity as a parameter (Bilateral heating with external critical heat flux).

70 kg/cm². Preliminary results show that in annular-dispersed flow the CHF is of the same order of magnitude as in cylindrical ducts; but too few experimental points are available to draw any quantitative conclusion. In Sweden still another experimental group is working on vertical clusters with steam-water upflow. Up to now published data (*120*) cover

the low pressure range (2.5 to 10 kg/cm^2). Experiments carried out with a three rod cluster show that in that range, critical steam quality decreases with increasing heat flux and decreasing pressure. Moreover they observed that critical steam qualities for rod clusters are much lower than those previously obtained for round ducts and described in previous reports.[5] This agrees in principle with results obtained in annuli: the process tube, usually not heated, acts as a water sink lowering the critical quality at constant heat flux, in comparison with the round tube case.

A general remark must be made about experiments on clusters: the fluid at the inlet is usually liquid water below the saturation temperature. Thus a portion of the heated channel is in single flow for a time and then

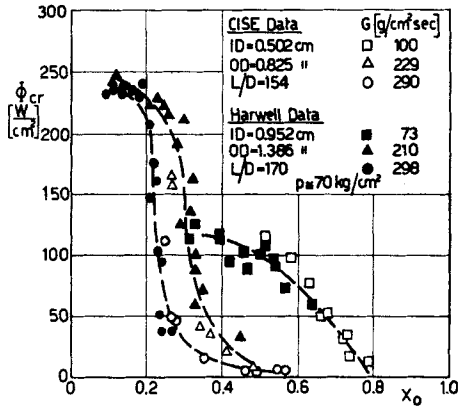

FIG. 26. Comparison of CHF data obtained at Harwell and at CISE for internally heated annuli.

in a multitude of two phase flow patterns before entering the annular-dispersed regime: the phase distribution at its boundary is the one imposed by geometry and by the heat input. Very probably different results would be achieved by imposing a pre-determined phase distribution through a mixer or similar device at the inlet of the heated section.

Other geometries were also studied mainly to simulate the behavior of a rod in a bundle: eccentric annuli, dumbbell-shaped cross section, maltese crosses etc. Nothing can be said here of these results, without going out of the scope of this chapter.

D. HEAT TRANSFER COEFFICIENT IN ANNULAR-DISPERSED FLOW

1. Heat Transfer Mechanism below the Crisis

In recent times an ever-increasing interest was put on the study of the mechanism of heat transfer in annular-dispersed flow. Today the

[5] See bibliography in reference (123)

amount of experimental data on the water-steam system in upward flow is quite large, and a list of references can be found in (*121*). Most of these data were taken at low pressure and a number of experimental correlations were developed. On the other hand, theoretical studies, aimed at describing possible heat transfer mechanisms, have not been particularly successful.

The following points must be taken into account:

(a) Only the measurement of local heat transfer coefficient is of scientific interest. Values averaged over a certain length, although in many cases of primary practical importance, are difficult to interpret, because the separate influence of flow pattern, heated length, quality variation, etc., cannot be easily separated.

(b) Heat transfer coefficients in annular-dispersed flow below the critical heat flux are usually very large. In high-pressure systems peak values up to 50 W/cm² °C are not uncommon. Since at high pressure (1) the ductwall must have a certain thickness (2) metals suitable for high temperature service, i.e., stainless steels have poor thermal conductivity, and (3) the temperature of the inner tube wall is deduced from that on the outer tube surface, the accuracy with which heat transfer coefficients are measured is usually very poor. With the best equipment and careful calibration the accuracy attainable in such measurements does not exceed the order of magnitude of 0.01 °C/W/cm², which means a 50% error on a value of 50 W/cm² °C.

(c) From the description of the crisis, as reported in Section III,A,2, it appears that h, below the critical heat flux, presents an "hysteresis" effect. Although this effect requires more careful experimental confirmations, it would be logical to conclude that, if things are so, only an upper and lower limit could be given for h. Below the critical heat flux, subject to some limitations, any value seems possible in between depending on the complicated flow subpattern configurations. At the critical heat flux, on the other hand, the value of the heat transfer coefficient seems unequivocally determined. A series of h measurements for a particular condition is presented in Fig. 27.

While the above picture is subject to confirmation, in what follows a number of correlations will be presented, which do not, of course, take into account these additional complications.

In bubble flow, and partially also in slug flow, the heat transfer mechanism is not substantially different from that which takes place in subcooled boiling.

The transition from nucleate boiling to evaporating mechanism is probably connected with hydrodynamic conditions prevailing in the annular dispersed regime, which is entered with increasing quality. This

transition could also be used as a tentative criterion to define the boundary between dispersed flow and other types of flow. Two resistances in series are met by heat going from a heated wall to a dispersed core: (a) heat must be transmitted through the liquid layer and (b) water must be evaporated from the liquid surface to the bulk with a mass transfer evaporative process. This picture is consistent with the hypothesis that no bubbles exist in the liquid film. Collier and Pulling (*121*) recently pointed out that Hau's (*122*) theory on the initiation of nucleate boiling may explain this phenomenon.

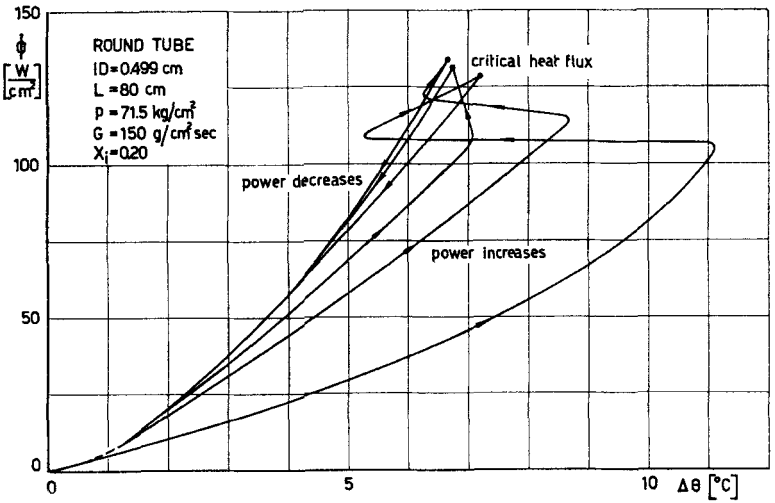

FIG. 27. Example of the wall to coolant temperature difference below CHF, as a multivalued function of the heat flux.

From an experimental point of view Dengler and Addoms (*123*) proposed for the temperature drop $\Delta\theta_f$ across a liquid layer, for which the nucleation begins, the following criterion:

$$\Delta\theta_f \cong 2(\bar{U}_\alpha)^{0.3} \tag{68}$$

where $\Delta\theta_f$ is in °C and $\bar{U}_\alpha$ in cm/sec and $\bar{U}_\alpha$ is the average mixture velocity calculated as $G/\bar{\rho}$, where $\bar{\rho} = \bar{\alpha}\rho_g + (1 - \bar{\alpha})\rho_l$.

This temperature drop was also checked by Davis and David (*124*) for horizontal flow. If the liquid thickness in equilibrium with $\bar{U}_\alpha$, at that particular heat flux is sufficiently small, the temperature drop $\Delta\theta_f'$ which allows such heat flux to pass only by a conductive mechanism through the liquid layer is smaller than $\Delta\theta_f$ and bubble nucleation should not set in.

Putting:

$$\Delta\theta_f' = \frac{\phi s}{K_l} \tag{69}$$

the condition:

$$\Delta\theta_f = \Delta\theta_f' \tag{70}$$

gives:

$$2\bar{U}_a^{0.3} = \frac{\phi f(\bar{U}, \phi)}{K} \tag{71}$$

where $s = f(\bar{U}, \phi)$.

Making the further hypothesis that $s \sim 1/\phi$, one has the equation:

$$\frac{f(\bar{U}_a)}{\bar{U}_a^{03}} = \text{const} \tag{72}$$

independent of the heat flux, and depending only on $\bar{U}_a$. This equation determines the mixture velocity, at which nucleation is suppressed.

This relationship is of the same type as that defining the boundary between slug flow and annular dispersed flow, although this boundary might not coincide with the one for which bubble nucleation is suppressed.

2. Heat Transfer Correlations below the Crisis

Subject to the aforementioned limitations, a list of correlations can be given. A first group is the equivalent, in the heat transfer field, of Martinelli correlations for pressure drops. Guerrieri and Talty (*125*) and Dengler and Addoms (*123*) summarized results obtained with steam-water and organic systems at low pressure, in the following way:

$$\frac{h}{h_e} = K\left(\frac{1}{X_{tt}}\right)^n \tag{73}$$

in which K and n are constants and h_e is the heat transfer coefficient calculated with the Dittus-Boelter correlation and the total flowrate flowing in the liquid phase (*123*) or the liquid flowrate flowing alone (*125*).

The above correlation was recently checked by Collier (*121*) for low pressure experiments with steam-water mixtures in upward motion in annuli. Properties of the liquid phase are, however, calculated not at the bulk (saturation) temperature, but at the mean film temperature $\bar{\theta}_f$, so defined:

$$\bar{\theta}_f = \theta_{\text{sat}} + 0.33(\theta_w - \theta_{\text{sat}}). \tag{74}$$

Schrock and Grossmann (*83*) present a correlation valid for both the nucleate boiling and the evaporating region. The boiling number:

$$N_{\text{BO}} = \frac{\phi}{GH_{gl}} \tag{75}$$

is assumed as a fundamental parameter for the first condition:

$$\frac{N_{Nu}}{(N_{Re})_l^{0.8}(N_{Pr})_l^{0.4}} = K_1 \, BO + K_2 \left(\frac{1}{X_{tt}}\right)^n \tag{76}$$

K_1, K_2 and n being constants. Most of the data for water-steam upflow in tubular ducts are correlated within $\pm 35\%$. The experimental range is very wide: 3 to 35 kg/cm² for pressure and 24 to 450 gm/cm² second for mass velocity. Sani (*126*) used the same correlation for his results, obtained in steam-water downflow at low pressure and low heat fluxes. However the "boiling number" suggested by him is different:

$$N_{BO}' = \frac{\phi}{GH_{gl}} \frac{V_g}{V_L} \tag{77}$$

A number of correlations, derived from the homogeneous model, were used by Groothuis and Hendal (*127*) and Davis and David (*124*). They are all of the form:

$$N_{Nu} = K N_{Re}^{n_1} N_{Pr}^{n_2} \tag{78}$$

in which K, n_1, n_2 are constants and in the Reynolds number the average mixture fluidity $1/\bar{\mu}$ is used (see formula 25a).

In the high pressure range ($p > 40$ kg/cm²) these correlations, compared with Perroud (*84*) and CISE (*13*) data, show a worse disagreement than at low pressure.

From a theoretical point of view, some attempts to calculate the heat transfer coefficient from a hydrodynamic description of the liquid film, as for instance those made by Anderson (*128*) and Hewitt (*55*) did not give satisfactory results. These theories usually neglect the resistance to heat transfer at the gas-liquid interface. On the other hand, a semi-empirical correlation developed at CISE (*129*), in which the predominant phenomenon was supposed to be the self-diffusion of steam molecules through the steam boundary layer adjacent to the liquid surface, gave reasonable agreement at low pressure, but failed at higher pressures.

In conclusion, it is probable that any theoretical model should take into account both resistances to transfer of heat: that through the liquid film, and that at the liquid-vapor interface. Additional complications would be the carry-over and deposition of liquid droplets, and the presence of waves or roughness on the liquid film profile. The "hysteresis" of the heat transfer coefficient would provide a further challenge to any theoretician.

3. Heat Transfer above the Crisis

Above the critical heat flux, the heat transfer capacity of a heated surface drops down considerably. It has been recognized, however, that

in annular-dispersed flow the temperature increase following a small increase of the heat flux is not catastrophic as in pool boiling. From this fact arose the suspicion that occurrence of the crisis was not due to a process of partial film boiling, but to the inadequacy of the crossflow of water droplets to take away the heat input. This was pointed out elsewhere [see also (*58*)]. Breakdown of the liquid film would bring the flow pattern to a dry wall or partially dry wall conditions. An interesting question arises, whether this new flow pattern, the so-called "liquid deficient regime," of which we spoke only vaguely in Section I,A,1, is enhanced by the heat flux, or can exist only in heat transfer conditions. Adiabatic experiments prove that the "liquid deficient regime" may exist even without heat transfer, but that moderate heat fluxes bring down

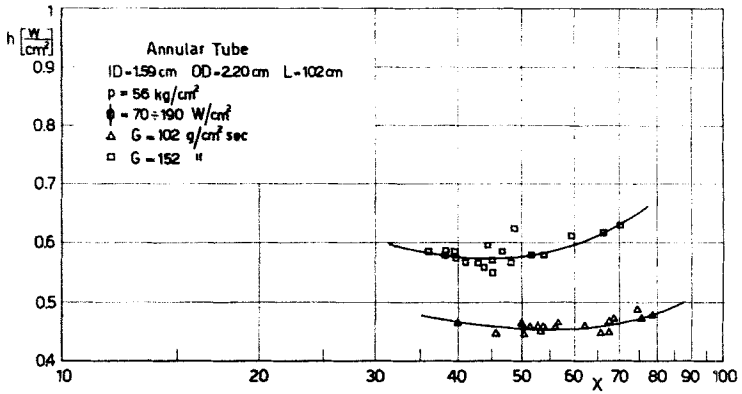

FIG. 28. Heat transfer coefficient vs. steam quality, beyond CHF (General Electric data).

the quality at which this happens. It is also evident that in vertical tubes there is a certain axial symmetry, while in horizontal tubes the liquid deficiency in the bottom of the cross section is reached downstream with respect to the top. Thus, in the latter case, the geometrical line connecting the "burnout points," at constant heat flux on the wall, is not a circumference, lying in a plane perpendicular to the axis, but is more or less an inclined ellipse.

The initiation of the liquid deficient region coincides, of course, with the occurrence of the crisis. Beyond this limit, experiments were not carried out in a systematic way. A number of heat transfer coefficients were measured by the Harwell group (*121*) at low pressure. Many data were collected at San Jose, at the General Electric Laboratories (*130*), in the first development of the once-through boiler. Here experiments were carried out at pressures of 56, 70, and 98 kg/cm² (800–1000–1400 psia),

in an annular vertical duct internally heated. They observed that h went down from the critical value to a minimum (in the 50–60% quality region) and then rose again to the dry saturated steam value. Temperature oscillations of varying amplitude occurred in this region, so that a mean value for h had to be taken into account. Some data are shown in Fig. 28.

Starting from the relationship:

$$N_{Nu} = C N_{Pr}^{1/3} N_{Re}^{0.8} \tag{79}$$

a correlation of experimental data was tried, neglecting the influence of water droplets, and introducing the gas flowrate GX and the hydraulic diameter αD. In this way, however, the minimum of h was not explained and an empirical correction was brought about (79) by substituting $(1 - X)X$ for X and $(1 - \alpha)/\alpha$ to α. For α, which is related to X, an empirical correlation of Larson's data (*47*) was used:

$$\alpha = \frac{1}{1 + \frac{1 - X}{X}\left(\frac{\rho_g}{\rho_l}\right)^{2/3}} \tag{80}$$

The final form of the correlation is the following:

$$\frac{N_{Nu}}{(N_{pr})^{1/3}} \frac{1 - \alpha}{\alpha} = 0.00136 \left(\frac{DG}{\mu} \frac{1 - X}{X}\right)^{0.853} \tag{81}$$

where G is the total mass flowrate and the physical properties refer to dry saturated steam. In this way, the authors claim that most of their data can be correlated better than 20%. Since, however, all experimental data are comprised between 0.4 and 0.8 $W/cm^2\,°C$ (800–1600 $BTU/ft^2h°F$) this result is certainly not surprising. Less acceptable seems the use of Larson's data, which were obtained in adiabatic flow, while beyond the crisis α is certainly different and the slip ratio should be very close to unity. Moreover, by introducing (*80*) into (*81*), one can see that h goes to infinity, for $X \to 1$, and this hardly seems a good approximation.

Another experimental analysis of the transition across the crisis was carried by Parker and Grosh (*131*). Experimental conditions were quite different from those of General Electric: low pressure (~2 kg/cm^2, 30 psia), very low heat flux (1–7 W/cm^2; 3–21.10^3 BTU/ft^2h), very high quality (89–100%). The steam-water system was studied in upward flow in a copper tube, 1 inch I.D., 4 feet long. The scheme they propose in order to handle the data is the following: if all droplets impinging on the wall are evaporated, the heat flux absorbed by them is:

$$\phi_{ev} = K_d C \lambda \tag{82}$$

where C is the concentration of water droplets and K_d is a diffusion coefficient (in velocity units). The temperature difference between the walls and the bulk of the fluids (assumed at the saturation temperature) is:

$$\theta_w - \theta_b = \frac{\phi - \phi_{ev}}{h} \tag{83}$$

where h is the heat transfer coefficient for saturated dry steam.

By definition, however:

$$\phi = h_{mist}(\theta_w - \theta_b) \tag{84}$$

where h_{mist} is the over-all heat transfer coefficient. In the end:

$$\frac{1}{h_{mist}} = \frac{1}{h_{dry}} \frac{\theta - \theta_{ev}}{\phi} \tag{85}$$

so that $\Delta\theta = (\theta_w - \theta_b)$ should rise more or less linearly from a value very close to zero for "burnout" conditions, to the dry steam value. An interesting remark is made by the authors: if $\Delta\theta$ reaches a value sufficiently high, the Leidenfrost phenomenon could arise (water droplets in spheroidal state, incapable of wetting the heated wall) and a sudden jump in temperature should precede the dry steam conditions, while the heat transfer coefficient should drop suddenly to this value. Some experimental runs seem to confirm this picture.

Experiments at very high quality (94–98%), moderate pressures (15–45 kg/cm²; 200–600 psia), mild heat fluxes (3–6 W/cm²; 10–20 × 10^3 BTU/ft²h) were performed by Rounthwaite and Clouston (*132*) in a long horizontal tube, 1.614 foot I.D., mild steel. Evidently they found that the upper portion of the tube perimeter enters the liquid deficient region before the bottom. Apparently the h value fell off by a factor of 20–25 from ~2.5 to ~0.1 W/cm^2 °C (5000 down to 200 BTU/ft²h°F).

At CISE, a number of heat transfer coefficients beyond the crisis were measured in a nonsystematic way (*82*). In a single case however a complete set of heat transfer coefficients were obtained under practically constant experimental conditions (pressure, flowrate, geometry, and quality). For this purpose a very short tube (L/D = 20) was used, so that the quality change due to heat input was negligible. Results are reported in Fig. 18, where the magnitude of recorded temperature oscillations are also indicated, while the heat transfer coefficients deduced from the same points are given in Fig. 29. The error which affects these heat transfer coefficients is generally low, owing to the higher $\Delta\theta$ measured, with respect to wet-wall conditions. As a general remark, it can be observed that over-all heat transfer coefficients are higher than predicted

for steam flowing alone, although coefficients found when increasing the heat flux above the critical value tend to the values corresponding to steam flowing alone (mass velocity GX). These experiments tend to confirm the hypothesis that the evaporation on the wetted area and a gas transmission elsewhere determine an average value of the heat transfer coefficient. By increasing the heat flux the wetted area of the wall decreases, until the temperature difference between the bulk and the wall is such that, possibly through the Leidenfrost phenomenon as suggested by Parker and Grosh, no more droplets wet the heated surfaces, even with quality steam. If this picture is true, the Leidenfrost temperature (function of many independent variables: p, G, X, D, etc.) will

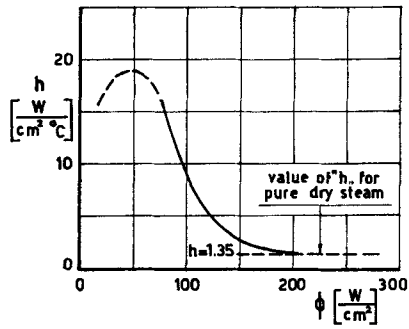

FIG. 29. Plot of the heat transfer coefficient beyond CHF (CISE's results, conditions equal to those of Fig. 18).

correspond for wet steam to a second critical heat flux. This second critical heat flux would be similar in nature to the burnout heat flux typical for subcooled and boiling water or low quality steam. The strong temperature oscillations observed during these experiments might be explained by the succession of wetting and nonwetting in the region where temperature is measured, although a not fully levelled power input could be partially responsible in a region of high $dT/d\phi$.

These oscillations reach a maximum when $\Delta\theta$ is about halfway up this intermediate region and should depend moreover on the thermal inertia of the heated element, the magnitude of the volume power density and so on. The picture is similar also with annuli externally or internally heated.

4. Analysis of the Heat Transfer Coefficient beyond the Crisis

In what follows a tentative analysis is made, to predict the order of magnitude of the average value of h in the liquid deficient region, fol-

lowing the assumptions presented above and in line with the approach made by Parker and Grosh (*131*).

Suppose that the critical heat flux is reached, and h_{cr} is the corresponding heat transfer coefficient. We have: $\Delta\theta_{cr} = \phi_{cr}/h_{cr}$. Then ϕ is increased above the ϕ_{cr} value and temperature recordings are taken for a sufficiently long time (at the same pressure, flowrate, and quality). The amount of water cross flow is still equal to ϕ_{cr}/λ. If the unit heat transfer area is taken into account, we ideally concentrate all the water crossflow on a fraction of this area, so that this area is just fully wet: this means that this area is in a critcal condition, with heat flux ϕ. The fractional area in wet condition will be ϕ_{cr}/ϕ, recalling that nothing has changed from the hydraulic point of view. The dry fractional area is then $(\phi - \phi_{cr})/\phi$. If we suppose that $\Delta\theta$ in the portion of the wet area is equal to $\Delta\theta_{wet} = \phi/h_{cr}$ while it is $\Delta\theta_{dry} = \phi/h_{dry}$ (where the subscript "dry" stands for dry saturated steam conditions) in the dry area, the value of $\Delta\theta$, weighted by the two areas, will be:

$$\begin{aligned}\Delta\theta &= \Delta\theta_{wet}\frac{\phi_{cr}}{\phi} + \Delta\theta_{dry}\frac{\phi - \phi_{cr}}{\phi} \\ &= \frac{\phi_{cr}}{h_{cr}} + \frac{(\phi - \phi_{cr})}{h_{dry}}\end{aligned} \tag{86}$$

while the average heat transfer coefficient $\bar{h}$, is:

$$\frac{1}{\bar{h}} = \frac{1}{h_{cr}}\left(\frac{\phi_{cr}}{\phi}\right) + \frac{1}{h_{dry}}\left(\frac{\phi - \phi_{cr}}{\phi}\right) \tag{87}$$

For $\phi = \phi_{cr}$, it is $\bar{h} = h_{cr}$, while for $X \to 1$, $\phi_{cr} \to 0$ and $\to \bar{h} \to h_{dry}$. In the intermediate region, $\bar{h}$ has intermediate values without excluding the possibility that $\bar{h}$ can go through a minimum in the upper quality region. In fact, neglecting the contribution of the water droplets to h_{dry}, but taking into account the volume occupied by the liquid phase in the bulk (and putting $S \sim 1$, beyond the crisis) one has, for the velocity of both phases, $\bar{U}^* = G\,(V_L + XV_{gl})$ and the apparent gas mass flowrate is:

$$G_g = \frac{U^*}{V_g} = G\left(\frac{V_L}{V_g} + X\frac{V_g - V_L}{V_g}\right) = G\frac{X + a}{1 + a} \tag{88}$$

Thus

$$h_{dry} = C\frac{K_g}{D}(N_{Pr})_g^{0.4}\left[\frac{G\dfrac{X + a}{1 + a}D}{\mu_g}\right]^{0.8} \tag{89}$$

At constant geometry and pressure h_{dry} is only a function of X.

Moreover, neglecting the term $\frac{\phi_{cr}}{H_{cr}}\frac{1}{\phi}$ in the $1/\bar{h}$ expression, one has:

$$\frac{1}{\bar{h}} \sim \left(1 - \frac{\phi_{cr}}{\phi}\right)\frac{1}{X^{0.8}} \tag{90}$$

A maximum for $1/\bar{h}$ is reached if:

$$\frac{d(1/\bar{h})}{dX} = 0; \qquad \text{that is: } \frac{0.8}{X}(\phi - \phi_{cr}) = -\frac{d\phi_{cr}}{dX} \tag{91}$$

The derivative $d\phi_{cr}/dX$ is always negative and it may happen that the above condition is satisfied for $X < 1$.

IV. Heat Transfer with Two-Phase, Two-Component Mixtures

Heat transfer with two-phase, two-component systems in annular flow was widely studied in the past and is being studied also today. The amount of theoretical and experimental work on condensation of steam in presence of an inert gas is very large. Most of it is concerned with downflow. In this condition the mass transfer process of H_2O molecules diffusing from the gas core through the gas boundary layer to the film liquid surface cannot be neglected in respect to the heat resistance of the liquid film itself.

This resistance may be calculated, as originally suggested by Nusselt (*133*), when the downflow is laminar; when it is mostly turbulent, better agreement with experiments is reached, if, for instance, more recent theories, like that of Duckler (*54*) are used. Heat transfer from the gaseous core to the liquid surface must take into account both heat convection and mass transfer. This is done by using the analogy suggested by Reynolds between convective heat transfer and momentum transfer also for the mass diffusion process. This method suggested by Colburn and Hougen in the 1930's (*134*, *135*, *136*), although somewhat laborious, allows a good evaluation of the over-all heat transfer coefficient in the condensation of a vapor from gas-vapor mixtures.

Experimental data on the evaporation of a two-phase two-component mixture in annular-dispersed flow are, on the contrary, very scarce.

Finzi *et al.* (*137*) evaluated the heat resistance from the liquid surface to the gaseous core in pure annular flow (both upward and downward in the water-steam-hydrogen system), by introducing a heat transfer coefficient calculated thus:

$$h = 0.023\frac{K}{D}(N'_{Pr})^{n}(N_{Re})^{0.8} \tag{92}$$

All physical properties, except the specific heat, refer to the gaseous mixture (steam + hydrogen), while, for the specific heat, the following expression is taken:

$$c' = c_m + \frac{M_v}{M_m} \frac{\lambda}{p - \pi} \frac{\Delta\pi}{\Delta\theta} \tag{93}$$

c_m is the true specific heat of the gaseous mixture; M_v, M_m are the molecular weights of the vapor and of the gaseous mixture, $\Delta\pi/\Delta\theta$ is the ratio of the vapor pressure to the temperature drop for the vapor between the liquid surface and the gaseous core. The exponent n in (*93*) has a value of 1.13. The agreement between results calculated with this method and with the Colburn method, in the case of condensation, is surprisingly good, but the reason is unknown.

Experiments with large heat fluxes, up to the crisis, in annular dispersed upward flow were carried out by Perroud and De la Rarpe (*138*) at CENG and by Lombardi (*139*) at CISE.

Perroud, with a method similar to that adopted by Colburn was able to correlate heat transfer coefficients from the liquid surface to the core. The presence of liquid droplets was neglected and the temperature drop in the liquid film on the wall was assumed to be a fixed fraction of the total. The results, obtained with different gas-steam-water mixtures, were well correlated, when this fraction was fixed at 0.2.

During experiments with hydrogen, pressures from 3 to 10 kg/cm² and an inlet temperature of 17°C, the crisis was reached. Heat fluxes so measured (24 experimental points) are proportional to the cube root of pressure, to exponent 0.6 of the inlet liquid flowrate and almost independent of the flowrate of the incondensable gas.

Experiments were carried out at CISE with the water-steam-nitrogen system, at low pressure (2.5 to 5 kg/cm²). The inlet mixture temperature varied between 14° and 90°C. A comparison between the heat transfer coefficients and the CHF's obtained in these conditions, and those obtained with the steam-water system (for equal water and steam mass flowrates, equal geometry, equal inlet temperatures, equal heat input, and equal outlet pressure) shows:

(a) that the presence of substantial amounts of nitrogen reduces the heat transfer coefficient by a factor of 2 to 3;

(b) that the critical heat flux is not appreciably altered;

(c) in consequence of this, the temperature difference between the heated wall and the bulk of the coolant at the CHF is higher by the same factor.

It was also observed that the temperature drop between the bulk and the heated wall showed a substantial reduction before the crisis was

reached, as it was later observed with steam-water mixtures. This reduction was more gentle with the presence of the noncondensable gas.

V. Practical Application of Annular-Dispersed Flow

The simultaneous flow of a gas and a liquid in a single duct, with and without heat transfer, is of a common occurrence in many industrial processes. The petroleum industry, for instance, is particularly concerned with the flow of two-phase mixtures in the reservoir, well bore, gathering lines, transmission lines, and processing plant equipment. Steam generators are another very important example of industrial plants operating with a two-phase flow. The interest in this field has considerably increased in recent years in connection with the construction of steam generating nuclear reactors. In fact, one of the characteristics of the in-reactor steam generation is that, below the critical pressure of water, two-phase flow exists at least in a portion of the reactor core.

Steam generating reactors are a wide class, whose development is still in its infancy, although considerable progress has been achieved in the past ten years. They can be defined as reactors which receive water at a particular enthalpy content from a condenser and eject saturated or superheated steam to the utilization plant. They can operate both on a direct or an indirect cycle, although the first design is more attractive, since a number of expensive components can be eleminated in principle.

In such reactors any kind of moderator can be envisaged in a pressure tube design. In the boiling water reactors, which are by far the most developed model of this class, light water behaves both as a coolant and moderator, while in the U.S.S.R. superheating reactor (*140*, *141*) graphite is used as a moderator and it seems that nothing prevents the use of heavy water.

As said above, liquid water entering the core with a certain enthalpy is ejected as steam. Achieving this in a single pass and with full vaporization of the water flow means a once-through design: thus, in each tube all kinds of flow patterns are met, from single-phase flow of liquid water to single phase flow of dry steam. Such a design, although attractive, incorporates a number of formidable obstacles, not the least important among them being that at constant flowrate a minor power surge produces a tremendous temperature increase at the superheated steam outlet. A two-pass or three-pass design seems to be more reliable, although complicated by the necessity of phase separation at a certain point of the cycle, and attention is here focused only on this arrangement.

In the superheated steam region heat transfer obeys the laws governing gas cooling. Problems exist with that mode of cooling, apart from the special problems arising from the use of a corrosive agent such as steam

at high temperatures. In the steam generating region, on the other hand, many possibilities exist, and a certain choice is permitted, in relation to the flow patterns allowed in the channel.

The simplest case is the use of saturated water to feed the heated channels. For the time being let us imagine that those channels are cylindrical and cooled from inside. In natural circulation boiling water reactors, the flowrate is mostly determined by the geometry of the circuit, while in forced circulation reactors the coolant flowrate can be imposed from the exterior. In the latter case, depending on the value of the flowrate, different steam qualities can be reached at the channel exit, which are usually much higher than those existing in boiling water reactors. To a certain extent, the predominant flow pattern existing along the channel may be selected as desired.

Up to now flow pattern charts, which are discussed in Section I, are not of general use and specific experiments are needed for specific cases. As previously mentioned, according to what has been found at CISE (*13*), at a pressure of 70 kg/cm² (~1000 psi) slug flow should not exist above a mean linear velocity of ~500 cm/second of the steam-water mixture, and, following the lines indicated in Section I,B,1, it would be impossible above 200–250 gm/cm². Above this mass velocity there is a smooth transition from bubble flow to dispersed flow. On the other hand, below this flowrate, slug flow can occur and maxima occur in the burnout heat flux, if special provisions are not taken at the channel inlet. Boiling water reactors usually operate in that region, but with a proper selection of flowrate and outlet quality most of the steam generating region of the reactor could operate in an annular-dispersed flow pattern. Thus the thermal and hydraulic properties of water-steam mixtures in these conditions are of considerable interest. Knowledge of the value of critical heat flux ϕ_{cr} and of the peculiarities of the crisis phenomenon (see Section III,C) is of primary importance.

One point should be emphasized in connection with the design criteria for a channel operating in annular-dispersed flow. A statement like "the maximum allowable heat power, shall not overcome the critical heat power" has an absolute nature, but what happens if the actual power overcomes the burnout power? Suppose that a tube 0.5 cm I.D., 80 cm long, operates in upflow at a pressure of 70 kg/cm² and constant heat flux of 100 W/cm². Outlet quality, just below the crisis, is 52.8% for G = 180 g/cm² second and 33.3% for G = 360 g/cm² second. To match the energy balance, inlet quality must be 27.6 and 21.5% respectively. A sudden power surge now brings the heat flux up to 150 W/cm² (outlet quality 63 and 39.2%). The temperature distribution along the tube is reported in Fig. 30.

Now in both cases the crisis begins at two-thirds of the heated length, but the maximum temperature jump is different. The one at higher flowrate is about two-thirds of that at lower flowrate. Thus safety beyond the crisis is different. Moreover the temperature increase beyond burnout is in itself quite moderate for such a high power surge, and periodical high frequency fluctuations of the heat transfer coefficient are of much more concern that the temperature increase itself.

In the previous example, inlet quality was not zero. To enter at zero inlet quality would be an interesting engineering condition, because there is no need for any steam blower or, worse, for an injection system at the bottom of the heated channel. With the higher flowrate no instability

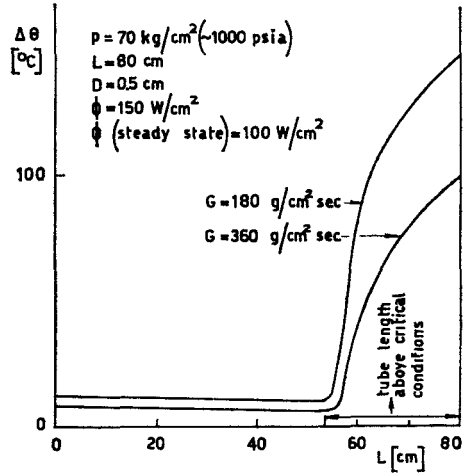

FIG. 30. Temperature distribution in a tube which operates partially below and partially beyond CHF, for two different mass velocities.

would occur, while with the lower one a small amount of instability does exist. Through moderately orificing the channel, it is not difficult to prevent this.

Orificing can be useful in another respect. Proper orificing would allow flashing of water, pressurized at a pressure higher than that of the mixture, in order to preheat water at a temperature higher than the temperature of the mixture. In this way any quality region which could present a slug flow is avoided for flowrates of most common use. It is interesting to note that, for a given flowrate, the average density of the coolant is not substantially different, in this case, from the one which would be obtained by entering at zero quality, without orificing.

For geometries which are more complicated than single tubes, like

annuli and clusters, experimental results are much less abundant. However, since any unheated surface, as pointed out elsewhere, acts as a water sink, it is of interest to eliminate them as much as possible from the heated channels to decrease the average coolant density.

There is also the possibility of increasing outlet quality (the CHF being constant) with the use of centrifugal fields. Very few experiments are available (*142*). However displacements of the outlet quality from 40–60 to 100% (at constant CHF) were achieved in some experiments by means of twisted ribbons inserted in a heated tube in a low pressure loop. Although practical application could be very difficult, it shows a path of improvement to reach higher qualities and to reduce the holdup water for a reactor designed for maximum neutron economy.

ACKNOWLEDGMENTS

I am much indebted to a number of my co-workers for the writing and the criticism of the manuscript. Without their help, this chapter could not have been written in the short time of four months. I want to recall here S. Bertoletti, L. Cravarolo, G. Peterlongo, and S. Villani. Particular thanks are due to I. Casagrande, who, in addition to personal contributions to the manuscript, helped me in rereading the manuscript as many times as necessary to increase internal consistency. I should also like to record particular thanks to G. Soldaini, who died in a tragic car crash last July, to whom I am indebted for much of the experimental results on heat transfer in annular-dispersed flow.

APPENDIX

In this chapter on "Fluid Mechanics and Heat Transfer of Two-Phase Annular-Dispersed Flow," reference to other two-phase flow patterns is only incidental. Since flow-pattern boundaries are not well defined, the boundary of the material collected, and the author's comments in this chapter, are correspondingly imprecisely defined. This should not be considered a complete fault of the author, but must be ascribed to the still vague nature of the problem.

The text does not start from the very beginning of the research work in this field. In a book on "Advances in Heat Transfer" it was considered reasonable to summarize the situation existing in 1954–1958 and to enter deeper into the recent advances. The chapter may be taken as up-to-date at about the middle of 1962. Although an effort was made to review all published literature, a number of papers escaped my attention. To prevent complete confusion of the reader, results of other papers examined subsequently could not be incorporated into the text. However, most of them are cited in the Supplementary List of References.

NOMENCLATURE

a	$\dfrac{V_1}{V_g - V_1}$
A	mass number, cross section area
c or c_p	specific heat at constant pressure
C	numerical constant
CHF	critical heat flux
D	diameter or distance beteewn parallel walls; also equiv. diameter
D_p	particle diameter
g	acceleration due to gravity
G	specific mass flowrate (or mass velocity)

GM	stands for Geiger-Müller (counters)
h	heat transfer coefficients; also liquid volume fraction (or liquid holdup)
H	enthalpy
k	thermal conductivity
K	parameter
L	length; also heated length
m	exponent or numerical constant
n	exponent
N_{Nu}	Nusselt number
N_{Pr}	Prandtl number
N_{Re}	Reynolds number
N_{We}	Weber number
p	pressure; also wetted perimeter
Q	volume flowrate
r	distance from the axis of the conduit
R	electrical resistance
s	film thickness or thickness in general
S	slip ratio (U_g/U_l)
U	linear velocity
V	specific volume
W	total power input
X	mass flow rate quality or Martinelli parameter
X_v	volume flow rate quality
X_M	molar flow rate quality
y	distance from the wall; also parameter equal to $\dfrac{1-X}{X+a}$
y^+	adimensional wall distance $\left(y^+ = \dfrac{y}{\mu_l}\sqrt{\tau_w \rho_l}\right)$
y_f	A_f/A_1
y_c	A_c/A_1
z	coordinate along the length
Z	atomic number
α	gas volume fraction (or void fraction)
β	contact angle
γ	surface tension
Γ	mass flowrate
Δ	difference
ΔS	$S-1$
ϵ	$2y/D$
θ	temperature
λ	latent heat of vaporization (also H_{gl})
μ	viscosity; also mass absorption coefficient (for radiation)
ρ	density; also electrical resistivity
σ	area
τ	shear stress
ϕ	heat flux; also Martinelli parameter

Subscripts

1,2	refer to sections 1 and 2 of a duct along its length
c	core
cr	refers to critical conditions
e	external
E	entrainment
f	friction; also film and fluid
g	gas (or steam)
gl	refers to the difference of any quantity in the vapor and liquid phase
h	heated
i	inlet or internal; also interfacial
l	liquid
m	refers to mixture
max	maximum
min	minimum
M	molar
o	outlet
( )o	refers to quantities calculated by attributing the total mass flow rate to a single phase (gas or liquid)
p	particle; also refers to impact pressure
s	solid or saturation
sub	refers to difference between saturation temperature and sub-cooled water temperature
tt	turbulent-turbulent
tv	turbulent-viscous
TP	two-phase (used only when necessary to distinguish from single-phase quantities)
v	volume
w	wall

Superscripts

$\bar{}$	average value (used only when necessary to distinguish from local value)

•	refers to superficial quantities (for instance specific flowrates, velocities etc.) of a single phase with respect to the total flow area; also refers to flowrate		density and specific volume of the mixture
			refers to frictional pressure drops according to momentum equation

REFERENCES

AERE = Atomic Energy Research Establishment (UK)
BMI = Battelle Memorial Institute (USA)
CEA = Commissariat à l'Energie Atomique (France)
GEAP = General Electric Atomic Power (Equipment Department) (USA)
ANL = Argonne National Laboratory (USA)
AECL = Atomic Energy of Canada Ltd. (Canada)
WAPD = Westinghouse Atomic Power Department (USA)
KAPL = Knolls Atomic Power Laboratory (USA)
AEEW = Atomic Energy Establishment Winfrith (UK)
UCRL = University of California—Radiation Laboratory (USA)
SNECMA = Société Nationale d'Etude et de Construction de Moteurs d'Aviation (France)
Ansaldo = Ansaldo Co. (Italy)
UKAEA = UK Atomic Energy Authority (UK)
HW = General Electric—Hanford Atomic Products Operation (USA)
MIT = Massachusetts Institute of Technology (USA)

1. R. C. Martinelli, L. M. K. Boelter, T. H. M. Taylor, E. G. Thomsen, and E. H. Morrin. *Trans. ASME* **66**, 139 (1944).
2. O. Baker. *Oil Gas J.* July 1954, p. 186.
3. H. S. Isbin, R. H. Moen, R. O. Wickey, D. R. Mosher, and H. C. Larson. *Nuclear Engineering and Science Conference*, A.I.Ch.E., Chicago, Illinois 1958.
4. L. I. Krasiakova. *AERE Trans.* **695**, January 1957.
5. G. E. Alves. *Chem. Eng. Progr.* **50**, 449 (1954).
6. T. W. Ambrose. General Electric Co., Hanford Labs, USAEC HW-52927, October 1957.
7. W. C. Galegar, W. B. Stàvall, and R. L. Huntington. *Petrol. Refiner* **33**, 208 (1954).
8. B. K. Kozlov. *Zh. Tekhn. Fis.* **24**, 2285 (1954).
9. J. H. Vohr. Columbia Univ., USAEC TID-11514, December 1960.
10. P. Griffith, G. B. Wallis. *J. Heat Transfer*, **83**, (1961).
11. D. J. Nicklin and J. F. Davidson. *Symposium on Two-Phase Fluid Flow*, London, February 1962.
12. G. B. Wallis. *International Heat Transfer Conference*, Boulder, Colorado, August 1961.
13. S. Bertoletti, J. Lesage, C. Lombardi, G. Peterlongo, M. Silvestri, G. Soldaini, and F. Weckermann. CISE Report R 36, April 1961.
14. S. Bertoletti, G. Soldaini. CISE. Unpublished results, 1962.
15. J. H. Perry. "Chemical Engineers' Handbook," 1950, p. 1019.
16. Quoted from G. H. Anderson and B. G. Mantzouranis, *Chem. Eng. Sci.* **12**, 233, (1960).
17. I. Casagrande and L. Cravarolo. *Energia Nucl.* **9**, p. 36 (1962).
18. G. A. Hughmark and B. S. Pressburg. *A.J.Ch.E. J.* **7**, 677, (1961).
19. P. G. Majiros and D. A. Dukler. *Develop. Mechanics*, **1**, (1961).

20. R. W. Lockhart and R. C. Martinelli. *Chem Progr.* (1949).
21. R. C. Martinelli and B. D. Nelson. *Trans. ASME* **70,** August 1948.
22. J. M. Chenoweth and M. W. Martin. *Petrol. Refiner* **34,** October 1955.
23. A. A. Armand. *AERE Trans.* **828,** 1959.
24. A. A. Armand and G. G. Treshchev. *AERE Trans.* **816,** 1959.
25. H. N. McManus. ASME publication 61-HYD-20, 1961.
26. M. Wicks and A. E. Duckler. *A.I.Ch.E. J.* September 1960.
27. G. W. Govier, B. A. Radford, and J. S. C. Dunn. *Can. J. Chem. Eng.* August 1957.
28. G. W. Govier and W. Leyh Short. *Can. J. Chem. Eng.* October 1958.
29. R. A. S. Brown, G. A. Sullivan, and G. W. Govier. *Can. J. Chem. Eng.* April 1960.
30. G. H. Anderson and B. G. Mantzouranis. *Chem. Eng. Sci.,* **12** (1960).
31. L. E. Gill and G. F. Hewitt. AERE R 3935 (1962).
32. S. G. Bankoff. *J. Heat Transfer* November 1960.
33. N. Adorni, I. Casagrande, L. Cravarolo, A. Hassid, M. Silvestri, and S. Villani. CISE Report R 26, October 1960.
34. N. Adorni, I. Casagrande, L. Cravarolo, A. Hassid, and M. Silvestri. CISE Report R 35, March 1961.
35. N. Adorni, I. Casagrande, L. Cravarolo, A. Hassid, M. Silvestri, and S. Villani. CISE Report R 41, June 1961.
36. I. Casagrande, L. Cravarol, A. Hassid, and M. Silvestri. CISE Report R 43, May 1962.
37. N. Adorni *et al.*, To be published. CISE. 1962.
38. I. Casagrande *et al.*, To be published. CISE. 1962.
39. L. Berkowitz, S. Bertoletti, J. Lesage, G. Peterlongo, G. Soldaini, and R. Zavattarelli. CISE Report R 27, October 1960.
40. N. Adorni, S. Bertoletti, J. Lesage, C. Lombardi, G. Peterlongo, G. Soldaini, F. J. Weckermann, and R. Zavattarelli. CISE Report R 30, December 1960.
41. N. Adorni, S. Bertoletti, J. Lesage, C. Lombardi, G. Peterlongo, G. Soldaini, F. J. Weckermann, and R. Zavattarelli. CISE Report R 31, January 1961.
42. G. M. Smith and Y. L. Hoe. CE 174 Report DL 118/6, Dominion Lab. Dept. Scientific and Industrial Research, New Zealand, September 1956.
43. C. E. Dengler. Ph. D. Thesis, Massachusetts Institute of Technology, Cambridge, Massachusetts (1952).
44. H. A. Johnson and A. H. Abon-Sabe. *Trans. ASME* 74, 977 (1952).
45. S. Yagi *et al. Chem. Eng.* (*Japan*) **17,** 216, (1953); quoted from (*19*).
46. H. S. Isbin, H. A. Rodriguez, H. C. Larson, and B. D. Pattie. *A.I.Ch.E. J.* **5,** December 1958.
47. H. C. Larson. Ph. D. Thesis, Univ. of Minnesota, Minneapolis, Minnesota (1957).
48. R. A. Egen, D. A. Dingee, and J. W. Chartain. BMI, 1163 (1957).
49. J. Huyghe, H. Mondin, and J. Villaneuve. *CEA* N. 055 (1961).
50. J. A. R. Bennet and J. D. Thornton. AERE R 3195, (1959).
51. G. F. Hewitt, R. D. King, and P. C. Lovegrove. AERE R 3921 (1962).
52. A. E. Dukler and D. P. Bergolin. *Chem. Eng. Progr.* **48,** (1952).
53. D. A. Charvonia. Purdue Univ. Report I-59-1 (1959).
54. A. E. Dukler. *Chem. Eng. Progr. Symp. Ser.* **56,** (1960).
55. G. F. Hewitt. AERE R 3680 (1961).
56. S. Calvert and B. Williams *A.I.Ch.E. J.*, March 1955.
57. M. Silvestri. VII$^{\text{èmes}}$ journées de l'Rydraulique, Paris, June 1962.
58. P. M. C. Lacey, G. F. Hewitt, and J. G. Collier. AERE R 3962 (1962).
59. G. B. Wallis and P. Griffith. M.I.T. Tech. Report No. 13, December 1958.

60. S. Vella and R. Zavattarelli. Final Report ANSALDO, October 1961.
61. S. Levy. GEAP report dated May 31 1961.
62. M. Petrick. ANL 5787, March 1958.
63. B. Richardson. ANL 5949, December 1958.
64. J. F. Marchaterre. ANL 5522, February 1956.
65. W. H. Cook. ANL 5621, (1956).
66. T. A. Hughes and W. Markest. Winter Meeting of the American Nuclear Society, San Francisco, California (1960).
67. G. W. Maurer. Bettis Technical Review, June 1960.
68. H. S. Isbin, N. C. Sher, and K. C. Eddy. *A.I.Ch.E. J.* March 1957.
69. D. Auson, R. E. Belin, and M. L. Horlor. Dominion Phys. Lab. Report R 239, New Zealand, February 1955.
70. D. English, P. T. Blacker, and W. E. Simmons. AERE ED/M 20 1955.
71. E. I. Nevstrueva and H. Gonsales. *Teploénerg.* No. 9, (1960).
72. J. J. Foglia, F. G. Peter, H. H. Epstein, R. O. Wooton, D. A. Dingee, and J. W. Chastain. BMI 1517, May 1961.
73. L. Cravarolo, A. Hassid, and S. Villani. *Energia Nucl.* **8**, December 1961.
74. E. W. Grohse. General Electric Research Lab., RL 1218, December 1954.
75. J. F. Cameron. *Radioisotopes in Scient. Res., Proc. Intern. Conf. I* Pergamon Press, London (1958).
76. Z. L. Miropol'skij and M. A. Styrikovič. *Izv. Akad. Nauk SSSR, Otd. Tekhn. Nauk.* No. 9, (1955).
77. S. Abid Husain and J. L. Putman. *Proc. Phys. Soc. Sect. A* **70** (1957).
78. R. Hours. CEA No. 521 (1955).
79. S. I. Kostarin, N. I. Semenov, and A. A. Točigin. *Teploenerg.* No. 1 (1961).
80. M. A. Styrikovič, A. V. Surnov, and Ja. G. Vinokur. *Teploenerg.* No. 9 (1961).
81. J. G. Bayly. AECL 1522, April 1962.
82. M. Silvestri. *Intern. Heat Transfer Conf.* Boulder, Colorado, August 1961.
83. V. E. Schrock and L. M. Grossman. Univ. of California, Institute of Engineering Research, November 1959.
84. P. Perroud, A. de La Harpe, and S. Rebière. CEA No. 1853, (1961).
85. R. A. De Bortoli, S. V. Green, B. W. Le Tournean, M. T. Roy, and A. Weiss. WAPD-188, October 1958.
86. G. F. Butenko and M. I. Radchenko. *Reactor Technol.* I, 3, 181, March 1960.
87. P. Griffith. WAPD-TM-210, December 1959.
88. L. S. Tong, H. B. Currin, and A. G. Thorp II. Trans. ANS **5** (1962). Also private communication by L. S. Tong.
89. G. S. Emmerson. *Nucl. Eng.* November 1960.
90. A. F. Pexton. UKAEA DEG 203 (R) (1961).
91. A. De la Harpe. *Étude Bibliogr.* CEA (1961).
92. J. M. Reynolds. MIT, Technical Report No. 10, July 1957.
93. J. Longo. KAPL-M-DIG-TD 1 and TD 2 (1958).
94. H. S. Isbin, R. Vanderwater, H. Fauske, and S. Singh. *Trans. ASME Series C,* May 1961.
95. D. W. Bell. *Nucl. Sci. Eng.* **7** March 1960.
96. A. Cicchitti, M. Silvestri, G. Soldaini, and R. Zavattarelli. *Energia Nucl.* **6** October 1959.
97. R. T. Jacobs and J. A. Merril. *Nucl. Sci. Eng.* **8** (1960).
98. R. W. Macbeth. AEEW-R 117, November 1961.
99. K. Goldman, H. Firstenberg, and C. Lombardi. *Trans. ASME Series C,* May 1961.

100. S. S. Kutateladze and M. A. Styrikovich. Gosuradstvennoye Energeticheskoye Izdatel'stvo, Moscow–Leningrad (1958).
101. A. A. Ivaškevič. *At. Energ.* USSR **8** January 1960.
102. A. A. Ivaškevič. *Teploenerg.* No. 10, (1961).
103. Z. L. Miropol'skij and M. E. Šicman. *At. Energ. USSR* **11,** No. 6, December 1961.
104. K. Goldman. *Intern. Heat Transfer Conf.*, Boulder, Colorado, August 1961.
105. B. S. Petukhov, E. A. Krasnoschekob, and V. S. Protopopov. *Intern. Heat Transfer Conf.*, Boulder, Colorado, August 1961.
106. M. A. Styrikovich and L. E. Factorovitch. *Soviet Phys. "Doklady"* **3** (1959).
107. M. A. Styrikovič, Z. L. Miropol'skij, M. E. Šicman, I. L. Mostinskij, A. A. Starovskij, and L. E. Faktorovič. *Teploenerg.* No. 5, (1960).
108. I. T. Aladyev, Z. L. Miropol'skij, V. E. Doroshchuk, and M. A. Styrikovich. *Intern. Heat Transfer Conf.*, Boulder, Colorado, August 1961.
109. GEAP 3781, August 1961.
110. GEAP 3709, September 1961.
111. S. Bertoletti, C. Lombardi, G. Soldaini, Unpublished results. CISE. 1962.
112. W. H. Cook. GEAP-3558, October 1960.
113. M. A. Styrikovich, Z. L. Miropol'skii, and Chzha-Yuan Shen. *Soviet Phys. "Doklady,"* **6** February 1962.
114. Z. L. Miropol'skij and I. L. Mostinskij. *Teploenerg.* No. 11 (1958).
115. A. W. Bennet, J. G. Collier, and P. M. C. Lacey. AERE-R 3804, (1961).
116. S. J. Green, G. W. Maurer, and A. Weiss. *ASME–A.I.Ch.E. Heat Transfer Conf.* Houston, Texas, August 1962.
117. E. Jaussen. GEAP 3467, June 1960.
118. G. M. Hesson. HW 63678 Rev, November 1960.
119. B. Matzner. Private communication. May 1962.
120. K. M. Becker. AE-74, Aktiebolaget Atomenergy, Sweden, May 1962.
121. J. G. Collier and D. J. Pulling. AERE R 3809, March 1962.
122. Y. Y. Hsu. *Trans. ASME Series C* Paper No. 61-WA-177, (1961).
123. C. E. Dengler and J. M. Addoms. *Chem Eng. Progr. Symp. Ser.* **52** (1956).
124. E. J. Davis and M. M. David. *Can. J. Chem. Eng.* **39,** June 1961.
125. S. A. Guerrieri and R. D. Talty. *Chem. Eng. Progr. Symp. Ser.* **52** (1956).
126. R. Le Roy Sani. UCRL 9023, January 1960.
127. H. Groothuis and W. P. Hendal. *Chem Eng. Sci.* **11** (1959).
128. G. H. Anderson, G. G. Haselden, and B. G. Mantzouranis. *Chem. Eng. Sci.* **16** (1961).
129. A. Cicchitti, C. Lombardi, M. Silvestri, G. Soldaini, and R. Zavattarelli. CISE Report 71, (1960).
130. E. E. Polomik, S. Levy, and S. G. Sawochka. GEAP 3703, May 1961.
131. J. D. Parker and R. J. Grosh. ANL 6291, January 1961.
132. C. Rounthwaite and M. Clouston. *Intern. Heat Transfer Conf.* Boulder, Colorado, August 1961.
133. W. Nusselt. ZVDI 60, 541, (1916).
134. A. P. Colburn and O. A. Hougen. *Ind. Eng. Chem.* **26** (1934).
135. A. P. Colburn. *Ind. Eng. Chem.* **26** (1934).
136. A. P. Colburn. *Proc. Inst. Mech. Eng.* **164** (1951).
137. S. Finzi, R. Renzoni, M. Silvestri, and S. Villani. *Energia Nucl.* **4** (1957).
138. P. Perroud and A. de La Harpe. CEA No. 1422, (1961).
139. C. Lombardi. Tesi di laurea in Ingegneria Nucleare presso il Politecnico di Milano (1959).

140. N. A. Dolležhal, A. K. Krasin, P. I. Aleshchenkov, A. N. Galanin, A. N. Grigoryants, I. Ja. Emel'janov, N. M. Kugushev, M. E. Minashin, U. I. Mityaev, B. V. Florinsky, and B. N. Sharapov. Proceedings of the *Intern. Conf. Peaceful Uses of Atomic Energy*, Geneva, **VIII**, 213a (1958).
141. N. A. Dolležal' P. I. Alescenkov, I. Ja. Emel'janov, Ju. I. Mitjaev, M. E Minašin, N. G. Morgunov, G. D. Knjazeva, L. I. Lunina, A. G. Filippov, V. N Smolin, Ju. I. Korjakin, and V. N. Mironov. *Power Reactor Experiments* **II**, *Proc. Symp. IAEA* (1961).
142. Private communication from SNECMA (France), (1962).

SUPPLEMENTARY LIST OF REFERENCES

G. F. Hewitt, L. E. Gill, and J. W. Hitchon. "Sampling probe studies of the gas core in annular two phase flow: Part I: Studies of the effect of length on phase and velocity distribution." *A.E.R.E.* R-3953 (1962).
N. Hall-Taylor and G. F. Hewitt. "The motion and frequency of large disturbance waves in annular two-phase flow of air-water mixtures." *A.E.R.E.* R-3952 (1962).
J. G. Collier. "Pressure drop data for the forced convective flow of steam/water mixtures in vertical heated and unheated annuli." *A.E.R.E.* R-3808 (1962).
D. J. Nicklin. "Two phase bubble flow." *Chem. Eng. Sci.* **17** (1962).
G. B. Wallis. "Two phase flow aspects of pool boiling from a horizontal surface." *A.E.E.W.* R-103 (1961).
G. B. Wallis. "The transition from flooding to upwards cocurrent annular flow in a vertical pipe." *A.E.E.W.* R-142 (1962).
H. S. Isbin, H. Fauske, T. Grace, and I. Garcia. "Two-phase steam water pressure drops for critical flows." *Symposium on Two-Phase Fluid Flow, London*, February 1962.
R. Moissis and P. Griffith. "Entrance effects in a two phase slug flow." *J. Heat Transfer*, February 1962.
S. Levy. "Steam slip: Theoretical prediction from momentum model." *J. Heat Transfer*, May 1960.
J. F. Marchaterre. "Two phase frictional pressure drop prediction from Levy's momentum model." *J. Heat Transfer* (1961).
D. J. Nicklin, J. O. Wilkes, and J. F. Davidson. "Two phase flow in vertical tubes." *Trans. Inst. Chem. Engr.* (1962).
H. C. Perkins, M. Yusuf, and G. Leppert. "A void measurement technique for local boiling." *Nucl. Sci. Eng.* **11** (1961).
H. N. McManus. An experimental investigation of film characteristics in horizontal annular two phase flow." *ASME publication 57-A-144.*
G. W. Govier and M. M. Omer. "The horizontal pipe line flow of air-water mixtures." *Can. J. Chem. Eng.*, June 1962.
G. F. Hewitt, I. King, and P. C. Lovegrove. "Holdup and pressure drop measurements in the two-phase annular flow of air-water mixtures." *A.E.R.E.* R 3764 (1961).
A. G. Németh. "Flow of gas-liquid mixtures in vertical tubes." *Ind. Eng. Chem.* **53**, February 1961.
M. Novakovic. "Two-phase, single-component pressure drop." *Bull. Inst. Nucl. Sci. "Boris Kidric,"* vol. **11**, March 1961.
J. J. Van Rossum. "Experimental investigation of horizontal liquid films. Wave formation, atomization, film thickness." *Chem. Eng. Sci.* **11** (1959).
M. R. Hatch and R. B. Jacobs. "Prediction of pressure drop in two-phase single-component fluid flow." *A.I.Ch.E. J.* **8**, March 1962.

G. A. Hughmark. "Holdup in gas-liquid flow." *Chem. Eng. Progr.* **58,** April 1962.

W. L. Owens, Jr. "Two-phase pressure gradient." *Intern. Heat Transfer Conf. Boulder (Colorado),* August 1961.

H. N. McManus, Jr. "An experimental investigation of liquid distribution and surface character in horizontal annular two-phase flow," ARO(D) Project 2117-E Grant DA-ORD-31-124-16-G28, October 1961.

M. A. Styrikovich and L. E. Faktorovich. "Effect of tube length on the magnitude of critical heat flow with forced convection of steam-water mixtures." *Soviet Phys. Tech. Phys.,* March 1958.

Z. L. Miropol'skij, M. E. Shitsman, I. L. Mostinskii, and A. A. Stavrovskii. "The effect of inlet conditions on the critical heat flux for the case of boiling water in tubes." *Teploenerg.* (1959).

J. A. R. Bennett, J. G. Collier, H. R. C. Pratt, and J. D. Thornton. "Heat transfer in two phase gas-liquid systems: Part 1. Steam-water mixtures in the liquid-dispersed region in an annulus." *A.E.R.E.* R-3159 (1959).

S. Levy and C. L. Swan. "Performance-two-phase pressure drop, burnout, and hydraulic oscillation of an inclined test section with net steam generation at 1000 PSIA." GEAP-3228, August 1959.

V. E. Doroshchuk and F. P. Frid. "The influence of the throttling of flow, and of heated proportion of the tube transfer, upon the critical intensities of heat transfer." *Teploenerg.* (1959).

R. P. Stein, J. W. Hoopes, Jr., M. Markels, Jr., W. A. Selke, A. J. Bendler, and C. F. Bonilla. "Pressure drop and heat transfer to nonboiling and boiling water in turbulent flow in an internally heated annulus." *Nucl. Eng.* (1960).

S. J. Green, B. W. Le Tourneau, and M. Troy. "Forced circulation Uniform flux burnout studies for high-pressure water." ASME 59-HT-25, July 1960.

A. E. Dukler. "Fluid mechanics and heat transfer in vertical falling film systems." *Heat Transfer* (1960).

Y. Y. Hsu and J. W. Westwater. "Approximate theory for film boiling on vertical surfaces." *Heat Transfer* (1960).

Yan-Po Chang and N. W. Snyder. "Heat transfer in saturated boiling." *Heat Transfer* (1960).

H. L. Foltz and R. G. Murray. "Two-phase flow rates and pressure drops in parallel tubes." *Heat Transfer* (1960).

L. Bernath. "A theory of local boiling burnout and its application to existing data." *Heat Transfer* (1960).

I. T. Aladyev, Z. L. Miropolsky, V. E. Doroshchuk, and M. A. Styrikovich. "Boiling crisis in tubes." International Heat Transfer Conference, Boulder (Colorado), August 1961.

W. L. Owens, Jr. "Two-phase pressure gradient." *Intern. Heat Transfer Conf. Boulder (Colorado),* August 1961.

P. M. C. Lacey. "The sensitivity of a resistance bridge for burn-out detection in two-phase heat transfer experiments." *A.E.R.E.* M-867, (1961).

H. S. Isbin, Yamazaki Y. Kvamme, I. Garcia, Jr., and C. M. Standahl. "Heat transfer to steam-water flows." *Proc. 1961 Heat Transfer Fluid Mechanics Inst.,* June 1961.

J. G. Collier. "Burnout in liquid cooled reactors-1." *Nucl. Power,* June 1961.

Yan-Po Chang. Section 1 "An analysis of the critical conditions and burnout in boiling heat transfer," Section 2 "A correlation of boiling heat transfer from the nucleation theory.—Including effects of system acceleration and forced convection." TID-14004, (1961).

G. G. Haselden. "The problem of predicting heat transfer to two-phase (vapour-liquid) fluids at moderate pressures." *Symp. Two-Phase Fluid Flow, London,* February 1962.

L. M. Grossman and V. E. Schrock. "Forced Convection Boiling in tubes." *Nucl. Sci. Eng.* **12** (1962).

N. Dinos. "Pressure drop for flow of boiling water at high pressure." DP-698, May 1962.

W. J. Levedahl. "Application of steam energy flow to reactor design." *Trans. Am. Nucl. Soc.* **5** (1962).

Z. L. Miropol'skij, M. E. Sicman, I. L. Mostinskij, and A. A. Starovskij. "Effects of the entrance conditions on the critical heat fluxes in tubes with boiling water." *Teploenerg. No 1* (1959).

M. A. Styrikovic and L. E. Faktorovic. "Effects of the heated length of a pipe on the critical heat fluxes with steam-water mixtures in forced flow." *Teploenerghetica No 2* (1959).

M. A. Styrikovic, Z. L. Miropol'skij, M. E. Sicman, I. L. Mostiuskij, A. A. Starovskij, and L. E. Faktorovic. "Influence of elements inserted upstream on the occurrence in boiling in steam generating pipes." *Teploenerg. No 5.*

M. A. Styrikovic and I. L. Mostiuskij. "On the effect of non uniform heating over the perimeter of a pipe on the critical heat fluxes." *Teploenerg. No 2* (1959).

V. E. Doroscuk and F. P. Fric. "On the problem of the influence of orificing and of the heated length of a pipe on the critical heat fluxes." *Teploenerg. No 9* (1959).

P. I. Povarnin and S. T. Semenov. "Investigation of boiling crisis in subcooled water flow in small diameter pipes at high pressure." *Teploenerg. No 1* (1960).

Z. L. Miropol'skij and L. E. Faktorovic. "Generalization of the experimental data on the influence of the heated length of the channel on the critical heat fluxes." *Teploenerg. No 6* (1961).

Author Index

Numbers in parentheses are reference numbers and indicate that an author's work is referred to although his name is not cited in the text. Numbers in italic show the page on which the complete reference is listed.

D

E

F

G

H

M

N

O

P

R

S

T

U

V

W

Y

Z

Subject Index

H

I

J

K

L

M

N

O

P

Q

R